Dinuclear Copper and Nickel Complexes of New Multidentate *N*-heterocyclic Carbene Ligands: Structures, Dynamics and Reactivity

Dissertation

zur Erlangung des mathematisch-naturwissenschaftlichen Doktorgrades

“Doctorum rerum naturalium“

der Georg-August-Universität Göttingen

im Promotionsprogramm Catalysis for Sustainable Synthesis (CaSuS)

der Georg-August University School of Science (GAUSS)

vorgelegt von

Stefan Günter Resch M.Sc.

aus Lebach

Göttingen, 2018

Betreuungsausschuss

Prof. Dr. Franc Meyer, Institut für Anorganische Chemie, Georg-August-Universität Göttingen

Prof. Dr. Sven Schneider, Institut für Anorganische Chemie, Georg-August-Universität Göttingen

Prof. Dr. Inke Siewert, Institut für Anorganische Chemie, Georg-August-Universität Göttingen

Mitglieder der Prüfungskommission

Referent: Prof. Dr. Franc Meyer, Institut für Anorganische Chemie, Georg-August-Universität Göttingen

Korreferent: Prof. Dr. Sven Schneider, Institut für Anorganische Chemie, Georg-August-Universität Göttingen

Weitere Mitglieder der Prüfungskommission:

Dr. Max M. Hansmann, Institut für Organische und Biomolekulare Chemie, Georg-August-Universität Göttingen

Dr. Matthias Otte, Institut für Anorganische Chemie, Georg-August-Universität Göttingen

Prof. Dr. Inke Siewert, Institut für Anorganische Chemie, Georg-August-Universität Göttingen

Prof. Dr. Marc Walter, Institut für Anorganische und Analytische Chemie, Technische Universität Braunschweig

Tag der mündlichen Prüfung: 19.12.2018

Zusammenfassung

Die vorliegende Dissertation ist in zwei Kapitel unterteilt und beschäftigt sich mit *N*-heterozyklischen Carbenkomplexen des Kupfers und Nickels, deren Strukturen, Dynamiken in Lösungen und Reaktionsmustern. Kapitel I beschäftigt sich thematisch mit Kupfer(I) NHC Komplexen und deren potentieller Anwendung in der Kupferabscheidung auf Oberflächen. Hierzu wurde ein Mesitylenkupfer(I)-NHC-Komplex wie auch ein dinuklearer Kupfer(I)-oxalato-Komplex synthetisiert und mittels thermogravimetrischer Analysemethoden untersucht. Ein Vergleich mit literaturbekannten Komplexen belegt das Potential für die Kupferabscheidung, jedoch sind weitere Untersuchungen in der Zukunft notwendig um fundierte, quantitative Aussagen über die Güte der Kupferabscheidung treffen zu können.

Ein größerer Fokus in Kapitel I liegt auf der Synthese von Kupfer(I)-Komplexen oligodentater NHC-Liganden, die primär hinsichtlich ihrer Dynamik in Lösung untersucht wurden. Hierbei stellte sich heraus, dass multinukleare Komplexe, welche drei oder sechs Kupferzentren in ihrer Festkörperstruktur aufweisen, sich beim Lösen in Acetonitril reorganisieren und als dinukleare Komplexe vorliegen. Dieses Verhalten der Komplexe wurde mit Hilfe mehrdimensionaler NMR-Spektroskopie, DOSY NMR-Spektroskopie wie auch ESI-MS analysiert. Die Ergebnisse belegen auf beeindruckende Weise die dynamische Diversität von oligonuklearen Kupfer(I)-NHC-Komplexen hinsichtlich der Konnektivität wie auch der Nuklearität in der Festkörperstruktur im Vergleich zur Lösung. Untersuchungen an mononuklearen und dinuklearen Kupfer(I)-pyridinyl/NHC-Komplexen unterstreichen die Dynamik solcher Systeme in Lösung. Wenngleich die Nuklearität dieser Komplexe in Lösung erhalten bleibt, konnte durch Analyse von dinuklearen Kupfer(I)-Komplexen gezeigt werden, dass unterschiedliche Koordinationsmotive des Liganden in einem kleinen Temperaturbereich ausgebildet werden. Ebenfalls war es möglich die temperaturabhängige Umwandlung zweier Ringkonformationen in einem dinuklearen Kupfer(I)-Makrozyklus mittels NMR-Spektroskopie zu belegen und die Energiebarriere dieser Konformationsänderung zu berechnen.

Die Verknüpfung von Kapitel I mit Kapitel II wird ermöglicht durch die Synthese eines neuen Kompartimentliganden mit zentraler Pyrazolbrücke und zwei Bis(imidazolium)-Chelatarmen in den 3- und 5-Positionen des Pyrazols. Dieses Ligandensystem besitzt das Potential multinukleare Komplexe der Münzmetalle auszubilden, welche in Lösung intakt bleiben, und präorganisierte, dinukleare Nickel(II)-NHC-Komplexe darzustellen. So erfolgten Unter-

suchungen der Prototropie an der Pyrazoleinheit des Liganden in verschiedenen Lösungsmitteln, inklusive der Bestimmung der Aktivierungsparameter dieser Austauschreaktion und es konnte gezeigt werden, dass der Ligand in Lösung agglomeriert. Nach Reaktion zweier Ligandenvariationen mit Silberoxid konnten supramolekulare Komplexe isoliert werden, die je nach Modifikation am Liganden eine unterschiedliche Architektur im Festkörper aufzeigen.

Kapitel II beschäftigt sich mit präorganisierten, zweikernigen Nickelkomplexen des neuen Pyrazol/NHC-Hybridliganden, die Koordination unterschiedlichster Ionen in der Kavität zwischen den beiden Nickelzentren wie auch das Verhalten der Komplexe gegenüber Säuren, Basen und kleinen Molekülen. **$[L^6Ni_2(OH)]^{2+}$** zeigt eine unterschiedlich starke Ausbildung von Wasserstoffbrückenbindungen zu Lösungsmitteln, welche anhand von Festkörperstrukturen, ^1H NMR-Spektroskopie wie auch IR-Spektroskopie belegt werden konnte. Die Substitutionskinetik der sehr stabilen Hydroxido-Brücke in **$[L^6Ni_2(OH)]^{2+}$** wurde anhand von H/D und $H_2{}^{16}O/H_2{}^{17}O$ Austauschexperimenten mittels ^1H NMR-Spektroskopie untersucht, die Aktivierungsparameter bestimmt und zwei verschiedene Austauschmechanismen, unterstützt durch experimentelle Befunde und erweiterte DFT Berechnungen, beschrieben. Ebenfalls war es möglich durch eine Deprotonierungsreaktion *in situ* **$[L^6Ni_2(O)]^+$** zu generieren, welches sich sehr schnell unter Protonenabstraktion einer unidentifizierten Quelle **$[L^6Ni_2(OH)]^{2+}$** zurückbildet. Durch Protonierungsreaktion von **$[L^6Ni_2(OH)]^{2+}$** mittels ethanolischer HCl konnte **$[L^6Ni_2Cl]^{2+}$** synthetisiert werden, welches die Synthese von μ-amido-, bis(cyanido)- und μ-sulfido-Komplexen ermöglichte.

Ein weiterer Fokus in diesem Kapitel waren Nickel-Schwefel-Verbindungen, die Charakterisierung dieser Komplexe, die Untersuchung der gegenseitigen Umwandlungen ineinander, wie auch deren Verwendung in HAT Reaktionen und als Katalysator in der Protonenreduktion. Die gegenseitige Umwandlung von **$[L^6Ni_2S]^+$** zu **$[L^6Ni_2(SH)]^{2+}$** über einen Begegnungskomplex **$[(L^6)_2Ni_4(SHS)]^{3+}$** wurde nachgewiesen wie auch der pK_s Wert von **$[L^6Ni_2(SH)]^{2+}$** mittels Titrationsexperimenten bestimmt. Mittels ^1H NMR-Spektroskopie war es ebenfalls möglich die Protonen-Selbstaustauschkinetik in dem Begegnungskomplex, bzw. zwischen **$[L^6Ni_2S]^+$** und **$[L^6Ni_2(SH)]^{2+}$**zu bestimmen. Ausgehend von **$[L^6Ni_2S]^+$** konnte durch Alkylierungsreaktion **$[L^6Ni_2(SCH_3)]^{2+}$** synthetisiert werden, welcher sich reversibel zu dem gemischtvalenten Ni^INi^{II} Komplex reduzieren lässt.

Ebenfalls wurde die Redoxchemie von **$[L^6Ni_2S]^+$** untersucht. Nach Oxidation von **$[L^6Ni_2S]^+$** lässt sich mittels verschiedenster analytischer Methoden, wie UV-vis-Spektroskopie, EPR-

Spektroskopie und DFT Rechnungen das erste ausschließlich zwischen zwei Nickelzentren stabilisierte Thiylradikal nachweisen. Diese kurzlebige Spezies dimerisiert sehr schnell zu dem Tetranickel(II)-μ_4-Persulfido-Komplex, welcher analysiert wurde und ein neues Nickel/Schwefel-Koordinationsmotiv darstellt. Durch die Bestimmung des pK_S Wertes von **$[L^6Ni_2(SH)]^{2+}$** und des Redoxpotentials $E_{1/2}$(**$[L^6Ni_2S]^+$**/**$[L^6Ni_2(S\cdot)]^{2+}$**) welches durch Simulationen der Cyclovoltammogramme bestimmt wurde, konnte die $BDFE_{(solv.)}$ der S-H Bindung in **$[L^6Ni_2(SH)]^{2+}$** ermittelt werden. Durch Kenntnis der S–H Bindungsstärke wurde weitergehend die HAT Reaktivität des **$[L^6Ni_2(S\cdot)]^+$** gegenüber schwachen O–H, N–H und C-H Bindungen untersucht und bestätigt. **$[L^6Ni_2(S\cdot)]^+$** ist somit der erste metallorganische Thiylradikal-Komplex, der für HAT Reaktivität erfolgreich verwendet wurde. Ebenfalls wurden **$[L^6Ni_2(SH)]^{2+}$** und **$[L^6Ni_2S]^+$** hinsichtlich ihres Vermögens zur chemischen und elektrochemischen Protonenreduktion untersucht. Beide Komplexe zeigen hierbei eine katalytische Aktivität, und analytische Untersuchungen geben einen ersten Einblick in den Mechanismus.

In dieser Arbeit konnten die Strukturen und Koordinationsmotive neuer metallorganischer Komplexe analysiert werden, deren Dynamik in Lösung belegt werden wie auch die Energiebarrieren ihrer Konformationsänderungen und der Austauschkinetiken an prä-organisierten Metallzentren bestimmt werden. **$[L^6Ni_2(S\cdot)]^{2+}$** stellt ein einzigartiges Thiylradikalsystem dar, welches HAT Reaktivität aufweist und als Modelsystem für bioanorganische und chemische Reaktionen dienen kann. Das neue Ligandensystem und dessen Komplexe bieten die Möglichkeit verschiedenste Reaktivitäten und Anwendungen zu untersuchen, neue Systeme zu synthetisieren und interessante und reaktive Spezies zu generieren, welche bereits in dieser Dissertationsarbeit aber auch in der Zukunft neue Erkenntnisgewinne in den Bereichen der metallorganischen, bioanorganischen Chemie und Katalyse ermöglichen.

Abstract

The present Ph.D. thesis is divided in two parts and describes *N*-heterocyclic carbene complexes of copper and nickel, their structures, dynamics in solution and reaction patterns. Part I deals thematically with copper(I) NHC complexes and their potential application for copper decomposition on surfaces. To achieve this, a mesitylen copper(I) NHC complex and a dinuclear copper(I) oxalato complex were synthesized and analyzed by thermogravimetric methods. A comparison of these complexes with complexes reported in the literature confirmed the potential for copper decomposition, but further investigations are necessary in the future to obtain quantitative results regarding the copper decomposition.

In Part I, the spotlight is mainly on the synthesis of copper(I) complexes of oligodentate NHC ligands, which are primarily investigated with respect to their dynamics in solution. Investigations show the rearrangement of multinuclear complexes, containing three or six copper cores in the solid state to dinuclear complexes in acetonitrile. Such a behavior is confirmed by 2D NMR spectroscopy, DOSY NMR spectroscopy and ESI-MS. The results verify the dynamic diversity of oligonuclear copper(I) NHC complexes concerning their connectivity and nuclearity in solid state and in solution. Investigations of mononuclear and dinuclear copper(I) pyridinyl/NHC complexes underline the dynamics of those complexes in solution. The change of the coordination pattern of the ligand to the metal centers in dinuclear copper complexes is observed in solution within a narrow temperature range. This rearrangement of the complex is highly temperature dependent and the nuclearity of such complexes does not change in solution. Further, the temperature dependent interconversion of the ring conformations in a macrocyclic dicopper(I) NHC complex is monitored *via* NMR spectroscopy and its energy barrier was determined.

Part I and Part II are linked by the successful synthesis of a new ligand bearing a central pyrazole bridge and two chelating bis(imidazolium) side arms in the 3- and 5-position of the pyrazole. This ligand system supports multinuclear complexes with coinage metals, which are stable in solution as well as preorganized dinuclear nickel(II) NHC complexes. The prototropy at the pyrazole unit in the ligand is investigated in different solvents allowing for the determination of the activation parameters for these exchange reaction. Furthermore, the formation of an aggregation of the ligand in solution to a dimer is confirmed. Two different supramolecular silver complexes in solid state are obtained by reaction of silver(I) oxide with two variations of the ligand.

Part II describes preorganized, dinuclear nickel complexes of the new hybrid pyrazole/NHC ligand, the coordination of different ions in the cavity between the nickel centers and their behavior with acids, bases and small molecules. A different strong hydrogen bond interaction between **$[L^6Ni_2(OH)]^{2+}$** and solvent molecules is observed and confirmed by the structure in solid state, ^{1}H NMR spectroscopy and IR spectroscopy. ^{1}H NMR investigations of the kinetics of the substitution reaction at the very stable hydroxido bridge in **$[L^6Ni_2(OH)]^{2+}$** by H/D und $H_2{}^{16}O/H_2{}^{17}O$ exchange reactions is investigated. The activation parameters were determined and two different mechanistic pathways are described based on experimental results and extended DFT calculations. In addition, the *in situ* formation of **$[L^6Ni_2(O)]^+$** is observed after deprotonation reaction and the fast back reaction to **$[L^6Ni_2(OH)]^{2+}$** after protonation by an unknown proton source. **$[L^6Ni_2Cl]^{2+}$** was obtained after protonation of **$[L^6Ni_2(OH)]^{2+}$** by ethanolic acid and allows for the synthesis of μ-amido, bis(cyanido) and μ-sulfido complexes.

Another focus of this part are nickel-sulfur compounds, their characterization, the investigation of their interconversion and their application in HAT reactions and as catalysts for proton reduction. The interconversion of **$[L^6Ni_2S]^+$** and **$[L^6Ni_2(SH)]^{2+}$** *via* an encounter complex **$[(L^6)_2Ni_4(SHS)]^{3+}$** is confirmed. The pK_a value of **$[L^6Ni_2(SH)]^{2+}$** was determined by titration experiments and the proton self-exchange kinetic of the encounter complex and **$[L^6Ni_2S]^+$** and **$[L^6Ni_2(SH)]^{2+}$**, respectively. Furthermore, **$[L^6Ni_2(SCH_3)]^{2+}$** is synthesized by alkylation of **$[L^6Ni_2S]^+$** and the reversible reduction of **$[L^6Ni_2(SCH_3)]^{2+}$** to the mixed valent Ni^INi^{II} is investigated.

In addition, the redox chemistry of **$[L^6Ni_2S]^+$** was explored. Different analytic methods, such as UV-vis spectroscopy, EPR spectroscopy and DFT calculations confirmed the observation of a unique thiylradical, exclusively coordinated between two nickel centers after oxidation of **$[L^6Ni_2S]^+$**. This short living species dimerized very fast to a tetranickel(II) μ_4-persulfido complex, which is further analyzed and represents a new coordination motif of nickel/sulfur. The $BDFE_{(solv.)}$ of the S–H bond in **$[L^6Ni_2(SH)]^{2+}$** is determined by the obtained pK_a value of **$[L^6Ni_2(SH)]^{2+}$** and the redox potential $E_{1/2}$(**$[L^6Ni_2S]^+$/$[L^6Ni_2(S\cdot)]^{2+}$**) *via* simulation of CV data's and a square scheme. The knowledge of the $BDFE_{(solv.)}$ allowed the investigation of the HAT reactivity of **$[L^6Ni_2(S\cdot)]^{2+}$** with weak O–H, N–H and C–H bonds. **$[L^6Ni_2(S\cdot)]^{2+}$** represents the first organometallic thiyl radical complex, with a thiyl radical exclusively stabilized between two nickel centers and HAT reactivity.

$[L^6Ni_2(SH)]^{2+}$ and **$[L^6Ni_2S]^+$** are tested with respect to electrochemical proton reduction. Both complexes show catalytic activity and analytical investigations give a first insight into the mechanism of proton reduction.

In this work, the structure and coordination motives of novel organometallic complexes are analyzed, their dynamics in solution are confirmed and the energy barriers of conformational changes and exchange kinetics at preorganized metal centers are determined. The new ligand system and its complexes give the possibility to investigate different kinds of reactivity and applications. In this thesis, a unique thiyl radical complex **$[L^6Ni_2(S\cdot)]^{2+}$** is obtained, which shows HAT reactivity and can be used as a model system for bioinorganic and chemical reactions. New systems and reactive species are presented, which allowed the contribution in the future to the areas of organometallic, bioinorganic chemistry and catalysis.

Acknowledgements – Danksagung

Die Erstellung dieser Arbeit mit ihren facettenreichen und diversen Themengebieten wäre niemals ohne die Unterstützung nachfolgender Personen möglich gewesen.

Allen voran möchte ich meinem Doktorvater Prof. Dr. Franc Meyer danken für seinen stetigen Optimismus. Ich danke dir, Franc, für die Bereitstellung dieser sehr anspruchsvollen und gleichzeitig sehr spannenden Themengebiete und die wissenschaftlichen Freiheiten, die ich während meiner Promotion genießen durfte. Ich empfinde diese gemeinsame Zeit als eine sehr prägende Zeit, die sicherlich meinen zukünftigen, beruflichen Werdegang maßgeblich beeinflussen wird.

Ebenfalls möchte ich meinem Betreuungsausschuss, Prof. Dr. Sven Schneider und Prof. Dr. Inke Siewert herzlich für ihre Unterstützung danken. Ich habe unsere zeitintensiven Statusgespräche mit sehr viel Freude, Enthusiasmus und sehr konstruktiven Feedback erlebt.

Mein Dank gilt Prof. Dr. Sven Schneider für die Übernahme des Korreferats und Herrn Dr. Max. M. Hansmann, Dr. Matthias Otte, Prof. Dr. Inke Siewert und Prof. Dr. Marc D. Walter für ihre Mitgliedschaft in meiner Prüfungskommission.

I am extremely grateful to have been hosted for one month at the DCM at the Université d‘Alpes Grenoble in the group of Dr. Carole Duboc and Dr. Marcello Gennari as well as at CEA in Grenoble in the group of Prof. Dr. Vincent Artero. Dear Carole, Marcello and Vincent, I would like to thank you for your permanent optimism, your interest in my research and the numerous and intense scientific conversations and your endearing personality. Furthermore, I would like to thank personally Marcello for technical support and patientience when I was working late. I thoroughly enjoyed my time in Grenoble and I am thankful for the support from the section Chimie Inorganique Redox at DCM of the Université Grenoble d‘Alpes, especially from Dr. Suzanne Adam, Florian Molton and Selime Sirach as well as the SolHyCat Team at CEA, here Jennifer Fize, Dr. Murielle Cavarot-Kerlidou and Dr. Matthieu Koep.

Des Weiteren möchte ich all den zahlreichen Personen an der Fakultät für Chemie danken, die mir halfen bürokratische, technische und analytische Hindernisse zu überwinden und ohne deren Hilfe diese Arbeit in der hier vorliegenden Form nicht existieren würde. Mein besonderer Dank gilt Dr. Michael John und Ralf Schöne, die mir halfen mein praktisches Wissen zur NMR-Spektroskopie grundlegend zu erweitern. Ich danke euch beiden für eure jahrelange Unterstützung, die vielen NMR-Messungen und Diskussionen über NMR-

Spektroskopie, das andauernde Interesse an meinen Experimenten und die stetige Bereitschaft mit mir ungewohntes NMR spektroskopisches Terrain zu betreten. Ebenfalls gilt mein Dank Frau Dr. Stückl, Frau Dr. Marie Bergner für EPR Messungen, Herrn Dr. Sebastian Dechert für X-ray Messungen und DFT Rechnungen, wie auch Prof. Dr. Ricardo Mata, Dr. Markus Finger für DFT Rechnungen.

Mein Dank gilt all denjenigen Studenten, die sich für meine wissenschaftlichen Arbeiten interessierten und sich dazu entschieden ihre Bachelorarbeit oder ihr Abteilungspraktikum unter meiner Aufsicht durchzuführen. Danken möchte ich Tobias Grothe, Katharina Wenderoth, Torben Rogge und Bastian Schluschaß für ihre praktische Unterstützung.

I would also like to thank all group members of AK Meyer for the time we spent together, the scientific discussions, the technical and scientific support and the parties. Especially I would like to thank all colleagues who shared over all the time with me laboratory T210 and office T209. Furthermore, I would like to thank Andreas Schwarz for the synthesis of the 3,5-dihydroxido-pyrazole. I would like to thank the Siewert working group for their technical support during collaboration and Prof. Dr. Inke Siwert for her support and simulations of the CV's. A Ph.D. thesis with this size needs the proofreading of many, ambitious people. I am so happy that so many people volunteered to correct my thesis or discussed with me about my work. I have to thank for proofreading of my work: Jérôme Günes, Roland Schulz, Josh Abbenseth, Dr. Christine Schiewer, Dr. Shoa-An Hua, Dr. Alexander Gers-Barlag, Dr. Oliver Mitevski, Dr. Marie Bergner, Dr. Suzanne Adam, Dr. Dennis Manz, Tal Dankovich, Dr. Munmun Gosh, Massimiliano Morganti, Kevin Lüken, Thomas Kothe, Hendrik Stevens, Prof. Dr. Andreas Steffen, Prof. Dr. Ricardo Mata, Dr. Christian Volkmann, Dr. Michael John, Dr. Claudia Stückl, Dr. Sandeep Gupta, Dr. Sebastian Dechert, Katharina Wenderoth, Manuel Oelschlegel and last but not least Dr. Allyssa Ann Massie. In addition, I would like to thank for long (non)scientific discussions and his friendship Dr. Alexander Brinkmeier.

Thanks go to all colleagues past and present of the IAC, as well as all people outside of the chemical department who become friends with me over the time, and who supported me during work and in private life in Göttingen. I had a great time with you in Göttingen.

Last but not least möchte ich meinen Freunden und meiner Familie danken. Mein größter Dank gilt hierbei meinen Eltern, ohne deren mentale und finanzielle Unterstützung meine zahlreichen Praktika, mein Studium in München, wie auch die vorliegende Arbeit nicht möglich gewesen wären. Ihr macht mich zu der Person die ich bin und ich liebe euch so sehr für eure unerschöpfliche Liebe und Unterstützung!

Für meine Familie

Wege entstehen beim Gehen.

(A. Machado y Ruiz)

Contents

Abbreviations

Compounds/ molecular fragments

$CoCp_2$	Cobaltocene
$Co(Cp^*)_2$	Bis(pentamethylcyclopentadienyl)cobalt(II)
CuAAC	Copper-catalyzed azide-alkyne cycloaddition
DCM	Dichloromethane
DiPP	2,6-di-isopropylphenyl
DMF	Dimethyl formamide
DMSO	Dimethylsulfoxide
Et_2O	Diethyl ether
EtOH	Ethanol
Fc/Fc^+	Redox couple ferrocene and ferrocenium
$FeCp_2$	Ferrocene
$[FeCp_2]PF_6$	Bis(cyclopentadienyl)iron(III) hexafluorophosphate
$Fe(Cp^*)_2$	Decamethylferrocene
$[Fe(Cp^*)_2]PF_6$	Decamethylferrocenium hexafluorophosphate
FurNeu	3,12-*N*-(*N*’,*N*’-dimethylaminoethyl)(2-pyridylmethyl)amino-dibenzofuran
GAO	Galactose oxidase
KO*t*Bu	Potassium *tert*-butanol
MeCN	Acetonitrile
MeOH	Methanol
Mes	Mesityl
Mes_4Cu_4	Mesitylcopper(I)
NHC	*N*-heterocyclic carbene
nacnac	*β*-diketiminate
OTf	Trifluoromethanesulfonate, triflate
Proton-sponge®	1,8-bis(*N*,*N*-dimethylamino)naphthalene
SIMes	1,3-dimesitylimidazolin-*2*-ylidene
tacn	triazacyclononane
THF	Tetrahydrofuran

Spectroscopy/Spectrometry

ATR IR	Attenuated total reflection *infra* red
br	Broad
COSY	Correlation Spectroscopy
CV	Cyclic voltammetry
d	Doublet
DOSY	Diffusion-Ordered NMR Spectroscopy
ESI	Electron Spray Ionization
EXSY	Exchange Spectroscopy
FAB	Fast Atom Bombardment
HMBC	Heteronuclear Multiple Bond Coherence
HMQC	Heteronuclear Single Quantum Coherence
NMR	Nuclear Magnetic Resonance
NOESY	Nuclear Overhauser Effect Spectroscopy
m	Multiplet
p	Pentet
q	Quartet
s	Singlet
SEC	Spectro-electro-chemistry
t	Triplet

Kinetic/Thermodynamic parameters and in formula used expressions

A	Pre-exponential factor
A	Ratio between R_{H1} and R_{H2} of two particles
D	Diffusion coefficient [$\mathrm{m^2 \cdot s^{-1}}$],
E or $E_{1/2}$	Potential or half potential [V]
E_a	Activation energy [$\mathrm{kJ \cdot mol^{-1}}$]
h	Planck's constant ($6.626070040 \cdot 10^{-34}$ J·s)
k	Rate constant [$\mathrm{s^{-1}}$]
k_b	Boltzmann's constant ($1.38064852 \cdot 10^{-23}$ $\mathrm{J \cdot K^{-1}}$)
η	Dynamic viscosity of the solvent [$\mathrm{kg \cdot m^{-1} \cdot s^{-1}}$]
R	Ideal gas constant ($8.3144598 \cdot \mathrm{J \cdot mol^{-1} \cdot K^{-1}}$]
R_H	Hydrodynamic radius [m]
$\Delta G^\ddagger$	Gibbs energy [$\mathrm{J \cdot mol^{-1}}$]
$\Delta H^\ddagger$	Enthalpy of activation constant
$\Delta S^\ddagger$	Entropy of activation constant [$\mathrm{J \cdot mol^{-1} \cdot K^{-1}}$]

Units

A	Ampere
a.u.	Arbitrary unit
atm	Atmosphere (1 atm = 1.0133 10^5 Pa)
°C	Degree Celsius
d	Day
h	Hour
Hz	Hertz (1 Hz = 1 sec^{-1})
I	Current [A]
J	Joule (1 J = 1 $\frac{\text{kg}\cdot\text{m}^2}{\text{s}^2}$)
$\text{J}\cdot\text{mol}^{-1}$	Joule per mol
$\text{J}\cdot\text{mol}^{-1}\cdot\text{K}^{-1}$	Joule per mol and Kelvin
K	Kelvin
mg	Milligram
min	Minute
mL	Milliliter
mol	Mol (1 mol = 12.0107 g)
ppm	Parts per million
T	Temperature [K]
T_c	Coalescence temperature [K]
t	Time [sec]
V	Volt

Miscellaneous

AACVD	Aerosol-assisted Chemical Vapor Deposition
ALD	Atomic Layer Deposition
3*c*2*e*	Three center two electron
CVD	Chemical Vapor Deposition
e.g.	*Exempli gratia*, lat.: for example
equiv.	Equivalents
et al.	*Et alii*, lat.: and other
HOMO	Highest occupied molecular orbital
Infra	Lat.: below
in vacuo	*In vacuo*, lat.: under reduced pressure
LUMO	Lowest unoccupied molecular orbital
IVCT	Intervalence charge transfer
LMCT	Ligand to metal charge transfer
n.d.	Not determined
pK_a	Logarithmic acid dissociation constant
PT	Proton transfer
r.t.	Room temperature
SOMO	Single occupied molecular orbiatl
TOF	Turn over frequency; $[\mathrm{TOF}] = \frac{\mathrm{mol(product)}}{\mathrm{mol(catalyst)\cdot h}}$
TON	Turn over number; $[\mathrm{TON}] = \frac{\mathrm{mol(product)}}{\mathrm{mol(catalyst)}}$
vs.	*Versus*, lat.: against

Part I

Copper(I) *N*-heterocyclic carbene complexes

1

A copper(I) *N*-heterocyclic carbene complex as potential precursor for copper deposition

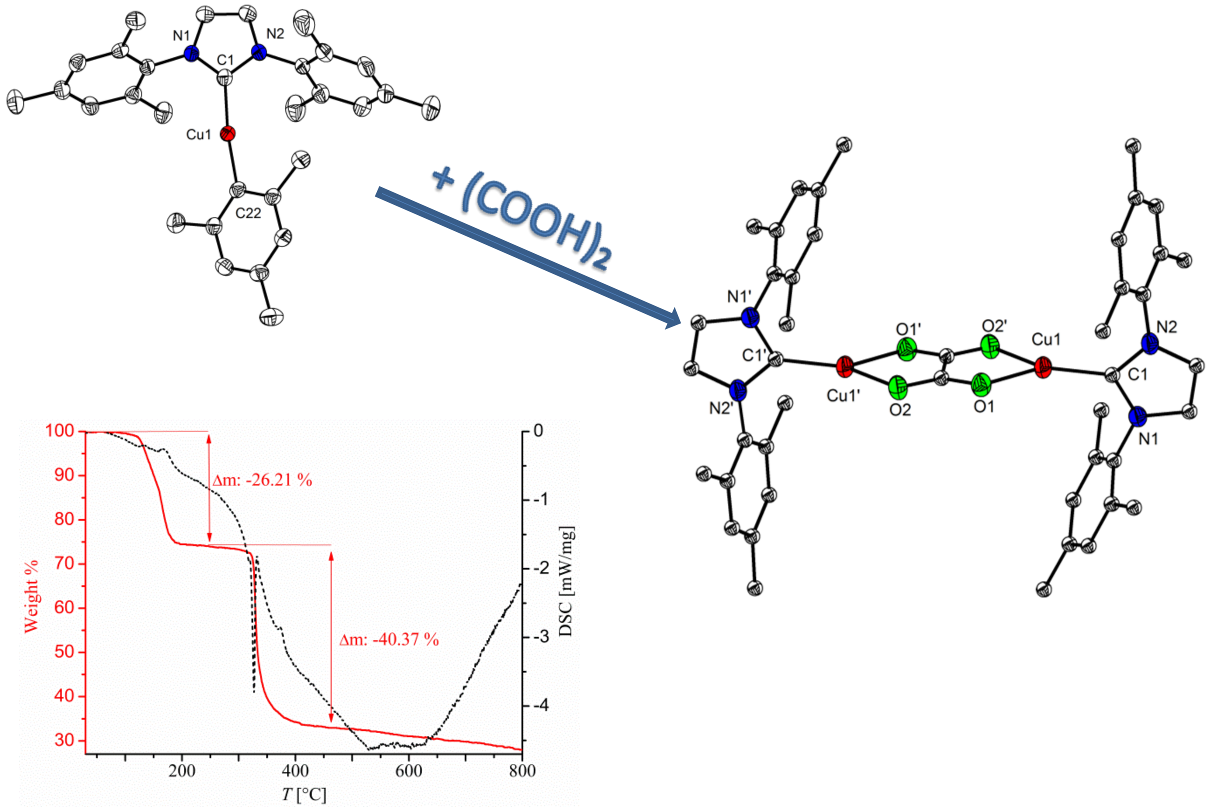

Abstract: Copper is a versatile material and is used in almost all areas of life. One of the most important processing steps of elemental copper in industries involves copper deposition on different kinds of surfaces, especially for the production of conducting materials in the microelectronic device industry. Chemical vapor deposition and especially atomic layer deposition receive high interest as processing methods for producing such materials. They require copper precursors that are cheap and easy to synthesize. Common copper precursors described in the literature are dicopper(I) oxalato complexes which are stabilized by different ligands. Here, the synthesis and characterization of a new σ-mesityl copper(I) NHC complex and the corresponding dinuclear copper(I) oxalate-bridged complex with an unsaturated backbone of the NHC ligand are presented. These two complexes are compared with closely related copper(I) complexes bearing the saturated variation of the NHC ligand scaffold, and that have been reported to be a useful precursor for copper deposition.

1.1 Introduction

Copper plays a crucial role in the electronic industry, due to its low electrical resistivity, which can increase the device performance.[1–3] Copper deposition on surfaces is an important processing step in industry and is widely applied in circuit manufacturing and microelectronic device industry.[4,5] Industry and research groups are looking for cheap, efficient and atom economical ways to optimize copper deposition reactions.

One possible way to achieve this is the optimization of deposition processes with respect to the thickness of the copper layer, its purity, the roughness of the surface and control of the decomposition. This can be achieved by changing the application method, for instance by use of chemical vapor deposition (CVD), aerosol-assisted CVD (AACVD), atomic layer deposition (ALD), spin coating or copper deposition from supercritical carbon dioxide.[1,6–8] An additional possibility for optimization is the use of alternative copper(I) or copper(II) precursors. Copper(II) complexes have several drawbacks, due to the need of external or internal reducing agents and often incomplete conversion to Cu^0. In the literature several evaporable, air stable organometallic copper(I) complexes are known, that are thermally stable up to relevant processing temperatures.

In the past several copper(I) β-diketonate complexes were established bearing neutral Lewis-bases (phosphine, alkyne or alkene) which show high potential for CVD applications.[1] Beside the desired elemental copper deposition, copper(II) (β-diketonate)$_2$ is additionally formed which lowers the efficiency of this process by 50%.[7] Meyer *et al.* presented a series of copper(I) μ-1,2,3,4-oxalato complexes, bearing alkyne modified Lewis bases. They show great potential for clean copper deposition reactions.[6] Additionally, the utilization of isocyanide or phosphine ligated copper(I) oxalato complexes results in the successful deposition of copper on surfaces.[7,9,10] The advantages of such complexes are their stability towards air, high solubility and the presence of an internal reducing agent, here the oxalate, which decomposes to CO_2. In addition, elemental copper in high purity can be obtained by generation of evaporable side products, like CO_2 and alkyne.

In 2016, Stollenz and Meyer *et al.*[8] further extended the field of dinuclear copper(I) μ-1,2,3,4-oxalato complexes, by introducing 1,3-dimesitylimidazolin-*2*-ylidene (SIMes) as a ligand for the synthesis of an air stable copper(I) complex for copper deposition.[8] Within a temperature range of 220 °C and 350 °C the complex decomposes to elemental copper with the release of volatile byproducts such as HCN, CO and CO_2 (**Scheme 1.1**). The development of volatile side products was monitored by mass spectrometry.[8] These results are the motivation for further investigation of dicopper oxalato-bridged complexes with respect to copper deposition.

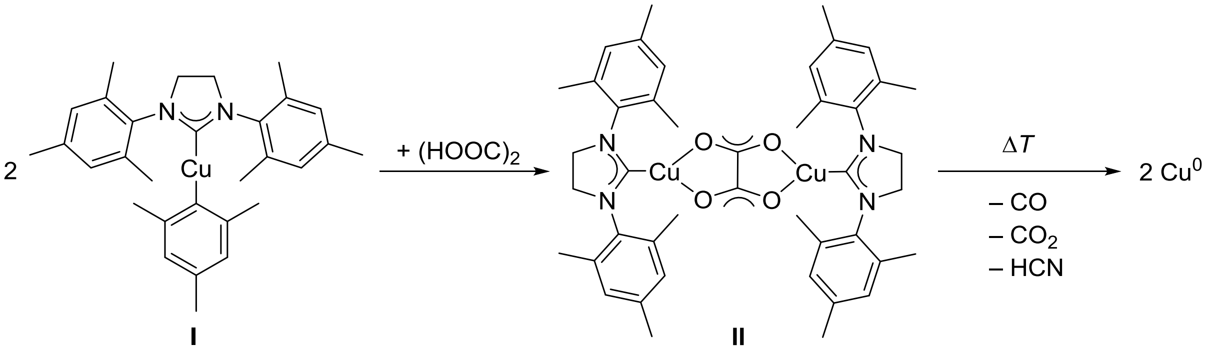

Scheme 1.1: Addition of oxalic acid to **I** led to the formation of **II** which decomposed between 220-350 °C to elemental copper under release of CO, CO_2 and HCN.[8]

In this chapter a new 1,3-dimesitylimidazol-*2*-ylidene copper(I) mesityl complex **1** is presented, its properties, the conversion to the corresponding dinuclear copper(I) μ-1,2,3,4-oxalato NHC complex **2**, along with the thermoanalysis of both complexes.

1.2 Results and Discussion

The σ-mesityl copper(I) NHC complex **1** is synthesized according to the method established for **I** (**Scheme 1.2**).[8] *In situ* deprotonation of 1,3-bis(mesityl) imidazolium chloride with *n*-BuLi and addition of Mes_4Cu_4 results in the formation of **1** as a colorless powder.

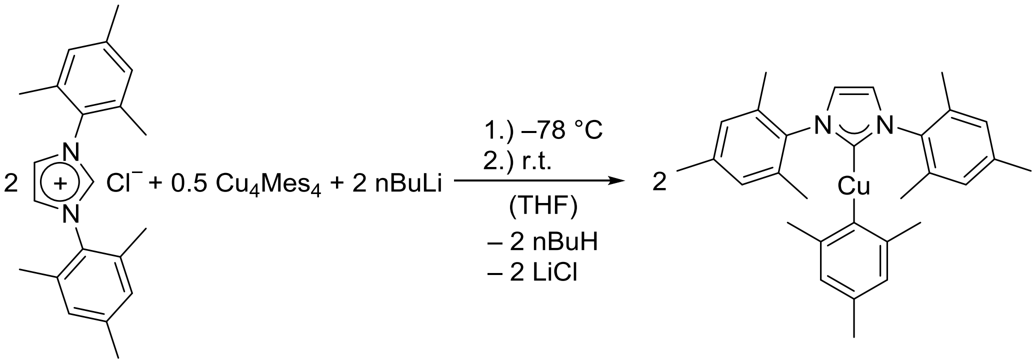

1

Scheme 1.2: Synthesis route of the formation of **1**.

Colorless single crystals are obtained by cooling a saturated complex solution of **1** in toluene at –24 °C for 4 days. **1** crystallizes in the space group $P2_1/c$ (**Figure 1.1**), like complex **I**[8]. The copper-carbene bond length Cu–C(1) in **1** is 1.903 Å (**Figure 1.1**) and in agreement with that of **I** (**Table 1.1**)[8] as well as in the range of in the literature known Cu–C NHC bonds and Cu–C NHC bond lengths described later in this thesis (**chapter 2**).[11,12] The distance between the copper ion and the mesityl ligand Cu–C(22) is 1.924 Å and the angle C(1)–Cu–C(22) is 173.43°. An almost linear coordination of the copper(I) ion by the two ligands is observed.[11] Compared to complex **I**, the Cu^I–C_{ipso} bond is slightly longer and the angle C(1)–Cu–C(22) is smaller (**Table 1.1**). One reason for these differences is the slightly different capability of both NHC ligands for undergoing π–back-donation from the metal. The π–donation from the p orbital of the two N atoms into the free p_π orbital of the carbene C atom results into a significant electronic charge in the formally empty p_π orbital of the carbene.[13] The π-delocalization in imidazol-*2*-ylidenes is higher than in imidazolin-*2*-ylidenes.[14,15] The imidazolin-*2*-ylidene ligand is a better π-acceptor than the imidazole-*2*-ylidene ligand, due to less electron delocalization in the carbene p_π orbitals from the N donors. Less π–backdonation from the copper(I) (d^{10}) to the imidazol-*2*-ylidene ligand results into an elongation of the copper-mesityl bond in comparison to the complex **I**.

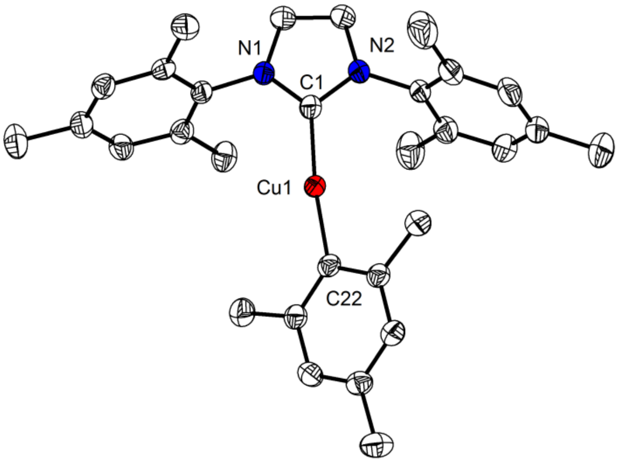

Figure 1.1: Molecular structure (50% probability thermal ellipsoids) of **1**. Hydrogen atoms are omitted for clarity.

Table 1.1: Comparison of bond lengths and angles of **1** and **I**[8].

Atoms	1	I
Cu–C(1)	1.90(3)	1.90(3)
Cu(1)–C(22)	1.92(4)	1.91(4)
C(1)–Cu–C(22)	173.4	175.5

Elemental analysis confirmed the expected composition of the complex and underlines the purity of the compound (see experimental section). In the context of copper deposition reactions this issue is of enormous importance, to avoid side reactions or accumulation of impurities on a surface. ESI-MS of **1** in THF shows two dominant peaks at $m/z = 671.40$ (100) **$[(NHC)_2Cu]^+$** and $m/z = 853.37$ (40) **$[(NHC)_2Cu_2Mes]^+$** which demonstrates the instability of the complex under ESI-MS conditions (**Figure 1.2**). These conditions degrade the complex and a more stable, linear coordinated **$[(NHC)_2Cu]^+$** complex cation is detected. This result is not surprising, since it emphasizes the intrinsic properties of NHCs, including the strong σ-donor character of the ligand[16], and it underlines the utility of this complex for undergoing substitution reactions at the mesityl position. **$[(NHC)_2Cu_2Mes]^+$** is a result of an aggregation process under ESI-MS conditions. It is proposed that the mesityl group takes the function of a linker between two NHC coordinated copper(I) cores.

Meyer and Stollenz *et al.*[17,18] reported several copper(I) mesityl complexes featuring a three-center two-electron (3*c*2*e*) coordination motif. The behavior of the complex is in agreement with the properties of **I**. Here degradation and aggregation under ESI-MS conditions in THF are also observed.[8]

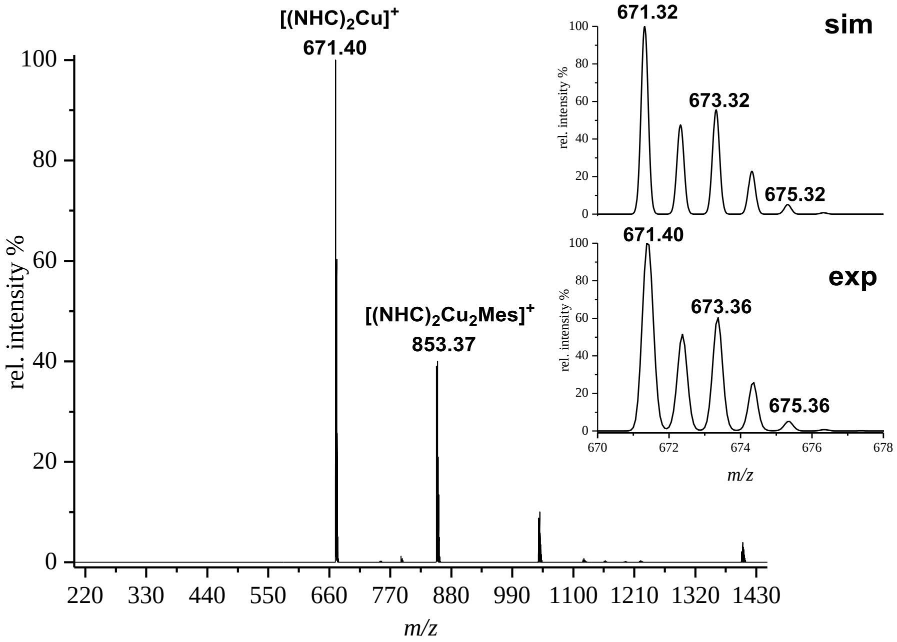

Figure 1.2: ESI-MS of **1** in THF. Inset shows the simulated (**top**) and experimental (**bottom**) isotopic distribution pattern of the peak at *m/z* = 671.40 (100) assigned to **[(NHC)$_2$Cu]$^+$**.

Thermal decomposition of **1** was determined *via* TG/DSC analysis (**Figure 1.3**). The decomposition of **1** occurs in two stages. The first decomposition of the complex occurs between approximately 100°C to 200 °C (Δm = –26.21%). A nearly thermostable behavior of the resulting product is observed in the temperature range from 200 °C to 330 °C. The second decomposition occurs from 330 °C to 450 °C (Δm = –40.15%) and at 800 °C is a residue of approximately 22.9% from the initial complex obtained. This does not correlate to the decomposition of elemental copper (13%). Similar results are observed for the related complex **I** (**Figure 1.3**, **right**) and no full decomposition to elemental copper is obtained. However, a comparison of the TG/DSC analysis of **1** with complex **I**[8] shows a significant difference (**Figure 1.3**, **right**). The decomposition of **1** takes place in two steps, with a temperature separation of almost 130 °C while the decomposition of **I** can be described as an almost continuous decomposition process. A comparison of mass differences between **1** and **I** suggests that in the first initiation phase probably C_9H_{12} (Δm = –24.62%) is released.

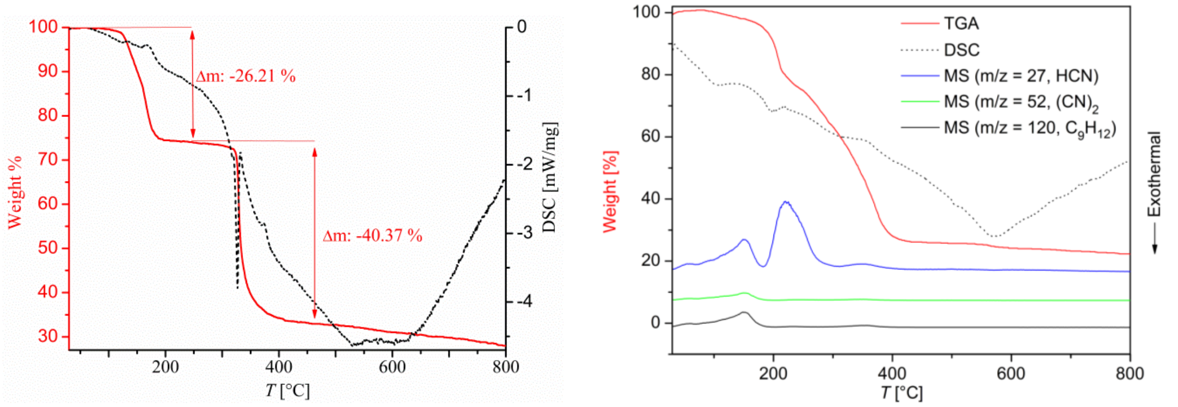

Figure 1.3: **Left** TG/DSC analysis of **1** with a heating rate of 5 K/min and **right** TG/DSC analysis combined with MS of **I** with the same heating rate.[8] © 2016 ELSEVIER.

The TG/DSC analysis of **1** motivates to synthesize the oxalate-bridged dinuclear copper(I) NHC complex **2**, which should also give a clean deposition to elemental copper, in agreement with the dicopper(I) *μ*-1,2,3,4-oxolato NHC complex **II**.

2 is synthesized according to the reaction in **Scheme 1.3** and analogous to the synthesis route for complex **II**.[8] Addition of one equivalent of oxalic acid at –78 °C to **1** and reaction of the components at r.t. overnight results in the formation of complex **2**. After further work-up (see experimental section) a colorless powder is obtained. Colorless single crystals are isolated after layering a saturated THF complex solution with cooled Et_2O at 4 °C (see experimental section).

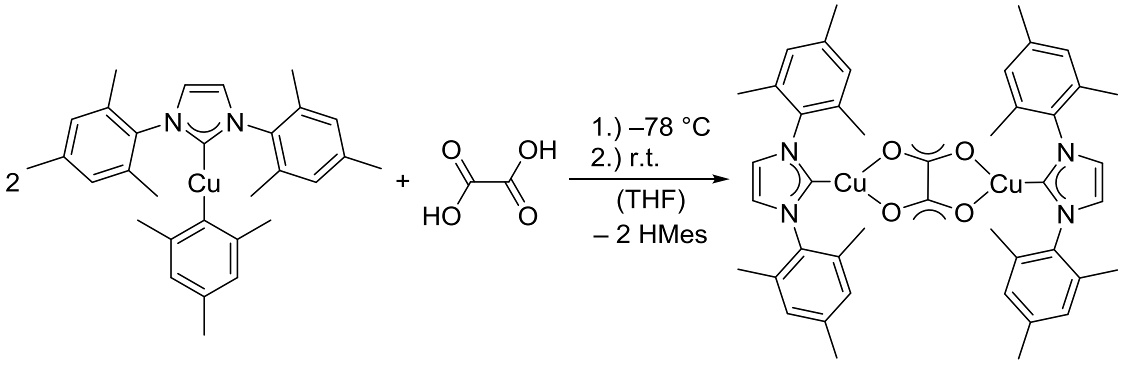

1 **2**

Scheme 1.3: Synthesis of the unsaturated dinuclear oxalato-bridged copper(I) NHC complex **2**.

2 crystallizes in the space group $P\bar{1}$. In agreement with the crystal structure of the imidazolin-2-ylidene complex **II**, the crystal structure of the imidazol-2-ylidene complex shows C_i symmetry (**Figure 1.4**). Each copper ion is coordinated in a distorted trigonal-planar fashion by one imidazol-2-ylidene ligand and the two oxygen ions of the oxalato bridge. The obtained bond lengths and binding angles of complex **2** are similar to **II** (**Table 1.2**). The Cu–C bonds in **2** and **II** are shorter than in complexes **1** and **I**, due to increasing electronegativity of the ancillary coligand.[8]

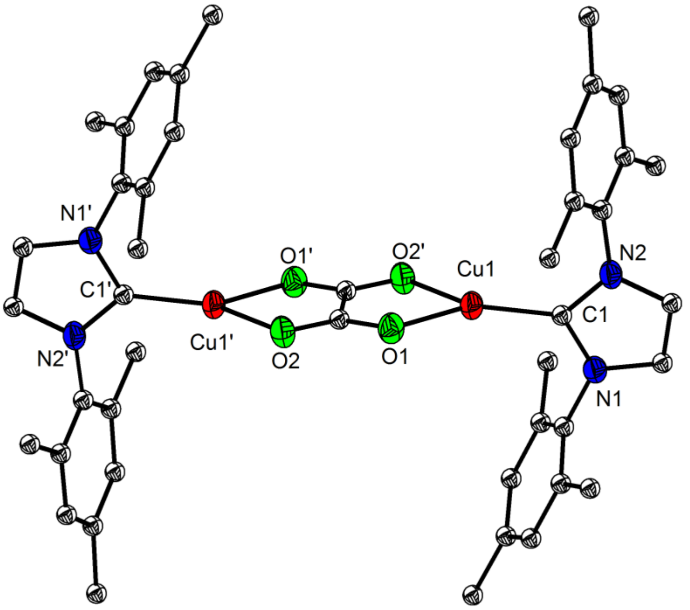

Figure 1.4: Molecular structure (50% probability thermal ellipsoids) of **2**. Hydrogen atoms are omitted for clarity.

An evaluation of the bonding situation in complex **II** and respective for **2** as well as a comparison of **II** with oxalato-bridged complexes has already been reported.[8] The Cu–O bonds in **2** and **II** lie in the range of the reported copper(I) oxalates with olefin or alkyne ligands (longer; 1.987(1)-2.004(2) Å) and isonitrile complexes (shorter, 2.081(2)-2.122(2) Å).[6,7] This is again related to the stronger π-acceptor character of the alkynes or alkenes and the σ-donor/π-acceptor character of isonitriles, respectively.[8]

Table 1.2: Comparison of selected crystallographic data of **2** and **II**[8].

Atoms	**2**	**II**
Cu–C(1)	1.860(5)	1.860(5)
Cu(1)–O(1)	2.039(4)	2.045(3)
Cu(1)–O(2‘)	2.042(3)	2.048(3)
O(1)–Cu(1)–O(2‘)	82.08(1)	81.93(1)
C(1)–Cu(1)–O(2‘)	137.9(2)	138.56(2)

The solid state ATR IR spectrum shows a very strong band at 1629 cm^{-1} (asymmetric COO stretch) and 1607.6 cm^{-1} (s)), reflecting the oxalato-bridge between the two copper ions (**Figure 1.5**). This stretching frequency is in good agreement with the corresponding values of in the dinuclear copper oxalato-bridged complexes, mentioned in the literature. Oxalato-complexes with alkene and alkyne co-ligands show COO stretches between 1642-1647 cm^{-1} and with isonitrile and phosphine co-ligands show COO stretches between 1617–1622 cm^{-1} and 1620-1635 cm^{-1})[6,7] respectively, according to its backbonding capabilities. The backbonding of the copper(I) ions (d^{10}) to the alkene or alkynes are the strongest and the back donation to the isonitrile is the weakest. In the ATR IR spectrum of the complex in solid state a very strong band at 1629 cm^{-1} (asymmetric COO stretch) and 1607.6 cm^{-1} (s) is observed, reflecting the oxalato-bridge between the two copper ions (**Figure 1.5**). This stretching frequency is in good agreement with the corresponding values of in the dinuclear copper oxalato-bridged complexes, mentioned in the literature. Oxalato-complexes with alkene and alkyne co-ligands show COO stretches between 1642-1647 cm^{-1} and with isonitrile and phosphine co-ligands show COO stretches between 1617-1622 cm^{-1} and 1620-1635 cm^{-1}[6,7] respectively, according to its backbonding capabilities. In complex **II** (1634 cm^{-1})[8] the COO stretch is around 5 cm^{-1} higher than in **2**. This features the slightly weaker π-acceptor capability of the unsaturated ligand in **2**. The reason is the significant electronic charge in the formally empty p_π orbital of the carbene in **2** and a higher π-delocalization in imidazol-*2*-ylidenes compared to imidazolin-*2*-ylidenes.[19]

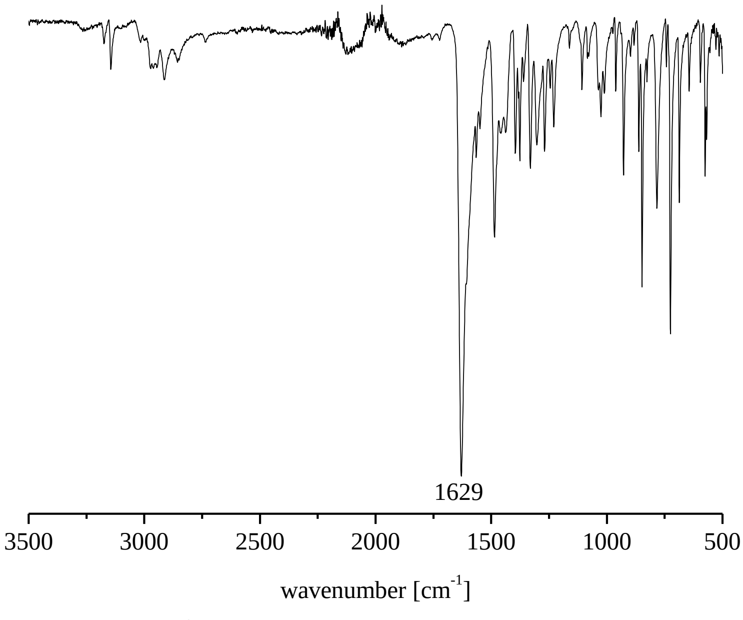

Figure 1.5: Solid state ATR IR of the oxalato-bridged dinuclear copper(I) NHC complex **2**. At 1629 cm^{-1} the asymmetrical COO stretching vibration of the oxalato bridge is observed.

In ^{1}H and ^{13}C{^{1}H} NMR spectra of **2** in THF-*d$_8$* only one set of singlets is observed. This reflects the high symmetry of the complex in solution (**Figure 1.6**) within the limitation of the NMR timescale (1-1000 Hz). The shift of the *4H*- and *5H*-backbone protons is in agreement with complexes, mentioned in the literature and with complexes described in this thesis. The carbene C^5 is low-field shifted to 185.2 ppm in the $^{13}C\{^1H\}$ NMR spectrum. At 170.8 ppm appears the ^{13}C NMR resonance of the quaternary C^6 atom of **2** (oxalato bridge of **II** $\delta = 170.7$ ppm)[8]. Moreover, the different electronic properties between NHCs, alkynes/alkenes and isonitriles and the effect on the electronic environment of the oxalato carbons are obvious. The ^{13}C signals in alkyne and alkene complexes are low-field shifted (171.8-171.4 ppm) and in the isonitrile complex slightly high-field shifted (169.2-168.9 ppm). In **II** the chemical shift of the carbene-C is observed at 206.5 ppm and is low-field shifted compared to complex **2**. This is a consequence of less electron density at the carbon atom.

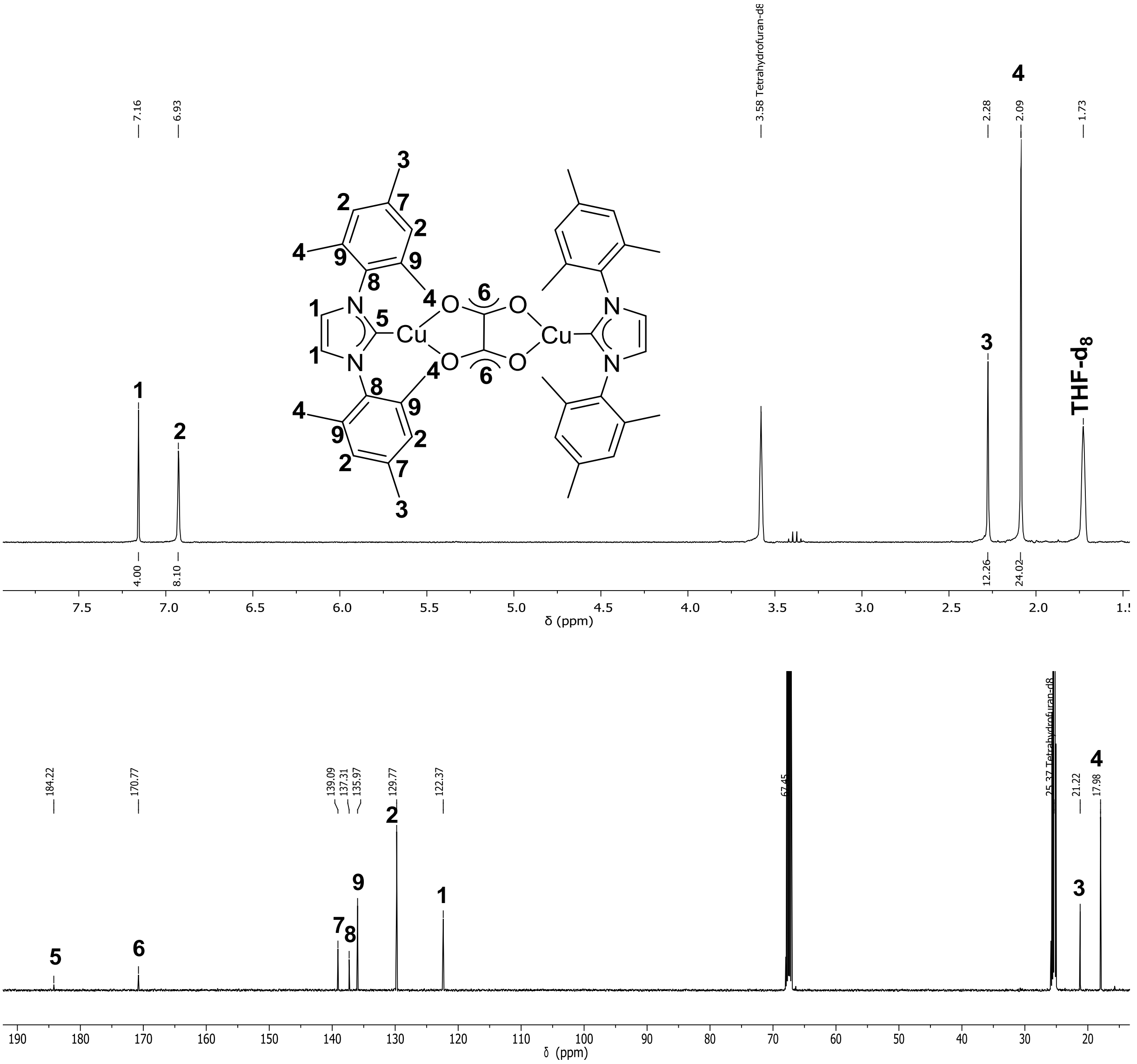

Figure 1.6: ^1H and $^{13}C\{^1H\}$ NMR spectra of **2** in THF-d_8 at 298 K. and (300 MHz and 75 MHz).

ESI-MS of **2** in THF shows one peak at $m/z = 671$, which is a result of a degradation of the complex under MS conditions. As described before by complexes **1**, **I** and **II**, the more stable mononuclear copper(I) dicarbene complex is formed under ionization conditions and no peaks of the dinuclear complex are observed. Elemental analysis confirmed the purity of the compound.

Preliminary thermal stability tests of **2** in a platinum crucible with a heating ramp applied from 25 °C to 800 °C and a heating rate of 5 K·min^{-1} shows a fast decomposition of **2**. After the thermostability test, a black decomposition product is obtained inside and outside the crucible. The removal of these deposits is only successful using strong acids. Due to this observation no TG/DSC analysis of **2** was possible. TG/DSC analysis of **II** suggested the deposition of elemental copper after thermolysis[8], but so far the exact identity of the resulting material after thermolysis of **2** has not be determined. A comparison of complex **1**, **2** with **I**[8] and **II**[8] indicate that complex **2** seems to be also a precursor for copper deposition, but further experiments are necessary to proof this thesis.

1.3 Conclusion and Outlook

The synthesis of a mononuclear *σ*-mesityl imidazol-*2*-ylidene copper(I) complex **1** was achieved and analytical data as well as thermostability were compared with data for a *σ*-mesityl imidazolin-*2*-ylidene copper(I) complex **I**. The thermal decomposition of complex **1** monitored by TG/DSC analysis shows a decomposition of the complex in two steps with a difference in temperature of 130 °C. **1** can be used as a precursor for the synthesis of a dinuclear, oxalato-bridged copper(I) NHC complex **2**, which was fully characterized and compared with complex **II**. Based on similarities between complexes **2** and **II**, confirmed by comparable analytical investigations, **2** appears to be a potential precursor for copper deposition, at even lower temperatures than **II**. In the future, employing an analytic instrument allowing TG/DSC measurements of complex **2**, or the testing of complex **2** in ALD experiments would be of great benefit to confirm the use of this complex for copper deposition on surfaces, in analogy to complex **II**.

2

Copper(I) complexes with multidentate NHC ligands and their dynamics in solution

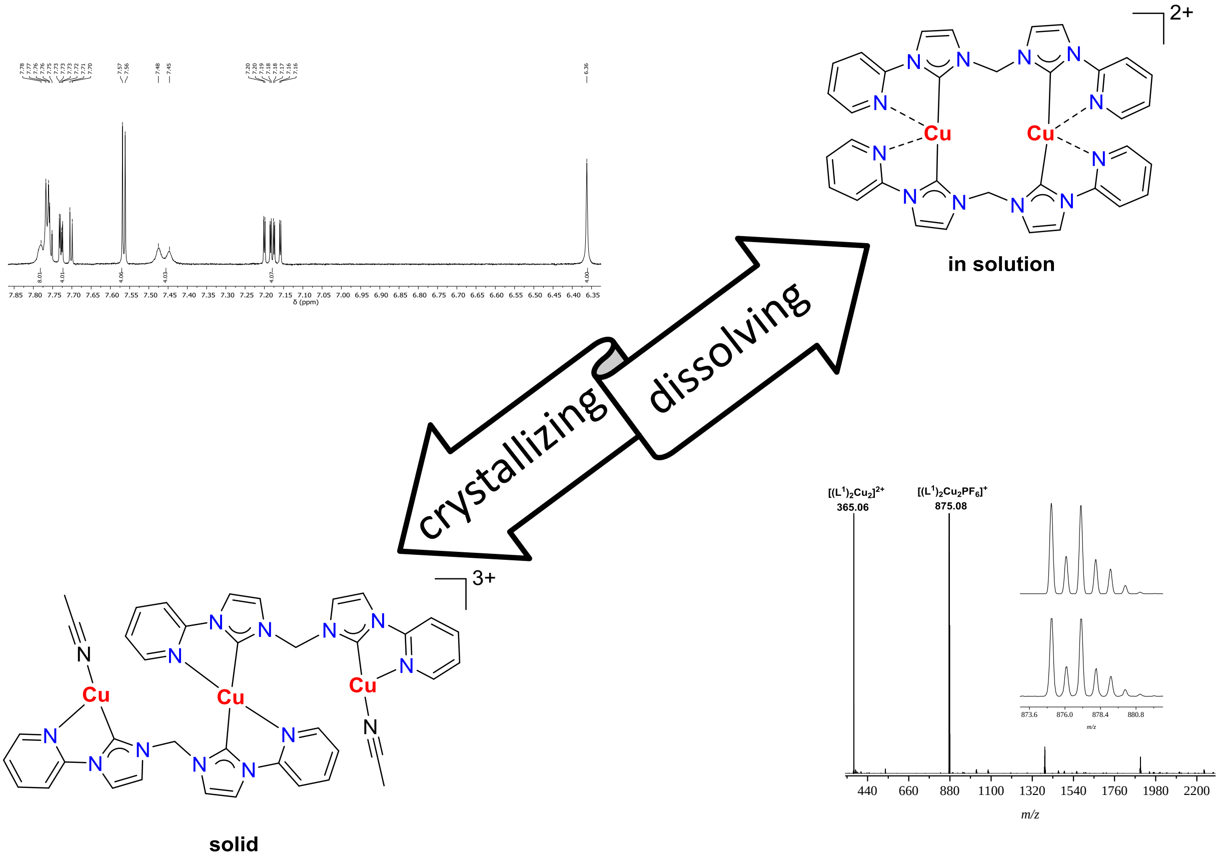

Abstract: Copper(I) complexes with oligodentate ligands containing *N*-heterocyclic carbenes (NHCs) have attracted great interest in academia over the past decade, especially in material science and catalysis. Numerous copper(I) complexes featuring oligodentate NHC ligands with various types of nuclearity in solid state have been reported, however accurate prediction of the geometry and nuclearity of these complexes is often difficult. Little knowledge is available regarding the dynamics of multinuclear copper(I) NHC complexes in solution, which raises the question whether dissolved complexes have the same constitution as in solid state. In this chapter a detailed study of three multinuclear Cu^I hybrid NHC/pyridine complexes is reported, which underlines the importance analyzing the dynamic behavior of such complexes in solution in comparison with their solid state structures. The ligand scaffold is varied by exchange of the central methylene bridge by propylene or pyridinyl units. In addition, the dynamics of a mononuclear copper(I) macrocycle and a dinuclear macrocycle is investigated and its activation parameters are determined.

2.1 Introduction

In the literature oligodentate ligands are widely used in several transition metal complexes and mono- or multinuclear metal complexes have been reported.[20–27] One class of these oligodentate ligands bearing *N*-heterocyclic carbenes and their corresponding complexes can be found in material chemistry, catalysis and medicinal chemistry.[20–28] The reason for this versatile use of NHC ligands is due to their intrinsic properties, for instance their high stability towards thermal stress, moisture and air, which is mainly due to the strong σ-donor strength of the NHCs.[29] In the past, NHCs were extensively combined with pyridine groups, to form a variety of oligodentate ligands. A short overview oligodentate pyridine/NHC hybrid ligands, known in the literature is given in **Figure 2.1**.

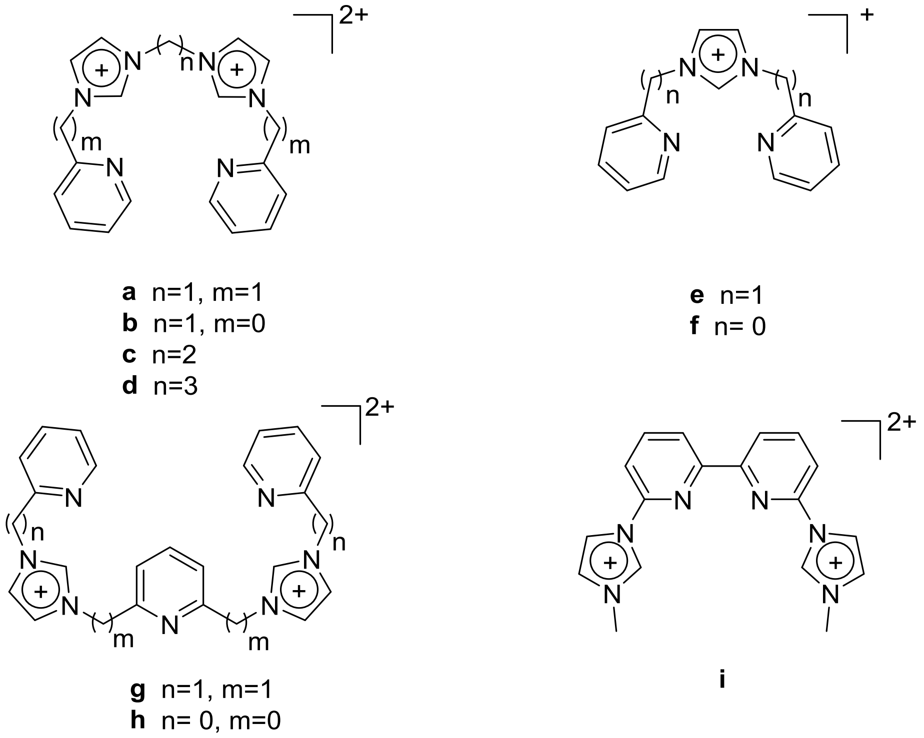

Figure 2.1: Selection of oligodentate hybrid NHC/pyridine ligands reported in the literature.[20–27]

With those ligands monodentate nickel(II)[25,30,31], palladium(II)[25,32], rhodium[33] and iridium(I)[34] complexes are described. In contrast to this, the combination of coinage metals with such ligands results into multinuclear metal complexes. Since coinage metal ions in the oxidation state +I prefer a linear coordination, especially by the NHCs, ligand design has a strong influence on the number of metal ions in the resulting complexes.

Multinuclear oligodentate NHC complexes of copper(I)[11,35–38], silver(I)[11,32,35,39–41] and gold(I)[11,40,42,43] have been described, but in contrast to $\mathrm{Au^I}$ and $\mathrm{Ag^I}$ complexes, relatively few copper(I) complexes have been presented so far.[11,35–38] In catalysis, di-, tri- and tetranuclear copper(I) NHC complexes are used. Xu *et al.*[44] published a tetranuclear copper(I) phenanthroline-based NHC complex which mediates the copper assisted azide-alkyne cycloaddition (CuAAC). In addition, oligodentate copper(I) NHC complexes have been tested as photoactive materials in optoelectronic devices.[45–47]

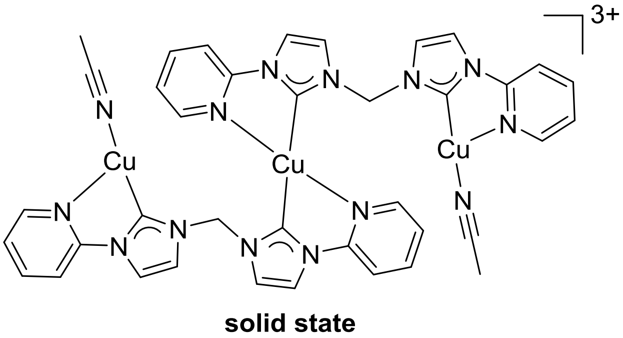

3

Figure 2.2: Trinuclear copper(I) NHC/pyridine hybrid complex **3**, first published by Chen and coworkers.[48]

In contrast to extensive studies of oligodentate copper(I) hybrid NHC/pyridine complexes in solid state, much less is known about such systems in solution.[49] One reason for this can be the lack of accurate analytic methods which allow determining the precise composition of the complexes in solution. Hofmann *et al.*[49] reported the dynamics of dinuclear Cu^I NHC complexes in solution, monitored by ^1H VT NMR spectroscopy. At low temperatures the structures of their complexes in solution are consistent with the obtained solid state structures.[49] At higher temperatures they were able to observe a fluxional process. In 2009, Chen and coworkers[48] described a trinuclear copper(I) complex **3** (**Figure 2.2**), which shows high symmetry in solution. After oxidation of this complex they obtained a dinuclear species. The high symmetry of the complex in solution, monitored by ^1H NMR spectroscopy, is in contrast to the symmetry of the trinuclear copper(I) NHC complex in the molecular solid state structure.

Here the first detailed studies of the trinuclear copper(I) NHC complex **3** in solution are presented. These results, reported below motivates to further study the influence of the central bridge on the nuclearity and the constitution in such complexes, and explore their behavior in solution. For this the methylene spacer between the two *2H*-imidazolium units is exchanged by propylene and by pyridine units. Furthermore, two macrocyclic complexes are synthesized and their behavior in solution is investigated.

2.2 Results and Discussion

2.2.1 Dynamic investigations of five copper(I) NHC complexes

The synthesis of the copper(I) NHC complexes **3-7** is achieved by the mesitylcopper(I) route, first reported by Danopoulos *et al.*[50] and further investigated and established by Kühn, Meyer and Resch *et al.*[8,51] The synthesis and structure determination of the three copper(I) NHC complexes **3-5** are already described in the Master thesis of Resch at TU Munich.[51] Here the focus will be mainly on the dynamics of the complexes in solution, which is primarily investigated as part of this work at the University of Göttingen. A detailed description of the complexes can be found in the Master Thesis.[51] An overview of the here presented complexes is shown in **Scheme 2.1**.

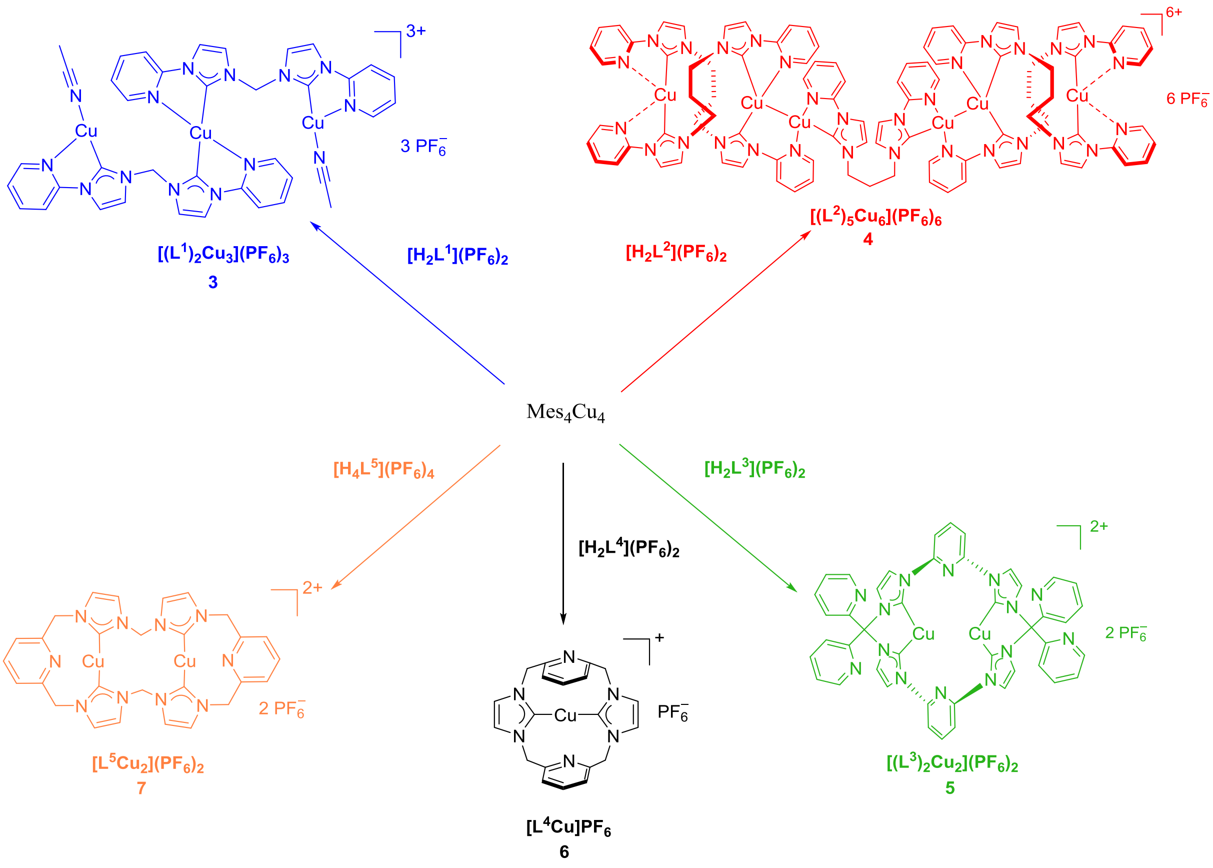

Scheme 2.1: Reaction scheme for the synthesized copper(I) NHC complexes by the Mes_4Cu_4 route.[51]

2.2.2 Dynamic of open-chained copper(I) NHC complexes in solution

Single crystals of complex **3** are obtained by Et_2O diffusion into a solution of the complex in MeCN. **3** crystalizes in the space group *P*21/n and consists of three copper(I) ions. The constitution of the complex in solid state is also confirmed by elemental analysis and fast atom bombardment mass spectrometry (FAB-MS) in agreement with the results published by Chen *et al.*[36] The ^1H NMR spectrum in MeCN-d_3 of **3** shows one set of signals and indicates a system with a symmetrical structure (**Figure 2.3**). These findings can be explained by a rearrangement of the trinuclear copper(I) NHC complex to a dinuclear copper(I) complex under release of one copper ion as $[Cu(CD_3CN)_4]^+$ in MeCN-d_3 (**Scheme 2.2**). Chen *et al.*[36] never mentioned this behavior of the complex and assumed the retention of the trinuclear complex in solution.

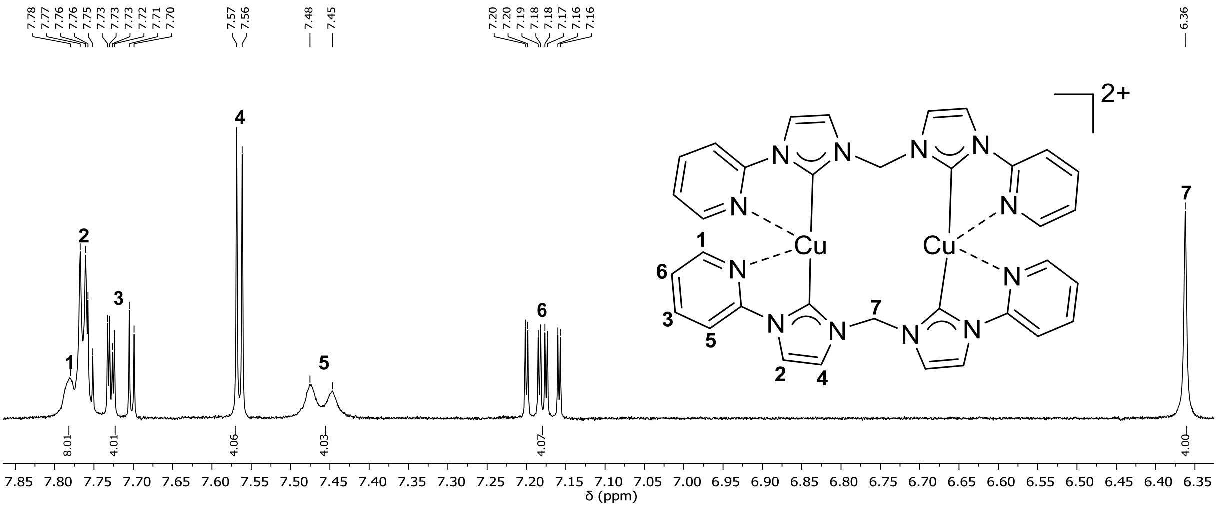

Figure 2.3: ^1H NMR spectrum of complex **5** in MeCN-d_3 at 298 K and 300 MHz. One set of signals is observed.

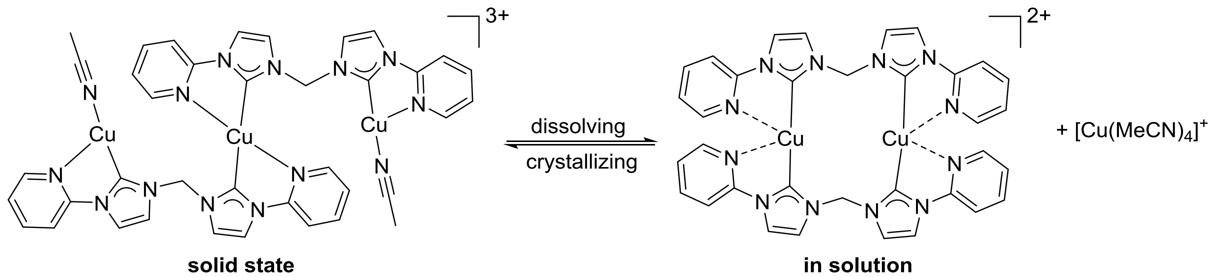

Scheme 2.2: A rearrangement of the trinuclear oligodentate copper(I) NHC complex in solid state to a dinuclear copper(I) NHC complex and a tetrakisacetonitrile copper(I) complex is proposed by dissolving the complex in MeCN.

2D NMR spectroscopy and ESI-MS analysis are used to elucidate the nuclearity of the complex in solution. VT NMR experiments were conducted in MeCN-d_3 in the range between

80 °C to –40 °C and confirm the presence of a species with higher symmetry in solution in comparison to the solid state structure (**Figure 2.4**). The imidazol-*2*-ylidene proton resonance H^4 is not affected by temperature variation, but broadening of all other peaks is observed. No decoalescence of the corresponding proton peaks, down to 233 K is observed. As a consequence of this behavior no activation parameters ($\Delta H^{\ddagger}$ or $\Delta S^{\ddagger}$) can be determined. A necessary condition for the determination of these parameters by NMR spectroscopy is the presence of well resolved spectra below the coalescence temperature to obtain peak widths at half heights of the peaks at a temperature where in ideal case no exchange occurs (see experimental section **10.2.2**).

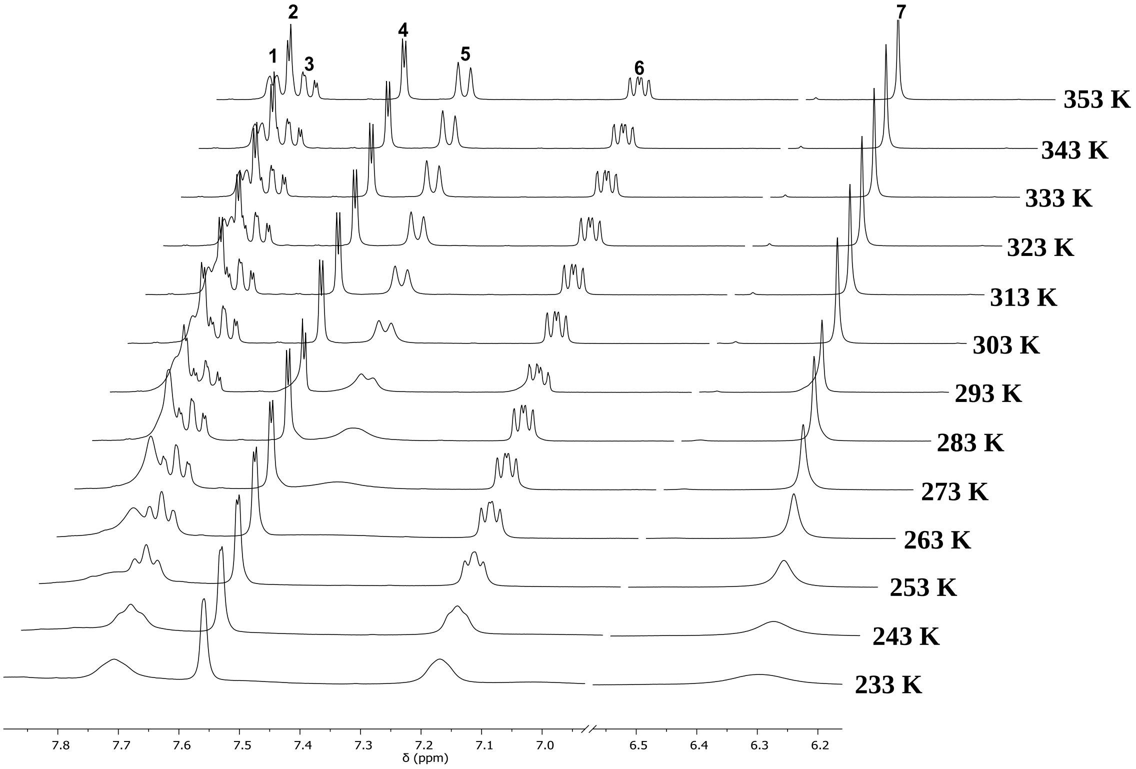

Figure 2.4: ^{1}H VT NMR spectroscopy of **3** between 80 °C and –40 °C in MeCN-d_3 (400 MHz).

$^1H^{15}N$ HMBC NMR measurements of the complex and the free ligand (**Figure 2.5**, **left**) indicate only weak binding of the pyridine-N to the copper ion with a small difference in chemical shift $\Delta\delta(N_{py}) = -14$ ppm. Pazderski *et al.*[52] have reviewed the ^{15}N NMR chemical shifts in transition metal complexes including pyridine. They reported a range of chemical shift differences between free pyridine and coordinated pyridine of 30-150 ppm. Kirchner *et al.*[53] discussed the chemical shift difference ΔN_{py} of tri- and tetracoordinated copper(I) complexes bearing bidentate SN ligands. They reported a shift of –30 ppm between the free ligand and the copper(I) complex. Regarding the solid state structure a larger $\Delta\delta(N_{py})$ is expected, because the pyridine donor atoms are bound to the peripheral copper ions.

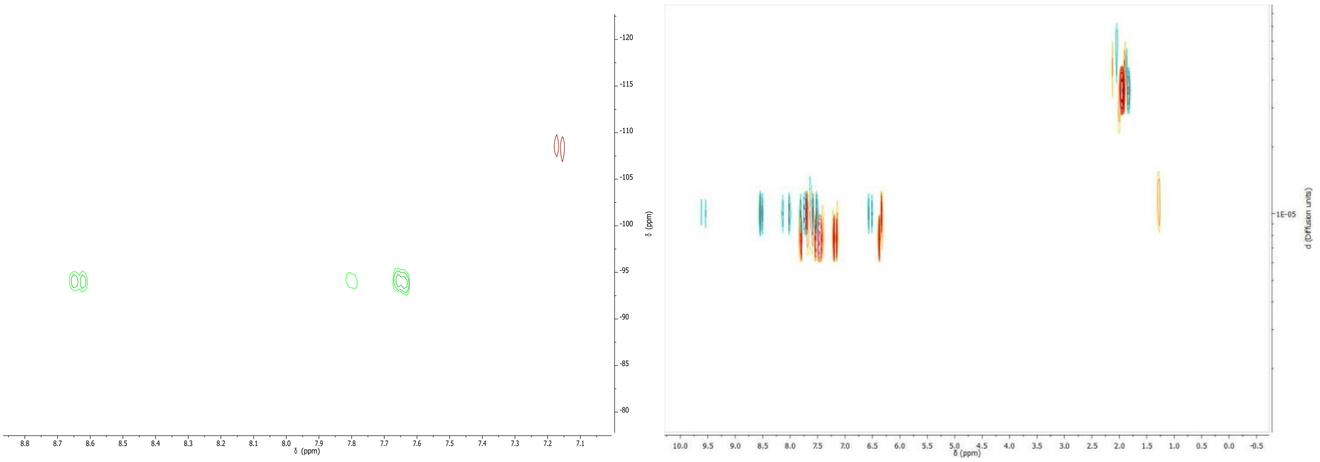

Figure 2.5: (**left**) Comparison of the ^{15}N chemical shift of the pyridine groups in complex **3** (**purple**) and **$H_2L^1(PF_6)_2$** (**green**) determined by ^{1}H^{15}N HMBC NMR spectroscopy. (**right**) ^{1}H DOSY NMR of the complex **3** (**red**) and **$H_2L^1(PF_6)_2$** (**blue**).

A ^{1}H DOSY NMR spectrum of **3** shows only one species in solution (**Figure 2.5**, **right red**) with a smaller diffusion coefficient ($D_{298} = 8.97 \cdot 10^{-6}\ \mathrm{m^2 s^{-1}}$) than the free ligand ($D_{298} = 1.07 \cdot 10^{-5}\ \mathrm{m^2 s^{-1}}$). Comparison of the hydrodynamic radii of **$[H_2L^1](PF_6)_2$** and **3** considering the Stokes-Einstein equation[54] (1), is in agreement with the composition **$[(L^1)_2Cu_2]^{2+}$**. The Stokes-Einstein equation has different restraints (e.g. it assumes spherical molecules) which leads to an inaccuracy of R_{Cu} and thus of **A** for non-spherical molecules.[54]

$$D = \frac{k_b \cdot T}{6 \cdot \pi \cdot \eta \cdot R_H} \tag{1}$$

$$\mathbf{A} = \frac{V_1}{V_2} = \left(\frac{R_{\mathrm{Cu}}}{R_{\mathrm{L}}}\right)^3 = \left(\frac{D_{\mathrm{L}}}{D_{\mathrm{Cu}}}\right)^3 = \left(\frac{D_{\mathrm{Cu}}}{D_{\mathrm{L}}}\right)^{-3} = \left(\frac{8.97 \cdot 10^{-6}}{1.07 \cdot 10^{-5}}\right)^{-3} = 1.70\ \approx 2 \tag{2}$$

Furthermore, one has to keep in mind that the ^{1}H DOSY NMR spectrum only can show the average of the dynamics of the molecules in solution based on the NMR instrument time scale and the resolution of the NMR spectra, which strongly depend on the spin-lattice relaxation time T_1, which has a strong influence on the signal intensity and the spin-spin relaxation time T_2, which has an influence of the line shape of the signal.

ESI-MS measurements of single crystals, dissolved in MeCN, confirm the presence of dinuclear species in solution. Two dominant peaks at m/z = 875.08 (100) **$[(L^1)_2Cu_2(PF_6)]^+$** and m/z = 365.06 (99) **$[(L^1)_2Cu_2]^{2+}$** are observed (**Figure 2.6**). Overall, the combined evidence from 2D NMR techniques with ESI-MS strongly suggests the presence of the dinuclear species **$[(L^1)_2Cu_2]^{2+}$** in MeCN solution.

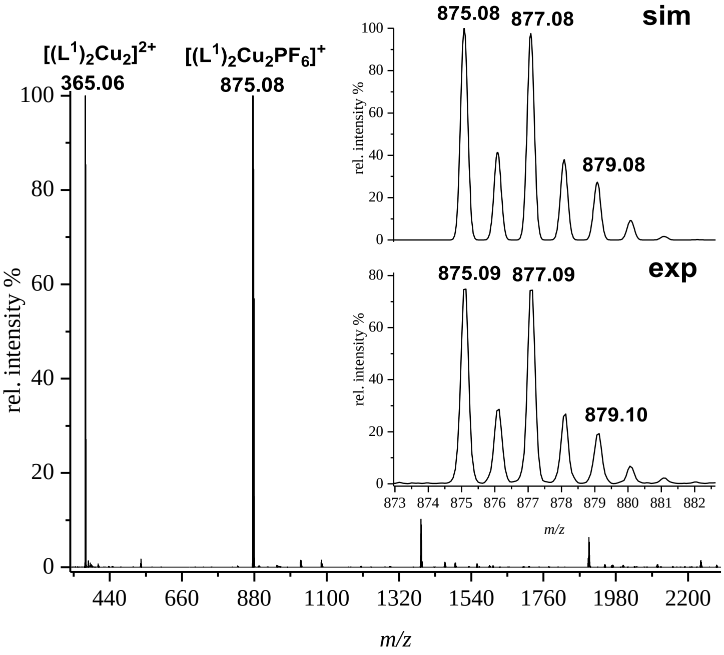

Figure 2.6: ESI-MS of **3** in MeCN. The inset shows the experimental and simulated isotopic distribution pattern for the peak at *m/z* = 875.08 (100) for $\mathbf{[(L^1)_2Cu_2\ (PF_6)]^+}$.

To further explore the influence of the central bridge on the nuclearity, connectivity and denticity in solid state as well as in solution, the 2*H*-imidazolium distance of the oligodentate ligand is extended by two CH_2 units. Synthesis of the ligand and its copper(I) complex using Mes_4Cu_4, is performed as described previously.[51,55]

In this work, single crystals of $\mathbf{[(L^2)_5Cu_6](PF_6)_6}$, suitable for X-ray measurements are obtained by slow diffusion of Et_2O into a complex MeCN solution. **4** crystalizes in the space group $P\bar{1}$. The previously described constitution[51], including bond lengths and bond angles in the complex can now be confirmed by the solid state structure. The exchange of the central unit of the bridge and as consequence thereof higher flexibility of the ligand, results into two trinuclear subunits which are linked to a fifth propylene-bridged ligand (**Figure 2.7** and **2.8**). In **Figure 2.8** the copper····copper distances are shown. The obtained crystal structure confirms a hexanuclear copper(I) NHC complex in solid state, where five ligands are surrounding the two trinuclear Cu^I subunits in a helical fashion (**Figure 2.7** and **2.8**). Cuprophilic interactions are observed within the two subunits, and weak interaction between the two internal copper(I) ions Cu(3) and Cu(4) (3.75 Å).

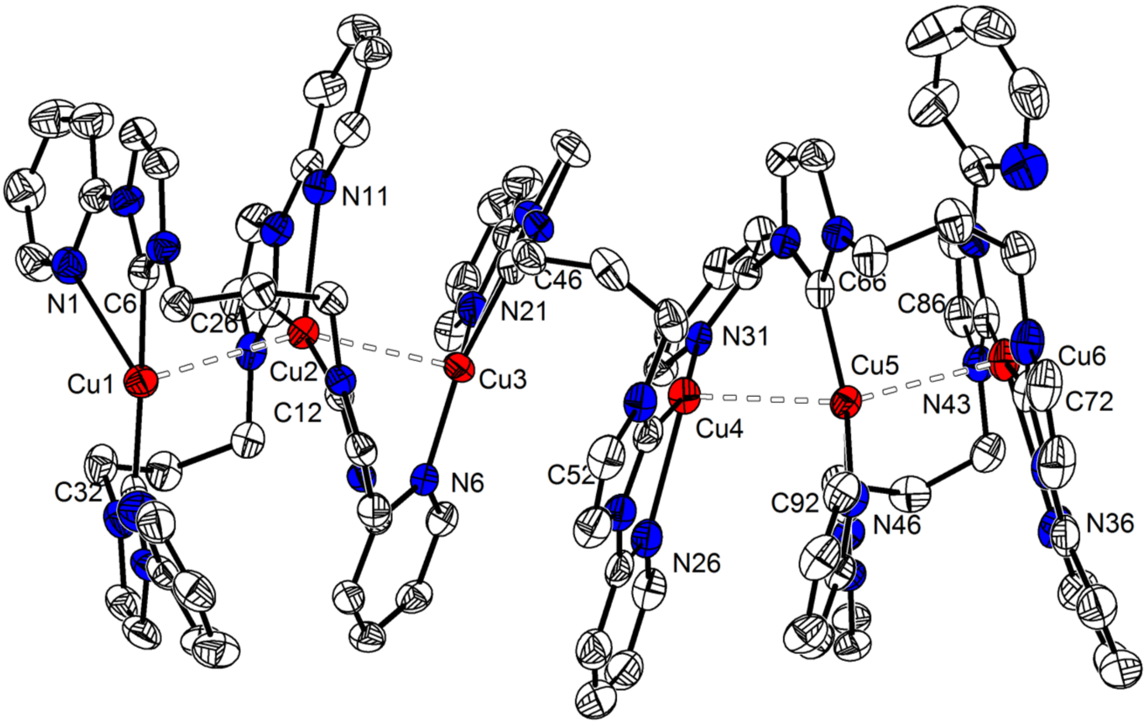

Figure 2.7: Molecular structure (30% probability thermal ellipsoids) of **4**. Counter ions and hydrogen atoms are omitted for clarity. Selected distances [Å] and angles [º]: Cu(1)····Cu(2) 2.8393(7), Cu(2)····Cu(3) 2.6501(7), Cu(3)····Cu(4) 3.7492(6), Cu(2)–N(11) 2.396(4), Cu(1)–C(6) 1.912(4), C(6)-Cu(1)-C(32) 174.93(2).

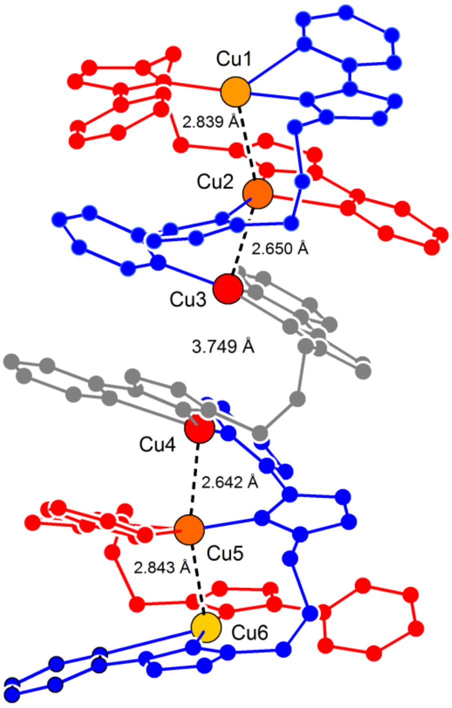

Figure 2.8: Schematic drawing of the helical structure of **4**. Six copper(I) ions are in the center of a helical structure, which is formed by coordination of five ligands.

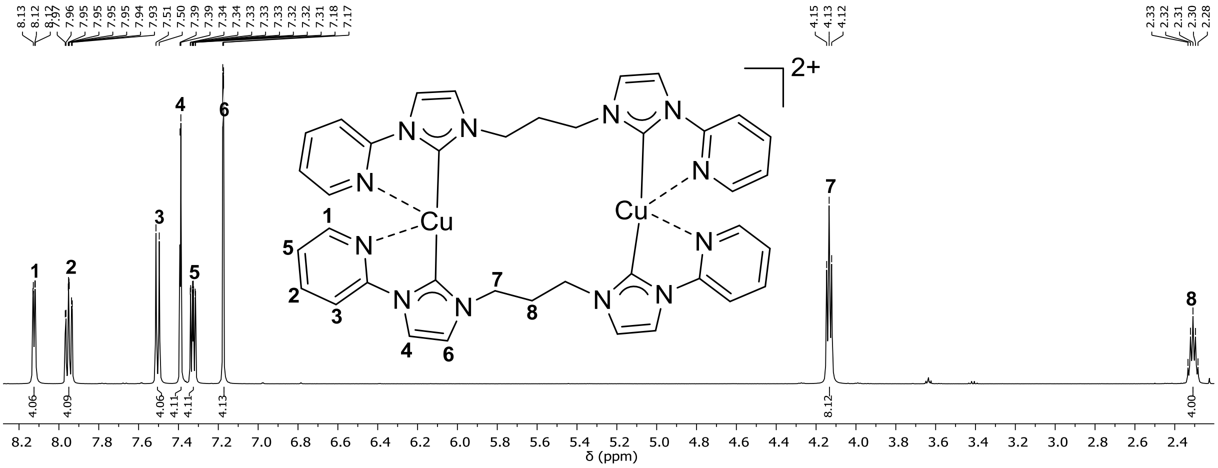

Figure 2.9: ^{1}H NMR spectrum of complex **5** in MeCN-d_3 at 298 K and 500 MHz. One set of signals is observed.

^{1}H NMR spectrum of complex **4** in MeCN-d_3 shows, in agreement with complex **3**, the presence of a species of higher symmetry than predicted from the molecular structure in solid state (**Figure 2.9**). VT ^{1}H NMR spectroscopy of complex **4** over a wide temperature range (80 °C to –40 °C) (**Figure 2.10**) does not show any decoalescence. The signals of the protons H^3 and H^4 are affected the most by decrease of the temperature from 353 K to 233 K, showing a high-field shift of $\Delta\delta = 0.25$ ppm and $\Delta\delta = 0.27$ ppm.

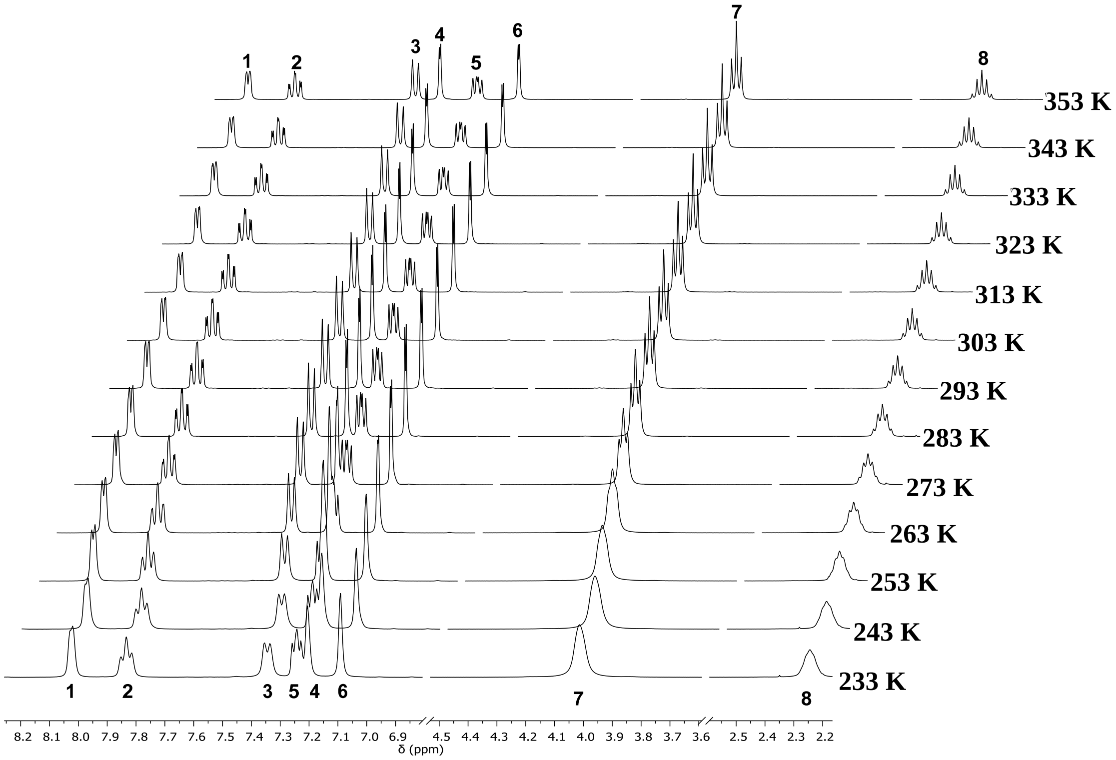

Figure 2.10: VT ^{1}H NMR spectra of complex **4** in the temperature range between 353 K and 233 K at 400 MHz in MeCN-d_3. The region between 6.9 ppm and 4.5 ppm was removed to obtain a higher resolution of the peaks.

^{1}H DOSY NMR spectroscopy of **4** confirms the presence of one species in solution on the timescale of the experiment, and similar diffusion coefficients of complex **3** and **4** suggests a comparable size of the two complexes (**Figure 2.11**, $D_{298} = 8.69 \cdot 10^{-6}$ m^{2}s^{-1}). The ratio between both complexes **4** and **3**, based on the Stokes-Einstein equation (2) is 1.09.

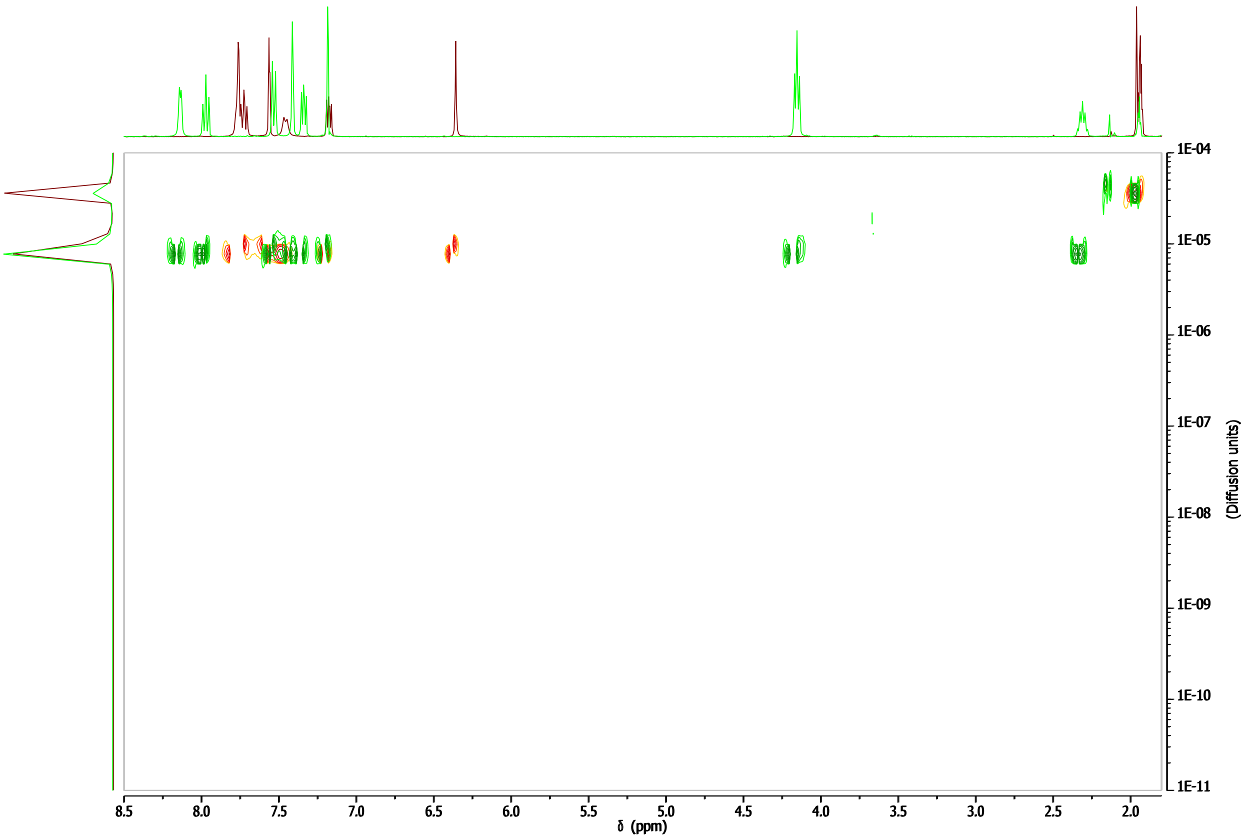

Figure 2.11: Stacked ^{1}H DOSY NMR spectra of **3** (**red**, $D_{298} = 8.97 \cdot 10^{-6}$ m^{2}s^{-1}) and **4** (**green**, $D_{298} = 8.69 \cdot 10^{-6}$ m^{2}s^{-1}) in MeCN-d_3 at room temperature.

The chemical shift of the pyridine nitrogen atom in **4** is $\delta(\mathrm{N_{py}}) = -105$ ppm, determined by ^{1}H^{15}N HMBC NMR spectroscopy which is almost the same shift like it is observed for complex **3** ($\mathrm{N_{py}} = -108$ ppm), suggesting a similar weak coordination of the pyridine groups to the copper ions. The dinuclearity of **4** is confirmed by ESI-MS measurement in MeCN (**Figure 2.12**). Two main peaks at *m/z* = 933.15 (99) for $\mathbf{[(L^2)_2Cu_2(PF_6)]^+}$ and at *m/z* = 395.09 (100) for $\mathbf{[L^2Cu]^+}$ are observed. The mononuclear species $\mathbf{[L^2Cu]^+}$ is observed upon fragmentation of $\mathbf{[(L^2)_2Cu_2(PF_6)]^+}$.

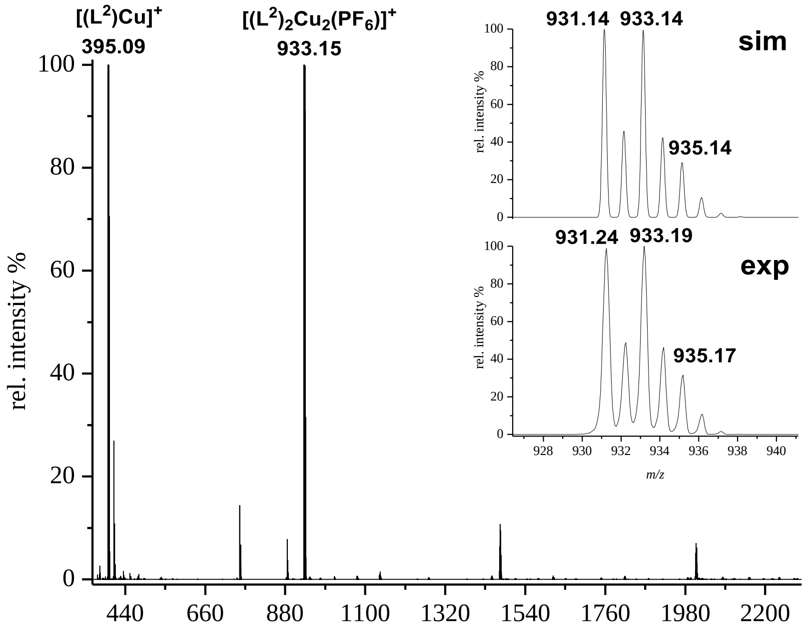

Figure 2.12: ESI-MS of complex **4** in MeCN. The inset shows the experimental and simulated isotopic distribution pattern for the peak at *m/z* = 931.14 (99) for **$[(L^2)_2Cu_2(PF_6)]^+$**.

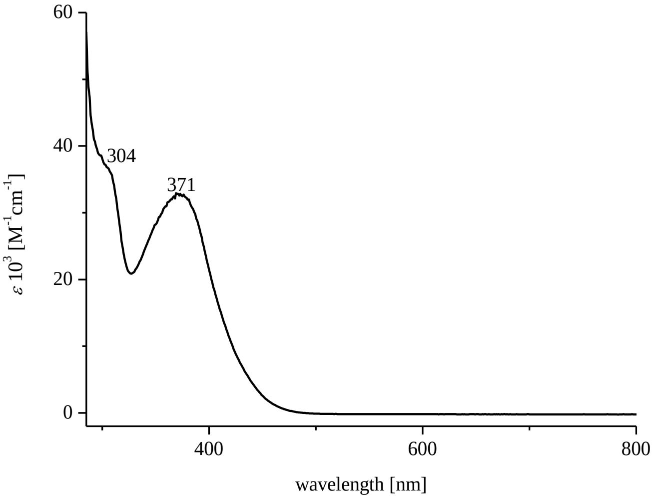

Figure 2.13: UV-vis spectrum of **4** in propionitrile at –80 °C showed one shoulder at 304 nm ($\varepsilon = 36.84 \cdot 10^3$ $M^{-1} \cdot cm^{-1}$) and a local maximum at 371 nm ($\varepsilon = 32.82 \cdot 10^3$ $M^{-1} \cdot cm^{-1}$).

The UV-vis spectrum of **4** in propionitrile at –80 °C shows two bands at 304 nm ($\varepsilon = 36.84 \cdot 10^3$ $M^{-1} \cdot cm^{-1}$) and 371 nm ($\varepsilon = 32.82 \cdot 10^3$ $M^{-1} \cdot cm^{-1}$) (**Figure 2.13**).

In 2015 Kühn *et al.*[55] investigated the influence of the alkylene bridge of oligodentate silver(I) NHC complexes on the nuclearity of the complex. They varied the bridge from ethylene to hexylene and observed a high structural diversity. The behavior of the copper ions is not comparable with the silver ions using the same ligand scaffold. An expansion of the alkylene bridge from methylene to propylene results in a higher nuclearity of the complex in solid state, but previous results showed that the two homologous ethylene[51] and propylene-bridged complexes have hexanuclear copper cores in solid state. A comparison between the two homologous copper and silver complexes shows that no prediction of the structure is possible not even upon slight changes of the ligand scaffold or by use of the higher homologous. In conclusion a hexanuclear propylene-bridged copper(I) NHC complex in solid state rearranged to a dinuclear copper(I) NHC complex in solution, bearing two ligands.

A dinuclear copper(I) NHC complex **5** is obtained in the solid state, by exchange of the methylene or propylene bridge by a pyridinyl bridge. Analysis of **5** in solid state[51] and in solution confirms the preservation of the dinuclear copper(I) NHC core. **5** crystalizes in the space group *Pnn2*.[51] In the crystal structure the two copper(I) ions interact with the central pyridinyl atom in a three-center two-electron (3*c*2*e*) configuration, while the external pyridinyl groups do not interact with the metals (**Figure 2.14** (**a**)). ^{1}H NMR spectroscopy of **5** in MeCN-d_3 (**Figure 2.14** (**b**) **top**) shows one set of signals, in analogy to the D_2 symmetry of the complex in solid state. A decrease of the temperature results in a rearrangement of the peaks in the ^{1}H NMR spectrum (**Figure 2.14** (**b**), **bottom**). The reason for this observation is the change of the coordination motif in the complex, which affects the chemical and electronic environment of the protons (**Figure 2.14** (**a**)). Proton resonances were assigned using 2D NMR spectroscopy. Discrimination between the two imidazol-*2*-ylidene backbone protons H^3 and H^7 is possible by observation of a NOE from the corresponding imidazol-*2*-ylidene protons to the *meta*-pyridinyl protons H^4 and H^5.

VT ^{1}H NMR spectra in the range 233-353 K give further insides in the highly dynamic behavior of the complex with different coordination modes of the copper cores. At high temperature a three-center two-electron interaction between the copper ions and the internal pyridinyl groups is observed. By decrease of the temperature a stronger interaction with the peripheral pyridinyl groups and the two copper ions is obtained (**Figure 2.14**). The interaction of the central pyridinyl groups with the two copper centers *via* a 3*c*2*e* bonding situation effects markedly the electronic situation of the protons H^1 and H^5. Increase of the temperature results into a low-field shift of the *para*-pyridine peak H^1 of almost 1 ppm. At 233 K, NOE between the imidazol-*2*-ylidene peak H^3 and the *meta*-pyridine H^4 is very strong.

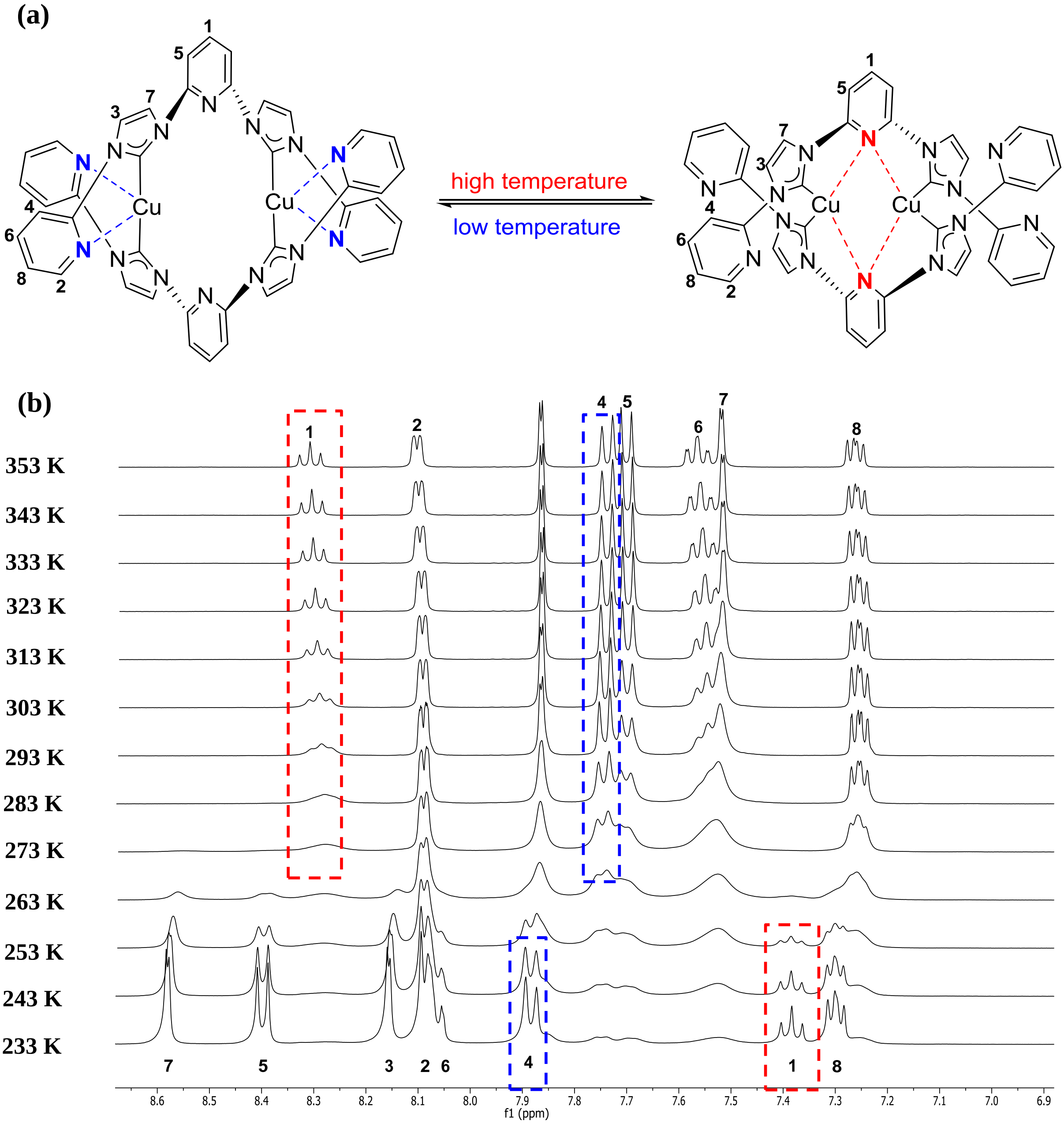

Figure 2.14: (**a**) Assumed coordination modes of **5** at different temperatures. (**b**) VT ^{1}H NMR spectra of complex **5** in the temperature range between 353 K and 233 K (400 MHz) in MeCN-d_3.

This finding corroborates the coordination of the external pyridinyl groups to the copper centers at low temperatures. Stronger interaction of the external pyridinyl groups with the copper ions leads to an increase of the rotation barrier of latter groups and a stronger coupling of the two protons (H^3 and H^4) through space. ^{13}C{^{1}H} NMR spectroscopy confirms the different kinds of interactions at low and high temperatures (**Figure 2.15**). The signals show the same trend like presented for the ^{1}H NMR shifts. An increase of the temperature results in a significant low-field shift of the ^{13}C–1 and ^{13}C–5 signals by a 3*c*2*e* interaction (approximately 3 ppm) concomitant a high-field shift of ^{13}C–6 (**Figure 2.15**).

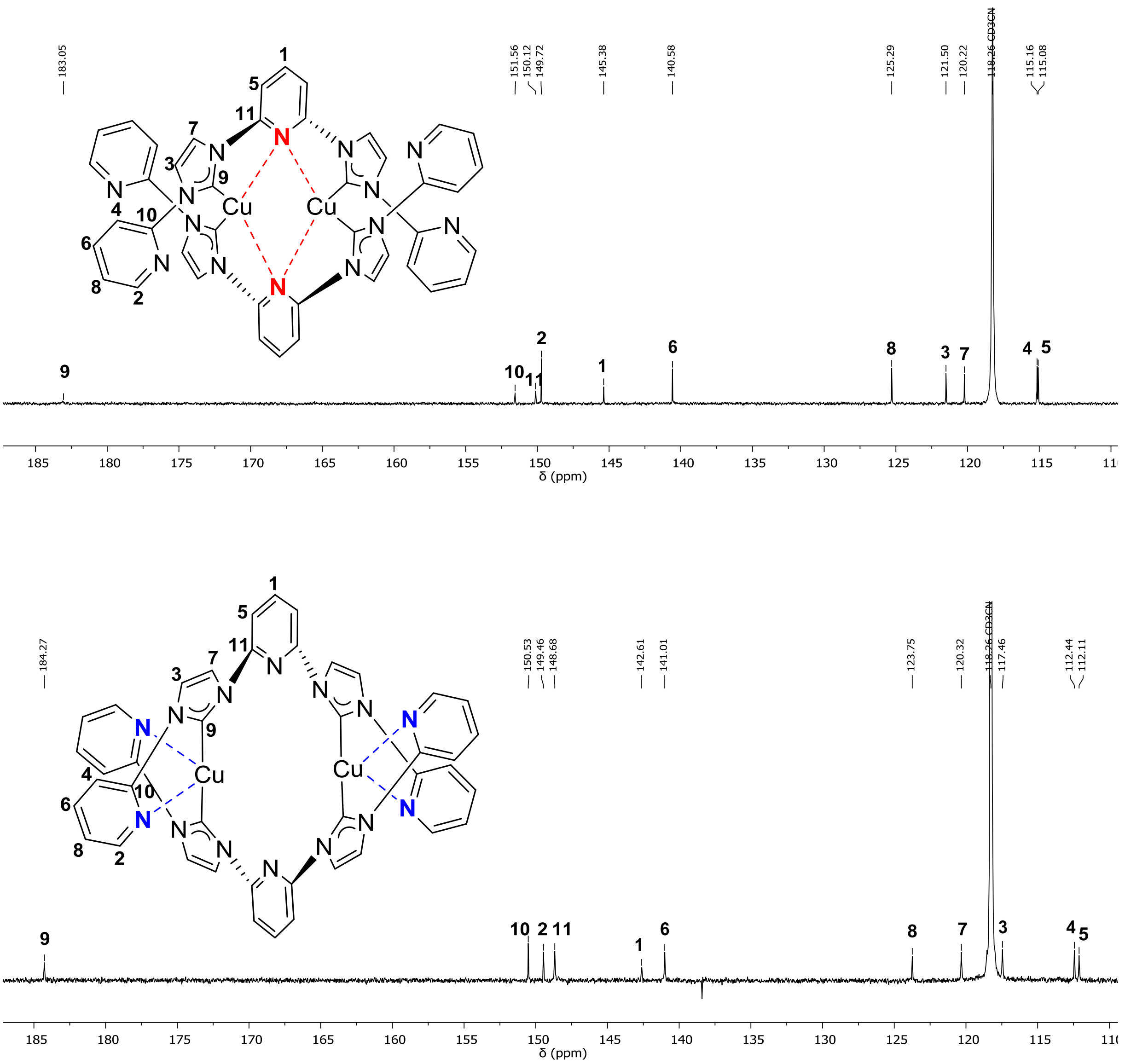

Figure 2.15: $^{13}C\{^{1}H\}$ NMR spectra of **5** at 353 K (**top**) and 233 K (**bottom**) (126 MHz) in MeCN-d_3.

Main parts of the results presented in this subchapter were published:

Y. Liu, S. G. Resch, I. Klawitter, F. Meyer *et al. Angew. Chem. Int. Ed.* **2019**, *58*, 2.

2.2.3 Dynamic of a macrocyclic copper(I) NHC complex in solution

The synthesis of the macrocyclic copper(I) complex **6** is possible following the described Mes_4Cu_4 route.[51] After work-up of the reaction mixture,[51] a yellow powder is obtained. Single crystals, suitable for X-ray measurements are collected after diffusion of Et_2O into a solution of the complex in MeCN.[51] The crystal structure shows a mononuclear complex, where the copper ion is coordinated by the two NHC carbene-C atoms in an almost linear fashion and the metal center is only weakly interacting with the pyridinyl nitrogen atoms. In 2001, Youngs *et al.*[40] reported the synthesis of the ligand and complexes with this ligand have been published, bearing Ag^{I}[56], Au^{I}[43], Ni^{II}[57], Hg^{II}[58], Pd^{II}[58] and Fe^{II}[59,60] ions. The higher homolog coinange metals showed disilver(I) and digold(I) complexes in contrast to the mononuclear copper complex **6**. The macrocyclic copper(II) NHC complex shows a saddle-shaped conformation of the ligand scaffold.[61] The central copper(II) ion is coordinated by two pyridinyl groups and two NHCs. This leads to contraction of the Cu–N bond distance of almost 0.6 Å (Cu^{II}–N = 2.09 Å), in agreement with the tendency of copper(II) ions to get stabilized by less polarized donor atoms. The copper(II)–C bond slightly increased compared to complex **6**.

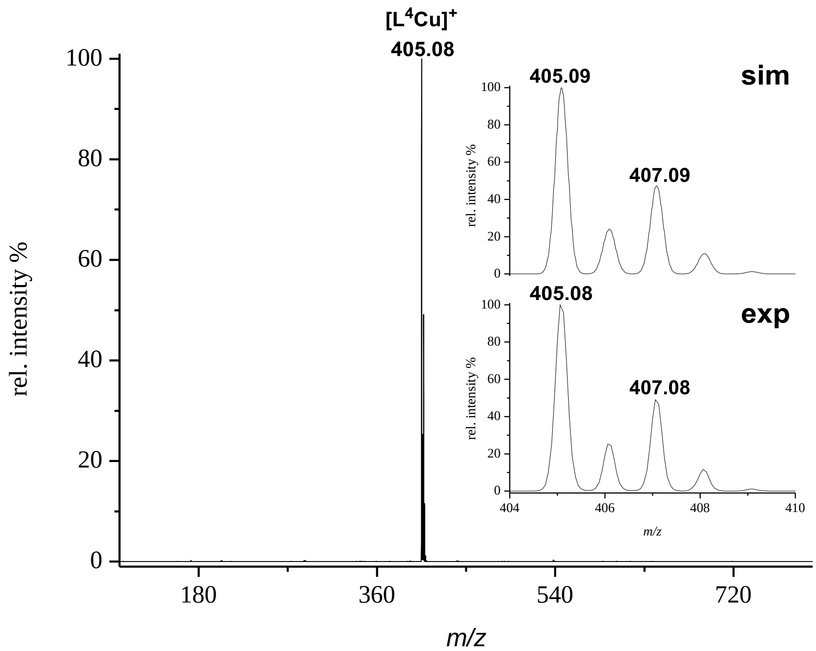

Figure 2.16: ESI-MS of complex **6** in MeCN. The inset shows the simulated (**top**) and the experimental (**bottom**) and isotopic distribution pattern for the peak at *m/z* = 405 (100) for **$[L^4Cu]^+$**.

Single crystals of complex **6** are dissolved in MeCN and an ESI-MS is measured. peak at *m/z* = 405 (100) is observed, according to **$[L^4Cu]^+$** (**Figure 2.16)**. Only one Detailed NMR spectroscopic investigations confirm the assignments in **Figure 2.17**[51] and ^{1}H DOSY NMR experiments indicate the existence of a mononuclear complex in solution (see experimental section). Only one set of signals in the ^{1}H NMR spectrum is observed (**Figure 2.17**). An apparent D_{2h} symmetric complex is obtained in MeCN-d_3 as a result of fast ring flip of the complex scaffold (**Scheme 2.3**). VT ^{1}H NMR experiments confirm this symmetry over a broad temperature range between 353 K to 233 K. No significant diastereotopic splitting of the CH_2 groups H^4 is observed concomitant with no observation of an energy barrier for the ring flip. This is in agreement with the long distance between the pyridinyl group to the copper ion in the molecular structure in solid state (2.71 Å)[51] and the weak interaction in solution.

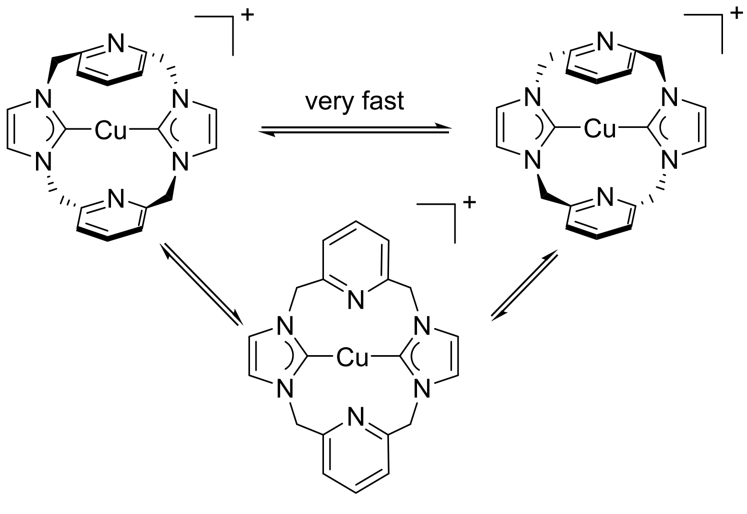

6

Scheme 2.3: An apparent D_{2h} symmetry of complex **6** is observed in the ^{1}H NMR spectrum in MeCN-d_3 as a result of fast ring flip.

The $^1H^{15}N$ HMBC spectrum shows a shift of the pyridinyl N at –67.45 ppm (**Figure 2.18**) and a shift of $\Delta\delta(N) = 10$ ppm compared to the free ligand underlines this weak interaction. In contrast to this Meyer and Kühn observed an energy barrier in the corresponding macrocyclic mono-iron(II) bisacetonitrile complex.[59] On the other hand, no change in the saddle shaped conformation was observed in the cyclic nickel complex over a broad temperature range.[57]

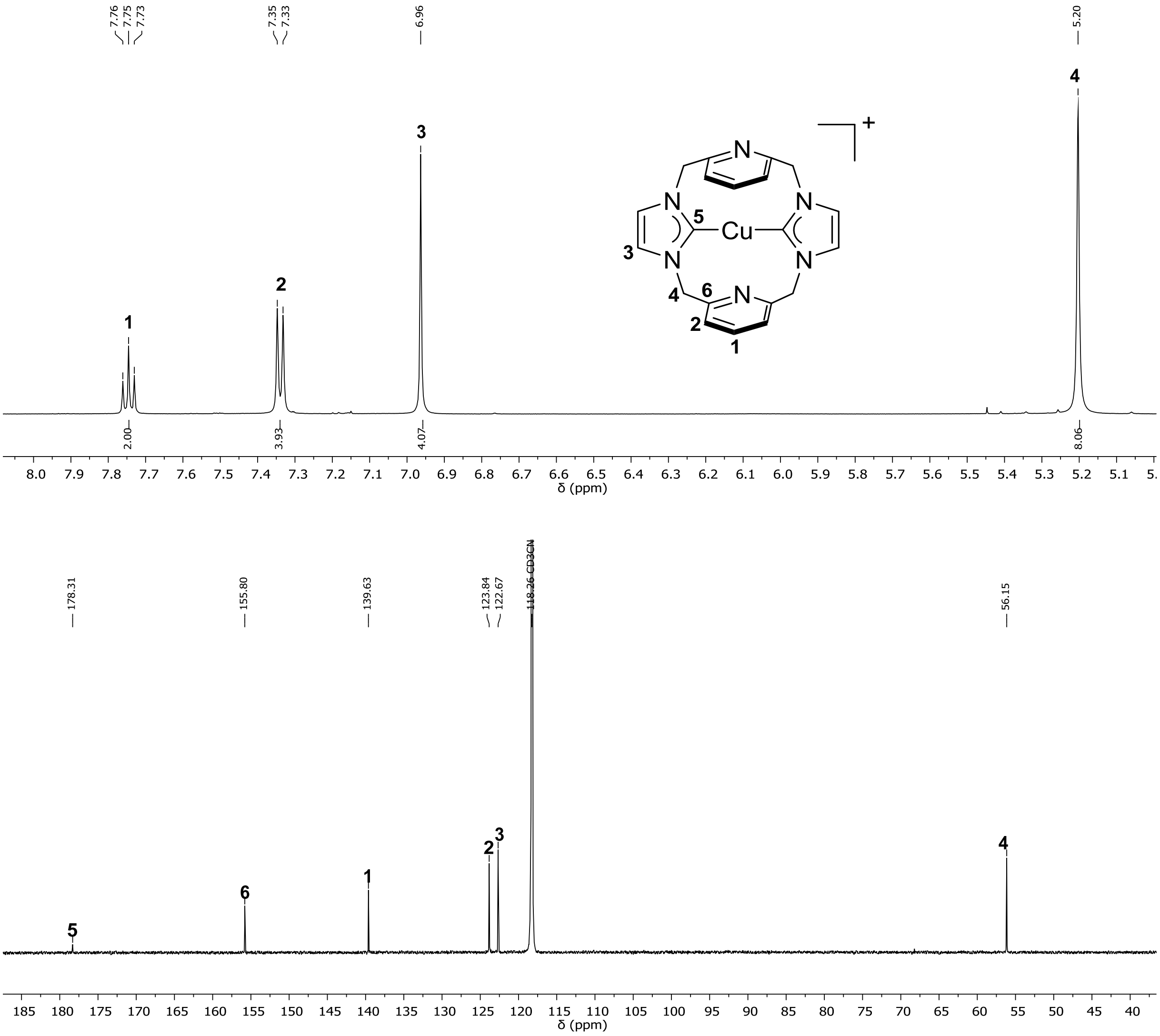

Figure 2.17: Top: ^{1}H NMR spectrum of complex **6** in MeCN-d_3 at 298 K (500 MHz) showes one set of proton signals. The singlet of the CH$_2$ groups H^4 are in agreement with an apparent D_{2h} symmetry of the complex in solution. **Bottom:** ^{13}C{^{1}H} NMR at 126 MHz shows the shift of the carbenes at 178.3 ppm.

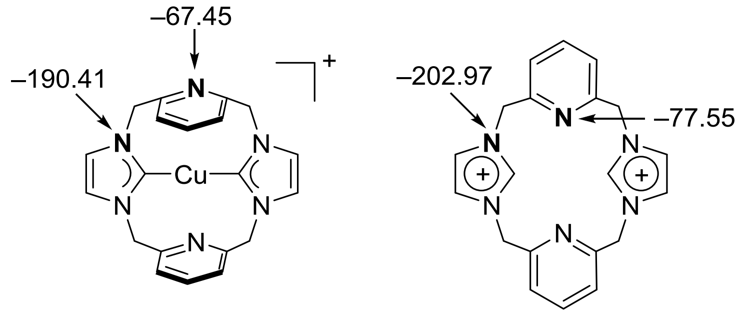

Figure 2.18: ^{15}N NMR shift in **6** based on ^{1}H^{15}N HMBC spectroscopy and right ^{15}N shifts in the free ligand.

CV of **6** was performed in MeCN (1.0 mM complex solution in 0.1 M NBu$_4$PF$_6$) at room temperature (see **appendix**, **Figure A.2.1**) and results are in agreement with the previously described *EC* meachnims of the copper(II) complex by Klawitter[61] as result of the conformational change of the ligand by change of the redox stage of the metal from Cu^{I} to Cu^{II} and *vice versa* (**Scheme 2.4**).

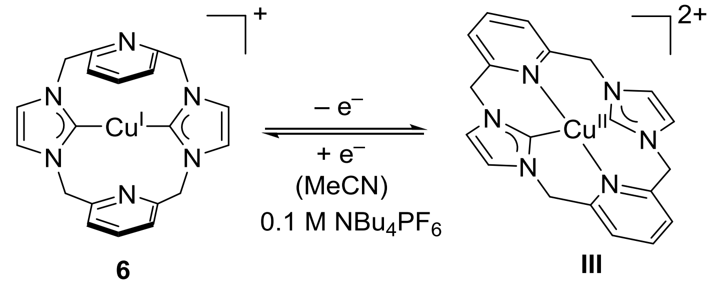

Scheme 2.4: Oxidation process of **6**. First oxidation results in the formation of the copper(II) NHC complex **III** concomitant with rearrangement of the ligand scaffold.

A comparison of the UV-vis spectra of **6** and **III** shows markedly differences. In the UV-vis spectrum of complex **6** one band at 331 nm ($\varepsilon = 2.17\cdot10^3\ M^{-1}\cdot cm^{-1}$) is observed, whereby in the copper(II) complex **7** two bands at 379 nm ($\varepsilon = 0.44\cdot10^3\ M^{-1}\cdot cm^{-1}$) and 485 nm ($\varepsilon = 0.15\cdot10^3\ M^{-1}\cdot cm^{-1}$) are obtained (**Figure 2.19**).

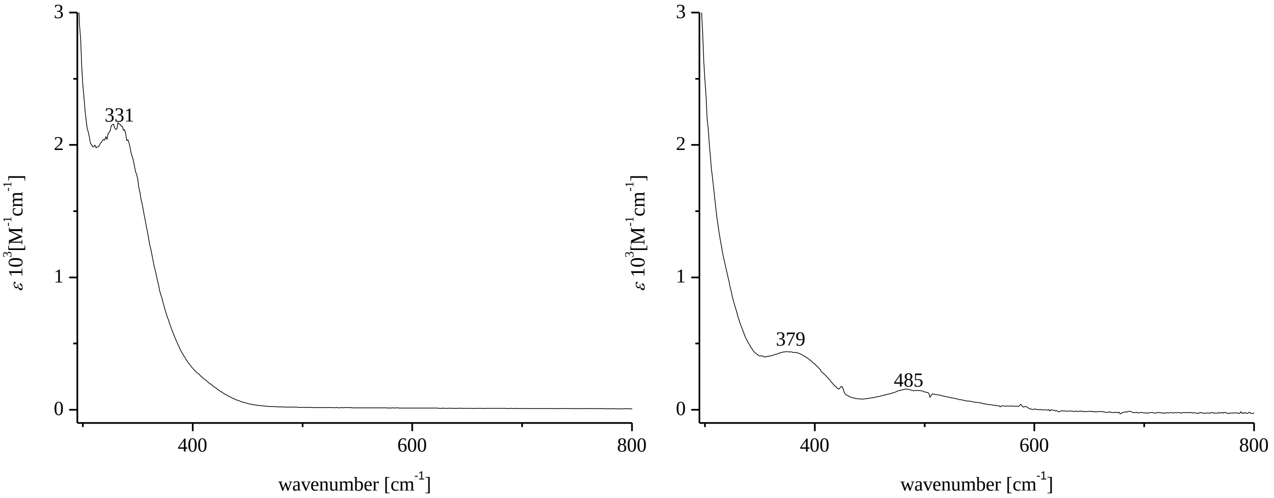

Figure 2.19: **Left:** UV-vis spectra of complex **6** at –35°C in MeCN shows one band at 331 nm and **right:** Two bands at 379 nm and 485 nm were observed in UV-vis spectrum of complex **III** at –40 °C in MeCN.

2.2.4 Dynamic of a macrocyclic dicopper(I) NHC complex in solution

7 was obtained by reaction of calix[4]-2*H*-imidazolium[2]pyridine with Mes_4Cu_4 in MeCN. After work-up of the reaction mixture (see experimental section) a pale yellow solid was obtained. Single crystals of **7** suitable for X-ray diffraction are collected, after diffusion of Et_2O into a complex solution in MeCN.

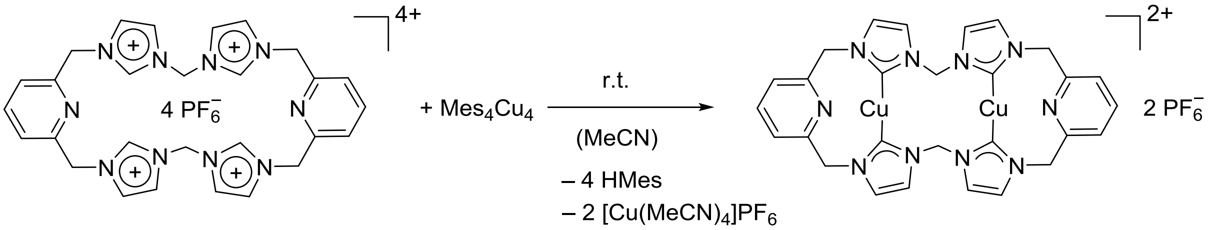

$H_4L^4(PF_6)_4$

7

Scheme 2.5: Reaction of calix[4]-2*H*-imidazolium[2]pyridine with Mes_4Cu_4 results in the formation of complex **7**.

7 crystallizes in the space group $P\overline{1}$. The molecular structure in solid state shows in agreement with the analogous silver(I) complex[62] a dinuclear complex, in which the metal ions are coordinated by two carbene-C atoms in an almost linear fashion (C13–Cu1–C2 175.9°) (**Figure 2.20**). In the corresponding silver complex a more acute angle of 169.9° is observed. **7** shows a Cu(1)/Cu(1') distance of 4.00 Å. This distance is quite large in comparison to the disilver complex (2.87 Å), which shows argentophilic interactions.[62] In the molecular structure in solid state, the ligand scaffold is twisted around the N(1)–Cu(1)–Cu(1')–N(1') axis (**Figure 2.20**, **right**). Cu(1)–C(2) and Cu(1)–C(13) distances are 1.90 Å, in agreement with in the literature known copper(I) carbene complexes.[36,63] The Cu(1)····N(1) distance of 2.26 Å indicates a weak interaction between these two atoms. In general, metal-pyridinyl bond lengths range between 1.9 Å and 2.1 Å.[26,64,65] Relevant bond lengths are summarized in **Table 2.1**. The ESI-MS shows two peaks at *m/z* = 314 (100) for **$[L^5Cu_2]^{2+}$** and *m/z* = 773 (22) for **$[L^5Cu_2(PF_6)]^+$** (**Figure 2.21**).

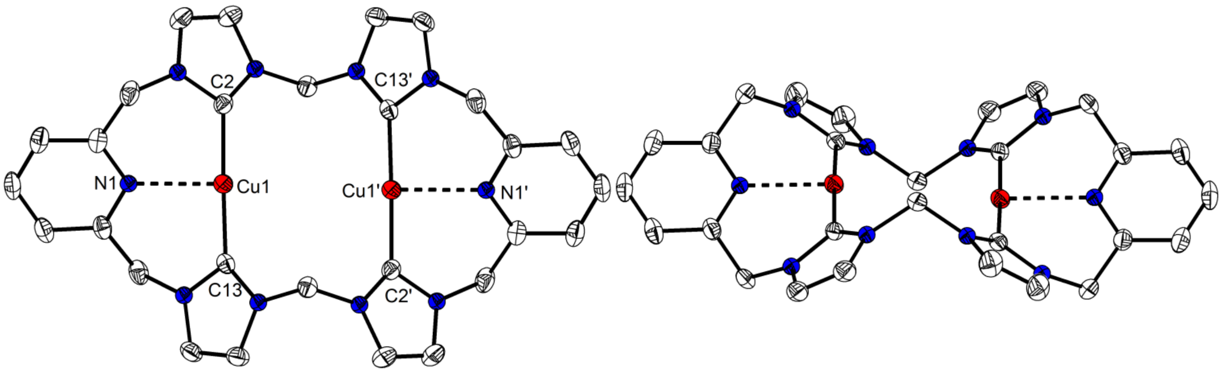

Figure 2.20: Molecular structure (50% probability thermal ellipsoids) of the cationic part of **7**. H atoms are omitted for clarity.

Table 2.1: Selected bond lengths [Å] and angles [°] of complex **7**.

Atoms	Bond lengths
Cu1–C13	1.90(0)
Cu1–C2	1.90(3)
Cu1–N1	2.25(7)
C13–Cu1–C2	175.9
C13–Cu1–N1	92.04
C2–Cu1–N1	89.67

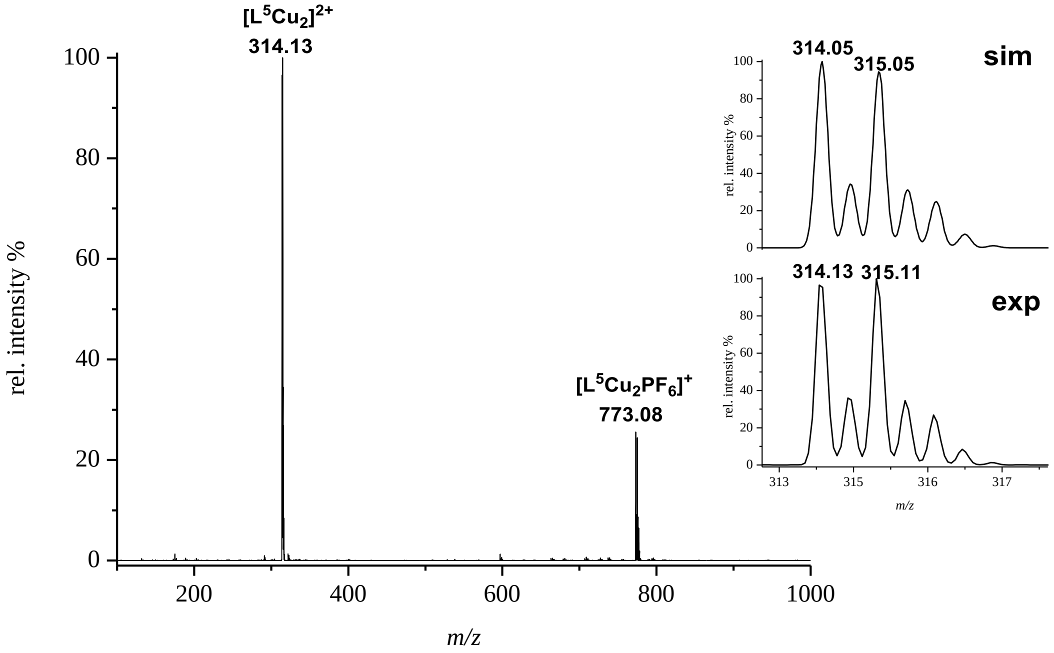

Figure 2.21: ESI-MS of **7** in MeCN. The inset shows the experimental and simulated isotopic distribution pattern for the peak at *m/z* = 314.05 (100) for $\mathbf{[L^5Cu_2]^{2+}}$.

^{1}H NMR spectrum of **7** in MeCN-d_3 shows one set of signals, with a diastereotopic splitting of the proton resonances H^5 of the two CH$_2$ groups. In view of the molecular structure in solid state one doublet of the AX spin system in the NMR spectrum is assigned to the two protons which are pointing towards the outside of the ring and the second doublet to the resonances of the two inner protons, orientated to the inside ring. In the latter, the protons are more shielded because of proximity to the two copper(I) ions resulting in a high-field shift of 426 Hz (**Figure 2.22**).

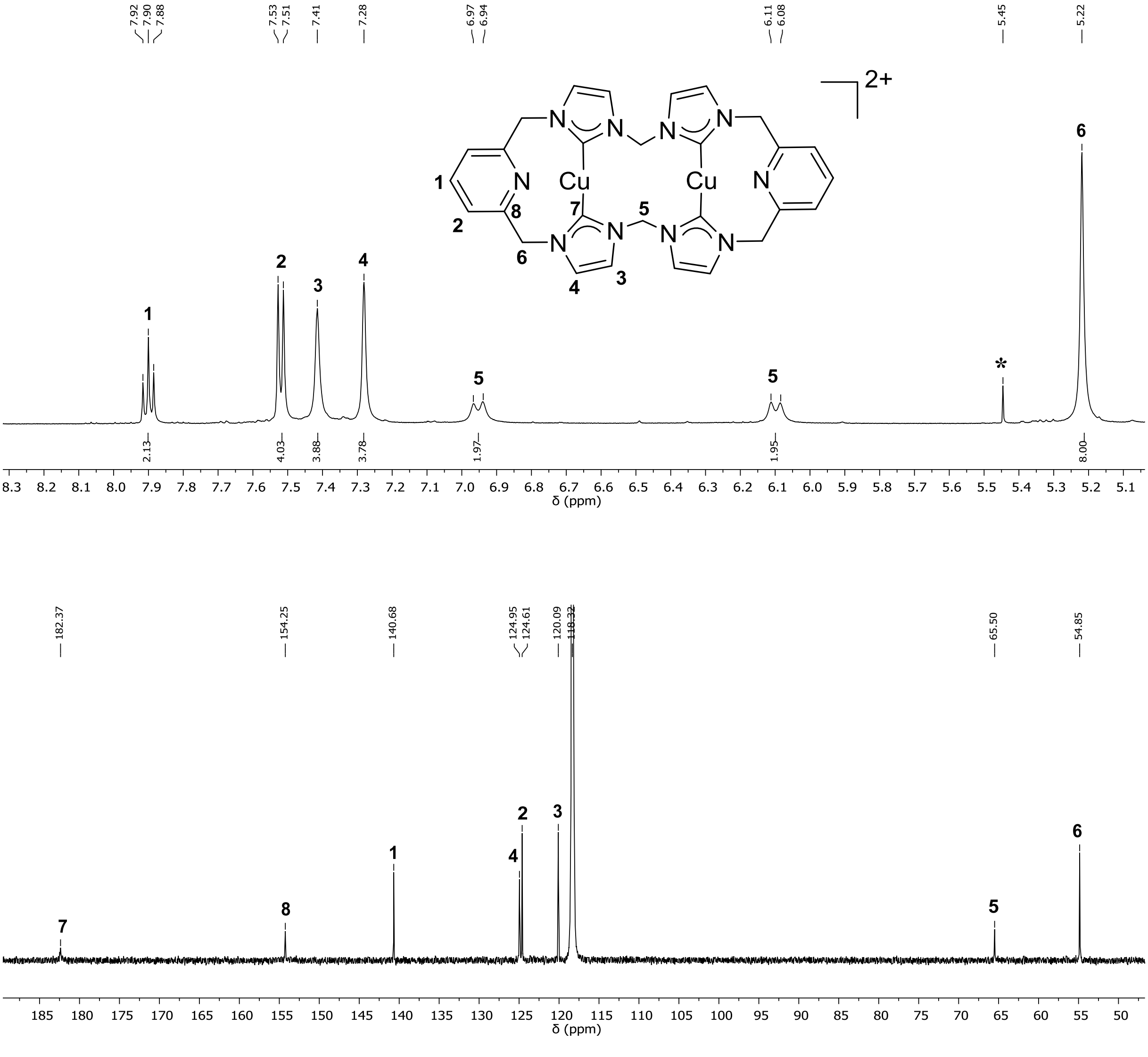

Figure 2.22: Top: ^{1}H NMR spectrum of **7** in MeCN-d_3 at 298 K and 500 MHz shows a diastereotopic splitting of the proton resonances H^5 of the CH$_2$ groups and a shift of the CH$_2$ groups of 426 Hz. (*****) shows DCM as an impurity. **Bottom:** In ^{13}C{^{1}H} NMR spectrum a carbene-C peak at 182.3 ppm and one set of signals are observed.

VT ^{1}H NMR spectra of complex **7** in MeCN-d_3 show a coalescence temperature of the proton resonances H^5 at T_c = 353 K (**Figure 2.23**) which allows to determine the rate constants k of the ring flip (**Scheme 2.6**) in the C_{2h} symmetric complex at different temperatures by line shape analysis of the CH_2 peaks H^5 in the ^1H NMR spectra (see experimental section 10.2.2).[66,67] The rate constants at different temperatures are listed in **Table 2.2**. Based on the temperature dependence of the rate constant k and an Eyring plot (**Figure 2.24**, **left**), an activation enthalpy of $\Delta H^‡ = 45.9\ kJ{\cdot}mol^{-1} \pm 0.92\ kJ{\cdot}mol^{-1}$ and an activation entropy of $\Delta S^‡ = -65.7\ J{\cdot}mol^{-1}{\cdot}K^{-1} \pm 1.3\ J{\cdot}mol^{-1}{\cdot}K^{-1}$ are determined, and by an Arrhenius plot the activation energy $E_a = 48.5\ kJ{\cdot}mol^{-1} \pm 0.97\ kJ{\cdot}mol^{-1}$ is obtained (**Figure 2.24**, **right**). A comparison of the kinetic data with similar copper, silver or gold complexes is not possible, because comparable data are unavailable in the literature.

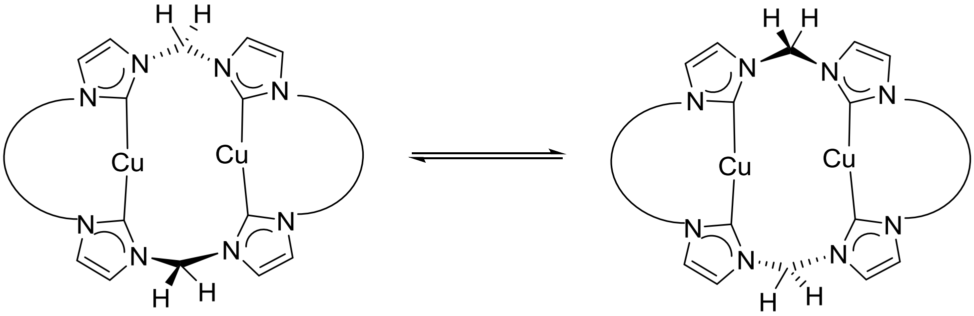

Scheme 2.6: Ring flip in the C_{2h} symmetric complex **7**.

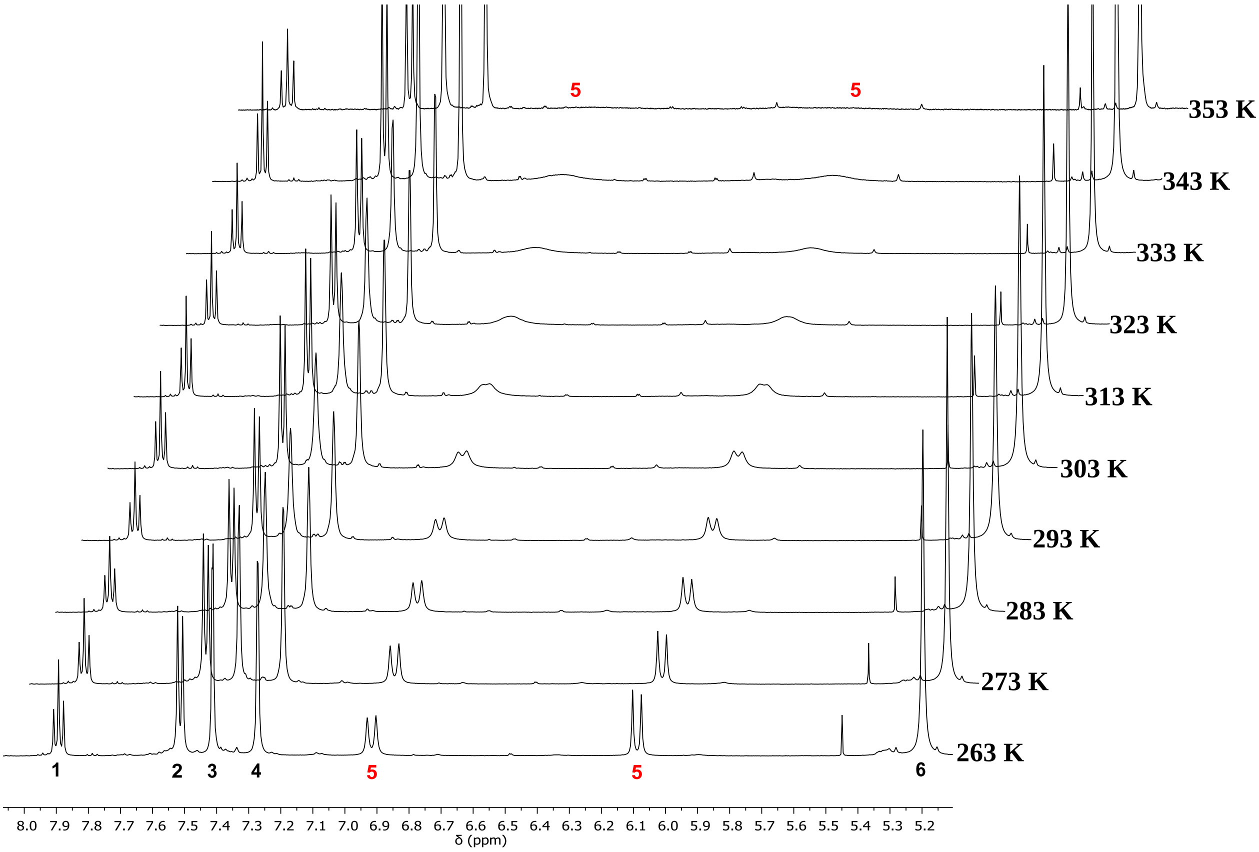

Figure 2.23: VT ^1H NMR spectra of **7** in the temperature range between 353 K and 263 K. The coalescence point of the AX spin system is approximately 353 K.

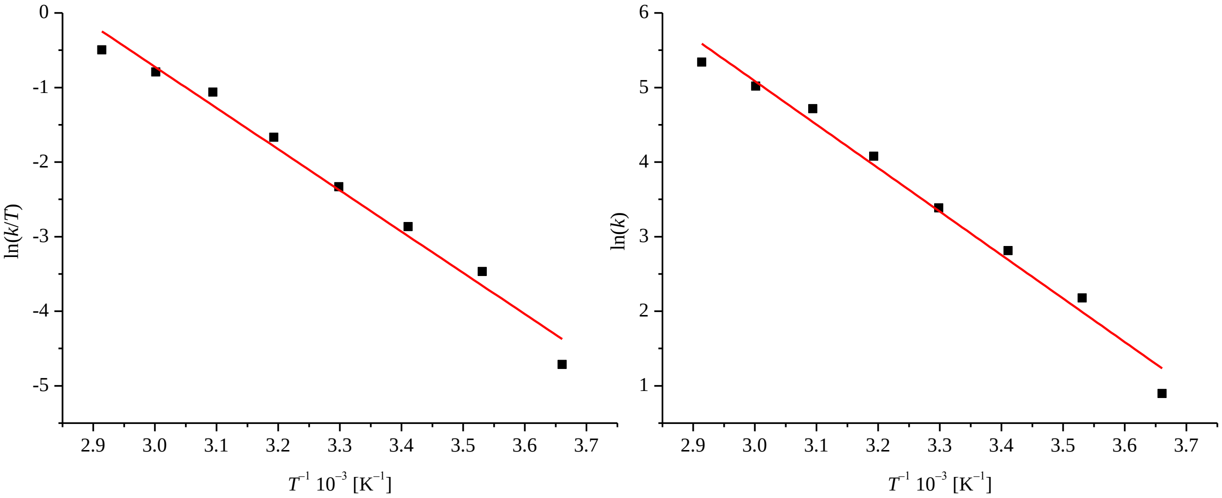

Figure 2.24: Eyring plot (**left**) and Arrhenius plot (**right**) based on the line broadening analysis of the diastereotopic splitting of the CH_2 groups H^5 in a temperature regime between 343 K and 273 K. An activation enthalpy of $\Delta H^{\ddagger} = 45.9 \pm 0.92$ kJ·mol^{-1} and an activation entropy of $\Delta S^{\ddagger} = -65.7 \pm 1.3$ J·mol^{-1}·K^{-1} were determined ($R^2 = 0.98$) as well as an activation energy of $E_a = 48.5 \pm 0.97$ kJ·mol^{-1} ($R^2 = 0.98$).

Table 2.2: Rate constants at different temperatures derived by line shape analysis of the ^{1}H NMR peaks of the CH_2 group H^5.

T [K]	$(\Delta\upsilon_e)_{1/2}$	$(\Delta\upsilon_0)_{1/2}$	k [s^{-1}]
343.2	69.22	2.77	208.76
333.2	50.85	2.77	151.05
323.2	38.27	2.77	111.51
313.2	21.56	2.77	59.03
303.2	12.16	2.77	29.50
293.2	8.08	2.77	16.67
283.2	5.58	2.77	8.84
273.2	3.55	2.77	2.45

Furthermore CV of **7** in MeCN (1 mM, 0.1 M NBu_4PF_6 in MeCN) shows a *quasi* reversible redox processes at –0.13 V and an irreversible redox event at 0.26 V *vs.* Fc/Fc$^+$ (**appendix**, **Figure A.2.2**).

2.3 Conclusion and Outlook

The presented results show the versatility of mesitylcopper(I) as a precursor for copper(I) carbene complex synthesis. Beside the previously presented synthesis of the complexes **3-6**, also the synthesis of **7** was successful, broadening the scope of new Cu^I NHC complexes by the mesitylcopper route. All complexes showed diverse structural properties. It was previously shown, that by variation of the central bridge (methylene, propylene or pyridinyl) different coordination motives and different nuclearities of the resulting copper complexes can be obtained. In this work it was shown that **3** and **4** strongly rearrange in MeCN from oligonuclear complexes to dinuclear copper(I) complexes.

The pyridinyl-bridged dinuclear copper(I) complex **5** shows a dynamic behavior in solution, monitored by VT ^1H NMR spectroscopy. At room temperature and elevated temperatures a three center two electron interaction of the internal pyridinyl groups with the copper(I) ions is observed. In contrast to this, at lower temperatures the copper(I) cores interact with the peripheral pyridinyl groups. This rearrangement affects the proton resonances in such a way, that chemical shift changes of up to 1 ppm are observed.

In **6**, a high flexibility of the ligand scaffold is monitored by ^1H NMR spectroscopy. No energy barrier over a broad temperature range is obtained, due to weak interaction of the pyridinyl groups with the copper(I) ion and a fast ring flip, which is reflected by an apparent D_{2h} symmetry of the complex in the ^1H NMR spectrum. Herein presented CV of complex **6**, as well as CV measurements of the copper(II) complex, confirmed a *EC* mechanism for the oxidation of the copper(I) complex or the reduction of the copper(II) complex. This observation is based on rearrangement of the ring by coordination or de-coordination of the pyridinyl groups to the copper center. In the future, this configurational change can be further analyzed by CV simulations at different complex concentrations, to obtain an estimated $E_{1/2}$ potential and data of the ring flip.

In contrast to **6**, **7** shows a coalescence temperature at approximately 353 K in MeCN and the activation parameters ($\Delta H^{\ddagger}$, $\Delta S^{\ddagger}$, E_a) for the ring flip of the complex are determined.

These five examples show the importance of detailed studies of copper(I) NHC in both solid state and in solution to understand the coordination environment of the metal ions and composition of the metal complexes in different states of matter. The ^1H DOSY NMR spectroscopy has several constraints and can only give an average picture of the movement of the molecules in solution, limited by the relaxation times and correlation time. Furthermore, the influence of the counter ion (here: PF_6^-) by possible ion pairing with the cationic copper complex is not investigated in this thesis. This interaction can have consequences on the dynamics of the molecule in solution and can change the ^{1}H DOSY NMR spectra. Additional experiments are necessary to prove the theory of a certain ion pairing.

3

Novel hybrid pyrazole/tetra-NHC ligand scaffolds for di- and multinuclear metal complexes

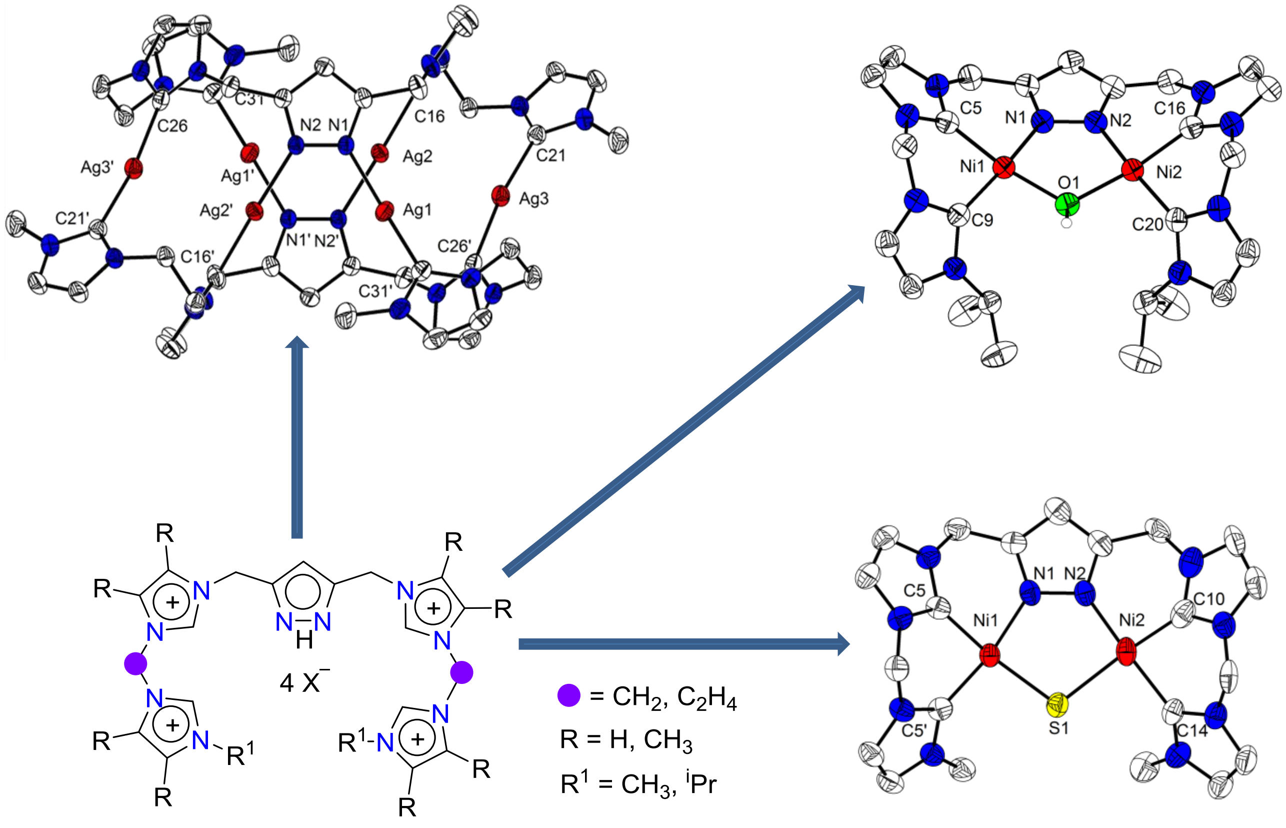

Abstract: Since the first modified pyrazolate-bridged dinuclear metal(II) complexes in 1985, this structural motive gained enormous interest and is one of the most popular systems for enabling the incorporation of two metals in one ligand scaffold with short intermetallic distances. Several complex systems are developed, capable of activating small molecules. On the other hand *N*-heterocyclic carbene complexes are found in a wide range of application, for instance in material science, medical chemistry or catalysis. The combination of both motifs, pyrazolate bridge and NHC donors in a single ligand scaffold is a promising and challenging task. However, so far only thirteen publications are known to report such systems, mainly related to their basic coordination chemistry. In the following chapters a novel hybrid pyrazole/tetra-NHC ligand and its modifications as flexible ligand scaffolds for building up di- and multinuclear metal complexes are presented. In this section the focus will be on new multinuclear silver(I) and copper(I) NHC complexes.

Main parts of the results presented in this chapter were published:

S. G. Resch, S. Dechert, F. Meyer, *Z. Anorg. Allg. Chem.* **2019**, *645*, 605.

3.1 Introduction

Cooperative effects[68,69] in di- and multinuclear metal systems play a key role in many enzymatic reactions.[70–72] Such cooperative effects can lead to more efficient and selective transformations, conformational control of substrates, higher local reagent concentration at the metal centers and stabilization of reactive species and complex intermediates.[73] Additionally, they can facilitate the accessibility of bimolecular reactions and be used to overcome entropic control.[73] The transfer of cooperative effects from biological systems to organometallic complexes is of great interest for the scientific and industrial communities. Strategic approaches for exploiting cooperative effects in catalysis have been applied in many reactions, as for example in epoxidation reactions[74] and olefin hydrogenations.[75] Cooperative effects can also play an essential role in the activation of small molecules at organometallic complexes and in the active centers of enzymes.

(Bio-)chemists are fascinated by these structural motives and are designing biomimetic or bioinspired model complexes to provide analytic data for the investigation and the understanding of biochemical and biological processes in nature as well as improving catalytic processes by adopting mechanism and strategies from nature. Since, the first hybrid pyrazolate bridging dinuclear nickel(II) and palladium(II) complexes, reported by Bosnich and coworkers[76] in 1985, this ligand motive gained enormous interest. It is one of the most popular system for enable the incorporation of two metals in a ligand scaffold with short connectivity.[77–79] Such ligands (**Scheme 3.1**) are able to synthesize well-defined bimetallic and multi-metallic complexes having flexible side arms and close metal distances. This can result in metal···metal interactions and hence to useful chemical, physical, catalytic, magnetic, optical and electronic properties.[42,77,78]

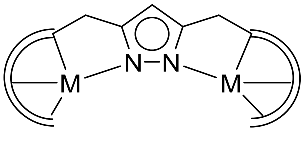

Scheme 3.1: Schematic representation of dinuclear pyrazolate-bridged metal complexes.[77]

Meyer *et al.*[77,78] are working on the development of highly pre-organized dinuclear metal complexes, many of which mediate bioinspired transformations of small substrates. Bioinspired model complexes, based on pyrazolate-bridged ligands are investigated for several enzymes[77,80,81] but also extended porphyrin systems, so called Siamese Twin porphyrins[82] and pyrazolate-bridged catalysts for water oxidation are reported.[83]

Surprisingly, the combination of the central pyrazole unit with *2H*-imidazolium is only mentioned in thirteen publications (**Figure 3.1**). Hence there is scope for the further development of pyrazole/imidazolium hybrid ligands with respect to thousands of literature known mono- and dinuclear metal NHC complexes and their reported manifold properties and applications, for instance in catalysis, material science and medicinal chemistry.

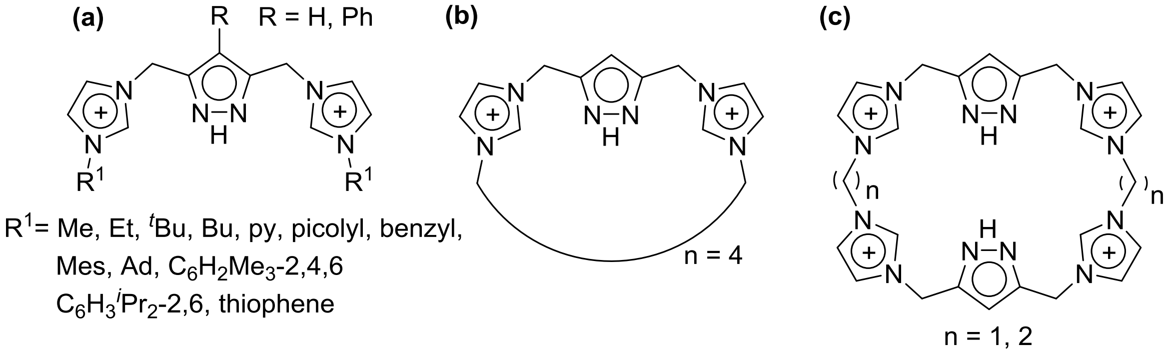

j **k** **l**

Figure 3.1: Overview of previously reported hybrid pyrazole/imidazolium ligands.[136,139-143]

In 2007, Chen and coworkers[42] published the first hybrid pyrazole/imidazolium ligand **j** (**Figure 3.1 (a)**) and its conversion to the corresponding silver and gold complexes. In the following years modifications of this ligand scaffold, synthesis of further silver complexes and investigation of their structural and physical properties mainly with respect to their luminescent properties were reported by Chen[84,85] (**Figure 3.1 (a)/(b)**) and Meyer *et al.*[86,87] (**Figure 3.1 (a)**). In addition, these complexes are tested as transmetallation reagents. The silver(I) pyrazolate/NHC complexes show a variety of structural motifs. Supramolecular silver(I) complexes with the ligand systems **j** and **k** were synthesized, bearing four or six Ag^+ with two to four ligands.

Supramolecular coinage NHC complexes have also found applications in host guest chemistry. In 2016 Pöthig *et al.*[88] showed that the reaction of silver(I) oxide with ligand **l** (**Figure 3.1 (c)**) results in an octanuclear supramolecular complex, a so called pillarplex[89] (**Figure 3.2 (a)**). Eight silver ions are forming the central ring, capped on top and bottom by two macrocycles. This tubular structure allows the hosting of small molecules, for instance 1,8-diaminooctane and the corresponding silver and gold complexes show photoluminescence.

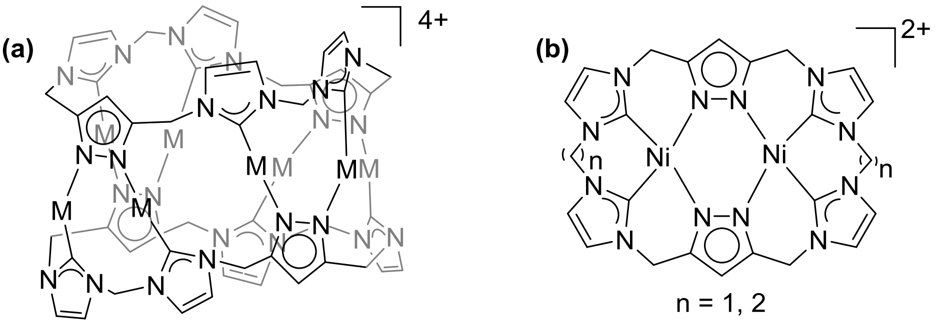

IV **V**

Figure 3.2: (a) Silver and gold pillarplexes published by Pöthig *et al.*[88] showing a tubular structure. **(b)** dinuclear nickel(II) complexes with methylene or ethylene linked NHCs.[90]

In 2017 Pöthig and coworkers[91] entered the field of molecular machines with their coinage di-pyrazolate/tetra-NHC complexes. They tested their pillarplexes as mechanical interlocked molecules (MIMs)[92,93], by synthesis of the corresponding rotaxanes. New features of this $[Ag_8(L^{Me})_2][2]Rot(OTf)_4$ complex **IV** are the easy transmetallation by gold(I) chloride and the pH dependent reversible acid/base assisted generation of the metal free rotaxane $[(\mathbf{l}^{Me})_2[3]Rot(OTf)_8$. Decrease of the pH results in the conversion of the metal free rotaxane, whereby an increase of the pH leads to the recovery of the multinuclear silver(I) complex.

The methylene-bridged macrocycle itself can function as a hydrogen bond sensor, by capturing for instance MeCN in the cavity of the ligand *via* hydrogen bond interactions.[94] Complexation of the ligands by nickel result in dinuclear complexes **V** (**Figure 3.2 (b)**) and the molecular structures in solid state show a saddle shaped conformation.[90,94] Inclusion of a halide (Cl^- or Br^-) under formation of a supramolecular host-guest complex in a tennis ball like fashion, a so called capsoplex is feasible by the macrocyclic ethylene-bridged dinickel(II) NHC complex.[90] Open-chained variations of this dinickel(II) pyrazolate-bridged complexes were already published by Chen *et al.*[64] and Waymouth and coworkers[95] in 2008. Reaction of the methyl-substituted ligand (**Figure 3.2 (a)**) results in self-assembly of two ligands and two nickel(II) ions. The use of the corresponding picolyl or 2-pyridinyl-substituted ligands lead to hydroxido-bridged dinickel(II) complexes (**Figure 3.3 (a)** and **(b)**). The latter complexes proved to be efficient catalysts for Suzuki-Miyaura or Kumada-Corriu cross coupling reactions.[64] The corresponding dicopper(II) μ-OH complex (in analogy to **Figure 3.3 (b)**) can catalyze the oxidative amination of arylboronic acids.[85]

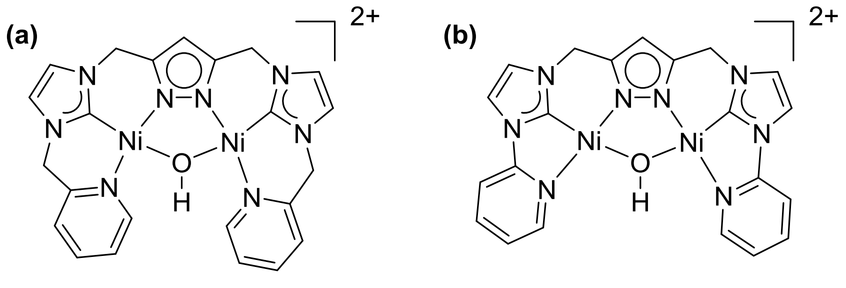

VI VII

Figure 3.3: Two dinickel(II) μ-OH complexes which are able to undergo Suzuki-Miyaura or Kumada-Corriu cross coupling reactions.[64]

In addition to first row transition metal complexes of the open-chained pyrazole/di-*2H*-imidazolium ligand, also late transition metal complexes are known. The successful synthesis of the corresponding Rh[95,96], Ir[95], Pd[97–99], and Ru[96] complexes were reported and the corresponding complexes were characterized.

To this day the chemistry of the pyrazolate/di-*N*-heterocyclic carbene complexes is limited to some basic coordination chemistry, luminescence investigations, supramolecular chemistry and two catalytic applications. The motivation of the herein presented results is to further explore the chemistry of this field of pyrazole/imidazolium ligands, and to combine the pyrazole unit for bio-inspired reactivity and metal cooperativity, with well-established properties of *N*-heterocyclic carbenes. In order to achieve this ambitious goal, a ligand system is designed which is able to coordinate two or more metal ions in close proximity. It is at the same time able to stabilize metals by three instead of just two chelating positions in a pincer-like fashion. This coordination motif can achieve a higher stabilization of the incorporated metals and features probably the stabilization of reactive intermediates and the coordination of ions in the cavity between the two metal centers.

Herein, the intrinsic properties of the ligand, the prototropy of the pyrazole NH and modifications of the ligand are presented. In addition, supramolecular coinage complexes of Cu^I and Ag^I are shown and its coordination chemistry is explored. Beginning in **chapter 4** dinuclear nickel complexes are presented and its intrinsic properties and its behavior towards small molecules, bases and acids are investigated (**chapter 5-7**). Also the electro-catalytic proton reduction by sulfur-bridged dinickel NHC complexes is presented in **chapter 9**.

3.2 Results and Discussion

3.2.1 Synthesis and characterization of new hybrid ligand scaffolds

In order to build up a ligand scaffold which allows the coordination of metal ions in a preorganized fashion, it was decided to combine four imidazolium units with a pyrazole unit. **Scheme 3.2** shows a novel pyrazole-bridged tetra-2*H*-imidazolium scaffold, which is modified at the labeled positions to tune the properties of the ligand.

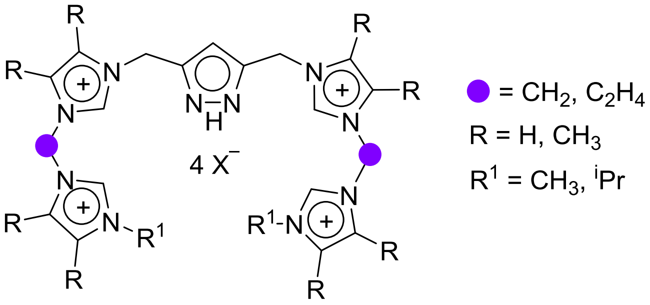

Scheme 3.2: Presentation of a novel 3,5-tetra-(2*H*-imidazolyl)-pyrazole ligand scaffold. The ligand is modified at the labelled positions; (●) variation of the distances between the imidazolium units (methylene or ethylene bridge); R^1 tuning of steric demand by variation between CH_3 or *iso*-propyl group; R: alkyl groups or H atoms at the 4/5 positions of the imidazolium-backbones.

The synthesis of different pyrazole-bridged ligands is already mentioned in several publications.[82,83,100–102] In the literature mainly two strategies are described. One is the step by step build-up of the side arms under formation of the central pyrazole building block *via* the corresponding diketone in the final step.[83] A second synthetic approach includes first the synthesis of a functionalized pyrazole unit, secondly the build-up of the side arms and finally fusion of the central unit with the side arms.[82,100–102] The synthesis of a new ligand scaffold **$[H_5L^6](PF_6)_4$**, first presented in this work, is achieved following the second route (**Scheme 3.3**).

3,5-bis(chloromethyl)-1-tetrahydropyran-2-yl-pyrazole **x**, is synthesized following an established synthetic protocol, starting from the 3,5-dimethylpyrazole.[76,103] In the next step **x** is transformed into the corresponding 3,5-bis(iodomethyl)-1-tetrahydropyran-2-yl-pyrazole **Y**, by a Finkelstein reaction using potassium iodide in acetone. This procedure was already described by Meyer *et al.*[101] and was later slightly modified in the group of Meyer.[104] Exchange of the leaving group from chloride to iodide at the pyrazole side arms is necessary to facilitate nucleophilic substitution by an imidazole. Waymouth *et al.*[95] already reported in

2008, that nucleophilic substitution of a chlorido pyrazole unit by a functionalized imidazole was not successful.

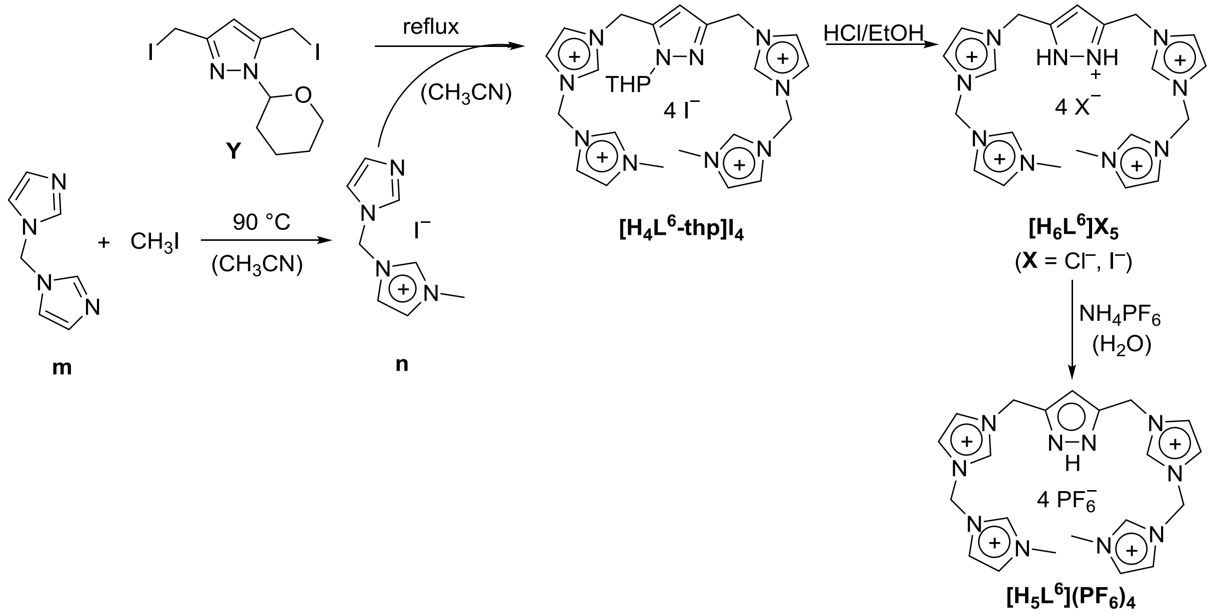

Scheme 3.3: Synthetic route of the ligand **$[H_5L^6](PF_6)_4$**.

To circumvent this problem, they added sodium iodide to the mixture in acetone and heated the mixture to 60 °C for 20 hours, to achieve the reaction. In this case an *in situ* Finkelstein reaction was used for a halide exchange at the side arm of the pyrazole unit, followed by a nucleophilic substitution of the halide ion by the functionalized imidazole. For the synthesis of the ligand **$[H_5L^6](PF_6)_4$**, protection of the pyrazole by a tetrahydropyranyl (thp) unit is also necessary to avoid undesired side reactions.

The side arms are synthesized in a two-step synthesis. First the 1,1'-(bisimidazolyl) methane **m** is synthesized in an improved manner and is characterized. According to a described route from Tejeda and coworkers[105] imidazole reacts with dichloromethane in the presence of sodium hydroxide and tetrabutylammonium bromide, used as a phase transfer catalyst in a dichloromethane/water two phase system at 40 °C. **m** is obtained in high purity by sublimation in a *Kugelrohr* at 140 °C and under high *vacuo* (10^{-5} mbar), confirmed by elemental analysis (see experimental section). Monoalkylation of **m** is achieved by addition of 0.4 equivalents of methyliodide in MeCN at 90 °C for 3 hours. **n** is obtained in high purity by dissolving the obtained raw product in methanol and conducting a fractionated precipitation with Et_2O, whereby in the first fraction the disubstituted bis(imidazolium) salt is obtained. **n** is isolated in the second and third fraction (see experimental section). Remaining **m** is recovered in an atom economical way from small impurities, mainly small amounts of monosubstituted product, by use of the *Kugelrohr* sublimation. **n** is fully characterized by

NMR spetroscopy, ESI-MS and IR spectroscopy, and X-ray crystallography (see experimental section and **appendix**, **Figure A.3.2**). The purity of the compound is confirmed by elemental analysis (see experimental section).

Kühn *et al.*[106] also described a synthesis route for **n** with 20% higher yield, but without any recycle step for the recovery of the starting material and without a full characterization of the product. **[H_5L^6-thp]I_4** is synthesized by adding a small excess (2.1 equiv.) of **n** to **Y** in MeCN and heating the resulting mixture for 4 days. The ^{1}H NMR spectrum in DMSO-d_6 of **[H_4L^6-thp]I_4** shows a diasterotopic splitting of the ligand protons of the two side arms, based on the asymmetry of the compound as a result of the thp protection group (see experimental section). By addition of a 6 M ethanolic HCl solution to a methanol solution of the ligand the thp group can be removed within 30 min. and the protonated ligand [**H_6L^6**]**X_5** (**X** = Cl^-, I^-) is obtained.

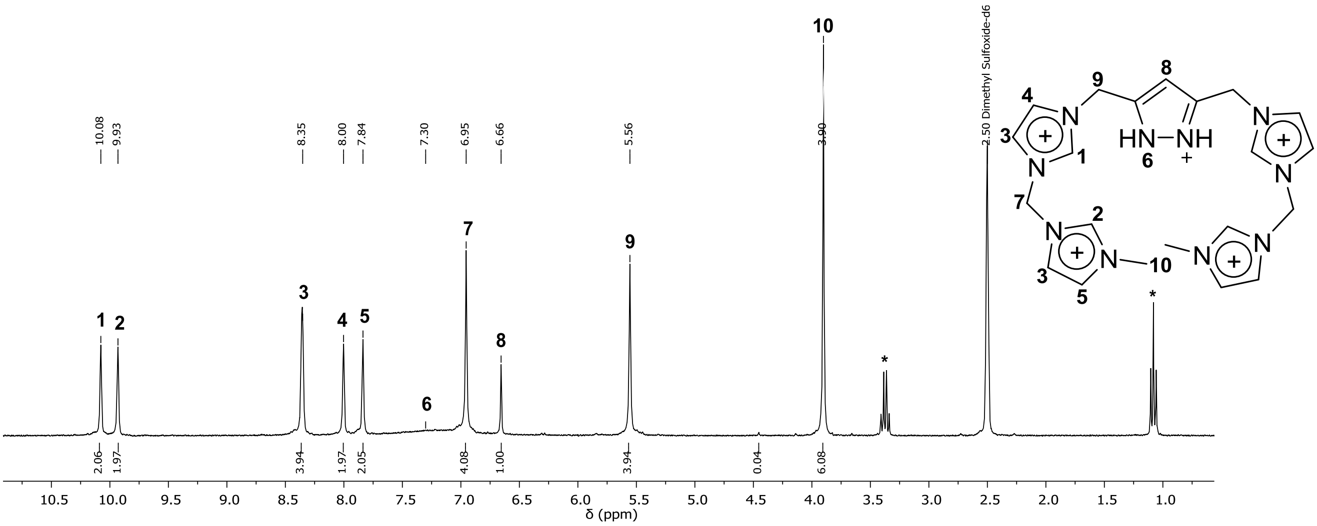

Figure 3.4: ^{1}H NMR spectrum of [**H_5L^6**]**X_5** (**X** = Cl^-, I^-) in DMSO-d_6 at 298 K and 300 MHz. An apparent C_{2v} symmetric molecule can be observed. The NH peak **6** is broadened. (*****) are impurities (Et_2O).

In the ^{1}H NMR spectrum of [**H_6L^6**]**X_5** (**X** = Cl^-, I^-) a molecule with an apparent C_{2v} symmetry is observed (**Figure 3.4**). After neutralization and counter ion exchange, using NH_4PF_6, **[H_5L^6](PF_6)$_4$** is isolated from an aqueous solution in 54% yield. Its purity is confirmed by elemental analysis. Furthermore the existence of the ligand is supported by ESI-MS analysis (**Figure 3.5**, **left**) showing dominant peaks at *m/z* = 855 (19) for **[H_5L^6(PF_6)$_3$]$^+$** and at *m/z* = 355 (100) for **[H_5L^6(PF_6)$_2$]$^{2+}$**, beside fragments of the ligand (*m/z* = 163 and *m/z* = 401).

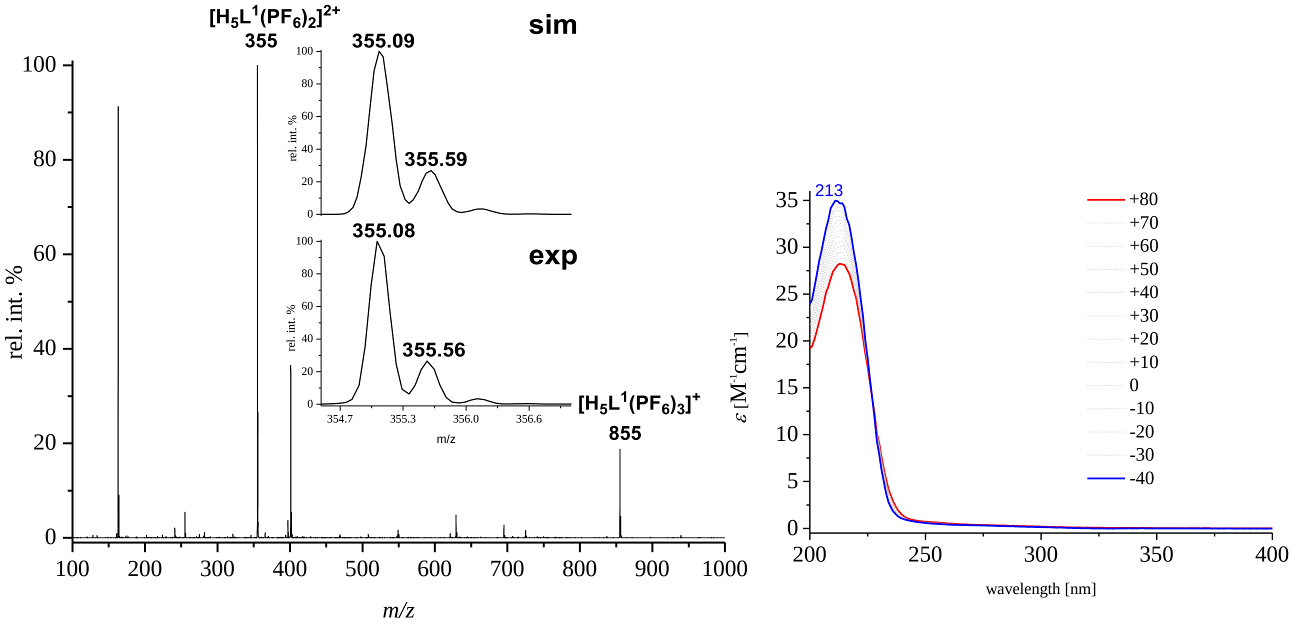

Figure 3.5: Left: ESI-MS of $\mathbf{[H_5L^6](PF_6)_4}$ in MeCN. The inset shows the experimental and simulated isotopic distribution pattern for the peak at *m/z* = 355.09 (100) for $\mathbf{[H_5L^6(PF_6)_2]^{2+}}$. **Right:** VT UV-vis spectra of $\mathbf{[H_5L^6](PF_6)_4}$ in MeCN and in the temperature range between 80 °C and –40 °C. © 2019 JOHN WILEY AND SONS.

In the UV-vis spectrum of $\mathbf{[H_5L^6](PF_6)_4}$ in MeCN one band at 213 nm with an extinction coefficient $\varepsilon = 31.76\ M^{-1}\cdot cm^{-1}$ at 20 °C (**Figure 3.5**, **right**) is observed. A decrease of the temperature from 80 °C to –40 °C results in an increase of this band ($\Delta\varepsilon = 6.73\ M^{-1}\cdot cm^{-1}$) and a light blue shift by 2 nm. The increase of the extinction coefficient by lowering the temperature likely has physical reasons, and also the tautomerism of the NH exchange at the pyrazole is slowed down. Comparison of the absorption spectrum of $\mathbf{[H_5L^6](PF_6)_4}$ with hybrid pyrazole/imidazolium ligands, described in the literature, is not possible, due to lack of available data.[84]

3.2.2 Prototropy of $[H_5L^6](PF_6)_4$

A ^1H NMR spectrum of $\mathbf{[H_5L^6](PF_6)_4}$ in dry MeCN-d_3 at 298 K shows broad resonances of the imidazolium protons H^2, H^4 and H^6 and distinct chemical shifts of the H^{10} resonances of the two CH_2 groups as a result of prototropy at the pyrazole (**Figure 3.6**). However the peak separation of the two CH_2 groups H^{10} is too small to distinguish between them at 298 K. The prototropy, a special form of tautomerism, is based on the movement of one proton, here between the two pyrazole N atoms. This form of tautomerism is well known for pyrazole and pyrazole-based ligands and was already described for some other ligand scaffolds in the literature.[100,107–109]

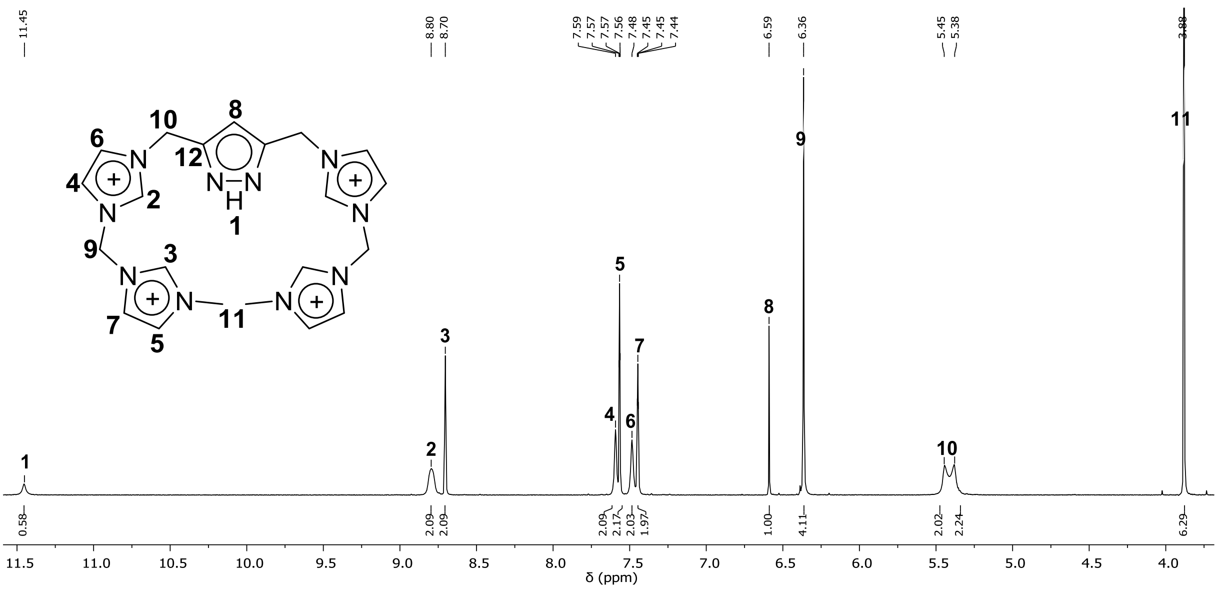

Figure 3.6: ^{1}H NMR spectrum of **$[H_5L^6](PF_6)_4$** at 298 K and 500 MHz in MeCN-d_3 suggests the dynamic NH exchange by the peak separation of the proton resonances H^{10} of the two CH_2 groups.

The proton resonances H^{10} of the CH_2 groups are in close proximity to the N–NH unit and will be affected the most by tautomerism. At 298 K in MeCN the exchange rate k of the prototropy is already in an intermediate or slow exchange range under the coalescence temperature T_c, monitored by the separation of the proton resonances H^{10} of the CH_2 groups. In the $^{13}C\{^1H\}$ NMR spectrum the prototropy at 298 K already leads to a peak separation of the C–4, C–6 and C–10 resonances. For C–10 a separation of 404.5 Hz between the two CH_2 groups is observed (see experimental section). A detailed study of ligands, described in the literature, documented that in some cases also a large peak separation of the CH_2 groups is observed (289.2 Hz to 389.9 Hz).[42,87] Consideration of $^1H^{15}N$ HMBC NMR spectroscopy allows the identification of the half of the nitrogen atoms in the ligand scaffold (**Figure 3.7, left**).

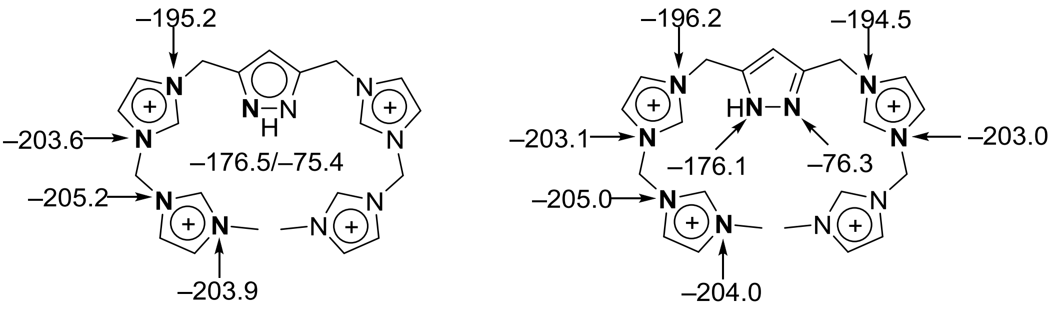

298 K

243 K

Figure 3.7: Chemical shift of the ^{15}N atoms, determined by $^{1}H^{15}N$ HMBC NMR spectroscopy (**left**) at 298 K and full assignment by $^{1}H^{15}N$ HSQC and $^{1}H^{15}N$ HMBC NMR spectra at 243 K (**right**). The chemical shifts of the not bold N atoms are identical to the bold N atoms at the other ligand side arm.

The discrimination between the two pyrazole nitrogen atoms (–176.5 ppm NH^{pz}/–75.4 ppm N^{pz}) by correlation with the H^{pz} peak H^8 is already possible. By lowering the temperature to 243 K and conducting several 2D NMR experiments it is possible to assign all protons of the two side arms. A $^{1}H^{15}N$ HSQC NMR spectrum at 243 K confirmed the correlation of the NH proton H^1 and the connected N atom with a shift of –176 ppm (see experimental section). Based on the $^{1}H^{15}N$ HMBC NMR spectrum at 243 K (**Figure 3.8** and experimental section), the shift of the second pyrazole N atom at –76.3 ppm is confirmed and a clear discrimination between the two CH_2 groups and hence the two side arms is possible (**Figure 3.8**). The obtained chemical shifts of the two pyrazole N atoms are in the range of the chemical shifts of a related *tacn*/pyrazole hybrid ligand measured in MeCN-d_3 (–174.3 ppm for NH and -87.2 ppm for N)[100] and shifts of unsubstituted pyrazole in DMSO-d_6, described in the literature (–173.1 ppm for NH and –79.8 ppm for N).[110,111] In addition, $^{1}H^{15}N$ HMBC NMR spectroscopy allows the discrimination of all ^{15}N chemical shifts in the ligand system (**Figure 3.8**). To the best of my knowledge no ^{15}N NMR assignments of the nitrogen atoms in previously described imidazolium/pyrazole ligands were performed.

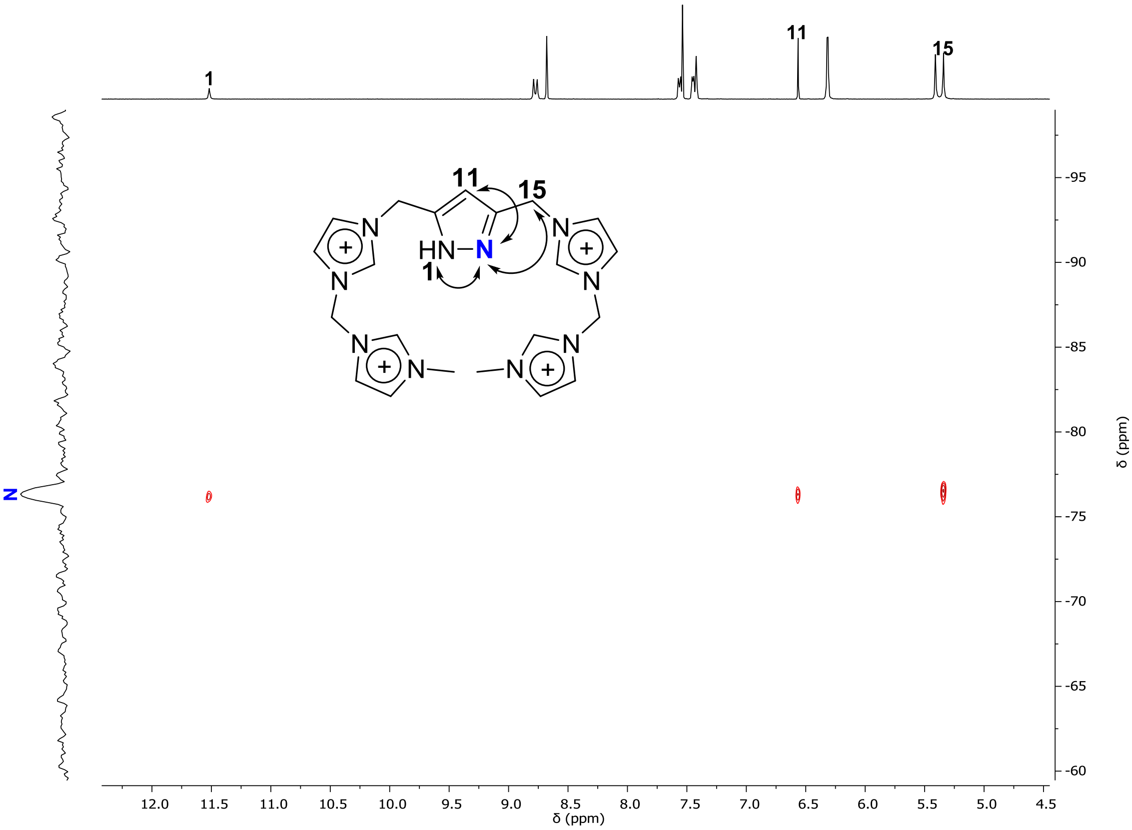

Figure 3.8: Excerpt of the $^1H^{15}N$ HMBC NMR spectrum of $\mathbf{[H_5L^6](PF_6)_4}$ at 243 K in MeCN-d_3 (500 MHz/50.7 MHz), shows the correlation between $\mathbf{^{15}N}$ at –76.3 ppm and the proton resonances H^1 of NH, $H^{pz\text{-}\mathbf{11}}$ and H^{15} of the CH_2 group and allows the discrimination between the two side arms.

In the ^1H NMR spectrum at 243 K are the two proton resonances H^{12} and H^{13} of the two CH_2 groups slightly separated but the external imidazolium groups are not affected by the prototropy, even at low temperature (**Figure 3.9**). Consequently one set of signals of both arms is observed. In the $^{13}C\{^1H\}$ NMR spectrum the splitting of the peaks, in dependence on the side arm is observed, but the separation between the two CH_2 groups C^{14} and C^{15} (400 Hz) is one magnitude higher than the largest separation between ^{13}C NMR signals for other side arm C atoms (**Figure 3.9**).

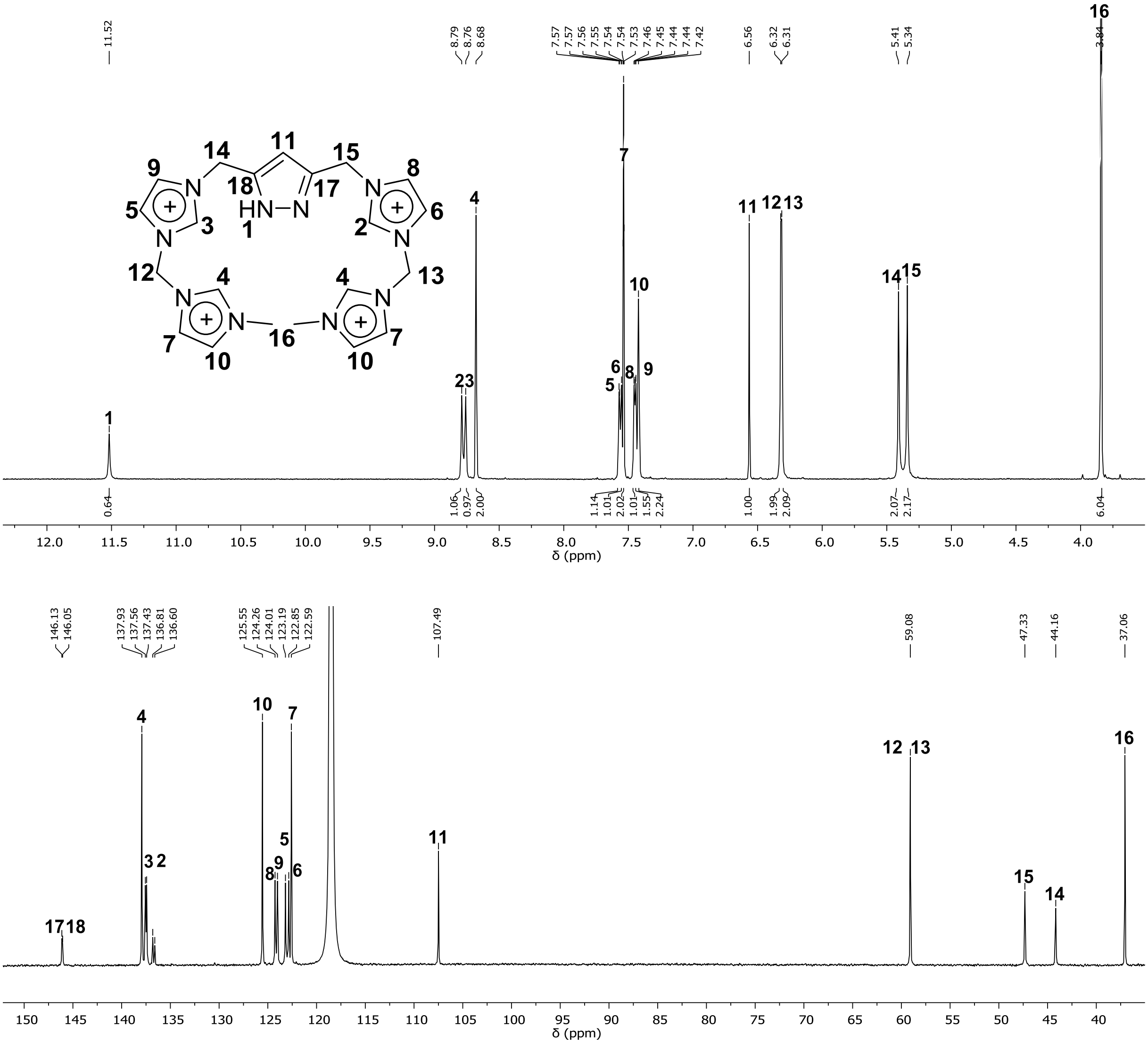

Figure 3.9: Top ^1H NMR spectrum and **bottom** $^{13}C\{^1H\}$ NMR spectrum of $\mathbf{[H_5L^6](PF_6)_4}$ at 243 K in MeCN-d_3 and 500 MHz/126 MHz.

The tautomerism in **$[H_5L^6](PF_6)_4$** is highly temperature dependent (**Figure 3.10**). This issue is already described in the literature for pyrazoles. To get a better insight into the prototropy of the herein presented ligand system, ^{1}H NMR experiments at VT are performed, to determine the activation parameters. The two resonances H^{14} and H^{15} of the CH_2 groups are evaluated, as these protons will be affected most by the prototropy and consequently will give a rough estimation of the NH exchange rate at various temperatures (**Figure 3.10**).[100] The coalescence temperature T_c of the CH_2 proton resonances H^{14} and H^{15} is 305 K. The determination of the rate constants k at different temperatures is done by line shape analysis of the corresponding CH_2 peaks in the ^{1}H NMR spectra (see experimental section).[66,67] In **Table 3.1**, the rate constants at different temperatures are listed.

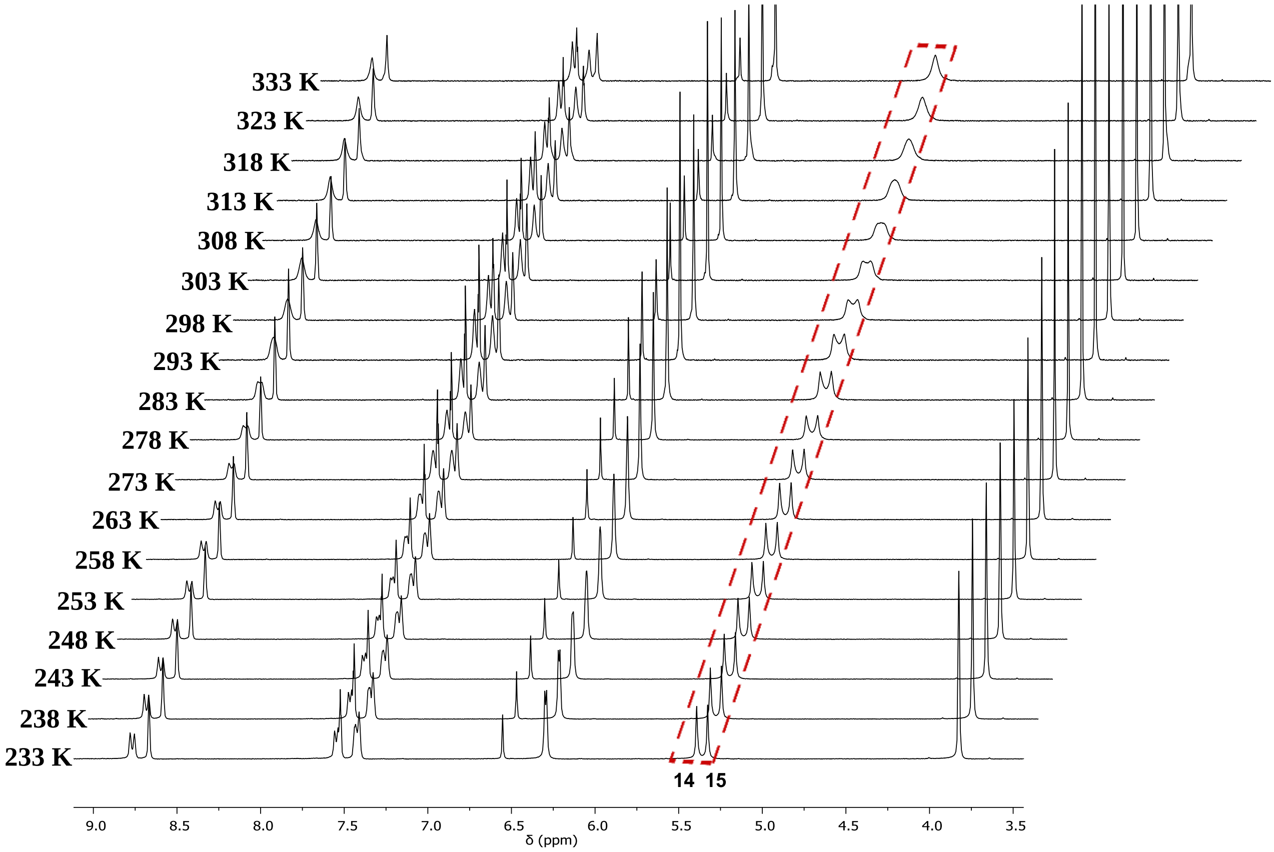

Figure 3.10: Detail of the ^{1}H VT NMR spectra of **$[H_5L^6](PF_6)_4$** in MeCN-d_3 and 400 MHz. Prototropy is indirectly investigated by the shift of the the proton resonances H^{14} and H^{15} (– – – –). © 2019 JOHN WILEY AND SONS.

Through the temperature dependence of the rate constant k and under consideration of an Eyring plot (**Figure 3.11**), an activation enthalpy of $\Delta H^{\ddagger} = 27.6\ kJ{\cdot}mol^{-1} \pm 0.55\ kJ{\cdot}mol^{-1}$ and an activation entropy of $\Delta S^{\ddagger} = -124.6\ J{\cdot}mol^{-1}{\cdot}K^{-1} \pm 2.5\ J{\cdot}mol^{-1}{\cdot}K^{-1}$ are determined. Litchman[112] investigated the proton exchange at the unsubstituted pyrazole in DMSO-d_6, in 1979. He observed an activation enthalpy of $\Delta H^{\ddagger} = 29.3\ kJ{\cdot}mol^{-1}$ and an activation entropy of $\Delta S^{\ddagger} =$

–104.6 J·mol^{-1}·K^{-1}. A proton exchange mechanism in pyrazole scaffolds can be described by a multinuclear pathway rather than a unimolecular one. The entropy of activation in **$[H_5L^6](PF_6)_4$** of $\Delta S^{‡}$ = -124.6 J·mol^{-1}·K^{-1}±2.5 J·mol^{-1}·K^{-1} is consistent with a multinuclear pathway. In this mechanism it is postulated that solvent molecules, pyrazole agglomerates and even the walls of NMR tubes can be involved.[113]

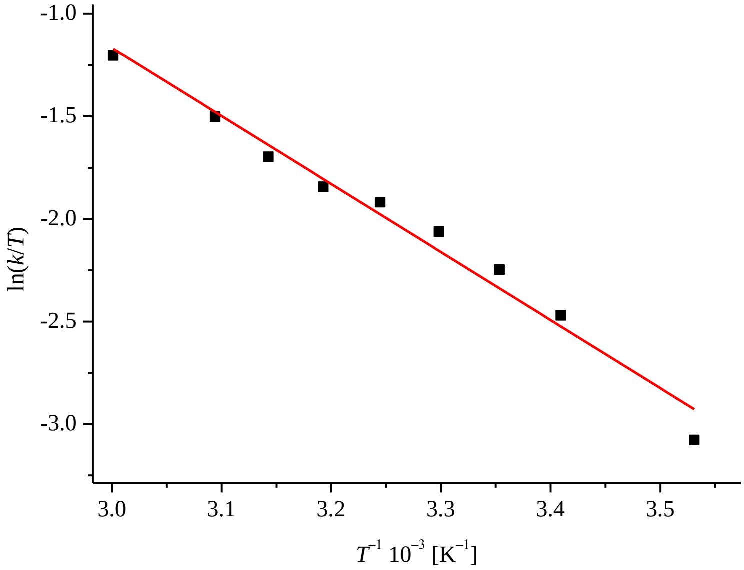

Figure 3.11: Eyring plot based on the line broadening of the pyrazole tethered CH_2 group (H^{14} and H^{15}) in a temperature regime between 323 K and 278 K. An activation enthalpy of $\Delta H^{‡}$ = 27.6±0.55 kJ·mol^{-1} and an activation entropy of $\Delta S^{‡}$ = –124.6±2.5 J·mol^{-1}·K^{-1}are determined. The red line shows the best fit (slope = –3314.5, intercept = 8.7765, R^2 = 0.9756). © 2019 JOHN WILEY AND SONS.

Table 3.1: Rate constants at different temperatures derived by line shape analysis of the ^{1}H NMR peaks of the CH_2 proton resonances H^{14} & H^{15}. © 2019 JOHN WILEY AND SONS.

T [K]	$(\Delta v_e)_{1/2}$	$(\Delta v_0)_{1/2}$	k [s^{-1}]
333.2	17.05	5.35	100.10
323.2	21.62	5.35	71.98
318.2	25.44	5.35	58.29
313.2	29.98	5.35	49.55
308.2	31.21	5.35	45.28
303.2	17.63	5.35	38.56
298.2	15.39	5.35	31.53
293.2	13.26	5.35	24.82
283.2	9.51	5.35	13.05

Meyer *et al.*[108] presented in 2017 a 1,1'-bis(pyrazole-4-yl) ferrocene system which shows agglomerate formation *via* N····H interactions between two pyrazoles in the solid state. ^{1}H DOSY NMR measurements of the ferrocene derivate in DMF-d_6 indicates the retention of such agglomerates in solution at low temperature.[108] **$[H_5L^6](PF_6)_4$** shows in MeCN-d_3 at different temperatures the same molecular size and dimerizes in solution. This is confirmed by comparative studies of the diffusion coefficient of the ligand with a dinickel complex **$[L^6Ni_2(OH)](PF_6)_2$**, which are determined by ^{1}H DOSY NMR measurements at 333 K, 298 K and 243 K (see **chapter 4** and experimental section for further details). By use of the Stokes-Einstein equation (formula (1) and (2), **chapter 2**) a molecular size ratio of 2:1 between **$[H_5L^6](PF_6)_4$** and the complex at different temperatures is found (**Table 3.2**).

Table 3.2: Diffusion coefficients of **$[H_5L^6](PF_6)_4$** and **$[L^6Ni_2(OH)](PF_6)_2$** at different temperatures.

T [K]	D [$m^2 \cdot s^{-1}$] **$[H_5L^6](PF_6)_4$**	D [$m^2 \cdot s^{-1}$] **$[L^6Ni_2(OH)](PF_6)_2$**	**$[H_5L^6](PF_6)_4$:$[L^6Ni_2(OH)](PF_6)_2$**
333	$1.21 \cdot 10^{-9}$	$1.50 \cdot 10^{-9}$	2:1
298	$7.74 \cdot 10^{-10}$	$9.77 \cdot 10^{-10}$	2:1
243	$3.17 \cdot 10^{-10}$	$3.89 \cdot 10^{-10}$	2:1

A significant influence of the solvent is quite obvious from the prototropy activation parameters for **$[H_5L^6](PF_6)_4$** in MeCN-d_3 compared to DMSO-d_6 (**Table 3.3**, and for rate constants see **appendix Table A.3.1**). Reasons for this may be manifold. Also the intrinsic properties of the ligand may play an important role for the proton exchange, *e.g.* intramolecular hydrogen bond interactions between the pyrazole NH and the side arms of the ligand.[100] The activation enthalpy of the proton exchange in **$[H_5L^6](PF_6)_4$** in MeCN is almost half ($\Delta H^{\ddagger} = 46.7$ kJ·mol^{-1}) and the entropy is almost twice ($\Delta S^{\ddagger} = -74.2$ J·mol^{-1}·K^{-1}) that of the previously described pyrazole-bridged *tacn* scaffold in MeCN-d_3 (**Table 3.3**).[100] A comparison of $\Delta G^{\ddagger}_{293K}$ of unsubstituted pyrazole dissolved in DMSO-d_6 and the *tacn*/pyrazole ligand in MeCN-d_3, with the herein presented ligand (in MeCN-d_3 or DMSO-d_6) shows comparable values (**Table 3.3**).

Table 3.3: Comparison of activation parameters of three different pyrazole based ligands.

	$[H_5L^6](PF_6)_4$	unsubstituted pyrazole[112]	*tacn*/pyrazole[100]

	MeCN	DMSO	DMSO	MeCN
$\Delta H^{\ddagger}$ [kJ·mol^{-1}]	27.6±0.55	40.4±0.80	29.3	46.7
$\Delta S^{\ddagger}$ [J·mol^{-1}·K^{-1}]	–124.6±2.5	–86.9±1.7	–104.6	–74.2
$\Delta G^{\ddagger}_{293K}$ [kJ·mol^{-1}]	64.1±1.3	65.9±1.3	59.9	68.4

The *tacn*/pyrazole ligand shows a hydrogen bond N···H···N between the *tacn* side arm and the pyrazole unit, in agreement with the solid state structure.[100] In **$[H_5L^6](PF_6)_4$** an interaction between the 2*H*-imidazolium proton and the non-protonated pyrazole nitrogen atom is possible. Based on the obtained activation parameters this interaction should be much weaker than the interaction observed in the pyrazole-bridged *tacn* ligand and therefore should play a minor role.

The absence of a significant shift of the 2*H*-imidazolium proton peak H^2 compared to peak H^3 even at low temperature supports the minor role of this possible interaction (**Figure 3.10**). Unfortunately, no crystal structure of **$[H_5L^6](PF_6)_4$** could be obtained to evidence any dimer formation as it is observed in solution. In the solid state structures of diimidazolium/pyrazole ligands, reported in the literature, no interaction between the pyrazole N and the 2*H*-imidazolium protons is observed. The side arm is turned in the opposite direction (see SI of referenced publications).[87,97]

3.2.3 Modification of $[H_5L^6](PF_6)_4$

Furthermore, modifications of the ligand (**$[H_5L^7](PF_6)_4$**, **$[H_5L^8](PF_6)_4$**, **$[H_5L^9](PF_6)_4$**) are possible and are summarized in **Scheme 3.4**. A detailed description of the synthesis and the characterization of the ligands can be found in the experimental section.

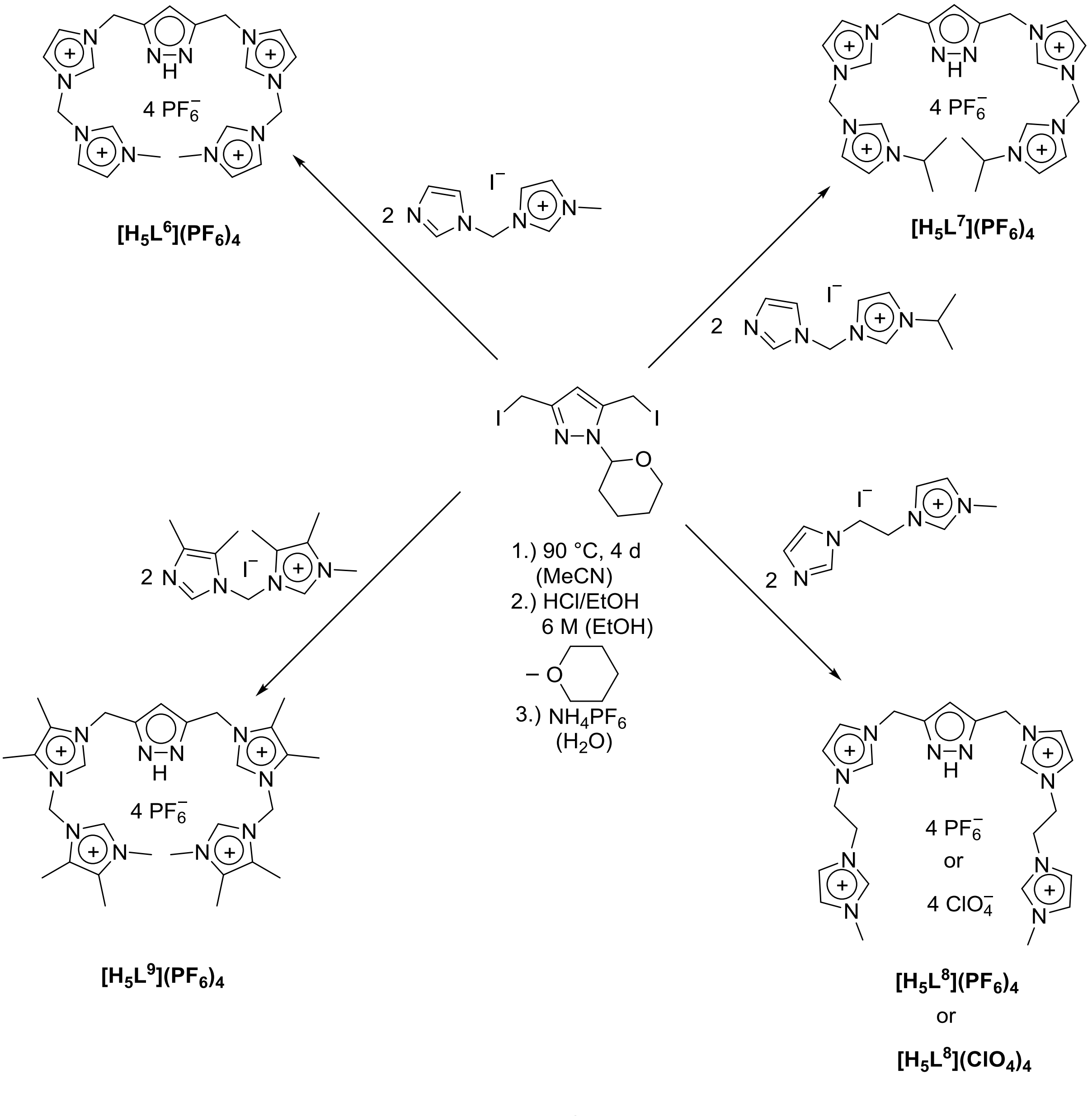

Scheme 3.4: Summary of the ligand modifications of **$[H_5L^6](PF_6)_4$**.

3.3 Supramolecular coinage hybrid pyrazole/tetra-NHC complexes

3.3.1 Supramolecular silver(I) hybrid pyrazolate/tetra-NHC complexes

In this subchapter the synthesis and characterization of multinuclear silver(I) NHC complexes with the **$[H_5L^8](PF_6)_4$** and **$[H_5L^6](PF_6)_4$** ligand scaffolds are described. **$[H_5L^8](PF_6)_4$** reacts with silver(I) oxide in MeCN at 55 °C for 25 hours under absence of light and after work-up a white solid is obtained in 59% yield (see experimental section). Single crystals suitable for X-ray diffraction are collected after slow diffusion of *tert*-butyl methyl ether into a MeCN solution of the complex. **$[(L^8)_2Ag_6](PF_6)_4$** crystallizes in the space group $P\bar{1}$. A hexanuclear silver(I) layer complex is formed, where the silver ions are capped by two ligands (**Figure 3.12**). The silver ions are coordinated by the carbene carbons and the pyrazolate nitrogen atoms of the two ligands in a linear fashion (**Figure 3.12**). The complex can be divided in three parts (ligand layer-silver layer-ligand layer). The metal part consist of two silver(I) ions located above and below a plane, which is formed by four inner Ag^+, so that the six silver ions are arranged in a chair like conformation (**Figure 3.12** and **3.13 left**).

The Ag hexagon can be separated into two triangles (Ag(1)–Ag(2)–Ag(3)) and a four membered parallelogram ($\sphericalangle$ Ag(1')–Ag(2')–Ag(1) 98.7° & $\sphericalangle$ Ag(2')–Ag(1)–Ag(2) 81.3°). Within the triangles (Ag(1)–Ag(2)–Ag(3) and Ag(1')-Ag(2')-Ag(3')) an identical bonding situation is observed. The Ag····Ag distances are listed in **Table 3.4**. The silver····silver distance between these two triangles (Ag(1)····Ag(2') and Ag(1')····Ag(2)) is 3.499 Å, which indicates only a weak metal····metal interaction, since the distance is above the sum of the corresponding van der Waals radii of 3.44 Å.[114,115] Such weak interactions are also observed within the triangle between Ag(2)····Ag(3) with 3.42 Å and Ag(2)····Ag(1) with 3.62 Å. The distance between Ag(1) and Ag(3) is 4.58 Å which opens the triangle on one side.

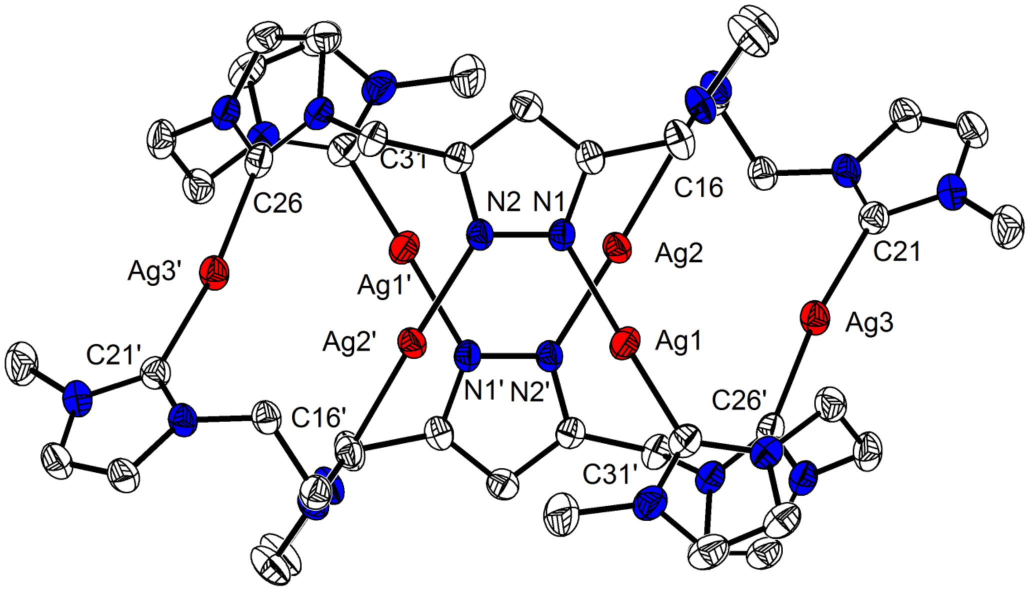

Figure 3.12: Molecular structure (50% probability thermal ellipsoids) of the cationic part of **$[(L^8)_2Ag_6](PF_6)_4$**. H atoms are omitted for clarity. Symmetry transformation used to generate equivalent atoms: (') 1–*x*, 1-*y*, 1–*z*. © 2019 JOHN WILEY AND SONS.

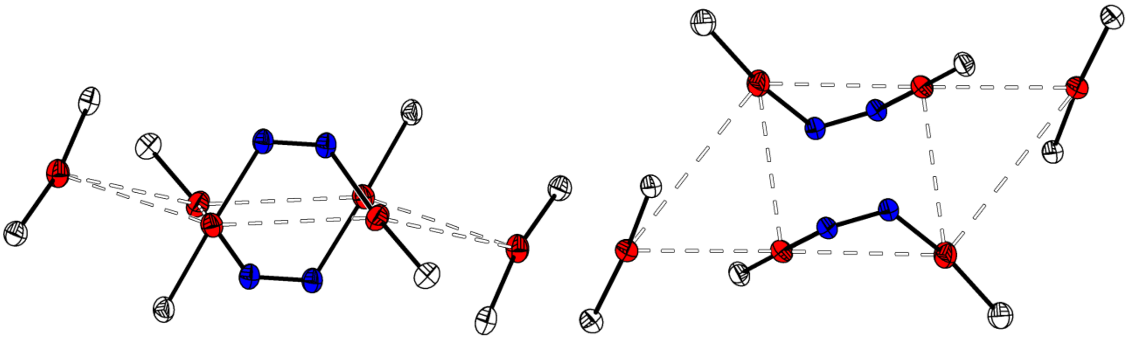

Figure 3.13: Left: side view on the coordination pattern of the silver(I) ions in **$[(L^8)_2Ag_6](PF_6)_4$** shows a chair like conformation of all six ions. **Right**: top view shows the separation of the six silver ions in a triangular coordination environment and a central parallelogram. © 2019 JOHN WILEY AND SONS.

Table 3.4: Selected Ag····Ag distances [Å] for **$[(L^8)_2Ag_6](PF_6)_4$**.

Atoms	Atom distances
Ag1····Ag2	3.617(3)
Ag1····Ag3	4.576(8)
Ag2····Ag3	3.417(6)
Ag1····Ag2’	3.499(1)

Table 3.5: Selected Ag–C and Ag–N bonds [Å] for **$[(L^8)_2Ag_6](PF_6)_4$**.

Atoms	Bond lengths
Ag1–C31’	2.06(2)
Ag1–N1	2.095(2)
Ag2–C16	2.073(3)
Ag2–N2’	2.103(2)
Ag3’–C26	2.082(3)
Ag3–C21	2.087(3)

Table 3.6: Selected bond angles [°] for **$[Ag_6(L^8)_2](PF_6)_4$**.

Atoms	Bond lengths
C31'–Ag1–N1	167.37(1)
C26'–Ag3–C21	170.05(1)
C16–Ag2–N2'	178.29(9)

The Ag–C bonds are in the range between 2.06-2.09 Å and the Ag–N bonds 2.10 Å in agreement with typical silver-carbene bonds and silver-pyrazole-N bonds of related silver imidazole/pyrazolate complexes (**Table 3.5**).[41,42,84,87] As a result of the different chemical environment of the protons of the complex in solution, a non-trivial ^{1}H NMR spectrum is observed for which no signal assignment is possible.

The ESI-MS of the complex (*m/z* and isotopic pattern) in MeCN suggests the retention of the hexanuclear silver(I) NHC complex in solution, by observation of a peak at *m/z* = 1969 (4.6) for **$[(L^8)_2Ag_6(PF_6)_3]^+$** and *m/z* = 912 (63) for **$[(L^8)_2Ag_6(PF_6)_2]^{2+}$** (**Figure 3.13**). All other peaks are assigned to fragments of the complex with lower nuclearity than six or to fragments of the free ligand.

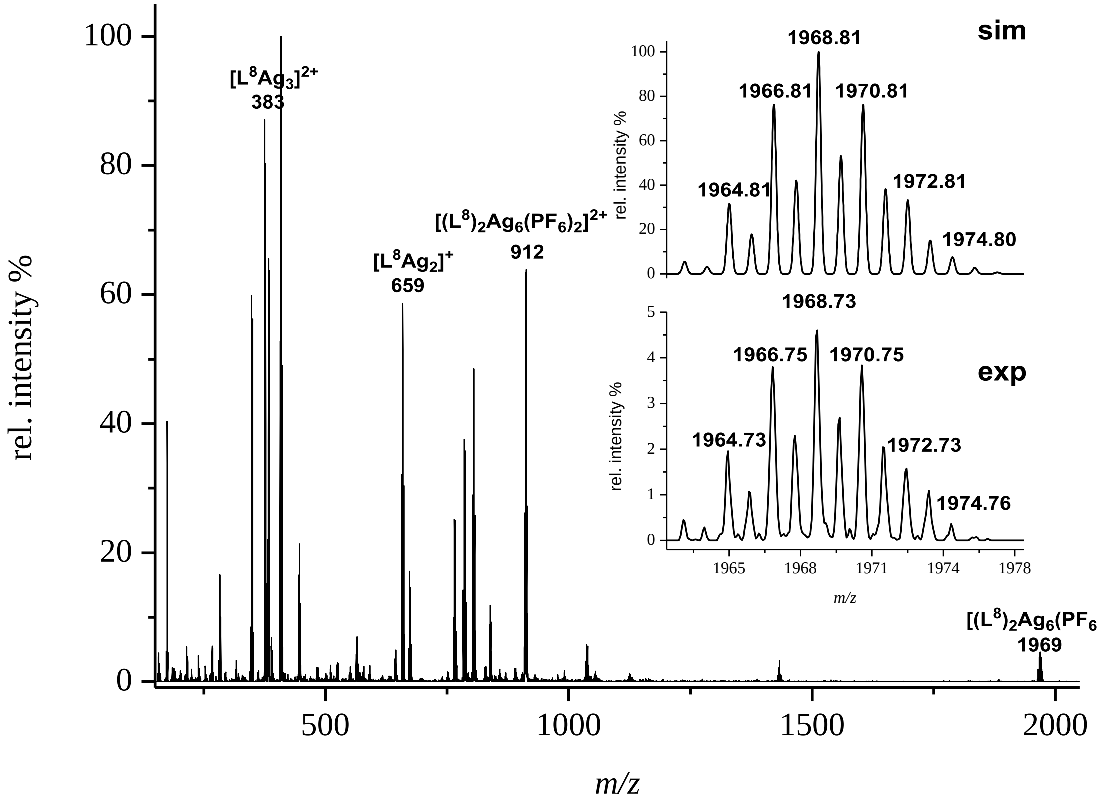

Figure 3.13: ESI-MS of **$[(L^8)_2Ag_6](PF_6)_4$** in MeCN. The inset shows the simulated (**top**) and experimental (**bottom**) isotopic distribution pattern for the peak at *m/z* = 1969 (4.6) for $[(L^8)_2Ag_6(PF_6)_3]^+$.

The reaction of Ag_2O with **$[H_5L^6](PF_6)_4$** also results in the formation of a hexanuclear silver(I) NHC complex, but with a different complex geometry (for synthetic details see experimental section).

The silver ions are coordinated by the carbene carbons and the pyrazolate nitrogen atoms of the two ligands in a linear fashion (**Figure 3.14**). The complex can be divided in three parts (ligand layer-silver and NHC layer-ligand layer). In **$[(L^6)_2Ag_6](PF_6)_4$** the silver ions are located in one layer but the coordination by the ligands occurs from the side, top and bottom (**Figure 3.15** and **3.15 left**). The metal part consist of two silver(I) ions located above and below a plane, which is formed by four inner Ag^+, so that the six silver ions are arranged in a chair like conformation (**Figure 3.15** and **3.15 left**). The Ag hexagon can be separated into two triangles (Ag(1)–Ag(2)–Ag(3)) and a four membered rectangle (Ag(1)–Ag(2)–Ag(1')–Ag(2'); 89.7° and 90.3°).

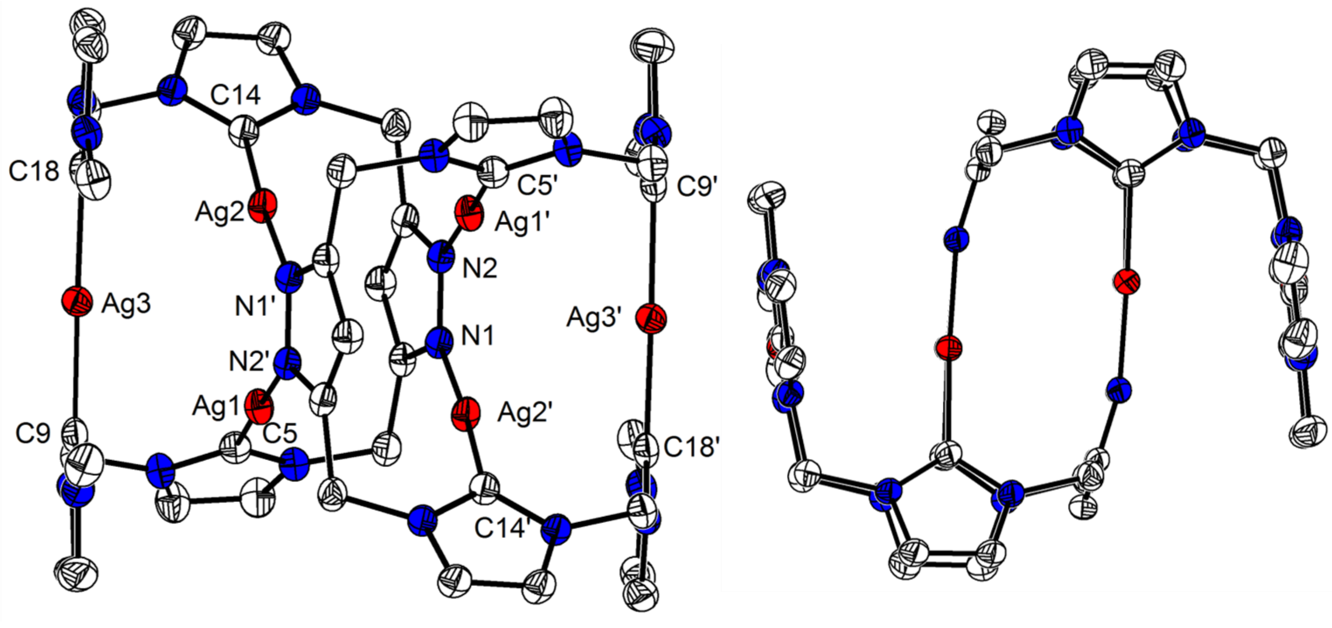

Figure 3.14: Left: ORTEP plot of **$[(L^6)_2Ag_6](PF_6)_4$** showing thermal ellipsoids at 50% probability level. H atoms are omitted for clarity. Symmetry transformation used to generate equivalent atoms: (') 1–*x*, 1–*y*, 1–*z*. **Right:** Top view of **$[(L^6)_2Ag_6](PF_6)_4$**.

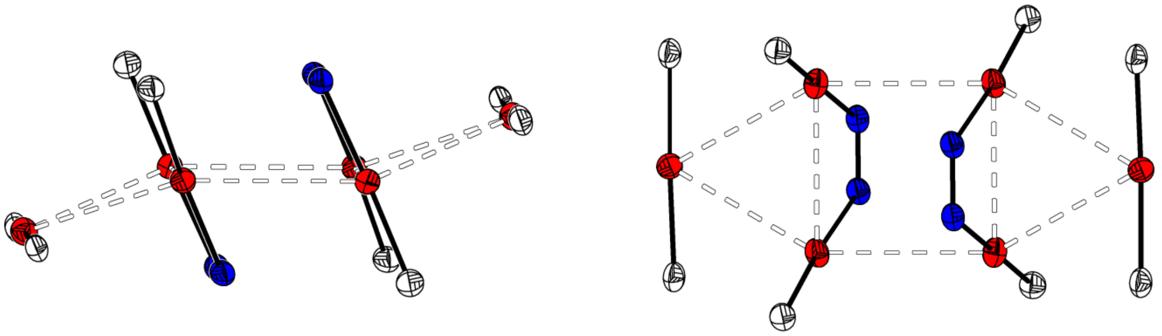

Figure 3.15: Left: side view on the coordination pattern of the silver(I) ions of **$[(L^6)_2Ag_6](PF_6)_4$** shows a chair like arrangement of all six ions. Here the external silver(I) ions are coordinated from the two carbene C atoms in the same layer where all silver ions are located. **Right:** top view shows the separation of the six silver ions in a triangular coordination environment and a central rectangle. © 2019 JOHN WILEY AND SONS.

Argentophilic interactions are observed within the triangle as well as in the square. The $Ag^+\cdots Ag^+$ distances are listed in **Table 3.7**. All observed distances are significantly lower than the sum of the corresponding van der Waals radii of 3.44 Å.[114] **$[(L^8)_2Ag_6](PF_6)_4$** and **$[(L^6)_2Ag_6](PF_6)_4$** crystallize both in the space group $P\bar{1}$. The square arrangement of the four central silver ions and the coordination pattern of the two ligands are in agreement with the tetranuclear silver(I) bisimidazole/pyrazolate complexes, published by Chen *et al*. and Meyer *et al*.[42,84,86,87] The two pyrazolate units are twisted by 180° and the two silver ions of the subunit are coordinated by a nitrogen atom of the pyrazolate unit of one ligand and one NHC-

C atom of the second ligand in an almost linear fashion (**Table 3.7**, **Figure 3.14**). In addition, the third silver(I) ion in the triangle is coordinated by two NHC-C atoms of one ligand. By use of the newly developed hybrid ligands the primary coordination sphere is extended to a second coordination sphere which allows the synthesis of silver(I) complexes in a hexanuclear coordination motif by using **$[H_5L^6](PF_6)_4$** or **$[H_5L^8](PF_6)_4$**.

In 2010, a similar Ag coordination motif was published by Chen and coworkers[85], where the ligand contained a picolyl unit as external group. In contrast to **$[(L^6)_2Ag_6](PF_6)_4$** Chen's complex shows shorter silver····silver interactions within the Ag_3-triangle (0.4 Å) and weaker silver-silver interactions between the two triangles. In **$[(L^6)_2Ag_6](PF_6)_4$** the interactions within the Ag_4 square are stronger compared to the Ag_3-triangle in the same complex, but argentophilic interactions can be also observed in the Ag_3-triangle (see discussion above and **Table 3.8**). In **$[(L^6)_2Ag_6](PF_6)_4$** the silver(I)-N and silver(I)-C atom distances are similar to the bond lengths in **$[(L^8)_2Ag_6](PF_6)_4$**. In Chen's complex each carbene-C atom is coordinated to two silver(I) ions in a 3*c*2*e* coordination mode, which results in an elongation of the Ag^+–C carbene bonds in contrast to **$[(L^8)_2Ag_6](PF_6)_4$** and **$[(L^6)_2Ag_6](PF_6)_4$**.

Table 3.7: Selected bond angles [°] for **$[(L^6)_2Ag_6](PF_6)_4$**.

Atoms	Bond angle [°]
C5–Ag1–N2'	177.86(9)
Ag2–Ag1-Ag3	60.078(7)
Ag2'–Ag1–Ag3	143.68(0)
C14–Ag2–N1'	176.32(9)
C14–Ag2–Ag1	117.31(8)
Ag1–Ag2–Ag3	62.763(7)
Ag1–Ag2–Ag1'	90.309(8)
Ag3–Ag2–Ag1'	146.28(4)
C18–Ag3–C9	173.30(1)
Ag2–Ag3-Ag1	57.159(7)
N10–C18–Ag3	126.06(2)
N9–C18–Ag3	130.71(19)

Table 3.8: Selected Ag····Ag bond lengths [Å] for **$[(L^6)_2Ag_6](PF_6)_4$**.

Atoms	**Bond lengths**
Ag1····Ag2	3.174(8)
Ag1····Ag3	3.359(7)
Ag2····Ag3	3.275(0)
Ag1'····Ag2	3.303(6)

Table 3.9: Selected Ag–C and Ag–N bonds [Å] for **$[(L^6)_2Ag_6](PF_6)_4$**.

Atoms	**Bond lengths**
Ag1–C5	2.076(3)
Ag1–N2'	2.105(2)
Ag2–C14	2.073(2)
Ag2–N1'	2.102(2)
Ag3–C18	2.103(3)
Ag3–C9	2.104(3)

Investigation of **$[(L^6)_2Ag_6](PF_6)_4$** in solution is not trivial, as already described for **$[(L^8)_2Ag_6](PF_6)_4$**. The ^{1}H NMR spectrum shows indicative of a low symmetric species with numerous peaks, according to the different environments of the protons of the two ligands. ESI-MS in MeCN suggests the retention of the hexanuclear complex in solution. A mass peak at *m/z* = 1912 (100) for $[(L^6)_2Ag_6\ (PF_6)_3]^+$ is observed (see experimental section).

3.3.2 Supramolecular copper(I) hybrid pyrazolate/tetra-NHC complexes

The corresponding copper(I) complexes **$[(L^6)_2Cu_6](PF_6)_4$** and **$[(L^8)_2Cu_6](PF_6)_4$** were synthesized following the mesitylcopper(I) route (see **chapter 2**, or **Scheme 3.5** and experimental section for details). Crystallization attempts failed until now, so that no structural information is available. It is hypothesized that with copper(I) the same structures will be obtained as with silver(I).

An evidence, that the hypothesis might be correct, is given by a single crystal X-ray measurement of **$[(L^6)_2Cu_6](PF_6)_4$** (see **appendix, Figure A.3.3**) in which the copper(I) ions have the same coordination motif like silver(I) in **$[(L^6)_2Ag_6](PF_6)_4$**. Unfortunately, **$[(L^6)_2Cu_6](PF_6)_4$** co-crystallized with a halide containing impurity **$[(L^6)_2Cu_8X_4](PF_6)_2$** (**X** = Cl^-, Br^-) and the resolution of the crystallographic data were insufficient to discuss the bonding situation in this complex in a proper way (see appendix). The UV-vis spectrum of **$[(L^6)_2Cu_6](PF_6)_4$** shows a band at 266 nm ($\varepsilon = 38.32\cdot10^3$ $M^{-1}\cdot cm^{-1}$) and a shoulder around 315 nm ($\varepsilon = 16.90\cdot10^3$ $M^{-1}\cdot cm^{-1}$) in propionitrile at 293 K (**Figure 3.16**). ESI-MS in MeCN confirmed the existence of a multinuclear copper NHC complex in solution, but the existence of a hexanuclear complex is not confirmed under ESI-MS conditions (**Figure 3.17**) in contrast to the observed hexanuclear silver(I) NHC complexes discussed above (**section** 3.3.1).

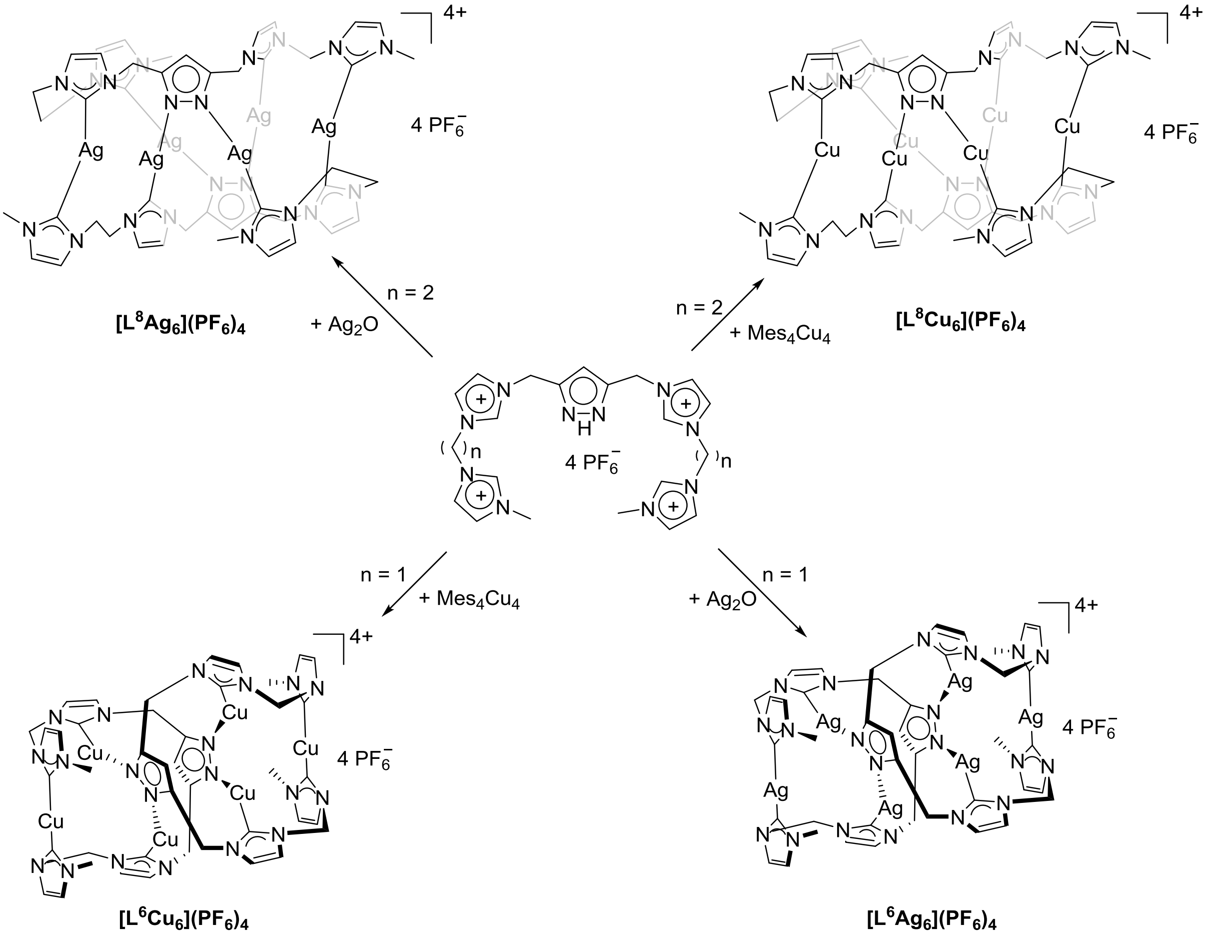

Scheme 3.5: Summary of obtained structures (for Ag) and proposed structures (for Cu) after reaction of the **$[H_5L^6](PF_6)_4$** or **$[H_5L^8](PF_6)_4$** with Ag_2O or Mes_4Cu_4, respectively.

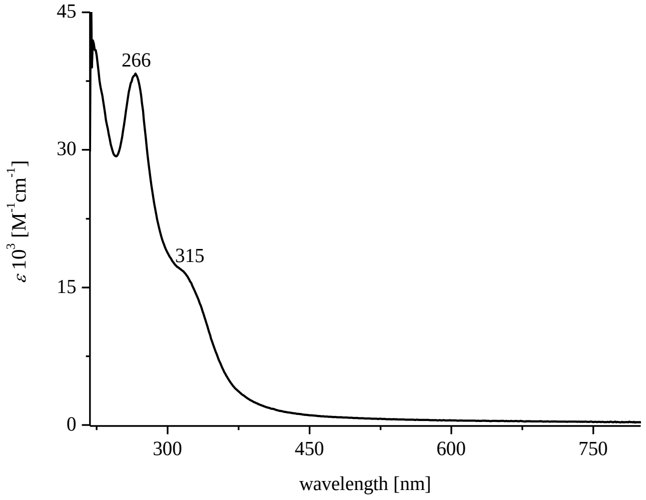

Figure 3.16: UV-vis spectrum of **$[(L^6)_2Cu_6](PF_6)_4$** in propionitrile at 293 K shows one band at 266 nm ($\varepsilon = 38.32 \cdot 10^3$ $M^{-1} \cdot cm^{-1}$) and a shoulder at around 315 nm ($\varepsilon = 16.90 \cdot 10^3$ $M^{-1} \cdot cm^{-1}$).

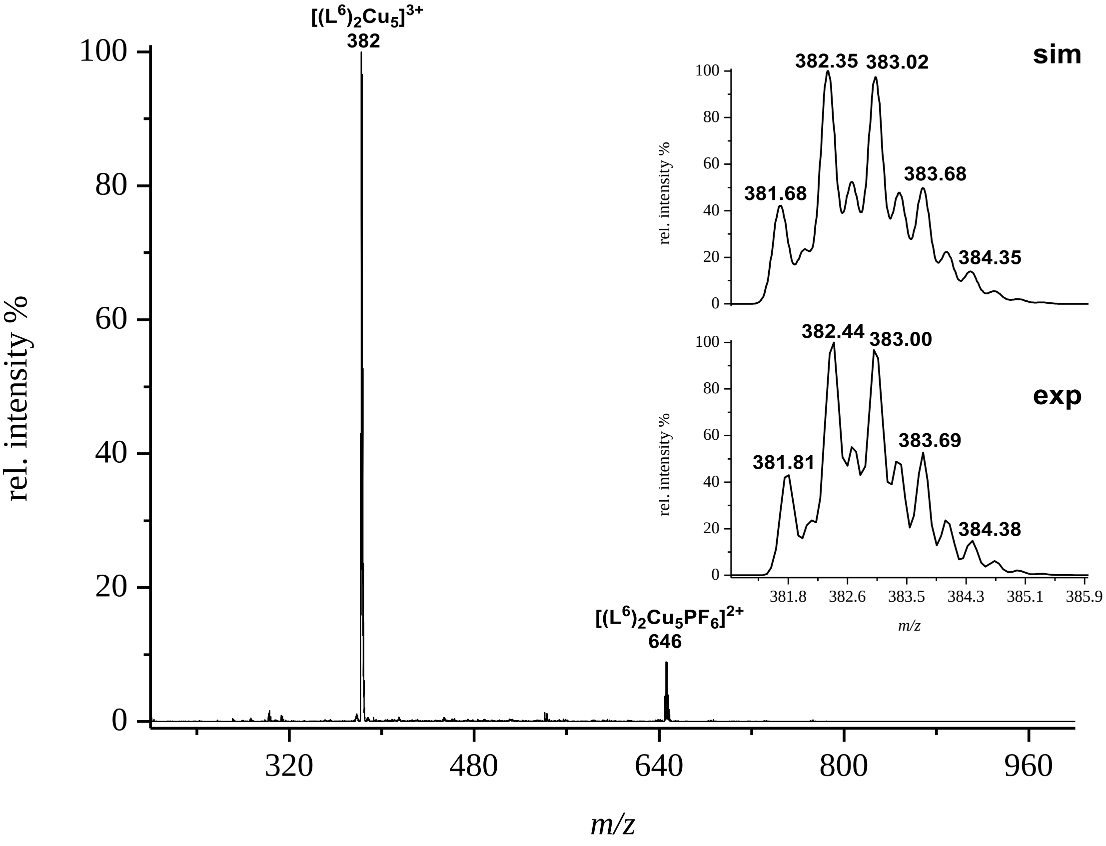

Figure 3.17: ESI-MS of **$[(L^6)_2Cu_6](PF_6)_4$** in MeCN. The inset shows the simulated (**top**) and experimental (**bottom**) isotopic distribution pattern for the peak m/z = 382 (100) for **$[(L^6)_2Cu_5]^{3+}$**.

In the negative ion ESI-MS of a $\mathbf{[(L^8)_2Cu_6](PF_6)_4}$ solution in MeCN a hexanuclear copper ion at *m/z* = 1993 (17.6) is detected corresponding to $[\mathbf{(L^8)_2Cu_6(PF_6)_5}]^-$ (**Figure 3.18**). In the positive ion ESI-MS (see experimental section) only pentanuclear ions and copper containing ions with a lower nuclearity are observed.

A copper(I) NHC complex in agreement with the solid state structure of $\mathbf{[(L^6)_2Ag_6](PF_6)_4}$ is expected but until now no single crystals suitable for X-ray analysis are obtained.

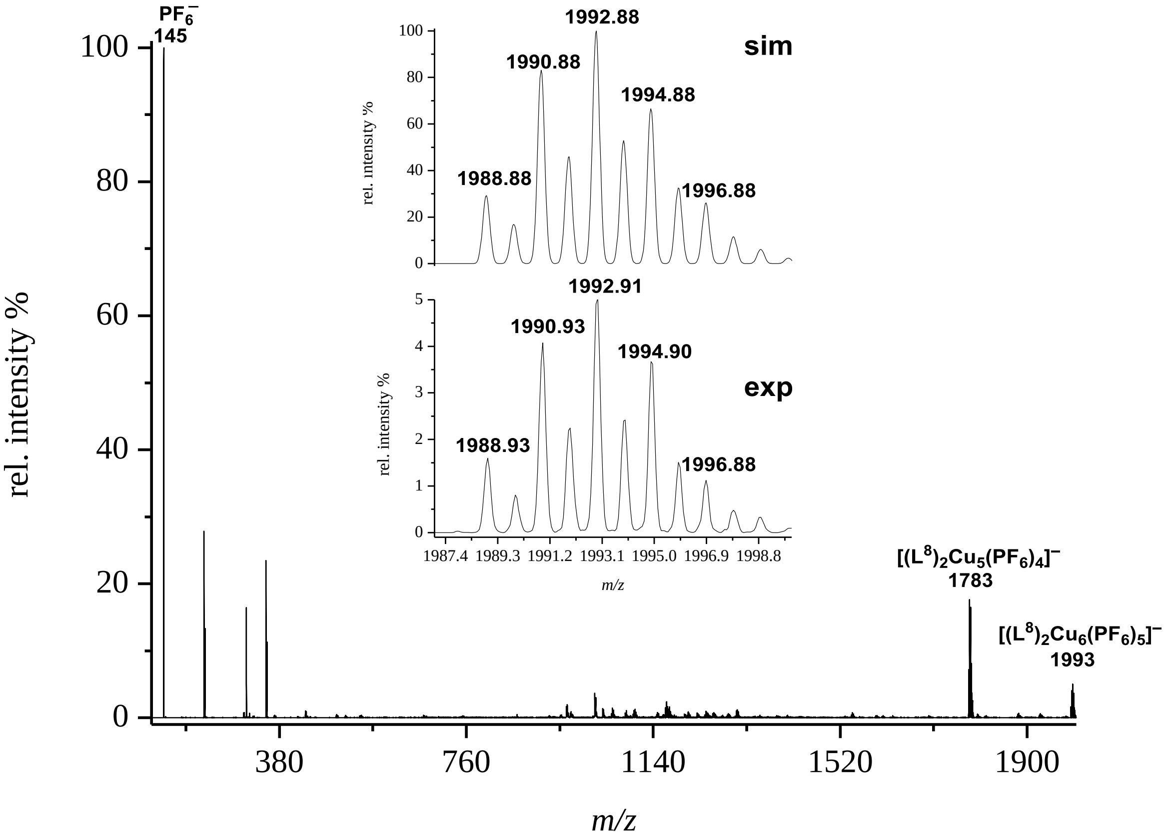

Figure 3.18: ESI-MS of $\mathbf{[(L^8)_2Cu_6](PF_6)_4}$ in MeCN. The inset shows the simulated (**top**) and experimental (**bottom**) isotopic distribution pattern for the peak *m/z* = 1993 (5) for $[\mathbf{(L^8)_2Cu_6(PF_6)_5}]^-$.

3.4 Conclusion and Outlook

In this chapter the successful synthesis of a new pyrazole-bridged ligand system bearing four imidazolium units was described. The prototropy of **$[H_5L^6](PF_6)_4$** was investigated and compared to the prototropy of unsubstituted pyrazole and literature known pyrazole-bridged ligands, and the effect of the solvent was examined. ^{1}H DOSY NMR experiments confirmed formation of agglomerates of the ligand over the whole applied temperature range. The diversity of this ligand system was confirmed by variation of the external alkyl substituent (**$[H_5L^7](PF_6)_4$**), change of the spacer between the bis(imidazolium) units (**$[H_5L^8](PF_6)_4$**) and alkylation of the 4/5 positions of the imidazolium units (**$[H_5L^9](PF_6)_4$**). With this ligand portfolio in hand, multinuclear coinage metal complexes of silver(I) and copper(I) were synthesized. Reaction of silver(I) oxide or Mes_4Cu_4 with **$[H_5L^6](PF_6)_4$** or **$[H_5L^8](PF_6)_4$** resulted in the formation of hexanuclear silver(I) or copper(I) complexes of the type **$[(L^x)_2M_6](PF_6)_4$**. The variation of the spacer between the two NHCs resulted in two different structural motifs for $M = Ag^+$. In the future, the photoluminescence properties of these complexes can be investigated and compared to the literature known multinuclear coinage complexes.

The ligands **$[H_5L^6/L^7/L^9](PF_6)_4$** are used in the next chapters for the synthesis of dinickel(II) complexes whose behavior towards small molecule activation or reactivity with acids and bases is explored.

Part II

Nickel *N*-heterocyclic carbene complexes

4

Preorganized pyrazolate-bridged dinickel(II) μ-OH tetra-NHC complexes and their reactivity

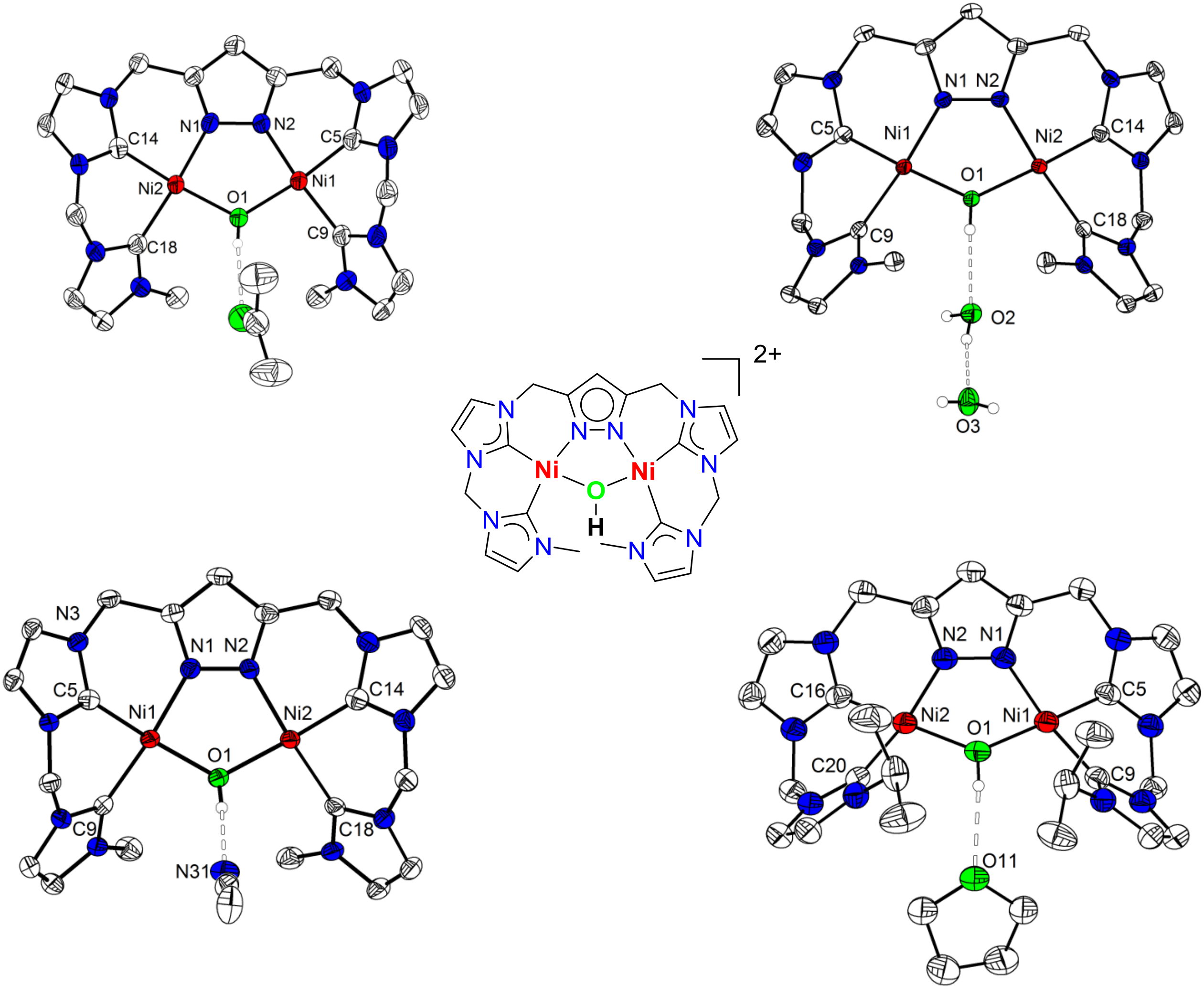

Abstract: In this chapter new dinickel(II) hybrid pyrazolate/NHC complexes are presented based on the ligand systems described in **chapter 3**. The H/D and $H_2{}^{16}O/H_2{}^{17}O$ exchange kinetics of a dinickel(II) μ-OH complex are investigated as well as the formation of an *in situ* generated μ-oxido complex. Destabilization and transformation of **[L^{6}Ni$_2$(OH)](PF$_6$)$_2$** into a μ-Cl complex **[L^{6}Ni$_2$Cl](PF$_6$)$_2$** is presented. **[L^{6}Ni$_2$Cl](PF$_6$)$_2$** is the starting compound for the generation of pyrazolate-bridged dinickel μ-amido and biscyanido tetracarbene complexes.

4.1. Introduction

The ligand family **[H_5L^{6-9}](PF_6)$_4$**, presented in **chapter 3**, exhibit the coordination of coinage metals in different fashions and the formation of supramolecular NHC complexes with six metal centers. Depending on the used metal, the ligand is proposed to stabilize dinuclear species with an intermetallic cavity for the coordination or activation of ions and small molecules. These promising properties make this system attractive for the investigation of reactions, where the stabilization of intermediates is in the focus of research. A useful synthon is hereby the pyrazole building unit, which provides a flexible substitution in the 3 and 5 position of the heterocycle by incorporating different side arms and allows the coordination of two metal centers with in close proximity and showing interesting cooperative effects.[77,78]

4.1.1 Pyrazolate-bridged dinickel(II) complexes

Dinickel(II) μ-pyrazolate complexes have already been described in the literature and have found application in catalytic reactions[64] and in modelling of binuclear metallbiosites[77]. Chen *et al.*[64] described pyrazolate-linked dinuclear nickel(II) μ-hydroxido complexes (**VI** and **VII** in **Figure 3.3**, **chapter 3**) in the context of catalytic cross coupling reactions, in specifically Suzuki-Miyaura and Kumada-Corriu coupling reactions. In the mechanism the reduction of the nickel(II) centers is proposed. In 2018, Meyer *et al.*[102,116] introduced a dinickel(II) complex **VIII** which allows the activation of dioxygen and phenylacetylene under release of dihydrogen (**Figure 4.1**).

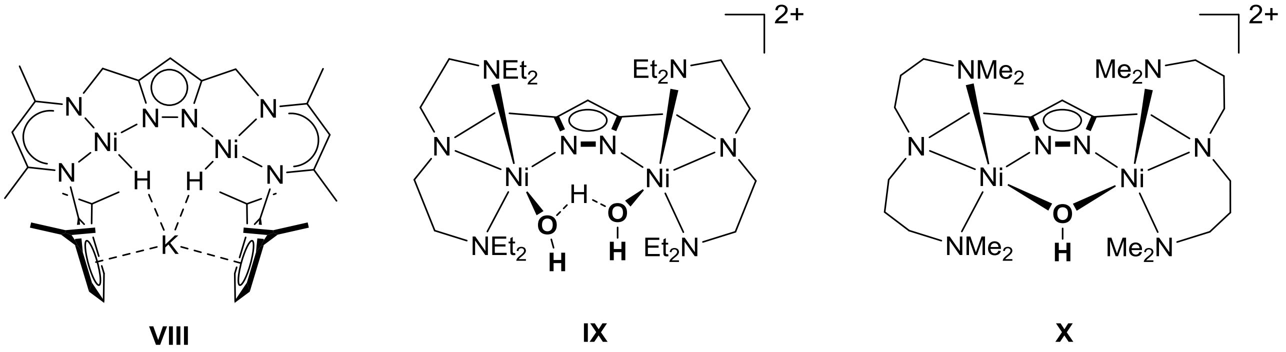

Figure 4.1: Left: Structures of complex **VIII**, which is able to activate dioxygen and phenylacetylene and **right:** an example of a H_3O_2 bridged dinickel(II) complex **IX** and a hydroxido-bridged complex **X**.[77,102]

Several pyrazolate-bridged dinickel(II) complexes are investigated as biomimetic or bioinspired model complexes of hydrolytic enzymes. Urease is an enzyme which can be found in plants, fungi and bacteria; it catalyzes the hydrolysis of urea to the final products, ammonia and carbon dioxide.[68,117–120] The co-factor of the enzyme contains two nickel(II) centers which are linked *via* a hydroxido bridge and a carboxylated lysine. One nickel ion is further coordinated by two histidine residues and a water molecule, whereby the second nickel ion is connected to one aspartic acid, two histidine residues and one water molecule (**Figure 4.2**). To date, several mechanism for the hydrolysis of urea at the active center are described.[120]

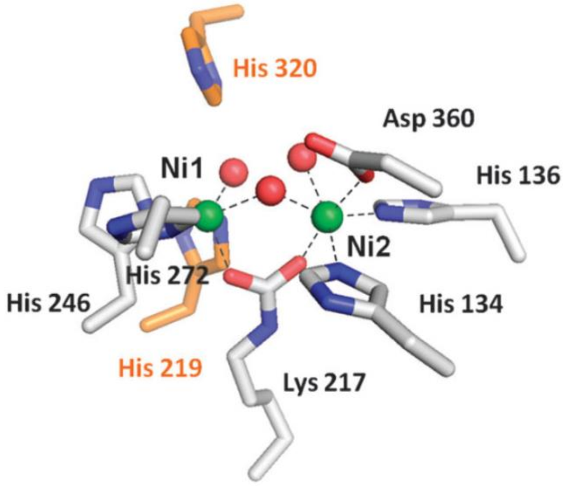

Figure 4.2: Active center of urease. Two nickel centers are bridged by a hydroxide and a carboxylated lysine. Ni1 is, in addition, coordinated by two histidine residues and one water molecule. Ni2 is coordinated by two histidine residues, one aspartic acid and one water molecule.[120] © 2009 ROYAL SOCIETY OF CHEMISTRY.

Pyrazolate-bridged dinickel model complexes for urease activity have been described in the literature.[77,121] Meyer and coworkers showed that complex **IX** (**Figure 4.1**) is able to coordinate ureate in a *N*,*O* fashion between the two nickel(II) centers.[77,121] This coordination is possible due to the large nickel····nickel distance of 4.5 Å in the molecular structure in solid state.[77,122] Degradation of the *N*,*O*-bridged ureate is not feasible by hydrolysis but by thermolysis under formation of a *N*,*O*-bridged cyanato complex and release of ammonia.[77,122,123] Hydrolysis of urea seems to be also possible without incorporation of ureate between the two nickel centers.[120,124] The hydroxido-bridged complex **X** (**Figure 4.1**) showed no activity towards urea and low nucleophilic reactivity of the OH-bridge in contrast to the putative urease enzyme.[77] To the best of my knowledge, no further reactivity of pyrazolate-bridged dinickel μ-OH complexes was previously described.

4.1.2 Reactivity of nickel hydroxido complexes

In contrast to dinickel complexes described above, several mononuclear nickel(II) hydroxido complexes and their reactivity towards organic substrates or small molecules were reported.[64,124–128] Activation of urea, CO_2 and successful cross coupling reactions were demonstrated. Monfette *et al.*[125] described nickel hydroxido complexes as intermediates in nickel-catalyzed Suzuki-Miyaura cross coupling reactions, and Holm and coworkers[126] presented a mononuclear nickel pincer complex **XI** with a terminal OH group enabling the activation of several small molecules (**Scheme 4.1**). Substitution reactions, for instance of DCM and MeOH, as well as activation of CO_2 were demonstrated, based on the nucleophilic character of the obtained OH unit.

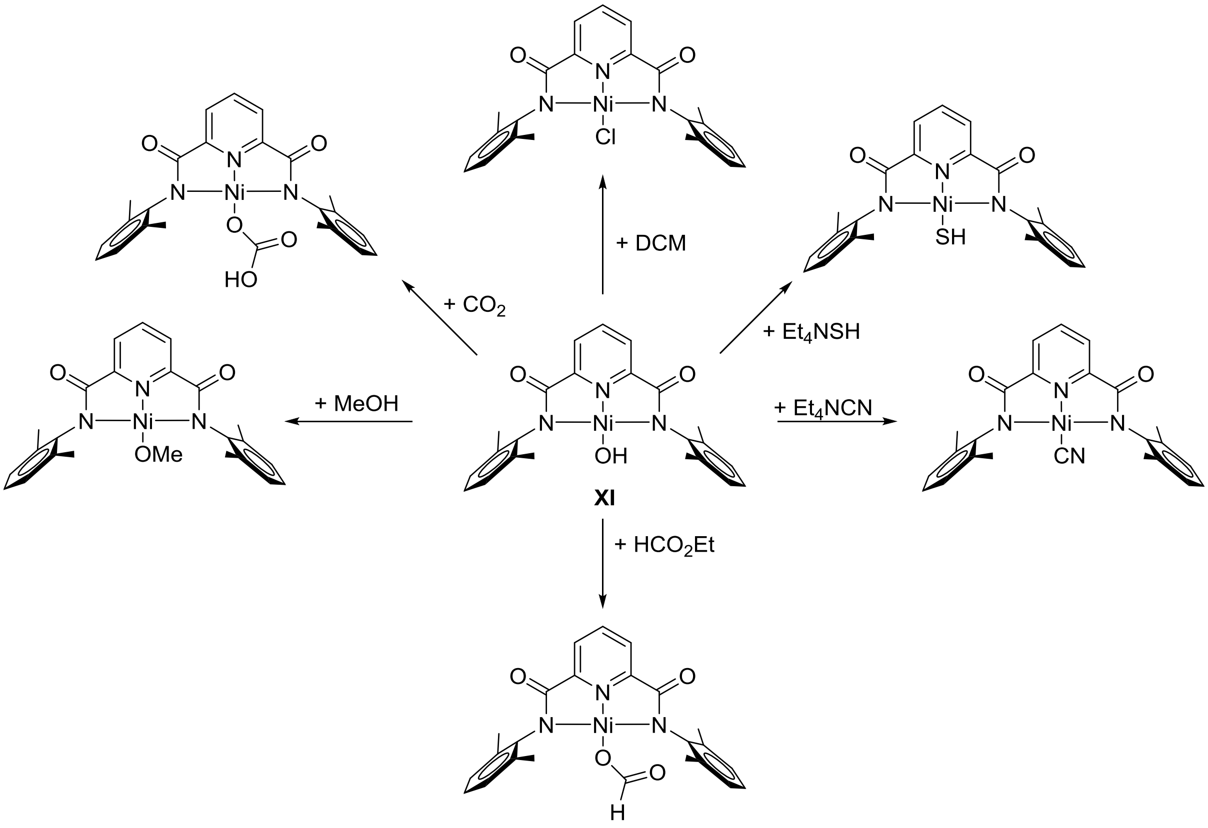

Scheme 4.1: Reactivity of the terminal hydroxido nickel(II) pincer complex **XI** with DCM, Et_4NSH, Et_4NCN, HCO_2Et, MeOH and CO_2.[126]

4.2. Objectives

The use of dinickel complexes described above in catalysis or substrate activation is rare. To date, only Chen *et al.*[64,85] reported dicopper(II) and dinickel(II) μ-OH complexes for catalytic cross coupling reactions. This lack of reactivity motivates the investigation of a new class of dinickel(II) μ-OH complexes (**Figure 4.3**) and their kinetic lability towards water exchange. Using exchange reactions with D_2O and $H_2{}^{17}O$, the activation parameters are derived to gain further insights into the potential reactivity of these compounds and the lability of the hydroxido bridge between the two nickel ions. Furthermore, reactivity studies for the destabilization of the OH-bridge as well as their behavior towards bases and acids are investigated.

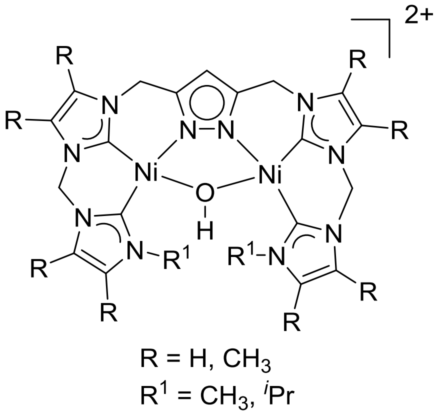

Figure 4.3: Proposed dinickel(II) μ-OH complexes with the ligands [$\mathbf{H_5L^6/H_5L^7/H_5L^9}$]$\mathbf{(PF_6)_4}$.

4.3 Results and Discussion

4.3.1. A [$L^6Ni_2(OH)](PF_6)_2$ complex and the interaction of its hydroxido group with solvent molecules

The synthesis of a dinuclear nickel(II) hydroxido-bridged complex **[$L^6Ni_2(OH)](PF_6)_2$** is achieved by reaction of **[$H_5L^6](PF_6)_4$** with nickel(II) acetate and sodium acetate in MeCN (p. a.) at room temperature (**Scheme 4.2**) according to a similar route.[129–131]

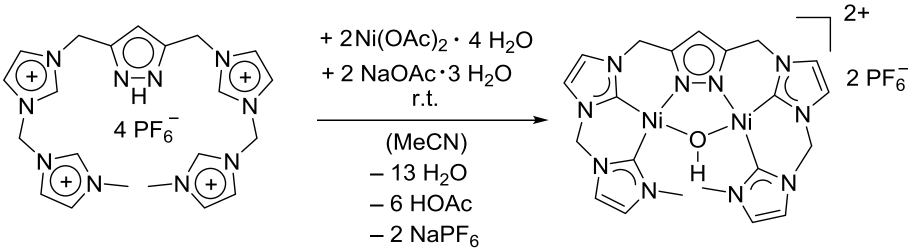

Scheme 4.2: Synthesis of **[$L^6Ni_2(OH)](PF_6)_2$**.

Pale yellow crystals are obtained by slow diffusion of Et_2O in an acetone solution of the complex at 5 °C. Crystallization of the complex is also possible by slow diffusion of THF or Et_2O into a solution of the complex in MeCN. **[$L^6Ni_2(OH)](PF_6)_2$** is obtained in two different space groups, depending on the crystallization conditions. **[$L^6Ni_2(OH)](PF_6)_2$** crystallizes in the space group $P2_1/c$ and in the space group $P\bar{1}$, by using MeCN as solvent. In solid state, the complex shows a saddle shaped conformation (**Figure 4.4**).

The two nickel(II) ions are each coordinated in a distorted square planar fashion by two carbene carbon atoms and a pyrazolate nitrogen atom, linked *via* a hydroxide ion. The nickel(II)····nickel(II) distance is with 3.26 Å shorter than previously reported dinickel μ-OH complexes (3.64-3.47 Å)[77,116] and similar to **VI** and **VII**.[64] In solid state an approximate (no-crystallographic) C_s symmetry of the molecule is obtained. Relevant atom distances and angles can be found in **Table 4.1** and **Table 4.2**. Nickel-carbene bonds in **[$L^6Ni_2(OH)](PF_6)_2$** are varying between 1.85-1.88 Å and selected bond lengths around the nickel centers are shown in **Scheme 4.3**. The nickel hydroxido bonds are 1.88 Å and 1.89 Å. Ni(1) is located 0.038 Å out of the N(1)–O(1)–C(9)–C(5) plane and Ni(2) 0.026 Å out of the N(2)-C(14)–C(18)–O(1) plane. The angle between both planes is 24.74°. Similar Ni–C, Ni–O and Ni–N bonds are observed in the molecular structures in solid state of **VI** and **VII**.[64]

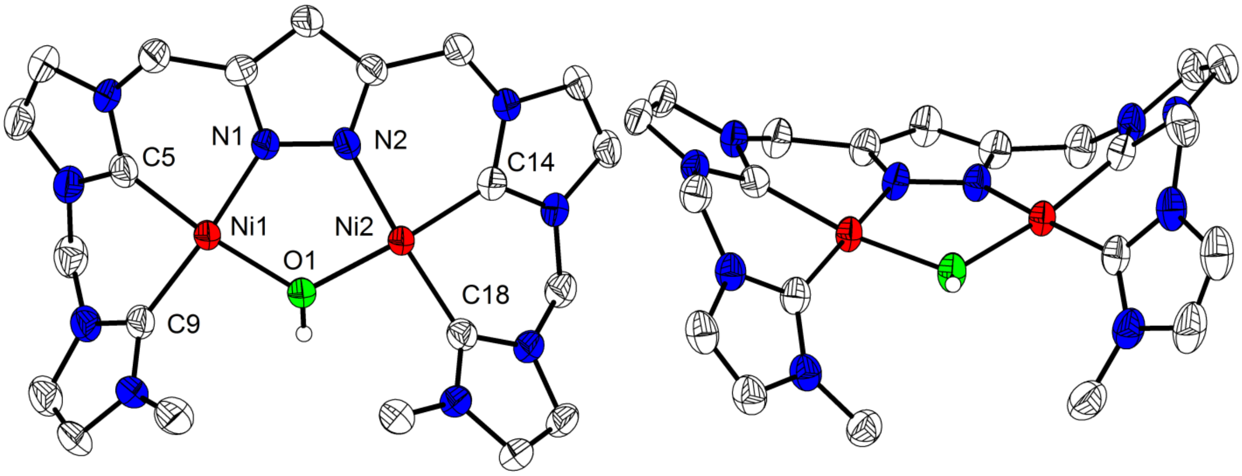

Figure 4.4: Molecular structure (50% probability thermal ellipsoids) of the cationic part of **[$L^6Ni_2(OH)](PF_6)_2$**. H atoms, except of the OH bridge, are omitted for clarity.

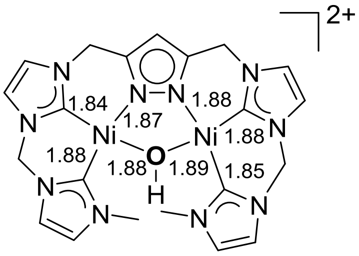

Scheme 4.3: Selected bond lengths **[Å]** in **[$L^6Ni_2(OH)](PF_6)_2$**.

Table 4.1: Selected bond lengths [Å] for **[$L^6Ni_2(OH)](PF_6)_2$.**

Atoms	**Bond lengths**
Ni····Ni	3.263(8)
Ni1–C5	1.842(3)
Ni1–N1	1.870(2)
Ni1–C9	1.881(3)
Ni1–O1	1.887(2)
Ni2–C14	1.852(3)
Ni2–C18	1.883(3)
Ni2–N2	1.885(2)
Ni2–O1	1.896(2)

Table 4.2: Selected bond angles [°] for **[L^{6}Ni$_2$(OH)](PF$_6$)$_2$**.

Atoms	Bond angles
C5–Ni1–N1	88.76(1)
C5–Ni1–C9	87.31(1)
N1–Ni1–O1	86.65(9)
C9–Ni1–O1	97.73(1)
C14–Ni2–C18	89.22(1)
C14–Ni2–N2	88.83(1)
C18–Ni2–O1	95.15(1)
N2–Ni2–O1	87.86(1)
Ni1–O1–Ni2	119.2(5)
C2–N1–Ni1	130.8(2)
N2–N1–Ni1	120.9(0)
C3–N2–Ni2	132.4(2)

^{1}H NMR spectroscopy of **[L^{6}Ni$_2$(OH)](PF$_6$)$_2$** shows an apparent C_{2v} symmetry of the complex at 298 K in MeCN-d_3 (**Figure 4.5 (a)**). At –0.04 ppm the proton resonance of the hydroxido bridge is obtained as a sharp singlet, which is supported by ^{1}H^{1}H NOESY NMR spectroscopy (**Figure 4.5** (**c**)). A NOE between proton resonances H^8 of the CH$_3$ groups and the OH group is observed. The slight low-field shift of the OH proton resonances compared to previously reported dinickel(II) μ-OH complexes as well as the high reactivity complex **XI** (δ(OH) = -4.95 ppm) is indicative of weak nucleophilicity reactivity (see **section 4.3.9**).[116,126] ^{13}C resonances for the carbene-C atoms C^9 and C^{10} are assigned in the ^{13}C{^{1}H} NMR spectrum at 161.2 ppm and 156.6 ppm (**Figure 4.5 (b)**). The sharp proton resonance of the hydroxido group allows further investigations of the influence of the solvent on this group.

Hydrogen bond interactions between the OH proton and one molecule of the solvent used for crystallization are observed in the molecular structures in solid state of the complex (**Figure 4.6**).

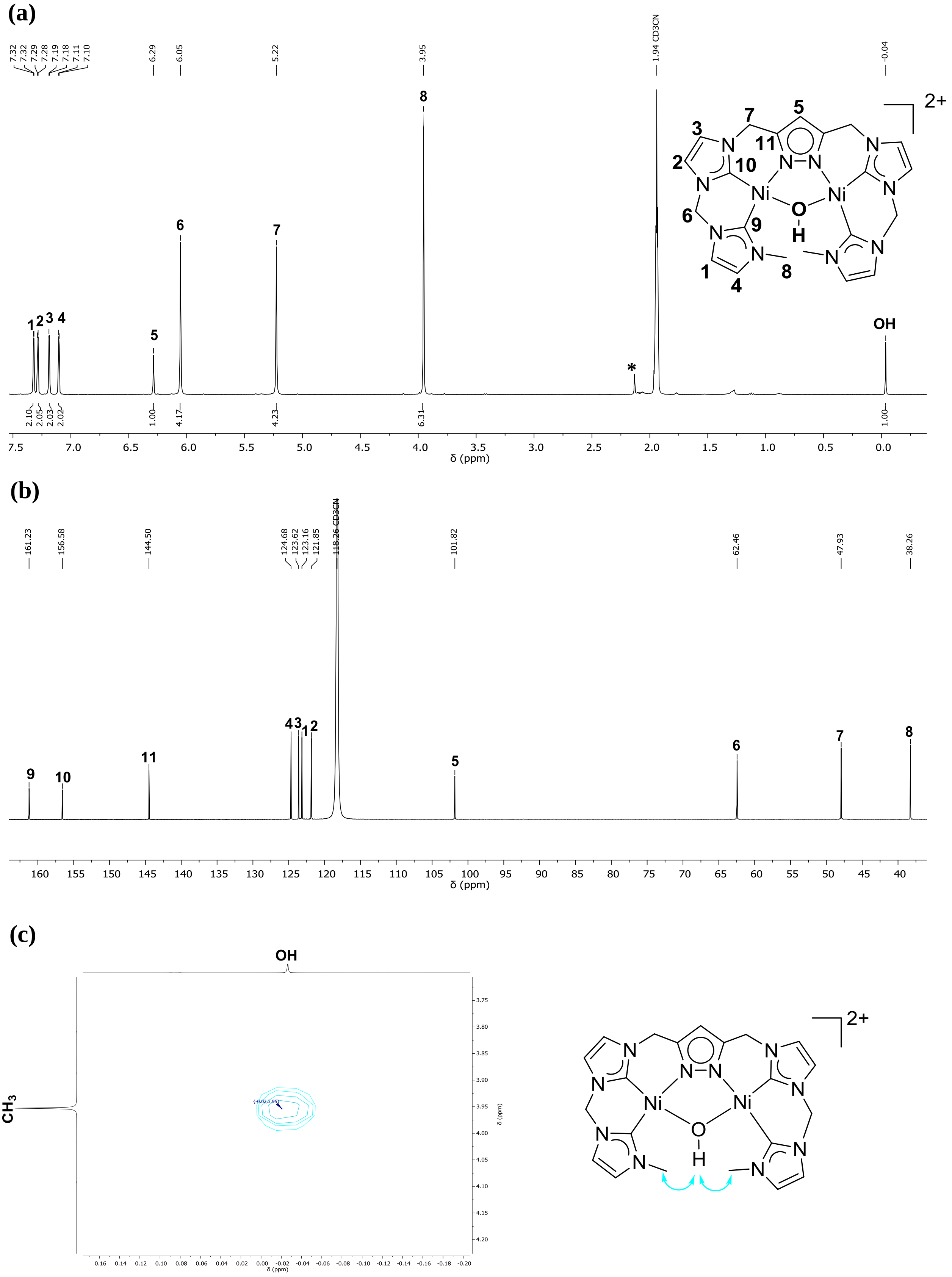

Figure 4.5: **(a)** ^{1}H NMR spectrum of **[L^{6}Ni$_2$(OH)](PF$_6$)$_2$** in MeCN-d_3 at 298 K and 400 MHz. The proton resonance of the OH group in MeCN-d_3 is observed at –0.04 ppm. (*) represents obtained traces of water. (**b**) ^{13}C{^{1}H} NMR spectrum at 126 MHz. (**c**) Excerpt of ^{1}H^{1}H NOESY spectrum showing NOE between the proton resonances of the peripheral CH$_3$ groups and the central OH bridge at 298 K in MeCN-d_3 (500 MHz).

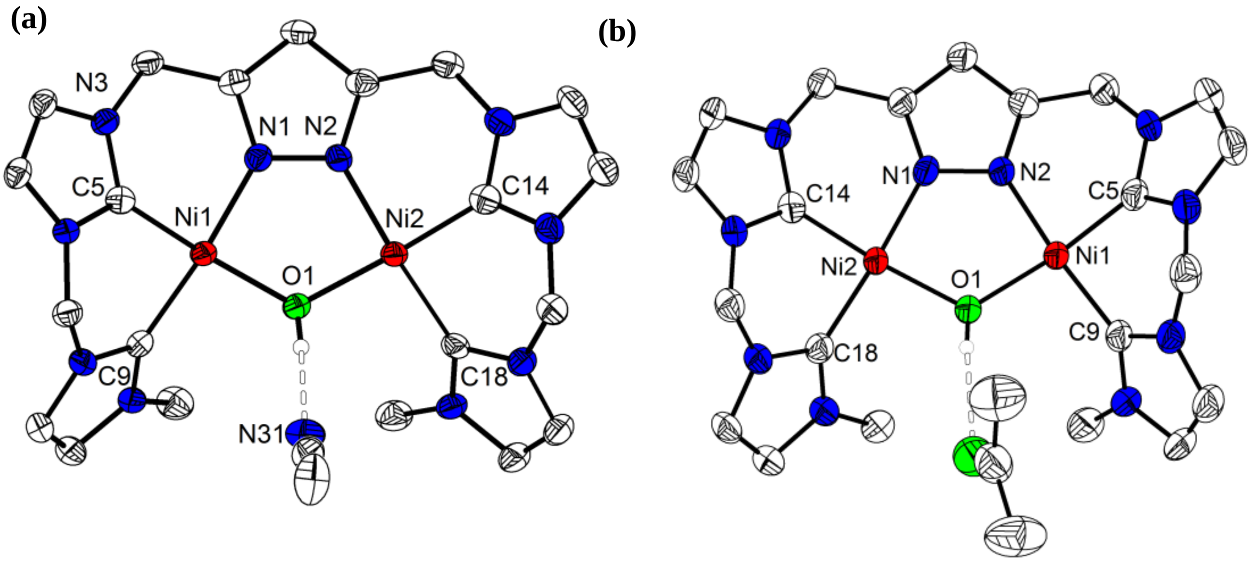

Figure 4.6: Depending on the solvent used for crystallization, hydrogen bond interactions of $\mathbf{[L^6Ni_2(OH)]^{2+}}$ to MeCN (**a**) or acetone (**b**) are observed.

Solvent-free compounds are isolated by re-dissolving crystalline material in acetone and evaporation of the solvent under reduced pressure. Elemental analysis of the obtained pale yellow solid confirms the purity and absence of solvent molecules. In addition, spectroscopic methods, for instance NMR and IR spectroscopy are performed to get further information about this interaction. A comparison of the ^1H NMR shifts of the OH proton resonance in different deuterated solvents clearly demonstrates the strong influence of the solvent on the hydroxido group (**Table 4.3**).

Table 4.3: Solvent effect on the shift of the OH peak in NMR and IR spectra of $\mathbf{[L^6Ni_2(OH)](PF_6)_2}$ at 298 K.

solvent	δ(OH) [ppm]	υ(OH) [cm^{-1}]
DMSO-d_6/DMSO	1.89	3389
Acetone-d_6/Acetone	1.15	–
MeCN-d_3/MeCN	–0.04	3503
Solid state	–	3600

These shifts are significantly higher than the shifts of the CH/CH_2 group peaks (average $\Delta\delta = 0.2$ ppm) (**Figure 4.7**). A stronger interaction between the OH group and the solvent molecule occurred from MeCN-d_3 to DMSO-d_6, due to increased H-acceptor ability of the used solvent. With increased hydrogen bond interaction, a greater de-shielding of the OH proton is observed. A low-field shift of the OH peak is obtained, as a consequence of the change of the electronic environment of the OH group by changing the solvent from MeCN-d_3 to acetone-d_6/DMSO-d_6 (**Figure 4.7**).

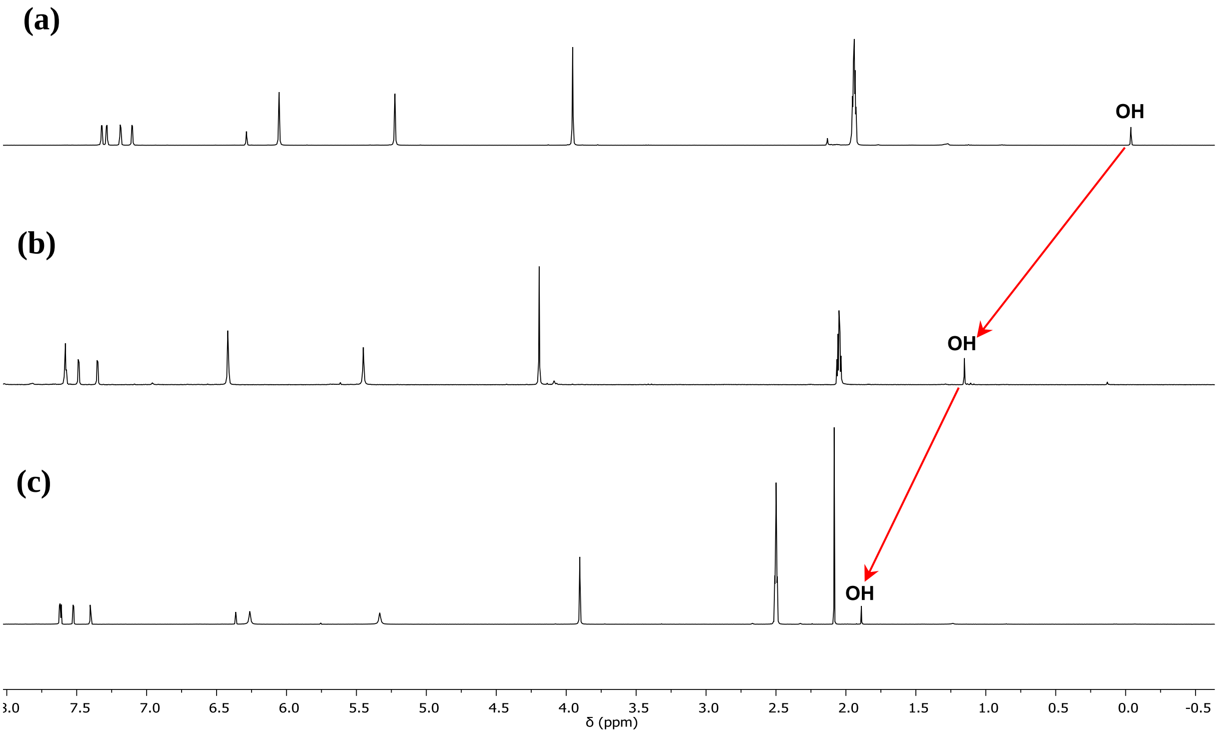

Figure 4.7: ^{1}H NMR spectra of **[$L^6Ni_2(OH)](PF_6)_2$** in (**a**) MeCN-d_3, (**b**) acetone-d_6 and (**c**) DMSO-d_6. Marked region (←) shows the shift of the proton resonances of the OH group in different solvents. Low-field shift from MeCN to DMSO is observed.

The IR spectrum of **[$L^6Ni_2(OH)](PF_6)_2$** in solid state shows a OH stretch at υ(OH) = 3600 cm^{-1} (**Figure 4.8**). Meyer *et al.*[116] reported a dinickel μ-OH complex **XII** with a OH stretch at υ(OH) = 3606 cm^{-1} in solid state (**Figure 4.9**). The OH stretching frequency of a dinickel, di-μ-OH complex is observed at υ(OH) = 3650 cm^{-1} in Nujol.[125] In contrast to this, Chen[64] and coworkers assigned the OH vibrations in their complexes **VI** and **VII** to bands at υ(OH) = 3441 cm^{-1} and υ(OH) = 3450 cm^{-1}. In the IR spectrum of **[$L^6Ni_2(OH)](PF_6)_2$** a red-shift of the OH stretch is observed in solution (**Table 4.3, Figure 4.8**). A stronger red shift is observed in dependence on the strength of the H-bonding interactions of the hydroxido group with the solvent (**Table 4.3**, **Figure 4.8**). In harmonic approximation (3) the stretching frequency depends on the force constant k and the reduced mass μ of the molecule. By changing the solvents, and simultaneous variation of the H-bonding interactions, the k values changed and as a result, the frequencies are shifted. (**Figure 4.8** and **Table 4.3**). A pronounced red shift from υ(OH) = 3600 cm^{-1} in solid state to υ(OH) = 3389 cm^{-1} in DMSO is observed.

$$\upsilon = \frac{1}{2\pi}\cdot\sqrt{\frac{k}{\mu}} \tag{3}$$

In conclusion, the electronic environment of the hydroxido bridge can be strongly influenced by variation of the solvent, due to the hydrogen bonding interaction between the selected solvents and the hydroxido bridge.

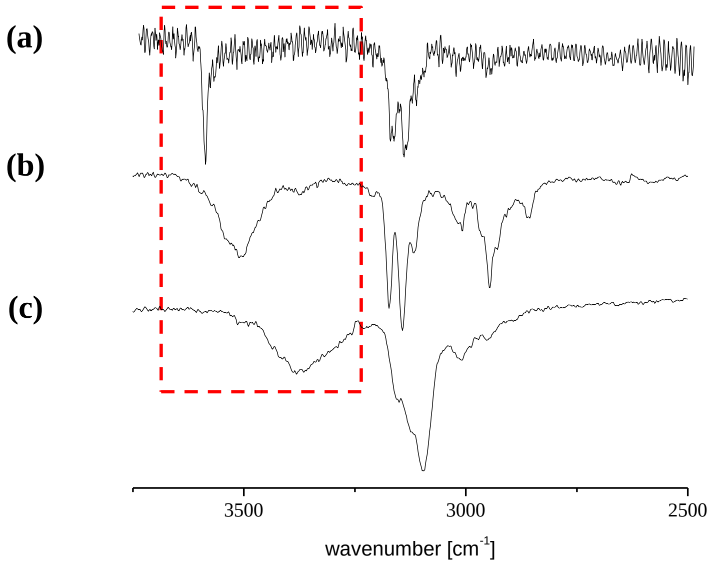

Figure 4.8: Comparison of the OH stretching frequencies (– – –) of $\mathbf{[L^6Ni_2(OH)](PF_6)_2}$ in (**a**) solid state $\upsilon_{(OH)}$ = 3600 cm^{-1}, (**b**) MeCN at $\upsilon_{(OH)}$ = 3503 cm^{-1} and (**c**) DMSO at $\upsilon_{(OH)}$ = 3389 cm^{-1} at r.t.

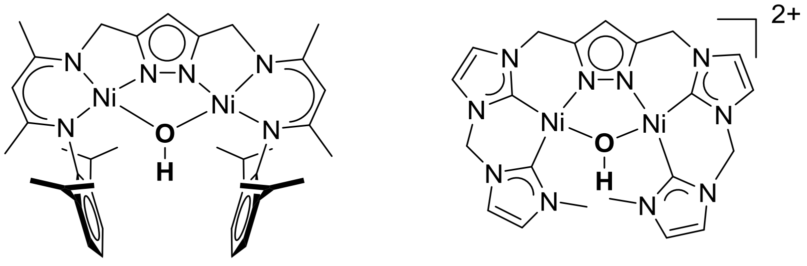

ν(OH) = 3606 cm^{-1}

XII

ν(OH) = 3600 cm^{-1}

Figure 4.9: Comparison of the υ(OH) of complex **XII** and $\mathbf{[L^6Ni_2(OH)]^{2+}}$ in solid state.

4.3.2 H/D and ^{16}OH/^{18}OH exchange at [L^{6}Ni$_2$(OH)](PF$_6$)$_2$

Proton exchange at the hydroxido bridge in **[L^{6}Ni$_2$(OH)](PF$_6$)$_2$** occurs upon addition of an excess of D_2O to a solution of the complex in MeCN. The ^{1}H NMR spectra of **[L^{6}Ni$_2$(OH)](PF$_6$)$_2$** shows a strong shift of the OH resonance in dependence on the amount of D_2O from initially –0.04 ppm in MeCN-d_3 to 0.08-0.28 ppm (25 equiv. to 100 equiv. D_2O at 298 K), before the peak vanished. ^{1}H NMR spectroscopy of **[L^{6}Ni$_2$(OD)](PF$_6$)$_2$** in MeCN-d_3 shows equal proton resonances compared to **[L^{6}Ni$_2$(OH)](PF$_6$)$_2$** and the absence of the OH proton resonance (**Figure 4.10**).

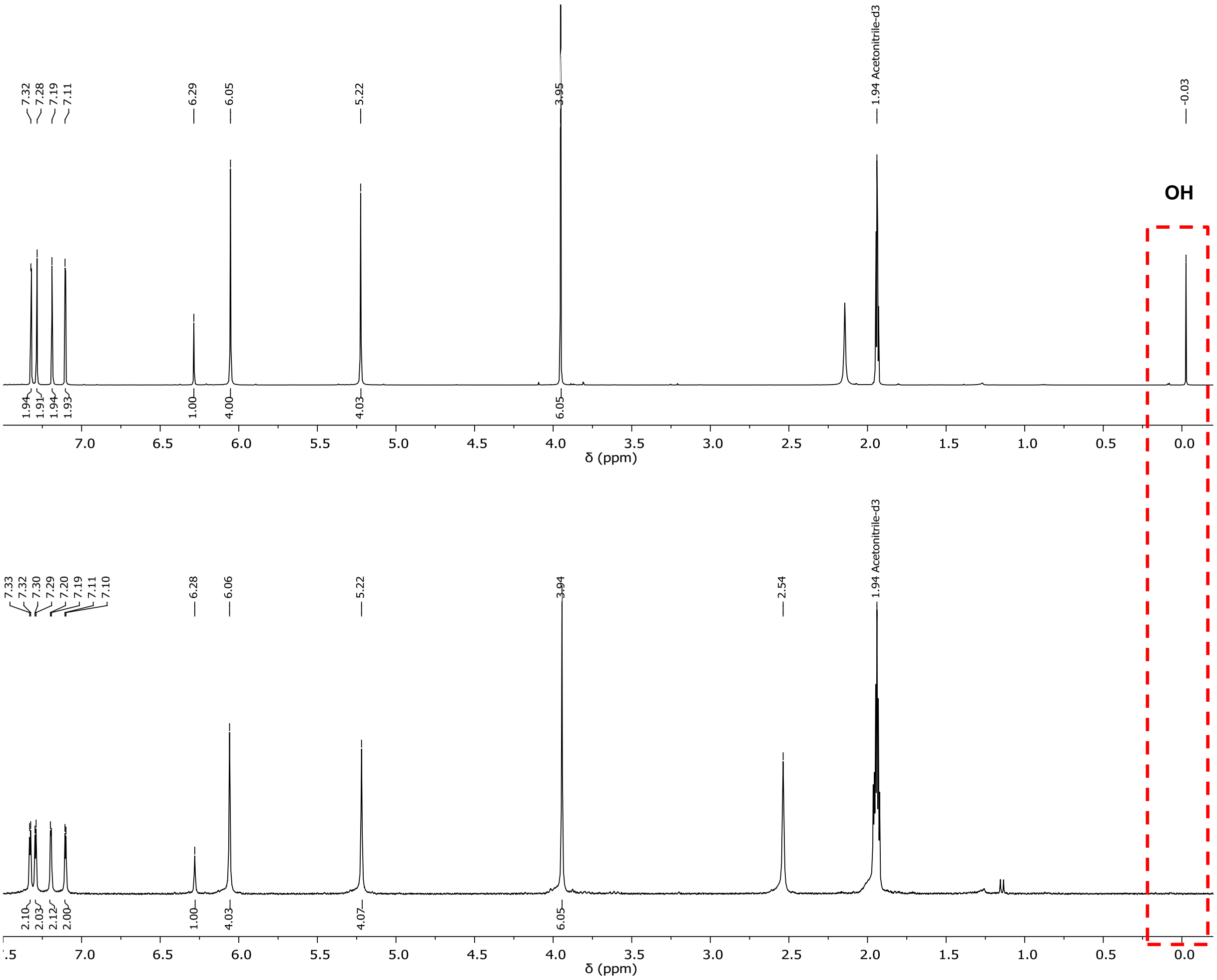

Figure 4.10: Top: ^{1}H NMR spectra of **[L^{6}Ni$_2$(OH)](PF$_6$)$_2$** and **bottom:** of **[L^{6}Ni$_2$(OD)](PF$_6$)$_2$** at 300 MHz both in MeCN-d_3. The labeled areas (– – –) show the disappearance of the OH proton resonance after total conversion to the OD-bridged complex.

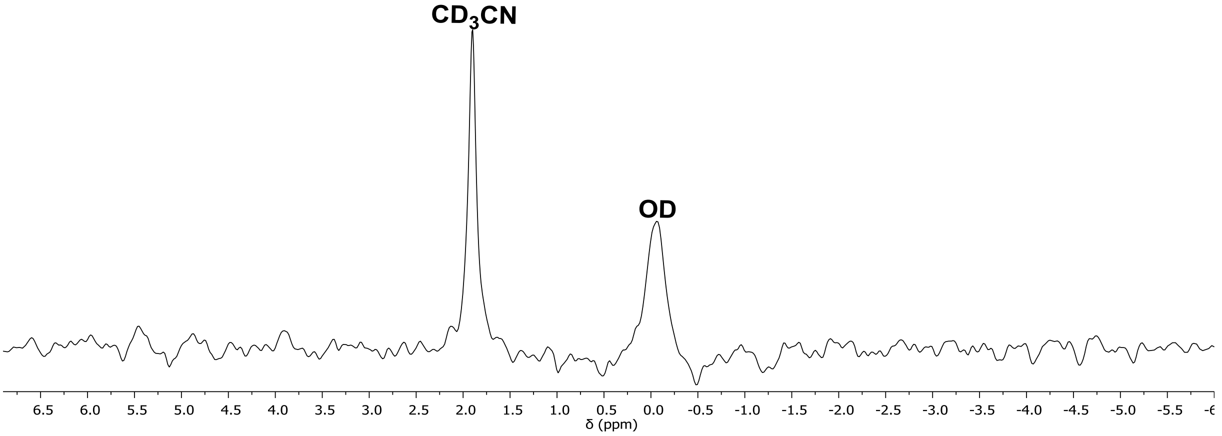

Figure 4.11: ^{2}H NMR spectrum of **[L^{6}Ni$_2$(OD)](PF$_6$)$_2$** in MeCN at 298 K and 61 MHz. One ^{2}H resonance at 0.06 ppm is assigned to the OD resonance of **[L^{6}Ni$_2$(OD)](PF$_6$)$_2$**.

^{2}H NMR spectroscopy of **[L^{6}Ni$_2$(OD)](PF$_6$)$_2$** in MeCN shows a broad peak at around 0.06 ppm for the OD resonance (**Figure 4.11**). In addition, the H/D exchange is confirmed by ESI-MS experiments (**Figure 4.12**, **right**). In the ESI-MS measurements of the labeled and unlabeled complexes two peaks of the doubly and singly charged complexes are obtained, respectively. The difference between [**L^{6}Ni$_2$(OD)PF$_6$**]$^+$ and [**L^{6}Ni$_2$(OH)PF$_6$**]$^+$ is $m/z = 1$ in agreement with the isotopic shift.

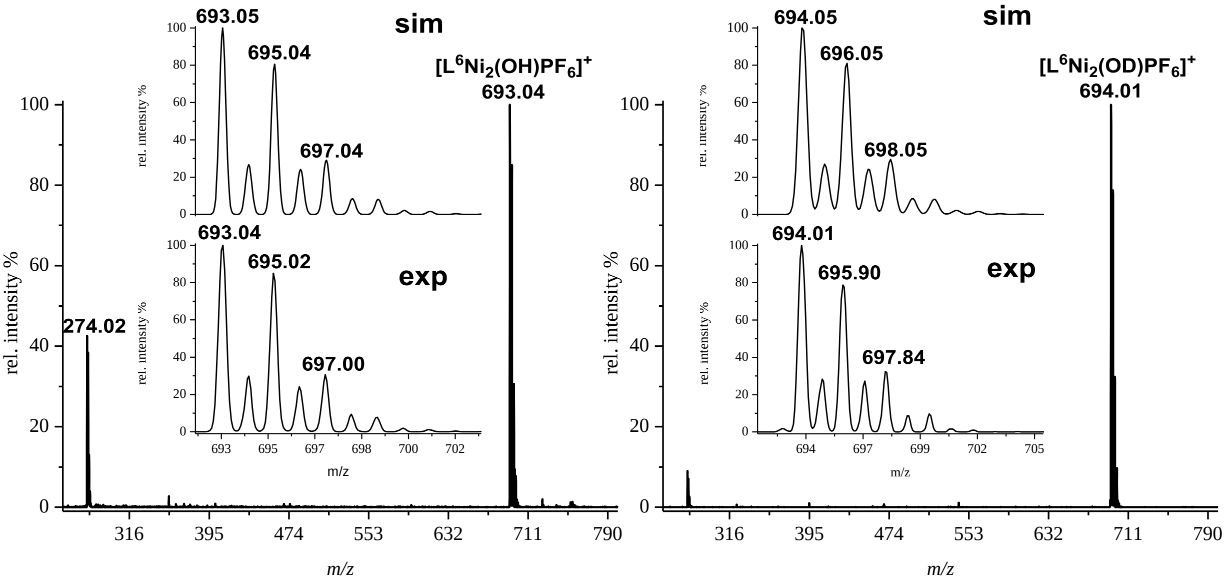

Figure 4.12: Left: ESI-MS of **[L^{6}Ni$_2$(OH)](PF$_6$)$_2$** in MeCN. The inset shows the simulated (**top**) and experimental (**bottom**) isotopic distribution pattern of the peak at *m/z* = 693 (100) for [**L^{6}Ni$_2$(OH)PF$_6$**]$^+$. **Right:** ESI-MS of **[L^{6}Ni$_2$(OD)](PF$_6$)$_2$** indicates the successful labeling of the complex. The inset shows the simulated (**top**) and experimental (**bottom**) isotopic distribution pattern of the peak at *m/z* = 694 (100) for [**L^{6}Ni$_2$(OD)PF$_6$**]$^+$.

Comparison of the IR spectra of **[L^{6}Ni$_2$(OH)](PF$_6$)$_2$** and **[L^{6}Ni$_2$(OD)](PF$_6$)$_2$** show an expected shift of the hydroxido stretching frequency from υ(OH) = 3518 cm^{-1} to υ(OD) = 2602 cm^{-1} (**Figure 4.13** and **Table 4.4**). Also a total exchange of the ^{16}OH bridge by H$_2$^{18}O is possible and confirmed by ESI-MS measurements (**Figure 4.14**). Two peaks are observed at *m/z* = 275 (15) for [**L^{6}Ni$_2$(^{18}OH)]$^{2+}$** and at *m/z* = 695 (100) for [**L^{6}Ni$_2$(^{18}OH)PF$_6$]$^+$**.

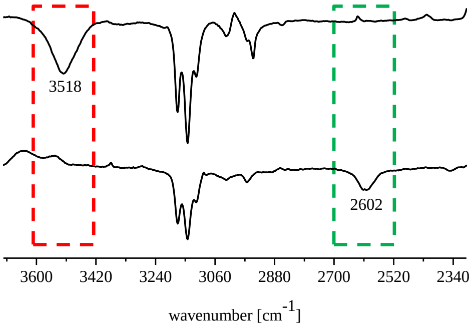

Figure 4.13: Excerpt of IR spectra of **[L^{6}Ni$_2$(OH)](PF$_6$)$_2$** (**top**): υ(OH) at 318 cm^{-1} (– – –) and **[L^{6}Ni$_2$(OD)](PF$_6$)$_2$** (**bottom**): υ(OD) at 2602 cm^{-1} (– – –) in MeCN.

Table 4.4: Comparison of the OH and OD stretches of [**L^{6}Ni$_2$(OH)](PF$_6$)$_2$** and [**L^{6}Ni$_2$(OD)](PF$_6$)$_2$** in MeCN.

	υ(OH) [cm^{-1}]	υ(OD) [cm^{-1}]	$\Delta\upsilon$ [cm^{-1}]	$\left[\frac{\upsilon(\mathrm{OH})}{\upsilon(\mathrm{OD})}\right]$
Experimental	3518	2602	916	1.35
harmonic approximation	3518	2560	958	1.37

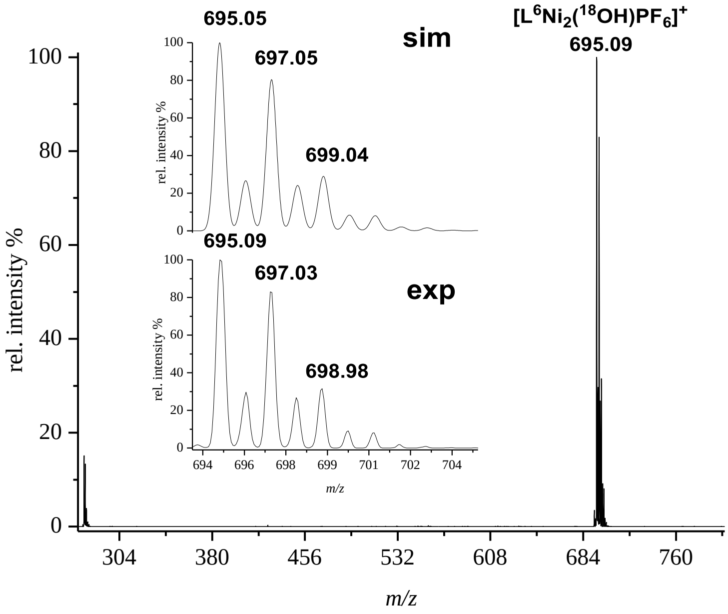

Figure 4.14: ESI-MS of [**L^{6}Ni$_2$(^{18}OH)](PF$_6$)$_2$** in MeCN. The inset shows the simulated (**top**) and experimental (**bottom**) isotopic distribution pattern of the peak at *m/z* = 695 (100) for [**L^{6}Ni$_2$(^{18}OH)PF$_6$]$^+$**.

4.3.3 H/D exchange kinetics at $[L^6Ni_2(OH)](PF_6)_2$

NMR studies are performed at different D_2O and $H_2{}^{17}O$ concentrations and different temperatures, to investigate the H/D and $^{16}OH/^{17}OH$ exchange kinetics. A substitution reaction at a square planar complex can be considered by the following general reaction equation (4)[132], wherein Y is the incoming nucleophile and X the leaving ligand. A rate law is formulated for such a case (5), wherein k_1 is a rate constant of a solvent assistant pathway, where the solvent has coordinating properties.[132] k_2 is the rate constant which is directly dependent on the entering nucleophile Y, here D_2O or $H_2{}^{17}O$, respectively.[132] Substitution reactions are carried out in an excess of Y. Hence a minimal amount of 10 equiv. to maximum of 100 equiv. of Y is used in relation to $[\mathrm{ML_3X}]$. $[\mathrm{Y}]$ can be assumed as a constant over the whole reaction time and the expression $(k_1 + k_2[\mathrm{Y}])$ in formula (5) is simplified to k (6).

$$[\mathrm{ML_3X}] + \mathrm{Y} \rightarrow [\mathrm{ML_3Y}] + \mathrm{X} \tag{4}$$

$$-\frac{\mathrm{d}[\mathrm{ML_3X}]}{\mathrm{dt}} = (k_1 + k_2[\mathrm{Y}]) \cdot [\mathrm{ML_3X}] \tag{5}$$

$$-\frac{\mathrm{d}[\mathrm{ML_3X}]}{\mathrm{dt}} = k \cdot [\mathrm{ML_3X}] \tag{6}$$

H/D exchange is followed by ^1H NMR spectroscopy. Substitution of a proton by a deuterium ion in the exchange reaction results in a decrease of the OH proton resonance in the ^1H NMR spectrum and concomitant increase of the **$[L^6Ni_2(OD)](PF_6)_2$** concentration in solution over time (**Figure 4.15** (**a**) and appendix). Plotting of the natural logarithm of c(**$[L^6Ni_2(OH)](PF_6)_2$**) *vs.* time allows the determination of the rate constants k of the *pseudo* first order reaction as the negative slope of a linear fit at a defined temperature and amount of D_2O (**Figure 4.15** (**b**) and **Table A.4.1** in appendix). The rate constants k_1 (intercept) and k_2 (slope) are determined by plotting the obtained k values at defined temperatures *vs.* c(D_2O) (**Figure 4.15** (**c**)). In **Table 4.5** all obtained k_1 and k_2 values are listed at four different temperatures (288 K, 298 K, 308 K and 318 K). In **Figure 4.15** (**c**), a linear fit supports the dependency of the exchange reaction on the D_2O concentration.[132,133] A comparison of the obtained k_1 and k_2 values shows that k_1 cannot be neglected at low c(D_2O). A solvent assistant mechanism has a certain influence on the overall reaction kinetic. The activation parameters $\Delta H^\ddagger$, $\Delta S^\ddagger$ and the activation energy E_a are determined by use of an Eyring plot and an Arrhenius plot (**Figure 4.16**) by consideration of k_2.

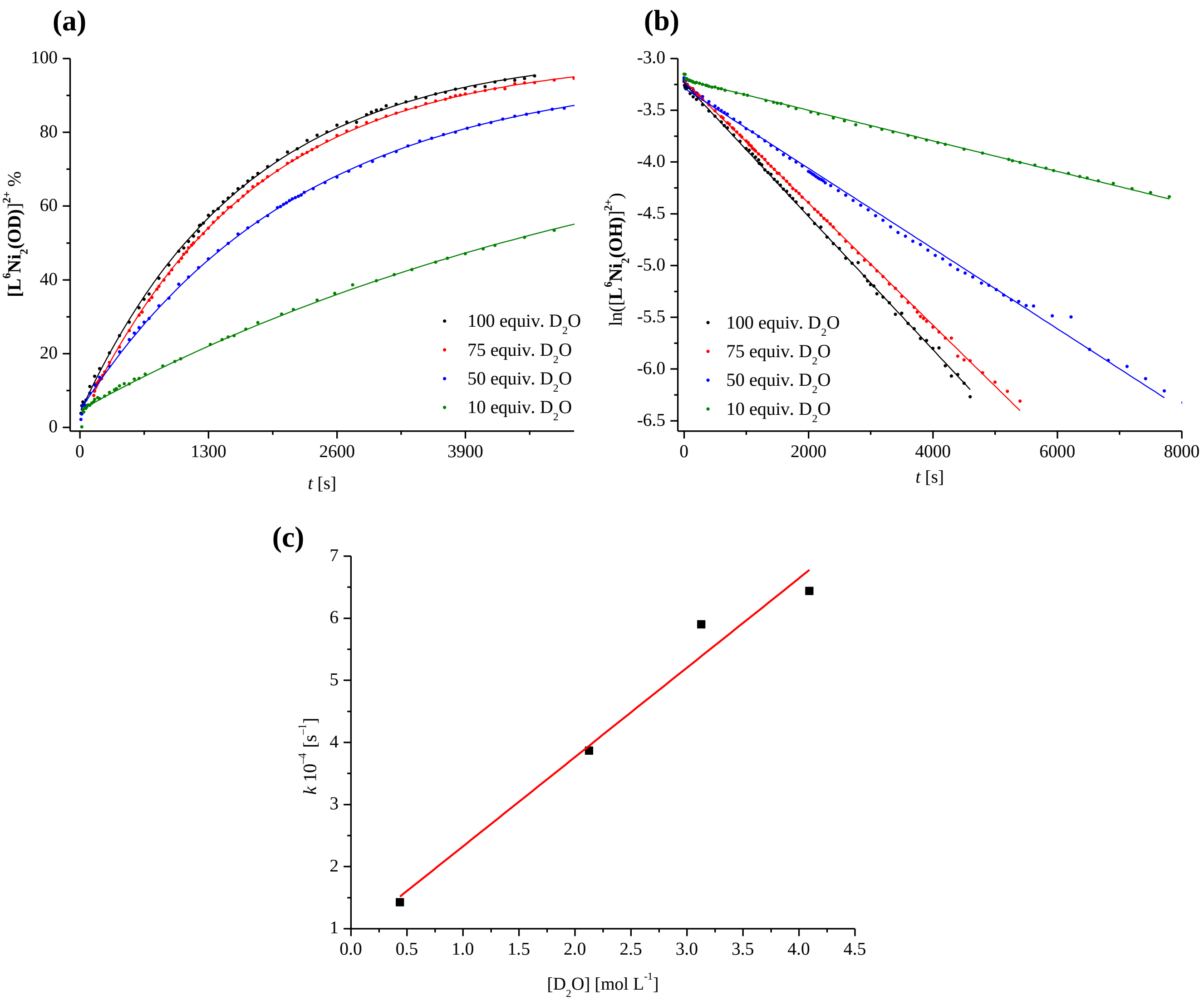

Figure 4.15: (**a**) Formation of **[$L^6Ni_2(OD)](PF_6)_2$** over time in the presence of different equiv. of D_2O at 308 K in MeCN-d_3. (**b**) Determination of k values at different D_2O concentrations at 308 K. (**c**) Dependency of k *vs.* [D_2O] at 308 K. The red line shows the best fit (slope = $1.439 \cdot 10^{-4}$, intercept = $8.869 \cdot 10^{-5}$, $R^2 = 0.9621$).

Table 4.5: Graphical determined rate constants k_1 and k_2 for H/D exchange of **[$L^6Ni_2(OH)](PF_6)_2$** by D_2O.

T [K]	k_1 10^{-4} [s^{-1}]	k_2 10^{-4} [$L \cdot mol^{-1} \cdot s^{-1}$]
288	0.24±0.02	0.34±0.02
298	0.99±0.01	0.97±0.01
308	0.89±0.04	1.44±0.06
318	5.43±0.18	5.50±0.19

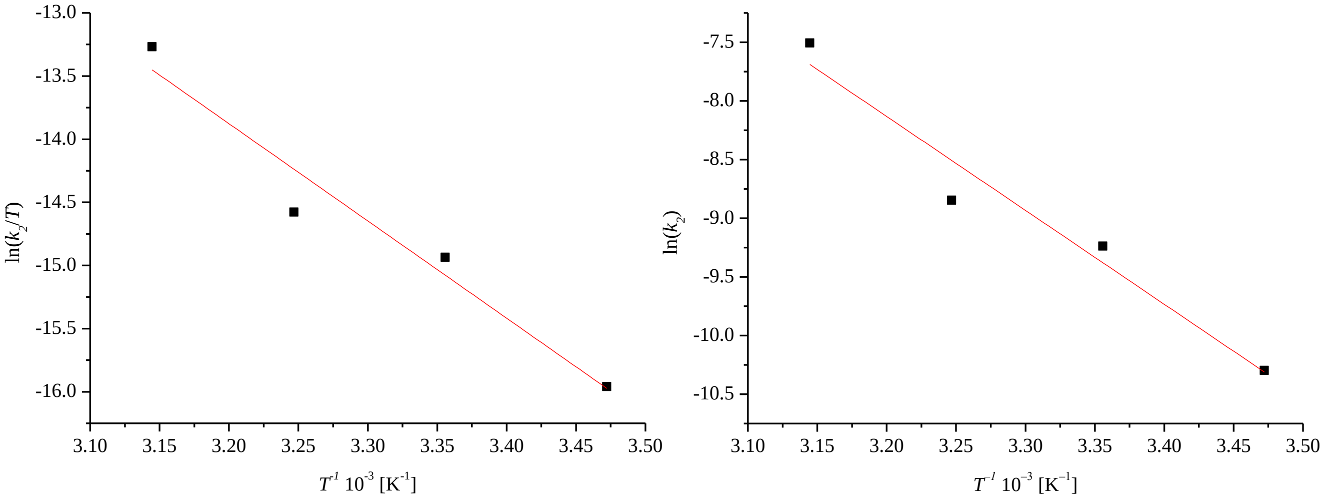

Figure 4.16: Left: Eyring plot (R^2 =0.9316). **Right:** Arrhenius plot (R^2 =0.9363) of the H/D exchange reaction of **[L^{6}Ni$_2$(OH)](PF$_6$)$_2$** by D_2O.

An activation enthalpy of $\Delta H^‡ = 64.0\ \mathrm{kJ{\cdot}mol^{-1}} \pm 9.0\ \mathrm{kJ{\cdot}mol^{-1}}$ and an activation entropy of $\Delta S^‡ = -108.0\ \mathrm{J{\cdot}mol^{-1}{\cdot}K^{-1}} \pm 15.1\ \mathrm{J{\cdot}mol^{-1}{\cdot}K^{-1}}$ are determined by an Eyring plot. The activation energy $E_a = 66.6\ \mathrm{kJ{\cdot}mol^{-1}} \pm 8.9\ \mathrm{kJ{\cdot}mol^{-1}}$ is obtained by an Arrhenius plot. The strongly negative entropy value is in accordance with an associative mechanism.[132] The obtained $\Delta S^‡$ value can just be considered as a first approximation, since the temperature window of $\Delta T = 30$ K (T =288-318 K) is small and results into a large error of the intercept with the y-axis. Discrimination between an associative mechanism and a concerted pathway (interchange reaction mechanism) is not trivial from activation parameters alone. However, evidence from a structure in solid state provides further mechanistic insights. It is obtained after addition of tetra-butyl ammonium chloride to **[L^{6}Ni$_2$(OH)](PF$_6$)$_2$** and crystallization of the reaction product **[L^{6}Ni$_2$(OH)]Cl$_2$·2 H$_2$O** (**Figure 4.17)**. This molecular structure in solid state shows a cluster of water molecules interacting with the hydroxido bridge *via* hydrogen bond interactions. In addition, the water molecules are hydrogen-bonded to the chloride counter ions of the complex. Based on this structure, a concerted H/D exchange seems to be possible. A possible mechanism is described in **Scheme 4.4**. A pre-equilibrium between **[L^{6}Ni$_2$(OH)]$^{2+}$** and **[L^{6}Ni$_2$(OH)]$^{2+}$·D$_2$O** can be described, which occurs fast after addition of D_2O to **[L^{6}Ni$_2$(OH)]$^{2+}$** and is mainly located on the site of **[L^{6}Ni$_2$(OH)]·D$_2$O**. In the next step, a second D_2O molecule coordinates to **[L^{6}Ni$_2$(OH)]$^{2+}$·D$_2$O** and two D_2O molecules are preorganized *via* hydrogen bond interactions with the μ-OH group of **[L^{6}Ni$_2$(OH)]$^{2+}$** and a simultaneously protonation/deprotonation step could occur (**Scheme 4.4)**. In such a mechanistic scenario the overall rate would be strongly dependent on the pre-equilibrium constant k and a higher order of the reaction is probably expected, which cannot be determined by a rate law in formula (5).

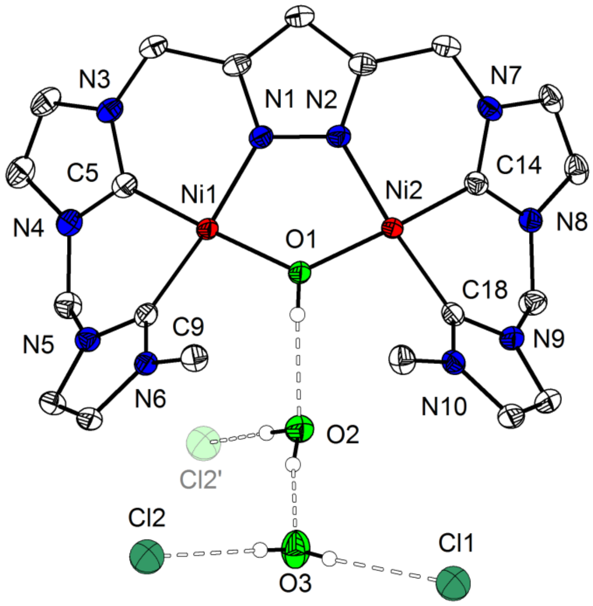

Figure 4.17: Structure (50% probability thermal ellipsoids) of **$[L^6Ni_2(OH)]Cl_2 \cdot 2\ H_2O$**. H atoms, except of the OH bridge and water molecules, are omitted for clarity. Hydrogen bond interactions of the OH bridge to water molecules are observed.

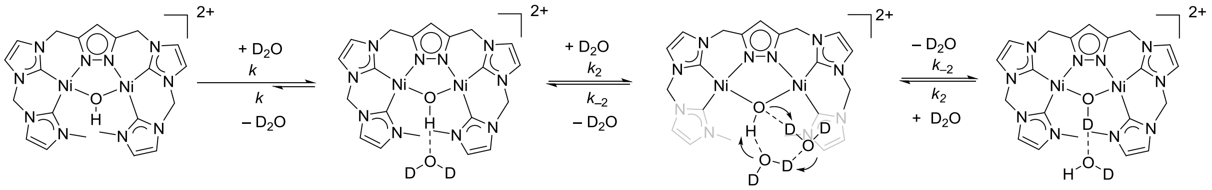

Scheme 4.4: Postulated reaction mechanism for the concerted H/D exchange reaction at **$[L^6Ni_2(OH)]^{2+}$** with D_2O.

4.3.4 $^{16}OH/^{17}OH$ exchange kinetics at $[L^6Ni_2(OH)](PF_6)_2$

Exchange of the hydroxido bridge occurs upon addition of an excess of $H_2{}^{17}O$ to the complex solution in MeCN-d_3 and is monitored by ^1H NMR spectroscopy. This indirect investigation of the exchange reaction is possible, due to the ^{17}O nuclear spin of 5/2, which results in an extreme broadening of the $H^{17}O$ resonance of **$[L^6Ni_2(^{17}OH)](PF_6)_2$** in the ^1H NMR spectrum and allows for monitoring the decrease of the $H^{16}O$ resonance over time. Measurement of the exchange reaction by ^{17}O NMR spectroscopy is not possible due to the long relaxation times of the nucleus. This leads to longer measurement times and also broad signals, which makes the fast reactions impossible to evaluate. ^{17}O NMR spectroscopy of **$[L^6Ni_2(^{17}OH)](PF_6)_2$** in MeCN-$d_3$ shows a broadened ^{17}OH resonance at –119.6 ppm (**Figure 4.18**).

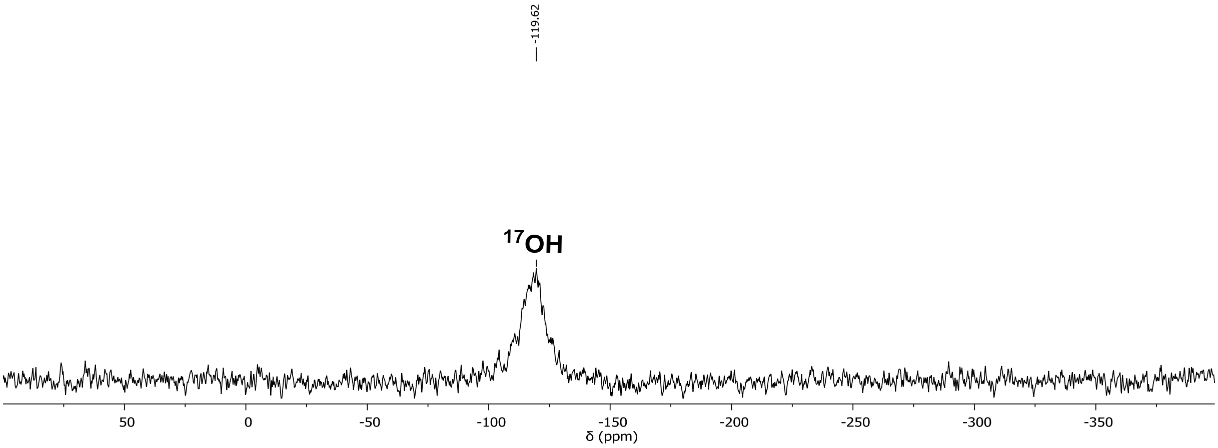

Figure 4.18: ^{17}O NMR spectrum of **$[L^6Ni_2(^{17}OH)](PF_6)_2$** shows one peak at –119.6 ppm for the ^{17}OH bridge at 298 K and 54 MHz.

Substitution of the ^{16}OH bridge in **$[L^6Ni_2(OH)](PF_6)_2$** by ^{17}OH results in a decrease of the ^{16}OH proton resonance in the ^1H NMR spectrum and concomitant increase of the **$[L^6Ni_2(^{17}OH)](PF_6)_2$** concentration in solution over time (**Figure 4.19** (**a**) and appendix). The corresponding ln[**$[L^6Ni_2(OH)](PF_6)_2$**] *vs.* time plot shows a linear trend of the reaction (**Figure 4.19** (**b**) and appendix). The overall rate of the $H_2{}^{16}O/H_2{}^{17}O$ exchange reaction is slower than the H/D exchange, supported by the obtained k values (see appendix). **Figure 4.19** (**c**) shows a linear dependency for the exchange rate on the $H_2{}^{17}O$ concentration. In **Table 4.6**, the rate constants k_1 and k_2 at four different temperatures (298 K, 308 K, 318 K and 328 K) are summarized. The linear fit in **Figure 4.19** (**c**) and the obtained k_1 and k_2 values support the strong dependency of the exchange reaction on the $H_2{}^{17}O$ concentration.[132,133] k_1 is at least a magnitude of ten lower than $k_2 \cdot [H_2{}^{17}O]$ can be neglected and a solvent assistant mechanism is excluded.[132,133]

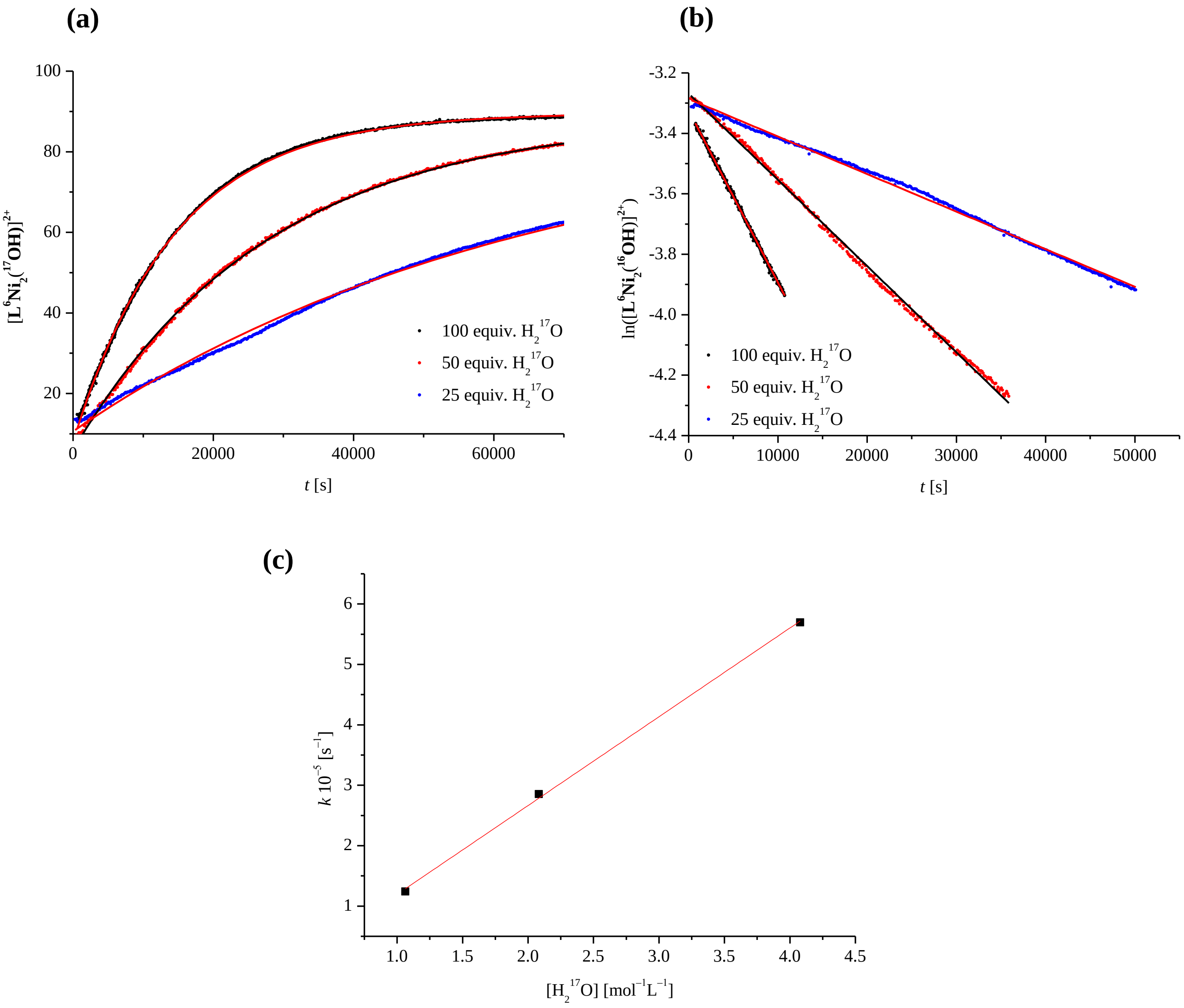

Figure 4.19: (**a**) Formation of **$[L^6Ni_2(^{17}OH)](PF_6)_2$** over time in the presence of different equiv. of $H_2{}^{17}O$ at 298 K in MeCN-d_3. (**b**) Determination of k values at different equiv. of $H_2{}^{17}O$ at 298 K. (**c**) Dependency of k *vs.* concentration of $H_2{}^{17}O$ at 298 K. The red line shows the best fit (slope = $1.439\cdot10^{-4}$, intercept = $8.869\cdot10^{-5}$, $R^2 = 0.9621$).

Table 4.6: Graphical determined rate constants k_1 and k_2 for $^{16}OH/^{17}OH$ exchange of **$[L^6Ni_2(OH)](PF_6)_2$** by $H_2{}^{17}O$.

T [K]	$k_1\ 10^{-5}$ [s^{-1}]	$k_2\ 10^{-4}$ [$L\cdot mol^{-1}\cdot s^{-1}$]
298	$-0.27\pm0.4\cdot10^{-3}$	$0.15\pm0.2\cdot10^{-3}$
308	2.54 ± 0.02	$0.34\pm0.3\cdot10^{-2}$
318	-2.53 ± 0.09	1.14 ± 0.04
328	$-6.09\pm0.3\cdot10^{-2}$	$3.55\pm0.2\cdot10^{-2}$

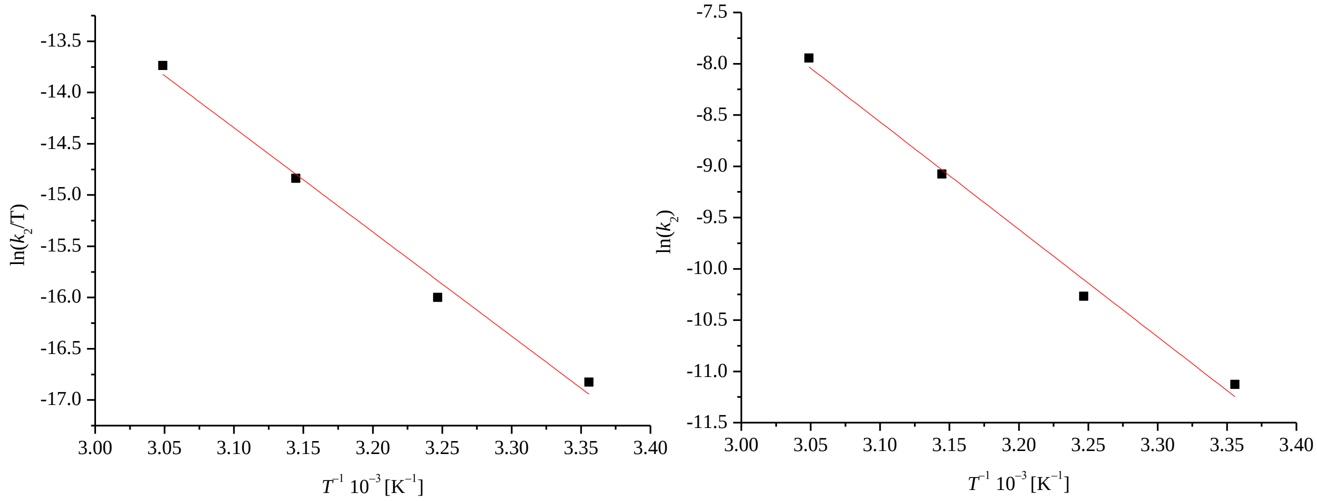

Figure 4.20: Left: Eyring plot (R^2 =0.9864) and **right** Arrhenius plot (R^2 =0.9870).

$\Delta H^{\ddagger}$ and $\Delta S^{\ddagger}$ are determined from an Eyring plot with k_2 values and calculated by formula (6) and (7) (**Figure 4.20**). A reaction enthalpy of $\Delta H^{\ddagger}$ = 84.5 kJ·mol^{-1}±2.1 kJ·mol^{-1} and a reaction entropy of $\Delta S^{\ddagger}$ = –54.8 J·mol^{-1}·K^{-1}±1.4 J·mol^{-1}·K^{-1} are obtained. An associative mechanism is supported by the negative activation entropy.[132] The kinetic parameters of the $H_2{}^{16}O/H_2{}^{17}O$ exchange differ significantly from the H/D exchange reaction values, in agreement with the observed faster H/D exchange rates. Two different mechanism are assumed in accordance with a large $\Delta\Delta H^{\ddagger}$ = 20.5 kJ/mol±6.9 kJ·mol^{-1} between the H/D (concerted pathway) and $^{16}OH/^{17}OH$ (associative pathway) exchange kinetics. A comparison of the $\Delta G^{\ddagger}{}_{303\,K}$ at 303 K shows an energy difference of 4.4 kJ·mol^{-1}±2.2 kJ·mol^{-1} (**Table 4.7**). In section 4.3.3., a concerted pathway for the H/D exchange reaction was already postulated (**Scheme 4.4**).

Table 4.7: Comparison of activation parameters for water exchange at **$[L^6Ni_2(OH)](PF_6)_2$**, **XIII**[134] and **DFT**[134] of **XIII** (Calculated values B3LYP-D3 and computed with the def2-TZVP basis set, based on BP86/def2-SVP optimized geometries.

	$[L^6Ni_2(OH)](PF_6)_2$		**XIII**[134]		**DFT XIII**[134]
	H/D exchange	$^{16}OH/^{17}OH$ exchange	H/D exchange	$^{16}OH/^{17}OH$ exchange	$^{16}OH/^{17}OH$ exchange
$\Delta H^{\ddagger}$ [kJ/mol]	64.0±9.0	84.5±2.1	86.0	88.0	84
$\Delta S^{\ddagger}$ [J/molK]	–108.0±15	–54.8±1.4	–80.0	–74.0	–
E_a [kJ/mol]	66.6±8.9	87.1±2.1	89.0	90.0	–
$\Delta G^{\ddagger}{}_{303}$ [kJ/mol]	96.8±13	101.1±2.1	110.0	109.0	91

In 2016, Manz[134] reported very slow H/D and $^{16}OH/^{17}OH$ exchange reactions at the dinickel(II) μ-OH complex **XIII** (**Figure 4.21**). Based on DFT calculations, they proposed an associative mechanism for both exchange reactions with an intermediary H_3O_2 bridge between the two nickel centers. The reported rates are three orders of magnitude lower than in

[L^{6}Ni$_2$(OH)](PF$_6$)$_2$, probably due to the steric hindrance of the exchange reaction by the Dipp groups in **XIII**. DFT calculations suggest the incorporation of a water molecule and the formation of a H_3O_2 bridge as an intermediate (in accordance to **Scheme 4.5**).[134]

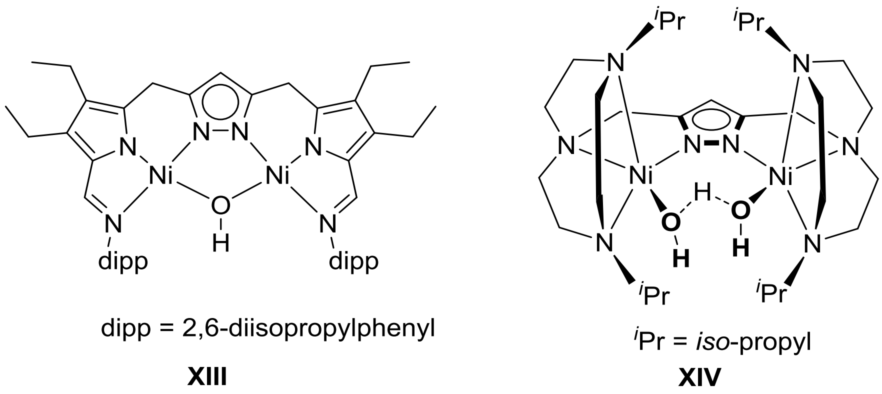

Figure 4.21: Left: A dinickel(II) μ-OH complex **XIII** and **right**: dinickel(II) μ-H_3O_2 complex **XIV**.

In 2002, Meyer *et al.*[123] published the molecular structures in solid state of dinickel(II) μ-H_3O_2 complexes **IX** and **XIV** (**Figure 4.1** and **4.21**) with nickel···nickel distances between 4.48 Å and 4.45 Å..[121,122,135] The nickel···nickel distance in **[L^{6}Ni$_2$(OH)](PF$_6$)$_2$** is 3.26 Å and a hypothetic dinickel μ-H_3O_2 complex is assumed to be unstable, since the incorporation of diatomic anions or molecules in a μ-η^1:η^1 fashion failed so far. The formation of this complex would be the rate determining step (**Scheme 4.5**). Extended DFT calculations of **[L^{6}Ni$_2$(OH)](PF$_6$)$_2$** can give further insights of an energetically favored pathway.

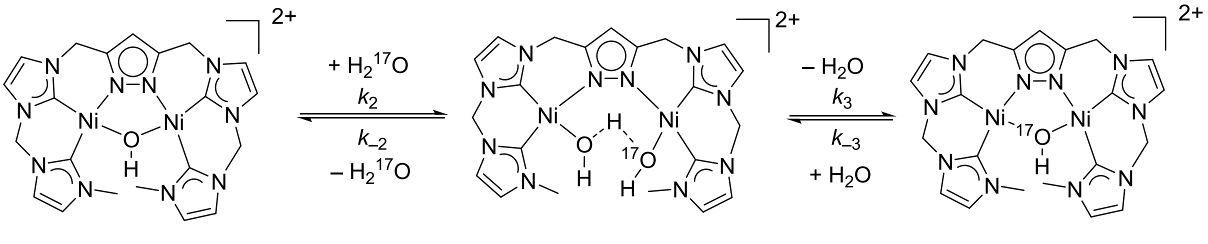

Scheme 4.5: Postulated associative reaction mechanism for the ^{16}OH/^{17}OH exchange *via* a μ-H_3O_2 intermediate.

4.3.5 DFT calculations of the ^{16}OH/^{17}OH exchange at [L^{6}Ni$_2$(OH)](PF$_6$)$_2$

Extended DFT calculations are performed to elucidate the mechanism for the $H_2{}^{16}O$/$H_2{}^{17}O$ exchange reaction at **[L^{6}Ni$_2$(OH)]$^{2+}$**. The ground state and starting point of the calculation is **[L^{6}Ni$_2$(OH)]$^{2+}$** interacting with one water molecule *via* a hydrogen bond (**Scheme 4.6**). In a first step the water molecule moves to one nickel center and the hydrogen bond interaction to the hydroxido bridge is repealed. In the next step the water molecule coordinates to a nickel center and forms a hydrogen bond interaction to the OH bridge. An elongation of the O–H bond of the water molecule and a distorted ligand scaffold in the transition state is observed. The distorted ligand scaffold is energetically not favored and leads to a high activation barrier which has to be overcome. A stronger interaction between the hydroxido bridge and the water molecule results in elongation of one Ni–O(H) bond and finally into a bond break and an incorporation of the water molecule between one nickel ion and the hydroxido ligand that is still bound to the other nickel ion. The previously postulated **$[L^6Ni_2(H_3O_2)]^{2+}$** is slowly formed and a strongly distorted ligand scaffold in the molecule is observed. A stable intermediate is found halfway along the substitution pathway, circa 60 kJ·mol^{-1} higher in energy than the starting structure. The short intermetallic distance disfavors the incorporation of H_3O_2 in contrast to the large dinickel distance, observed in the molecular structures of **IX** and **XIV**.[121,122,135] The distortion of the ligand scaffold in **$[L^6Ni_2(OH)]^{2+}$** and the formation of **$[L^6Ni_2(H_3O_2)]^{2+}$** are both energetically not favored and are the rate determining steps in the hydroxide exchange reaction. In the next steps $H_2{}^{16}O$ and ^{17}OH are formed, $H_2{}^{16}O$ is released out of the bridge, μ-^{17}OH is formed and the exchange is completed after decoordination of $H_2{}^{16}O$. Also a reverse reaction pathway from **$[L^6Ni_2(H_3O_2)]^{2+}$** under release of $H_2{}^{17}O$ is energetically favorable. However, the release of water is faster than the association. Based on theoretical results, a mechanism is proposed that explains the rather low reaction rates of the ^{16}OH/^{17}OH exchange reaction compared to the H/D exchange reaction. The calculated $\Delta H^{\ddagger}$ lies between 91.8-99.6 kJ·mol^{-1} depending on the functional used. This is in fair agreement with the experimentally determined value (84.5 kJ·mol^{-1}) and a strong argument in favor of the proposed mechanism (**Table 4.8**). The ^{16}OH/^{17}OH exchange reaction follows an associative mechanism *via* **$[L^6Ni_2(H_3O_2)]^{2+}$** in agreement with DFT calculations, whereby the H/D exchange reaction probably follows mainly a concerted mechanism.

Table 4.8: Comparison of experimental and theoretical determined activation parameters for water exchange at **$[L^6Ni_2OH](PF_6)_2$**, (BP86-D3 and B3LYP-D3).

	^{16}OH/^{17}OH exchange at **$[L^6Ni_2(OH)](PF_6)_2$**		
	Experimental	**BP86**	**B3LYP**
$\Delta H^{\ddagger}$ [kJ/mol]	84.5±2.1	91.8	99.6
$\Delta S^{\ddagger}$ [J/molK]	–54.8±1.4	–	–
$\Delta G^{\ddagger}_{298}$ [kJ/mol]	100.8±2.5	100.9	108.8

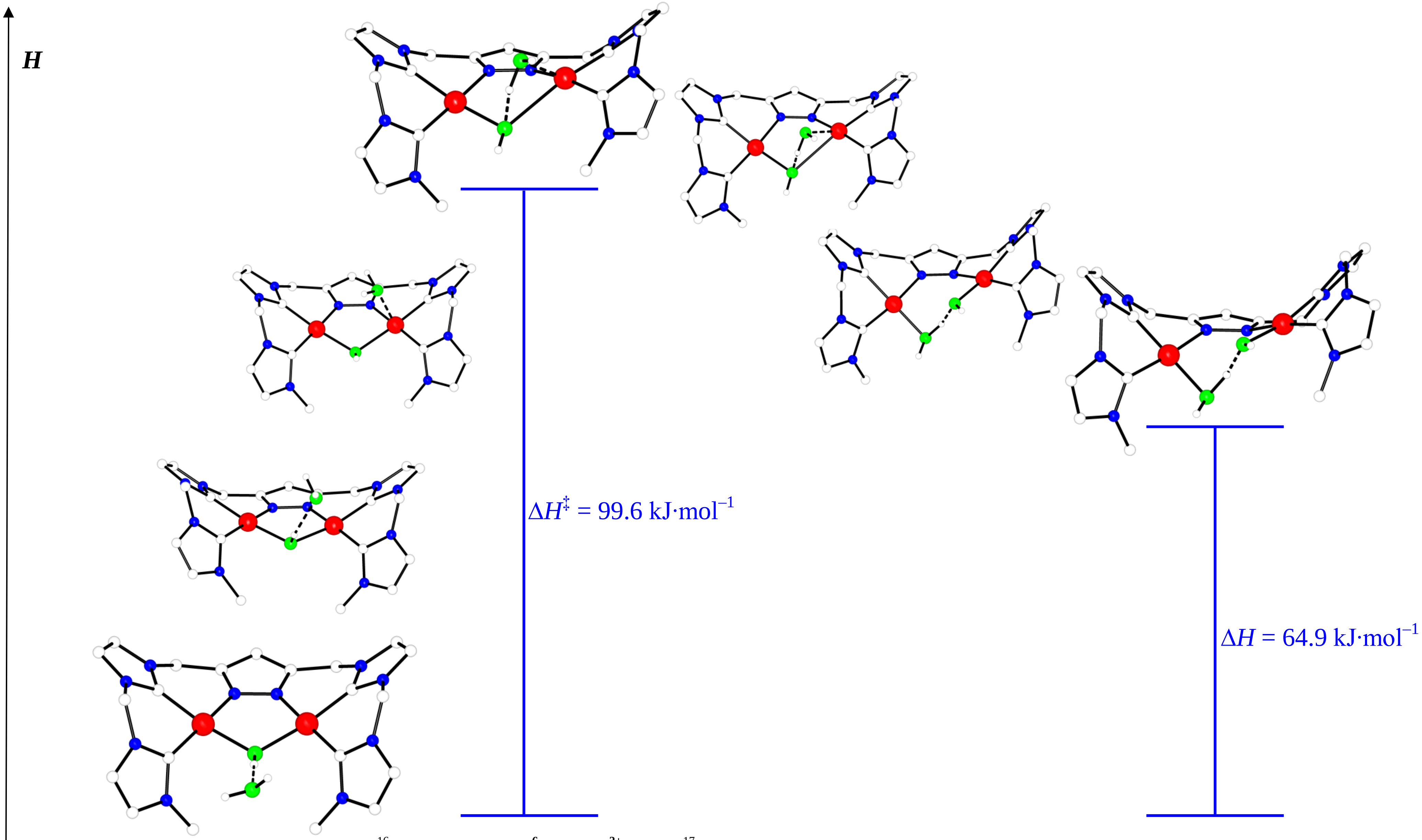

Scheme 4.6: Half of the energy profile for the *μ*-^{16}OH exchange of **[L^{6}Ni$_2$(OH)]$^{2+}$** with H$_2$^{17}O based on DFT calculations (B3LYP-D3).

4.3.6 Dynamics of $[L^6Ni_2(X)]^{y+}$ in solution

The ^1H NMR spectrum of **$[L^6Ni_2(OH)](PF_6)_2$** at 298 K shows an apparent C_{2v} symmetry in solution (**Figure 4.5** (**a**)), indicating high flexibility of the ligand. In the molecular structure in solid state, only an approximate (non-crystallographic) C_s symmetric molecule is isolated. In the following a general description of the interconversion of possible conformers of **$[L^6Ni_2(X)]^{y+}$** in solution is presented, and afterwards the energy barrier of **$[L^6Ni_2(OH)](PF_6)_2$** is determined.

In theory, **$[L^6Ni_2(X)]^{y+}$** can exist in three conformations of different symmetry, C_s, C_2 and C_{2v}. VT ^1H NMR experiments are performed to investigate the interconversion of conformers in solution. In the VT ^1H NMR spectra of all complexes (except of **$[L^6Ni_2(SH)]^{2+}$**), a decrease of the temperature leads to the observation of a diastereotopic splitting of both CH_2 proton resonances (AB spin system) of **$[L^6Ni_2(X)]^{y+}$**. This diastereotopic splitting excludes the presence of C_{2v} symmetry complex and **$[L^6Ni_2(X)]^{y+}$** is present as the two C_2 symmetric enantiomers or as the C_s symmetric complex. Three different scenarios are possible, depending on the most thermodynamic stable conformer (C_2 or C_s). In **Scenario 1** the C_s symmetric conformer is the thermodynamic stable complex. After passing a transition state, the C_2 symmetric complex is formed, which is a high energy intermediate and will be quickly converted into the identical C_s symmetric complex (**Scheme 4.7**). A small population of the C_2 symmetric complex below the detection limit of the NMR instrument is the consequence, due to a large energy difference of the two conformational diastereomers. Only the proton resonances of the C_s symmetric complexes are observed in the ^1H NMR spectrum. In **Scenario 2** (**Scheme 4.8**) the C_2 symmetric conformer is the thermodynamic stable complex and the C_s symmetric diastereomer is the unobservable high energy complex. **Scenario 3** (**Scheme 4.9**) differs from **Scenario 1** according to the relative energetic levels of the two diastereomers. The C_2 symmetric complex has a ground state energy that is comparable to the C_s symmetric complex. The proton resonances of the C_s symmetric complex and the C_2 symmetric complexes are both observed in the ^1H NMR spectrum and in dependence on the more energetically preferred conformer differs the ratio between C_s:C_2.

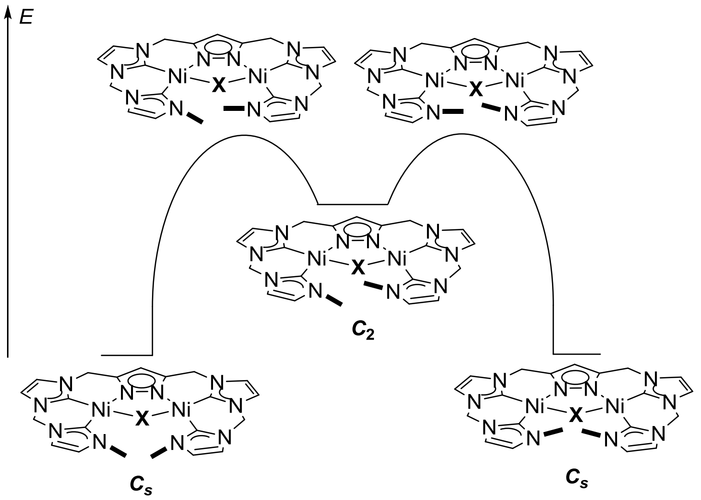

Scheme 4.7: Scenario 1: Energy profile of the interconversion of the C_s symmetric conformer into the C_s symmetric conformer *via* a high energy lying C_2 symmetric complex.

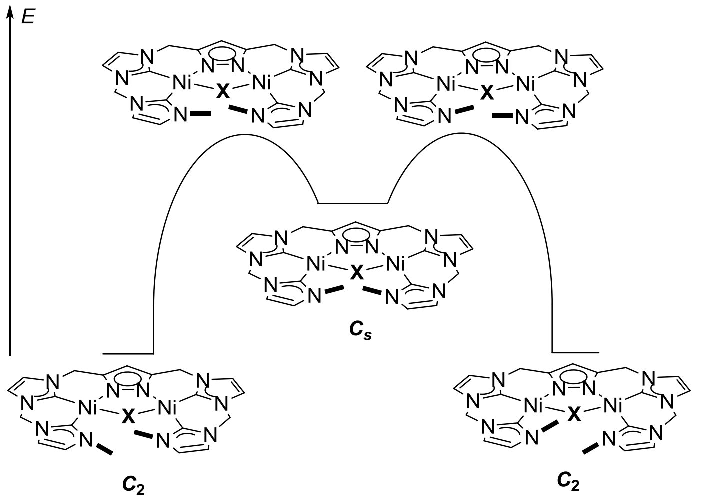

Scheme 4.8: Scenario 2: Energy profile of the interconversion of the C_2 symmetric conformer into the C_s symmetric conformer *via* a high energy lying C_2 symmetric complex.

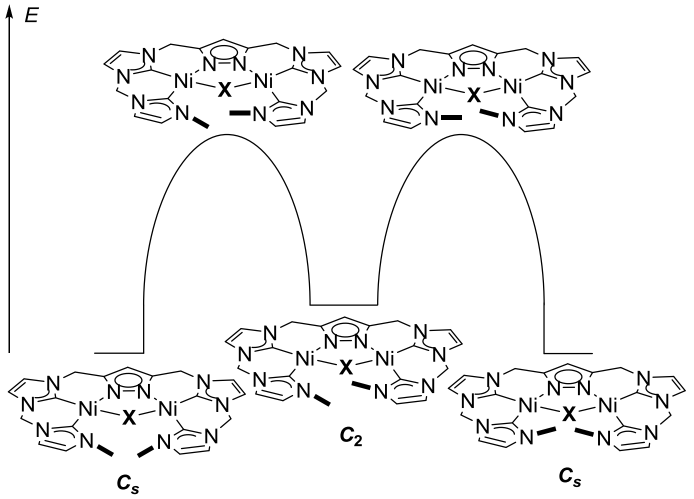

Scheme 4.9: Scenario 3: Energy profile for the interconversion of the C_s symmetric conformer into the C_s symmetric conformer *via* a C_2 symmetric complex of comparable energy.

4.3.7 Dynamics of [$L^6Ni_2(OH)](PF_6)_2$ in solution

VT ^{1}H NMR spectra of **[$L^6Ni_2(OH)](PF_6)_2$** in MeCN-d_3 (**appendix, Figure A.4.10**) show a diastereotopic splitting of the CH_2 groups (AB spin system) by decrease of the temperature. Only one diastereomer is observed in the ^{1}H NMR spectra, which indicates an interconversion of the C_s or C_2 symmetric complexes *via* **Scenario 1** or **Scenario 2** (**Scheme 4.7** or **Scheme 4.8**). The population of one diastereomer is below the detection limit of the NMR instrument and cannot be observed in the NMR spectra. No experimental possibility exists which would allow the discrimination between the C_s or C_2 symmetric complex as the more thermodynamic stable conformer in solution. The coalescence temperature T_c for both methylene groups is observed between 253 K and 263 K in MeCN-d_3 (**appendix, Figure A.4.10**). Determination of the kinetic parameters in such an AB system, where a simultaneous spin exchange in each CH_2 group is observed, is not trivial. A general description for the determination of the exchange rate k for the three different temperature regimes: (fast exchange, at coalescence temperature and slow exchange) is explained in the experimental section. These formulae cannot be used for an AB spin system, as observed for **[$L^6Ni_2(OH)](PF_6)_2$** and the complexes described herein below the coalescence point (see experimental section **10.2.2**). A possible way to determine k values for slow and intermediate exchange rates of such AB spin systems is the use of computational programs.

Since the number of accessible spectra below the coalescence temperature is too low in MeCN-d_3 to obtain reliable $(\Delta\upsilon_0)_{1/2}$ and $\Delta\upsilon_0$ values (see **10.2.3**), the determination of kinetic parameters for the dynamic process is instead performed in acetone-d_6 (**Figure 4.22**). An activation enthalpy of $\Delta H^‡ = 74.4\ \mathrm{kJ{\cdot}mol^{-1}} \pm 0.35\ \mathrm{kJ{\cdot}mol^{-1}}$ and an activation entropy of $\Delta S^‡ = 79.2\ \mathrm{J{\cdot}mol^{-1}{\cdot}K^{-1}} \pm 0.37\ \mathrm{J{\cdot}mol^{-1}{\cdot}K^{-1}}$ as well as an activation energy E_a of $76.5\ \mathrm{kJ{\cdot}mol^{-1}} \pm 0.35\ \mathrm{kJ{\cdot}mol^{-1}}$ for the interconversion is obtained by an Eyring plot or an Arrhenius plot (**Figure 4.23**). Based on the positive activation entropy, it is suggested that this value is related to the dissociation of an interacting acetone molecule *via* hydrogen bond interaction to the complex (**Figure 4.6**). The ^{1}H NMR spectroscopic investigations do not give any information which conformer is observed at low temperature (Cs or C_2 symmetry). Considering the obtained molecular structure in solid state, it is proposed that a C_s symmetric molecule is observed.

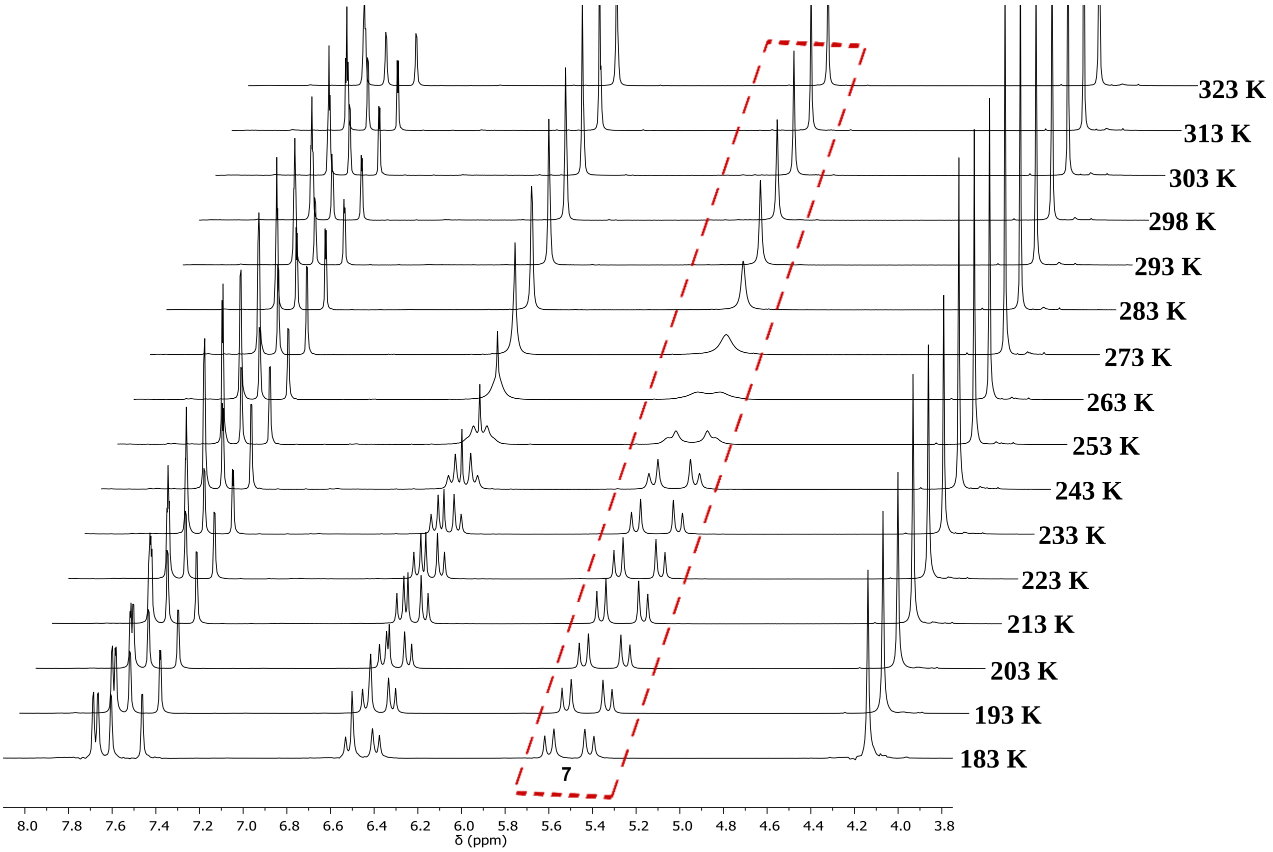

Figure 4.22: VT ^{1}H NMR spectra of **[L^{6}Ni$_2$(OH)](PF$_6$)$_2$** in acetone-d_6 in the temperature range between 323 K and 183 K. A T_c between 273 K and 263 K is observed. The labeling (– – –) highlights the diastereotopic splitting of the proton resonances H^7 of the CH$_2$ groups.

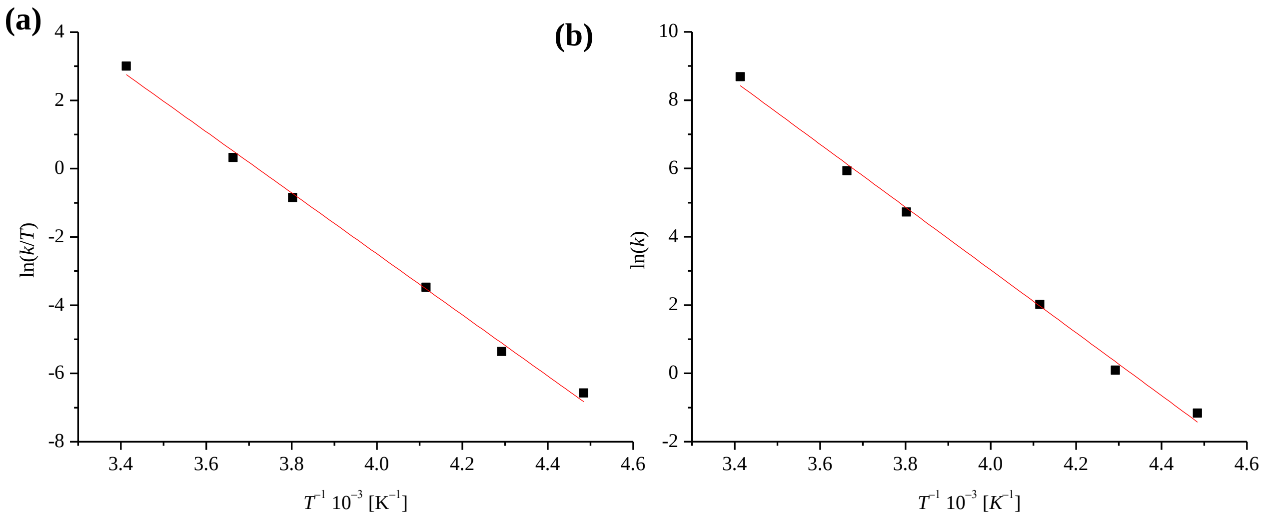

Figure 4.23: (**a**) Eyring plot (R^2 = 0.9953), (**b**) Arrhenius plot (R^2 = 0.9955).

Table 4.9: Rate constants at different temperatures derived by line shape analysis of the ^{1}H NMR resonances of the CH_2 group using the simulation program WinDNMR.

T [K]	k [s^{-1}]
293.2	5913
273.2	377
263.2	112
243.2	7.52
233.2	1.10
223.2	0.32

4.3.8 Redox properties of [L^{6}Ni$_2$(OH)](PF$_6$)$_2$

The UV-vis spectrum of **[L^{6}Ni$_2$(OH)](PF$_6$)$_2$** in MeCN at –40 °C shows three bands at 213 nm ($\varepsilon = 23.6 \cdot 10^3$ M$^{-1}\cdot$cm^{-1}), at 304 nm ($\varepsilon = 25.6 \cdot 10^3$ M$^{-1}\cdot$cm^{-1}), and at 371 nm ($\varepsilon = 1.19 \cdot 10^3$ M$^{-1}\cdot$cm^{-1}), where the bands at 213 nm and 303 nm seems to be characteristic for this ligand system and the band at 371 nm primarily depends on the bridge between the two metal centers (see **chapter 5** for further discussion) (**Figure 4.24**). The peak at 213 nm is already observed in the ligand **[H$_5$L^6](PF$_6$)$_4$** (**chapter 3**). VT UV-vis spectroscopy of **[L^{6}Ni$_2$(OH)](PF$_6$)$_2$** in MeCN shows an influence of the intensity of the bands but does not lead to the appearance of new bands or significant shifts of previously observed bands. By cooling down the solution, an increase of the extinction coefficients is monitored by UV-vis spectroscopy and has physical reasons. In the UV-vis spectrum of solid state **[L^{6}Ni$_2$(OH)](PF$_6$)$_2$**, an additional weak band around 623 nm is obtained.

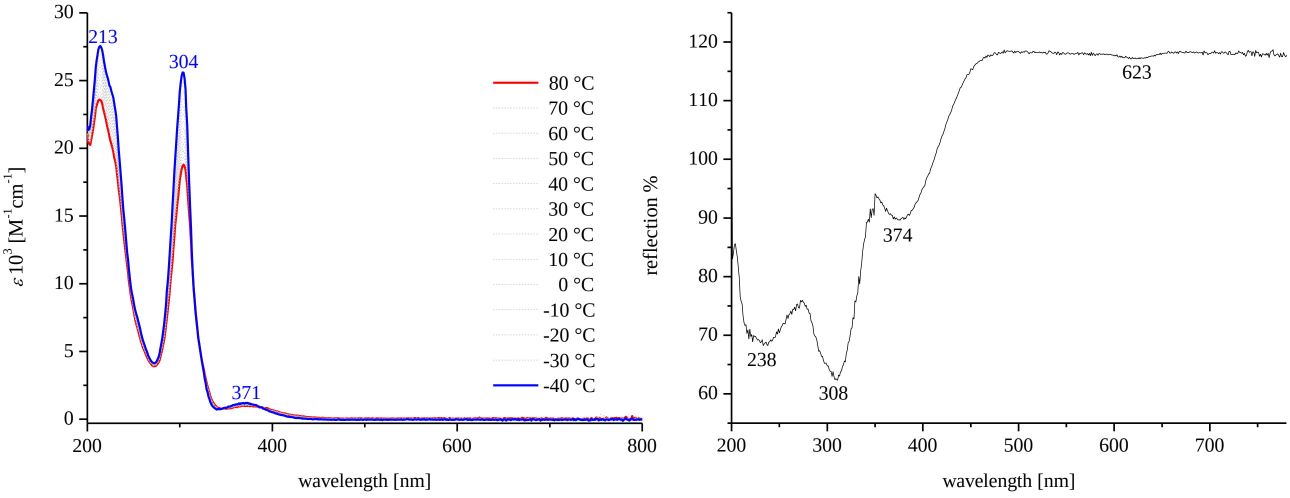

Figure 4.24: Left: VT UV-vis spectrum of **[L^{6}Ni$_2$(OH)](PF$_6$)$_2$** in MeCN. **Right:** UV-vis spectrum of **[L^{6}Ni$_2$(OH)](PF$_6$)$_2$** in solid state.

The redox behavior of **[L^{6}Ni$_2$(OH)](PF$_6$)$_2$** is investigated by CV experiments. In the CV one oxidation event at approximately 1.01 V and a corresponding reduction process at –0.08 V are observed. Reduction of the complex leads to two waves at –2.24 V and –2.54 V *vs.* Fc/Fc$^+$ which are assigned to Ni^{I}Ni^{II} and Ni^{I}Ni^{I} and a new wave appeared at –0.87 V in the reverse scan (**Figure 4.25**). A detailed measurement of the first reductive wave at different scan rates shows quasi reversible behavior of this process. The peak separation is under 150 mV but the integral values for the reductive and oxidative process are not the same, and in addition, a second, very broad wave appears at higher potentials (–0.87 V). Measurements with different batches show that this new wave also corresponds to the complex and is a product of the oxidation of a second species, which is formed after reduction of $\mathbf{[L^6Ni_2(OH)](PF_6)_2}$ and further reaction. An ECE process is observed.

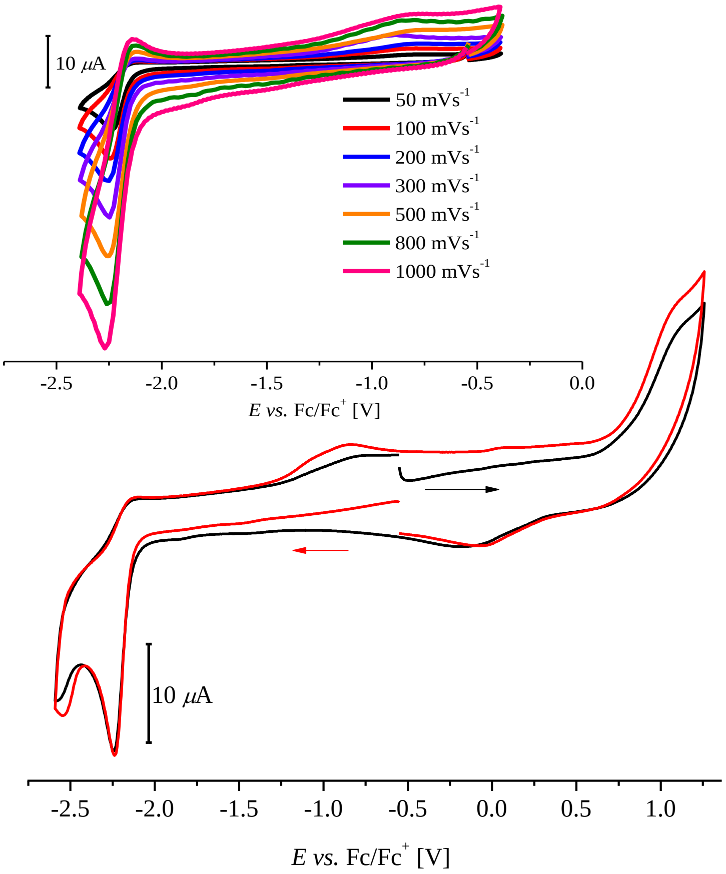

Figure 4.25: CV of $\mathbf{[L^6Ni_2(OH)](PF_6)_2}$ at a scan rate of 100 mV·s^{-1} in MeCN; inset shows the scan rate dependence of the first reduction process at –2.18 V *vs.* Fc/Fc$^+$.

Table 4.10: Peak potentials of the reduction process *vs.* Fc/Fc$^+$ [V].

Scan rate [mVs^{-1}]	$E_{1/2}^{\mathrm{red}}$ [V]	ΔE^{red} [mV]
50	–2.163	148.0
100	–2.179	128.0
200	–2.181	140.0
300	–2.188	120.0
500	–2.188	134.8
800	–2.191	140.0
1000	–2.206	130.0
2000	–2.201	140.0
3000	–2.216	130.1
5000	–2.216	129.8

This reduction process is further investigated by a SEC UV-vis experiment at room temperature. After applying a potential at –2.2 V *vs.* Fc/Fc$^+$ an increase and simultaneously a shift of the band at 372 nm occurs, and a new band at 366 nm is obtained. No isosbestic point is observed and a new broad band with a maximum at approximatively 560 nm is observed. The reduction process is completed after three minutes (**Figure 4.26** (**a**)).

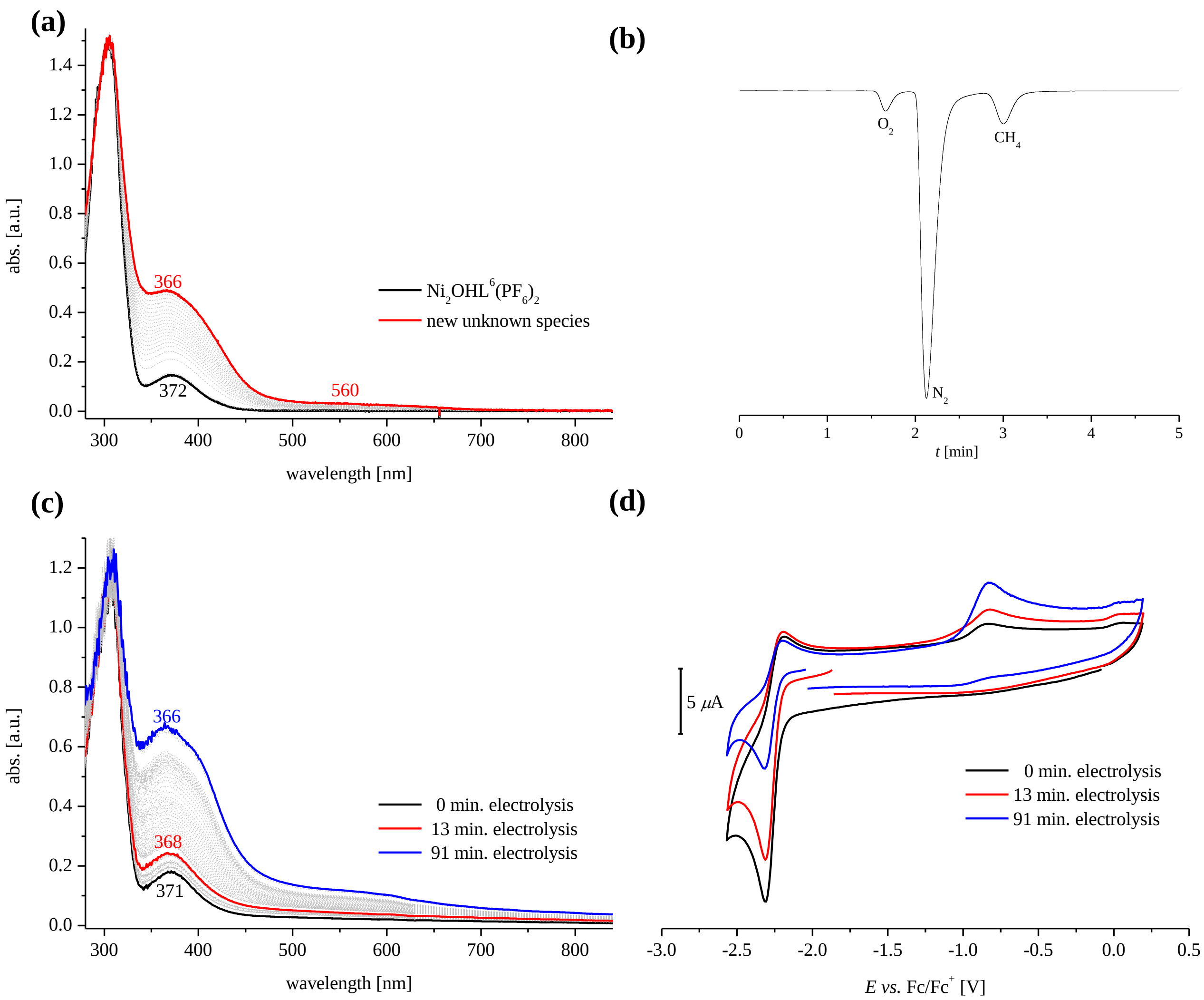

Figure 4.26: **(a)** SEC-UV-vis measurement of **[$L^6Ni_2(OH)$](PF_6)$_2$** at r.t. Increase and shift of the bands at 372 nm to 366 nm. (**b**) GC-TCD analysis of the bulk electrolysis of **[$L^6Ni_2(OH)$](PF_6)$_2$** at –2.4 V *vs.* Fc/Fc$^+$, showing the absence of H_2. At a retention time of 1.67 min O_2 can be observed, based on the method, nitrogen at 2.13 min, as the used inert gas and methane at 3.00 min as used reference for quantifying the amount of produced gas. (**c**) SEC-UV-vis measurement at –40 °C. (**d**) Single CV's between the bulk electrolysis of the complex at 233 K.

After transformation of **[$L^6Ni_2(OH)$](PF_6)$_2$**, a decrease of the bands and decomposition is observed. The resulting product, after electrochemical reduction, seems to be not stable at room temperature, evidenced by a decrease of the newly formed bands. Additional electrochemical experiments are conducted at 233 K (**Figure 4.26** (**c**)). CV measurements of **[$L^6Ni_2(OH)$](PF_6)$_2$** at this temperature show no changes in comparison to the CV obtained at 298 K. Furthermore a bulk electrolysis experiment of **[$L^6Ni_2(OH)$](PF_6)$_2$** at 233 K, monitored by *in situ* UV-vis spectroscopy is performed, leading to the same results. No additional bands arise. After 13 min and 91 min of bulk electrolysis, 200 μL aliquots of the electrolysis mixture are collected and EPR samples are prepared. EPR measurements recorded at 100 K and 22 K show no signal. An increase of the temperature of the electrolyzed solution to r.t. leads to a color change and precipitation is observed, which indicates the instability of the reduced species.

Gas Chromatography-Thermal Conductivity Detection (GC-TCD) of the head space after electrolysis is performed after 10 min and after 40 min of bulk electrolysis (**Figure 4.26** (**b**)). No H_2 is detected after electrolysis and excludes the proton reduction at the OH group. Only methane as internal standard, dioxygen and nitrogen from air are detected by GC-TCD. Also no dihydrogen is detected after 40 additional minutes of controlled potential coloumetry (CPC).

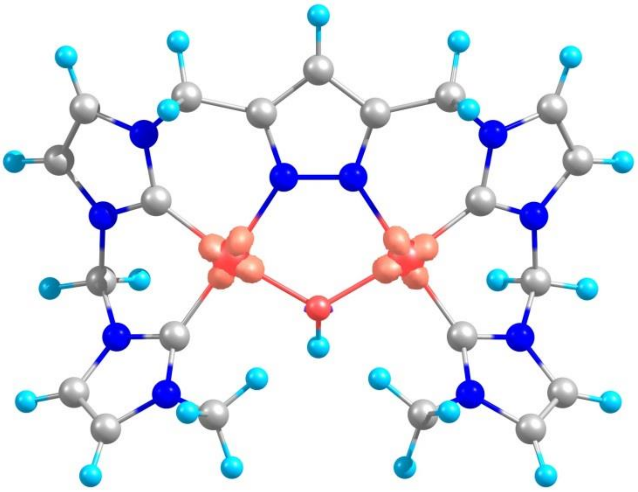

Figure 4.27: Calculated molecular structure of **$[L^6Ni_2(OH)]^+$** showing the spin density. Starting point of the single point calculations is the crystallographic structure of **$[L^6Ni_2(OH)]^{2+}$**. The first reduction process in **$[L^6Ni^{II}Ni^{II}(OH)]^{2+}$** mostly occurs at the nickel centers with an overall Mulliken spin population of 55%.

DFT calculations suggest a mostly metal centered reduction process in the first step (**Figure 4.27**). The Mulliken spin population on both nickel atoms is in total 55% and balanced on both metal centers, due electron delocalization. Following a metal centered reduction in the first step, transformation to the second, EPR silent species is a very fast process, which is faster than the timescale for performing UV-vis measurements. Hence, the life time of any mixed valent Ni^INi^{II} species is very short. The reduced species is not observed by UV-vis spectroscopy and not detected *via* EPR spectroscopy. Based on these experiments, **$[L^6Ni_2(OH)](PF_6)_2$** is reduced to a very unstable intermediate. This intermediate shows quasi reversibility at high scan rates, but in general reacts further to a new species, which can be monitored by UV-vis spectroscopy. Afterwards, the new species decomposes or further reacts to unknown compounds.

4.3.9 Reactivity of $[L^6Ni_2(OH)](PF_6)_2$

Holm and coworker[126] describe a nickel-hydroxido complex **XI**, which is able to undergo several reactions with small molecules (**Scheme 4.1**). No reaction of **$[L^6Ni_2(OH)](PF_6)_2$** is observed with acetic acid, carbon dioxide, ethyl formate and urea. Meyer *et al.*[77] describe that the activation of urea by a dinuclear nickel(II) hydroxido bridged complex derived from **X** and **XIV** is not possible. The reaction of urea with **$[L^6Ni_2(OH)](PF_6)_2$** at 70 °C for several weeks, followed *via* ^1H NMR spectroscopy, does not lead to any product formation. The synthesis of **$[L^6Ni_2H](PF_6)_2$** is also not achieved by reaction of **$[L^6Ni_2(OH)](PF_6)_2$** with two different silanes (Ph_3SiH or Et_3SiH). **$[L^6Ni_2(OH)](PF_6)_2$** is a particularly stable and inert species (see also **chapter 5** and **8**).

4.3.10 Deprotonation reactions of $[L^6Ni_2(OH)](PF_6)_2$

In the literature, nickel oxido systems are described as reactive compounds, able to activate C-H bonds.[136] However, to date no single crystal structure of nickel or copper μ-oxido complexes have been obtained. Driess *et al.*[136] reported the *in situ* formation of an oxido nickel(II) complex (**Scheme 4.10**, **XV**). This complex takes a proton out of the solvent or the silica walls of the flask to form the hydroxido-bridged complex.[136] To the best of my knowledge, no analytical characterization of a dinickel(II) μ-oxido complex has been described in the literature.

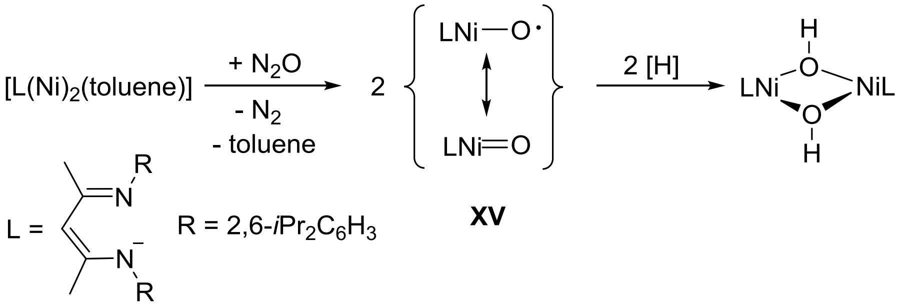

Scheme 4.10: Proposed *in situ* formation of a nickel(II) oxido complex and its transformation to a dinickel(II) bis-hydroxido-bridged complex **XV**.

Reaction of $\mathbf{[L^6Ni_2(OH)](PF_6)_2}$ with $KHBEt_3$ at low temperature leads to an immediate color change from pale yellow to orange. ESI-MS analysis of the reaction mixture shows one dominant peak at *m/z* = 547 (100) which is assigned to the ion $\mathbf{[L^6Ni_2O]^+}$ (**Figure 4.28**, **top**). By comparison with the ESI-MS of $\mathbf{[L^6Ni_2(OH)](PF_6)_2}$, this peak is a result of a chemical reaction. In the ESI-MS of $\mathbf{[L^6Ni_2(OH)](PF_6)_2}$ (**Figure 4.11**, **left**) two peaks are observed at *m/z* = 693.04 (100) for $\mathbf{[L^6Ni_2(OH)PF_6]^+}$ and at *m/z* =274.02 (43) for $\mathbf{[L^6Ni_2(OH)]^{2+}}$. To elucidate the origin of the removed proton, a second experiment is performed. The reaction is repeated and D_2O is added after the color changed from yellow to orange, causing an inverse color change from orange back to yellow (**Scheme 4.11**). ESI-MS of the quenched reaction exclusively shows $\mathbf{[L^6Ni_2(OH)](PF_6)_2}$ labeled and unlabeled (**Figure 4.28**, **bottom**). A shift of *m/z* = 1 in comparison to $\mathbf{[L^6Ni_2(OH)](PF_6)_2}$ confirmed the formation of a labeled species. These findings are interpreted as deprotonation of $\mathbf{[L^6Ni_2(OH)](PF_6)_2}$ after addition of $KHBEt_3$ and *in situ* formation of $\mathbf{[L^6Ni_2O]^+}$.

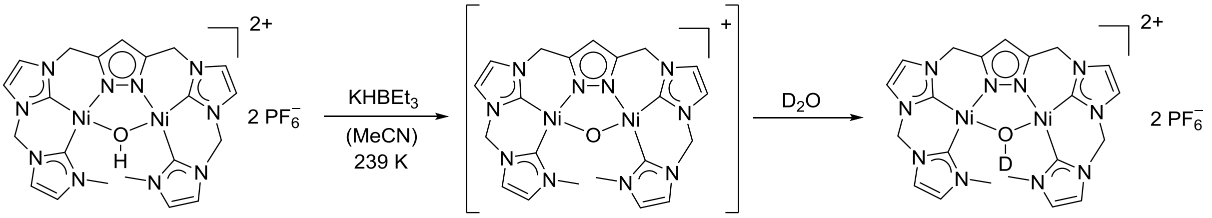

Scheme 4.11: *In situ* deprotonation of $\mathbf{[L^6Ni_2(OH)](PF_6)_2}$ and conversion to $\mathbf{[L^6Ni_2(OD)](PF_6)_2}$ after addition of D_2O.

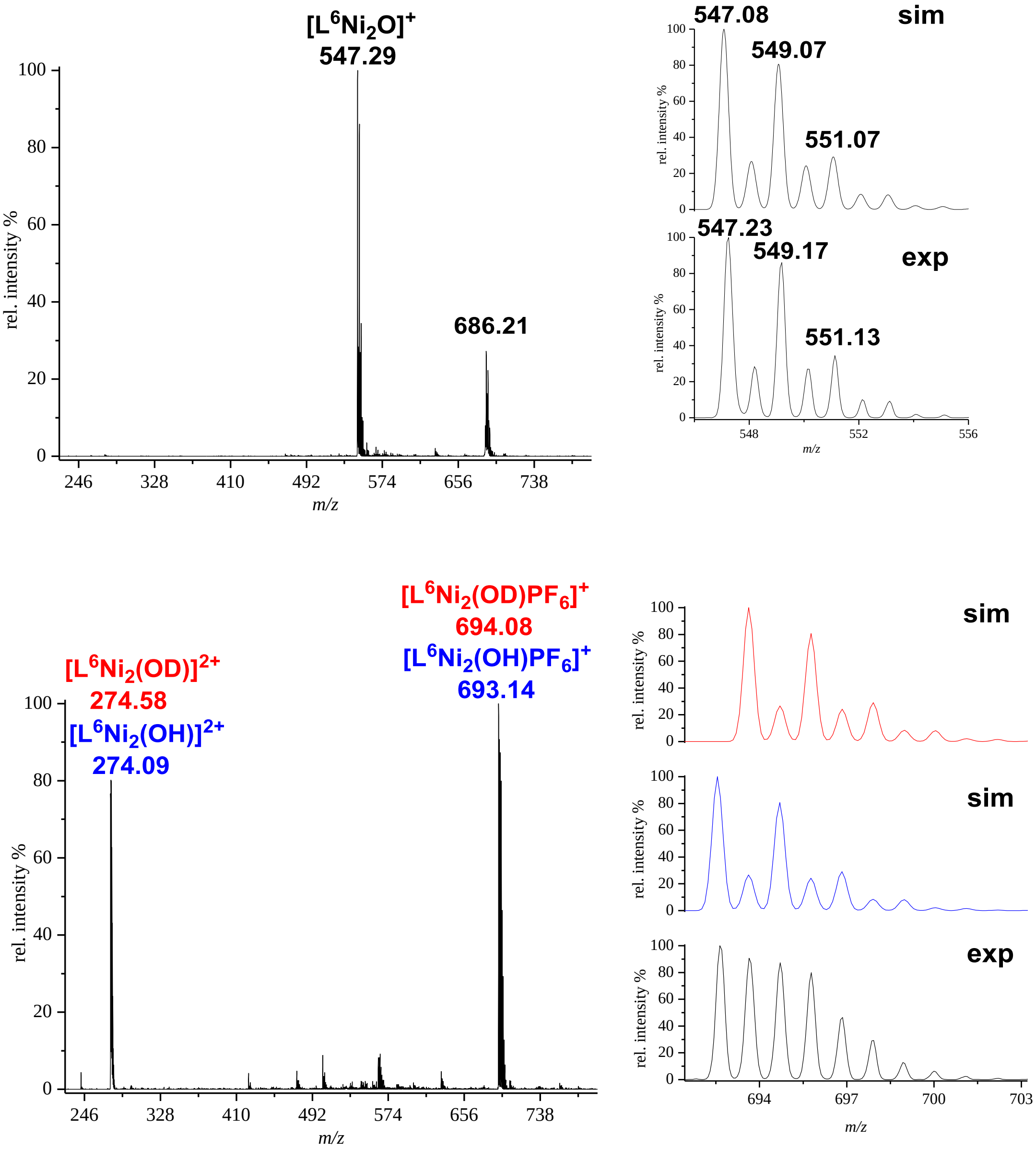

Figure 4.28: Top: ESI-MS of a postulated $[\mathbf{L^6Ni_2O}]^+$ complex in MeCN. The inset shows the simulated (**top**) and experimental (**bottom**) isotopic distribution pattern of the peak at *m/z* = 547 (100) for $[\mathbf{L^6Ni_2O}]^+$. **Bottom**: ESI-MS of D_2O quenched reaction. The inset shows the simulated (**top**) and experimental (**bottom**) isotopic distribution pattern of the peak at *m/z* = 693 and 694 (100) for $[\mathbf{L^6Ni_2(OH)PF_6}]^+$ and $[\mathbf{L^6Ni_2(OD)PF_6}]^+$.

Additional, NMR experiments are performed to further investigate this reaction. $\mathbf{[L^6Ni_2(OH)](PF_6)_2}$ is converted to $\mathbf{[L^6Ni_2(OD)](PF_6)_2}$ and a ^{2}H NMR spectrum in MeCN is measured at 238 K (**Figure 4.29**). One ^{2}H resonance at 0.06 ppm is assigned to the OD group of the complex. Afterwards, $KHBEt_3$ is added at low temperature and the reaction is immediately freeze quenched. A ^{2}H NMR measurement now shows the vanishing of the OD resonance (**Scheme 4.12**, **Figure 4.29**). The combination of the above described experiments lead to the conclusion that the proton abstraction at the OH group of $\mathbf{[L^6Ni_2(OH)](PF_6)_2}$ is achieved.

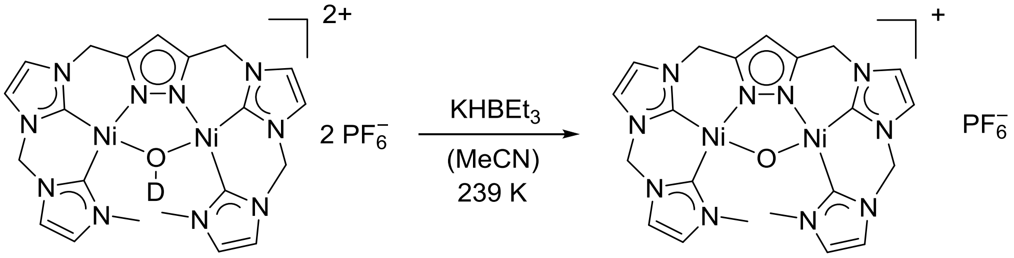

Scheme 4.12: Deprotonation reaction of $\mathbf{[L^6Ni_2(OD)](PF_6)_2}$ followed by ^{2}H NMR in MeCN.

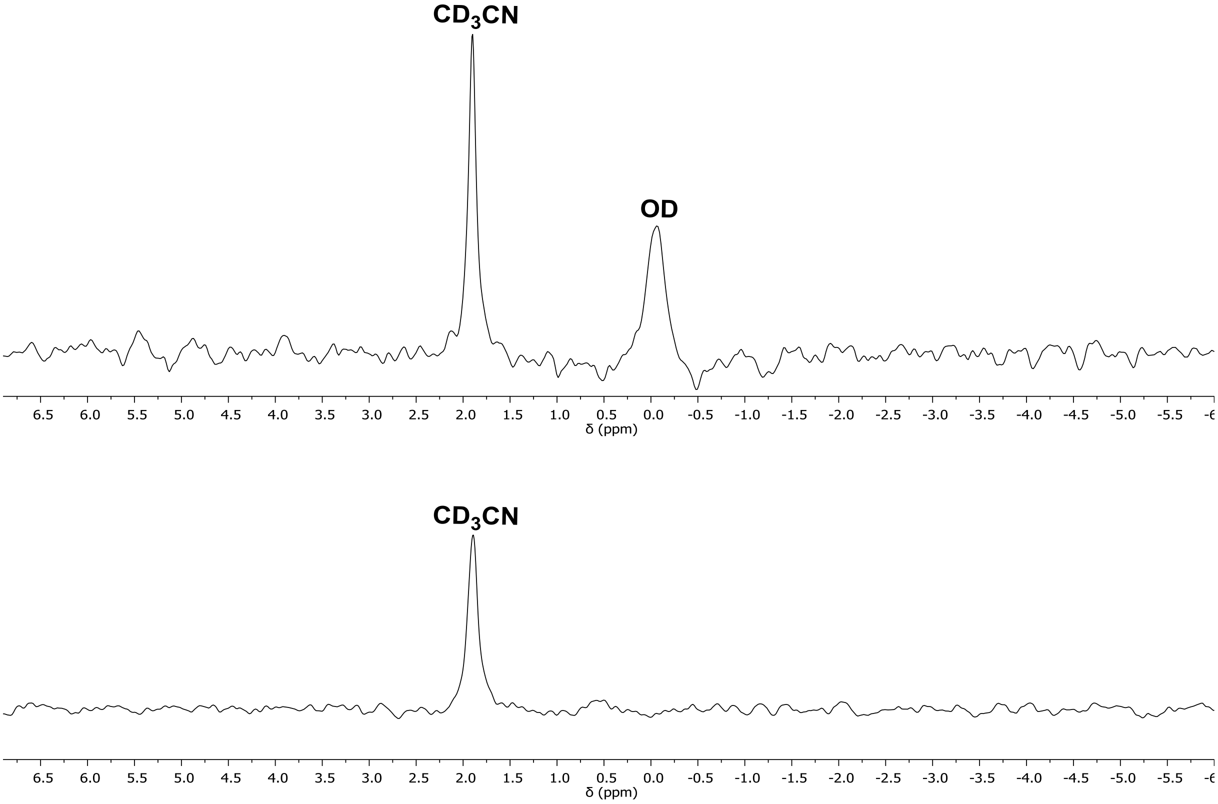

Figure 4.29: Top: ^{2}H NMR spectrum of $\mathbf{[L^6Ni_2(OD)](PF_6)_2}$ at 238 K and 500 MHz in MeCN and **bottom:** ^{2}H NMR spectrum after addition of $KHBEt_3$ to the complex solution.

Further NMR experiments are performed and confirm an unprecedented behavior of the deprotonated complex in MeCN-d_3. **[$L^6Ni_2(OH)](PF_6)_2$** is dissolved in MeCN, the solution is cooled down to 238 K and $KHBEt_3$ is added. Afterwards Et_2O is added to the orange solution and a brownish solid is isolated. This solid is washed several times with Et_2O, to remove triethylborane and dried under reduced pressure. The solid is redissolved in MeCN-d_3 and a ^1H NMR spectrum is recorded (**Figure 4.30**) after one day. A decrease of the integral value for the CH_2 proton resonances H^7 and a vanishing of the OH resonance are observed. In addition, a splitting of the MeCN-d_3 quintet is observed. The complex in solution is further analyzed *via* ESI-MS which shows one dominant peak of the complex at m/z = 696.

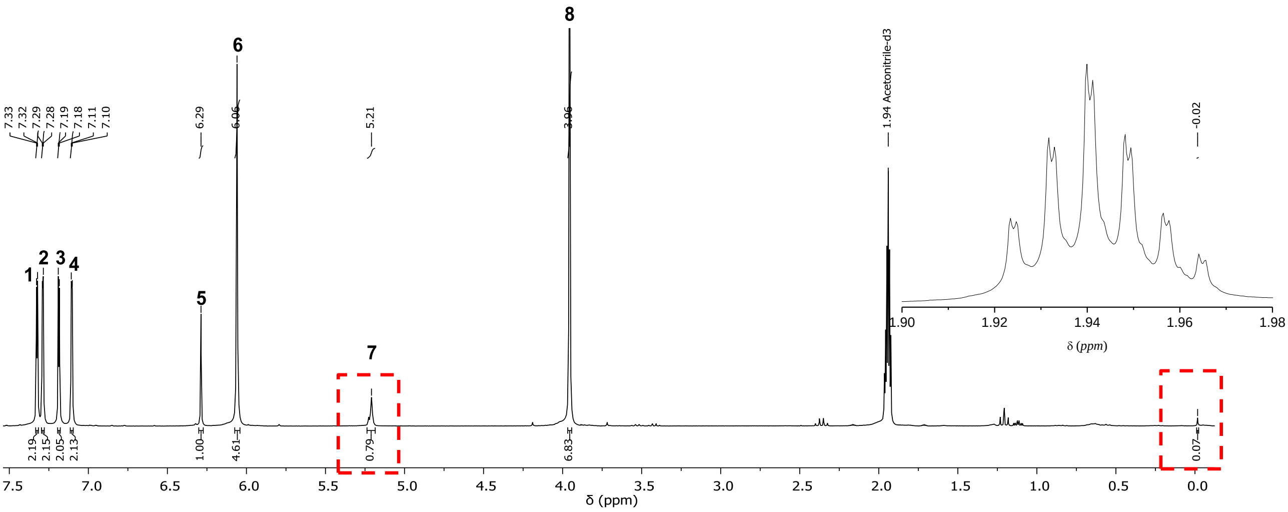

Figure 4.30: ^1H NMR spectrum of **[$L^6Ni_2O]PF_6$** after storing for one day in MeCN-d_3. A decrease of the integral value of the CH_2 groups H^7 is observed and the OH resonance disappeared. Inset shows the change of MeCN-d_3.

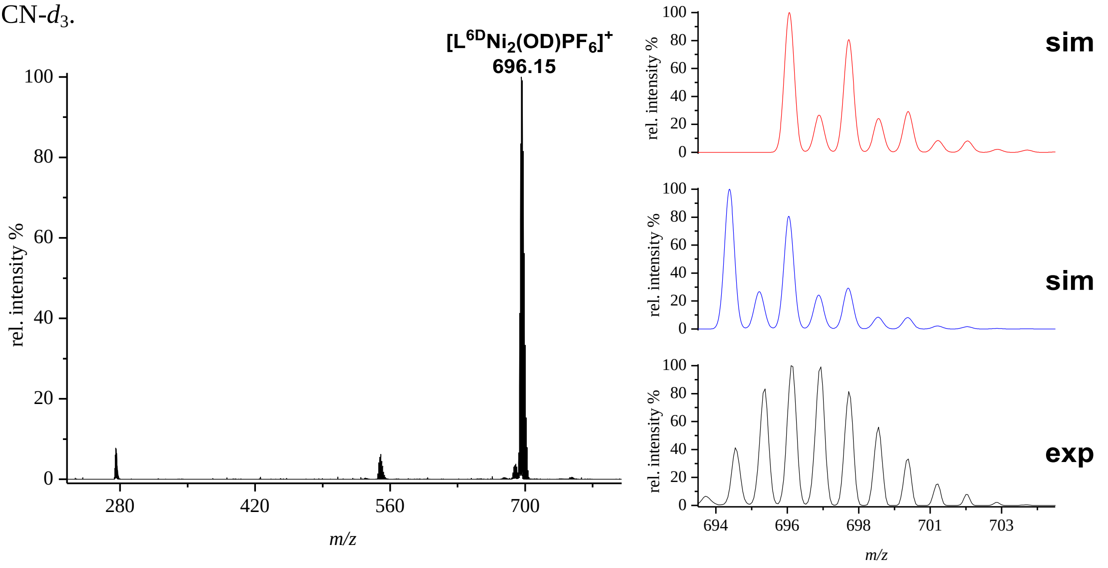

Figure 4.31: ESI-MS of **[$L^6Ni_2O]PF_6$** after several hours in MeCN-d_3. Inset shows the experimental isotopic distribution pattern at m/z = 696 (100) (**bottom**) in comparison to exemplary chosen isotopic distribution pattern of single deuterated [**$L^{6D}Ni_2(OH)PF_6$**]$^+$ (**blue**) or triple deuterated [**$L^{6D3}Ni_2(OH)PF_6$**]$^+$ (**red**) complexes.

An analysis of the experimental isotopic distribution pattern supports the existence of several deuterated species in solution (**Figure 4.31**). IR spectroscopy of the NMR solution shows the appearance of an OD stretching frequency at $\upsilon(OD) = 2600\ cm^{-1}$ of the complex. Assignments in the finger print region, where the CH_2 stretching frequencies are located is not trivial, but a red shift of some vibrational bands in comparison to **$[L^6Ni_2(OH)](PF_6)_2$** is discernible (**Figure 4.32**).

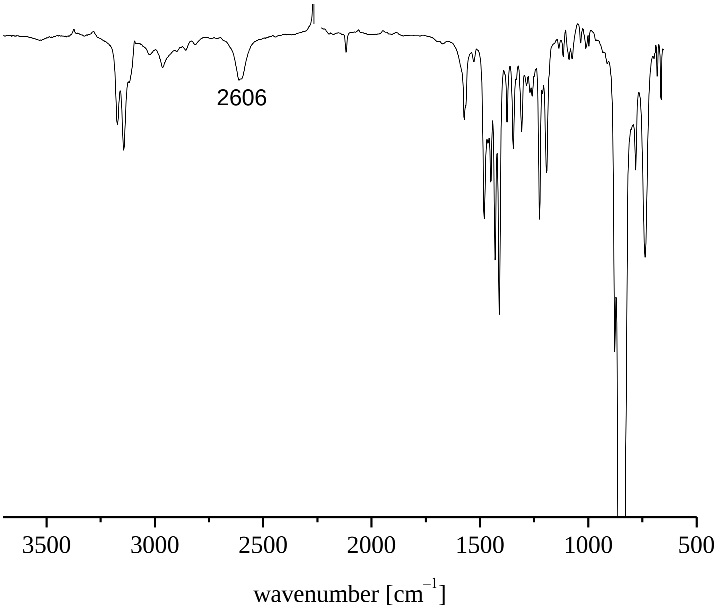

Figure 4.32: IR spectrum of **$[L^6Ni_2O]PF_6$** after aging for one day in MeCN-*d*$_3$. Stretching frequency at $\upsilon(OD) = 2606\ cm^{-1}$ confirmed the reprotonation of **$[L^6Ni_2O]PF_6$** by a deuterium ion.

The behavior of **$[L^6Ni_2(OD)](PF_6)_2$** in MeCN-*d*$_3$ is monitored over one month by ^1H NMR spectroscopy to further investigate the H/D exchange at the CH_2 groups H^7. After four days this peak is vanished and a decrease of the imidazol-*2*-ylidene resonances is detected. Surprisingly, the decrease of the proton resonances is observed with retention of the molecule symmetry (**Figure 4.33**). 31 days later only the proton resonances of the pyrazole synthon H^5 and the proton resonances H^8 of the CH_3 groups remain. A H/D exchange reaction, a labeling of the weakest C–H bonds in the ligand scaffold of **$[L^6Ni_2(OH)](PF_6)_2$**, with MeCN-*d*$_3$ is observed. ^2H NMR spectroscopy of the labeled complex in MeCN confirmed this hypothesis (**Figure 4.34**) but the previously observed chemical shift of OD is disappeared. A reason for this can be a H/D exchange under reformation of the *μ*-OH complex. Since the analytic data confirm the existence of **$[L^6Ni_2(OD)]^{2+}$** in MeCN-*d*$_3$, **$[L^6Ni_2(OH)](PF_6)_2$** can be only observed *in situ* for a short time. No clear evidences are obtained, which explain why the ligand scaffold undergoes an H/D exchange with MeCN-*d*$_3$. A reason for this exchange reaction can be the presence of a base, which cannot be detected by ESI-MS and NMR spectroscopy. Exchange of MeCN-*d*$_3$ by MeCN shows a decrease of the ^{2}H resonances in the ^{2}H NMR spectrum and an appearance of the ^{1}H resonances in the ^{1}H NMR spectrum. The H/D exchange in MeCN is reversible, which indicates that it is not easy possible to remove the potential base out of the system.

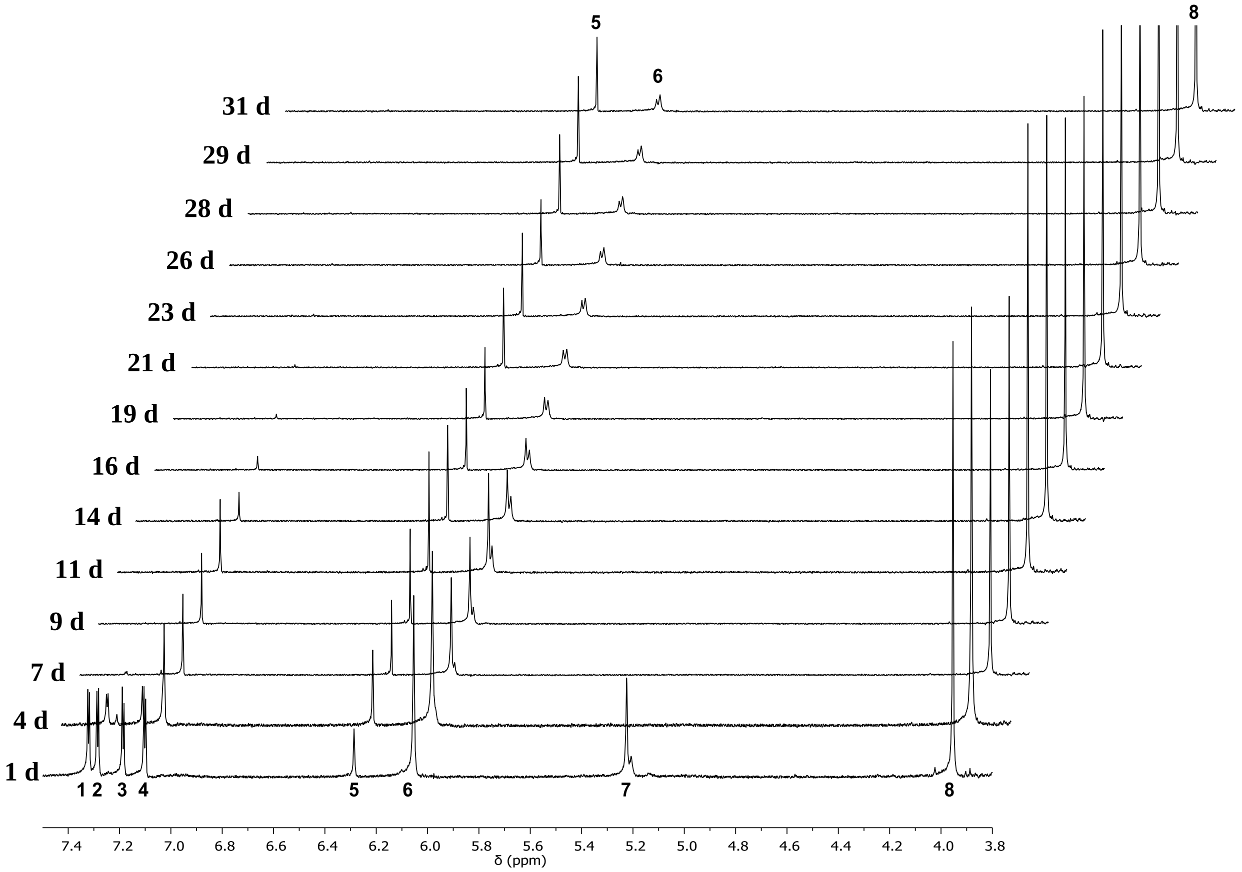

Figure 4.33: ^{1}H NMR spectra of the deprotonation reaction of **[$L^6Ni_2(OH)](PF_6)_2$** monitored over time. After one month a persistent of the proton resonances H^5 and H^8 is observed, wherein under retention of the molecule symmetry all other signals are vanished.

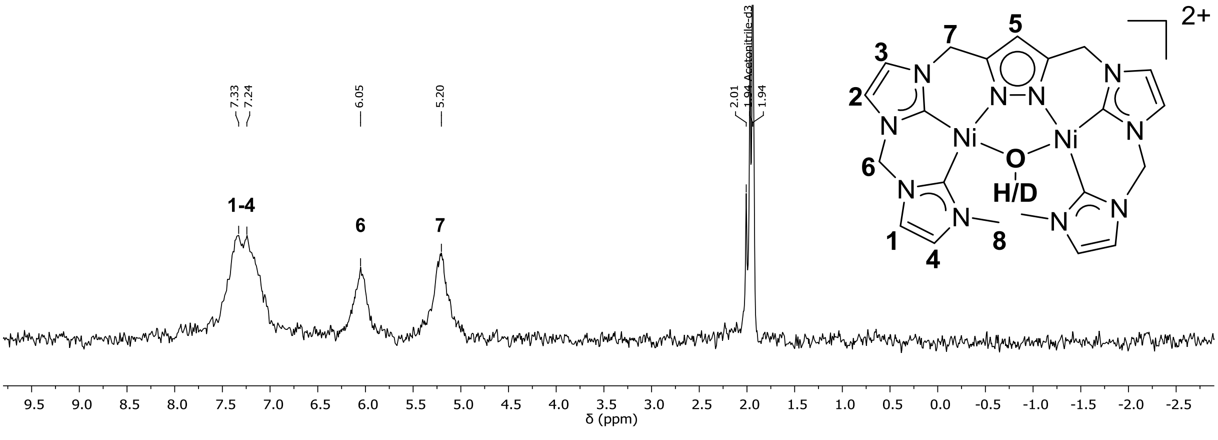

Figure 4.34: ^{2}H NMR spectrum of labeling reaction. In **Figure 4.33** vanished proton resonances are observed again as ^{2}H resonances.

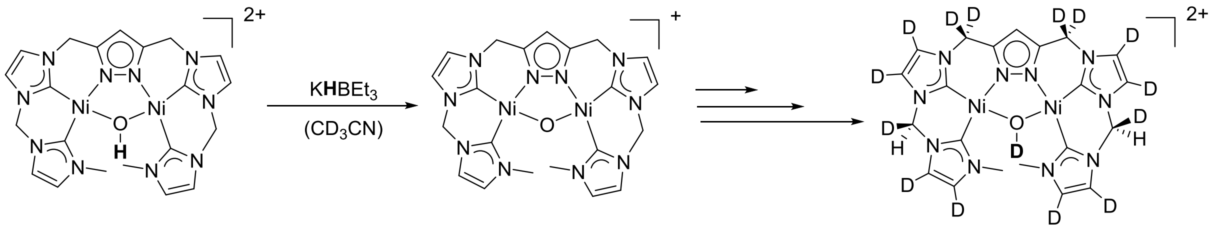

Scheme 4.13: H/D exchange of C–H groups in **[L^{6}Ni$_2$(OH)](PF$_6$)$_2$** after reaction with KHBEt$_3$ in MeCN-*d*$_3$.

Addition of KHBEt$_3$ to **[L^{6}Ni$_2$(OH)](BAr^F)$_2$** in THF-*d*$_8$ also lead to a color change for a short time. Afterwards the color changed again and the ^{1}H NMR spectrum of the reaction mixture shows the proton resonances of the starting compound. No change of the ^{1}H NMR spectrum is observed over several months. In conclusion, the presented experiments confirm the *in situ* formation of [**L^{6}Ni$_2$O](PF$_6$)** by reaction of [**L^{6}Ni$_2$(OH)](PF$_6$)$_2$** with KHBEt$_3$. Under presence of MeCN-*d*$_3$ an H/D exchange reaction with the ligand scaffold is observed, which is reversible in MeCN. These findings are supported by ^{1}H NMR, ^{2}H NMR and IR spectroscopy. The participation of traces of an unknown base cannot be excluded and can be a reason for the H/D exchange. A similar behavior is not observed in THF-*d*$_8$, indicating that MeCN-*d*$_3$ plays an essential role in this reaction. The re-protonation of [**L^{6}Ni$_2$O]$^+$** occurs upon reaction with traces of water or with protons on the wall of the silica surface.

4.3.11 [$L^7Ni_2(OH)](PF_6)_2$ and **[**$L^9Ni_2(OH)](PF_6)_2$

4.3.11.1 [$L^7Ni_2(OH)](PF_6)_2$

[$L^7Ni_2(OH)](PF_6)_2$ and **[$L^9Ni_2(OH)](PF_6)_2$** are synthesized in accordance to **[$L^6Ni_2(OH)](PF_6)_2$**. **[$L^7Ni_2(OH)](PF_6)_2$** crystalizes as pale yellow crystals in the space group $P2_1/n$ by slow diffusion of THF in a complex solution in acetone at 5 °C. Single crystals, suitable for X-ray diffraction confirmed the constitution of the complex in the solid state. A saddle shaped conformation is obtained with an approximate (non-crystallographic) C_s symmetry (**Figure 4.35**). As already described in **[$L^6Ni_2(OH)](PF_6)_2$**, two nickel(II) ions are each coordinated in a distorted square planar fashion by two carbene-C atoms and a pyrazolate-N atom, linked *via* a hydroxide ion. The nickel(II)····nickel(II) distance is 3.28 Å. Further crystallographic data can be found in the appendix (**Table A.4.3** and **A.4.4**).

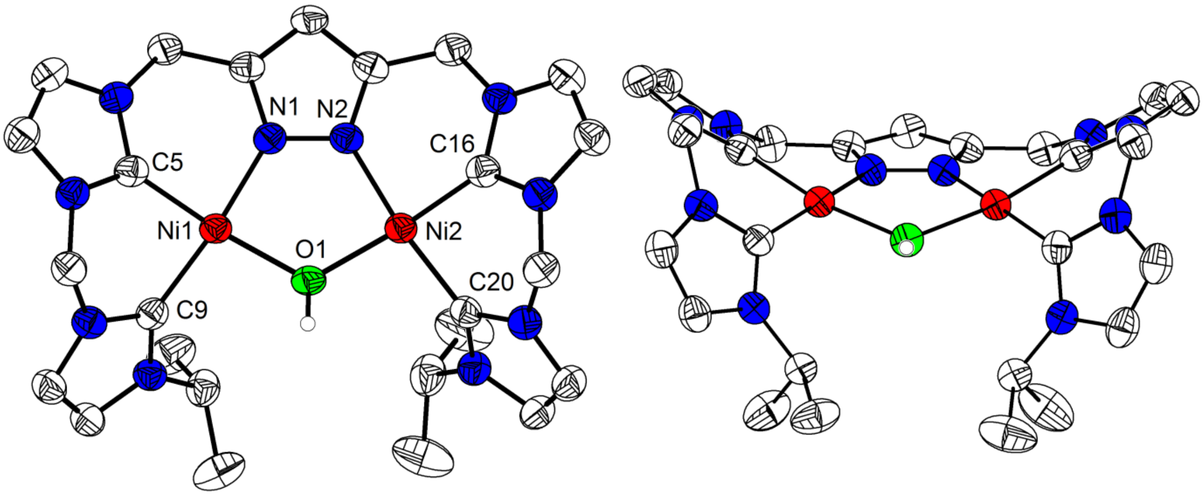

Figure 4.35: Molecular structure (50% probability thermal ellipsoids) of the cationic part of **[$L^7Ni_2(OH)](PF_6)_2$**. H atoms, except of the OH bridge, are omitted for clarity.

Also **[$L^7Ni_2(OH)](PF_6)_2$** co-crystalized with solvent molecules, in this case THF and a hydrogen bond interaction is observed between the OH bridge and the molecule (**Figure 4.36**).

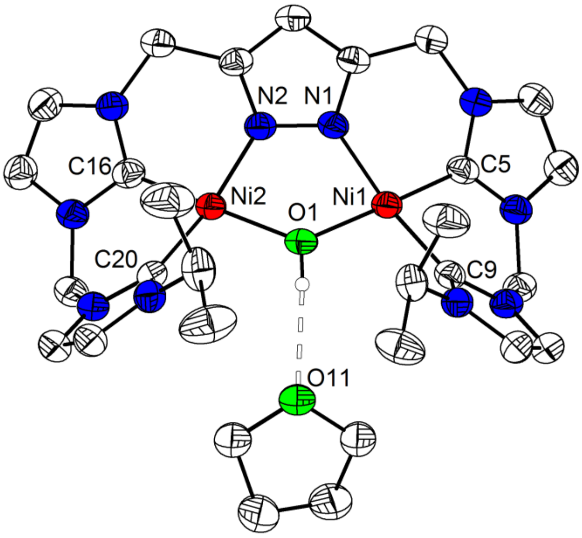

Figure 4.36: ORTEP plot of **$[L^7Ni_2OH](PF_6)_2$** showing the cationic part with co-crystalized THF molecule showing the hydrogen bond interaction between the OH bridge and the THF molecule.

In the ^{1}H NMR spectrum of **$[L^7Ni_2(OH)](PF_6)_2$** in MeCN-d_3 an apparent C_{2v} symmetry of the complex is observed and the proton of the OH group resonates at $\delta = 0.07$ ppm. ESI-MS analysis of **$[L^7Ni_2(OH)](PF_6)_2$** in MeCN shows one mass peak at $m/z = 749$ (100) for the singly charged complex **$[L^7Ni_2(OH)PF_6]^+$** (**Figure 4.38**) and the second peak at $m/z = 302$ (79) for the doubly charged complex **$[L^7Ni_2OH]^{2+}$**.

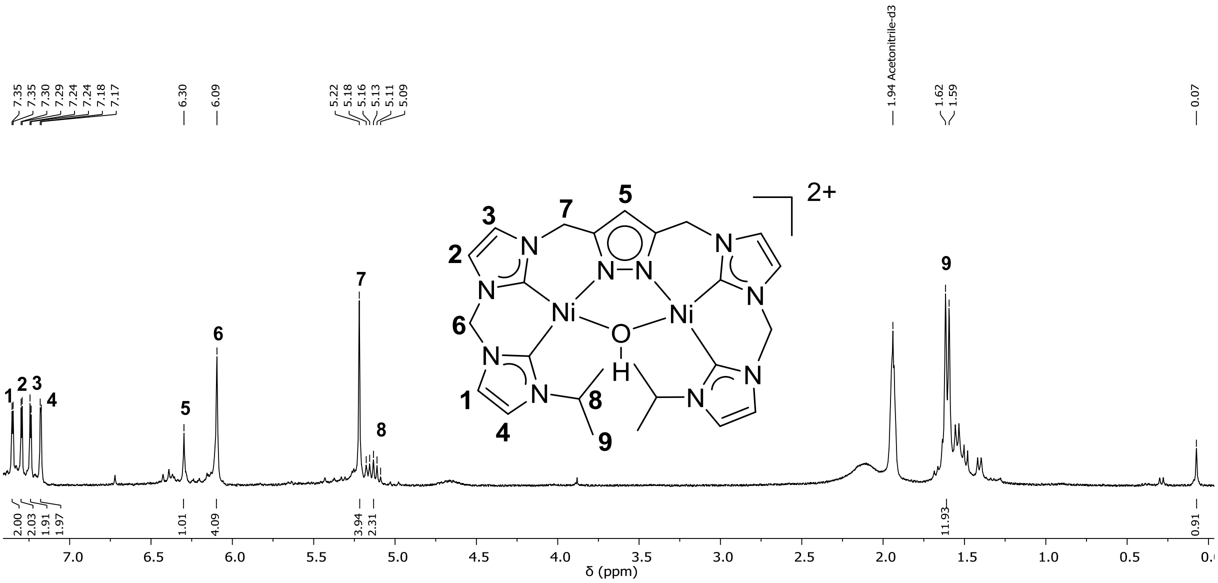

Figure 4.37: ^{1}H NMR spectrum of **$[L^7Ni_2(OH)](PF_6)_2$** in MeCN-d_3 at 298 K shows an apparent C_{2v} symmetric complex. (*) water and residue signals are assigned to not fully converted ligand.

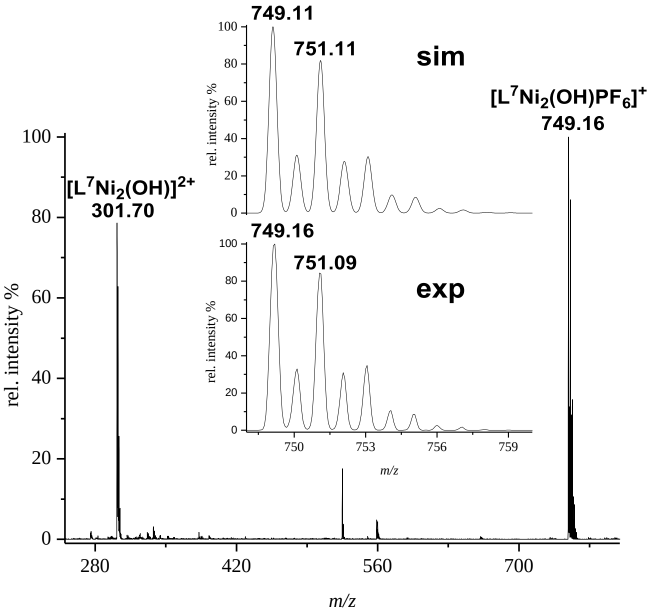

Figure 4.38: ESI-MS of [$\mathbf{L^7Ni_2(OH)](PF_6)_2}$ in MeCN. The inset shows the simulated (**top**) and experimental (**bottom**) isotopic distribution pattern of the peak at *m/z* = 749 (100) for $\mathbf{[L^7Ni_2(OH)PF_6]}^{2+}$.

4.3.11.2 [$L^9Ni_2(OH)](PF_6)_2$

Reaction of **[$H_5L^9](PF_6)_4$** with nickel(II) acetate and sodium acetate results in the formation of **[$L^9Ni_2(OH)](PF_6)_2$**. The corresponding ^{1}H NMR spectrum shows one set of signals, wherein the proton resonances of the CH_3 groups in the 4/5-imidazol-*2*-ylidene position are superimposed as two singlets (**Figure 4.39**). A pronounced high-field shift of the OH proton resonance at δ = –0.21 ppm is observed for **[$L^9Ni_2(OH)](PF_6)_2$**. Alkylation of the imidazol-*2*-ylidene backbone protons leads to a higher electron density in the system compared to **[$L^6Ni_2(OH)](PF_6)_2$**, which leads to a lower acidity and higher nucleophilicity of the OH bridge (δ(OH) = –0.21 ppm), monitored by a high-field shift of the OH peak of 0.17 ppm in the ^{1}H NMR spectrum compared to the OH resonance of **[$L^6Ni_2(OH)](PF_6)_2$** (δ(OH) = –0.04 ppm). Also a high-field shift of the carbene-C resonances of **[$L^9Ni_2(OH)](PF_6)_2$** is observed by a chemical shift of 2 ppm (159.2 ppm and 154.1 ppm) compared to **[$L^6Ni_2(OH)](PF_6)_2$**. (161.2 ppm and 156.6 ppm). ESI-MS measurement of the complex are assigned to two mass peaks at *m/z* = 805 (41) to the singly charged complex **$[L^9Ni_2(OH)PF_6]^+$** and at *m/z* = 330 (100) for the doubly charged complex **$[L^9Ni_2(OH)]^{2+}$** (**Figure 4.40**).

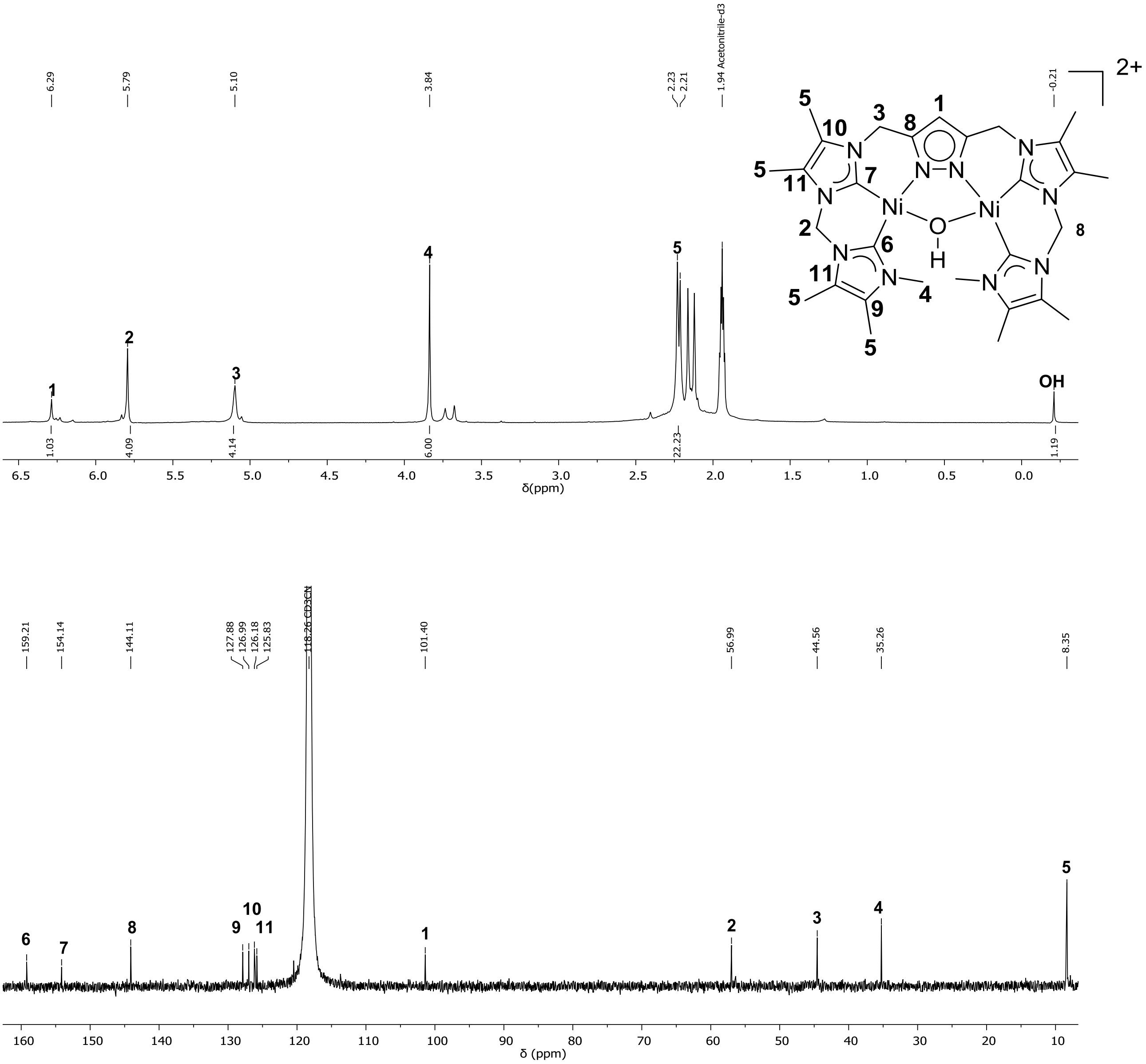

Figure 4.39: Top: ^{1}H NMR spectrum of **[L^{9}Ni$_2$(OH)](PF$_6$)$_2$** in MeCN-d_3 at 298 K (300 MHz) shows a pronounced high-field shift of the OH proton resonance compared to **[L^{6}Ni$_2$(OH)](PF$_6$)$_2$**. **Bottom:** ^{13}C{^{1}H} NMR spectrum at 75 MHz.

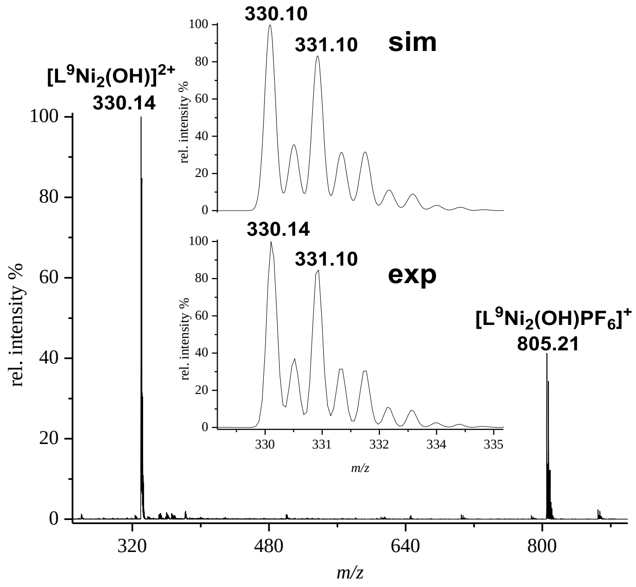

Figure 4.40: ESI-MS of $\mathbf{[L^9Ni_2(OH)](PF_6)_2}$ in MeCN. The inset shows the simulated (**top**) and experimental (**bottom**) isotopic distribution pattern of the peak at *m/z* = 330 (100) for $\mathbf{[L^9Ni_2(OH)]^{2+}}$.

4.4 A μ-chlorido dinickel(II) NHC complex

4.4.1 Destabilization of the hydroxido bridge in $[L^6Ni_2(OH)]^{2+}$

Reaction of **$[L^6Ni_2(OH)](PF_6)_2$** with a strong acid, like ethanolic HCl ($pK_a^{[137]}$ = 8.9 in MeCN) in a 1:1 ratio results in quantitative formation of **$[L^6Ni_2Cl](PF_6)_2$**. This substitution reaction is established in this work as a standard method for the synthesis of **$[L^6Ni_2Cl](PF_6)_2$**. A proposed mechanism can be the protonation of **$[L^6Ni_2(OH)](PF_6)_2$**, *in situ* formation of **$[L^6Ni_2(OH_2)]^{3+}$** and nucleophilic attack of the chloride with release of water (**Scheme 4.14**). The equilibrium of the reaction is shifted to the product side by removal of the solvent. By applying this strategy, **$[L^6Ni_2(OH)](PF_6)_2$** is used as a starting compound for the synthesis of **$[L^6Ni_2Cl](PF_6)_2$** which can be further transformed into amido (**chapter 4.3.11**), bis(cyanido) (**chapter 4.3.12**), sulfido (**chapter 5**), hydrosulfido (**chapter 6**) and disulfido complexes (**chapter 8**).

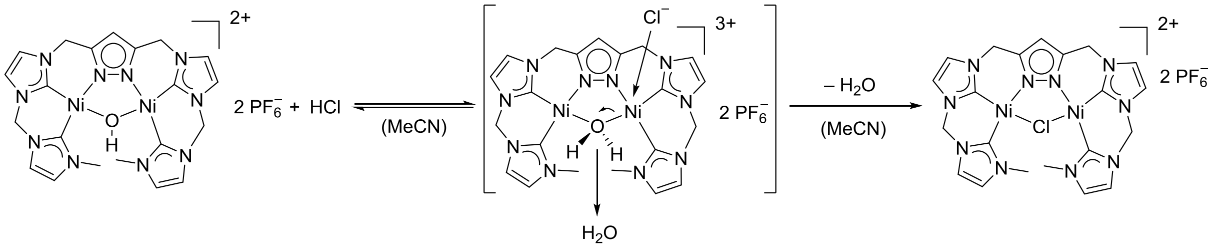

Scheme 4.14: Proposed reaction mechanism for the transformation of **$[L^6Ni_2(OH)](PF_6)_2$** to **$[L^6Ni_2Cl](PF_6)_2$** *via* a potential **$[L^6Ni_2(OH_2)]^{3+}$** intermediate.

Elemental analysis confirms that the purification of the complex is possible by removal of the solvent. Pale greenish crystals are obtained by slow diffusion of Et_2O into a concentrated complex solution. Due to intrinsic problems of the molecular structure in solid state, containing a 'forbidden virtual mirror plane', no reliable bond lengths and angles are obtained. A virtual mirror plane in the resulting molecular structure in solid state leads to a virtual duplication of atoms. DFT structure optimization calculations confirm that the obtained atom distances are reasonable and the molecular structure shown in **Figure 4.41** can be considered for a description of the molecule.

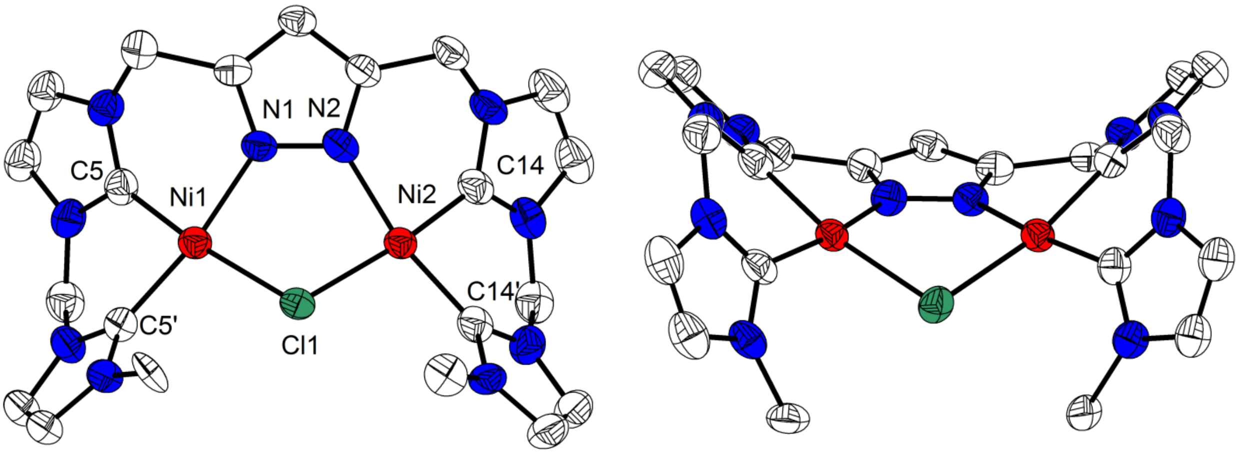

Figure 4.41: Molecular structure (50% probability thermal ellipsoids) of the cationic part of [**$L^6Ni_2Cl](PF_6)_2$**. H atoms are omitted for clarity.

[$L^6Ni_2Cl](PF_6)_2$ crystalizes in the space group *Pmn*2_1. The Ni(1)····Ni(2) distance is 3.46 Å and as expected larger than in **[$L^6Ni_2(OH)](PF_6)_2$** (3.26 Å). Also, this complex crystalizes in a saddle shape conformation with an approximate (non-crystallographic) C_s symmetry. The Ni(1) ion is 0.08 Å out of the N(1)–C(5)–C(5')–Cl(1) plane and Ni(2) 0.10 Å out of the Cl(1)–N(2)–C(14)–C(14') plane. The angle between both planes is 35.7° and 11° larger than in **[$L^6Ni_2(OH)](PF_6)_2$** (24.7°). The Ni–Cl bond length is 2.19 Å and the Ni-carbene carbon bond lengths are 1.86 Å and listed in **Table 4.11**. These bond lengths are exactly the same as the average of the Ni–$C^{Carbene}$ bond lengths in **[$L^6Ni_2(OH)](PF_6)_2$**. The atom distances around the two nickel(II) ions are presented in **Scheme 4.15**.

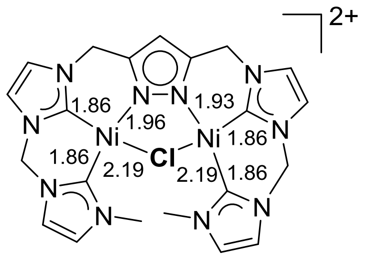

Scheme 4.15: Selected bond lengths **[Å]** in **[$L^6Ni_2Cl]^{2+}$**.

Table 4.11: Selected bond lengths in [Å] for **$[L^6Ni_2Cl](PF_6)_2$**.

Atoms	Bond lengths
Ni1····Ni2	3.464(3)
Ni1–C5'	1.861(8)
Ni1–C5	1.861(8)
Ni1–Cl1	2.198(2)
Ni1–N1	1.958(1)
Ni2–C14	1.864(8)
Ni2–C14’	1.864(8)
Ni2–Cl1	2.196(1)
Ni2–N2	1.932(1)

Table 4.12: Selected bond angles [°] for **$[L^6Ni_2Cl](PF_6)_2$**.

Atoms	Bond angles
C5'–Ni1–C5	87.1(5)
C5–Ni1–N1	85.6(5)
C5’–Ni1–Cl1	99.6(3)
N1–Ni1–Cl1	88.3(6)
C14–Ni2–N2	83.7(5)
C14’–Ni2–C14	86.0(6)
C14’–Ni2–Cl1	99.8(3)
N2–Ni2–Cl1	90.4(6)

ESI-MS of **$[L^6Ni_2Cl](PF_6)_2$** shows two peaks corresponding to the complex with one counter ion at *m/z* = 713 (100) for **$[L^6Ni_2(Cl)PF_6]^+$** and as the doubly charged complex at *m/z* = 284 (8) for **$[L^6Ni_2Cl]^{2+}$** (**Figure 4.42**). In the ^{1}H NMR spectrum of **$[L^6Ni_2Cl](PF_6)_2$** an apparent C_{2v} symmetry is observed, like in **$[L^6Ni_2(OH)](PF_6)_2$**. In MeCN-d_3 the imidazol-*2*-ylidene proton resonances of H^1 and H^2 overlap to an integral value of 4. Besides this, one set of proton resonances is observed (**Figure 4.43**). ^{1}H DOSY NMR spectroscopic analysis confirms the existence of a dinuclear complex in solution ($D_{298K} = 9.81\cdot10^{-10}$ m$^2\cdot$s^{-1}) in comparison with **$[L^6Ni_2(OH)](PF_6)_2$** ($D_{298K} = 9.77\cdot10^{-10}$ m$^2\cdot$s^{-1}) and **$[H_5L^6](PF_6)_4$** ($D_{298K} = 7.74\cdot10^{-10}$ m$^2\cdot$s^{-1}). ^{13}C resonances of the two chemically different carbene-C atoms C^9 and C^{10} are located at δ = 156.0 ppm and δ = 152.8 ppm in the ^{13}C{^{1}H} NMR spectrum. A high-field shift is observed, compared to **$[L^6Ni_2(OH)](PF_6)_2$**, due to lower σ donor strength of the chlorido bridge than the OH bridge.[138]

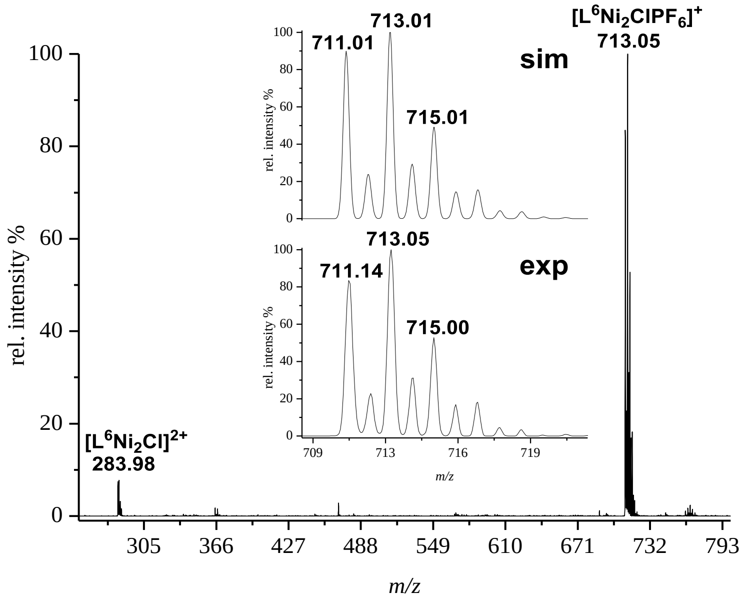

Figure 4.42: ESI-MS of **[L^{6}Ni$_2$Cl](PF$_6$)$_2$** in MeCN. The inset shows the simulated (**top**) and experimental (**bottom**) isotopic distribution pattern of the peak at *m/z* = 713 (100) for **[L^{6}Ni$_2$ClPF$_6$]$^+$**.

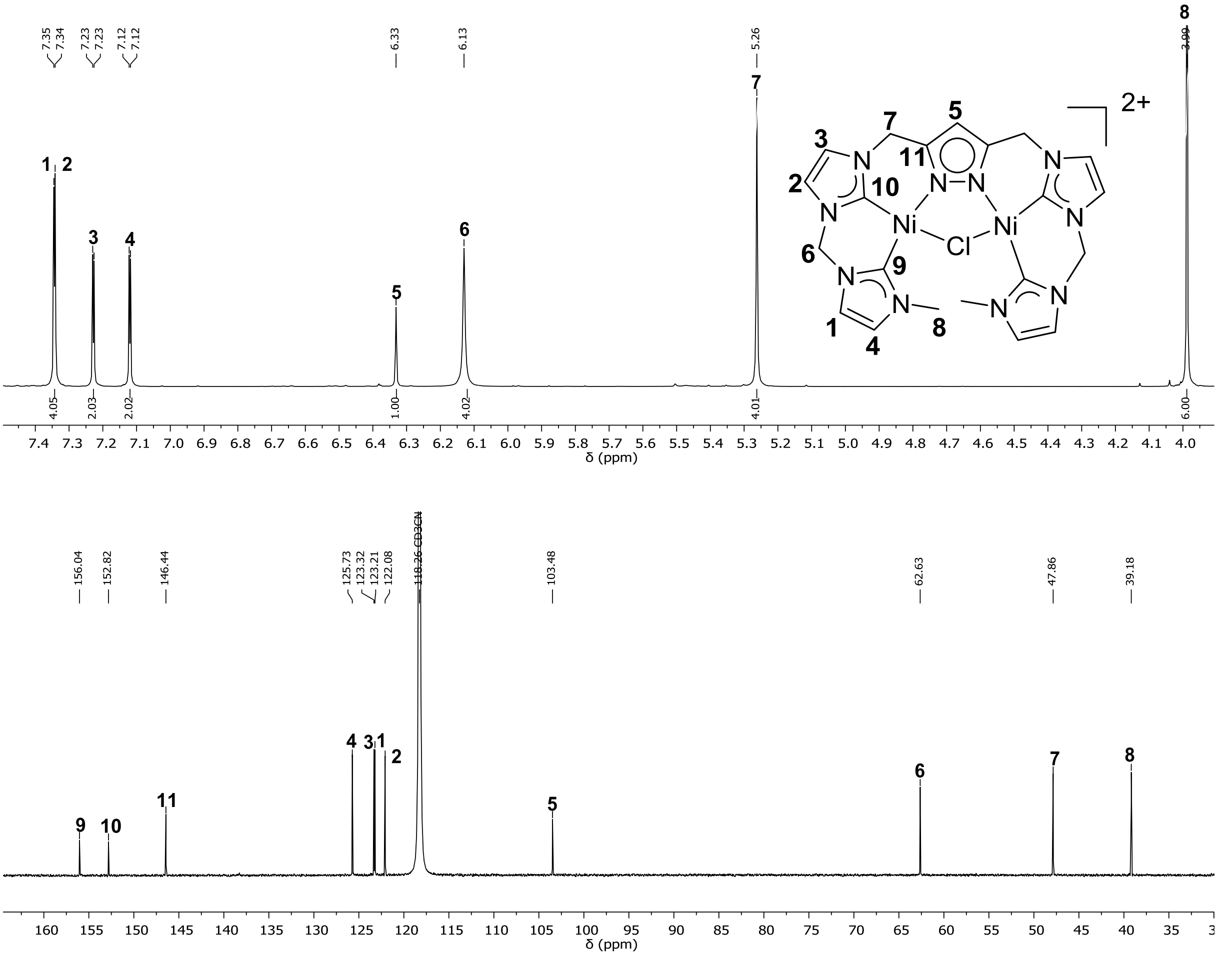

Figure 4.43: Top: ^{1}H NMR spectrum of **[L^{6}Ni$_2$Cl](PF$_6$)$_2$** showing an apparent C_{2v} symmetry of the complex in MeCN-d_3 at 500 MHz. **Bottom:** ^{13}C{^{1}H} NMR spectrum of **[L^{6}Ni$_2$Cl](PF$_6$)$_2$** at 126 MHz and 298 K.

UV-vis spectroscopy of **[L^{6}Ni$_2$Cl](PF$_6$)$_2$** in MeCN at –40 °C shows three absorption bands at 211 nm ($\varepsilon = 35.5\cdot10^3$ M$^{-1}\cdot$cm^{-1}), 297 nm ($\varepsilon = 21.9\cdot10^3$ M$^{-1}\cdot$cm^{-1}) and 375 nm ($\varepsilon = 0.84\cdot10^3$ M$^{-1}\cdot$cm^{-1}) (**Figure 4.44**). Increase of the temperature leads to a decrease of the bands at 211 nm ($\Delta\varepsilon = 1.9\cdot10^3$ M$^{-1}\cdot$cm^{-1}) and 296 nm ($\Delta\varepsilon = 2.1\cdot10^3$ M$^{-1}\cdot$cm^{-1}) as well as a decrease of the band at 375 nm concomitant with a shift of this absorbance to 382 nm ($\varepsilon = 0.73\cdot10^3$ M$^{-1}\cdot$cm^{-1}). The UV-vis spectrum of the complex in solid state shows three bands at 236 nm, 294 nm and 392 nm, which indicates a non-negligible solvent influence on these transitions (**Figure 4.44**).

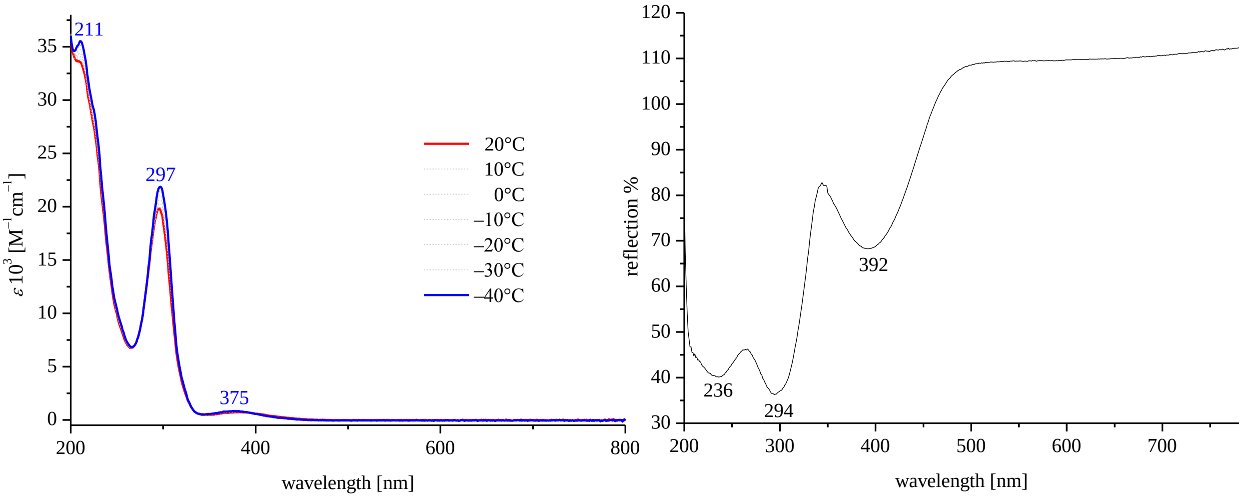

Figure 4.44: Left: VT UV-vis spectra from **[L^{6}Ni$_2$Cl](PF$_6$)$_2$** in MeCN in the temperature range from 20 °C to –40 °C. Absorbance bands are observed at –40 °C, at 211 nm ($\varepsilon = 35.5\cdot10^3$ M$^{-1}\cdot$cm^{-1}), 297 nm ($\varepsilon = 21.9\cdot10^3$ M$^{-1}\cdot$cm^{-1}) and 375 nm ($\varepsilon = 0.84\cdot10^3$ M$^{-1}\cdot$cm^{-1}). **Right:** UV-vis spectrum of the complex in solid state with three bands at 236 nm, 294 nm and 392 nm.

4.4.2 Redox properties of [L^6Ni_2Cl](PF_6)$_2$

CV of **[L^6Ni_2Cl](PF_6)$_2$** (**Figure 4.45**) shows an irreversible oxidation event at 0.95 V *vs.* Fc/Fc$^+$ and a resulting reduction process in the cathodic region at –1.38 V. By sweeping to a reductive potential, the CV shows two reductive waves at –1.83 V and –2.21 V and a new wave at –0.32 V in the reverse scan. This new wave also appears after the first reduction occurs. The reduction event at –1.83 V shows quasi reversible behavior at higher scan rates, in analogy to the observation for **[$L^6Ni_2(OH)$](PF_6)$_2$** (**Table 4.13**).

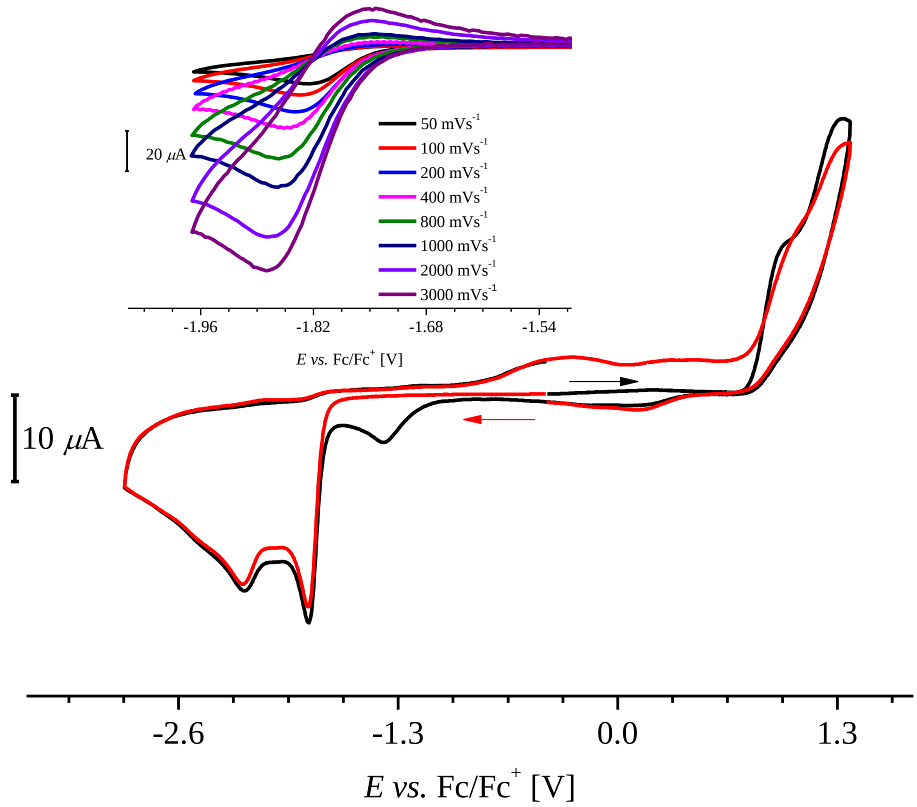

Figure 4.45: CV of **[L^6Ni_2Cl](PF_6)$_2$** at 100 mV·s^{-1} (0.1 M NBu_4PF_6 in MeCN). One wave at 0.95 V is observed in the anodic region (→) and two waves at –1.83 V and –2.21 V in the cathodic region (←). Inset shows the behavior of the first reductive wave by increase of the scan rate.

Table 4.13: Peak potentials of the 1st reduction process *vs.* Fc/Fc$^+$ [V].

Scan rate [mVs^{-1}]	$E_\mathrm{p}^\mathrm{red}$ [V]	$\Delta(E_p^a - E_p^c)$ [mV]
50	–1.825	–
100	–1.837	–
200	–1.843	–
400	–1.807	99.95
800	–1.807	111.9
1000	–1.804	119.9
2000	–1.813	131.9
3000	–1.813	131.9

Increase of the scan rates did not suppress the second wave at –0.32 V. This irreversibility of the reductive wave at –1.83 V is not based on the removal of the bridged chloride. To support this thesis the CV experiment is repeated using NBu_4Cl as electrolyte. The obtained CVs show no reversibility. Consequently, the presence of a higher concentration of chloride ions in the solution, do not affect the irreversible process. To further investigate the first reduction process, SEC UV-vis measurements at room temperature are performed. After applying a potential of –1.92 V *vs*. Fc/Fc$^+$ the band at 389 nm increased and shifts to 362 nm. In addition, a broad band at 551 nm is observed. The reaction is completed after approximately 3 min and only a small subsequent decrease of the bands is observed, in contrast to **[$L^6Ni_2(OH)$](PF_6)$_2$**, where a rapid decomposition of the reduced species is observed at room temperature. Since the stability of the reduced complex is higher, a second potential at –0.36 V *vs*. Fc/Fc$^+$ is applied to investigate the reversibility of this transition. The oxidation process leads to a decrease of previously observed bands and formation of a new band at 382 nm. Also comparison of the initial and final spectrum underlines the synthesis of a new species after the second process and not the reformation of the starting complex (**Figure 4.46** (**a**) and (**b**)).

In order to investigate the behavior of **[L^6Ni_2Cl](PF_6)$_2$** at low temperature, a bulk electrolysis of the complex is performed at –20 °C and the reaction is monitored *via* UV-vis spectroscopy. In addition, three EPR samples are collected, one before electrolysis, one after 5 minutes of electrolysis and one after one hour of bulk electrolysis. At –20 °C, no new bands are observed during the bulk electrolysis of **[L^6Ni_2Cl](PF_6)$_2$** and the same bands are obtained like at room temperature. EPR spectra of all three samples are silent.

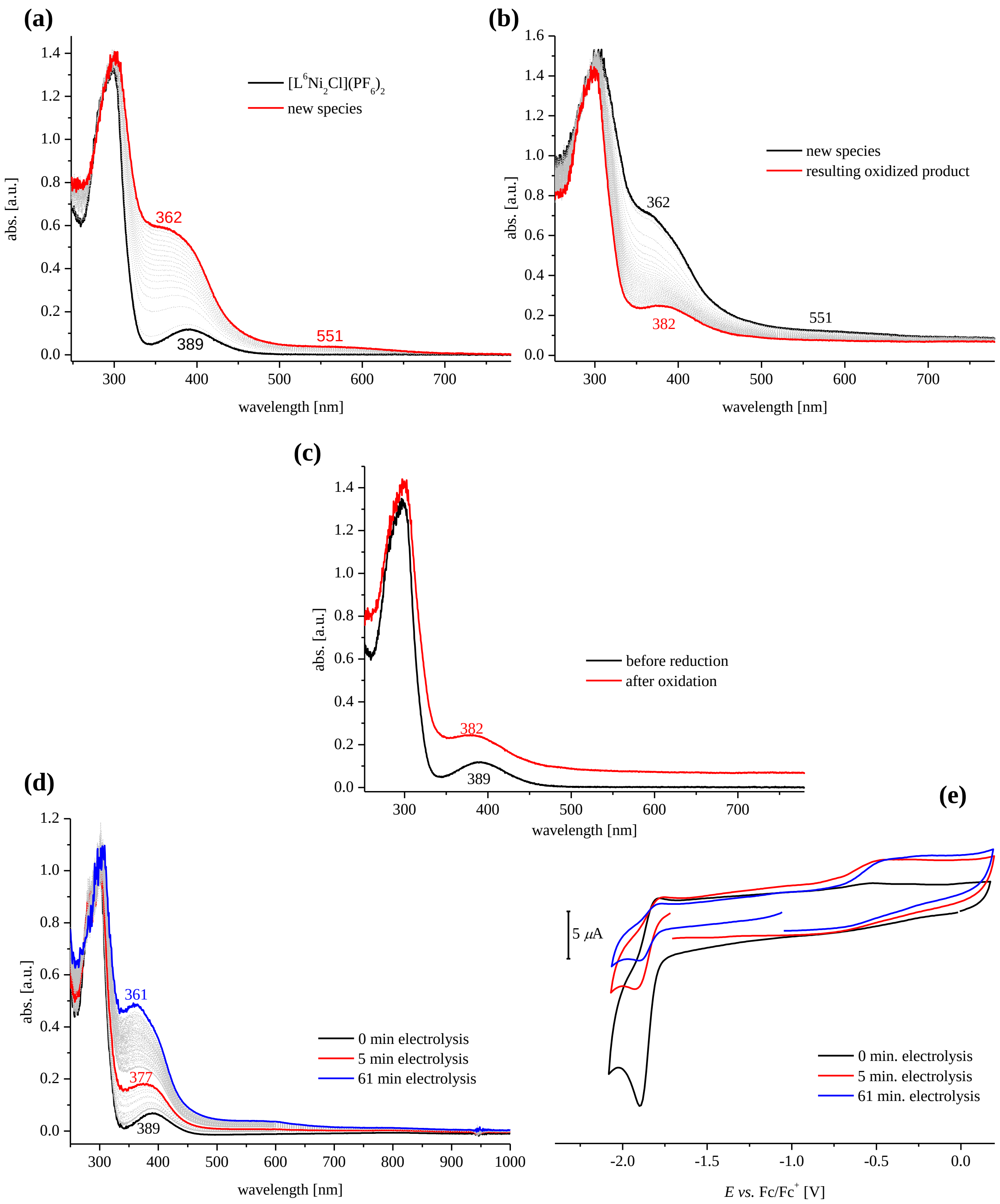

Figure 4.46: SEC UV-vis spectra monitored (**a**) reduction of **$[L^6Ni_2Cl](PF_6)_2$** at –2.0 V *vs.* Fc/Fc$^+$ (**b**) oxidation of the new species at 0 V *vs.* Fc/Fc$^+$ (**c**) reduction of **$[L^6Ni_2Cl](PF_6)_2$** at –20 °C *vs.* Fc/Fc$^+$ (**d**) CV of **$[L^6Ni_2Cl](PF_6)_2$** between bulk electrolysis.

DFT calculations based on the coordinates from **$[L^6Ni_2Cl](PF_6)_2$** of the reduction process suggests, that the reduction is mainly metal based (**Figure 4.47**). The calculation of the one electron reduced molecule shows a spin population at the nickel centers of 55%, which indicates the reduction of the nickel(II) to a nickel(I) species. SEC UV-vis data and the bulk electrolysis experiments at –20 °C propose that this reduced species will be immediately transformed into another species, which is EPR silent and whose signature can be followed by UV-vis spectroscopy. The generation of the reduced species is further followed by ^{1}H NMR spectroscopy and ESI-MS analysis, whereby the complex is chemically reduced by Co(Cp*)$_2$. ^{1}H NMR spectroscopy confirms the formation of new species and ESI-MS supports a possible activation of MeCN and formation of nickel alkyl or cyanido species. In conclusion, the reduction of **[L^6Ni_2Cl](PF_6)$_2$** shows the formation of a species, which could not be stabilized but reacted to an unknown diamagnetic species.

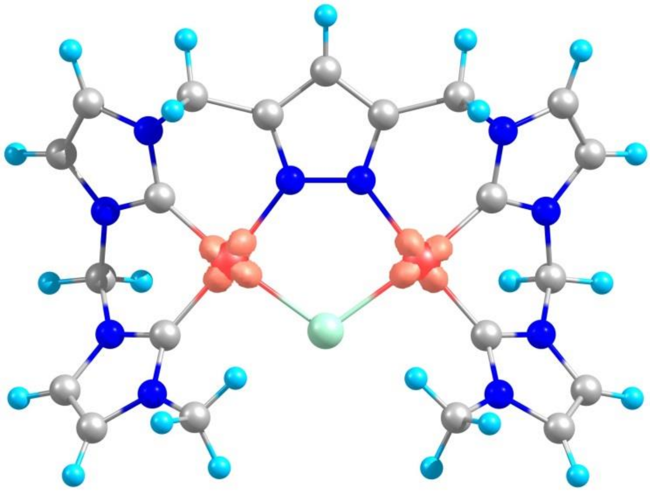

Figure 4.47: Calculated molecular structure of **[L^6Ni_2Cl]$^+$** showing the spin density. Starting point of the single point calculations is the crystallographic structure of **[L^6Ni_2Cl]$^{2+}$**. The first reduction process in **[L^6Ni_2Cl]$^{2+}$** appeared at the nickel centers with an overall Mulliken spin population of 55% at both Ni atoms.

4.4.3 Synthesis of an amido-bridged complex

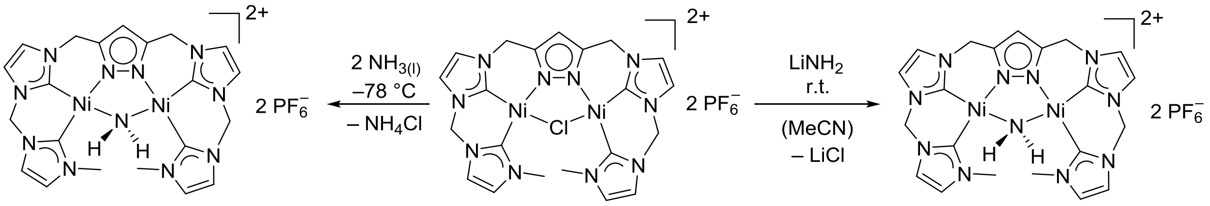

Scheme 4.16: Left: Reaction of **[L^{6}Ni$_2$Cl](PF$_6$)$_2$** with liquid ammonia give **[L^{6}Ni$_2$(NH$_2$)](PF$_6$)$_2$**. **Right:** Synthesis of **[L^{6}Ni$_2$(NH$_2$)](PF$_6$)$_2$** by salt metathesis of **[L^{6}Ni$_2$Cl](PF$_6$)$_2$** with LiNH$_2$.

Reaction of **[L^{6}Ni$_2$Cl](PF$_6$)$_2$** with lithium amide in MeCN at room temperature leads to a color change from pale green to orange (**Scheme 6.12**, **right side**). After filtration and evaporation of the solvent, an orange solid is obtained. **[L^{6}Ni$_2$(NH$_2$)](PF$_6$)$_2$** is generated upon reaction of **[L^{6}Ni$_2$Cl](PF$_6$)$_2$** with liquid ammonia (**Scheme 4.16**, **left side**). ESI-MS analysis confirms the transformation of **[L^{6}Ni$_2$Cl](PF$_6$)$_2$** to the amido complex. Two peaks are observed, related to doubly charged ion **[L^{6}Ni$_2$(NH$_2$)]$^{2+}$** at *m/z* = 273 (83) and singly charged complex **[L^{6}Ni$_2$(NH$_2$)(PF$_6$)]$^+$** at *m/z* = 692 (100) (**Figure 4.48**).

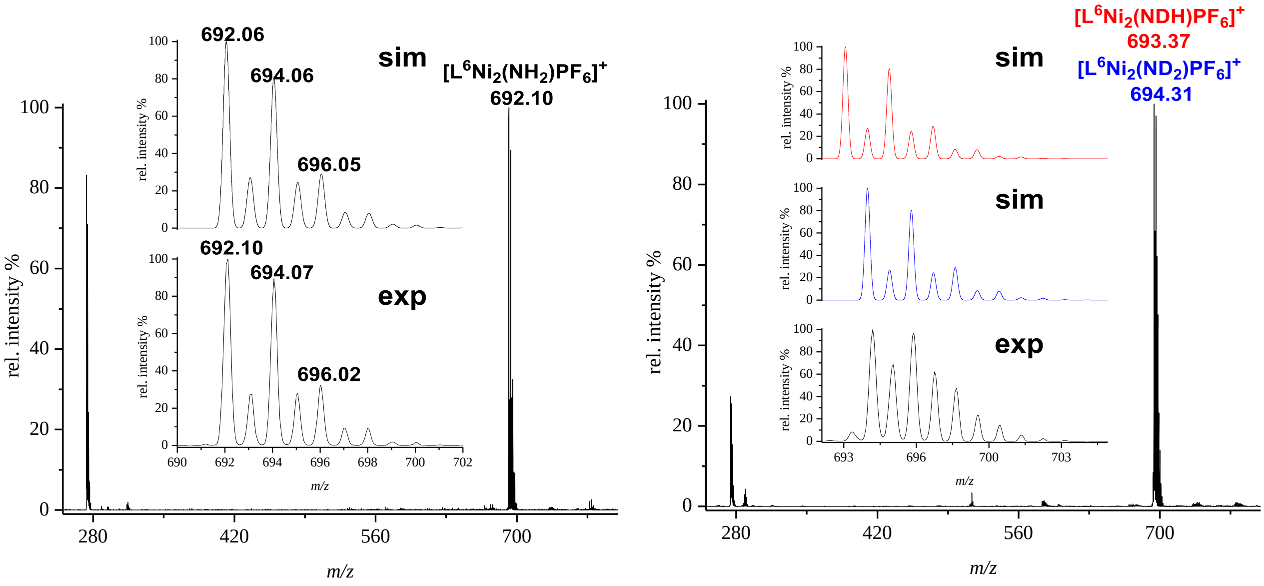

Figure 4.48: Left: ESI-MS of **[L^{6}Ni$_2$(NH$_2$)](PF$_6$)$_2$** in MeCN. The inset shows the simulated (**top**) and experimental (**bottom**) isotopic distribution pattern at *m/z* = 692 (100) for **[L^{6}Ni$_2$(NH$_2$)(PF$_6$)]$^+$**. **Right:** ESI-MS of the labeled complex. Inset shows the simulated isotopic distribution pattern for **[Ni$_2$ND$_2$L^6](PF$_6$)$_2$** (**blue**) and for **[Ni$_2$NDHL^6](PF$_6$)$_2$** (**red**) and experimental isotopic distribution pattern of the peaks at *m/z* = 693.

IR spectroscopy of **[L^{6}Ni$_2$(NH$_2$)](PF$_6$)$_2$** in MeCN shows two pronounced bands at 3474 cm^{-1} and 3379 cm^{-1} which are assigned to the symmetric and asymmetric stretching modes of the μ-NH$_2$ group in the complex. In 2009, Ikariya and co-workers[139] reported diruthenium and diiridium μ-NH$_2$ complexes with corresponding vibrational bands of the NH$_2$ group around

3300 cm^{-1}. Also NH stretches of μ-NH$_2$ groups at υ(NH) = 3351/3277 cm^{-1} and υ(NH) = 3333/3183 cm^{-1} of two dinuclear platinium(II) complexes are presented in the literature.[140] In 2016, Manz presented the first molecular solid state structure of a dinuclear nickel(II) μ-NH$_2$ complex and vibrational bands at υ(NH) = 3348 cm^{-1} and 3333 cm^{-1} in the IR spectrum.[134] Unfortunately, no crystals of **[L^{6}Ni$_2$(NH$_2$)](PF$_6$)$_2$** suitable for X-ray measurement were obtained. Based on a theoretical expected molecular structure in solid state, frequency calculations are performed, to determine the N–H stretching frequencies in **[L^{6}Ni$_2$(NH$_2$)](PF$_6$)$_2$** (**Figure 4.49**). By these calculations, vibrational bands at υ(NH) = 3467 cm^{-1} and 3357 cm^{-1} are determined, which are in good agreement with the experimental values (3474 cm^{-1} and 3379 cm^{-1}).

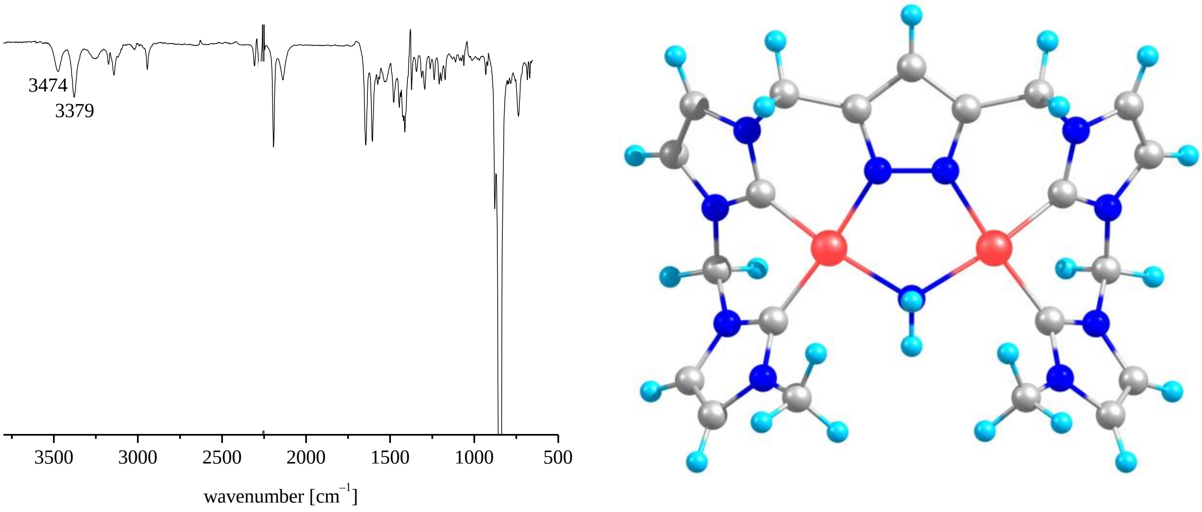

Figure 4.49: Left: IR spectrum of **[L^{6}Ni$_2$(NH$_2$)](PF$_6$)$_2$** in MeCN shows two vibrational bands for the μ-NH$_2$ group at υ(NH) = 3474 cm^{-1} and 3379 cm^{-1}. **Right:** Calculated molecular structure of **[L^{6}Ni$_2$(NH$_2$)]$^{2+}$**.

Re-dissolving the complex in MeCN-d_3 and recording a ^{1}H NMR spectrum confirmed a symmetric compound in solution. One set of peaks is observed, which could be assigned to the corresponding proton resonances of the complex, using 2D NMR spectroscopy (**Figure 4.50**). The NH$_2$ proton resonances could not be detected. ESI-MS analysis of the complex in MeCN-d_3 shows a shift of the mass peaks (**Figure 4.48**, **right**) by $m/z = 1$ and $m/z = 2$ for the mono charged species, likely reflecting H/D exchange at the NH$_2$ group. Also the isotopic pattern distribution and the mass shift of the doubly charged complex at $m/z = 274$ (27) is in agreement with the theoretical isotopic distribution pattern of **[L^{6}Ni$_2$(ND$_2$)]$^{2+}$**(**Figure 4.48**, **right**). The generated complex seems to be highly basic and a H/D exchange between the MeCN-d_3 and the μ-NH$_2$ group is observed.

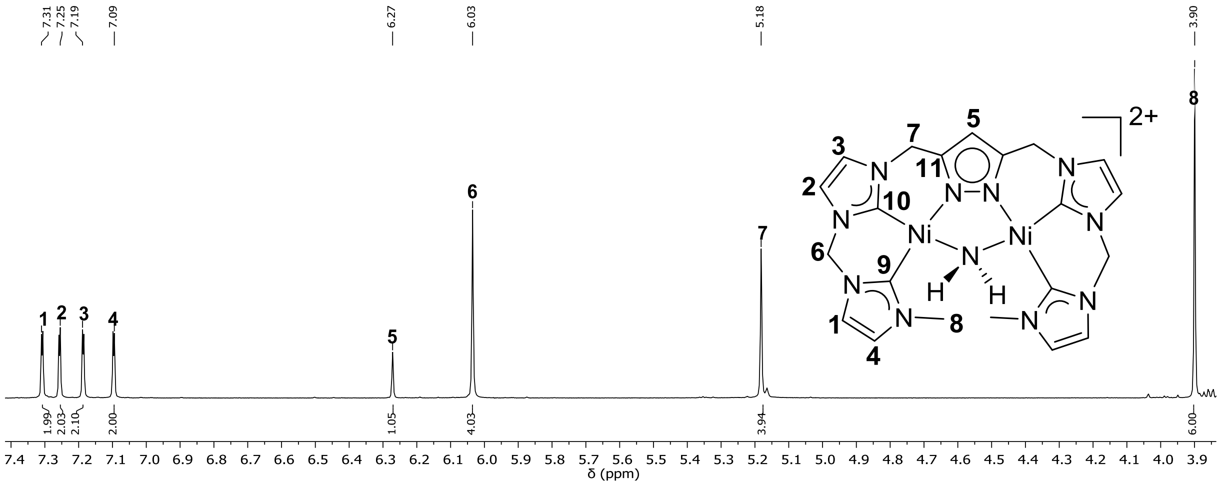

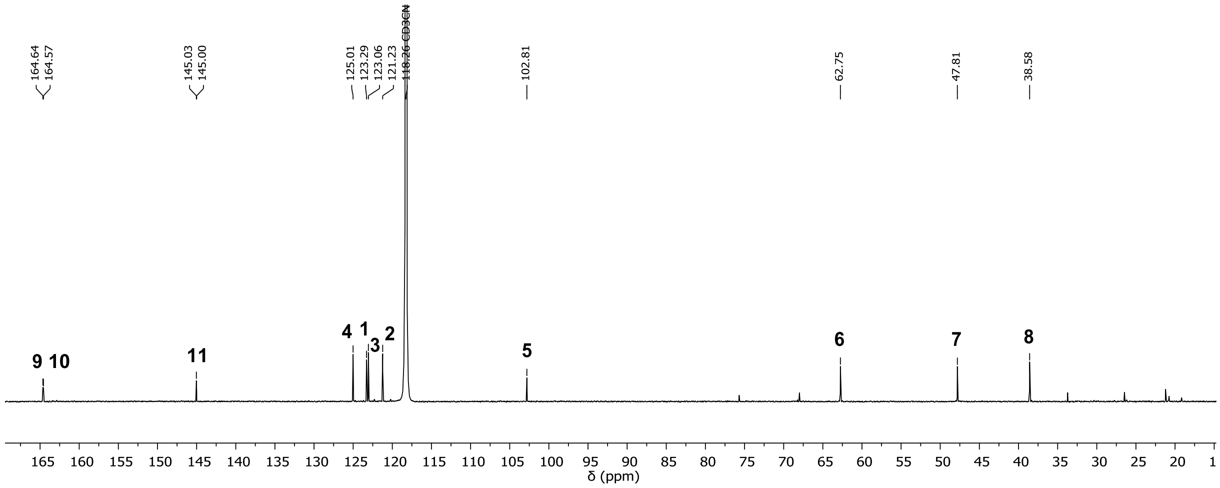

Figure 4.50: Top: ^{1}H NMR spectrum of **[L^{6}Ni$_2$(NH$_2$)](PF$_6$)$_2$** in MeCN-d_3 showing an apparent C_{2v} symmetry of the complex in solution at 500 MHz. **Bottom:** ^{13}C resonances of the carbene carbon atoms are found at 164 ppm in the ^{13}C{^{1}H} NMR spectrum at 126 MHz.

These findings are also supported by H/D exchange IR spectroscopy. In **Figure 4.51** the stretching frequencies of the unlabeled and the labeled species are compared. A red shift of the ND$_2$ stretch is observed by H/D exchange according to the increase of the reduced mass μ in formula (3). The bands at υ(NH) = 3467 cm^{-1} and 3357 cm^{-1} disappear and new vibrational bands are obtained at υ(ND) = 2614 cm^{-1} and ν(ND) = 2465 cm^{-1}.

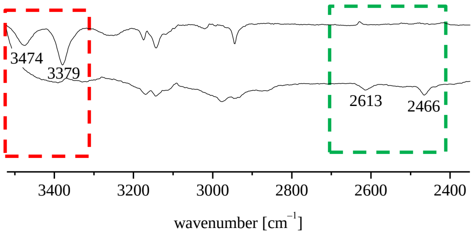

Figure 6.51: Excerpt of IR spectra of **[L^{6}Ni$_2$(NH$_2$)](PF$_6$)$_2$ top:** υ(NH$_2$) at 3474 cm^{-1} and 3379 cm^{-1} (– – –) in MeCN and **[L^{6}Ni$_2$(ND$_2$)](PF$_6$)$_2$ bottom**: υ(ND$_2$) at 2613 cm^{-1} and 2466 cm^{-1} (– – –) in MeCN-d_3.

The calculated IR stretching frequencies of **$[L^6Ni_2(ND_2)](PF_6)_2$** for the μ-ND_2 vibrations are at $\upsilon(ND) = 2558\ cm^{-1}$ and $\upsilon(ND) = 2420\ cm^{-1}$. Hence, the theoretic values are in good agreement with the experimental observed ones (**Tabel 4.14**). In addition, this H/D exchange allows to confirm the previously assigned υ(NH) and represent to the best of my knowledge the first υ(ND) values of a bimetallic μ-ND_2 complex. The combination of ESI-MS, NMR spectroscopy and IR spectroscopy confirms the synthesis of **$[L^6Ni_2(ND_2)](PF_6)_2$**. To the best of my knowledge, this is the first preorganized dinickel(II) amido-bridged NHC complex and the second dinickel(II) amido-bridged complex in the literature.

Table 4.14: Comparison of NH and ND stretching frequencies in **$[L^6Ni_2(NH_2)](PF_6)_2$** and **$[L^6Ni_2(ND_2)](PF_6)_2$**, respectively. DFT* (def2-tzvp def2-tzvp/j bp86). Harmonic approximation gives $\frac{\boldsymbol{\upsilon(NH)}}{\boldsymbol{\upsilon(ND)}}$ = 1.33.

	$\upsilon(NH_2)$ [cm^{-1}]	$\upsilon(ND_2)$ [cm^{-1}]	$\Delta\upsilon$ [cm^{-1}]	$\left[\frac{\upsilon(NH)}{\upsilon(ND)}\right]$
Experimental	3474	2613	861	1.33
	3379	2466	913	1.37
Theoretical*	3467	2558	909	1.35
	3357	2420	937	1.38

4.4.4 Reactivity of the [L^{6}Ni$_2$Cl](PF$_6$)$_2$ complex towards potassium cyanide

A biscyanido dinickel(II) complex is obtained after a salt metathesis reaction of **[L^{6}Ni$_2$Cl](PF$_6$)$_2$** with potassium cyanide (**Scheme 4.17**). The composition of the complex is confirmed by ESI-MS analysis. Only one mass peak is observed in the ESI-MS at *m/z* = 583 (100), which fit to the singly charged complex **[L^{6}Ni$_2$(CN)$_2$]$^+$** (**Figure 4.52**) The IR spectrum of **[L^{6}Ni$_2$(CN)$_2$]PF$_6$** in MeCN shows a pronounced vibrational band at 2116 cm^{-1} which is assigned to the CN stretches in the complex (**Figure 4.52**). This band is shifted to lower frequencies in comparison to known CN complexes, for instance [Ni$_2$(CN)$_2$(S$_2$N$_2$H)]$^{2-}$[141,142] or [Ni(CN)$_4$]$^{-}$[143] due to the strong σ donor character of the NHCs.

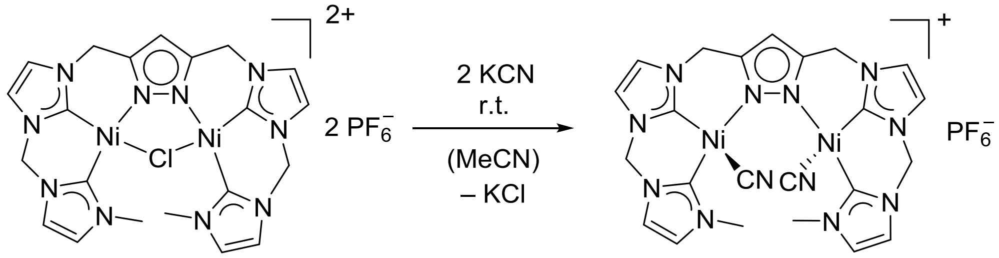

Scheme 6.17: Synthesis of **[L^{6}Ni$_2$(CN)$_2$]PF$_6$** by salt metathesis of **[L^{6}Ni$_2$Cl](PF$_6$)$_2$** with KCN.

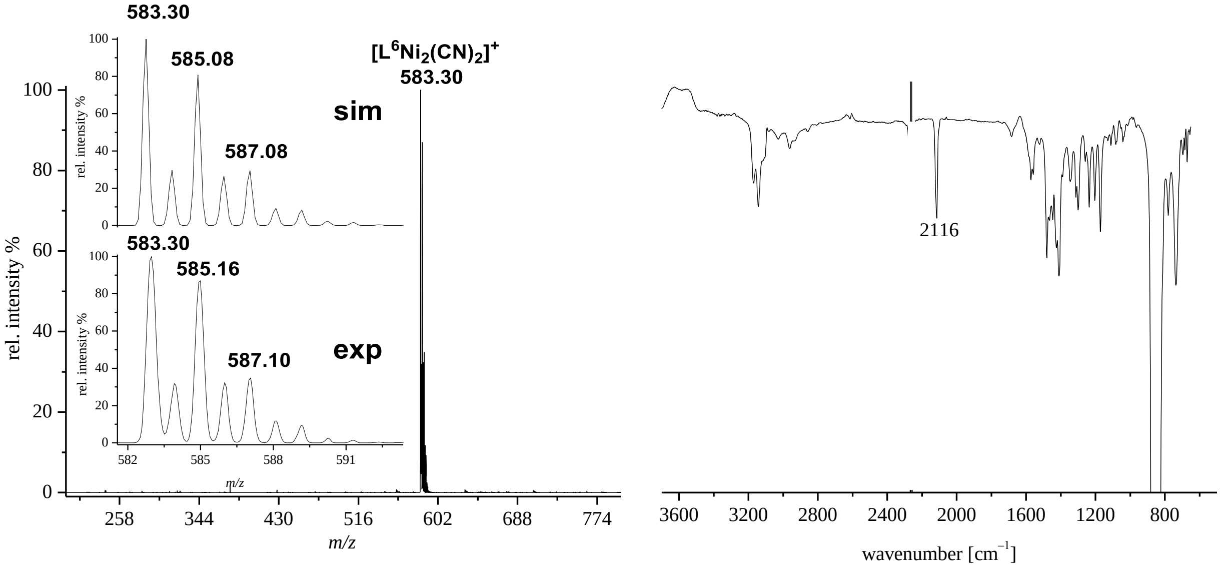

Figure 4.52: Left: ESI-MS of **[L^{6}Ni$_2$(CN)$_2$](PF$_6$)** in MeCN. Inset shows the simulated (**top**) and experimental (**bottom**) isotopic distribution pattern at *m/z* = 583 (100) for **[L^{6}Ni$_2$(CN)$_2$]$^+$**. **Right:** IR spectrum of **[L^{6}Ni$_2$(CN)$_2$](PF$_6$)** in MeCN shows a pronounced band at 2116 cm^{-1} which is assigned to the CN stretches of the complex.

The increased electron density at the nickel(II) ions results into a π-backdonation from the metal into the π* orbitals of the CN triple bond and leads to a decrease of the CN stretching frequency. A [Ni$_2$(CN)$_2$(S$_2$N$_2$H)]$^{2-}$[141,142] complex is described in the literature, which shows a CN stretch at $\upsilon(\mathrm{CN}) = 2128\ \mathrm{cm}^{-1}$ in the IR spectrum and cyanide complex of **XI**, shows a CN band at $\upsilon(\mathrm{CN}) = 2127\ \mathrm{cm}^{-1}$.[126] In the IR spectrum, $[\mathrm{Ni(CN)_4}]^{-}$ shows a CN stretch at $\upsilon(\mathrm{CN}) = 2149\ \mathrm{cm}^{-1}$.[143]

The ^{1}H NMR spectrum of **$[L^6Ni_2(CN)_2]PF_6$** in MeCN-*d*$_3$ shows a diastereotopic splitting of the proton resonances H^5 and H^6 of the CH_2 groups as well as a broadening of the resonances H^8 of the CH_3 groups. The chemical shift between the two doublets of the AX spin system of the CH_2 groups H^5 is $\delta = 241$ Hz. A reason for this diastereotopic splitting can be the orientation of the CN groups in the cavity of the complex relative to the CH_3 groups of the ligand. In theory, several conformers are possible as described for **$[L^6Ni_2(OH)](PF_6)_2$**, but in addition the CN groups can probably point in opposite directions out of the ligand plane. C^{carbene} resonances of the complex are assigned at $\delta = 169.5$ ppm and $\delta = 163.4$ ppm in the $^{13}C\{^1H\}$ NMR spectrum of **$[L^6Ni_2(CN)_2]PF_6$** in MeCN-*d*$_3$. In agreement with in the literature known, ^{13}C chemical shifts of CN in metal complexes range from 160 ppm to 120 ppm, and the CN resonance of **$[L^6Ni_2(CN)_2]PF_6$** is observed at 143.1 ppm.[144,145] ^{13}C resonances of **$[\mathrm{Ni(CN)_4}]^{2-}$** are found at 135.5 ppm.[145] (**Figure 4.53**)

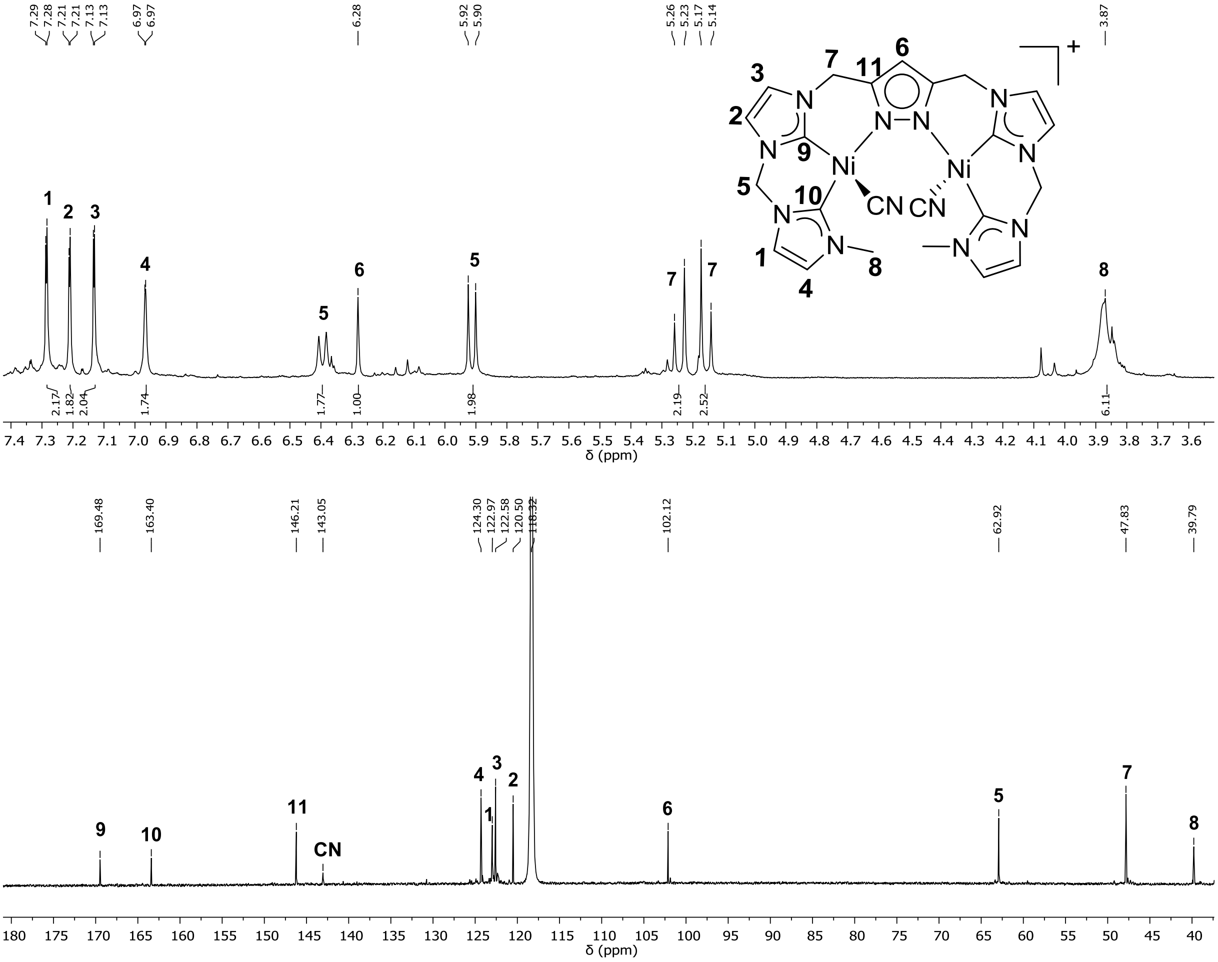

Figure 4.53: Top: ^{1}H NMR spectrum of **$[L^6Ni_2(CN)_2]PF_6$** at 500 MHz and 298 K. **Bottom:** $^{13}C\{^1H\}$ NMR spectrum in MeCN-*d*$_3$ at 298 K and 126 MHz. The ^{13}C resonance of the CN groups was assigned at 143.1 ppm.

4.5 Conclusion and Outlook

The synthesis and characterization of dinickel(II) complexes, bearing a OH^{-}, Cl^{-}, NH_2^{-} -bridged or two CN^{-} groups between the two metal centers is presented here. The strong interaction of the hydroxido-bridged complex with solvent molecules *via* hydrogen bond interaction is investigated in solid state by IR spectroscopy and NMR spectroscopy. In addition the H/D and $H_2{}^{16}O/H_2{}^{17}O$ exchange kinetics for the substitution of the OH group are determined. The complex shows slow exchange kinetics and the derived activation parameters propose a concerted pathway for the H/D exchange and an associative reaction mechanism for the $H_2{}^{16}O/H_2{}^{17}O$ exchange in agreement with extended DFT calculations. *In situ* deprotonation of the OH proton is possible and ^{1}H NMR spectroscopy and ESI-MS suggest the formation of a dinickel(II) μ-oxido complex. With HCl, the protonation of the OH group in **$[L^6Ni_2(OH)](PF_6)_2$** is possible and leads to the substitution of the bridge under release of water. This example shows that the stable OH bridge between the two nickel centers of a pyrazolate can be substituted in these types of bimetallic complexes. **$[L^6Ni_2Cl](PF_6)_2$** is used for the synthesis of **$[L^6Ni_2(NH_2)](PF_6)_2$** and **$[L^6Ni_2(CN)_2]PF_6$**.

5

A Dinickel(II) μ-sulfido tetracarbene/pyrazolate complex and its manifold properties

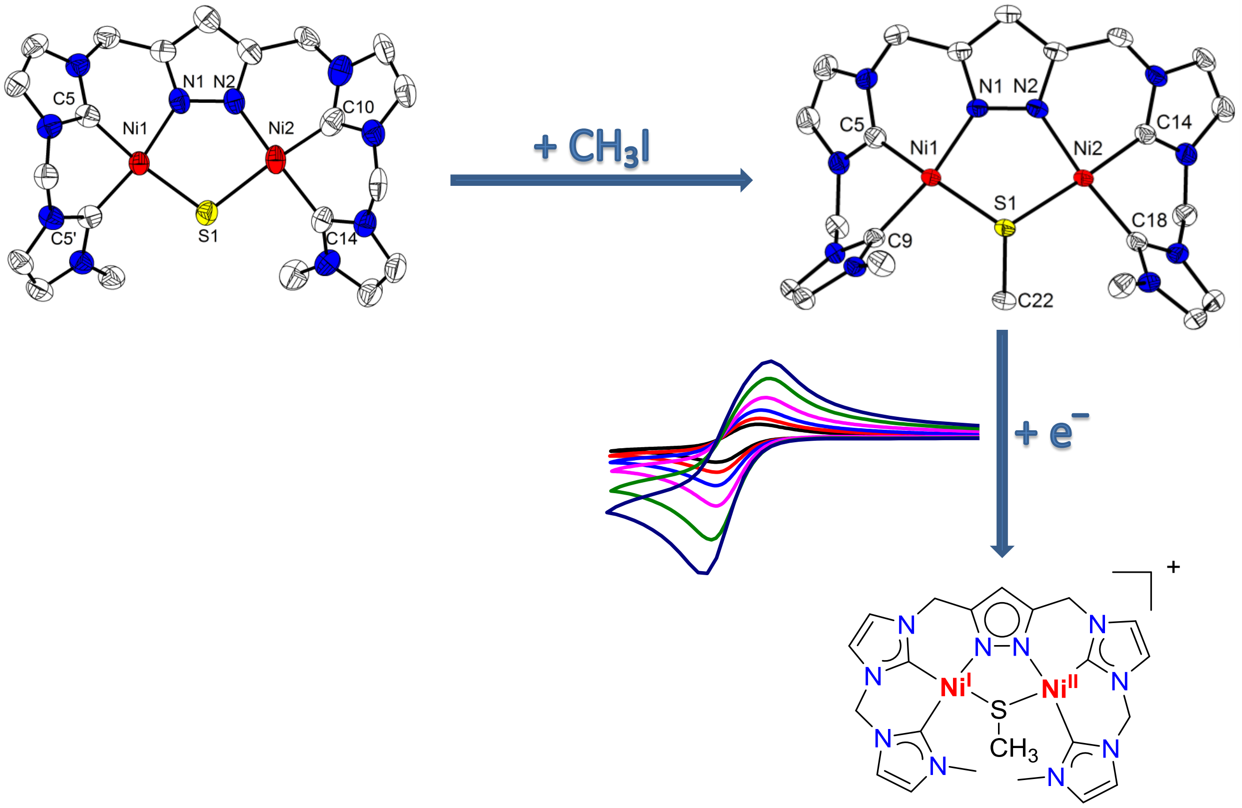

Abstract: Nickel sulfur containing complexes are important in large industrial processes, like in hydrodesulphurization reactions for petroleum feedstocks and are promising as electrode material in photocatalytical water oxidation reactions. The catalytic active center of [NiFe] hydrogenases, methyl-coenzyme M reductase (MCR) and acetyl coenzyme A synthase (ACS) contain mono- or dinickel sulfur units and the role of the co-factors is still in focus of ongoing research. In academia mono and dinuclear nickel(I) or nickel(II) sulfur complexes are studied as model complexes of the active centers of enzymes or are investigated with respect to the activation of small molecules, such as N_2O, NO, CO, O_2 and H_2. Herein, a novel dinuclear dinickel(II) μ-sulfido complex is presented, encompassing intrinsic properties, its transformation to the corresponding thiolato complex and its reactivity towards small molecules. The dinickel(II) μ-thiolato complex is reversibly reduced to a mixed valent Ni^INi^{II} complex, showing an axial-symmetric EPR spectrum.

5.1 Introduction

5.1.1 Sulfur containing metal complexes and their application in chemical reactions

Metal sulfido-bridged complexes have gained enormous interest in the last two decades, due to their presence in nature and their broad applicability in chemical reactions.[146–153] Nickel and cobalt promoted heterogeneous molybdenum sulfide catalysts have a huge impact on industrial catalysis due to their role in hydrodesulphurization reactions of petroleum feedstock.[146,154–157] The sulfur containing organic feedstock is hydrogenated to their aromatic or aliphatic petroleum compounds under release of H_2S.[158] Metal sulfido-bridged clusters, for instance Mo_2S_4, are also used in industrial hydrogenation, hydrocracking and hydrodeoxygenation reactions, in which C–C, C–S and C–H bonds are activated and cleaved.[146,159,160] Solid nickel sulfur composites are tested as cathode material in lithium batteries[161] and heterogeneous nickel sulfur catalysts are used in hydrodenitrogenation reactions or to produce dihydrogen from water on a photocatalytic way.[162,163] Cubane-type Mo_3NiS_4 is described as a catalyst for intramolecular cyclization reactions of alkynoic acids to enol lactones[164] and a molecular dinickel bis-*μ*-sulfido NHC complex **XVI** is able of activating heterolytically dihydrogen or pinacolborane (**Scheme 5.1**).[165,166]

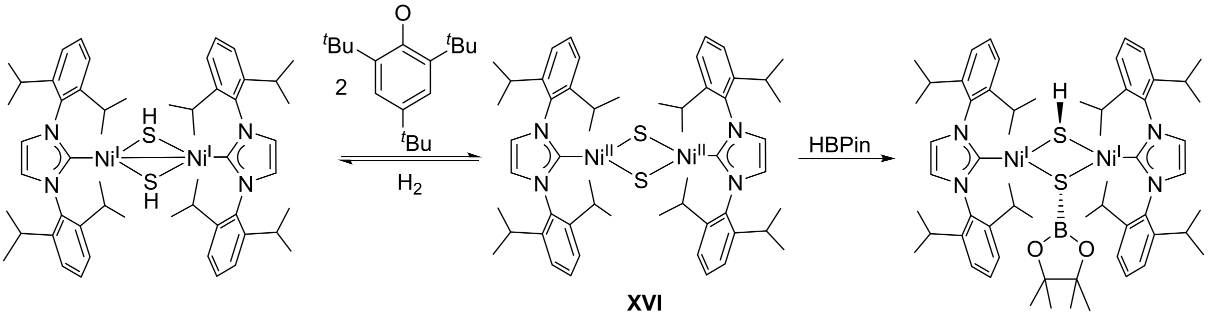

Scheme 5.1: **XVI** and its heterolytic cleavage of dihydrogen and pinacolborane. The resulting dinickel(I) *μ*-dihydrosulfido complex can be converted to the starting compound by HAT process with 2,4,6-*tert*-butylphenoxy radical.[165,166]

In 2015, Hayton *et al.* presented a “masked Ni-S···[KL]” *nacnac* complex ([KL] = [K($C_{12}H_{24}O_6$)]), **XVII** which shows reactivity towards nitrous oxide[167], carbon monoxide[168], nitric oxide[168] and carbon disulfide[169] (**Scheme 5.2**).

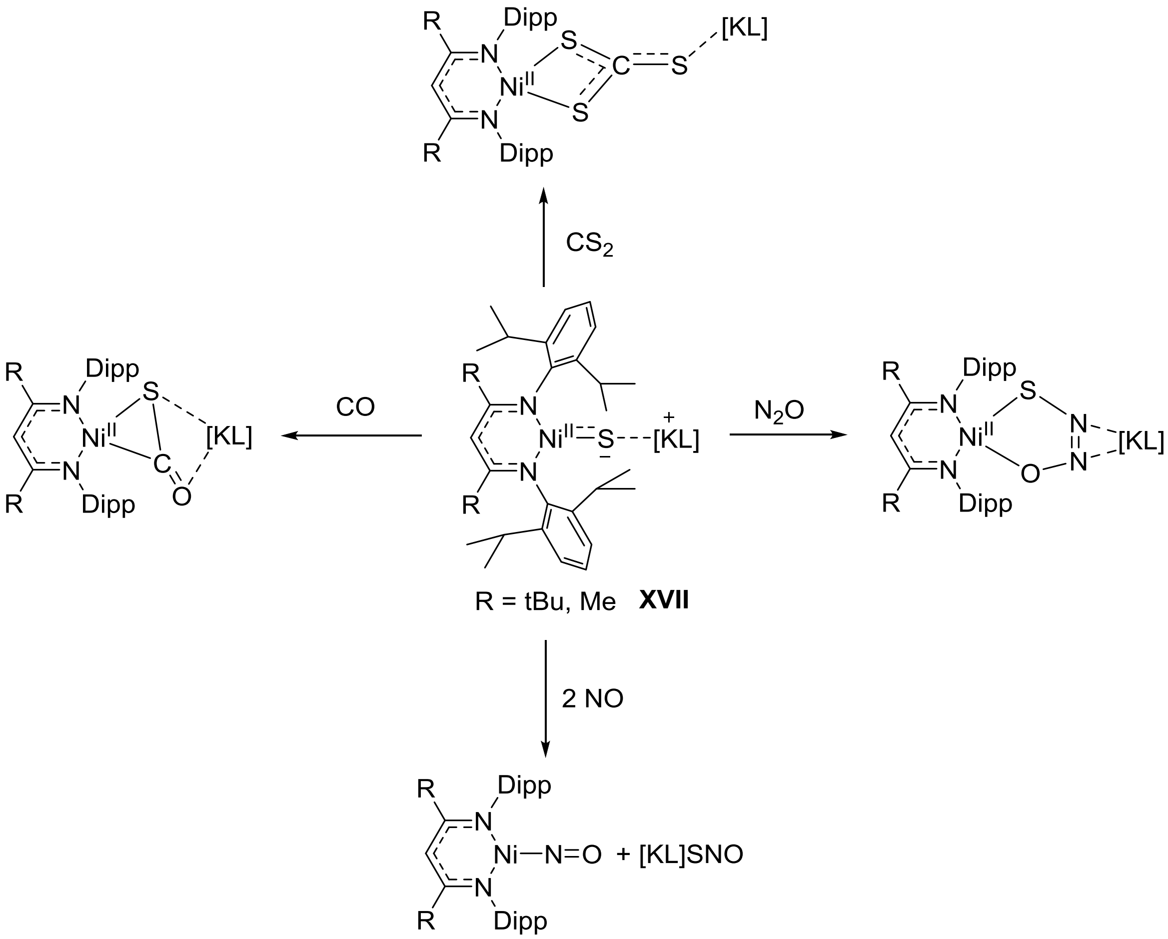

Scheme 5.2: Versatile reactivity of a "masked Ni-S···[KL]" *nacnac* complex **XVII** ([KL] = [K($C_{12}H_{24}O_6$)]). Reactivity with CS$_2$, N$_2$O, NO and CO are described in the literature.[167–169]

5.1.2 Metal-sulfur containing co-factors in nature

Iron, nickel, molybdenum and copper co-factors bearing sulfur ligands are omnipresent in nature. Iron sulfur clusters are used in biological processes in electron transfer cascades and proton-coupled electron transfer reactions. In the latter case, the most prominent examples are the [FeFe] or [Fe] hydrogenases[170,171] and the [2Fe-2S] Rieske cluster[172–180]. Nickel cysteine based enzymes are able to activate and convert small molecules for energy storage, to protect the organism or to build up relevant substrates for the organism. Several enzymes, bearing nickel ions in the active center are known, but there is still a lack of knowledge on how the mechanism of substrate conversions at these active sites can occur. In 2017, Limberg *et al.*[181] described the progress in the ongoing work of research of model complexes containing nickel(I) as an active site. In several enzymes, catalytic active species with nickel in the oxidation state +I or +III are mentioned.

5.1.2.1 Coenzyme M reductase and acetyl coenzyme A synthase

There is an ongoing debate regarding the mechanism of methyl-coenzyme M reductase (MCR).[182–184] This enzyme, found in methanogen *archae bacteria*, is catalyzing the reaction of methyl coenzyme M and coenzyme B to methane and CoB-S-S-CoM. Two mechanisms are proposed: in mechanism I, the change of the oxidation states from nickel(I) to nickel(III) is proposed in the catalytic cycle (**Scheme 5.3**). The initial step is the formation of a nickel(III)-methyl complex[148–153,185] wherein mechanism II a radical mechanism with a Ni^{I}/Ni^{II} redox stage and homolytic splitting of the H_3C-SCoM bond is postulated.[186,187] Nevertheless, the generation and stabilization of a nickel(I) species seems to be the initial step for the activation of the substrate.

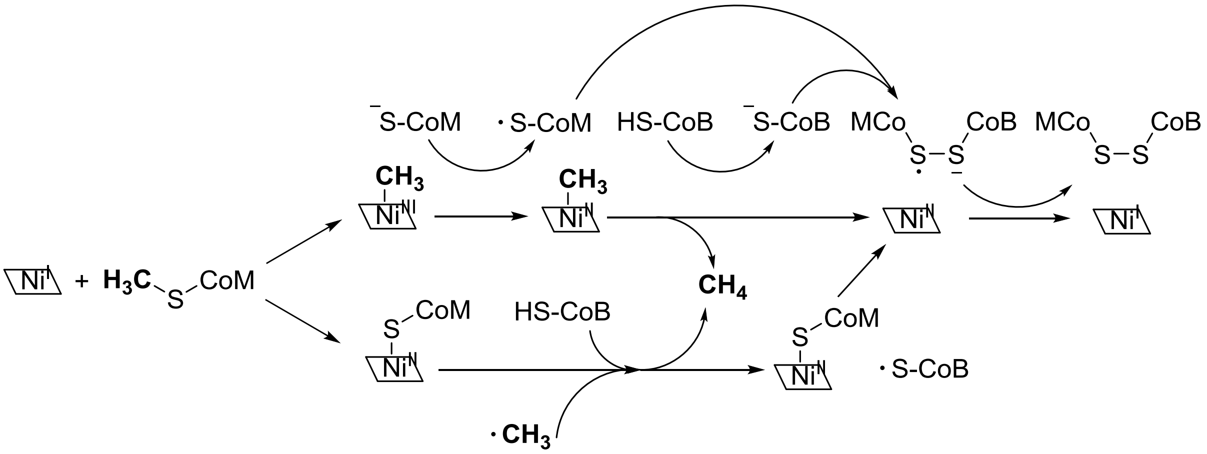

Scheme 5.3: Mechanistic investigations of the methyl-coenzyme M reductase. Mechanism I (**top**): heterolytic cleavage of the H_3C-SCoM and formation of Ni^{III}-methyl complex. Mechanism II (**bottom**): homolytic cleavage of the methyl-S bond, followed by a radical mechanism.[188]

A second example is the active center of the acetyl coenzyme A synthase (ACS) with an ongoing debate regarding the two proposed pathways.[189,190] (**Scheme 5.4**).

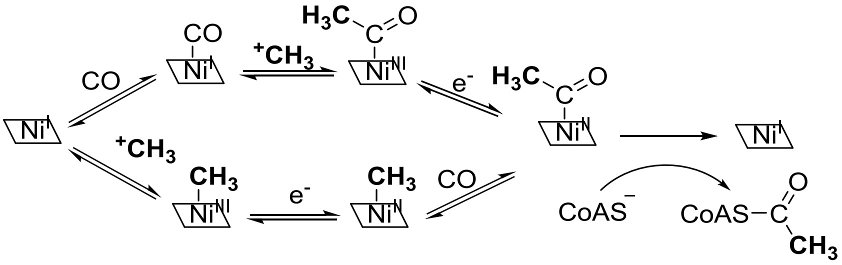

Scheme 5.4: Two proposed pathways with the different intitial steps: **Top:** Association of CO, bottom: oxidative addition of $^{+}CH_3$.

5.1.2.2 Hydrogenases and sulfur mediated protein folding

In [NiFe] hyrogenases, nickel has an important role as non-innocent metal during the conversion of protons to dihydrogen. In the nickel-R state a nickel(I) and in the nickel-M state a nickel(III) complex is postulated.[191] Most [NiFe] hydrogenases are air sensitive and their activity can be (ir)reversible inhibited under presence of dioxygen.[191–195] A possible inhibition pathway is the formation of a sulfinate or sulfonate ligated nickel complex.[192,196] To date, only four dioxygen tolerant [NiFe] hydrogenases from *Ralstonia eutropha* (*RE*) are known[197,198], but the reason for this O_2 tolerance is still unknown.[196] A possibility is the reversible oxygenation of one of the bridging cysteine S amino acids. Model complexes are developed for comparison with O_2 tolerant hydrogenases, to get further insights in such a mechanism and to provide spectroscopic data.[199–201] In 2017, Driess and coworkers[199] reported the synthesis of the first heterobimetallic S-oxygenated [NiFe] hydrogenase model complex and its chemical properties.

Dioxygen can also be used for the refolding of sulfur containing enzymes. The folding and unfolding of proteins by disulfides plays in nature an important role. Randomly coiled polypeptide chains, formed by reduction of disulfide groups can be refolded by air oxidation of the cysteine side chains under presence of transition metals, like copper.[192,202] Herein, the copper assists the electron transfer from the ionized sulfhydryl groups to molecular dioxygen by the change of its oxidation states from copper(II) to copper(I), concomitant with formation of a thiyl radical, which dimerizes to a disulfide.

5.2 Objectives

In this chapter, the focus is on the synthesis and characterization of **[L^6Ni_2S]PF_6** as the key compound for the transformation to a thiolato-bridged complex **[$L^6Ni_2(SCH_3)$](PF_6)$_2$** (**Scheme 5.5**). Furthermore the interconversion of **[$L^6Ni^{II}Ni^{II}(SCH_3)$](PF_6)$_2$** to **[$L^6Ni^{I}Ni^{II}(SCH_3)$](PF_6)$_2$** is investigated, which is a potential key complex for further reactivity studies of mixed valent dinickel complexes. Also, the reactivity of **[L^6Ni_2S]PF_6** with O_2, N_2O and NO is investigated.

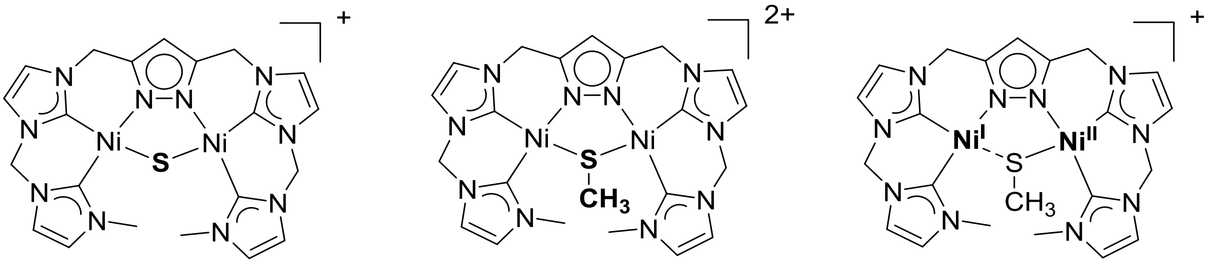

Scheme 5.5: Proposed structures for [**L^6Ni_2S]PF_6**, [**$L^6Ni^{II}Ni^{II}(SCH_3)$](PF_6)$_2$** and [**$L^6Ni^{I}Ni^{II}(SCH_3)$](PF_6)$_2$**.

5.3. Results and Discussion

5.3.1 A μ-sulfido dinickel(II) NHC complex

The synthetic starting point from the most reactions in the following chapters is a sulfido-bridged complex [$\mathbf{L^6Ni_2S]PF_6}$. The synthesis of $\mathbf{[L^6Ni_2S]PF_6}$ is achieved by reaction of $\mathbf{[L^6Ni_2Cl](PF_6)_2}$ with sodium sulfide. A direct synthesis route of [$\mathbf{L^6Ni_2S]PF_6}$ from the ligand is not possible, due to the tendency of *in situ* formation of the $\mathbf{[L^6Ni_2(OH)](PF_6)_2}$ complex (see also **chapter 4**).

Upon addition of solid Na_2S to a solution of $\mathbf{[L^6Ni_2Cl](PF_6)_2}$ an immediate color change is observed at the surface of the solid particles of Na_2S from greenish-yellowish to orange. During further reaction time the suspension turned red-orange. After reaction over three days and work-up of the complex (see experimental section) red crystals are obtained by diffusion of Et_2O into a complex solution in MeCN. The complex crystallizes in the space group *P*nma and the molecular structure in solid state shows an approximate (non-crystallographic) C_s symmetry of the complex, in agreement with the structures of $\mathbf{[L^6Ni_2(OH)](PF_6)_2}$ and $\mathbf{[L^6Ni_2Cl](PF_6)_2}$ (**chapter 4**). Ni(1) is 0.13 Å out of the C(5')–C(5)–N(1)–S(1) plane and Ni(2) is 0.047 Å out of the S(1)–N(2)–C(10)–C(14) plane. The angle between these two planes is 17.21° and the most acute angle of all crystallized dinickel(II) μ-pyrazolate complexes presented in this work. The Ni(1)····Ni(2) distance is 3.48 Å and compared to dinickel(II) distances of the $\mathbf{[L^6Ni_2(OH)](PF_6)_2}$ (3.26 Å) and to $\mathbf{[L^6Ni_2Cl](PF_6)_2}$ (3.46 Å) larger. The Ni-$C^{carbene}$ bond lengths are listed in **Table 5.1** and are in the range between 1.87-1.94 Å in agreement with the literature known values[165] and bond lengths described in this work. The elongated Ni–C bond (1.94 Å) is the longest Ni–$C^{Carbene}$ bond of all pyrazolate/NHC complexes presented in this work. An overview of the most important nickel ligand distances is presented in **Scheme 5.6**. In the crystal structure (**Figure 5.1**), the two methyl groups are orientated both away from the pyrazolate-dinickel plane. The distance between the two CH_3 groups is 4.67 Å and distance between CH_3 groups and S(1) are 3.24 Å and 3.33 Å.

The average Ni–S bond lengths (2.18 Å) is in the range of nickel sulfur single bonds and in agreement with 'bent' (Ni–S–Ni angle << 178-180°) dinickel disulfido complexes (2.18-2.20) (**Figure 5.2**)[203,204] In 2014, complex **XVI** (**Scheme 5.1**) was presented with a short Ni–S bond of 2.09 Å.[165] All bent nickel sulfido complexes, described in the literature, have two sulfido bridges between the nickel centers. To the best of my knowledge, no comparable structural motive like in **[L^{6}Ni$_2$S]PF$_6$** is found. In the literature, dinickel μ-sulfido complexes bearing just one sulfur ion as bridge show an almost linear Ni–S–Ni angle (178-180°) and a very short Ni–S bond of 2.03-2.07 Å.[205,206]

Compared to this, the Ni-S bond length in the "masked complexes" **XVII** (**Scheme 5.2**) is similar to the latter complexes (2.06-2.08 Å). The Ni–S bond can be described as an intermediate bond between nickel-sulfur single and double bond. The additive covalent radii of Ni–S single bonds are 2.13 Å and 1.95 Å for Ni–S double bonds.[167]

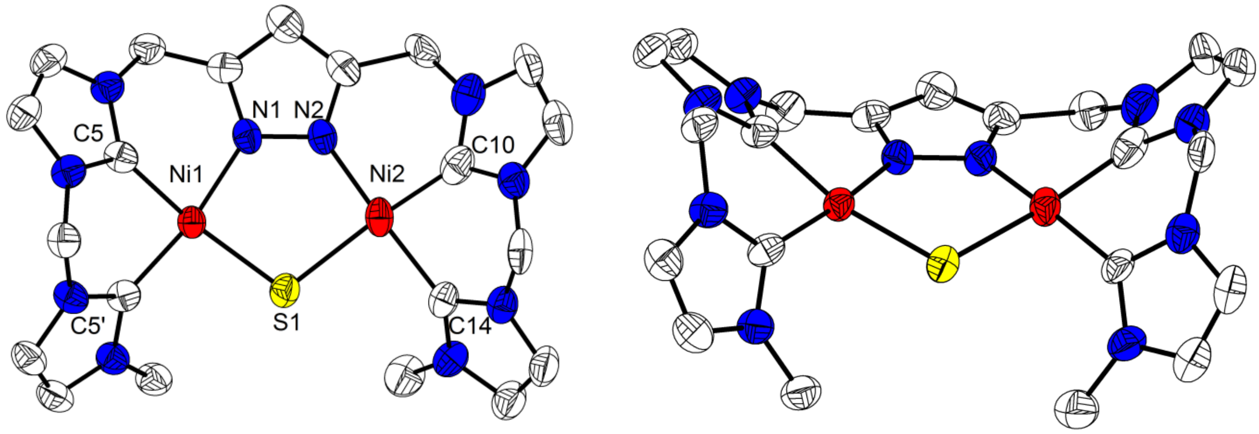

Figure 5.1: Molecular structure (50% probability thermal ellipsoids) of the cationic part of **[L^{6}Ni$_2$S]PF$_6$**. H atoms are omitted for clarity. Symmetry transformation used to generate equivalent atoms: (') x, 1/2-y, z.

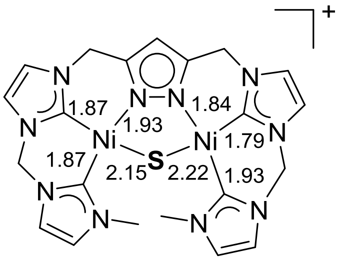

Scheme 5.6: Selected bond lengths **[Å]** in **[L^{6}Ni$_2$S]$^+$**.

Table 5.1: Selected bond lengths [Å] for **[L^{6}Ni$_2$S]PF$_6$**.

Atoms	Bond lengths
Ni1····Ni2	3.480(8)
Ni1–C5'	1.872(4)
Ni1–C5	1.872(4)
Ni1–S1	2.148(2)
Ni1–N1	1.933(6)
Ni2–C10	1.787(1)
Ni2–C14	1.940(1)
Ni2–S1	2.220(2)
Ni2–N2	1.836(6)

Table 5.2: Selected bond angles [°] for **$[L^6Ni_2S]PF_6$**.

Atoms	Bond angles
C5'–Ni1–C5	88.0(2)
C5–Ni1–N1	84.4(2)
Ni1–S–Ni2	105.(7)
C5–Ni1–S1	96.9(1)
C10–Ni2–N2	93.4(4)
C10–Ni2–C14	86.0(6)
C14–Ni2–S1	90.0(3)

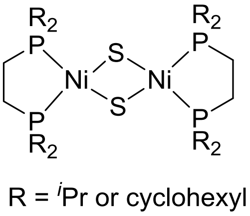

Figure 5.2: Example of a complex with a 'bent' Ni–S–Ni bond.

The ESI-MS of the complex in MeCN shows only one peak at m/z = 563 (100), which can be assigned to the singly charged **$[L^6Ni_2S]^+$** (**Figure 5.3**).

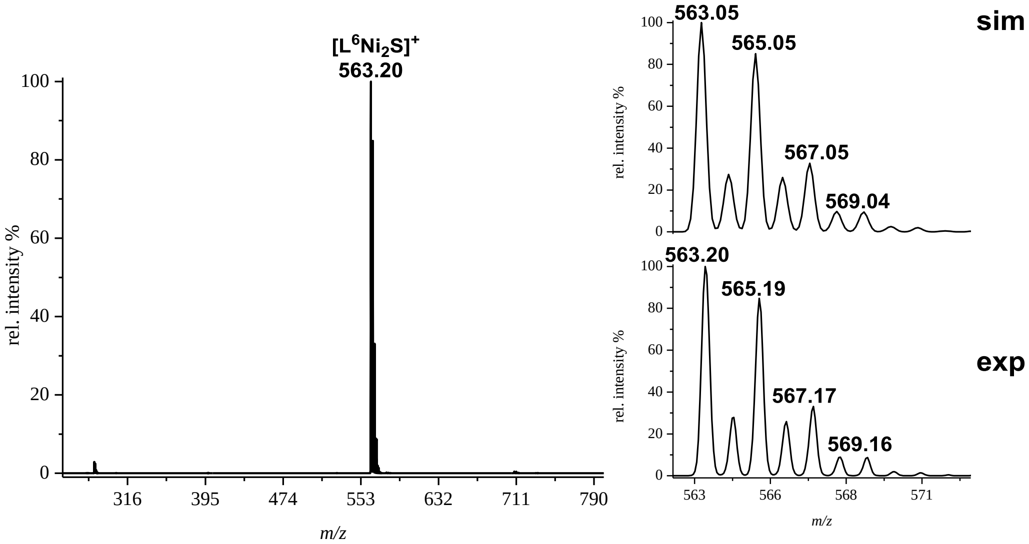

Figure 5.3: ESI-MS spectrum of **$[L^6Ni_2S]PF_6$** in MeCN. Inset shows the simulated (**top**) and experimental (**bottom**) isotopic distribution pattern at m/z = 563 (100) for **$[L^6Ni_2S]^+$**.

5.3.2 UV-vis spectroscopy of [L^6Ni_2S]PF_6

The UV-vis spectrum of the complex in solid state shows at r.t. five bands (246 nm, 310 nm, 345 nm, 396 nm and 433 nm) (**Figure 5.4**). The UV-vis spectrum of **[L^6Ni_2S]PF_6** in MeCN at 293 K shows three bands at 230 nm ($49.98 \cdot 10^3$ $M^{-1} \cdot cm^{-1}$), 306 nm ($48.32 \cdot 10^3$ $M^{-1} \cdot cm^{-1}$) with a shoulder around 337 nm and at 395 nm ($10.75 \cdot 10^3$ $M^{-1} \cdot cm^{-1}$) with a shoulder around 433 nm ($7.53 \cdot 10^3$ $M^{-1} \cdot cm^{-1}$). In solution spectrum the bands around 395 nm and 433 nm are dramatically decreased relative to the bands at 230 nm and 306 nm (approximately 20%).

A UV-vis spectrum was obtained by TD-DFT calculations (**Figure 5.4**), but no clear transitions in the molecule can be assigned, due to admixture of several metal and ligand orbitals in the ground states as well as in the excited states.

A decrease of the temperature leads to an increase of the bands at 230 nm ($\Delta\varepsilon = 2.73 \cdot 10^3$ $M^{-1} \cdot cm^{-1}$), at 306 nm ($\Delta\varepsilon = 2.77 \cdot 10^3$ $M^{-1} \cdot cm^{-1}$), and blue shift of the band at 395 nm to 393 nm concomitant with a slight increase of the band ($\Delta\varepsilon = 0.13 \cdot 10^3$ $M^{-1} \cdot cm^{-1}$). The shoulder at 433 nm is decreasing ($\Delta\varepsilon = 0.15 \cdot 10^3$ $M^{-1} \cdot cm^{-1}$).

[L^6Ni_2S]PF_6 is in contrast to the previously described **[L^6Ni_2Cl](PF_6)$_2$** or **[$L^6Ni_2(OH)$](PF_6)$_2$** partly soluble in THF, due to its lower overall charge. No extinction coefficient is determined since the poor solubility of the complex in THF does not allow the determination of the concentration. The corresponding UV-vis spectrum of the complex at r.t. differs compared to the UV-vis spectrum at 293 K in MeCN. The band at 306 nm in MeCN is only slightly shifted to 308 nm but the former bands at 396 nm and 433 nm are significant red shifted respectively to 402 nm and 445 nm in THF (**Table 5.3**). The former shoulder at 433 nm in MeCN has a higher absorption in THF than the former band at 393 nm, which is now at 402 nm. The intensities have changed, which can affect different strong interactions of the solvent molecules with the complex. All UV-vis bands are compared in **Table 5.3** in dependence on the solvent.

Table 5.3: Comparison of the UV-vis bands of **[L^6Ni_2S]PF_6** in solid state, MeCN and THF at 293 K.

UV-vis bands [nm]		
Solid	**MeCN**	**THF**
246	230	–
310	306	308
345	337	337
396	395	402
433	433	445

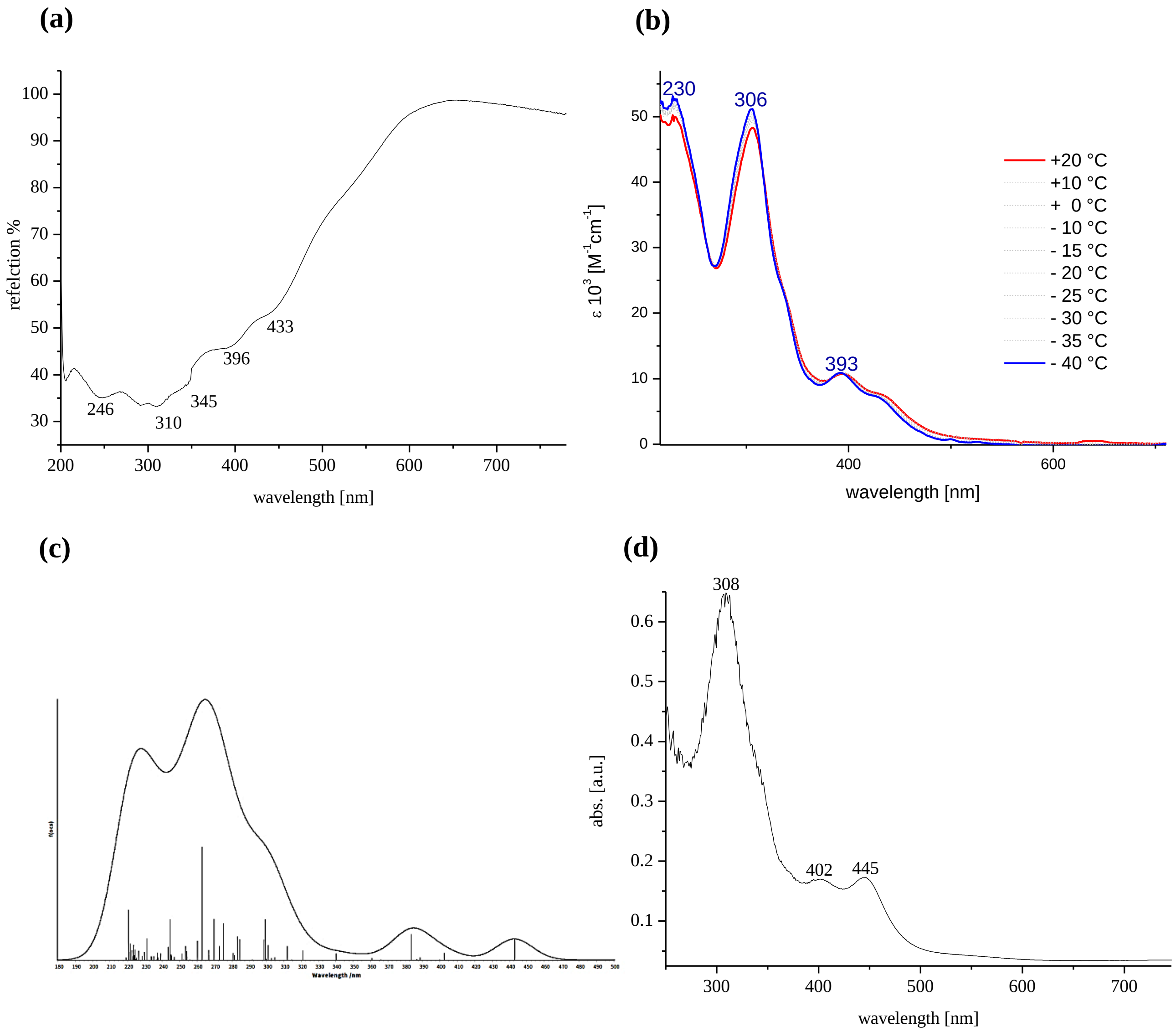

Figure 5.4: (a) Solid state UV-vis of **[L^{6}Ni$_2$S]PF$_6$** at r.t.; (b) Variable temperature UV-vis spectra in MeCN in the range between +20 °C and –40 °C; (c) TD-DFT calculated UV-vis spectrum (d) UV-vis spectrum of **[L^{6}Ni$_2$S]PF$_6$** in THF at r.t.

5.3.3 NMR spectroscopy of [L^{6}Ni$_2$S]PF$_6$

The ^{1}H NMR spectrum of **[L^{6}Ni$_2$S]PF$_6$** in MeCN-d_3 at 298 K shows an apparent C_{2v} symmetry of the complex in solution with slight line broadening of peaks H^7 and H^8. The combination of ^{1}H NMR spectroscopy with ^{13}C{^{1}H} NMR spectroscopy and 2D NMR measurements allow the assignment of all proton resonances (**Figure 5.5**). The strong σ donor ability of the sulfido ion in comparison to the hydroxido and chlorido ions is clearly observable in the ^{1}H NMR spectrum, based on the chemical shift of the corresponding proton resonances (**Figure A.5.1** in **appendix**). The largest shift is observed for the pyrazolate proton resonance H^5 at 6.09 ppm. This signal is high-field shifted (in average approximately

0.2 ppm) in comparison to the H^{pz} signals of **[$L^6Ni_2(OH)$](PF_6)$_2$** and **[L^6Ni_2Cl](PF_6)$_2$** (δ(OH^-) H^{pz} = 6.26 ppm and δ(Cl^-) H^{pz} = 6.33 ppm) (**Figure 4.5** and **Figure 4.43**). The broadening of the singlet of the CH_2 groups H^7 and the CH_3 groups H^8 at room temperature suggests a dynamic effect which is further investigated by VT ^1H NMR spectroscopy.

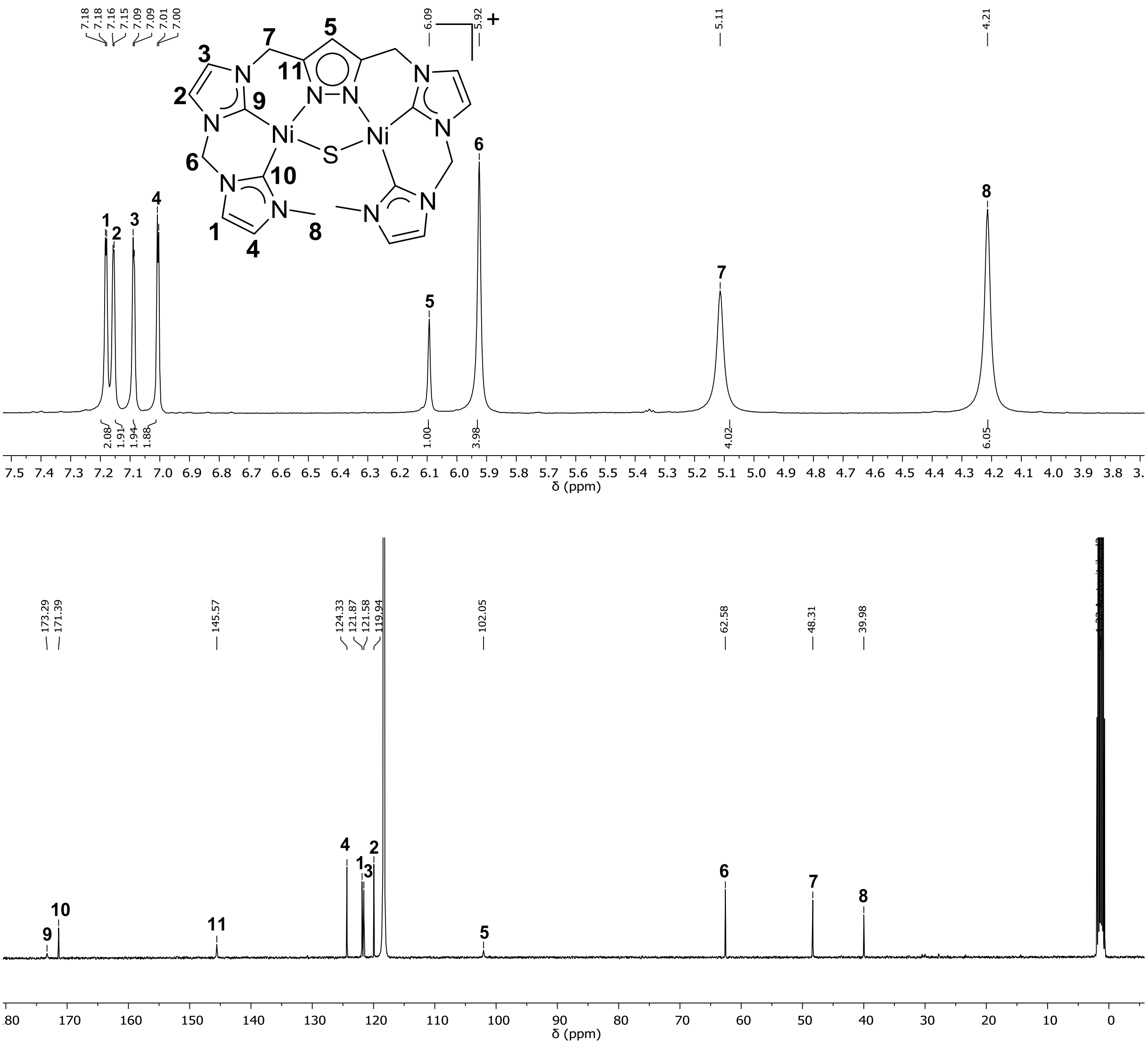

Figure 5.5: Top: ^1H NMR spectrum of **[L^6Ni_2S]PF_6** at 298 K, 500 MHz in MeCN-d_3. Line broadenings are observed of peak H^7 and H^8. **Bottom:** $^{13}C\{^1H\}$ NMR spectrum of **[L^6Ni_2S]PF_6** at 298 K and 126 MHz.

VT ^1H NMR spectroscopy is performed in a temperature range from 333 K to 233 K (**Figure 5.6**). An increase of temperature leads to a decrease of the peak line width. The decrease of the temperature triggers a broadening of the peaks for H^6, H^7 and H^8 at 283 K. Below 283 K two pyrazolate proton signals for H^5 (- - - -) are observed, and at the same temperature peaks of the CH_2 groups H^6 and H^7 are split into an AB spin system. Two sets of proton signals are obtained, confirming the formation of two diastereomers. The energetically most stable conformers for **[L^{6}Ni$_2$S]PF$_6$** are depicted in **Scheme 5.7** and show C_s and C_2 symmetry. The ratio of the two species is 2:1 at 263 K, based on the ratio of H^8 (- - - -) and H^{pz} (- - - -) proton resonances. A temperature dependent equilibrium of the two C_2 symmetric enantiomers of **[L^{6}Ni$_2$S]PF$_6$** and the C_s symmetric diastereomer and *vice versa* is observed (**Scheme 5.7**). The determination of the thermodynamically more stable diastereomer is not possible from the present data. Since the molecular structure in solid state of the complex only shows the C_s symmetric complex, it is assumed that this could be the more stable one in solution.

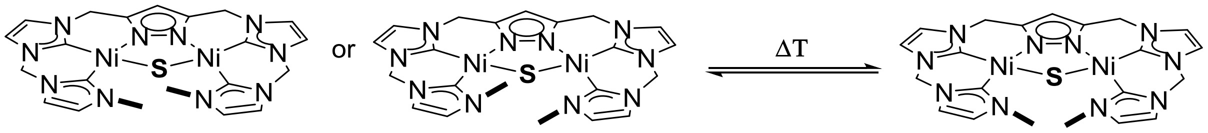

Scheme 5.7: Interconversion of the two energetically not discriminable enantiomers with C_2 symmetry (**left**) into the C_s symmetric conformer (**right**).

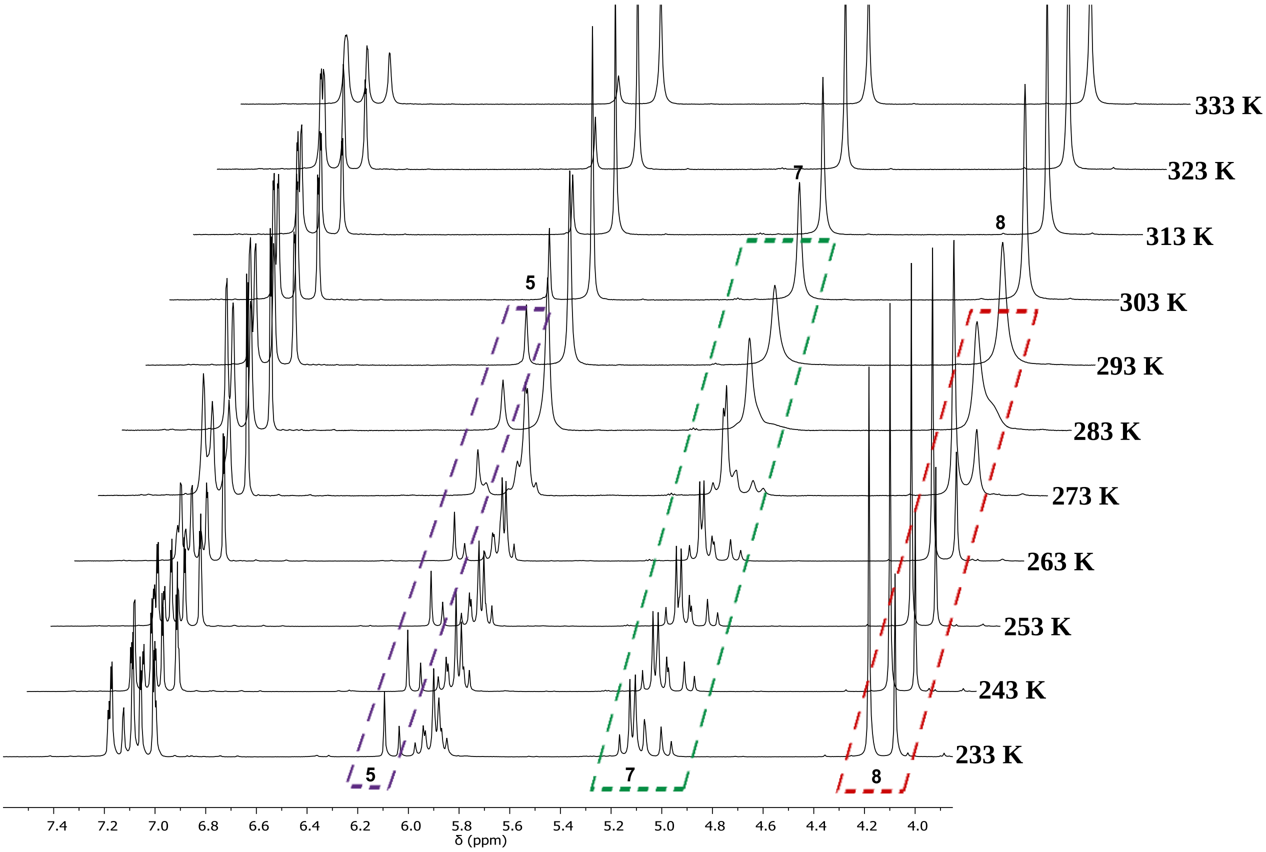

Figure 5.6: VT ^{1}H NMR spectra of **[L^{6}Ni$_2$S]PF$_6$** in the temperature range between 233 K and 333 K (400 MHz, CD$_3$CN). A decrease of temperature leads to the interconversion of the apparent C_{2v} symmetric molecule into two conformers with C_2 and C_s symmetry.

In **chapter 4**, possible scenarios for the interconversion of the two diastereomers for **$[L^6Ni_2(X)]^{y+}$** are described (**Scheme 4.6-4.8**). Since two diastereomers are observed in the ^{1}H NMR spectrum of **$[L^6Ni_2S]PF_6$**, the interconversion of the conformers occurs by **Scenario 3**, whereby for **$[L^6Ni_2(OH)](PF_6)_2$** and **$[L^6Ni_2Cl](PF_6)_2$** an interconversion of the C_2 or C_s symmetric complexes are observed by **Scenario 1** or **Scenario 2**. In the ^{1}H NMR spectrum the singlet peaks of the corresponding CH_3 groups H^8 are well separated at 263 K and below, which allows to determine the energetic difference of the ground states of both diastereomers, using a van't Hoff plot (**Figure 5.7** and **Scheme 5.8**). The equilibrium constant K is determined by comparison of the integral values of the separated peaks of H^8 at four different temperatures (263 K to 233 K). The difference of the enthalpy ΔH^o of the two ground states is $-1.1\ kJ\cdot mol^{-1} \pm 3.3\ J\cdot mol^{-1}$.

The exchange rate between the two conformers is determined under consideration of $^1H^1H$ EXSY NMR experiments of the CH_3 resonances (**Figure 5.7** (**b**) for instance) at five different temperatures (273 K to 233 K). Using the program EXSYCALC, k_1 and k_2 values are determined by evaluation of the four integral values of the diagonal peaks in the $^1H^1H$ NOESY NMR spectra at each temperature (**Table 5.4**). The calculated k values allow determining further kinetic parameters under consideration of the Eyring and Arrhenius plot (**Scheme 5.8** and **Figure 5.7**). Alternatively, the k values can also be derived by line shape analysis of the signals of the CH_3 group, using GSD method of the NMR program MESTRENOVA.

Based on the approximated (non-crystallographic) C_s symmetric conformer in the molecular structure in solid state, it is postulated that the thermodynamically favored complex is the C_s symmetric complex. Unfortunately, the experiment failed to dissolve crystals of exclusively C_s symmetric molecules at 243 K in MeCN-d_3 and conducting a ^{1}H NMR spectrum at 233 K to obtain a spectrum dominated by the proton resonances of the C_s symmetric species. No new ratio between the two diastereomers is observed. Reasons for this are the low solubility of the crystals and the fast exchange rate between the two conformers, even at 233 K. These results make a discrimination and final assignment of the two species impossible. Also DFT calculations will not give further insights into the thermodynamic favored conformer, due to the small energetic difference between those conformers, which would be in the error range of the DFT calculations.

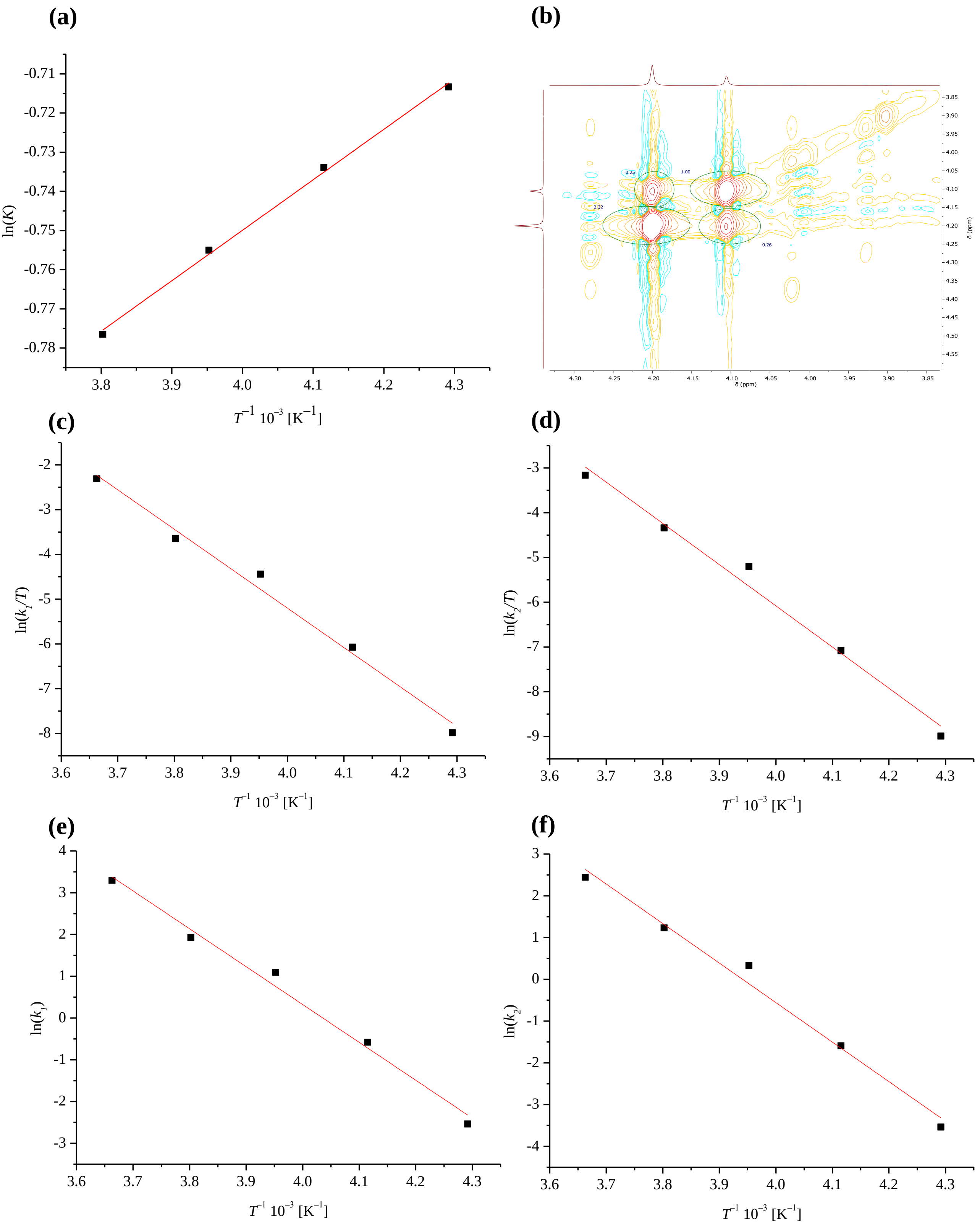

Figure 5.7: (**a**) van’t Hoff plot, (**b**) $^1H^1H$ NOESY NMR spectrum showing the exchange between the two CH_3 groups. (**c**)-(**d**) Eyring plots and (**e**)-(**f**) Arrhenius plots for the interconversion of the *Cs* symmetric and C_2 symmetric conformers in temperature dependency.

Only advanced methods, like generation of a chiral environment by stepwise titration of a chiral complex to $\mathbf{[L^6Ni_2S]PF_6}$ and performing ^{1}H NMR experiments could allow the determination of the thermodynamic stable complex. By use of the obtained parameters derived from the van’t Hoff plot (energy difference of ground states) as well as from Eyring plot (enthalpy of activation and entropy of activation) and Arrhenius plot (activation energy) **Scheme 5.8** is generated, showing all parameters summarized for the interconversion of the two C_2 symmetric enantiomers into the C_s symmetric conformer. The obtained barrier for the interconversion of the diastereomers of $\mathbf{[L^6Ni_2S]PF_6}$ is similar to the obtained barrier for the AB spin exchange in $\mathbf{[L^6Ni_2(OH)](PF_6)_2}$ (**Table 5.8**). The splitting into the AB system in $\mathbf{[L^6Ni_2S]PF_6}$ and the splitting into the two diastereomers occurs at the same temperature. This may indicate that the spin exchange occurs *via* the opposite conformation. The interconversion of the C_s symmetric conformer in its C_s symmetric conformer occurs *via* the C_2 symmetric diastereomer (**Scenario 3**). The barrier for the AB spin exchange in $\mathbf{[L^6Ni_2S]PF_6}$ is equal to the barrier for the interconversion of the two diastereomers. These results for $\mathbf{[L^6Ni_2S]PF_6}$ strongly support that the interconversion of the conformers of $\mathbf{[L^6Ni_2(OH)](PF_6)_2}$ occurs *via* the opposite conformation, which is below the detection limit of the NMR instrument (**Scenario 1**).

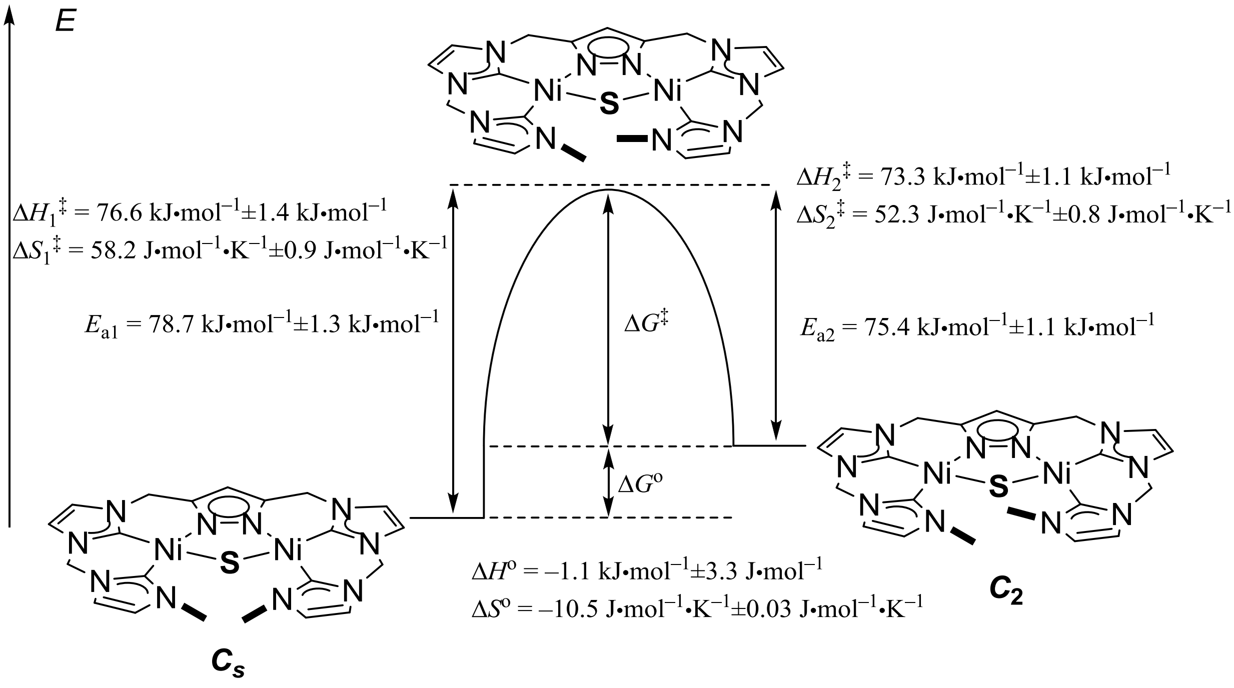

Scheme 5.8: Reaction scheme for the interconversion of the two different C_2 and C_s symmetric conformers of $\mathbf{[L^6Ni_2S]^+}$. Based on the crystal structure the C_s symmetric conformer is tentatively assigned to be the more stable complex.

Table 5.4: Rate constants for the exchange reaction of the two conformers, determined by $^1H^1H$ EXSY NMR spectroscopy.

T [K]	k_1 [s^{-1}]	k_2 [s^{-1}]
233	0.079	0.029
243	0.560	0.203
253	2.977	1.387
263	6.885	3.423
273	27.100	11.517

5.3.4 Redox properties of [L^6Ni_2S]PF_6

In order to get an insight in the redox properties of **[L^6Ni_2S]PF_6** CV experiments are performed. In dependence on the scan direction a different number of redox events are observed. Sweeping first to a negative potential (←) shows one irreversible reduction event at very low potential (0.5 mM, E_p^{red}= –2.76 V *vs.* Fc/Fc^+), which is very close to the reduction of MeCN (–3.0 V, electrolyte: NBu_4PF_6)[207]. Increase of the scan rate leads to a more negative current (inset, **Figure 5.8**). A very broaden wave as oxidative response of the reduction process at approximately –2.76 V appears at around –1.46 V. This wave is not observed, when the potential window in the cathodic area is smaller and does not include the complex reduction. A similar oxidation event in the CV is also observed for **[$L^6Ni_2(OH)$](PF_6)$_2$** and **[L^6Ni_2Cl](PF_6)$_2$**. As already described before (**chapter 4**), the *in situ* UV-vis spectra of **[$L^6Ni_2(OH)$](PF_6)$_2$** and **[L^6Ni_2Cl](PF_6)$_2$** during bulk electrolysis (–25 °C and –40 °C) do not show the direct transformation of the starting complexes to the reduced species. No further investigations are considered, based on these previous results and due to the small ΔE^{red} of the complex and the solvent.

The reduction process of **[L^6Ni_2S]PF_6** is proposed to occur at one nickel atom as in **[$L^6Ni_2(OH)$](PF_6)$_2$** and **[L^6Ni_2Cl](PF_6)$_2$** with *in situ* formation of a Ni^INi^{II} species. Calculations based on the proposed nickel(I)/nickel(II) mixed valent sulfido complex confirm that the unpaired electron is mostly located on one nickel (Mulliken spin population 55%). In comparison to the calculations of the mixed valent Ni^INi^{II} μ-hydroxido and μ-chlorido NHC complexes, the unpaired electron is mainly located on one nickel center and not distributed over both metal centers. This situation gives the opportunity to have a look at the bonds in the calculated mixed valent complex structure. The calculated molecular structure of this mixed valent complex shows an elongation of the Ni^I–S (2.24 Å) bond in comparison to the Ni^{II}–S bond (2.20 Å) (**Figure 5.9**). Previously in this work, the bond lengths of the molecular structure in solid state of **[L^6Ni_2S]PF_6** are described. The bond lengths differed significantly, with shortened Ni(1)–S(1) bonds (2.15 Å) and a longer bond of Ni(2)–S(1) (2.22 Å) in **[L^6Ni_2S]PF_6**. Also bond elongation of the Ni–N^{pyr}, and Ni–$C^{Carbene}$ *trans* to the μ-S are observed in comparison to the $Ni^{II}Ni^{II}$ NHC complex.

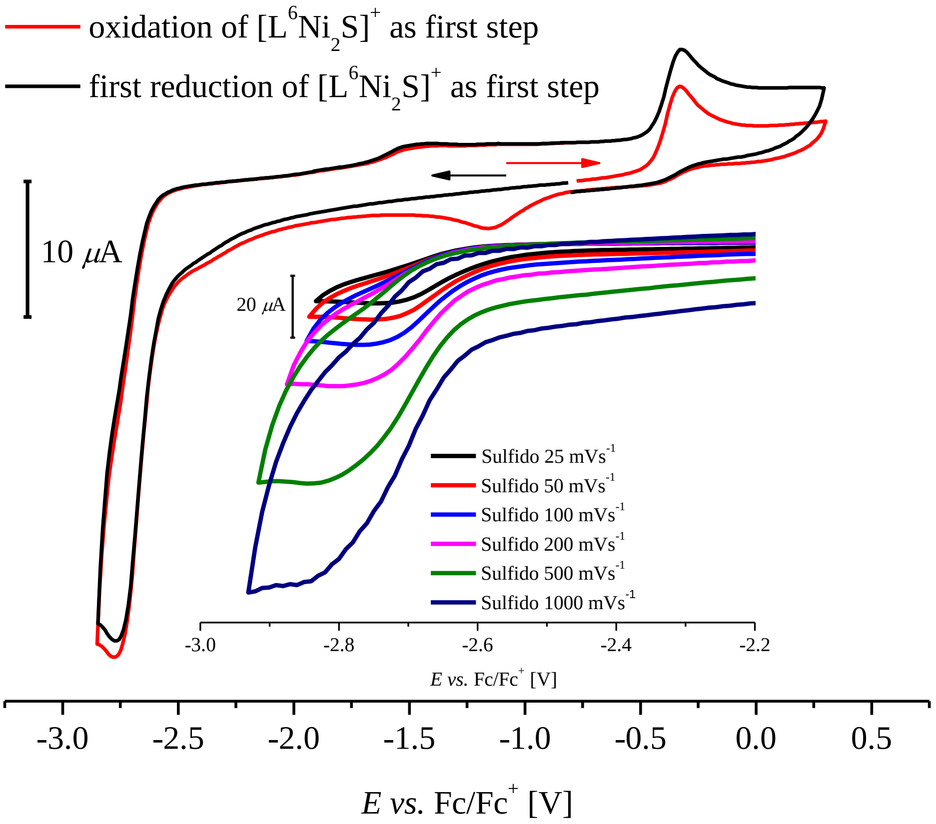

Figure 5.8: CV of **[L^6Ni_2S]PF_6** (0.5 mM, 0.1 M NBu_4PF_6 in MeCN, 100 mV·s^{-1}). Inset showed the reduction process at E_p^{red}= –2.76 V *vs.* Fc/Fc$^+$ at different scan rates (25 mV·s^{-1} to1000 mV·s^{-1}).

By sweeping to an anodic potential first (→), one oxidative event at a peak potential of E_p^{ox} = –0.33 V is observed. As a consequence of this oxidation process a new wave at –1.16 V is obtained. The large peak separation points towards an *EC* mechanism in which the oxidized **[L^6Ni_2S]PF_6** rapidly reacts to a new species that is then reduced at much more negative potential. This new species is later identified as a tetranickel persulfido complex (see **chapter 7** and **chapter 8**). A detailed study concerning this redox event, the analytic investigation of the *in situ* formed thiyl radical complex and the analytic and structural evidence of the formation of the first persulfido-bridged tetranickel complex is presented in **chapter 7** and **8**.

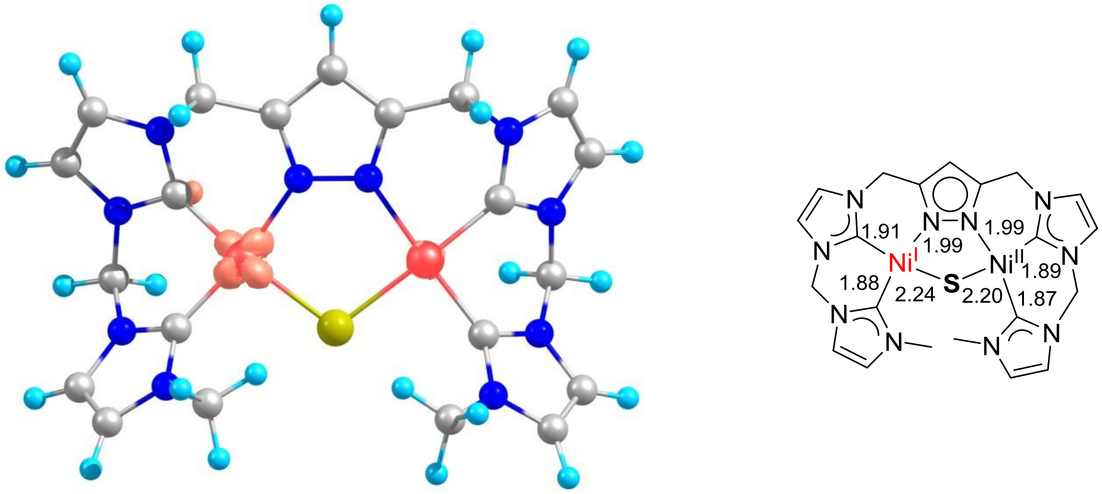

Figure 5.9: Left: Calculated molecular structure of **[L^{6}Ni$_2$S]** showing the spin density. Starting point of the single point calculations is the crystallographic structure of **[L^{6}Ni$_2$S]**$^+$. The unpaired electron is mostly located on one nickel atom (Mulliken spin population 55%). **Right:** Selected bond lengths of the calculated mixed valent complex.

5.3.5 Reactivity of [L^{6}Ni$_2$S]PF$_6$ towards small molecules and acids

In the previous section the intrinsic properties of **[L^{6}Ni$_2$S]PF$_6$** are presented. As already mentioned, metal sulfido complexes are interesting due to their existence in enzymes, their applications in catalytic processes and their ability to activate small molecules. With respect to this reactivity of literature known complexes, the reactivity of **[L^{6}Ni$_2$S]PF$_6$** towards some molecules and the behavior towards protons is investigated. **Scheme 5.9** summarizes the obtained results. Further information concerning the reactivity of **[L^{6}Ni$_2$S]PF$_6$** with NOBF$_4$, NO and acids will be given in **chapters 8** and **9**.

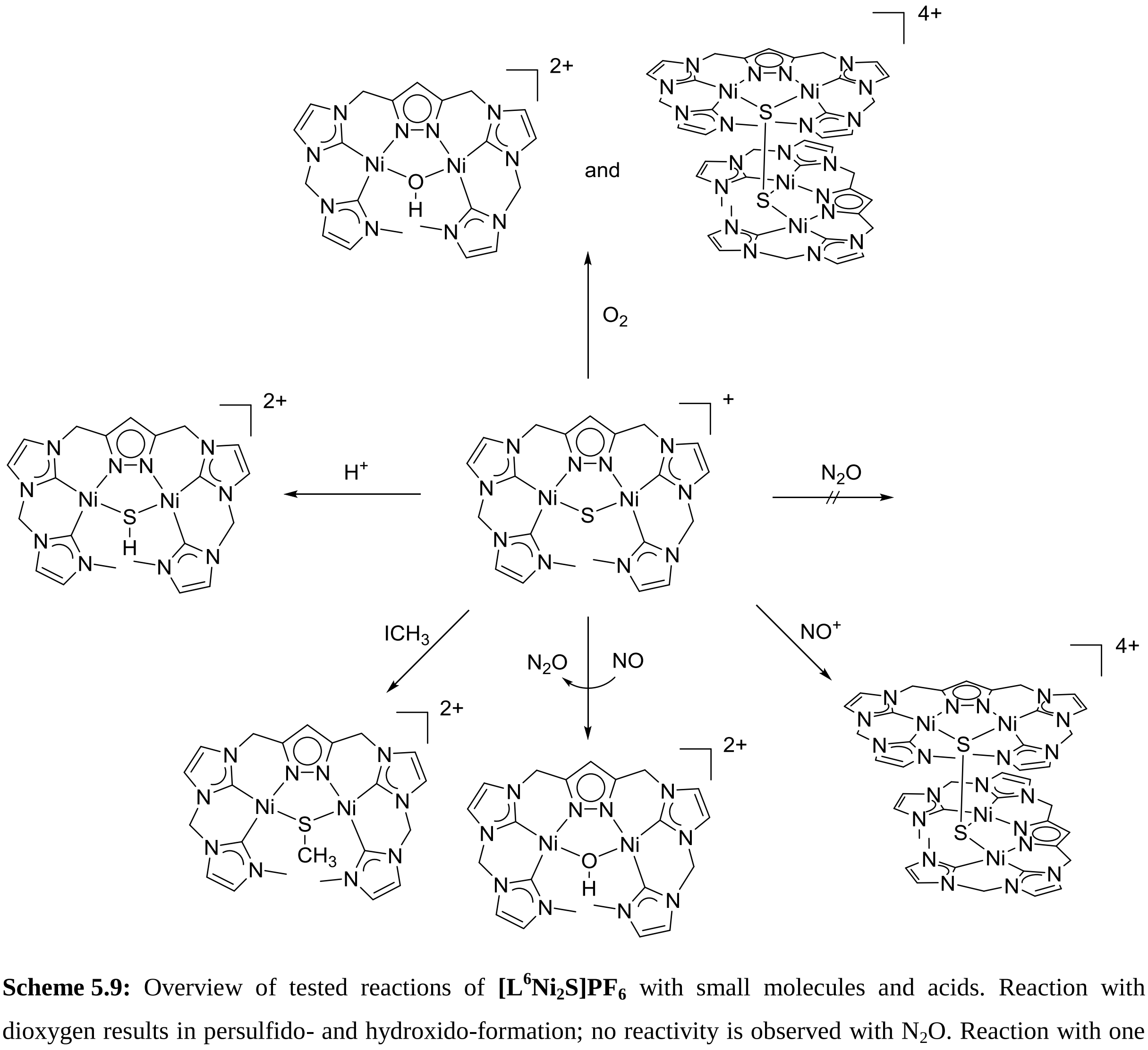

Scheme 5.9: Overview of tested reactions of **[L^{6}Ni$_2$S]PF$_6$** with small molecules and acids. Reaction with dioxygen results in persulfido- and hydroxido-formation; no reactivity is observed with N$_2$O. Reaction with one equivalent of NO$^+$ results in formation of **[(L^6)$_2$Ni$_4$(S$_2$)](PF$_6$)$_4$** and reaction of **[L^{6}Ni$_2$S]PF$_6$** with NO at 233 K leads to **[L^{6}Ni$_2$(OH)](PF$_6$)$_2$** and N$_2$O; alkylation of **[L^{6}Ni$_2$S]PF$_6$** leads to the μ-SCH$_3$ complex and protonation of **[L^{6}Ni$_2$S]PF$_6$** to the corresponding SH-bridged complex.

5.3.5.1 Reactivity of [L^6Ni_2S]PF_6 with dioxygen

When **[L^6Ni_2S]PF_6** dissolved in a MeCN-d_3 solution is exposed to dry dioxygen gas an immediate color change from red to yellow is observed. ^{1}H NMR spectroscopy confirmed the reaction of **[L^6Ni_2S]PF_6** to **[$L^6Ni_2(OH)$](PF_6)$_2$** and to the tetranickel(II) persulfido complex **[(L^6)$_2Ni_4(S_2)$](PF_6)$_4$** in a 1.34:1 ratio (**Figure 5.10**). Further information about **[(L^6)$_2Ni_4(S_2)$](PF_6)$_4$**, its properties and reactivity are reported in **Chapter 8**. The redox properties of dioxygen makes a mechanistic analysis complicated. The oxidation potential of **[L^6Ni_2S]PF_6** is $E_{1/2} = –0.255$ V, based on CV simulations (see **chapter 7**) and low compared to the redox potential of O_2. The one electron oxidation of **[L^6Ni_2S]PF_6** to an intermediate thiyl radical is possible and results in the formation of the dimerized persulfido complex **[(L^6)$_2Ni_4(S_2)$](PF_6)$_4$**.

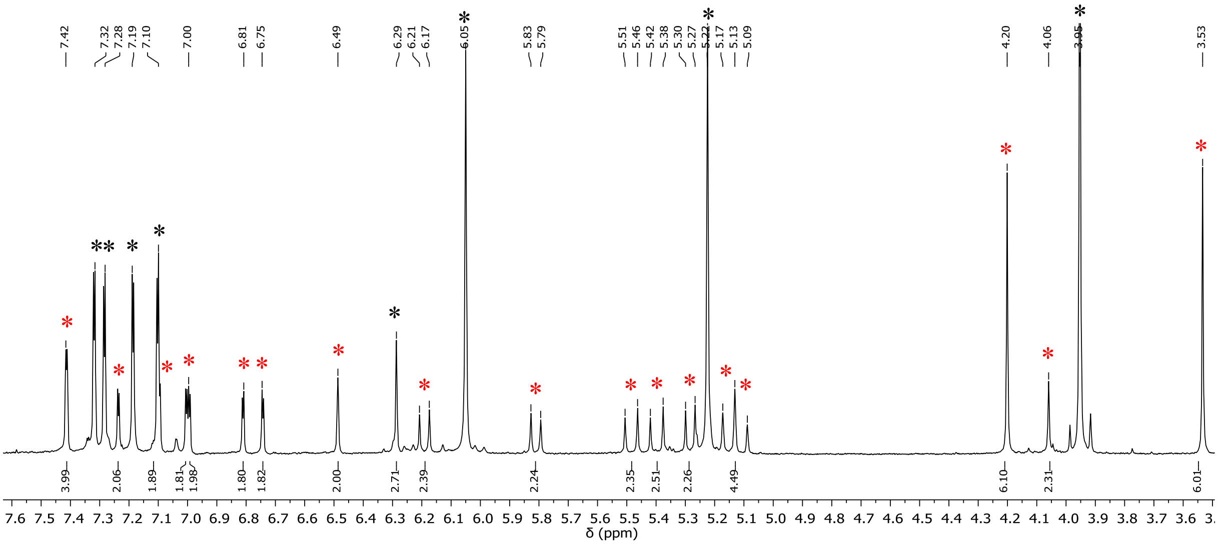

Figure 5.10: ^{1}H NMR spectrum of the reaction product after reaction of **[L^6Ni_2S]PF_6** with O_2 at 298 K (400 MHz) in MeCN-d_3. Proton resonances of the persulfido complex (**chapter 8**) are labeled with * and proton resonances of **[$L^6Ni_2(OH)$](PF_6)$_2$** are labeled with *.

The dimerization reaction is fast, according to CV experiments (**chapter 7**). These findings are in agreement with disulfide formation in protein and structural regeneration of coiled polypeptide chains by dioxygen in the presence of a transition metal.[192,202] It is quite challenging to investigate if the nickel ion is involved in the reaction of **[L^6Ni_2S]PF_6** with dioxygen, in line with the already described disulfide formation by copper containing enzymes. No evidence for a S-oxygenated complex are found. The formation of **[$L^6Ni_2(OH)$](PF_6)$_2$** seems to be the result from a further reactivity of **[(L^6)$_2Ni_4(S_2)$](PF_6)$_4$** or **[L^6Ni_2S]PF_6** with O_2. The origin of the hydroxido bridge is further explored by ESI-MS analysis. **[L^6Ni_2S]PF_6** in MeCN reacts with $^{18}O_2$ and the resulting product is analyzed by mass spectrometry. Mass peaks at *m/z* = 695 for **[(L^6)Ni_2(^{18}OH)PF_6]$^+$** and *m/z* = 274 for **[(L^6)Ni_2(^{18}OH)]$^{2+}$** confirm the incorporation of labeled oxygen originated from O_2. The source of the proton is unknown, but as already described in **chapter 4**, a potential *in situ* generated **[L^6Ni_2O]$^+$** is strongly basic and takes a proton from solvent molecules or from the wall of glass ware. Reaction attempts at 234 K also result in formation of the same reaction mixture.

5.3.5.2 Stability of [L^6Ni_2S]PF_6 towards N_2O

Hayton *et al.*[167] described the reactivity of a “masked (nacnac)Ni^{II}=S” complex **XVII** with nitrous oxide to the first thiohyponitrite complex (**Scheme 5.2**). Since N_2O is also a mild oxygen transfer agent, the reactivity of nitrous oxide with **[L^6Ni_2S]PF_6** is tested, but no reactivity is observed. ^1H NMR experiments in MeCN-d_3 only show the starting complex, and variation of temperature from 249 K to 318 K does not affect the reactivity.

5.3.5.3 Reactivity of [L^6Ni_2S]PF_6 with $NOBF_4$ and NO gas

Reaction of **[L^6Ni_2S]PF_6** with one equivalent of $NOBF_4$ (E^o = 0.87 V in MeCN)[208] leads to one electron oxidation of **[L^6Ni_2S]PF_6** and dimerization of the formed thiyl radical complex to the persulfido-bridged tetranickel(II) complex (see **chapter 7** for thiyl radical complex and **chapter 8** for NO reactivity). **[$L^6Ni_2(OH)$](PF_6)$_2$** and N_2O are immediately formed from **[L^6Ni_2S]PF_6** and NO at 233 K. A detailed description of these reactions and their analysis can be found in **chapter 8**.

5.3.5.4 Alkylation of [L^6Ni_2S]PF_6

Alkylation of **[L^6Ni_2S]PF_6** with methyl iodide in MeCN leads to an insoluble **[$L^6Ni_2(SCH_3)$](PF_6)I** complex, which can be re-dissolved in MeCN after counter ion exchange, using $AgPF_6$ (**Scheme 5.10** and experimental section). Brownish single crystals are obtained by diffusion of Et_2O into a **[$L^6Ni_2(SCH_3)$](PF_6)$_2$** complex solution in MeCN. The complex crystallizes in the space group $P2_1/c$. Again a complex in a saddle shaped conformation is observed in the molecular structure in solid state, bearing now a SCH_3 bridge between the two nickel(II) centers. The Ni(1) ion is 0.033 Å out of the C(9)–C(5)–N(1)–S(1) plane and Ni(2) is 0.0269 Å out of the S(1)–N(2)–C(14)–C(18) plane. The angle between these two planes is 31.88°. This acute angle is almost double than in **[L^{6}Ni$_2$S]PF$_6$** (17.21°) but in the same range as the angle in **[L^{6}Ni$_2$Cl](PF$_6$)$_2$**. The Ni(1)····Ni(2) distance is 3.45 Å.

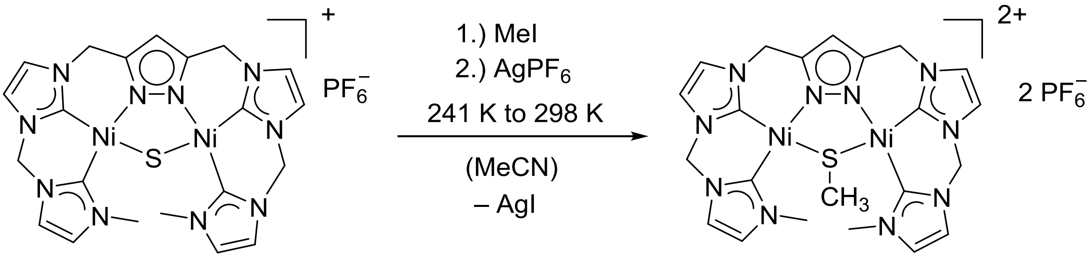

Scheme 5.10: Alkylation reaction of **[L^{6}Ni$_2$S]PF$_6$** to [L^6**Ni$_2$(SCH$_3$)](PF$_6$)$_2$**.

The nickel carbene bonds are in the range between 1.86-1.88 Å (**Table 5.5**). The bond lengths in this complex are different compared to **[L^{6}Ni$_2$S]PF$_6$** in the molecular structure in solid state (**Scheme 5.6**). The Ni–C$^{\text{carbene}}$ bond lengths are all in the same range. The Ni–S bonding situation (2.20 Å) is for both nickel ions almost the same and in the range of the literature known Ni$_2$ μ-SCH$_3$ complexes (2.18-2.22 Å).[209] Alkylation of the sulfur ion results in an elongation of the Ni–S bonds compared to **[L^{6}Ni$_2$S]PF$_6$** (average bond lengths in Ni μ-S: 2.18 Å).

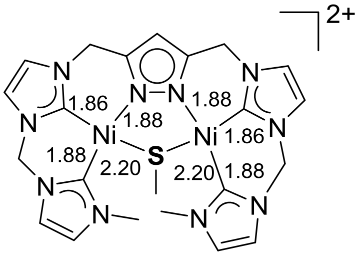

Scheme 5.11: Selected bond lengths [Å] in **[L^{6}Ni$_2$(SCH$_3$)]$^{2+}$**.

In the molecular structure in solid state (**Figure 5.11**), the two methyl groups are orientated both away from the dinickel-pyrazolate plane. The distance between the two CH$_3$ groups is 5.46 Å and distances between CH$_3$ groups and S(1) are 3.39 Å and 3.33 Å. The sulfur ion is surrounded by two nickel ions and the CH$_3$ group. The sulfur ion is located 0.78 Å out of the Ni(1)–Ni(2)–C(22) plane and forms the top of a trigonal pyramid. The corresponding angles around the sulfur are 106.5° Ni(1)–S(1)–C(22), 103.0° Ni(1)–S(1)–Ni(2) and 109.6° for C(22)–S(1)–Ni(2).

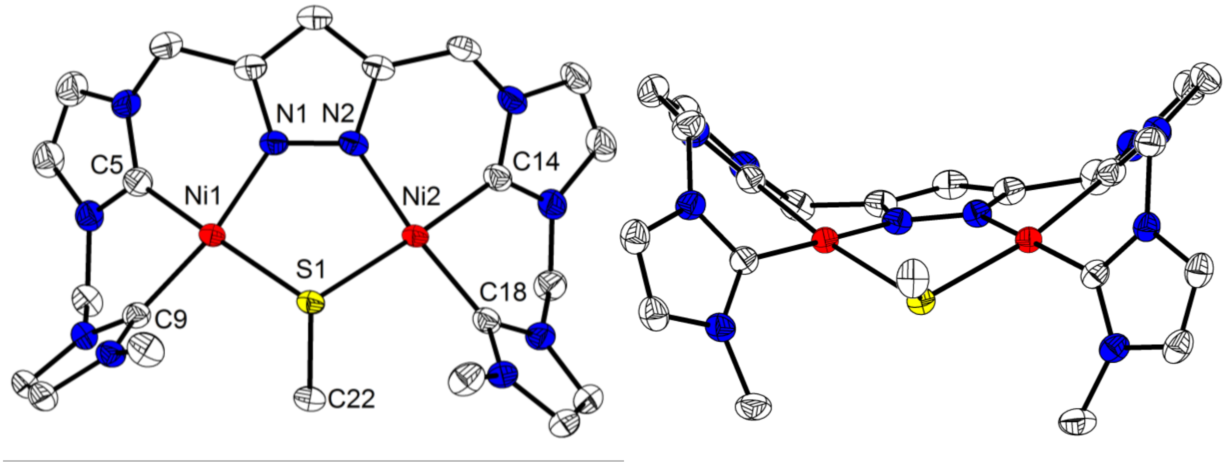

Figure 5.11: Molecular structure (50% probability thermal ellipsoids) of the cationic part of **[$L^6Ni_2(SCH_3)$](PF_6)$_2$**. H atoms are omitted for clarity.

Table 5.5: Selected bond lengths [Å] for **[$L^6Ni_2(SCH_3)$](PF_6)$_2$**.

Atoms	Bond lengths
Ni1····Ni2	3.450(9)
Ni1–C5	1.862(3)
Ni2–C14	1.865(3)
Ni2–C18	1.880(3)
Ni1–C9	1.879(3)
Ni1–N1	1.884(2)
Ni2–N2	1.889(2)
Ni1–S1	2.205(2)
Ni2–S1	2.205(4)

Table 5.6: Selected bond angles [°] for **[$L^6Ni_2(SCH_3)$](PF_6)$_2$**.

Atoms	Bond angles
C5–Ni1–C9	86.8(5)
C5–Ni1–N1	88.2(8)
C9–Ni1–S1	95.9(0)
N1–Ni1–S1	90.5(8)
C14–Ni2–C18	86.5(4)
C14–Ni2–N2	88.3(2)
C18–Ni2–S1	96.6(9)
N2–Ni2–S1	88.8(4)
C22–S1–Ni2	109.(5)
Ni1–S1–Ni2	102.(9)

5.4 Characterization of [$L^6Ni_2(SCH_3)$](PF_6)$_2$: dynamics in solution and redox properties

5.4.1 Dynamics of [$L^6Ni_2(SCH_3)$](PF_6)$_2$ in solution

In the ^{1}H NMR spectrum of **[$L^6Ni_2(SCH_3)$](PF_6)$_2$**, a diasterotopic splitting of the proton resonances H^6 and H^7 of the CH_2 groups is observed at 298 K in MeCN-d_3 (**Figure 5.12 (a)**). A reason for this observation can be the different orientation of the SCH_3 group compared to the CH_3 groups of the ligand, which leads to an AB spin system of the corresponding peaks in the spectrum (**Figure 5.12 (b)**). In addition, a spin exchange in the AB systems between the two protons is observable (roof top effect), which leads to a broadening and signal decrease of the outer peaks of the doublets. The chemical shift of the proton resonances H^5 is 6.32 ppm and the signal is 0.23 ppm down-field shifted, compared to the H^{pz} proton resonance of **[L^6Ni_2S]PF_6** due to reduced donor ability of the thiolato bridge compared to the sulfido bridge (**Figure A.5.1**, **appendix**). The proton resonance of the SCH_3 group is assigned to a peak at 1.57 ppm. In the ^{1}H^{1}H NOESY NMR spectrum a NOE effect between the proton resonances of the CH_3 groups H^8 from the ligand and SCH_3 is observable (**Figure 5.12** (**c**)). Based on 2D NMR measurements all peaks in the ^{1}H and ^{13}C{^{1}H} NMR spectra are assigned.
The dynamic behavior of **[$L^6Ni_2(SCH_3)$](PF_6)$_2$** is further explored by VT ^{1}H NMR measurements, which show a T_c of the CH_2 groups H^6 at 323 K and a T_c of the CH_2 groups H^7 between 303 K and 313 K. An increase of the temperature leads to an apparent C_{2v} symmetry of the molecules in the ^{1}H NMR spectrum. A decrease of the temperature just affects the line width of the doublets of the CH_2 groups and a sharpening of the peaks is observed. No further conformer of **[$L^6Ni_2(SCH_3)$](PF_6)$_2$** is observed in contrast to **[L^6Ni_2S]PF_6**. In analogy to considerations of the dynamic behavior of **[$L^6Ni_2(OH)$](PF_6)$_2$** and **[L^6Ni_2Cl](PF_6)$_2$** the interconversion according **Scenario 1** (**Scheme 4.6**, **chapter 4**) is assumed, wherein the high energetic C_2 symmetric conformers are not observed in the ^{1}H NMR time scale, due to fast interconversion and low population of this enantiomers. The exchange kinetic for the interconversion of the C_s symmetric conformers is determined by line shape analysis of the proton resonances H^6 of the CH_2 groups. Using the simulation program WinDNMR, k values for these interconversions are obtained between 298 K and 253 K (υ_0 at 253 K). k values are derived by use of a calibration curve (experimental section **10.2.2.1**) and are summarized in **Table 5.7**.

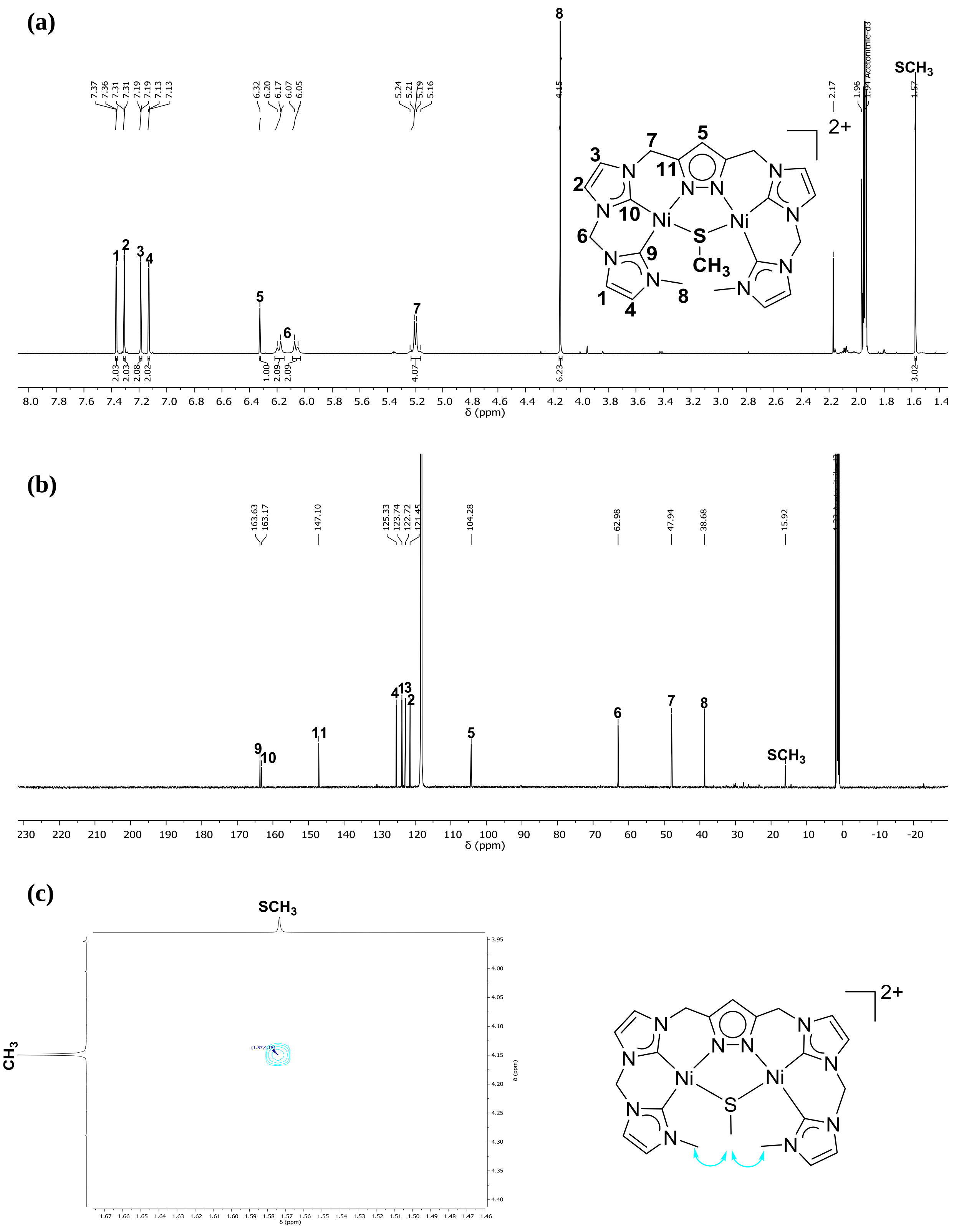

Figure 5.12: (**a**) ^{1}H NMR spectrum of **$[L^6Ni_2(SCH_3)](PF_6)_2$** in MeCN-d_3 at 400 MHz and 298 K. A diastereotopic splitting of the proton resonances H^6 and H^7 of the CH_2 groups is observed. (**b**) $^{13}C\{^1H\}$ NMR spectrum at 298 K and 126 MHz. (**c**) $^1H^1H$ NOESY NMR spectrum of **$[L^6Ni_2(SCH_3)](PF_6)_2$** at 500 MHz and 298 K, shows the through space correlation of the proton resonances between the CH_3 groups H^8 and the SCH_3 group and confirm the SCH_3 bridge between the two nickel ions in solution.

An activation enthalpy $\Delta H^{\ddagger} = 59.57\ \mathrm{kJ{\cdot}mol^{-1}} \pm 1.2\ \mathrm{kJ{\cdot}mol^{-1}}$ and an activation entropy $\Delta S^{\ddagger} = -24.62\ \mathrm{J{\cdot}mol^{-1}{\cdot}K^{-1}} \pm 0.5\ \mathrm{J{\cdot}mol^{-1}{\cdot}K^{-1}}$ as well as an activation barrier of $E_a = 62.02\ \mathrm{kJ{\cdot}mol^{-1}} \pm 1.2\ \mathrm{kJ{\cdot}mol^{-1}}$ are calculated. The negative entropy observed in **[$L^6Ni_2(SCH_3)](PF_6)_2$** is in contrast to the positive entropy of **[$L^6Ni_2(OH)](PF_6)_2$** and supports the hydrogen bond interaction of **[$L^6Ni_2(OH)]^{2+}$** with solvent molecules A comparison of the $\Delta G^{\ddagger}$ values at 293 K between **[$L^6Ni_2(SCH_3)](PF_6)_2$** ($\Delta G^{\ddagger}_{293K} = 66.78\ \mathrm{kJ{\cdot}mol^{-1}} \pm 1.5\ \mathrm{kJ{\cdot}mol^{-1}{\cdot}K^{-1}}$), **[$L^6Ni_2S]PF_6$** ($\Delta G^{\ddagger}_{293K} = 59.55\ \mathrm{kJ{\cdot}mol^{-1}} \pm 1.1\ \mathrm{kJ{\cdot}mol^{-1}}$) and **[$L^6Ni_2(OH)](PF_6)_2$** ($\Delta G^{\ddagger}_{293K} = 51.18\ \mathrm{kJ{\cdot}mol^{-1}} \pm 0.24\ \mathrm{kJ{\cdot}mol^{-1}}$) shows a higher energy barrier for **[$L^6Ni_2(SCH_3)](PF_6)_2$**. These findings are in agreement with the corresponding VT ^1H NMR spectra. An interconversion of the C_s symmetric conformers of **[$L^6Ni_2(SCH_3)](PF_6)_2$** occurs at a significantly higher temperature than it is observed for **[$L^6Ni_2(OH)](PF_6)_2$**. **Table 5.8** summarizes all activation parameters for the three complexes

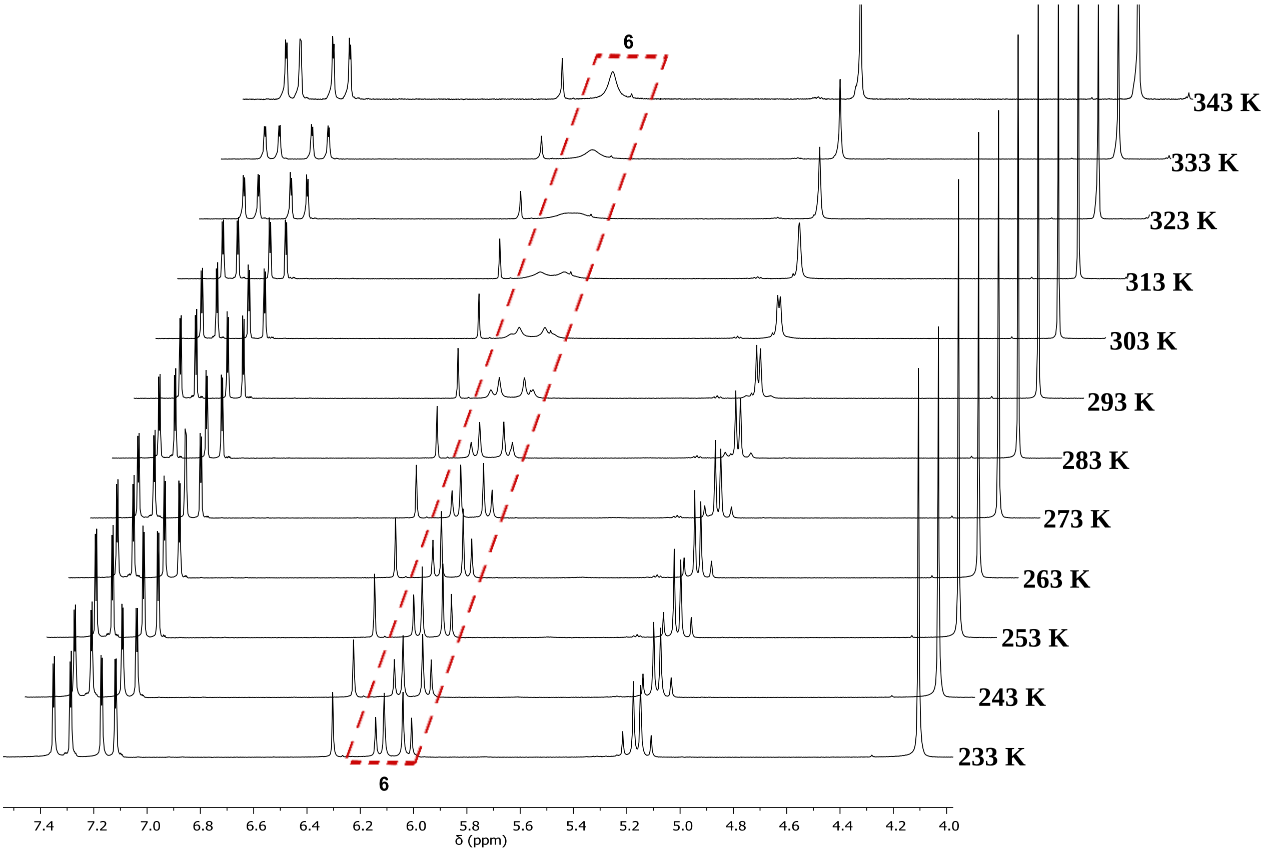

Figure 7.13: ^1H NMR spectra of **[$L^6Ni_2(SCH_3)](PF_6)_2$** in the range between 343 K and 233 K in MeCN-d_3 (400 MHz). The labeling highlights the diastereotopic splitting of the proton resonances H^6 of the CH_2 groups (- - - -).

The C_s symmetric conformer of **[$L^6Ni_2(SCH_3)](PF_6)_2$** is assumed to be the thermodynamic more stable complex compared to the C_2 symmetric enantiomers, since the preferred pyramidal geometry of the sulfur atom in the complex forces the linked CH_3 group of SCH_3 in a direction away from the ligand plane, which prefers the C_s symmetric conformation of the molecule according to the solid state structure.

Table 5.7: Rate constants at different temperatures derived by line shape analysis of the ^{1}H NMR proton resonances of the CH_2 groups H^6 and by the simulation program WinDNMR.

T [K]	k [s^{-1}]
343.2	215.831
333.2	122.207
323.2	93.132
313.2	61.365
293.2	10.216
283.2	3,876
273.2	1,306
263.2	0.223
253.2	0.146

Figure 5.14: Comparison of experimental and simulated ^{1}H NMR spectra of the proton resonances H^6 of the CH_2 group of **$[L^6Ni_2(SCH_3)](PF_6)_2$**.

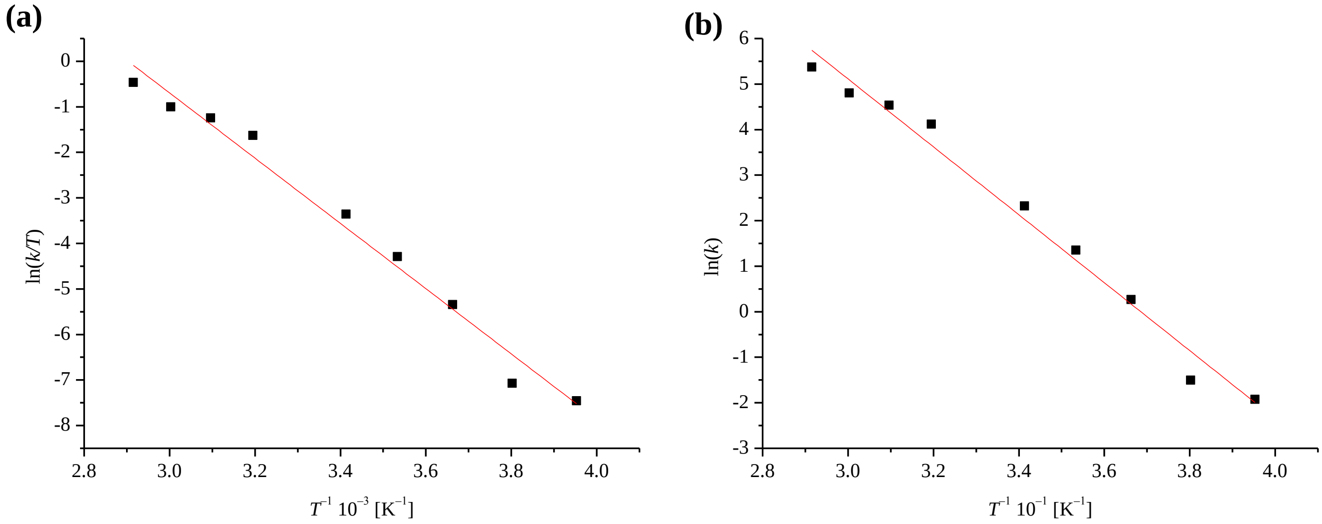

Figure 5.15: **(a)** Eyring plot ($R^2 = 0.9796$) and **(b)** Arrhenius plot ($R^2 = 0.9815$) of the conformer interconversions of **$[L^6Ni_2(SCH_3)](PF_6)_2$**.

Table 5.8: Comparison of activation parameters for the conformer interconversions in **$[L^6Ni_2(OH)](PF_6)_2$**, **$[L^6Ni_2S]PF_6$** and **$[L^6Ni_2(SCH_3)](PF_6)_2$**.

	$[L^6Ni_2(OH)](PF_6)_2$	**$[L^6Ni_2S]PF_6$**	**$[L^6Ni_2(SCH_3)](PF_6)_2$**
$\Delta H^‡$ [kJ/mol]	74.4±0.35	76.6±1.4	59.7±1.2
$\Delta S^‡$ [J/molK]	79.2±0.37	58.2±0.9	–24.6±0.5
$\Delta G^‡_{293}$ [kJ/mol]	51.2±0.24	59.6±1.1	66.8±1.5

5.4.2 ESI-MS and UV-vis spectroscopy of [L^{6}Ni$_2$(SCH$_3$)](PF$_6$)$_2$

[L^{6}Ni$_2$(SCH$_3$)](PF$_6$)$_2$ can be characterized by ESI-MS and UV-vis spectroscopy to give further insights. Two dominant peaks of **[L^{6}Ni$_2$(SCH$_3$)](PF$_6$)$_2$** are observed in the ESI-MS at *m/z* = 723 (100) **[L^{6}Ni$_2$(SCH$_3$)PF$_6$]$^+$** and *m/z* = 289 (25) **[L^{6}Ni$_2$(SCH$_3$)]$^{2+}$** (**Figure 5.16 (a)**) which further supports the composition of the complex in solution. The UV-vis spectrum of **[L^{6}Ni$_2$(SCH$_3$)](PF$_6$)$_2$** in MeCN shows four bands (225 nm, 266 nm, 308 nm and 375 nm) (**Figure 5.16** (**b**)). The bands around 225 nm and 308 nm are transitions of the ligand scaffold. These bands change only slightly depending on changes of the bridge between the two nickel centers. A general trend of these bands in dependence on the coordinated anion is given in **Figure A.5.1**. In contrast to this, the bands at 266 nm and 375 nm are assigned to the transition states between the nickel centers with the thiolato bridge (complicated LMCT bands, see below). The band around 400 nm shifts with the incorporated ion and has a local maximum at 375 nm in the thiolato-bridged complex. Surprisingly, an intense band at 266 nm is observed.

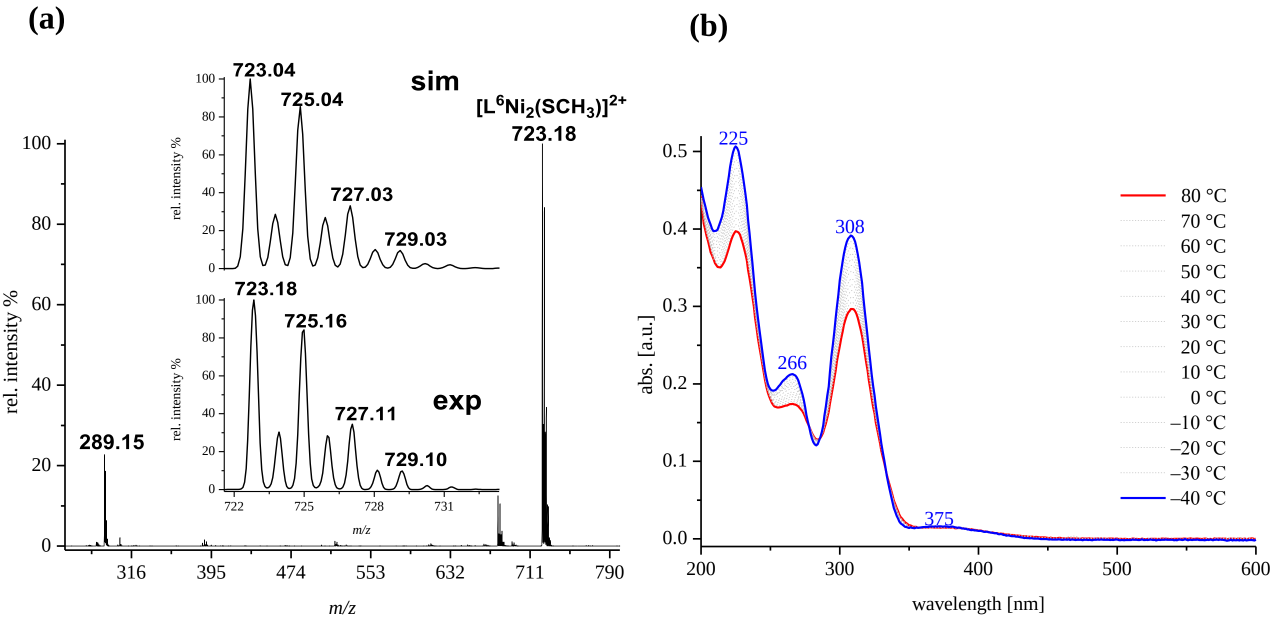

Figure 5.16: (a) ESI-MS in MeCN of **[L^{6}Ni$_2$(SCH$_3$)](PF$_6$)$_2$**. The inset shows the simulated (**top**) and experimental (**bottom**) distribution pattern at *m/z* = 723 (100) for **[L^{6}Ni$_2$(SCH$_3$)PF$_6$]$^+$**. **(b)** UV-vis spectra of **[L^{6}Ni$_2$(SCH$_3$)](PF$_6$)$_2$** in MeCN in the temperature range between +80 °C and –40 °C, showing an increase of all bands.

The increase of temperature to 80 °C leads to a decrease of all bands, while the decrease of temperature results in an increase of the bands at 225 nm, 266 nm and 308 nm, whereby the band at 375 nm is only minimally affected by the temperature. By decreasing the temperature from 80 °C to –40 °C one isosbestic point at 286 nm is assigned. These observations are based on physical phenomena.

Solomon *et al.*[210] calculated the transitions in UV-vis spectra of metal thiolato complexes, assigning the region of the observed bands in the UV-vis spectra to LMCT processes. As already mentioned, the accurate assignment of transitions *via* TD-DFT calculations for **$[L^6Ni_2S]PF_6$** and the herein presented complexes is not so simple due to the admixture of orbitals. In contrast to Solomon's results, which show LMCT transition from well-defined orbitals of the ligands and the metals, TD-DFT calculations of **$[L^6Ni_2(SCH_3)]^{2+}$** show a much more complicated situation. In **$[L^6Ni_2(SCH_3)]^{2+}$** transitions are observed from a nickel-SCH_3 mixed orbital ground state to orbitals of the ligand (**Figure 5.17 (b)**) or to the $Ni(d_{x^2-y^2})$ orbital (**Figure 5.17 (c)**). The band at 375 nm is assigned to a transition from a dinickel-SCH_3 mixed-orbital 149a (59% Ni d character and 21% $S(p_z)$; 30% S(p)) to the orbitals of the ligand (Orbital 151a). The theoretical calculations confirm that the bridge has a central influence on the transition of the bands around 400 nm, here to the excited state of the ligand. A further distinct transition from a dinickel-SCH_3 mixed orbital ground state is observed, here from orbital 140a (Ni d character: 64% and $S(p_x)$: 27%) to the d orbitals of the dinickel atoms (orbital 150a, Ni d character: 49%) is observed for the band at 266 nm.

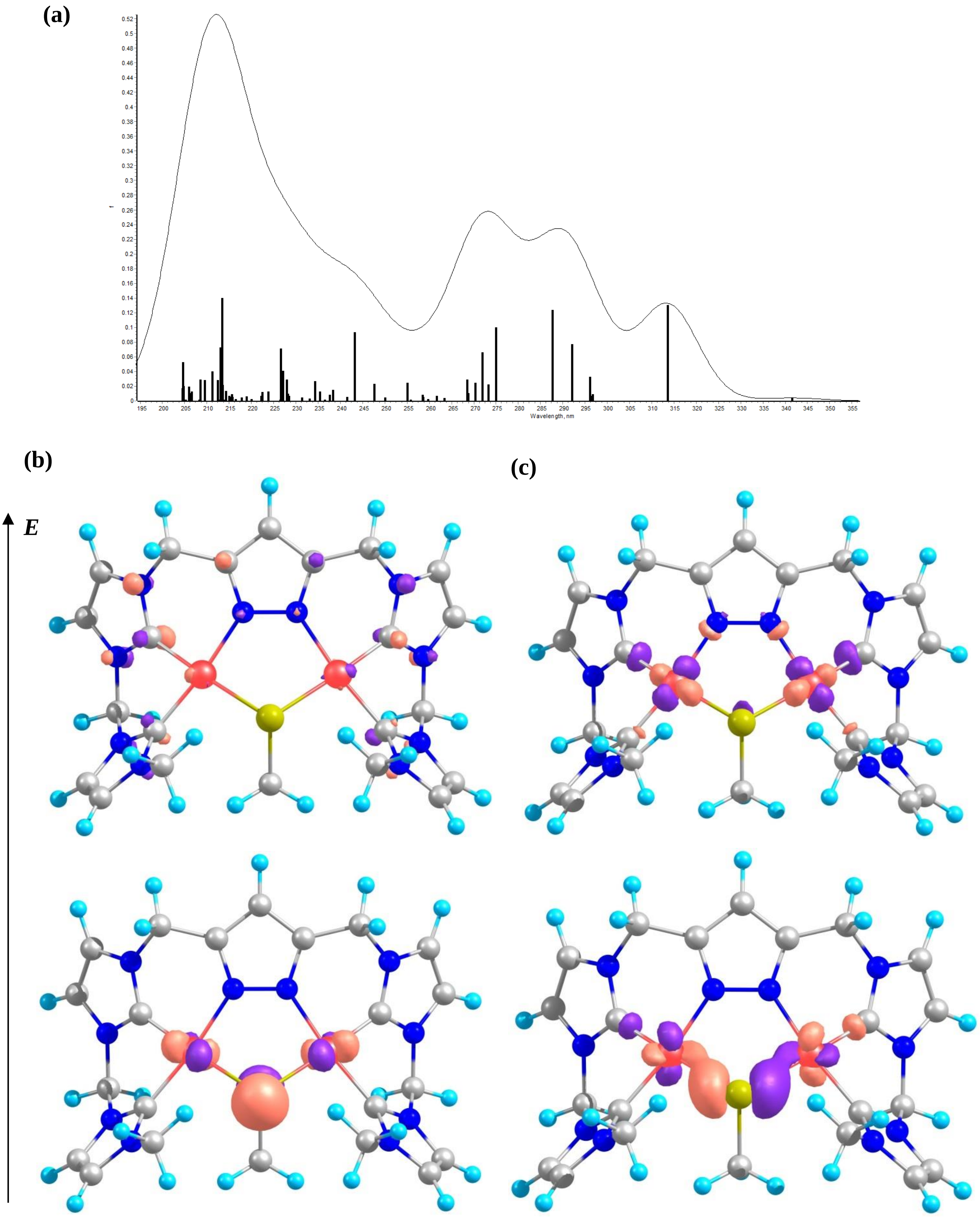

Figure 5.17: (**a**) TD-DFT UV-vis spectrum of [**L^{6}Ni$_2$(SCH$_3$)**]$^{2+}$. According to the bands in the experimental determined UV-vis spectra, a dinickel-SCH$_3$ to ligand CT band (**b**) at 375 nm is observed and identified as the excitation from Orbital 149a, (Ni d: 59%;and S(p$_z$): 21%, S(p) 30%) to the ligand Orbital 150a. Furthermore a dinickel-SCH$_3$ to dinickel CT band (**c**) is observed at approximately 266 nm from Orbital 140a (Ni d: 64%;and S(p$_x$): 27%) % to 151a Ni d (49%).

5.4.3 A mixed valent [$L^6Ni^INi^{II}(SCH_3)]^+$ complex

5.4.3.1 CV of [$L^6Ni^{II}Ni^{II}(SCH_3)](PF_6)_2$

In the potential window of the CV no chemical response of **[$L^6Ni_2(SCH_3)](PF_6)_2$** is observed by sweeping to an anodic potential up to 2.0 V *vs.* Fc/Fc^+, first. The CV of the complex shows two reductive processes, by scanning the cathodic potential. The first wave describes a reversible reduction event (**Figure 5.19**), whereby the second wave is irreversible (**Figure 5.18**). An increase of the scan rate does not show any reversibility for the second reduction event around E_p^{red} = –2.46 V (**Figure 5.18**, **inset**). The first wave is assigned to a $Ni^INi^{II}/Ni^{II}Ni^{II}$ redox process and the second wave at E_p^{red} = –2.46 V to the reduction of the mixed valent Ni^INi^{II} complex to an *in situ* generated Ni^INi^I complex. The postulated Ni^INi^I complex undergoes a further reaction which leads to a shift of the wave of the responding oxidation process (**Figure 5.18**). The peak separation between the first reduction and the first oxidation is ΔE = 236 mV and two further oxidation events at –1.36 V and –1.17 V *vs.* Fc/Fc^+ are observed.

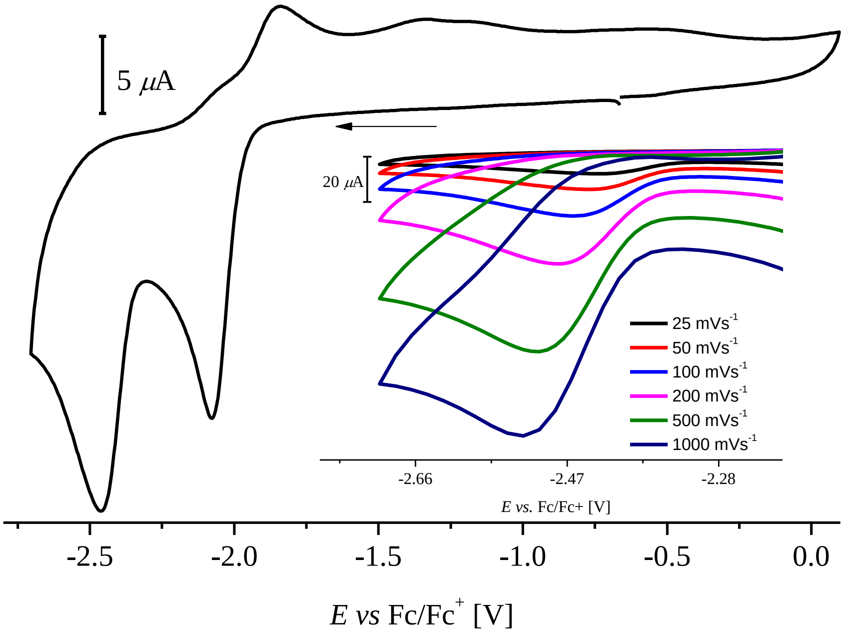

Figure 5.18: CV of **[$L^6Ni_2(SCH_3)](PF_6)_2$** (1.0 mM, 0.1 M NBu_4PF_6 in MeCN, 100 mV·s^{-1}). Two reduction processes are observable in the cathodic region. Inset shows the scan rate dependence of the second reductive wave at E_p^{red} = –2.46 V.

The first reduction event at $E_{1/2}$ = –2.03 V *vs.* Fc/Fc^+ shows a reversible redox behavior at scan rates from 25 mV·s^{-1} to 1 V·s^{-1} (**Figure 5.19 (a)**). At higher scan rates a higher peak separation is observed (ΔE = 92 mV to 150 mV) and a $i_{p,c}$ *vs.* $\upsilon^{1/2}$ plot shows a linear fit according to a diffusion controlled process (**Figure 5.19 (b)**). The reduction of **$[L^6Ni_2(SCH_3)](PF_6)_2$** leads to a new complex, which shows higher stability than the previously reported reduction processes of **$[L^6Ni_2(OH)](PF_6)_2$**, **$[L^6Ni_2Cl](PF_6)_2$** and **$[L^6Ni_2S]PF_6$** (**chapter 4 and 5**) and can be re-oxidized (**Figure 5.19**). In order to confirm the temperature dependency of the first reduction process, a solution of **$[L^6Ni_2(SCH_3)](PF_6)_2$** in 0.1 M NBu_4PF_6/MeCN electrolyte is prepared and cooled down to 233 K (**Figure 5.19 (d)**). The conducted CVs show an increased peak separation by increase of the scan rate. Afterwards, the complex solution is warmed up to 298 K and CVs are measured, confirming the retention of a reversible redox event (**Figure 5.19 (d)**). In addition, simulations of the CVs at room temperature and low temperature are performed, wherein the electron transfer rate and the diffusion constant are derived (**Figure 5.20** and **Table 5.8**).

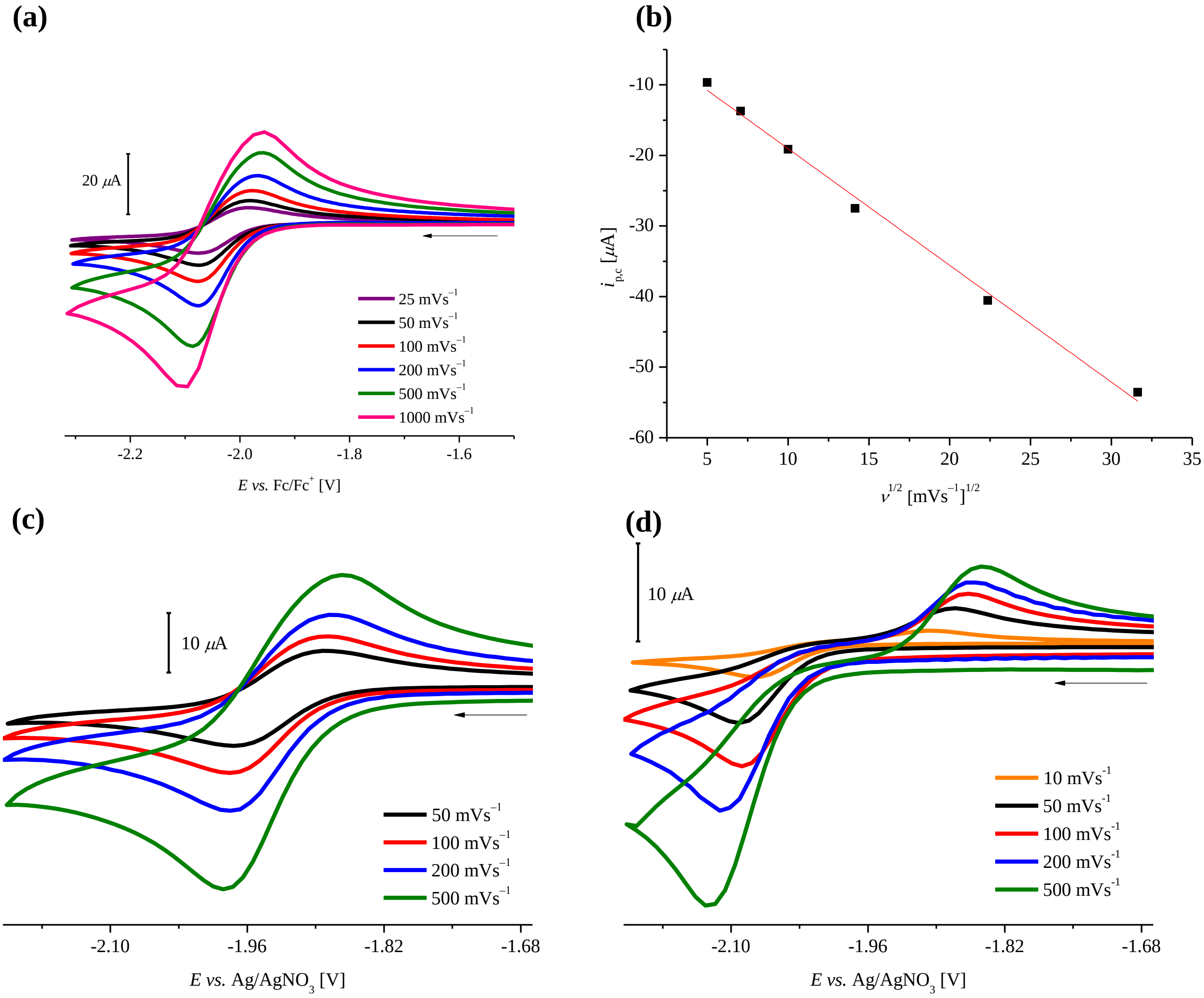

Figure 5.19: (**a**) CV of the first reduction event of **$[L^6Ni_2(SCH_3)](PF_6)_2$** at different scan rates *vs.* Fc/Fc^+. **(b)** i_p *vs.* $\upsilon^{1/2}$ plot shows the linear behavior of the wave at different scan rates (R^2 = 0.9941). (**c**) Peak separation of the first reduction process of **$[L^6Ni_2(SCH_3)](PF_6)_2$** at r.t. *vs.* $Ag/AgNO_3$ and **(d)** at 233 K.

A cathodic shift of E^0 from –1.93 V to –1.97 V is observed upon lowering the temperature from 298 K to 233 K. A decrease of the temperature results in a decrease of the diffusion coefficient (**Table 5.8**) as expected by the Stokes-Einstein equation (formula (1), **chapter 1**).[54] The diffusion coefficient depends on the temperature T and the inverse dynamic viscosity η. Hence, the decrease of the temperature leads to an increase of η(MeCN) from 0.347 mPa at 298 K to 0.831 mPa at 233 K (**Table 5.8**).

The temperature influence on the reference electrode is neglected, due to the set-up of the reference electrode, which allows a constant temperature of latter one at 298 K. In contrast to this is a decrease of the standard rate constant of almost a factor of 16 observed. The rate of mass transport is faster than rate of electron transfer, based on increasing viscosity of the solvent, but the change of intrinsic properties of the complex during the reduction can also have an influence.

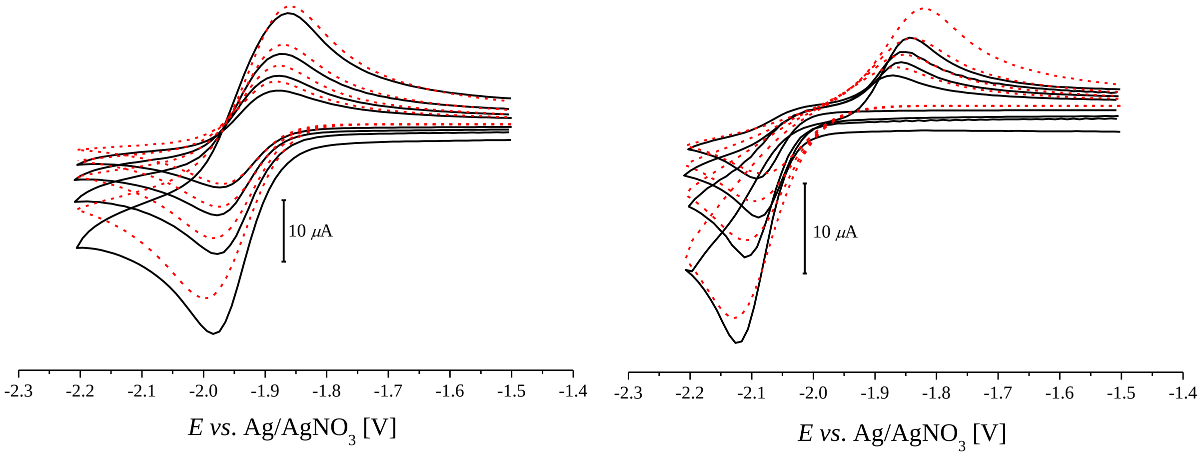

Figure 5.20: Simulation of the first reduction process of $\mathbf{[L^6Ni_2(SCH_3)](PF_6)_2}$ at 298 K (**left**) and 233 K (**right**).

Table 5.8: Obtained kinetic parameters obtained by CV simulations of the first reduction event of $\mathbf{[L^6Ni_2(SCH_3)](PF_6)_2}$ at 298 K and 233 K.

	298 K	233 K
E^0 [V]	–1.93	–1.97
k_S [cm·s^{-1}]	0.005	0.0003
$D^{(Ox/Red)}$ 10^{-6} [cm^2·s^{-1}]	7.5	4.0
η [mPa]	0.347	0.831

5.4.3.2 Analysis of $[L^6Ni^INi^{II}(SCH_3)]PF_6$

UV-vis SEC of **$[L^6Ni_2(SCH_3)](PF_6)_2$** at room temperature shows a dramatic increase and red shift of the observed bands (**Figure 5.21** (**a**)). The absorbance of the band at 373 nm increases markedly and shifts to 383 nm. In addition, a new band at 525 nm rises which has an absorbance too high to be a d–d transition and might be an intervalence charge transfer band (IVCT). Also a band in the NIR region appears, with a maximum at 786 nm (233 K) (**Figure 5.21** (**c**)). After no changes in intensity are observed by applying a reductive potential, re-oxidation of the reduced species to the oxidized species at –1.8 V is followed *via* UV-vis spectroscopy. A difference spectrum confirms the electro-chemical reversibility of **$[L^6Ni^INi^{II}(SCH_3)]^+$** (**Figure 5.21** (**b**)).

Since the reduction potential of the complex in MeCN is too low for the use of a chemical reducing agent, bulk electrolysis is performed at 233 K to further analyze the observed species by *in situ* UV-vis spectroscopy, CV and EPR spectroscopy (**Figure 5.21** (**c**)-(**f**)). After 30 min and 79 min 200 μL aliquots of the CV solution are taken and EPR samples are prepared. In addition, CVs are conducted to prove the progress of the chemical reduction of the complex. The UV-vis spectra which are obtained during the electrolysis and during the preparation of the EPR samples (**red** and **blue** **Figure 5.21**) lead to no further information. With the *in situ* dip probe it is possible to measure in a large spectral range, so that also the above described band at 780 nm is observed (**Figure 5.21** (**c**)). After the process is finished, further CVs are measured to confirm the reversibility of this process. CV measurements of the generated mixed valent complex show the same oxidation events as previously described by the CV of **$[L^6Ni_2(SCH_3)](PF_6)_2$**. The determined Q value supports a one electron reduction process. The EPR spectra of the aliquots at 100 K show the increase of the signal intensity of the reduced species during bulk electrolysis (**Figure 5.21** (**e**)). The green spectrum, 4 h after the end of the bulk electrolysis, shows slight instability of the complex at low temperature.

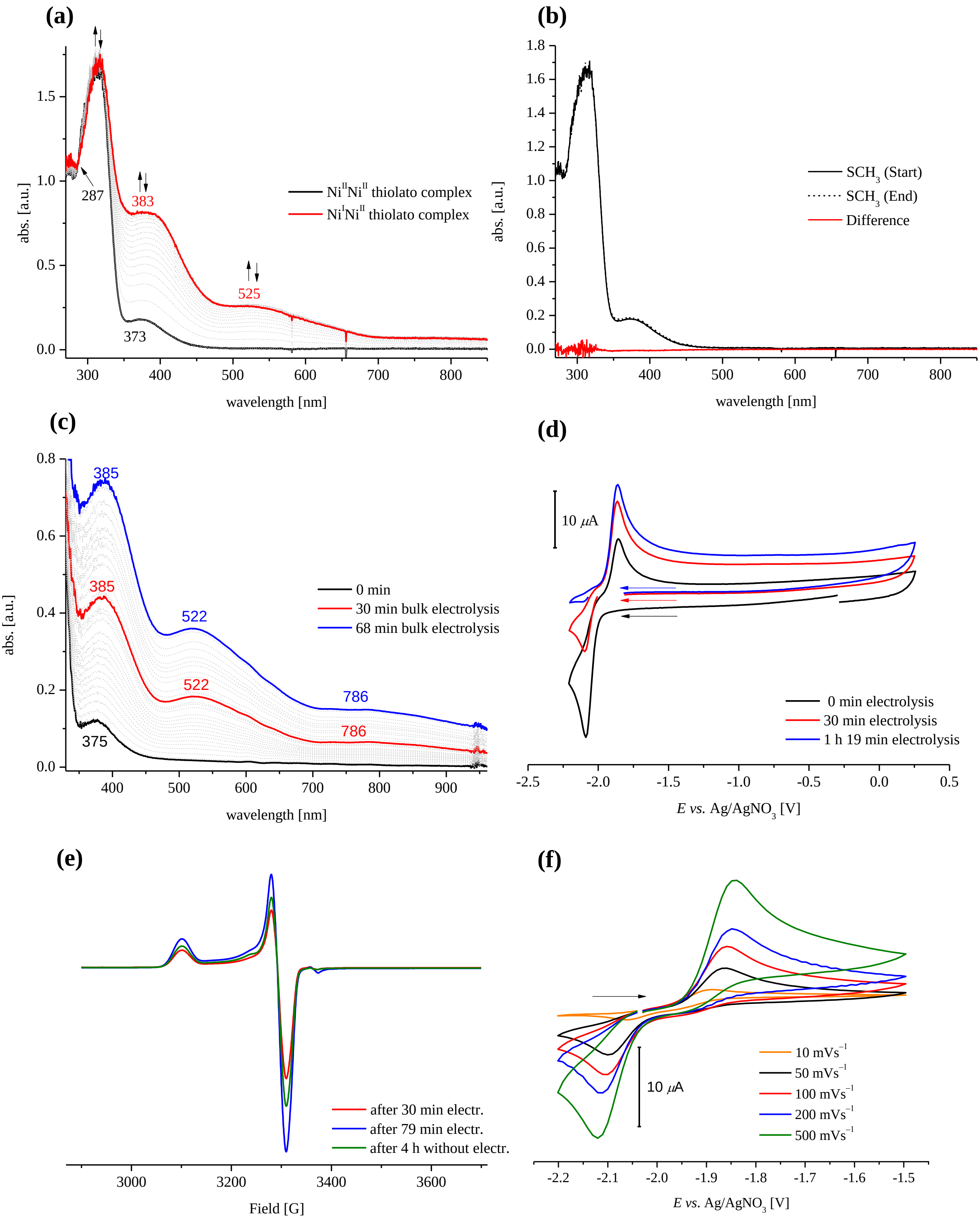

Figure 5.21: (**a**) SEC UV-vis spectra of **[$L^6Ni_2(SCH_3)](PF_6)_2$** in MeCN. (**b**) Difference spectra after re-oxidation of **[$L^6Ni^INi^{II}(SCH_3)]^+$**. (**c**) *In situ* UV-vis spectra recorded during bulk electrolysis of **[$L^6Ni_2(SCH_3)](PF_6)_2$** at 233 K. (**d**) CV of **[$L^6Ni_2(SCH_3)](PF_6)_2$** before starting the bulk electrolysis (**black**), after the first 30 min. of bulk electrolysis (**red**) and after 79 min of bulk electrolysis (**blue**). (**e**) Monitoring of the reduction reaction by EPR spectroscopy at 100 K, shows a quasi-axial symmetric signal for **[$L^6Ni^INi^{II}(SCH_3)]^+$** and increasing intensity with longer electrolysis time. (f) Scan rate dependency CV measurements, starting from **[$L^6Ni^INi^{II}(SCH_3)]^+$** at 233 K.

The EPR spectrum shows a quasi-axial signal with g_1 = 2.18, g_2 = 2.05 and g_3 = 2.04 values (**Figure 5.22**). In 2016, Duboc *et al.*[211] published a heteronuclear nickel(I)/iron(II) complex, which shows an axial EPR spectrum with comparable *g* values ($g_{\parallel}$ = 2.168, $g_{\perp}$ = 2.060). In the literature, tetraaza macrocyclic nickel(I) and porphyrinic complexes are described with axial symmetric or quasi-axial symmetric EPR spectra and with slightly rhombic character.[212,213] The catalytically active nickel(I) F_{430} center in methyl coenzyme M reductase (MCR), also exhibited an axial symmetric EPR spectrum.[213] In contrast to this several four coordinated nickel(I) complexes are reported with rhombic EPR signals.[214–216] *T*-shaped Ni^I complexes, for instance published by Lee, Tilley and Schneider and coworkers[217–219] also show a rhombic spectrum. In the EPR spectrum of **[$L^6Ni^INi^{II}(SCH_3)$]$^+$** a quasi-axial symmetry is observed which is based on the asymmetric environment around the single occupied orbital along the *x* and *y* axes.

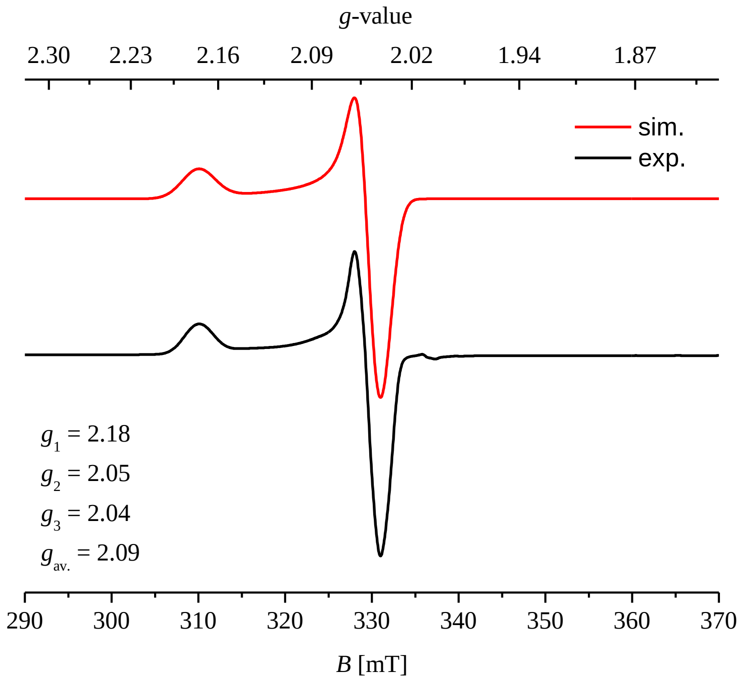

Figure 5.22: Experimental derived EPR spectrum of **[$L^6Ni^INi^{II}(SCH_3)$]$^+$** (**black**) in MeCN at 100 K and frequency: 9.44 GHz and simulation (**red**). A quasi-axial symmetric spectrum is obtained with the *g* values: g_1 = 2.18, g_2 = 2.05 and g_3 = 2.04 (9.443 GHz).

Based on theoretical calculations, the SOMO has a large nickel d character (Mulliken spin population: each 45%), mostly which is assumed to be the $d_{x^2-y^2}$ orbitals, which are directly orientated towards the corresponding ligands (**Figure 5.23**). The observation of the quasi-axial symmetry of the signal in the EPR spectrum leads to the conclusion, that the anisotropy in *x* and *y* direction is almost the same. Indeed the average bond lengths in *x* (C–Ni–S) and *y* direction (N–Ni–C) of the theoretically calculated **[$\mathbf{L^6Ni^INi^{II}(SCH_3)}$]$^+$** complex shows a slightly higher bond elongation in *x* direction (0.11 Å) than in the *y* direction, which can lead to a different anisotropy in the two directions and can be the explanation for the slightly different in-plane *g* values. Based on equal contribution of the electron populations on both nickel centers, the elongation of the Ni–SCH$_3$ bond is low in the calculated structure (0.03 Å) compared to Ni–SCH$_3$ in **[$\mathbf{L^6Ni_2(SCH_3)](PF_6)_2}$**.

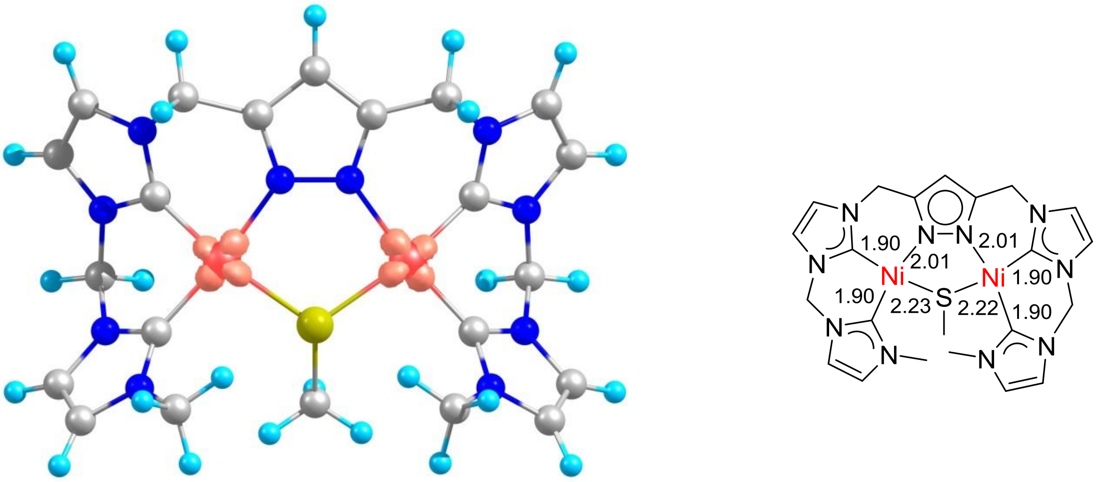

Figure 5.23: **Left:** Calculated molecular structure of [$\mathbf{L^6Ni^INi^{II}(SCH_3)}$]$^+$ showing the spin density. Starting point of the single point calculations is the crystallographic structure of [$\mathbf{L^6Ni^{II}Ni^{II}(SCH_3)}$]$^{2+}$.The unpaired electron is distributed over the d orbitals of the nickel centers with a Mulliken spin population of 45%. Calculations show a bond elongation of all bonds in comparison to [$\mathbf{L^6Ni_2(SCH_3)](PF_6)_2}$, but most significant for the Ni–N bond (elongation of approximately 0.13 Å).

Additional EPR measurements at 22 K do not give further information about the system. The experimental findings confirm the reduction of **[$\mathbf{L^6Ni^{II}Ni^{II}(SCH_3)}$]$^{2+}$** to a mixed valent **[$\mathbf{L^6Ni^INi^{II}(SCH_3)}$]$^+$** complex, where the unpaired electron is mostly metal centered in a quasi-axial environment. Unfortunately, crystallization attempts failed until now. The electrochemical redox potential of this complex is very low, due to the strong donor properties of the thiolato bridge as well as the strong σ donor properties of the NHC ligand scaffold which results in a strong ligand field and a high energetically $d_{x^2-y^2}$ orbital.

DFT calculations are performed, to get further information about the reduction process which occurs at $E_\mathrm{p}^\mathrm{red} = -2.46$ V *vs.* Fc/Fc$^+$. These calculations show that the reduction probably occurs at the nickel atoms under formation of **[$\mathbf{L^6Ni^INi^I(SCH_3)}$]**. A Broken-Symmetry calculation revealed a magnetic coupling of the unpaired electrons ($J = -136$ cm^{-1}).

5.5 Conclusion and Outlook

In this chapter the manifold properties of **$[L^6Ni_2S]PF_6$** were presented. In solution the complex shows at low temperature the formation of two different conformers and it was possible to determine $\Delta S^{\ddagger}$, $\Delta H^{\ddagger}$, ΔS^{o}, ΔH^{o} and E_a for this interconversion. Furthermore, these values were compared with the activation parameters for the interconversion of the conformers in **$[L^6Ni_2(OH)](PF_6)_2$** and [**$L^6Ni_2(SCH_3)](PF_6)_2$**.

Oxidation of the complex results in the formation of a tetranickel(II) persulfido complex, which will be further described in **chapter 8**. First reactivity studies of **$[L^6Ni_2S]PF_6$** towards small molecules were investigated and give the motivation to further explore the behavior of this complex with respect to small molecule activation. Also the reactivity of **$[L^6Ni_2S]PF_6$** with oxygen transfer agents, in analogy to experiments of Driess *et al.* can be further explored. In the next chapters the protonation of **$[L^6Ni_2S]PF_6$** will be explored. **$[L^6Ni_2S]PF_6$** and the protonated species will be investigated with respect to electro-chemical proton reduction, and in addition the reaction of **$[L^6Ni_2S]PF_6$** towards NO^+ and NO gas is probed.

Alkylation of the complex results in [**$L^6Ni_2(SCH_3)](PF_6)_2$** formation. This complex can be reversibly reduced to a mixed-valent Ni^INi^{II} μ-SCH_3 complex at low potential. The mixed valent complex was further investigated by CV, UV-vis and EPR spectroscopy, the latter showing a quasi-axial spectrum. Even though the redox potential is very low this complex can be an interesting starting point for studying bio-inspired reactivity. MCR and ACS reactivity can be an interesting starting point. Also the crystallographic and further electronic characterization of [**$L^6Ni^INi^{II}(SCH_3)]PF_6$** is a challenging and important task, which has to be considered in the future.

6

Interconversion of a dinickel(II) μ-sulfido complex and a μ-hydrosulfido complex *via* a supramolecular encounter complex

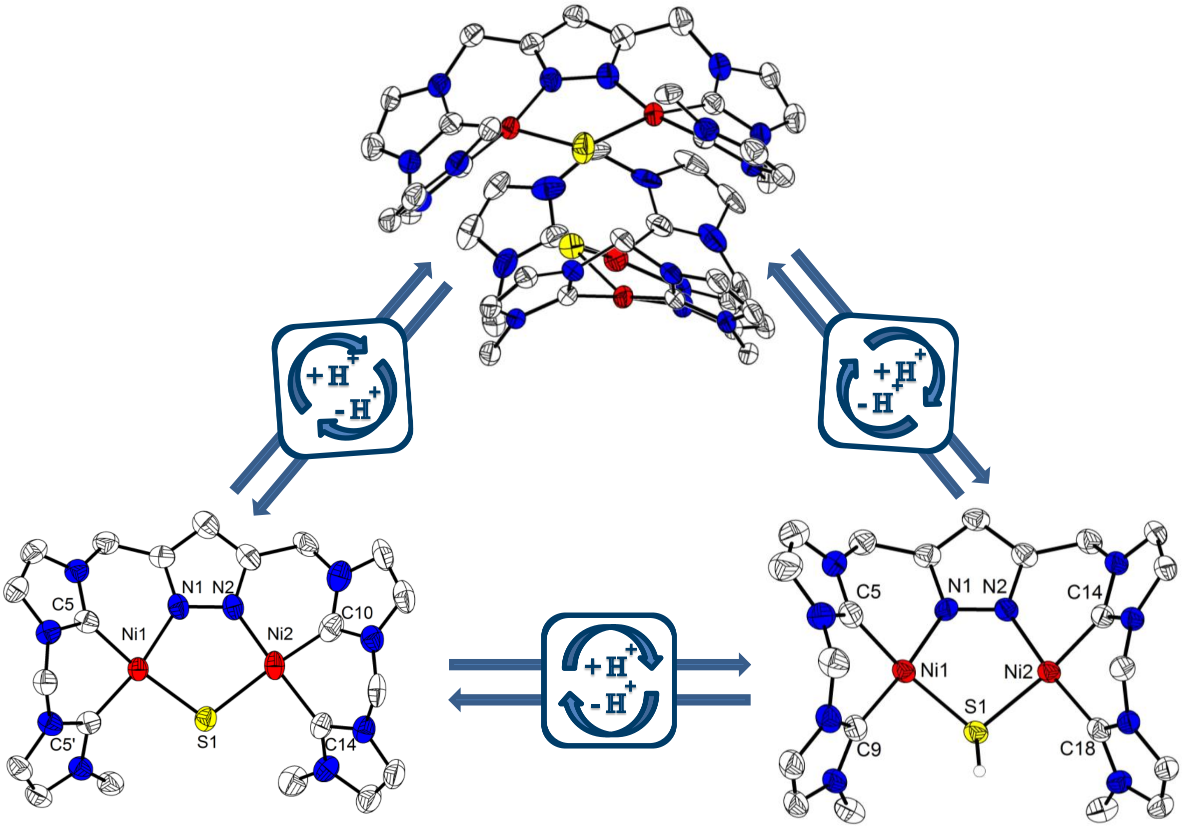

Abstract: The focus of this chapter is the interconversion of a dinickel(II) μ-sulfido complex and its μ-hydrosulfido complex. This transformation occurs *via* an intermediate supramolecular encounter complex, wherein a proton is located between two dinickel(II) μ-sulfido complexes. The proton transfer self-exchange rate between the sulfido- and hydrosulfido-bridged complexes is approximately ~10^4 $M^{-1}\cdot s^{-1}$. In addition, a pK_a value of 18.4 is determined for the dinickel(II) μ-SH complex *via* NMR titration experiments.

6.1 Introduction

In **chapter 5** the importance of metal sulfido complexes in hydrodesulphurization, hydrogenation, hydrocracking and hydrodeoxygenation reactions is mentioned. Also metal hydrosulfido complexes play an essential role in this context.[220] Dinuclear complexes **XVIII**[165,166], **XIV** or **XV**[221] (**Figure 6.1**) impressively show heterolytic cleavage of dihydrogen or pinacolborane[165,166] (**chapter 5, Scheme 5.1**). Also the electrocatalytic potential of complex **XIV** or **XV** for proton reduction has been reported by DuBois and coworkers[221], and the protonation of the sulfido-bridged ligand is proposed as the initial step of the catalytic mechanism.

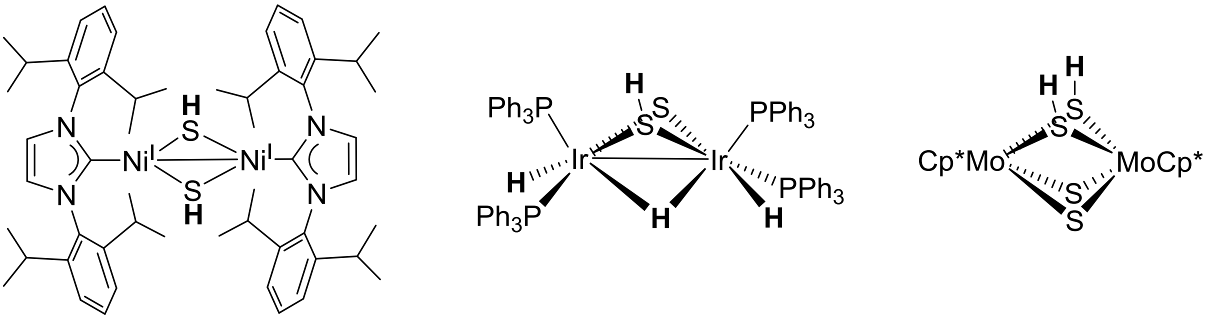

XVIII **XIV** **XV**

Figure 6.1: Selection of hydrosulfido-bridged complexes **XVIII**-**XV**.[166,221,222]

S–H bonds play in nature an important role and participate in catalytic processes, for instance in proton coupled electron transfer processes.[223] Two prominent examples are the reduction of nucleotides to deoxynucleotides by *E. coli* (class Ia RNR)[224] or the reversible proton reduction to H_2 by [FeFe], [Fe] and [NiFe] hydrogenases.[225] In 2015, Lubitz *et al.*[226] solved the protein crystal structure of a [NiFe] hydrogenase and reported a S–H protonated cysteine (C546) in the **Ni–R** state next to the active heterobimetallic center (**Figure 6.2**, **left**). These results are still part of an ongoing debate, but lead to the question "what is the mechanism of the enzyme catalyzed proton oxidation or dihydrogen reduction?" Several organometallic model complexes have been investigated, wherein the protonation of a sulfur containing ligand is discussed.[166,227,228] In 2016, Darensbourg *et al.*[227] investigated hemilabile bridging thiolate ligands as possible proton shuttles in the electro-catalytic proton reduction process of a [NiFe] hydrogenase model complex. Complex **XVI** features a hydrosulfido unit in the ligand backbone and shows electro-catalytic activity for proton reduction (**Figure 6.2**).[228]

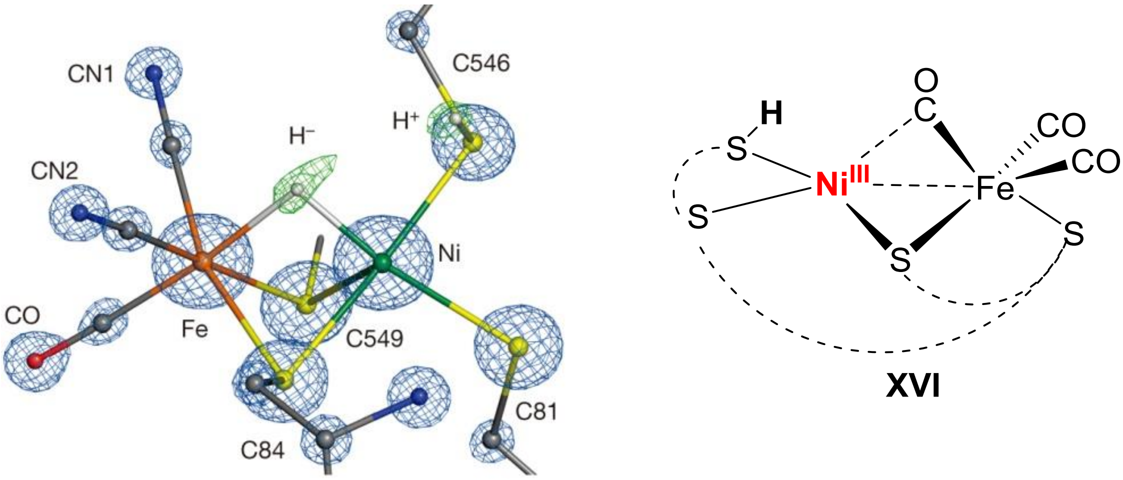

Figure 6.2: Left: Protein crystal structure of the active center of the [NiFe] hydrogenase in the **Ni–R** state. © 2015 SPRINGER NATURE. **Right:** [NiFe] model complex, with a protonated thiolate in the ligand backbone, close to the nickel center.[226,228]

In 2016, Duboc *et al.*[211,229] presented a bioinspired [NiFe] model complex (see **chapter 9**) and in 2018, they confirmed by detailed DFT calculations the protonation of the thiolate bridge by $[HNEt_3]^+$ after reduction of the nickel(II) center. An important step in understanding the mechanism of electro-catalysts or enzymes is the investigation of the factors which control the reaction rates and the mechanism of protonation in such systems.[230] Important factors in such elementary reactions are the pK_a value of the hydrosulfide and the S–H bond strength. However, only few experimentally determined pK_a values of metal hydrosulfido complexes have been described in the literature; especially for complexes, wherein the catalytic activity for proton reduction is demonstrated.[221,230] The number of experimentally determined S–H bond strengths is even lower and to the best of my knowledge are reported exclusively in the work of Franz and DuBois.[220,221,231–233]

6.2 Objectives

In the previous **chapter 5** the synthesis and reactivity of **[L^{6}Ni$_2$S]PF$_6$** is described. In this chapter the synthesis of a hydrosulfido-bridged complex *via* protonation of **[L^{6}Ni$_2$S]PF$_6$** is reported (**Figure 6.3**). Furthermore, the interconversion of **[L^{6}Ni$_2$S]$^+$** and **[L^{6}Ni$_2$(SH)]$^{2+}$** is investigated. The pK_a value and the proton self-exchange reaction of **[L^{6}Ni$_2$(SH)]$^{2+}$** is determined, as well as its redox properties. This analytical data will be useful to further understand the reactivity of the presented complexes in proton reduction reactions and HAT processes.

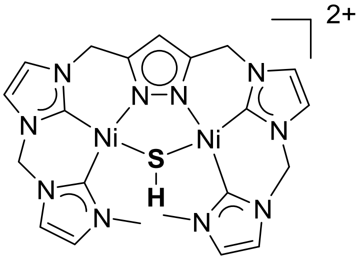

Figure 6.3: Proposed dinickel(II) μ-hydrosulfido complex.

6.3 Results and Discussion

6.3.1 A hydrosulfido-bridged dinickel(II) hybrid pyrazolate/NHC complex

The reaction of **[L^{6}Ni$_2$S]PF$_6$** with 2,6-lutidinium triflate results in an immediate color change from red to yellow (**Scheme 6.1**). Pale yellow crystals suitable for X-ray diffraction are obtained by slow diffusion of Et$_2$O in a MeCN solution of the complex.

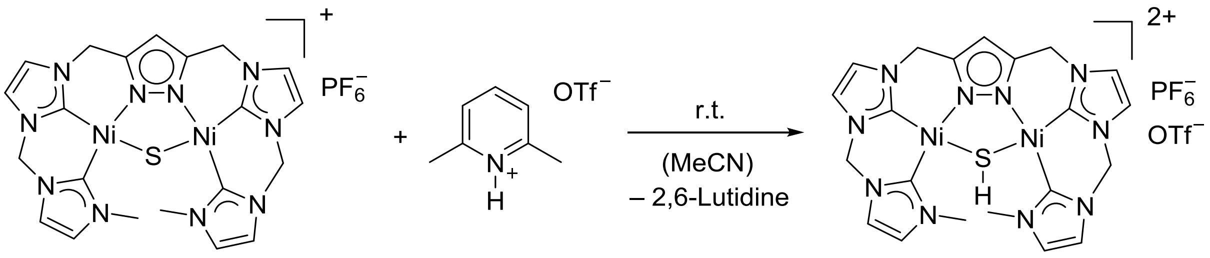

Scheme 6.1: Synthesis route of **[L^{6}Ni$_2$(SH)](PF$_6$)(OTf)**.

[L^{6}Ni$_2$(SH)](PF$_6$)(OTf) crystallizes in the space group *C*2/*c*. **[L^{6}Ni$_2$(SH)]$^{2+}$** shows a saddle shaped conformation of the molecular structure in solid state (**Figure 6.4**). The Ni(1)····Ni(2) distance is 3.29 Å and the CH$_3$ separation is 5.73 Å, and larger than in **[L^{6}Ni$_2$S]$^+$** (4.67 Å).

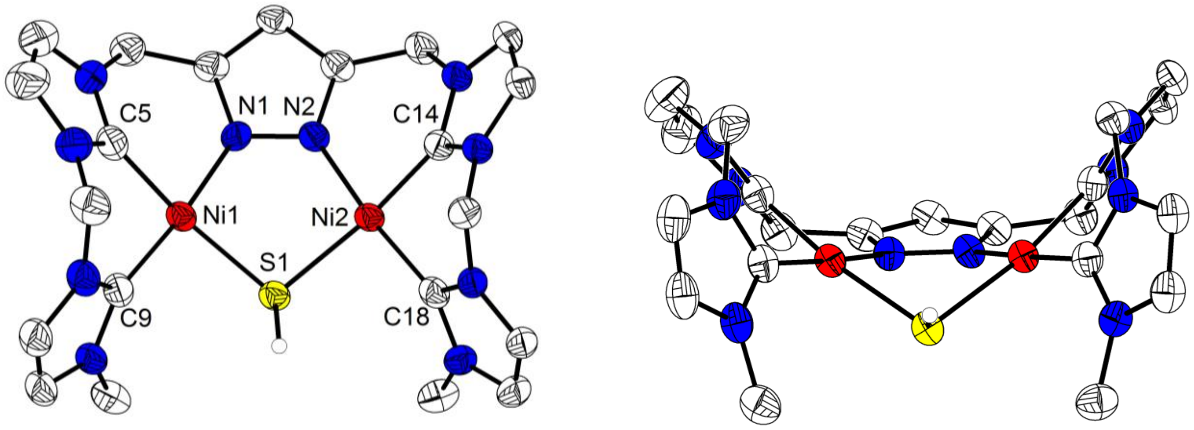

Figure 6.4: Molecular structure (50% probability thermal ellipsoids) of the cationic part of **[L^{6}Ni$_2$(SH)](PF$_6$)(OTf)**. H atoms, except of the SH proton, are omitted for clarity.

Ni(1) is –0.05 Å out of the C(5)–N(1)–S(1)–C(9) plane, and Ni(2) is –0.06 Å out of the N(2)–C(18)–C(16)–S(1) plane. The angle between the two planes is 52.1° and the largest angle which is observed for the dinickel(II) complexes described in this thesis (see also **Table A.6.1** and **Figure A.5.1** in **appendix**). Relevant bond lengths and bond angles of the complex are summarized in **Table 6.1** and **Table 6.2**.

Table 6.1: Selected bond lengths [Å] for **[L^{6}Ni$_2$(SH)](PF$_6$)(OTf)**.

Atoms	Bond lengths
Ni1····Ni2	3.291(0)
Ni1–C5	1.859(4)
Ni1–C9	1.888(4)
Ni1–N1	1.889(3)
Ni1–S1	2.213(9)
Ni2–C14	1.855(4)
Ni2–N2	1.877(3)
Ni2–C18	1.882(4)
Ni2–S1	2.204(1)

Table 6.2: Selected bond angles [°] for **[L^{6}Ni$_2$(SH)](PF$_6$)(OTf)**.

Atoms	Bond angles
C5–Ni1–C9	87.4(8)
C5–Ni1–N1	87.2(6)
C9–Ni1–S1	96.4(9)
N1–Ni1–S1	88.9(1)
C14–Ni2–N2	87.3(6)
C14–Ni2–C18	87.5(4)
N2–Ni2–S1	89.4(5)
C18–Ni2–S1	96.0(4)
Ni2–S1–Ni1	96.3(0)
C5–Ni1–C9	87.4(8)

Four peaks are detected in the ESI-MS of **[L^{6}Ni$_2$(SH)](PF$_6$)(OTf)** and are assigned at *m/z* = 709 (58) to [**L^{6}Ni$_2$(SH)PF$_6$**]$^+$, at *m/z* = 713 (73) to [**L^{6}Ni$_2$(SH)OTf**]$^+$, at *m/z* = 563 (36) to [**L^{6}Ni$_2$S**]$^+$ and at *m/z* = 282 (100) to **[L^{6}Ni$_2$(SH)]$^{2+}$** (**Figure 6.5**, **left**). MS/MS analysis of the cations at *m/z* = 709 ([[**L^{6}Ni$_2$(SH)PF$_6$**]$^+$) or *m/z* = 713 ([**L^{6}Ni$_2$(SH)OTf**]$^+$) show the formation of a peak at *m/z* = 563 for [**L^{6}Ni$_2$S**]$^+$. Cations **[L^{6}Ni$_2$(SH)X]$^+$ (X = PF$_6$**, **OTf**) are not stable under ESI conditions and is partly converted to [**L^{6}Ni$_2$S**]$^+$. In the IR spectrum of a solid sample of the complex, one band at υ(SH) = 2588 cm^{-1} is assigned to the S–H stretch (**Figure 6.6**). The band is weak due to the high covalency of the S–H bond. The S–H stretch for a macrocyclic dinickel(II) μ-SH complex is observed at 2552 cm^{-1}, for H_2S at 2550 cm^{-1} and for potassium hydrosulfide at 2556 cm^{-1}.[234–236] In order to confirm the assignment of the S–H stretching band in this work, the S–D labeled complex **[L^{6}Ni$_2$(SD)](PF$_6$)(OTf)** is synthesized. ESI-MS analysis of **[L^{6}Ni$_2$(SH)](PF$_6$)(OTf)** shows a shift of *m/z* = 1 for the singly charged complexes (**Figure 6.5**, **right**), confirming the successful H/D exchange. The unlabeled complex is also observed in the ESI-MS, due to fast H/D exchange with water.

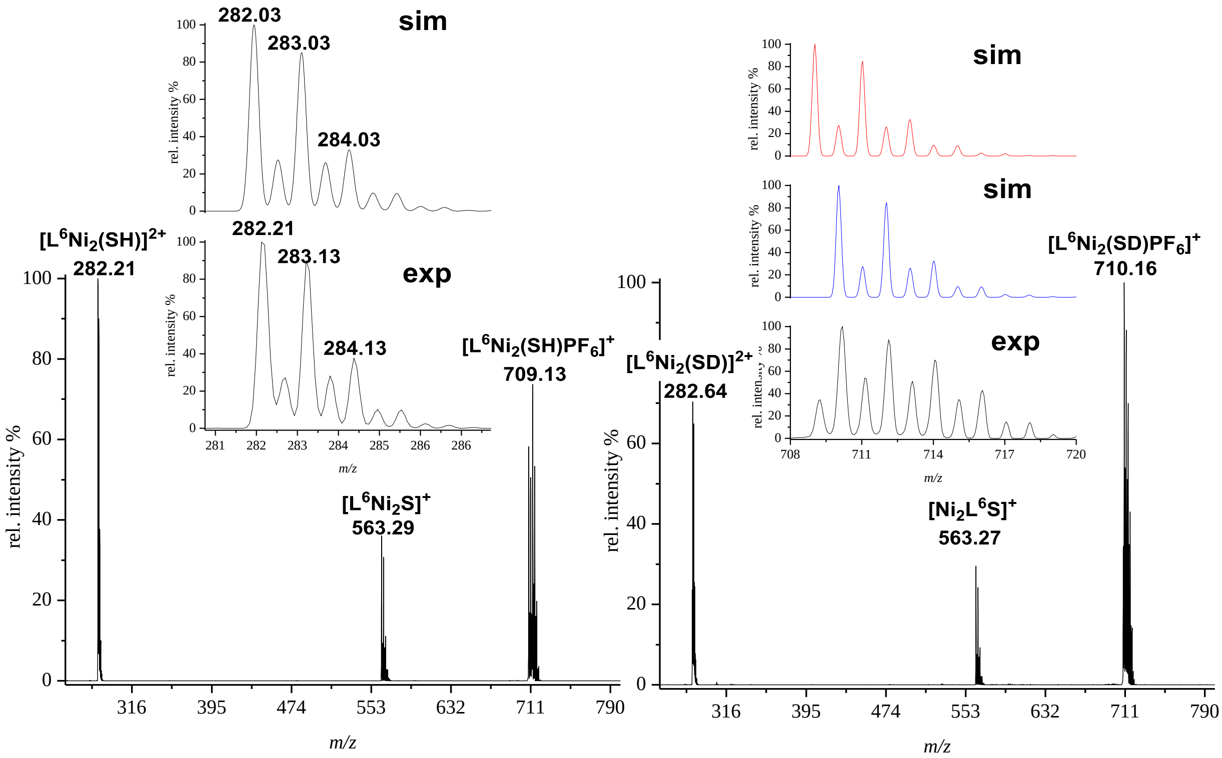

Figure 6.5: **Left:** ESI-MS of **[L^{6}Ni$_2$(SH)](PF$_6$)(OTf)** in MeCN. Inset shows the simulated (**top**) and experimental (**bottom**) isotopic distribution pattern of the peak at $m/z = 282$ (100) assigned to **[L^{6}Ni$_2$(SH)]**$^{2+}$. **Right:** ESI-MS of **[L^{6}Ni$_2$(SD)](PF$_6$)(OTf)** in MeCN. Inset shows the simulated (**top**) and experimental (**bottom**) isotopic distribution pattern of the peak at 710 (100) assigned to [**L^{6}Ni$_2$(SD)PF$_6$**]$^+$ (**blue sim**) and [**L^{6}Ni$_2$(SH)PF$_6$**]$^+$ (**red sim**).

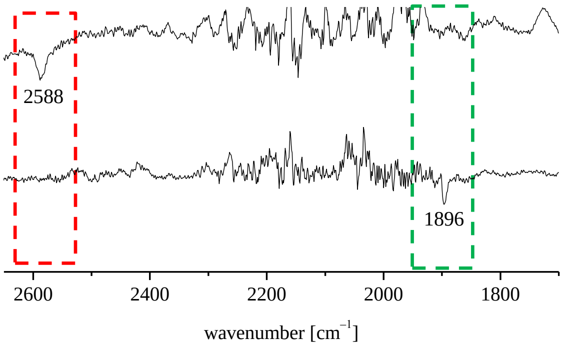

Figure 6.6: Excerpt of IR spectra of **[L^{6}Ni$_2$(SH)](PF$_6$)(OTf)** (**top**): υ(SH) at 2587 cm^{-1} (– – –) and **[L^{6}Ni$_2$(SD)](PF$_6$)(OTf)** (**bottom**): υ(SD) at 1896 cm^{-1} (– – –).

The IR spectrum of a crystalline sample of **[L^{6}Ni$_2$(SH)](PF$_6$)(OTf)** shows a weak band at υ(SD) = 1896 cm^{-1} (**Figure 6.6**). The shift between the labeled complex (υ(SD) = 1896 cm^{-1}) and unlabeled complex (υ(SH) = 2588 cm^{-1}) is in the range of the theoretical expected value. Additionally, DFT calculations of the IR stretching frequencies of the labeled and unlabeled complexes are performed. A comparison of the experimental S–H/S–D stretches with the calculated stretching frequencies confirms the correct assignment of the bands in the IR spectrum (**Table 6.3**).

Table 6.3: Comparison of experimental (ATR IR) SH and SD stretching frequencies in **$[L^6Ni_2(SH)](PF_6)(OTf)$** and **$[L^6Ni_2(SD)](PF_6)(OTf)$** and DFT* calculated frequencies (def2-tzvp def2-tzvp/j bp86). Harmonic approximation gives $\frac{\upsilon(SH)}{\upsilon(SD)}$ = 1.39.

	υ(SH) [cm^{-1}]	υ(SD) [cm^{-1}]	$\Delta\upsilon$ [cm^{-1}]	$\left[\frac{\upsilon(SH)}{\upsilon(SD)}\right]$
Experimental	2588	1896	692	1.365
Theoretical*	2576	1850	726	1.392

^{1}H NMR spectrum of **$[L^6Ni_2(SH)](PF_6)(OTf)$** in MeCN-d_3 shows an apparent C_{2v} symmetry of the complex and all signals are assigned by 1D and 2D NMR measurements (see experimental section). The SH proton signal is observed at 0.32 ppm as a slightly broadened singlet (**Figure 6.7** (**a**)). ^{1}H^{1}H NOESY NMR spectroscopy shows a NOE effect between the SH proton resonance and the proton resonances of the CH_3 groups H^8 (**Figure 6.8**). The ^{1}H NMR spectrum of the *in situ* generated **$[L^6Ni_2(SD)](PF_6)(OTf)$** complex shows a disappearance of the SH proton resonance at 0.32 ppm and otherwise identical proton resonances compared to **$[L^6Ni_2(SH)](PF_6)(OTf)$ (Figure 6.7** (**b**)). Re-dissolving of crystalline **$[L^6Ni_2(SD)](PF_6)(OTf)$** complex in MeCN-d_3 leads to an immediate H/D exchange with traces of water. The ^{2}H NMR spectrum of the *in situ* generated **$[L^6Ni_2(SD)](PF_6)(OTf)$** complex shows a broad signal at 0.75 ppm in MeCN. ^{13}C resonances of the two chemical inequivalent carbene-C atoms C^9 and C^{10} are assigned at 162.3 ppm and 160.7 ppm in the ^{13}C{^{1}H} NMR spectrum. The ^{1}H DOSY NMR spectrum of **$[L^6Ni_2(SH)](PF_6)(OTf)$** confirms the presence of a dinuclear complex in solution ($D_{298\,K} = 9.89\cdot10^{-10}$ m^{2}s^{-1}) in agreement with the diffusion coefficients of the previously observed complexes as well as the free ligand **$[H_5L^6](PF_6)_4$**.

VT ^{1}H NMR spectra of the complex show the conservation of the apparent C_{2v} symmetry over a broad temperature range (313 K to 233 K) (**appendix**). In contrast to this, the dinickel(II) complexes described in the previous chapters, **$[L^6Ni_2X]^{y+}$** (X = OH, S, SCH_3), show a diastereotopic splitting of the CH_2 groups at temperatures below 298 K.

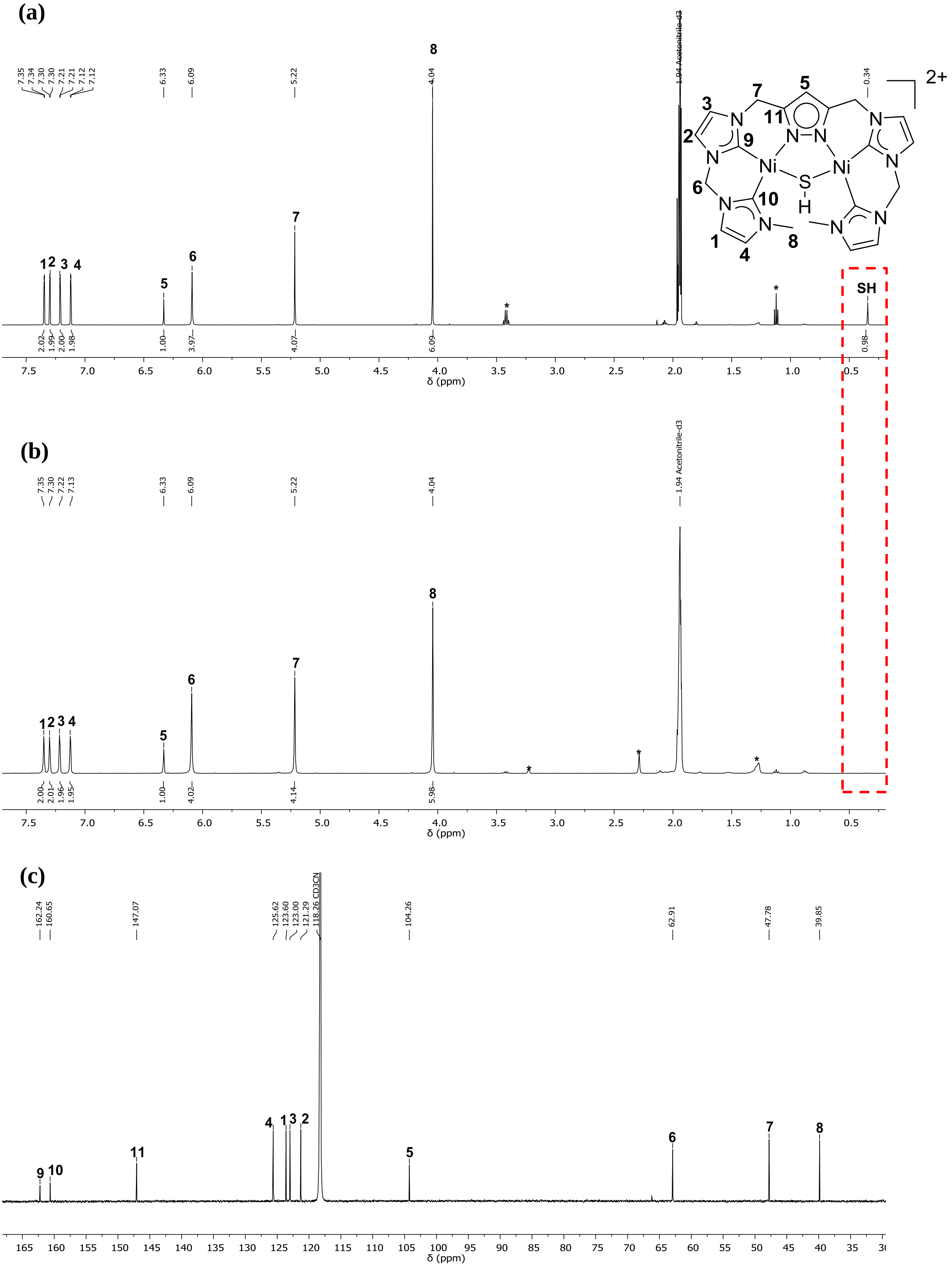

Figure 6.7: (**a**) ^{1}H NMR spectrum of **[L^{6}Ni$_2$(SH)]$^{2+}$** in MeCN-d_3 at 298 K and 500 MHz (**b**) ^{1}H NMR spectrum of the labeled complex **[L^{6}Ni$_2$(SD)]$^{2+}$** in MeCN-d_3 at 400 MHz shows the disappearance of the signal at δ(SH) = 0.32 ppm. (**c**) ^{13}C{^{1}H} NMR spectrum of **[L^{6}Ni$_2$(SH)]$^{2+}$** with carbene-C resonances for C^9 and C^{10} at 162.3 ppm and 160.7 ppm.

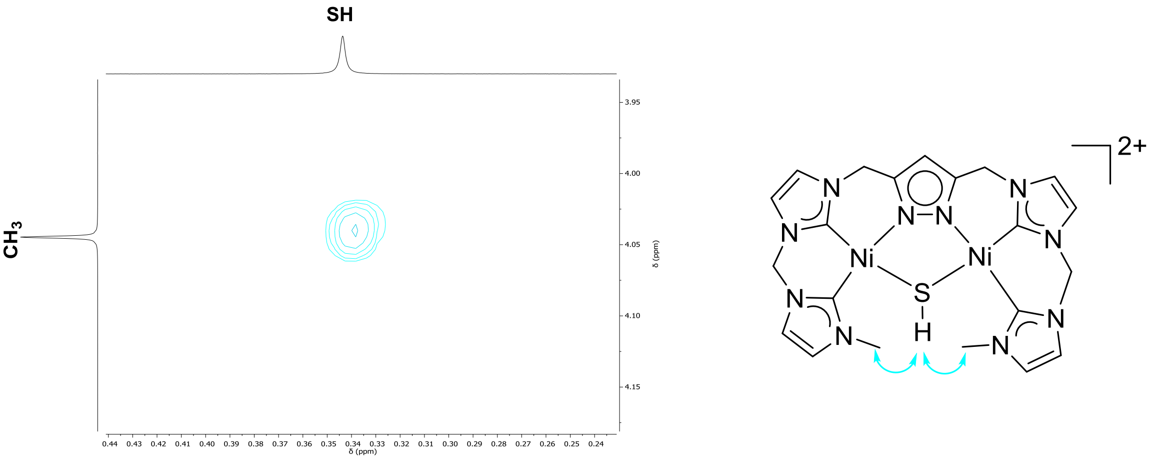

Figure 6.8: ^{1}H^{1}H NOESY NMR spectrum of **[L^{6}Ni$_2$(SH)]**$^{2+}$ in MeCN-d_3 at 298 K and 500 MHz shows a NOE effect between the proton resonances of the CH_3 groups and the SH protons.

A reason for the retention of the apparent C_{2v} symmetry and the high flexibility of the ligand can be the large distance of the CH_3 groups in **[L^{6}Ni$_2$(SH)](PF$_6$)(OTf)**, with 5.73 Å in the molecular structure in solid state. This distance is significant larger (2.08 Å to 0.26 Å), than in the previously reported complexes and allows a fast dynamic of the ligand scaffold due to a low energy barrier of the conformer interconversions.

VT UV-vis spectra of **[L^{6}Ni$_2$(SH)](PF$_6$)(OTf)** in MeCN show an increase of the observed extinction coefficient by decrease of the temperature. Furthermore, a band appears at 260 nm (ε = 19.8 10^3 M^{-1}·cm^{-1}). Additional bands are observed at 218 nm (ε = 56.8·10^3 M^{-1}·cm^{-1}), 305 nm (ε = 45.5·10^3 M^{-1}·cm^{-1}) and 378 nm (ε = 3.0·10^3 M^{-1}·cm^{-1}), beside this new transition. A red shift of the previously described bands is observed in the UV-vis spectrum of the complex in solid state (**Figure 6.9**).

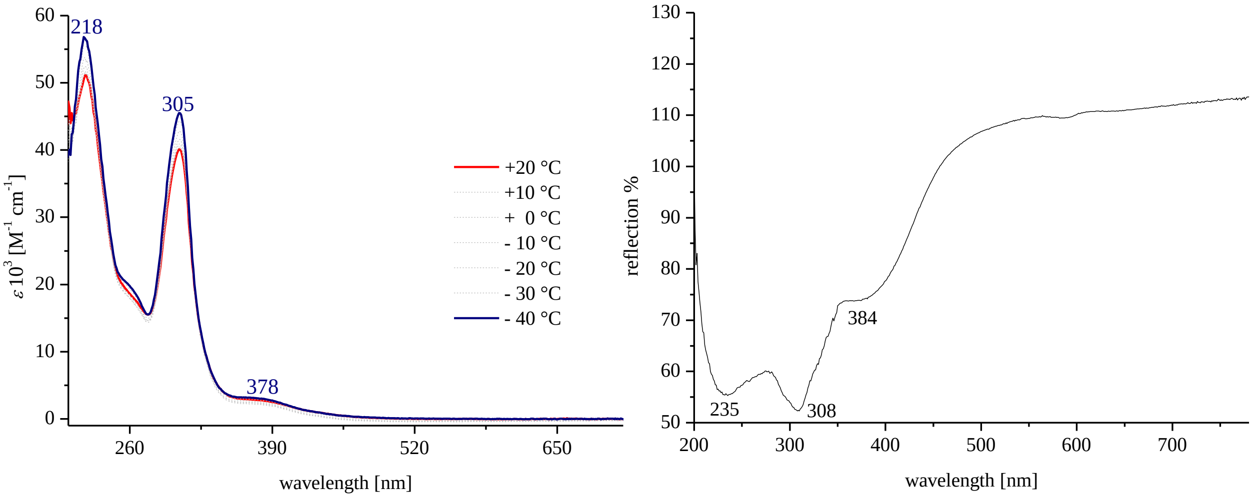

Figure 6.9: Left: VT UV-vis spectra of **[L^{6}Ni$_2$(SH)]**$^{2+}$ in MeCN, **right**: UV-vis spectrum of a solid sample of **[L^{6}Ni$_2$(SH)]**$^{2+}$.

6.3.2 Redox properties of [$L^6Ni_2(SH)]PF_6OTf$

CV experiments of **[$L^6Ni_2(SH)](PF_6)(OTf)$** are performed in MeCN (**Figure 6.10**). After first applying an anodic potential, no oxidation process is observed. The oxidation of **[$L^6Ni_2(SH)](PF_6)(OTf)$** is not possible in the range up to 2.0 V *vs.* Fc/Fc^+. Reduction of the complex is observed at –1.93 V *vs.* Fc/Fc^+. The resulting product can be oxidized and a wave at –0.28 V is obtained in anodic scan (**chapter 5**, **7** and **8**). These findings suggest that **[$L^6Ni_2(SH)]^{2+}$** is reduced at –1.93 V to **[$L^6Ni_2S]^+$** under release of dihydrogen and the product can be oxidized to the persulfido complex **[$(L^6)_2Ni_4(S_2)]^{4+}$** at –0.28 V. After performing a CV in a second cycle modus, the reduction of **[$(L^6)_2Ni_4(S_2)]^{4+}$** to **[$L^6Ni_2S]^+$** is observed at –1.5 V (see **chapter 5** and **7–9** for more details).

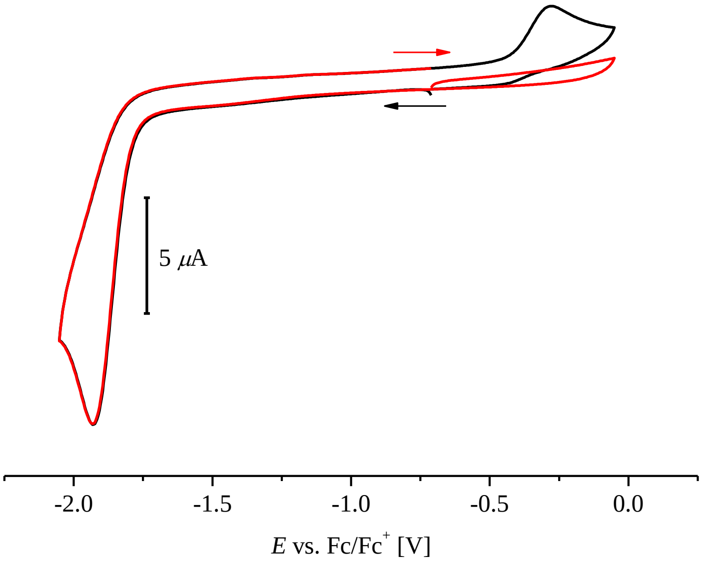

Figure 6.10: CV of **[$L^6Ni_2(SH)](PF_6)(OTf)$** at a scan rate of 100 mV·s^{-1} in MeCN (0.1 M NBu_4PF_6); after applying an anodic step potential first (→) an electric response is observed at –1.93 V *vs.* Fc/Fc^+ and starting with a cathodic potential (←) results in observation of a wave at –1.93 V and a corresponding oxidation process at –0.28 V.

6.3.3 pK_a determination of [$L^6Ni_2(SH)$](PF_6)(OTf)

UV-vis spectroscopic and NMR spectroscopic titration experiments are performed to determine the pK_a value and in addition the BDFE$_{(solv.)}$ of the S–H bond in **[$L^6Ni_2(SH)$](PF_6)(OTf)** by a square scheme (**chapter 7**). The pK_a value is of importance to understand better the mechanism of the electrocatalytic proton reduction of the complex (**chapter 9**). The final pK_a determination is achieved by a ^{1}H NMR spectroscopic titration experiment with **[$L^6Ni_2(SH)$](PF_6)(OTf)** and 1,8-bis(*N*,*N*-dimethylamino)naphthalene (proton-sponge®, pK_a = 18.62 in MeCN)[237]. The progress of deprotonation of **[$L^6Ni_2(SH)$]$^{2+}$** is followed by the chemical shift of the pyrazolate proton of the complex in the ^{1}H NMR spectrum depending on the amount of added base (NMR spectra, **see appendix**). In addition, the transformation is followed by the decrease of the integral value of the SH proton resonance relative to the pyrazolate H peak. Determination of the pK_a value with proton sponge© *via* UV-vis spectroscopy is not possible, since the bands of the base are covering the bands of the complexes at higher base concentrations (**appendix**, **Figure A.6.4**). The reaction equation (7) is considered for the calculation of the pK_a value.

$$[L^6Ni_2(SH)]^{2+} + B \rightleftharpoons [L^6Ni_2S]^{+} + HB^{+} \tag{7}$$

Equation (8) is derived based on (7) and in a further step the activity *a* is substituted in a first approximation by the concentration (9).

$$\Delta pK_a = pK_a(HB^+) - pK_a([L^6Ni_2(SH)]^{2+}) = \log\frac{a(HB^+)\cdot a\left([L^6Ni_2S]^+\right)}{a(B)\cdot a([L^6Ni_2(SH)]^{2+})} \tag{8}$$

$$\Delta pK_a = pK_a(HB^+) - pK_a([L^6Ni_2(SH)]^{2+}) = \log\frac{[HB^+]\cdot\left[[L^6Ni_2S]^+\right]}{[B^+]\cdot[[L^6Ni_2(SH)]^{2+}]} \tag{9}$$

Rearrangement of formula (9) results in expression (10).[238]

$$pK_a([L^6Ni_2(SH)]^{2+}) = pK_a(HB^+) - \log\frac{[HB^+]\cdot\left[[L^6Ni_2S]^+\right]}{[B^+]\cdot[[L^6Ni_2(SH)]^{2+}]} \tag{10}$$

The concentrations of **[$L^6Ni_2(SH)$]$^{2+}$**, **[L^6Ni_2S]$^+$** as well as the concentrations of the protonated and deprotonated proton-sponge® are derived by mass balance.[238] Chemical shifts of the proton sponge® and its protonated form are negligible and will be excluded. Since the concentration of the protonated base [HB^+] at a defined time *t* is equal to the concentration of the deprotonated complex **[L^6Ni_2S]$^+$** at this time, equation (10) can be simplified to (11):

$$\mathrm{p}K_a([\mathrm{L}^6\mathrm{Ni}_2(\mathrm{SH})]^{2+}) = \mathrm{p}K_a(\mathrm{HB}^+) - \log\frac{\left[[\mathrm{L}^6\mathrm{Ni}_2\mathrm{S}]^+\right]_t^2}{[\mathrm{B}^+]_t\cdot[[\mathrm{L}^6\mathrm{Ni}_2(\mathrm{SH})]^{2+}]_t};\ [\mathrm{HB}^+]_t = [[\mathrm{L}^6\mathrm{Ni}_2\mathrm{S}]^+] \quad (11)$$

$$\mathrm{p}K_a([\mathrm{L}^6\mathrm{Ni}_2(\mathrm{SH})]^{2+}) = \mathrm{p}K_a(\mathrm{HB}^+) - \log K \quad (12)$$

Equation (11) can also be rewritten to (12). The equilibrium constant K depends on three different concentrations and is determined by the slope of the plot (**Figure 6.11**)[238] of

$$\frac{[[\mathrm{L}^6\mathrm{Ni}_2\mathrm{S}]^+]_t^2}{[[\mathrm{L}^6\mathrm{Ni}_2(\mathrm{SH})]^{2+}]_t}\ vs.\, [\mathrm{B}^+]_t\,.$$

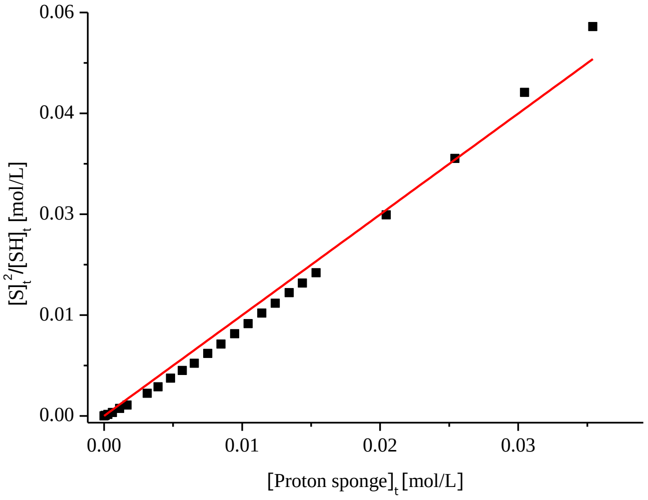

Figure 6.11: $[S]^2_t/[SH]_t$ *vs.* [Proton-sponge®]$_t$ plot. The slope of the linear fit is 1.58±0.22 and equal to *K*.

A *K* value of 1.58±0.22 is graphically determined by the slope of the plot in **Figure 6.11**. Under consideration of the literature known pK_a value of the protonated proton-sponge®[237] a p*K*a value of 18.42±0.06 is calculated according to (13).

$$\mathrm{p}K_a([\mathrm{L}^6\mathrm{Ni}_2(\mathrm{SH})]^{2+}) = 18.62 - \log 1.58 = 18.42 \pm 0.06 \quad (13)$$

The curvature of the plot in **Figure 6.11** leads to the conclusion that the determined pK_a value does not represent only the pK_a of **$[L^6Ni_2(SH)]^{2+}$**. It is more likely that the pK_a value is the average of the pK_a value of a supramolecular encounter complex (see **subchapter 6.3.5**), which has also a pK_a value and the pK_a value of **$[L^6Ni_2(SH)]^{2+}$**. The calculated p*K*a value of 18.42±0.06 will be further used as pK_a value of **$[L^6Ni_2(SH)]^{2+}$**, in a first approximation, since no discrimination between both pK_a values is possible. The reliability of this value is confirmed by an NMR titration experiment, using $HNEt_3OTf$ (pK_a[237] = 18.82 in MeCN). After addition of more than 6 equiv. a conversion of the sulfido complex to the hydrosulfido complex is observed (**chapter 9**). These results indicate similar pK_a values of both systems, and only an excess of HNEt$_3$OTf leads to protonation of **[L^{6}Ni$_2$S]PF$_6$** (**chapter 9**). The titration of **[L^{6}Ni$_2$S]PF$_6$** by 2,6-lutidinium triflate (pK_a[137] = 14.4 in MeCN) is followed by UV-vis spectroscopy (**Figure 6.12**) and ^{1}H NMR spectroscopy (**Figure 6.13**) and a K value of 5.4 is obtained. Determination of K is achieved by analysis of the UV-vis spectra by the program *spec fit*. This value also confirmed the region of the pK_a around 19.5. 2,6-Lutidinium triflate is a too strong acid and the ΔpK_a is too large for the determination of a precise pK_a value of **[L^{6}Ni$_2$(SH)](PF$_6$)(OTf)**. In addition, the UV-vis spectrum of the titration experiment did not show any isosbestic point, which supports the formation of an intermediate (**chapter 6.3.4**).

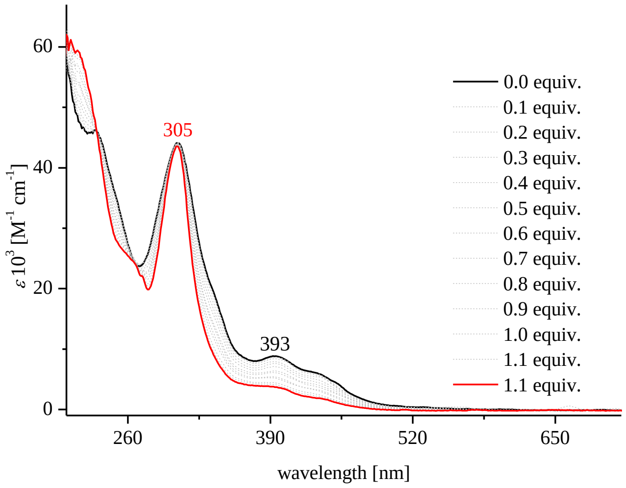

Figure 6.12: UV-vis spectrum of the titration of **[L^{6}Ni$_2$S]PF$_6$** by 2,6-lutidinium triflate in aliquots of 0.1 equiv.

The control experiments confirm that the determined pK_a value of 18.42±0.06 in MeCN is reasonable. pK_a values of mononuclear nickel(II) arylthiolato complexes are reported between 15.1-15.8[230] and the pK_a of complex **XVII** is 16.0 in MeCN (**Figure 6.13**).[220] In contrast to this, pK_a values of the S–H group in (Cp*)Mo$_2$S$_4$ clusters (*e.g.* **XV**) are found between 4.9 to 10.4.[232] Unfortunately, the pK_a values of many organic thiols are determined in the gas phase or in aqueous medium.[223] The pK_a value of thiophenol is 10.3 in DMSO.[223]

In **chapter 7** the pK_a value is used to determine the BDFE$_{\text{(solv.)}}$ of the S–H bond of **[L^{6}Ni$_2$(SH)](PF$_6$)(OTf)** by a square scheme.

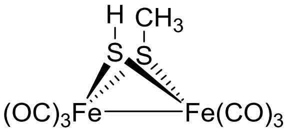

XVII

pK_a = 16

Figure 6.13: complex **XVII** and its pK_a value.

6.3.4 Proton transfer self-exchange rates

To gain further insight in the protonation reaction and to get a better understanding of the mechanism, further ^{1}H NMR spectroscopic titration experiments were performed. The ^{1}H NMR spectra of **[L^{6}Ni$_2$S]PF$_6$**, after titration with 2,6-lutidinium triflate at 298 K, show a linear trend for the chemical shift of the pyrazolate resonance, according to the amount of used acid (**Figure 6.14** and **6.15 (a)**). After addition of 0.8 equiv. of acid, the shift of the pyrazolate H resonance did not change any further. 1.0 equiv. of acid is not necessary, probably due to experimental errors. Furthermore, only one set of the ligand resonances is observed during the protonation experiment, which indicates rapid proton transfer self-exchange on the NMR time scale.[239] Since only one set of proton resonances for the two species is observed, the rate of intermolecular proton transfer (PT) cannot be determined accurately.[239] The self-exchange rate between **[L^{6}Ni$_2$S]$^+$** and **[L^{6}Ni$_2$(SH)]$^{2+}$** has to be at least the same rate or higher as the rate constant to achieve coalescence.[239] k_{obs} is derived by formula (14)[67] from the H$^{\mathrm{pz}}$ peak separation of the two complexes.

$$k_{obs} = \frac{\pi \cdot \delta \cdot \nu}{\sqrt{2}} \tag{14}$$

$$k = \frac{k_{obs}}{[\mathrm{complex}]} \tag{15}$$

A first-order rate constant of $k_{\mathrm{obs}} = 204.3\ \mathrm{s}^{-1}$ is calculated for the proton self-exchange rate at 298 K in MeCN-d_3. With a complex concentration of 17.9 mM the second-order rate constant $1.1 \cdot 10^4\ \mathrm{M}^{-1} \cdot \mathrm{s}^{-1}$ is obtained (15), which represents the lower limit of the H$^+$ exchange rate. This exchange rate is in the same range of PT self-exchange rates of synthetic [2Fe–2S] complexes reported by Mayer *et al.*[239], which are assumed as model complexes for Rieske and mitoNEET clusters. Comparison of the *k* values for the *in situ* observed PT exchange reaction in the presence of 2,6-lutidine, with the exchange rate obtained in the absence of base, shows the same values within the error range. A 2,6-lutidine assisted proton self-exchange is thus excluded.

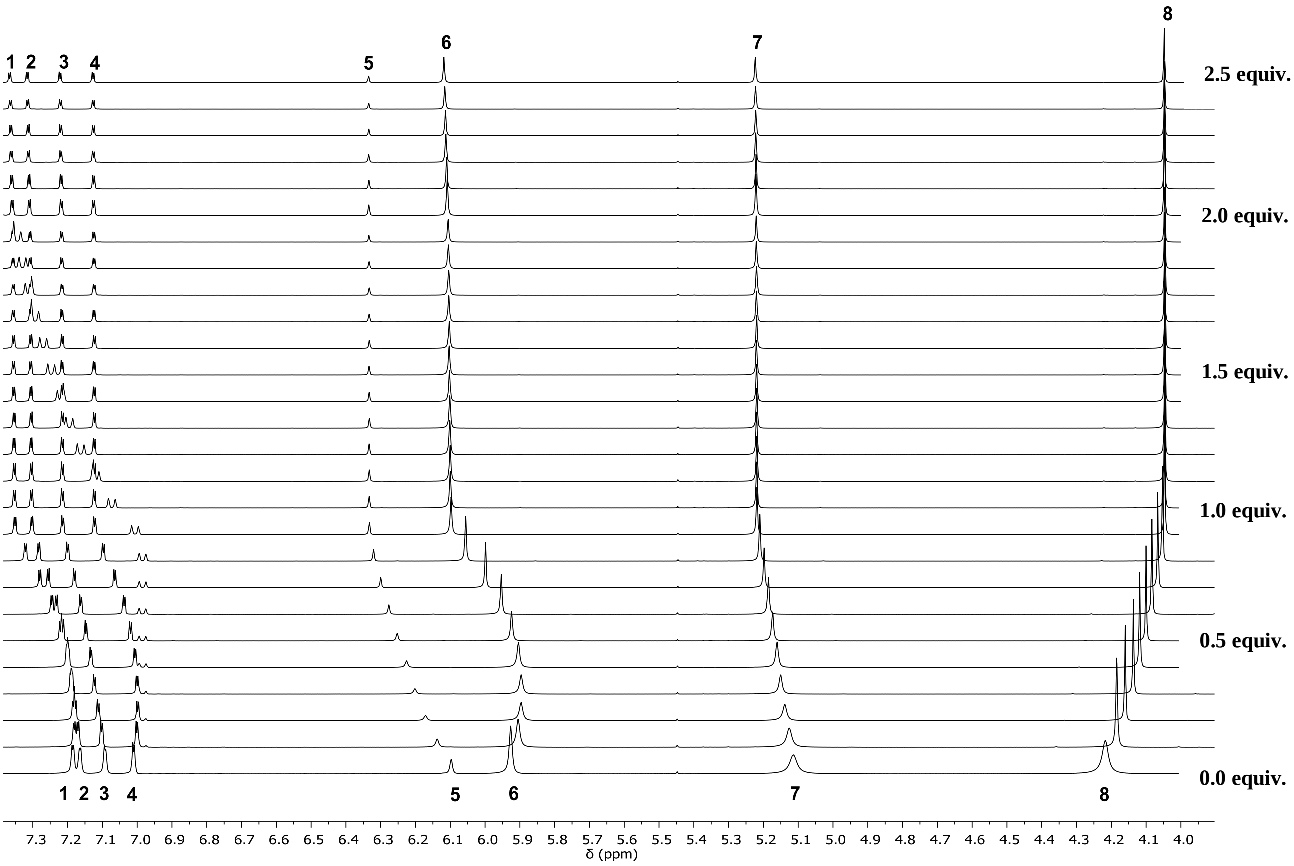

Figure 6.14: ^{1}H NMR titration experiments of **[Ni_2SL^6]PF_6** with 2,6-lutidinium triflate. Addition of 0.1 equiv. acid per spectrum.

This reaction is repeated at two further temperatures (233 K and 253 K) to determine the influence of the temperature on the exchange rate (**Figure 6.15 (b)** and for NMR spectra see **appendix**). A non-linear correlation between the chemical shift of the pyrazolate proton resonance and the amount of added acid is observed at lower temperature (**Figure 6.1 (b)**). The decrease of the temperature results as expected in a decrease of the PT exchange rate (**Table 6.4**). The parameters $\Delta H^{\ddagger}$ and $\Delta S^{\ddagger}$ as well as E_a are determined by an Eyring plot and an Arrhenius plot (**Figure 6.16**). Since no accurate determination of the rate constants is possible, also the kinetic parameters represent just a rough estimation (**Table 6.5**). For the proton self-exchange reaction at 298 K, a $\Delta G^{\ddagger}_{298\,K}$ of $49.79\,kJ \cdot mol^{-1} \pm 2.21\,kJ \cdot mol^{-1}$ is calculated. Mayer *et al.*[240] reported a value of $\Delta G^{\ddagger}_{298\,K} = 37.66\,kJ \cdot mol^{-1}$ for the proton self-exchange reaction at NH groups in Fe^{III}(Hbim).

Table 6.4: Determined k_{obs} and k values for the PT self-exchange reaction at 298 K, 253 K and 233 K.

T [K]	k_{obs} [s^{-1}]	k 10^4 [$M^{-1} \cdot s^{-1}$]
298	209.3	1.17
253	188.9	1.06
233	186.8	1.04

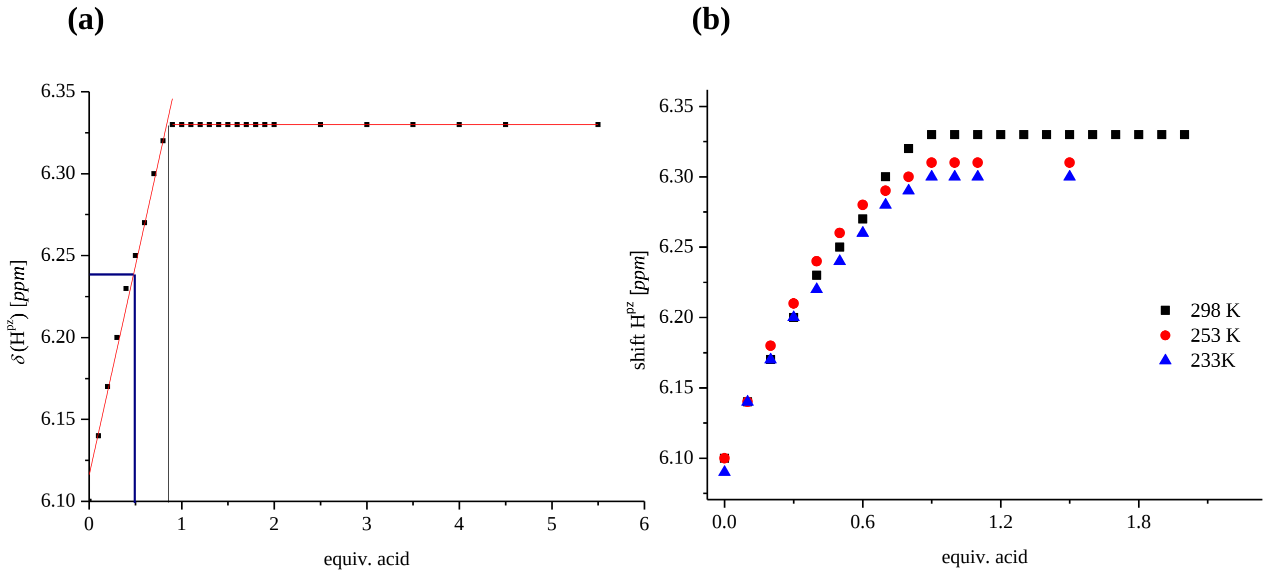

Figure 6.15: (**a**) Linear fit of the $\delta(\mathrm{H}^{\mathrm{pz}})$ *vs.* equiv. (2,6-lutidinium triflate) plot at 298 K. Blue line shows the correlation between $\delta(\mathrm{H}^{\mathrm{pz}})$ of the crystalized encounter complex (see section **6.3.5**) and the number of protons between the two subunits. (**b**) Comparison of the $\delta(\mathrm{H}^{\mathrm{pz}})$ *vs.* equivalents of acid plot at 298 K, 253 K and 233 K.

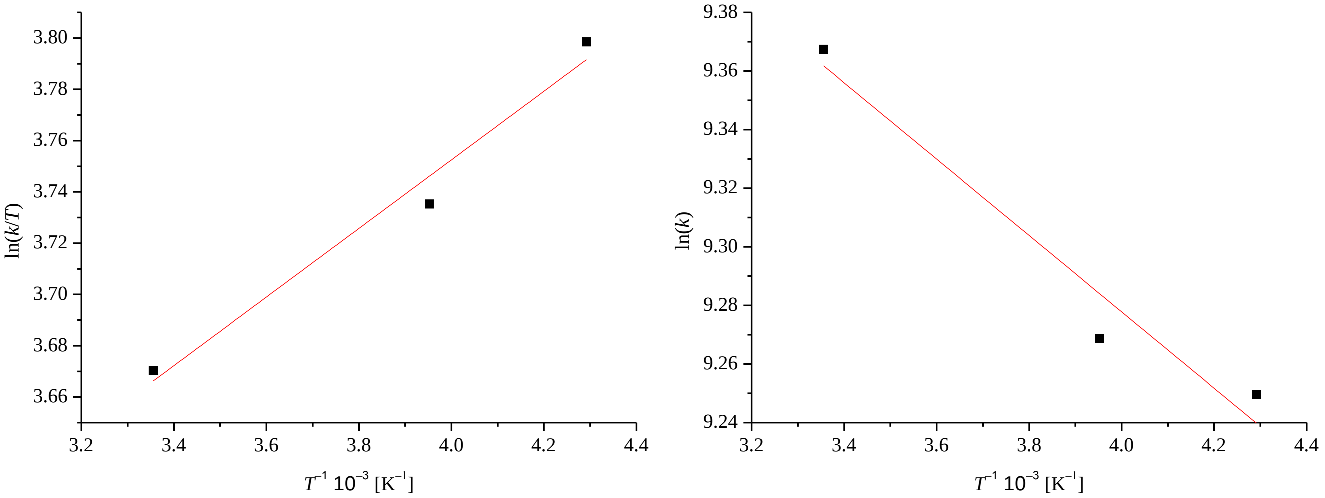

Figure 6.16: **Left**: Eyring plot ($R^2 = 0.9553$), **right**: Arrhenius plot ($R^2 = 0.9091$) of the PT self-exchange reaction at 298 K, 253 K and 233 K.

Table 6.5: Obtained thermodynamic parameters for the PT self-exchange reaction.

	PT self-exchange
$\Delta H^{\ddagger}$ [kJ·mol^{-1}]	–1.11±0.05
$\Delta S^{\ddagger}$ [J·mol^{-1}·K^{-1}]	–170.80±7.6
$\Delta G^{\ddagger}_{298\ \mathrm{K}}$ [kJ·mol^{-1}]	49.79±2.21
E_a [kJ·mol^{-1}]	1.08±0.10

6.3.5 A supramolecular encounter complex $[(L^6)_2Ni_4(SHS)](PF_6)_3$

The titration experiment with 2,6-lutidinium triflate shows no isosbestic point in the UV-vis spectra, which suggests the formation of an intermediate during the conversion from $\mathbf{[L^6Ni_2S]^+}$ to $\mathbf{[L^6Ni_2(SH)]^{2+}}$ (**Figure 6.12**). In addition, the ^{1}H NMR titration experiments of $\mathbf{[L^6Ni_2S]^+}$ with 2,6-lutidinium triflate show a non-linear variation of the CH_2 groups H^6 and the imidazol-*2*-ylidene protons $H^{1\text{-}4}$. Repetition of this experiment at 253 K and 233 K leads to the same findings (**appendix**). This observation motivates to further investigate this reaction and to characterize the formed intermediate. The hypothesis of the existence of an intermediate is further supported by the reaction shown in **Scheme 6.2**.

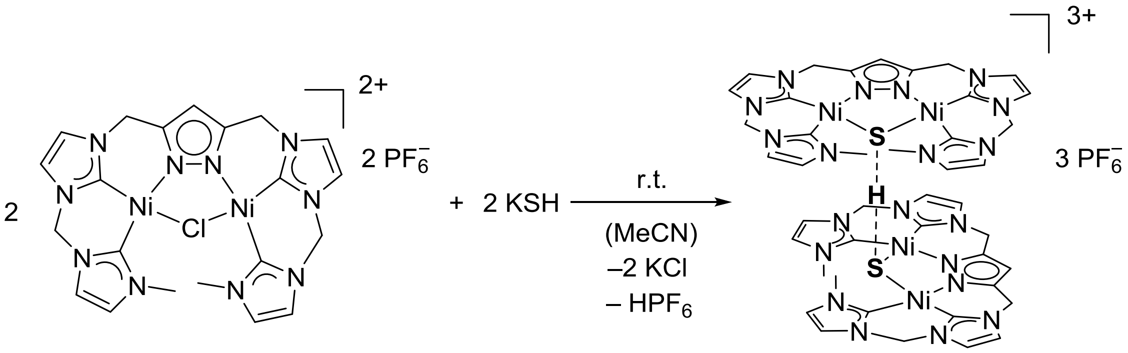

Scheme 6.2: Synthesis of $\mathbf{[(L^6)_2Ni_4(SHS)](PF_6)_3}$ by salt metathesis of $\mathbf{[L^6Ni_2Cl](PF_6)_2}$ with KSH.

After reaction of $\mathbf{[L^6Ni_2Cl](PF_6)_2}$ with potassium hydrosulfide (**Scheme 6.2**) and work-up of the reaction mixture (experimental section) red-orange crystals are obtained, suitable for X-ray diffraction. Two complexes are co-crystallized in the space group $P2_1/n$. The molecular structure in solid state (**Figure 6.17**) shows two $\mathbf{[L^6Ni_2S]^+}$ complexes which are closely orientated associative with each other, and three hexafluorophosphate counter ions. The two complexes are twisted with respect to each other by approximately 90°. Unfortunately, it is not possible to assign the position of the proton between the two complexes. The S····S distance is 3.76 Å and is too long for a covalent bonding of the two complexes *via* a disulfido bridge, since the van der Waals radius of S is 180 pm and the ionic radius of S^{2-} is 184 pm.[241] In **chapter 8** the molecular structure of a persulfido complex in solid state is described with a S–S distance of 2.13 Å. Nickel····nickel distances are observed between 3.52 Å and 3.47 Å. Pöthig *et al.*[90] described the formation of a similar capsoplex by titration of halide ions to a macrocyclic complex **V** (**chapter 3**). The halides are interacting with the metal centers and are centered in a tennis ball like shape (**chapter 3**).

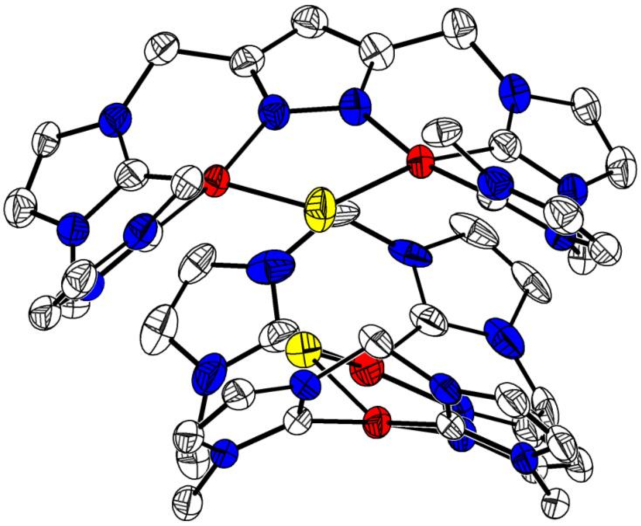

Figure 6.17: Molecular structure (30% probability thermal ellipsoids) of the cationic part of $\mathbf{[(L^6)_2Ni_4(SHS)](PF_6)_3}$. H atoms are omitted for clarity.

The ^1H NMR spectrum of $\mathbf{[(L^6)_2Ni_4(SHS)](PF_6)_3}$ confirms the existence of one proton within the encounter complex with a chemical shift at 1.00 ppm (**Figure 6.18**) in MeCN-*d*$_3$. The integral ratio between the pyrazolate proton resonances of the two subunits and the proton resonance of S···H···S is 2:1. In **Figure 6.15 (a)** the intersection point of $\delta(H^{pz})$ = 6.23 ppm of $\mathbf{[(L^6)_2Ni_4(SHS)](PF_6)_3}$ with the linear fit of the titration experiment is depicted (– – –). A 1:0.48 ratio between $\mathbf{[L^6Ni_2S]PF_6}$ and H^+ is graphically determined. The conversion of $\mathbf{[(L^6)_2Ni_4(SHS)](PF_6)_3}$ to $\mathbf{[L^6Ni_2S]PF_6}$ by addition of 0.5 equiv. of DBU (pK_a[237] = 24.34 in MeCN) to the encounter complex is successfully monitored by ^1H NMR spectroscopy and supported by ESI-MS analysis of the product.

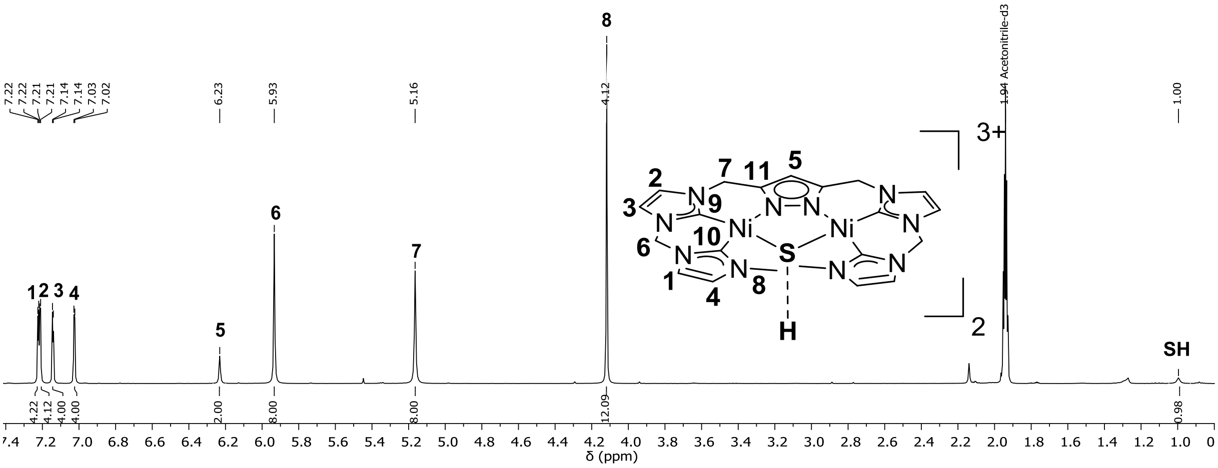

Figure 6.18: ^1H NMR spectrum of $\mathbf{[(L^6)_2Ni_4(SHS)](PF_6)_3}$ in MeCN-*d*$_3$ at 400 MHz and 298 K. A chemical shift of the SH proton resonance is assigned to a signal at 1.00 ppm.

The UV-vis spectrum of crystalline material of **[(L^6)$_2$Ni$_4$(SHS)](PF$_6$)$_3$** dissolved in MeCN fits with the UV-vis spectrum of the titration experiment after addition of 0.48 equiv. of acid ($\Delta\varepsilon_{394\text{nm}} = 1.0 \cdot 10^3$ M$^{-1}\cdot$cm^{-1}) (**Figure 6.19** (**a**)). VT UV-vis spectra of **[(L^6)$_2$Ni$_4$(SHS)](PF$_6$)$_3$** show an increase of the extinction coefficient of all bands by decreasing the temperature. In addition, a shift of the band at 396 nm (80 °C) to 392 nm (–40 °C, $\Delta\varepsilon = 2.8 \cdot 10^3$ M$^{-1}\cdot$cm^{-1}) and from 307 nm to 305 nm is observed ($\Delta\varepsilon = 11.7 \cdot 10^3$ M$^{-1}\cdot$cm^{-1}) (**Figure 6.19** (**b**)). The UV-vis spectrum of the complex in solid state differs from the spectra in solution. A discrimination from the spectra of **[L^{6}Ni$_2$S]PF$_6$** or **[L^{6}Ni$_2$(SH)](PF$_6$)(OTf)** in solid state is possible. An additional broad band at around 483 nm is observed (**Figure 6.19** (**c**)). The interaction between the two complexes is described as a weak interaction. At low concentrations like in the UV-vis solution, the host-guest complex largely dissociates into **[L^{6}Ni$_2$S]$^+$** and **[L^{6}Ni$_2$(SH)]$^{2+}$** and a spectrum similar to **[L^{6}Ni$_2$S]$^+$** is observed, but with just half of the extinction coefficient of **[L^{6}Ni$_2$S]$^+$** in agreement with the UV-vis data after addition of 0.5 equiv. of 2,6–lutidinium triflate to **[L^{6}Ni$_2$S]$^+$**.

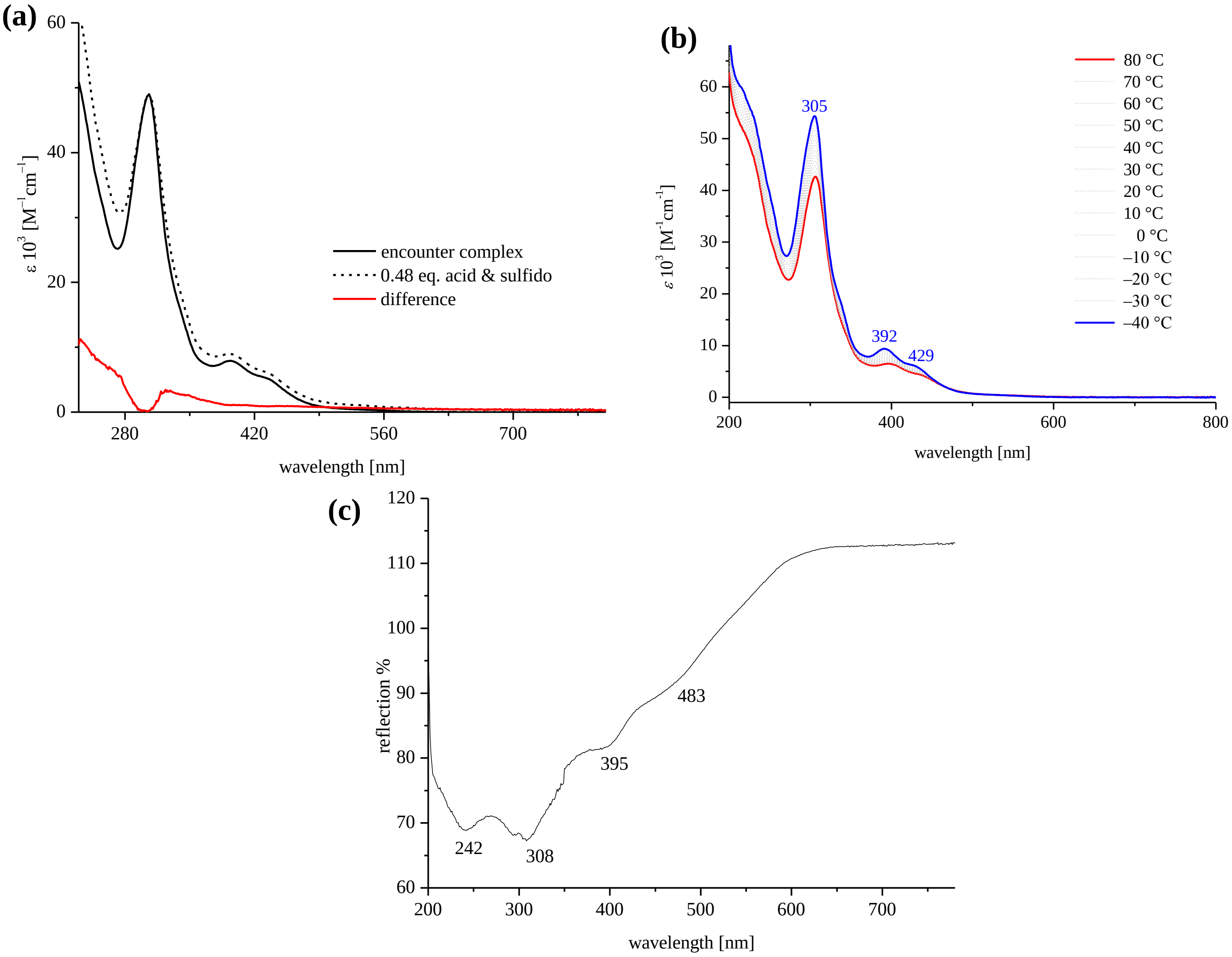

Figure 6.19: (**a**) Comparison of the UV-vis spectra of the encounter complex with **[(L^6)$_2$Ni$_4$(SHS)](PF$_6$)$_3$** after addition of 0.48 equiv. in MeCN at 20 °C. (**b**) VT UV-vis spectrum of **[(L^6)$_2$Ni$_4$(SHS)](PF$_6$)$_3$** in the temperature range of 80 °C to –40 °C in MeCN. (**c**) UV-vis spectrum of **[(L^6)$_2$Ni$_4$(SHS)](PF$_6$)$_3$** in solid state.

VT ^{1}H NMR spectra of **$[(L^6)_2Ni_4(SHS)](PF_6)_3$** in MeCN-$d_3$ show a diastereotopic splitting of the CH_2 groups H^6 and H^7 below 273 K and a pronounced low-field shift of $\Delta\delta$(SH) = 0.79 ppm of the SH proton resonance from 1.05 ppm (293 K) to 1.84 ppm (243 K) (**Figure 6.19**). **$[L^6Ni_2(SH)](PF_6)(OTf)$** shows only a high-field shift of the SH proton resonance of $\Delta\delta$(SH) = 0.09 ppm for the same temperature range. In the temperature range from 253 K to 233 K, the formation of a second conformer of **$[(L^6)_2Ni_4(SHS)](PF_6)_3$** is observed (**Figure 6.20**). In **chapter 5** the interconversion of the two conformers of **$[L^6Ni_2S]PF_6$** is observed at temperatures below 283 K. The observation of the second conformer of **$[(L^6)_2Ni_4(SHS)](PF_6)_3$** occurs more than 20 K lower than in the sulfido-bridged complex, as a possible consequence of the spatial approach of two complexes.

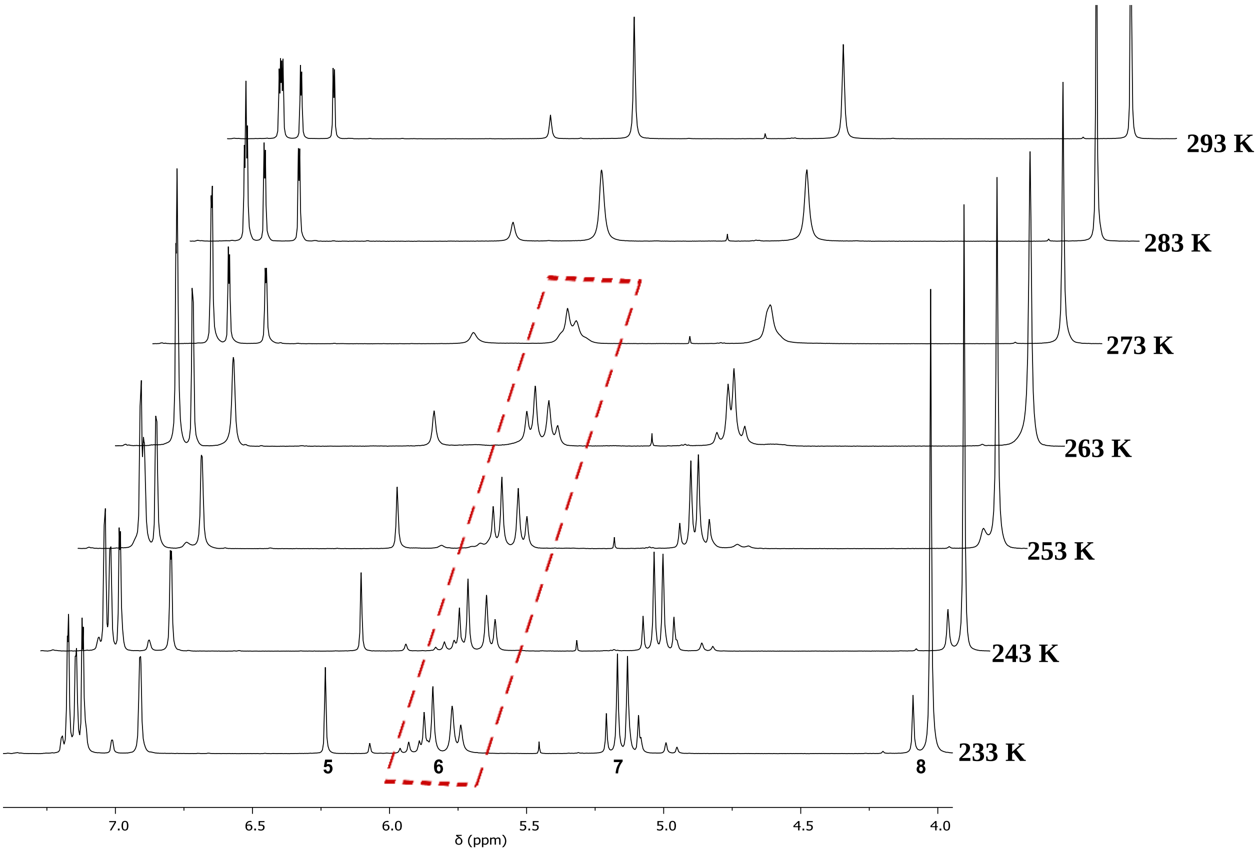

Figure 6.20: VT ^{1}H NMR spectra of **$[(L^6)_2Ni_4(SHS)](PF_6)_3$** in MeCN-$d_3$ between 293 K and 233 K at 400 MHz. Labeling highlights the diastereotopic splitting of the proton resonances H^6 of the CH_2 groups (– – –).

A comparison of all three complexes, **$[L^6Ni_2(SH)](PF_6)(OTf)$**, **$[(L^6)_2Ni_4(SHS)](PF_6)_3$** and **$[L^6Ni_2S]PF_6$** at 233 K underlines the differences (**Figure 6.21**). The largest peak separations of the CH_2 groups H^6 and H^7 are observed in **$[(L^6)_2Ni_4(SHS)](PF_6)_3$**, whereas **$[L^6Ni_2(SH)](PF_6)(OTf)$** does not show any diastereotopic splitting of the CH_2 groups. An especially large $\Delta\upsilon$ = 38.7 Hz is observed for the AB spin system of the CH_2 group H^6 in **$[(L^6)_2Ni_4(SHS)](PF_6)_3$** (– – –), which is more than double the peak separation in **$[L^6Ni_2S]PF_6$**

with Δυ = 16.7 Hz and indicates different chemical environments of the two protons. This findings support the existence of the encounter complex $\mathbf{[(L^6)_2Ni_4(SHS)](PF_6)_3}$. A similar Δυ is also observed during the titration experiment of $\mathbf{[L^6Ni_2S]PF_6}$ with 0.5 equiv. of acid (Δυ = 43.7 Hz) at 233 K.

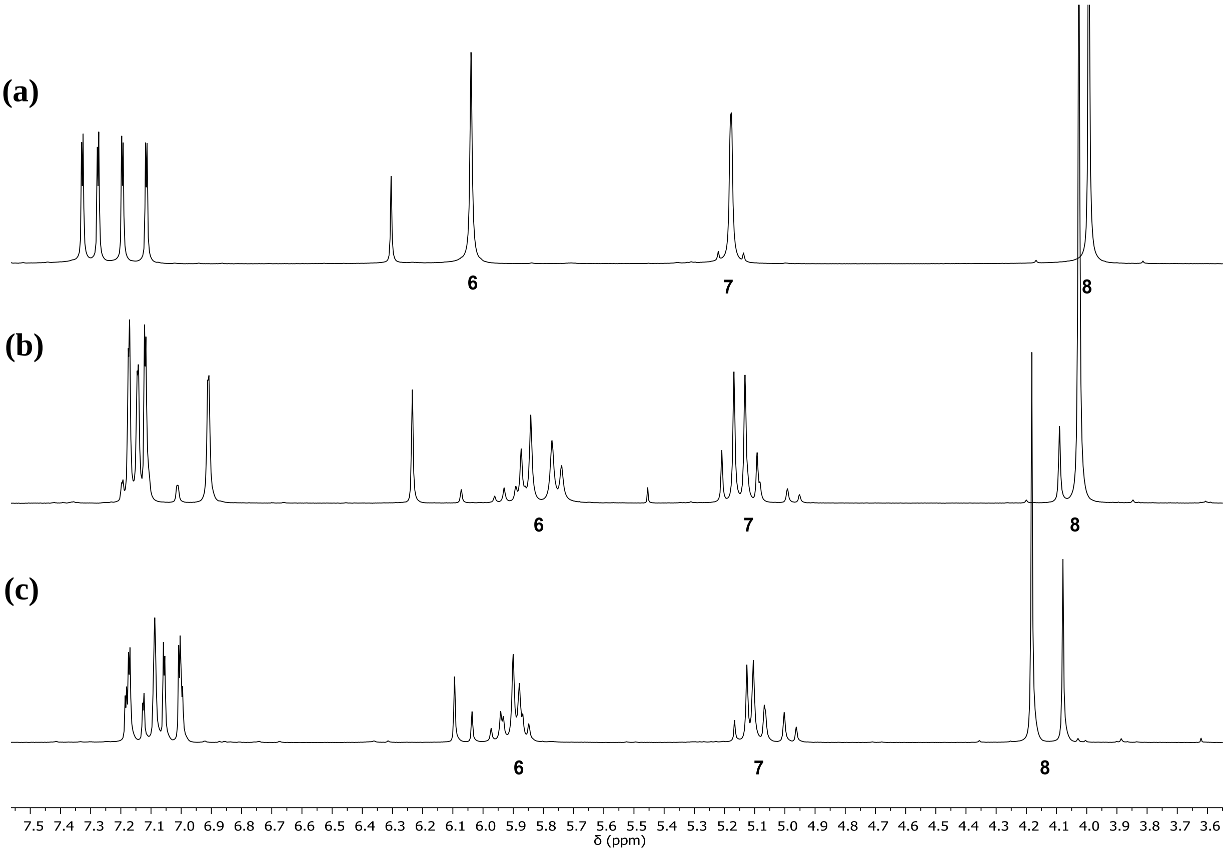

Figure 6.21: Comparison of ^{1}H NMR spectra of (**a**) $\mathbf{[L^6Ni_2(SH)](PF_6)(OTf)}$, (**b**) $\mathbf{[(L^6)_2Ni_4(SHS)](PF_6)_3}$ and (**c**) $\mathbf{[L^6Ni_2S](PF_6)}$ at 233 K in MeCN-d_3 at 400 MHz.

A detailed analysis of the crystalized complex $\mathbf{[(L^6)_2Ni_4(SHS)](PF_6)_3}$ and comparison of the spectroscopic data for the intermediate observed during titration experiments confirm this species as an encounter complex. The conversion of $\mathbf{[L^6Ni_2S]PF_6}$ to $\mathbf{[L^6Ni_2(SH)](PF_6)(OTf)}$ or *vice versa* occurs *via* an encounter complex $\mathbf{[(L^6)_2Ni_4(SHS)]^{3+}}$, which can also be described as an host-guest complex in which one proton is located in between two sulfido-bridged dinickel(II) complexes (**Scheme 6.2**). It is confirmed by several experiments that the interconversion of all three species occurs upon (de-)protonation reactions. Even though the non-linear variation, which is obtained during titration experiments and the VT NMR experiments as well as the UV-vis spectra, underlines the existence of the encounter complex, it is not possible to confirm such a supramolecular complex by ^{1}H DOSY NMR spectroscopy at different temperatures. A reason for this can be a fast dynamics between the individual compounds and the encounter complex, which is below the NMR instrument timescale.

6.4 Conclusion and Outlook

In this chapter the successful transformation of **$[L^6Ni_2S]PF_6$** to **$[L^6Ni_2(SH)](PF_6)(OTf)$** by protonation with 2,6-lutidinium triflate is demonstrated. Also, the deprotonation reaction of **$[L^6Ni_2(SH)](PF_6)(OTf)$** with proton-sponge® is possible. Titration experiments of the deprotonation reaction of **$[L^6Ni_2(SH)](PF_6)(OTf)$** with proton-sponge® as a base, monitored by ^{1}H NMR spectroscopy, allow the determination of the p*K*a value of 18.42±0.06 for **$[L^6Ni_2(SH)](PF_6)(OTf)$** in MeCN, which will allow to determine the $BDFE_{(solv.)}$ of the S–H bond by a square scheme in **chapter 7**. To gain further information about the interconversion of **$[L^6Ni_2S]PF_6$** and **$[L^6Ni_2(SH)](PF_6)(OTf)$**, UV-vis and NMR experiments have been conducted and confirm the existence of an intermediate, which is passed during the (de-)protonation reaction. The molecular structure in solid state confirms a supramolecular encounter complex **$[(L^6)_2Ni_4(SHS)](PF_6)_3$**, wherein the proton is encapsulated by two complex molecules. Furthermore, it is shown that deprotonation of this capsoplex by 0.5 equiv. DBU leads to the formation of **$[L^6Ni_2S]PF_6$**. The conversion of the encounter complex to the *μ*-SH complex is also successful (**Scheme 6.3**). The PT self-exchange rate between **$[L^6Ni_2(SH)]^{2+}$** and **$[L^6Ni_2S]^+$** is ~10^4 $M^{-1}\cdot s^{-1}$. With this portfolio of dinickel(II) complexes in hand, the reactivity with respect to hydrogen atom transfer reactions (HAT), oxidation chemistry of **$[L^6Ni_2S]PF_6$** as well as electrochemical proton reduction processes will be further investigated in the following chapters.

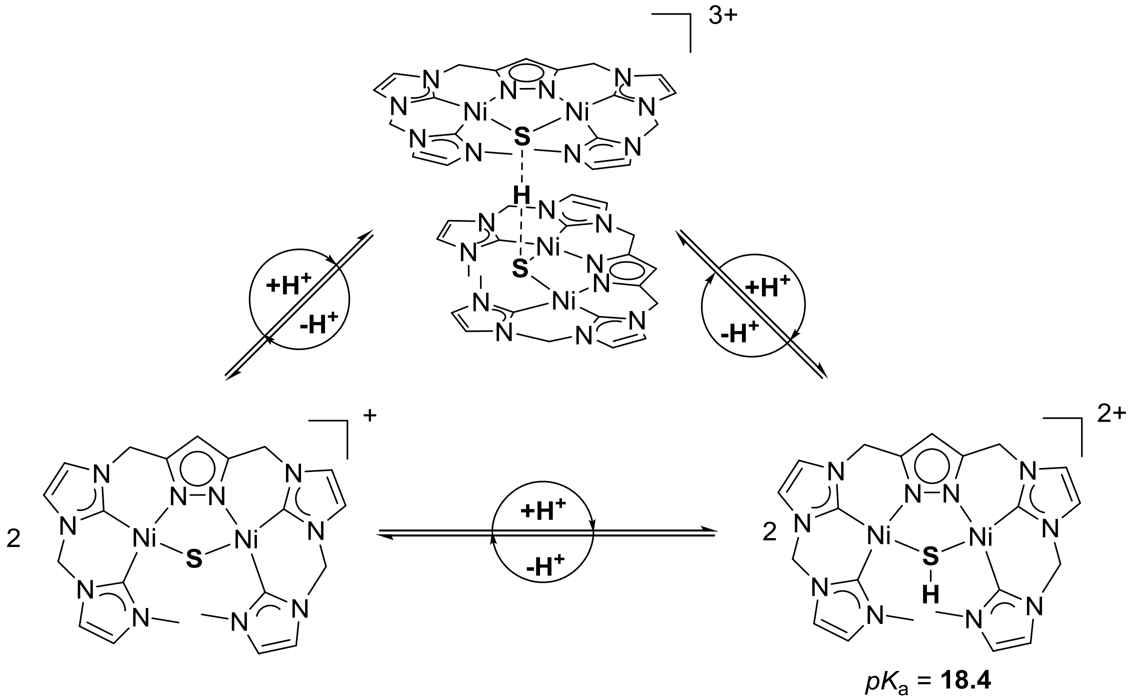

Scheme 6.3: Interconversion of **$[L^6Ni_2S]^+$** and **$[L^6Ni_2(SH)]^{2+}$** *via* **$[(L^6)_2Ni_4(SHS)]^{3+}$**.

7

A unique dinickel μ-thiyl radical complex – $Ni^{III}Ni^{II}$-μ-S *vs.* $Ni^{II}Ni^{II}$-μ-S·

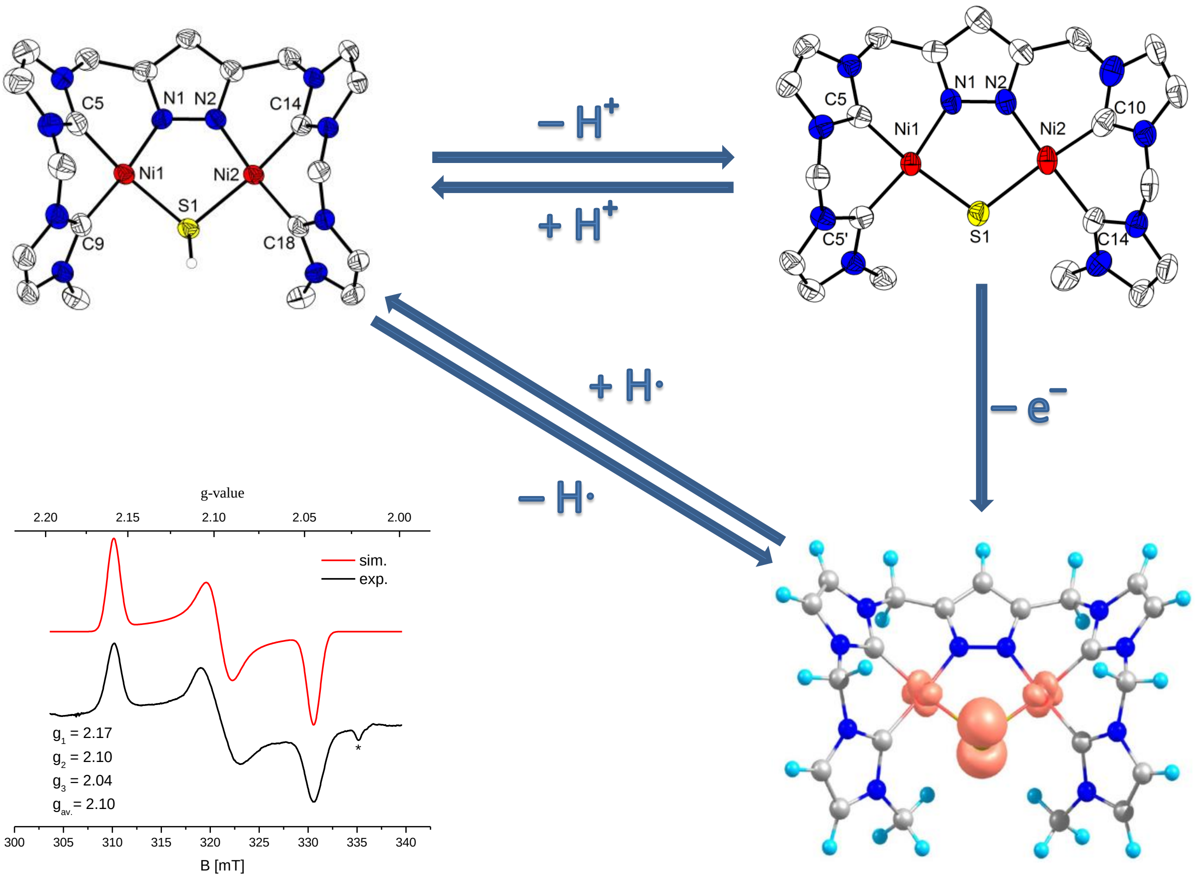

Abstract: Thiyl radicals play an important role in nature. Protein-derived radicals are essential in metabolism, DNA biosynthesis, prostaglandin biosynthesis or acetyl-coenzyme A production. They are also used in stoichiometric and catalytic reactions as well as in near-infrared chromophores in dyes. The monitoring of most thiyl radicals is challenging due to their temperature instability and their tendency towards dimerization. The reactivity and characteristics of thiyl radicals bridged between two metal centers is mainly unexplored. Here the first pyrazolate-bridged dinickel complex which bears a thiyl radical between the two nickel centers is presented. The location of the electron in the singly occupied S(p_z) orbital is supported by EPR spectroscopy and DFT calculations and, reactivity studies of HAT processes of this complex with organic substrates have been studied, based on the $BDFE_{(solv.)}$ values of the reaction partners.

7.1 Introduction

7.1.1 Relevance of thiyl radicals

In nature, radicals play an important role. Protein-derived radicals are essential in metabolism, DNA biosynthesis, prostaglandin biosynthesis or acetyl-coenzyme A production.[242–245] Thiyl radicals are an important actor in biology, especially in enzyme catalyzed processes like in those processes of the three known classes of ribonucleotide reductase (RNR).[246,247] The main function of RNR is the production of DNA building blocks. The enzyme catalyzes the reduction of nucleotides (CDP, GDP, UDP, ADP) into their deoxynucleotides, whereby the carbon bound hydroxyl group at C–2' is replaced by hydrogen.[247–251] This key step is the bottleneck reaction in *de novo* DNA synthesis in all living organisms.[247,249,252] All classes of RNR are associated to metallo-cofactors, which are able to form tyrosyl- (Class I), 5'-deoxyadenosyl- (Class II) or glycyl-radicals (Class III). These radicals are not able to catalyze the reduction of ribonucleotides by themselves[243,252] and primary act as an initiator to generate a thiyl radical. The thiyl radical has the power to trigger the reduction process of nucleotides. In *E. coli* (Class Ia), the distance between the cysteine (C_{439}) and the diferric-tyrosyl radical cofactor is more than 35 Å[253,254] and the generation of the thiyl radical occurs *via* sequential proton-coupled electron transfer (PCET) events.[249,255,264–266,256–263] Lassmann *et al.*[246] presented the direct detection of R–S· in a R1 protein from *E.coli*, which is a representative of class Ia RNR proteins.

In a first step of the mechanism of deoxynucleotide synthesis (**Scheme 7.1**), the thiyl radical abstracts the 3'-hydrogen atom from the nucleotide, forming a thiol and a substrate radical. This step facilitates the protonation of the 2'-hydroxido group under release of water and the formation of an intermediate (3). This intermediate is reduced to the 3'-keto-deoxynucleotide under formation of a disulfide anion radical (subsulfide).[224] A 3'-deoxynucleotide radical (5) is formed after a PCET process of the disulfide anion radical and glutamic acid with the keto-deoxynucleotide.[224] The hydrogen atom transfer (HAT) process of the initially formed cysteine S–H to the 3'-deoxynucleotide radical leads to the regeneration of the former thiyl radical along with deoxynucleotide formation.[224,243,252,267–270]

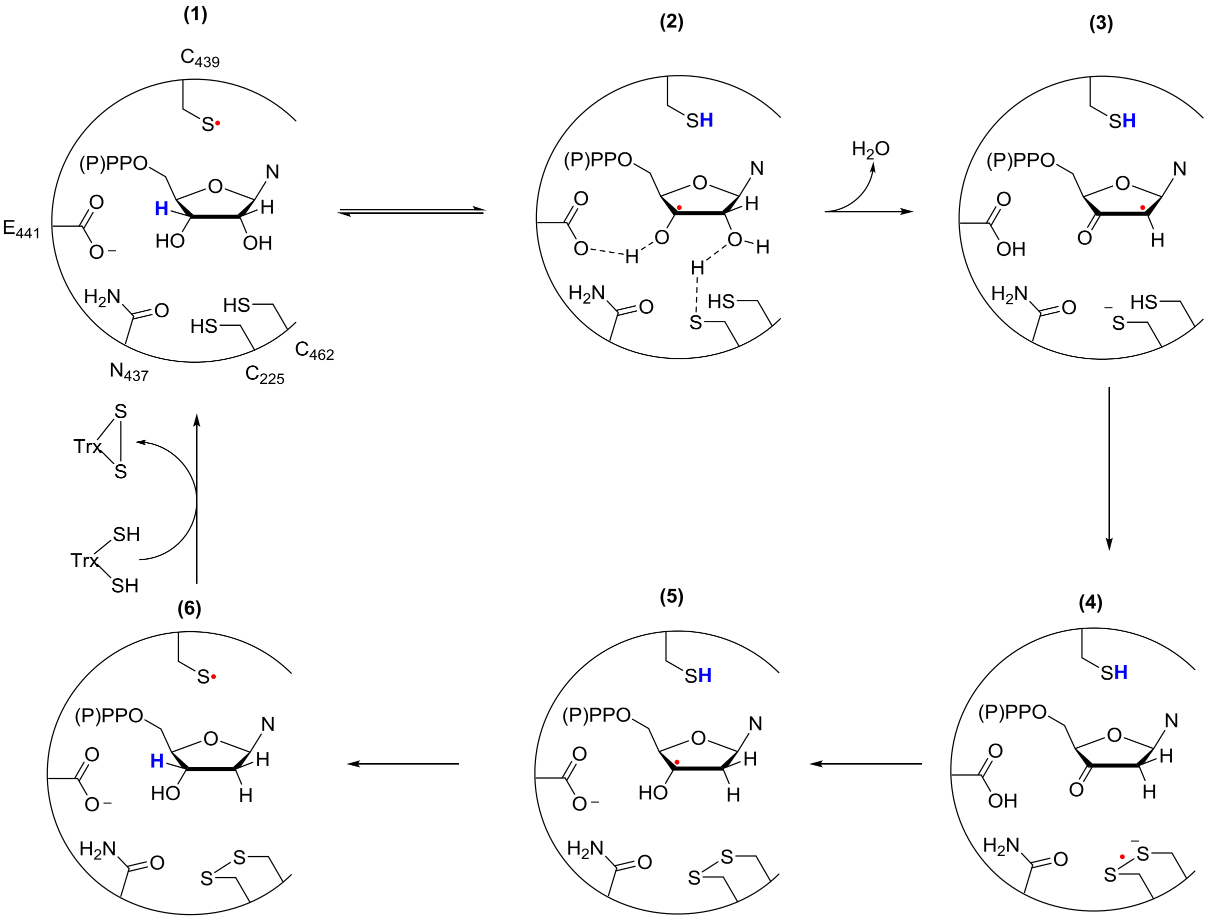

Scheme 7.1: Proposed mechanism for the reduction of nucleotides to deoxynucloetides by *E. coli* (class Ia RNR) according to Stubbe *et al.*[224] Abstraction of 3’-H by initiated thiyl radical (1); protonation of 2’-OH and release of water (2-3), formation of intermediate (3); reduction of intermediate (3), formation of disulfide anion radical (4); PCET process and formation of 3’-deoxynucleotide radical (5); HAT process and formation of deoxynucleotid; redox process and formation of thiyl radical.[224]

In class II RNR from *Lactobacillus leichmannii*, the thiyl radical is formed in a concerted mechanism during homolytic cleavage of the cobalt alkyl bond in adenosylcobalamin under formation of 5’-deoxyadenosine and cob(II)alamin.[243,252] It is possible to detect this radical *via* EPR spectroscopy at Cys–208. The EPR spectrum shows a strong magnetic interaction with the Co^{2+} nucleus ($I = 7/2$).[243,271] Direct evidence for the thiyl radical in class III proteins has remained elusive.

The role or presence of thiyl radicals in [NiFe] hydrogenases is still under investigation and part of ongoing debate. In these proteins the catalytically inactive **Ni–A** and **Ni–B** states of the enzyme show paramagnetic behavior, which has primarily been assigned to the nickel ion in the oxidation state +III, but containing also cysteine thiyl radical character.[272–276] Thiyl radicals are also proposed to be involved in the transport of NO out of red blood cells (RBCs).[277–279] In the first step, S-nitrosylated hemoglobin [SNOHb] is formed. In the next step NO can be transferred to another thiol which is located at the membrane of the RBC *via* a transnitrosylation process.[277,278] The role of thiyl radicals during the reaction of nitrite with deoxyhemoglobin in red blood cells is also under discussion and part of current research.[279] Rifkind *et al.* investigated the reaction of nitrite with deoxyhemoglobin, producing an intermediate with properties of Hb(II)NO^+ and Hb(III)NO and an unexpected stability[280] of these intermediates in the presence of a free thiol group (β93). They proposed equilibrium of these two intermediates with a thiyl radical. It is postulated that thiyl radicals are also involved as intermediates in the synthesis of co-factors, for instance in galactose oxidase, and it is also postulated that they play a role in biosynthesis, e.g. biological sulfur insertion reactions.[281]

In situ generated thiyl radicals also play an important role in catalytic applications for the synthesis of relevant organic molecules. Thiyl radicals as (co)-catalysts have been proposed to be generated *in situ* from phenyldisulfide in photocatalytic reactions, for instance in the photoreductive hydrodifluoroacetamidation of alkanes with Hantzsch ester or in the *anti*-Markovnikov hydroamination of alkenes for the synthesis of phenethylamine derivates.[282,283] Organic thiyl radicals are also used in polarity reversal catalysis.[284–286] In recent years the interest in metal linked thiyl radicals is continuously increasing, and metal thiyl radicals have already been described for applications in catalysis, electrochromic NIR dyes and magnetic materials.[287–291] In 2001, Stiefel *et al.*[288] described the electrochemical and selective reaction of a nickel 1,2-enedithiolate complex **XVIII** with ethene in a multicomponent gas-stream, including H_2S, H_2, CO, H_2O. After oxidation of the nickel thiolate complex, an *in situ* generated thiyl radical selectively attacks ethene under formation of **XIX (Scheme 7.2)**.

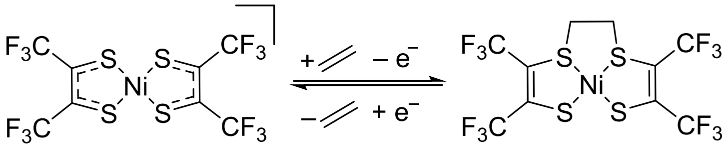

XVIII

XIX

Scheme 7.2: Selective and reversible reaction of complex **XVIII** with ethylene in a multicomponent stream.[288]

This reaction is reversible, after applying a cathodic potential. The anionic nickel complex can be regenerated under release of ethylene. This reversible reaction offers a multitude of possibilities, due to the high tolerance of the complex towards other gases and thus the possibility to purify the very important feedstock ethylene, which is the starting material for the synthesis of several industrially relevant products (alcohols, polymers, esters).

7.1.2 EPR spectroscopy of organic thiyl radicals

Thiyl radicals are postulated in several relevant biological processes. The direct detection of such thiyl radicals is quite challenging, due to its proximity to non-innocent metal ions or its tendency to further react under formation of S–H or S–S bonds. The detection of R–S· is often performed in an indirect way *via* a spin trap.[243,292] The detection of thiyl radicals in proteins can be done after chemical oxidation or by photochemically induced release of NO from nitrosothiols[292] and spin trapping. Lassmann *et al.*[246] confirmed the existence of thiyl radicals of *bovine serum albumin* (BSA) and R1 of *Escherichia coli* RNR by oxidation of the proteins with a Ce^{IV} salt and detecting the EPR signal of a spin trap. Also a limited number of directly detected thiyl radicals are known as well.[246] Based on the intrinsic properties of the thiyl radical and its environment, their spectra can differ significantly, especially the *g*-values. The EPR signal of the thiyl radical will be often indirectly obtained. This is possible by subtraction of the EPR spectra, where the thiol functions are blocked during the irradiation process from the EPR spectra, where the thiyl radical is formed. In the literature, also thiyl radicals of smaller molecular organic compounds are known in frozen solution or in single crystals. They are mainly formed by X-, γ- and UV-irradiation in frozen solution, solid matrices or in single crystals.[292] Neese *et al.*[293] summarized EPR data of organic thiyl radicals known in the literature. EPR parameters of thiyl radicals from proteins and small organic molecules are summarized in **Table 7.1**. The interpretation of some reported EPR spectra is still part of ongoing discussion, since other sulfur radicals can also be formed during irradiation processes. For instance perthiyl, sulfinyl or thiyl peroxyl radicals can be formed and show *g* values closer to the spin only value of the free electron ($g = 2.0023$).[292,294] Those radicals are also proposed to be “thiyl radicals”, raising questions on how EPR spectra of real organic thiyl radicals look like and why it is so challenging to observe this radical. In 2003, Lubitz *et al.*[292] reported an EPR spectrum (**Figure 7.1**) of an almost pure cysteine radical after UV photolysis. In 1987, Symons and coworkers[295] presented EPR spectra of $[S_8\cdot]^+$ in two different conformations and Jenne *et al.*[296] confirmed Simons assignment including the molecular structure in solid state of $[S_8\cdot]^+$. One conformer of $[S_8\cdot]^+$ has a crown conformation ($g_x = 2.069$, $g_y = 2.057$, $g_z = 1.997$, $g_{\text{av.}} = 2.041$) and will be interconverted into the more stable *exo*-*endo* conformation ($g_\text{x} = 2.044$, $g_\text{y} = 2.034$, $g_\text{z} = 2.0035$, $g_\text{av} = 2.027$).[296] In the EPR spectrum a rhombic signal is observed and a strong influence of the environment, here the geometry and the resulting orbital interactions which strongly affects all three *g* values.

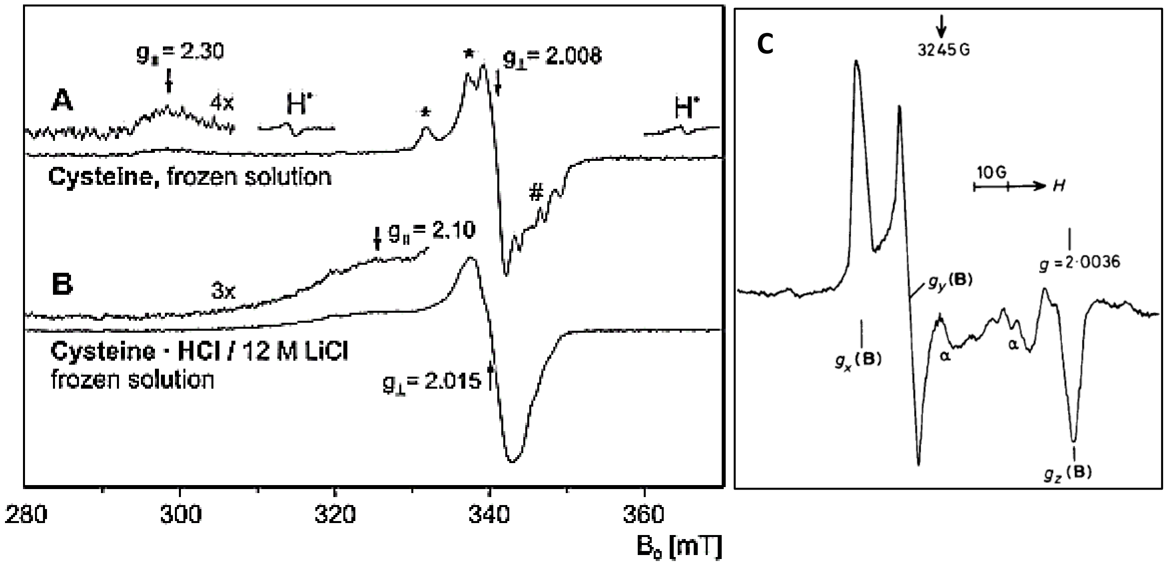

Figure 7.1: EPR spectra of the thiyl radical of **A** cysteine in frozen solution **B** cysteine and 12 M LiCl in frozen solution. **B** The EPR spectrum shows a radical signal with high purity of the cysteine radical. The corresponding g factors for the radical are $g_{\parallel}$ = 2.10 and $g_{\perp}$ = 2.015.[292] © 2003 ROYAL SOCIETY OF CHEMISTRY. **C** EPR spectrum of $[S_8\cdot]^+$with g_x = 2.044, g_y = 2.034, g_z = 2.0035, $g_{av.}$ = 2.027.[295] ©1987 ROYAL SOCIETY OF CHEMISTRY.

The EPR spectra of organic thiyl radicals show large and anisotropic g-factors and broad EPR line widths (**Table 7.1**)[293], which is more reminiscent of EPR spectra of paramagnetic transition metals than expected for a chalcogene radical. The general physical reason for this behavior is the large spin-orbit coupling of the sulfur which results in a fast spin-spin relaxation (short T_2 times) and large anisotropic g factors. Thiyl radicals are strongly influenced by the chemical environment, due to the degeneracy of their p_π orbitals (axial symmetry in the x-y plane). As a result the detection of a rhombic signal of thiyl radicals is only possible by a lift of the degeneracy of those orbitals; the orbit angular momentum is quenched.[294] Hence, this is the reason why thiyl radicals linked with alkyl groups or especially aryl groups are much easier detectable than the corresponding radicals from HS•, since they are able to undergo a *Jahn-Teller* distortion and the p_π orbitals are no longer degenerated. In case of the linked aryl group an interaction of the π orbitals takes place which lifts the degeneracy of the orbitals.[292] The necessity to quench the orbit degeneracy in order to detect an EPR signal leads to the detection of signals which show deviation from axial symmetry. Thiyl radicals show rhombic symmetry in EPR spectra, due to strong environmental interactions. This interaction can occur, for instance by formation of hydrogen bonds with polar, protic solvents.

Table 7.1: Selected EPR data from (bio)-organic thiyl radicals.[293]

Compound, method	*g*-values		
	g_x	g_y	g_z
Cysteine (HCl), Single crystal, e$^-$, 77 K	2.29	1.99	1.99
Cysteine (HCl), Single crystal, UV, 77 K	2.251	2.004	1.985
Cysteine (HCl), Single crystal X, 4 K	2.244	2.001	1.984
Pennicillamine (HCl), Single crystal, X, 4 K	2.297	2.037	1.921
Compound, method	$g_\parallel$		$g_\perp$
BSA, 4 mM, pH 7, 20 mM ascorbate	2.17		2.008
BSA lyophilized	2.16		2.006
Cysteine (HCl), 300 mmM, pH 3, 12 M LiCl, 150 K	2.10		2.015
Cysteine, crystalline powder	2.15		2.011
Cysteine, 300 mM, pH 3	2.30		2.008

Lubitz and coworkers have shown that by addition of lithium chloride to those radicals their properties will be affected by a highly polar isotropic environment, which leads to an increase of the g_z ($g_\perp$) value, whereby the $g_\parallel$ decreases. As already mentioned the properties of the thiyl radicals are strongly depending on their environment, especially their polarity and their connectivity. This observed effect plays a certain role, if thiyl radicals are linked to metal complexes.

7.1.3 EPR spectroscopy of metal-bound thiyl radicals

In literature, mainly thiyl radicals of organic compounds or in proteins are described. In comparison, there is little knowledge regarding the nature of metal thiyl radicals. One reason for the difficulties in characterizing these species is the challenge of the distinction between a metal- or sulfur-based radical. In addition, thiyl radicals are often short living species and strongly temperature sensitive and have the tendency to dimerize very fast to form disulfides, which makes them hard to be detected by EPR spectroscopy.[297–299] Phenyl-thiyl radicals decay at a rate of ca. 10^9 M^{-1} s^{-1}.[300] Since the dimerization occurs also very fast at metal complexes, several authors have described the formation of a disulfide bridge concomitant with the appearance of linked metal complexes which are EPR silent.[297–299] They have proposed the *in situ* generation of metal bound thiyl radicals. Nevertheless, also room temperature stable or longer living thiyl radicals which are bound to metals are detected and received increasing interest, due to their relevance to biological chemistry and their interesting behavior based on their non-innocent ligands.[257,301–306] Due to these interesting properties of redox-active ligands, in general, such complexes are investigated with respect to stoichiometric reactions, catalytical reactions,[288–291,307–312] and as near-infrared chromophores in dyes.[287]

Stubbe *et al.*[243] described a thiyl radical (C_{408}) which interacts with the cobalt nucleus in *L. leichmannii* reductase. A similar interaction between R–S· and metal centers was observed by Sarkar *et al.*[313] They described a dangling thiyl radical which is surprisingly well stabilized by Cu^I ion in a Cu/W complex. Small molecular complexes are also described earlier. In 1990, Darensbourg and Amatore *et al.*[297] presented mono- and dinuclear chromium carbonyl complexes, bearing a thiolate as a ligand (**Figure 7.2** (**a**)). In case of mononuclear complexes oxidation leads to a fast degradation and dimerization of alkylthiyl radicals, while in case of the dinuclear complexes it was possible to detect in the temperature range from –50 °C to –70 °C labile thiyl radical bridged dichromium complexes. Those complexes show rhombic spectra with g_1 and g_2 values which are much larger than the spin only value ($g = 2.0023$), due to spin orbit coupling of S.[297,314] Based on theoretical calculations the unpaired electron is mainly located in the p_z orbital of the sulfur and is antibonding in a π bonding fashion with the Cr d orbitals. This is one rare example, where the thiol/thiyl radical is bridged between two metal centers without linkage to a larger ligand scaffold.

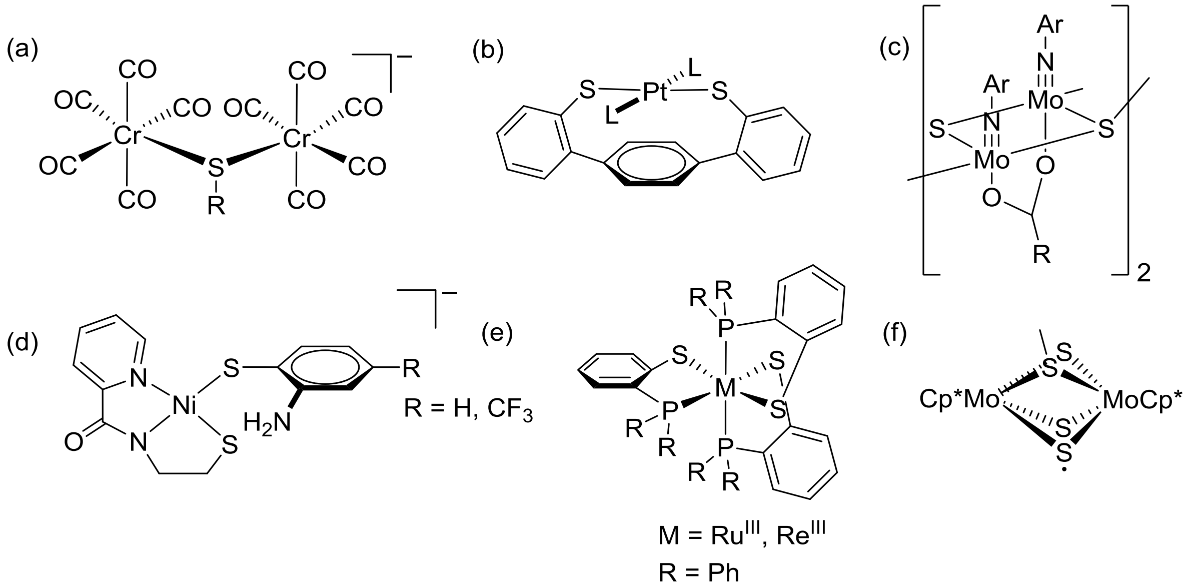

Figure 7.2: Examples of starting compounds, which are forming thiyl radicals. (**a**), (**b**), (**d**), (**f**) are observing directly EPR signals, (**c**) EPR signal of *in situ* generated thiyl radical monitored by spin trap (**e**) is antiferromagnetic coupled due to spin coupling.

In the literature, a series of thiolate complexes are described which are able to generate thiyl radicals, as part of the ligand scaffold. Prominent metal complex representatives which bear directly or indirectly detectable thiyl radicals are known from chromium[297], manganese[306], vanadium[315,316], molybdenum[146,233,299,301], copper[313], ruthenium[291,317,318], rhenium[289,319], cobalt[320], iridium[321], iron[302,322], platinum[287,323] and nickel[320,323–325]. Most of the thiyl radicals are postulated, based on their reactivity (Ru, Re, Ni), their dimerization behavior (Ga, Fe) or the resulting diamagnetism based on the coupling of the thiyl radical with the open-shell metal (Re, Ru). An outstanding system was published by DuBois and coworkers.[231,233,326] They have described a persistent free radical in the dinuclear molybdenum complex (**Figure 7.2** (**f**)). This family of complexes are able to perform proton reduction and hydrogen activation, including a switch of the redox stages at the Mo(IV/III) and the formation of bridging thiyl radicals. In 2008, they also published an EPR spectrum of their $(Cp^*)_2(Mo_2S_4Me)_2$ system, which may contain a thiyl radical (**Figure 7.3**). To the best of my knowledge, no clear assignments and exact interpretation with respect to the thiyl radical is done, while the reactivity, described above, indicates the existence of a thiyl radical.[233]

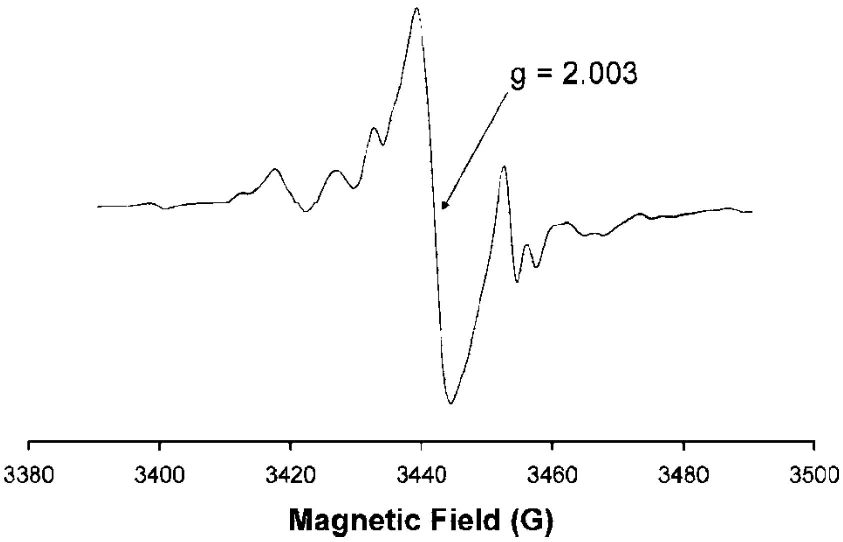

Figure 7.3: EPR spectrum of complex (**f**) (5 mM, in toluene at 296 K). A *g* factor of 2.003 is obtained.[233] Adapted with permission from Ref. [233] © 2008 AMERICAN CHEMICAL SOCIETY.

Wieghardt and coworkers used EPR spectroscopy to demonstrate the presence of thiyl radicals in close contact to nickel(II) complexes.[323,325] Harrop *et al.*[327] presented a nickel(II) thiolate system which showed electronic properties between nickel(III)/ RS^- and nickel(II)/ RS· after oxidation of the complex (**Figure 7.2** (**d**)). This is one of several examples in which the exact location of the unpaired electron remains uncertain, and a discussion arises whether the obtained radical has more nickel(III) character or more thiyl character. Simultaneously will this be the starting point for the discussion about the nature of the dinickel μ-thiyl NHC complex presented in this chapter.

7.1.4 Metal subsulfido complexes

In the literature, the metal mediated reduction of elemental sulfur is described, resulting in different kinds of metal bonded disulfide species.[328] A formal reduction of elemental "S_2" to two S^{2-} requires four electrons in total. By a stepwise reduction, three oxidation states of the "S_2" are passed, namely the supersulfide ($S_2^{-\cdot}$), the disulfide (S_2^{2-}) and the subsulfide ($S_2^{3-\cdot}$). Whereby several dinuclear metal complexes are described, bearing S^{2-} or S_2^{2-} units, a small number of supersulfide and subsulfide complexes exist.[328–330] One reason for the small amount of reported subsulfide complexes is the lack of knowledge about the electronic structure of such complexes. Here the spin density can be distributed over the coordinated metal and the chalcogenides. In 2015, Berry *et al.*[329] performed a global electronic structure analysis of M_2S_2 complexes. Starting point for this analysis was a previous debate regarding the oxidation states in a $[Cu_3S_2]^{3+}$ core, which seems to bear a subsulfido unit, stabilized by three copper(II) anions. This assignment was confirmed by a detailed analysis of the complex, including X-ray absorption spectroscopy (XAS) and computational studies. Also other homoleptic or heteroleptic subsulfido complexes are postulated and are summarized in **Figure 7.4**. Driess and coworkers reported the synthesis of heterobimetallic nickel(II)/platinum(II) and nickel(II)/iron(II) subsulfido complexes by reaction of a dimerized nickel(II) *side-on* supersulfido (μ-$S^{\cdot-}$) complex[331] with iron(0) or platinum(0) sources (Figure 7.4, **XX** and **XXI**).[328,330] All those complexes have a diamond shaped [MS_2M] core, wherein the disulfur unit is coordinated in a *side-on* mode. All obtained complexes show a weak attractive S····S interaction, and in the molecular structures in solid state S····S distances between 2.5 Å and 2.9 Å are determined. These distances are in between S····S distances of metal disulfido (2.0-2.3 Å) and metal bis(sulfido) complexes (>3 Å).

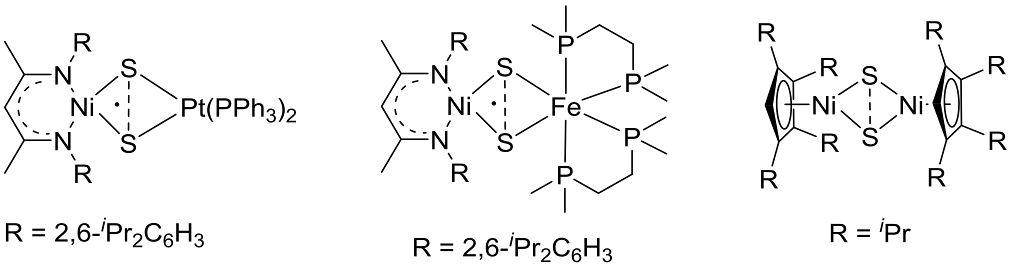

R = 2,6-^{i}Pr$_2$C$_6$H$_3$ R = 2,6-^{i}Pr$_2$C$_6$H$_3$ R = ^{i}Pr

XX **XXI** **XXII**

Figure 7.4: Dinuclear subsulfido complexes, described in the literature.[328–330,332]

A direct assignment of the presented subsulfido character based on EPR spectroscopy seems to be difficult, since the presence of non-innocent metals like nickel can result in large *g* anisotropies, as it is observed in the heteroleptic compounds, or even can result in the formation of diamagnetic complexes. Computational studies show (DFT and CASSCF methods), that in complex **XXII** the Ni_2S_2 bonding is quite covalent and a variety of Ni d and S p orbitals have to be considered. Hence, the E–E σ* orbital in the isolated S_2^{3-} unit is a two electron occupied orbital, which seems to be equally shared by the nickel and the sulfur and the system is best described as a (Ni_2^{5+})(S_2^{3-}) core.[329] Since this orbital is no frontier orbital, the subsulfide showed no "radical" character and the EPR spectrum is silent. This example impressively shows that the assignment of a metal subsulfido complex is not trivial and the non-innocence of the coordinated metal can strongly influence the electronic environment of the subsulfido unit, starting from the observation of EPR spectra with *g* values reminiscent of open-shelled metals[328,330] to EPR silent complexes.[329]

7.2 Objectives

As already mentioned the detection of thiyl radicals is feasible but challenging. All described examples show the impact and diversity of thiyl radicals in biology and chemistry. There is one property all model complexes have in common: the thiyl radical binds to the metal core or is close to a metal center, but in addition also linked to an alkyl or aryl group (except of $(Cp^*)_2Mo_2S_4$) and consequently part of the ligand scaffold. Except of the chromium and molybdenum complexes, described for instance by Noble, Franz, DuBois and coworkers, to the best of my knowledge no further examples of thiyl radicals, stabilized between two metal centers have been reported. In the latter case, the detection of the *in situ* generated thiyl radical after photolysis of the persulfido bridge is monitored by EPR spectroscopy by employing a spin trap (4-phenyl-1,2,4-triazoline-3,5-dione) (**Figure 7.2** (**c**)) and in $(Cp^*)_2Mo_2S_4$ the formation of the persistent thiyl radical is monitored by EPR spectroscopy. In the latter, to the best of my knowledge the explanation of the obtained EPR spectrum is still missing.

The target in this chapter is to provide the first spectroscopic data of a thiyl radical which is stabilized exclusively between two nickel centers (**Figure 7.5**) and to investigate its reactivity towards X–H bond activation (X = O, N, C) *via* HAT processes.

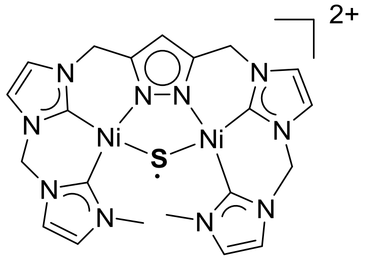

Figure 7.5: Proposed structure of a μ-**S·** dinickel(II) complex.

7.3 Results and Discussion

7.3.1 Spectroscopic characterization of the first dinickel *μ*-thiyl radical complex

The presented cyclic voltammogram of **$[L^6Ni_2S]PF_6$** (**Figure 7.6** and **chapter 5**) shows one irreversible oxidative wave, with a peak potential of $E_p = -0.35$ V *vs.* Fc/Fc$^+$ (1.0 mM, 0.1 M NBu_4PF_6, in MeCN, 100 mV·s^{-1}). This oxidation event is assigned to an oxidation process at the sulfido bridge of **$[L^6Ni_2S]PF_6$** and the formation of a thiyl radical, which rapidly dimerized to form **$[(L^6)_2Ni_4(S_2)]^{4+}$** (**chapter 8**). The dimerized product can again be reduced at a potential which is cathodically shifted by 870 mV in comparison to the oxidative wave. This reduction event can only be observed after a previous oxidation process, confirmed by two cycle measurements applying first a cathodic potential and comparison of one cycle starting first at an anodic potential or starting first at a cathodic potential (**Figure 7.6**). The interpretation of the chemical processes behind the observed redox events was achieved by chemical redox reactions and further analytical measurements.

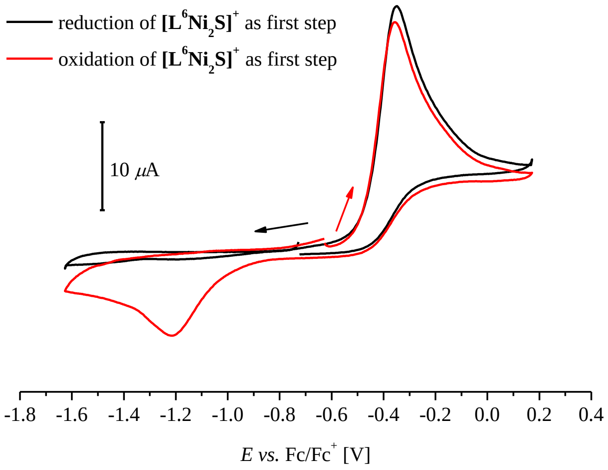

Figure 7.6: CV of **$[L^6Ni_2S]PF_6$** (1.0 mM) in 0.1 M MeCN/NBu_4PF_6 solution at a scan rate of 100 mV·s^{-1}, Pt counter electrode, GC working electrode, Ag reference electrode. Shown are CV's applying a cathodic potential (**black**) or anodic potential (**red**) first.

The chemical oxidation of **$[L^6Ni_2S]PF_6$** by 1.0 equiv. of $[FeCp_2]PF_6$ ($E_{1/2} = 0$ V in MeCN) leads to **$[(L^6)_2Ni_4(S_2)](PF_6)_4$** (**chapter 8**). This complex can again be chemically reduced to **$[L^6Ni_2S]PF_6$** by adding the reducing agent cobaltocene (2.0 equiv.) to the isolated complex **$[(L^6)_2Ni_4(S_2)](PF_6)_4$** in MeCN. This reaction is followed by ^{1}H NMR spectroscopy (experimental section) and confirms the chemical reversibility. With the UV-vis spectroscopic characteristics of **$[L^6Ni_2S]PF_6$** (**chapter 5**) and **$[(L^6)_2Ni_4(S_2)](PF_6)_4$** (**chapter 8**) being known, SEC UV-vis experiments are conducted (**Figure 7.7** (**a**)), starting from **$[L^6Ni_2S]PF_6$**. After applying a potential at +0.3 V *vs*. Fc/Fc$^+$ the bands at 393 nm and the shoulder in the UV-vis spectrum are decreasing and a broad band with a local maximum at 400 nm is observed. After no change in the UV-vis spectra is observed, a cathodic potential at –1.5 V *vs*. Fc/Fc$^+$ is applied, which results in the reversible regeneration of the original bands. The difference spectrum (**Figure 7.7** (**b**)) also demonstrates the electrochemical reversibility of the interconversion of **[L^{6}Ni$_2$S]PF$_6$** and **[(L^6)$_2$Ni$_4$(S$_2$)](PF$_6$)$_4$**. In addition, the SEC UV-vis experiments suggest a very fast dimerization reaction of the oxidized **[L^{6}Ni$_2$S]PF$_6$** complex, after the thiyl radical is formed.

Furthermore, EPR experiments are performed. First attempts of using 5,5-dimethyl-*1*-pyrroline *N*-oxide (DMPO) as a radical trap during the oxidation process of **[L^{6}Ni$_2$S]PF$_6$** with [Fe(Cp*)$_2$]PF$_6$ failed, due to faster recombination of the thiyl radicals and formation of **[(L^6)$_2$Ni$_4$(S$_2$)](PF$_6$)$_4$** than reaction of the *in situ* generated radicals with the radical trap. The use of a spin trap results in EPR silent spectra.

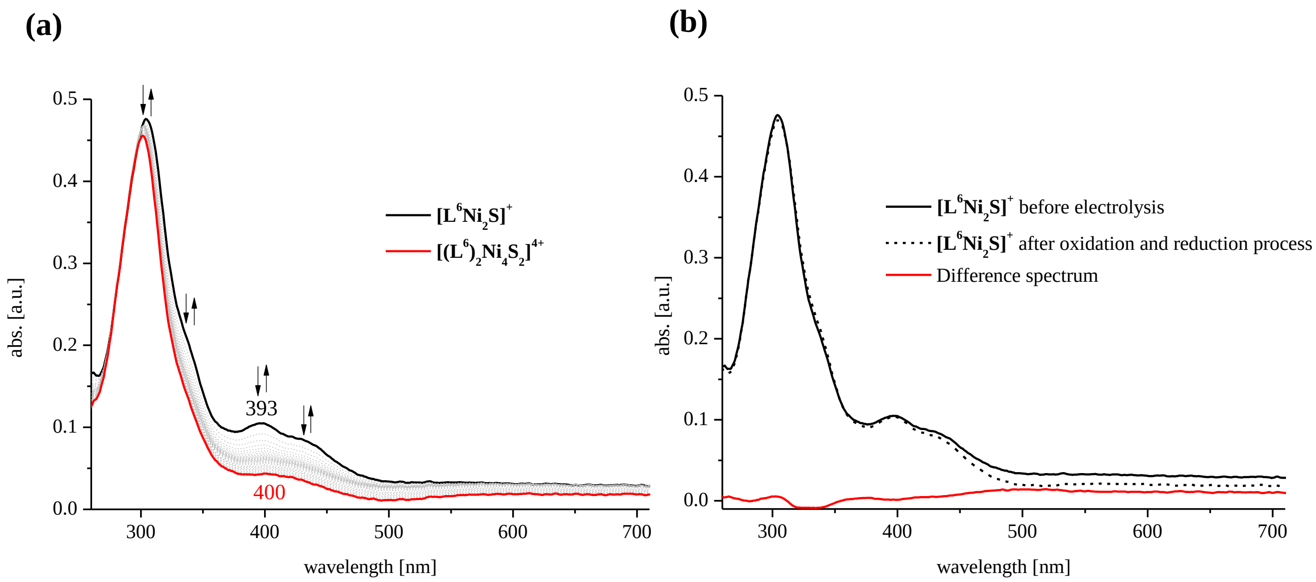

Figure 7.7: (**a**) SEC UV-vis of the sulfido complex (1.2 mM) in 0.1 M MeCN/NBu$_4$PF$_6$ solution, Pt mesh working electrode, Pt wire counter electrode, Ag wire reference electrode. Applying a potential of +0.3 V *vs.* Fc/Fc$^+$ and cross polarization after 2 min at –1.5 V *vs*. Fc/Fc$^+$ and observation of reformation of the sulfido complex. (**b**) Difference spectra confirm the interconversion of the two complexes (oxidation to persulfido and reduction back to sulfido complex).

Reproducible EPR spectra of the thiyl radical are recorded after a freeze-quench reaction of [Fe(Cp*)$_2$]PF$_6$ ($E_{1/2}$ (MeCN) = –0.59 V *vs.* Fc/Fc$^+$)[333] with **[L^{6}Ni$_2$S]PF$_6$**. The frozen solution shows three different colors. Red from the not reacted sulfido complex, green from not reacted [Fe(Cp*)$_2$]PF$_6$ and orange/yellow from the thiyl radical and already formed **[(L^6)$_2$Ni$_4$(S$_2$)](PF$_6$)$_4$** as well as the formed Fe(Cp*)$_2$. [Fe(Cp*)$_2$]PF$_6$ is chosen, because blank tests of $[Fe(Cp^*)_2]PF_6$ at 140 K show no EPR activity of the Fe^{III} ion.[334] The reason for this can be the spin-lattice or spin-spin relaxation processes in $[Fe(Cp^*)_2]^+$.[335] Walter and coworkers[335] published EPR spectra of different $[Fe(Cp^R)_2]^+$ derivates, with bulky substituents in order to investigate these phenomena. An interesting fact is that all EPR measurements are conducted at 2-22 K. In the literature, the axial symmetric EPR spectrum of $[Fe(Cp^*)_2]PF_6$ is reported at 12 K ($g_\parallel = 4.43$, $g_\perp = 1.35$).[334] As a positive side effect of this behavior of $[Fe(Cp^*)_2]PF_6$, at 142 K only the complex signal, resulting from oxidation of **$[L^6Ni_2S]PF_6$** is observable (**Figure 7.8**). **$[L^6Ni_2(S\cdot)]^{2+}$** shows a rhombic EPR spectrum with shifted *g*-factors ($g_1 = 2.17$, $g_2 = 2.10$ and $g_3 = 2.04$, $g_{av} = 2.10$) compared to the spin only value (2.0023). The experimental values are in good agreement with *g* values, derived by DFT calculation of EPR signatures from **$[L^6Ni_2(S\cdot)]^{2+}$**, which are performed by Dr. Finger and shows the three *g* values: $g_1 = 2.12$, $g_2 = 2.10$ and $g_3 = 2.04$.

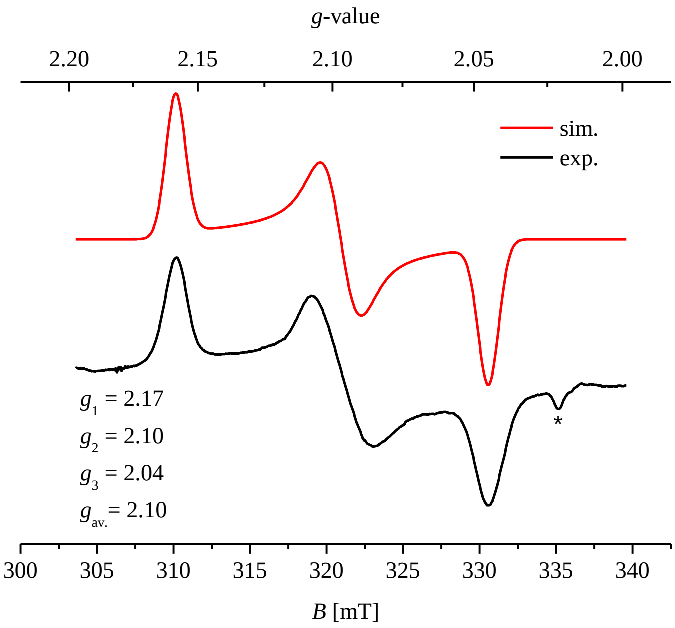

Figure 7.8: EPR spectrum of **$[L^6Ni_2(S\cdot)]^{2+}$** in MeCN at 142 K, frequency 9.45 GHz, showing a rhombic spectrum with the three anisotropic *g* values: $g_1 = 2.17$, $g_2 = 2.10$ and $g_3 = 2.04$, $g_{av} = 2.10$.

The narrow half-width of g_1 is 1.74 mT and of g_3 is 1.95 mT. The latter value is at the lower border of $g_\perp$of organic thiyl radicals (2-4 mT).[292] As expected the resulting spectrum is reminiscent of the spectra of paramagnetic transition metal complexes with large, anisotropic *g* factors, but with narrow half-widths. Compared to organic thiyl radicals the *g* factors are larger. The reason for this is a lower degeneracy of the $S(p_\pi)$ orbitals (axial symmetry in the x–y plane) caused by the nickel ions than can occur by alkyl or aryl substituents in the free organic radicals. Breaking of the degeneracy of the p_π orbitals the angular momentum about the molecular z axis will be quenched, which results in an increase of g_1 and g_2, decreasing in g_3 and change from an axial symmetric spectrum to a rhombic spectrum. In the presented EPR spectrum, also g_3 (equal to g_z) increases a lot compared to the spin only value. This can be explained in analogy to the observation by Lubitz *et al*. when lithium chloride is added to their organic thiyl radicals. The enhancement of the polar environment around the thiyl radical leads to an increase of the g_z value and decrease of g_x and g_y values in case of isotropic lithium cations. Here, increase of polarity around the thiyl radical induced in an anisotropic way by the two nickel ions in the x, y and z direction.

Due to the unique environment and the high covalency of the thiyl radical, a strong interaction with the nickel cores can be observed. This behavior can be better understood by taking a closer look at the spin density distribution in the complex and the bonding situation of the μ-thiyl radical. DFT calculations are conducted and relevant results are shown in **Figures 7.9** and **7.10**. The calculated molecular structure of **[L⁶Ni₂(S·)]²⁺** shows a high density on the S in the p_z orbital (Mulliken atomic spin population 67.1%), as well as equal contribution of spin density (each 16.2%) on the two nickel centers (d_{xz}).

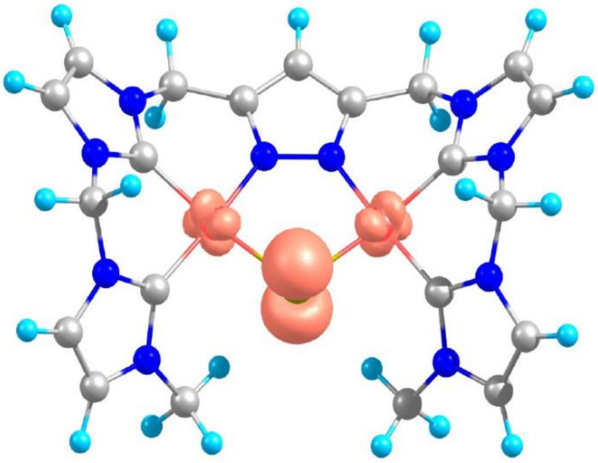

Figure 7.9: Calculated molecular structure of **$[L^6Ni_2(S\cdot)]^{2+}$** with 67.2% Mulliken atomic spin population at the $S(p_z)$ orbital and 32.4 % on the nickel ions (d_{xz}), equally distributed (Ni(1) 16.2%, Ni(2) 16.2%).

The local spin population (32.4%) at the nickel atoms explain the high *g* factors and the similarity of the obtained spectra with EPR spectra of Ni^{III} complexes. EPR spectra of several nickel(III) complexes from literature, can be found and in **Table A.7.1** (**appendix**), the *g* values of some postulated nickel(III) complexes are summarized. The listed values represent higher g_x and g_y factors than in **$[L^6Ni_2(S\cdot)]^{2+}$**, which indicates that a thiyl radical is observed *via* EPR spectroscopy, whereby the admixture of the nickel *d* orbitals is not negligible in this case. Unfortunately, a direct comparison of the EPR spectrum with other dinuclear pyrazolate-bridged nickel(III)/nickel(II) complexes is not possible, due to lack of reported spectra. To the best of my knowledge, so far only one example of a pyrazolate-bridged mixed valent $Ni^{III}Ni^{II}$ complex is presented with the metal ions in an octahedral environment.[336] In this case the nickel(III) core is also antiferromagnetically interacting with the high-spin nickel(II) center in the complex and high g values are observed ($g_1 = 5.29$, $g_2 = 3.20$, $g_3 = 2.08$). Also non pyrazolate-bridged, mixed valent Ni^{III}/Ni^{II} complexes show larger g values.[337]

The electronic structure of the thiyl radical is strongly dependent on the particular combination of nickel ions and the thiyl radical.[287] Front orbital considerations can give an insight in these interactions (**Figure 7.10**). An interaction between the nickel nuclei and the S radical in all three directions is observed, which results in an increase of anisotropy and an increase of the g factors in all three spatial directions. Bonding interactions between the thiyl radical and the nickel ions are observed in the molecule plane (**a**) Ni d_{xy}: 11% (orbital character composition); S p_x: 15%, (**b**) Ni d_{z^2}: 15%; S p_y: 14% and antibonding interactions in the z direction (**c**) Ni d_{xz} (d_{yz}) 11% (4.3%); S p_z: 25% (S p_y: 10.6%). In this work, an EPR spectrum of a unique thiyl radical complex is obtained with contribution of spin density at the nickel centers.

The influence of MeCN (the solvent used) on the thiyl radical is not investigated, but may also be relevant. In the literature mainly the influence of protic solvents was investigated. In general hydrogen bonding interactions between the radical and the solvent molecules lead to a polar environment and to an energetic lift of the degeneracy of the $S(p_{\pi})$ orbitals.

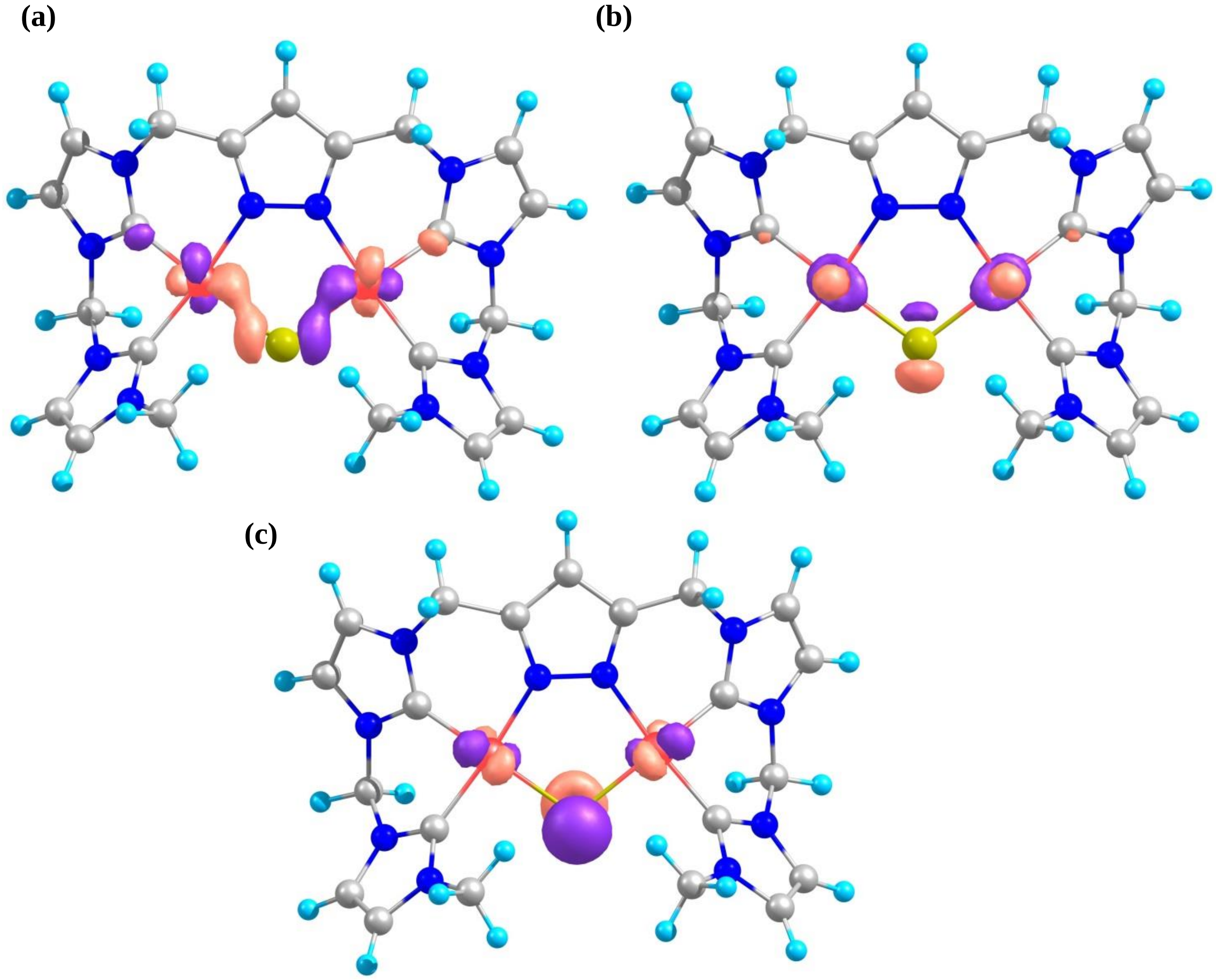

Figure 7.10: Frontier orbital consideration in $[\mathbf{L^6Ni_2(S\cdot)}]^{2+}$: (**a**) Orbital 135a, Ni d_{xy}: 11% (orbital character composition); S p_x: 15%, (**b**) Orbital 137a, Ni d_{z^2}: 15%; S p_y: 14%, (**c**) HOMO (Orbital 145a) Ni d_{xz} (d_{yz}) 11% (4.3%); S p_z: 25% (S p_y: 10.6%).

The instability of the thiyl radical is evidenced by the following experiments. The frozen solution with the detected rhombic signal is warmed up for about 20 s to –30 °C and afterwards the reaction is stopped immediately by freezing the solution in liquid nitrogen. After warming up to –30 °C a color change of the solution to yellow occurred, indicating the formation of $\mathbf{[(L^6)_2Ni_4(S_2)](PF_6)_4}$ and the previously observed EPR signal vanished. Also by warming the frozen solution to room temperature and shaking a disappearance of the EPR signal is observed, which indicates the further transformation of $[\mathbf{L^6Ni_2(S\cdot)}]^{2+}$.

Stopped-Flow UV-vis spectroscopy experiments at –40 °C are conducted that underline the fast dimerization reaction of the formed $[\mathbf{L^6Ni_2(S\cdot)}]^{2+}$ complex. $\mathbf{[L^6Ni_2S]PF_6}$ is mixed with $[FeCp_2]PF_6$ at –40 °C in MeCN in the single mixing mode and a series of UV-vis spectra are measured. **Figure 7.11** gives a summary of the obtained results. After addition of $[FeCp_2]PF_6$ to $\mathbf{[L^6Ni_2S]PF_6}$ and recording the UV-vis spectrum of the mixture every 1.7 ms a markedly decrease of the former bands around 393 nm are observed and an increase of a broad band with a local maximum of approximately 603 nm is observed, which decreases under formation of a band at 400 nm which can be assigned to **$[(L^6)_2Ni_4(S_2)](PF_6)_4$**. Furthermore, the decrease of the band at 603 nm is monitored over time and the disappearance of the band after approximately 2 s is observed (**Figure 7.11** (**a**), **inset**). In addition, a TD-DFT calculation of **$[L^6Ni_2(S\cdot)]^{2+}$** is performed, indicating a spectrum with a band around 600 nm for a excitation process from the dinickel-S mixed Orbital 135 to the HOMO (**Figure 7.11** (**b**)-(**d**)).

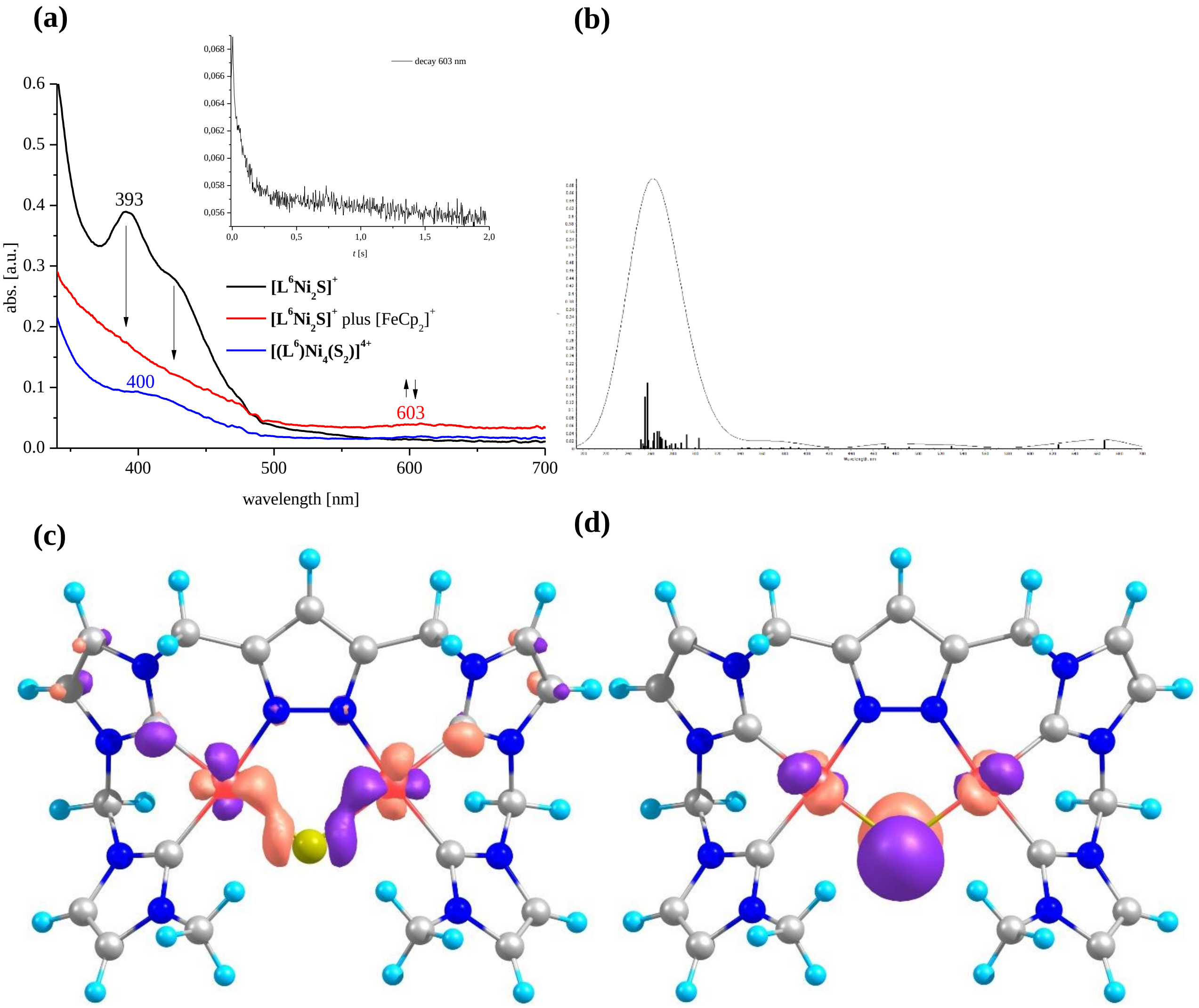

Figure 7.11: (**a**) Stopped-Flow UV-vis spectra of the reaction of **$[L^6Ni_2S]^+$** with $[FeCp_2]^+$ in MeCN at –40 °C. (**b**) TD-DFT UV-vis spectrum of **$[L^6Ni_2(S\cdot)]^{2+}$** shows a band at 666 nm according to the excitation from (**c**) Orbital 135b, Ni d character 32.6% (Ni d_{xy}: 26%); S p_x: 11% to (**d**) HOMO (Orbital 145b) Ni d character 31.9%, (Ni d_{xz}/d_{yz}) 28%; S p_z: 45%).

In conclusion, the first dinickel *μ*-thiyl radical complex is monitored, with around 67% spin location on the sulfur ion. To the best of my knowledge the direct detection of a thiyl radical, exclusively stabilized by metal ions and without support of a spin trap, is not clearly described in the literature to date. The closest example is a dinuclear molybdenum thiyl radical complex reported by Franz *et al*.[233] which lacks a detailed description of an EPR spectrum (g = 2.003) recorded at 296 K. Reasons for this can be the high complexity of the spectrum, including several complex isomers and the possible interaction with the Mo nuclei (I = 5/2) as well as admixture of Mo and S orbitals.[233] The assignment of **$[L^6Ni_2(S\cdot)]^{2+}$** is further supported by the observation of a short living species by stopped-flow UV-vis spectroscopy, in agreement with TD-DFT UV-vis spectroscopy. A further insight in **$[L^6Ni_2(S\cdot)]^{2+}$** would be possible by magnetic circular dichroism (MCD) spectroscopy or NEXAFS/XANES spectroscopy studies. The analysis of the *K*-edge of the S and the Ni ions would give further insights into the electronic distribution. Unfortunately, because of the low concentration of the thiyl radical as part of a mixture of several complexes in frozen solution and due to the instability of the system at higher temperatures, those experiments have not yet been conducted.

7.3.2 Mechanistic investigations of the dimerization reaction of the thiyl radical

The CV of $\mathbf{[L^6Ni_2S]^+}$ is described in **chapter 7.3.1** and shows an irreversible oxidative wave, with a peak potential of $Ep = -0.35$ V *vs.* Fc/Fc$^+$ (1.0 mM, 0.1 M NBu_4PF_6, in MeCN, 100 mV·s^{-1}). In all performed CV's an *EC* mechanism is proposed at room temperature, wherein a fast chemical reaction of the thiyl radical complex to $\mathbf{[(L^6)_2Ni_4(S_2)](PF_6)_4}$ (**chapter 8**) occurs. $\mathbf{[(L^6)_2Ni_4(S_2)](PF_6)_4}$ is also synthesized chemically and its analytical characteristics are identical to the spectroscopic results of the electrochemical oxidation of $\mathbf{[L^6Ni_2S]^+}$ (see **chapter 7.3.1** and **chapter 8**). The stopped-flow UV-vis experiments in MeCN at 233 K as well as the EPR studies underline the existence of an intermediate with a short lifetime and radical character. CV experiments are performed at scan rates from 200 V·s^{-1} to 1 kV·s^{-1} at 239 K to further confirm that the intermediate is a short-living species, and the result of a reversible oxidation event of $\mathbf{[L^6Ni_2S]^+}$. Indeed, a reversible oxidation of $\mathbf{[L^6Ni_2S]^+}$ is observed in a CV at scan rate of 700 V·s^{-1} (**Figure 7.12**) and in CV's with higher scan rates.

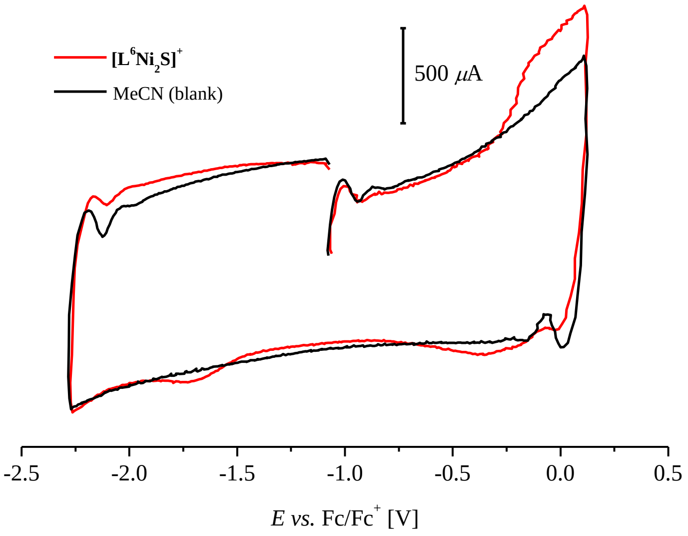

Figure 7.12: CV of $\mathbf{[L^6Ni_2S]^+}$ (0.5 mM) in 0.1 M MeCN/NBu_4PF_6 solution at a scan rate of 700 V·s^{-1} and 239 K; Pt counter electrode, GC working electrode, Ag reference electrode. Shown is the CV of the complex (**red**) in comparison to the CV of MeCN (**black**) at 700 V·s^{-1} to confirm the existence of reversible wave of the complex at a very high scan rate.

The observation of this reversible wave is an important result and the only proof of the reversible (electro-)chemical oxidation of $\mathbf{[L^6Ni_2S]^+}$. CV can be a useful tool, as indirect analytic method for the observation of the thiyl radical complex, to get a better insight into the redox properties of the complex. After the confirmation of an reversible oxidation process of $\mathbf{[L^6Ni_2S]^+}$ to $\mathbf{[L^6Ni_2(S\cdot)]^{2+}}$ *via* CV experiments at high scan rates and low temperatures, further mechanistic investigations of the dimerization pathway of **$[L^6Ni_2(S\cdot)]^{2+}$** to **$[(L^6)_2Ni_4(S_2)]^{4+}$** are possible. Furthermore, the important proof of the (electro-)chemical reversibility will allow to determine $E_{1/2}$(**$[L^6Ni_2S]^+$**/**$[L^6Ni_2(S\cdot)]^{2+}$** by CV experiments and its simulations. $E_{1/2}$([**$L^6Ni_2S]^+$**/[**$L^6Ni_2(S\cdot)]^{2+}$** is an important parameter for the determination of the $BDFE_{(solv.)}$ of the S–H bond in **$[L^6Ni_2(SH)]^{2+}$**. In **chapter 6**, the pK_a value of the S–H bond in **$[L^6Ni_2(SH)](PF_6)(OTf)$** is already determined. In addition, the determination of $E_{1/2}$([**$L^6Ni_2S]^+$**/[**$L^6Ni_2(S\cdot)]^{2+}$** will allow the calculation of the $BDFE_{(solv.)}$ by a square scheme (**section 7.3.3**).

Due to the importance of the $BDFE_{(solv.)}$ of the S–H bond, mainly with respect to subsequent HAT reactivity studies, CV simulations are carried out in cooperation with Prof. Dr. Siewert. Before presenting the results of the CV experiments, it is important to understand the mechanism of the chemical reaction of [**$L^6Ni_2(S\cdot)]^{2+}$** to form **$[(L^6)_2Ni_4(S_2)](PF_6)_4$**. Two reasonable pathways as the basis for the CV simulations of the formation of **$[(L^6)_2Ni_4(S_2)](PF_6)_4$** (**Model 1** and **Model 2**) are presented in **Scheme 7.3**.

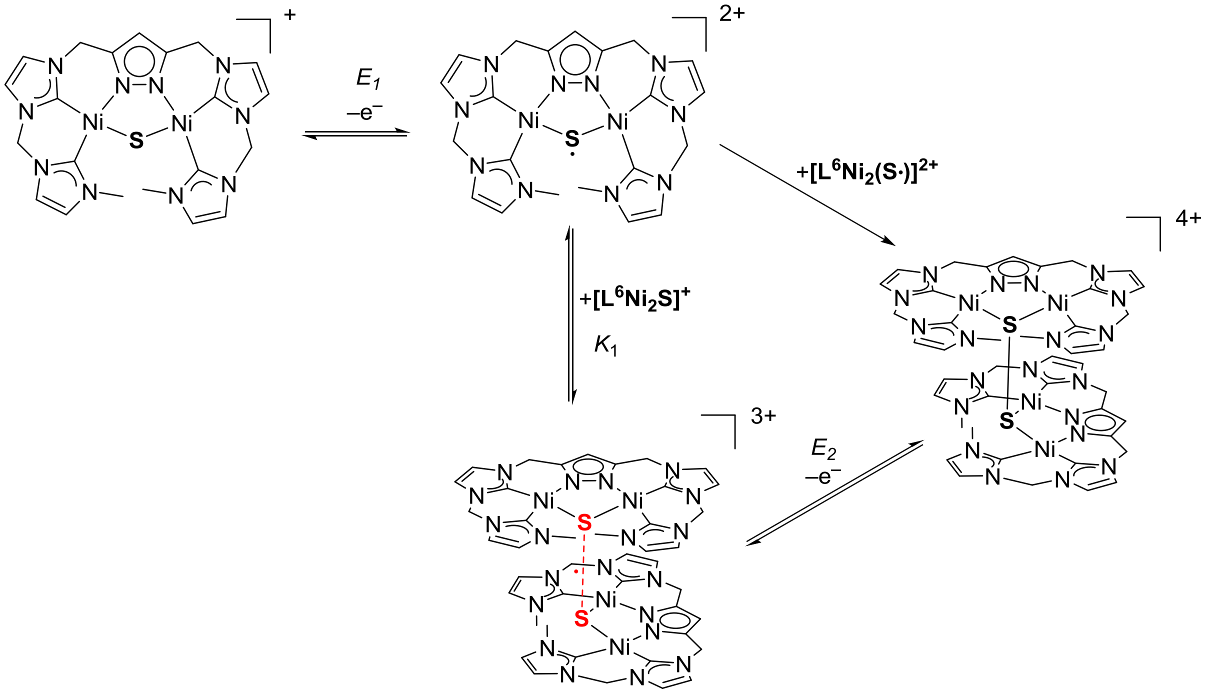

Scheme 7.3: Proposed mechanism based on **Model 1:** dimerization of [**$L^6Ni_2(S\cdot)]^{2+}$**and **Model 2:** first formation of [**$L^6Ni_2S\therefore SNi_2L^6]^{3+}$** and one electron oxidation under formation of **$[(L^6)_2Ni_4(S_2)]^{4+}$**

In **Model 1** an oxidation of [**$L^6Ni_2S]^+$** to [**$L^6Ni_2(S\cdot)]^{2+}$** and concomitant dimerization to **$[(L^6)_2Ni_4(S_2)]^{4+}$** is proposed. In the literature, dimerization reactions of organic molecules of $RS\cdot$ with RS^- to $RSSR^{\cdot-}$ are described (R = alkyl or aryl)[294,339–341] with rate constants of $10^9\ M^{-1}\cdot s^{-1}$ for the dimerization reaction.[342] Since the existence of dimetal subsulfido complexes is confirmed in other cases, an alternative mechanism for the oxidation of

$[L^6Ni_2S]^+$ is considered (**Model 2**, **Scheme 7.3**). **Model 2** assumes that after oxidation of **$[L^6Ni_2S]^+$** to **$[L^6Ni_2(S\cdot)]^{2+}$** no direct recombination of the two radicals occurs, but a reaction with the starting compound and the formation of **$[L^6Ni_2S\therefore SNi_2L^6]^{3+}$**. This subsulfido complex is further oxidized under formation of **$[(L^6)_2Ni_4(S_2)]^{4+}$** (**Scheme 7.3**).

In **Figure 7.13 (a)**, the CV's at three different concentrations (**2.0 mM**, **1.0 mM** and **0.5 mM**, 100 mV·s^{-1}) are exemplary compared.

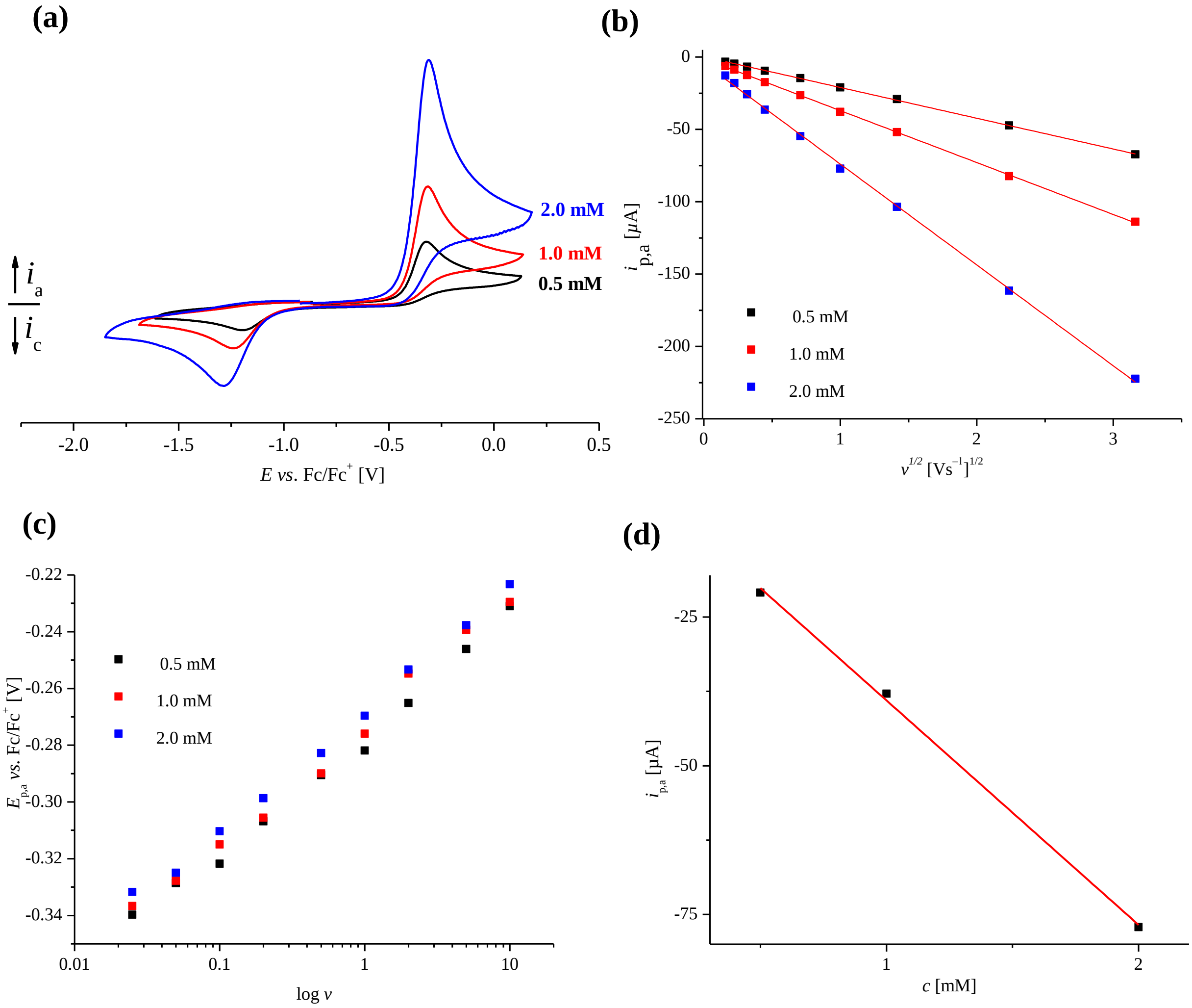

Figure 7.13: (**a**) CV of **$[L^6Ni_2S]PF_6$** at different concentrations at r.t. and a scan rate of 100 mV·s^{-1}, (**b**) $i_{p,a}$ *vs.* $\upsilon^{1/2}$ plot, (**c**) $E_{p,a}$ vs. log υ plot, (**d**) $i_{p,a}$ *vs.* **$[L^6Ni_2S]PF_6$**.

A linear correlation between the peak current and the square root of the scan rate is observed. The current decrease linearly with the square root of the scan rate and indicates a diffusion controlled process for the oxidation event (**Figure 7.13** (**b**)). Also the peak potential shifts linearly by the decade logarithm of the scan rate, which can be in general a hint for an irreversible electron transfer (**Figure 7.13** (**c**)). This is not the case for this reaction, since the CV experiments at high scan rates at 239 K prove a reversible electron transfer as consequence of the observation of a reversible wave. Furthermore, a cathodic shift of the peak potential for the reaction is observed by increase of the complex concentration (**Figure 7.13** (**c**)). This cathodic shift indicates a fast bimolecular reaction. Furthermore, this statement is supported by the low temperature CV experiments. No reversibility of the wave is observed below 500 $V{\cdot}s^{-1}$, which underlines the very fast speed of the dimerization reaction. In **Figure 7.13 (d)**, the peak current of the oxidation event shows a linear dependency of the complex concentration. This linear regression indicates proportionality between i_a and [complex].

The first oxidation of $\mathbf{[L^6Ni_2S]^+}$ to $\mathbf{[L^6Ni_2(S\cdot)]^{2+}}$ as a reversible electron transfer is proposed as the first step in both **Models** (**1** & **2**), followed by a very fast chemical reaction. The assumption is done by conducting CV measurements at 239K and fast scan rates from 200 $V{\cdot}s^{-1}$ up to 1 $kV{\cdot}s^{-1}$. A small reversibility of the redox event is observed at 1 kVs^{-1}. The determination of the speed constant k_1 for the dimerization reaction is possible by consideration of the CV's at high scan rates at 239 K (**Table 7.2**). No reversibility of the electrochemical process is observed below 500 Vs^{-1} (lower limit), whereby reversibility is observed at 1 kVs^{-1} (upper limit). **Model 1** fits under assumption of a reversible electron transfer and a fast chemical reaction after oxidation of $\mathbf{[L^6Ni_2S]^+}$.

Table7.2: Postulated **Model 1** and **Model 2** for the description of the oxidation event of $\mathbf{[L^6Ni_2S]PF_6}$.

	Model 1	**Model 2**
	$\mathrm{Ox} + \mathrm{e}^- \xrightleftharpoons{E_1} \mathrm{Red}$ $2\,\mathrm{Ox} \xrightarrow{k_1} \mathrm{Ox2}$	$\mathrm{Ox} + \mathrm{e}^- \xrightleftharpoons{E_1} \mathrm{Red}$ $\mathrm{Ox} + \mathrm{Red} \xrightleftharpoons{k_1,\,K} \mathrm{OxRed}$ $\mathrm{Ox2} + \mathrm{e}^- \xrightleftharpoons[\text{irrev.}]{E_2} \mathrm{OxRed}$
E_1	−0.255 (10) V	−0.240 (10) V
α_1	0.5 eV	0.5 eV
$k_{s,1}$	0.04 $cm{\cdot}s^{-1}$	0.04 $cm{\cdot}s^{-1}$
E_2	–	−0.92 V
α_2	–	0.5 eV
$k_{s,2}$	–	$1{\cdot}10^{-5}$ $cm{\cdot}s^{-1}$
k_1	$1{\cdot}10^{9}$ $({\cdot}10^{\pm1})$ $M^{-1}{\cdot}s^{-1}$	$1{\cdot}10^{7}$ $M^{-1}{\cdot}s^{-1}$
K_1	–	$1{\cdot}10^{7}$ M^{-1}
$D^{(Ox\mid Red)}$	$5{\cdot}10^{-6}$ $cm^2{\cdot}s^{-1}$	$5{\cdot}10^{-6}$ $cm^2{\cdot}s^{-1}$
$D^{(Ox2\mid Red2)}$	$2.5{\cdot}10^{-6}$ $cm^2{\cdot}s^{-1}$	$2.5{\cdot}10^{-6}$ $cm^2{\cdot}s^{-1}$

A rate constant k_1 for the dimerization reaction in **Model 1** is derived of approximately $1{\cdot}10^9$ $M^{-1}{\cdot}s^{-1}$ (lower limit $5{\cdot}10^8$ $M^{-1}{\cdot}s^{-1}$ and upper limit $5{\cdot}10^9$ $M^{-1}{\cdot}s^{-1}$) which is close to the value for diffusion controlled processes. k_1 is in agreement with in the literature known rate constants of organic thiyl radicals[338] like the reaction rate for the decay of phenyl-thiyl radicals (ca. $10^9\ M^{-1}\cdot s^{-1}$).[300]

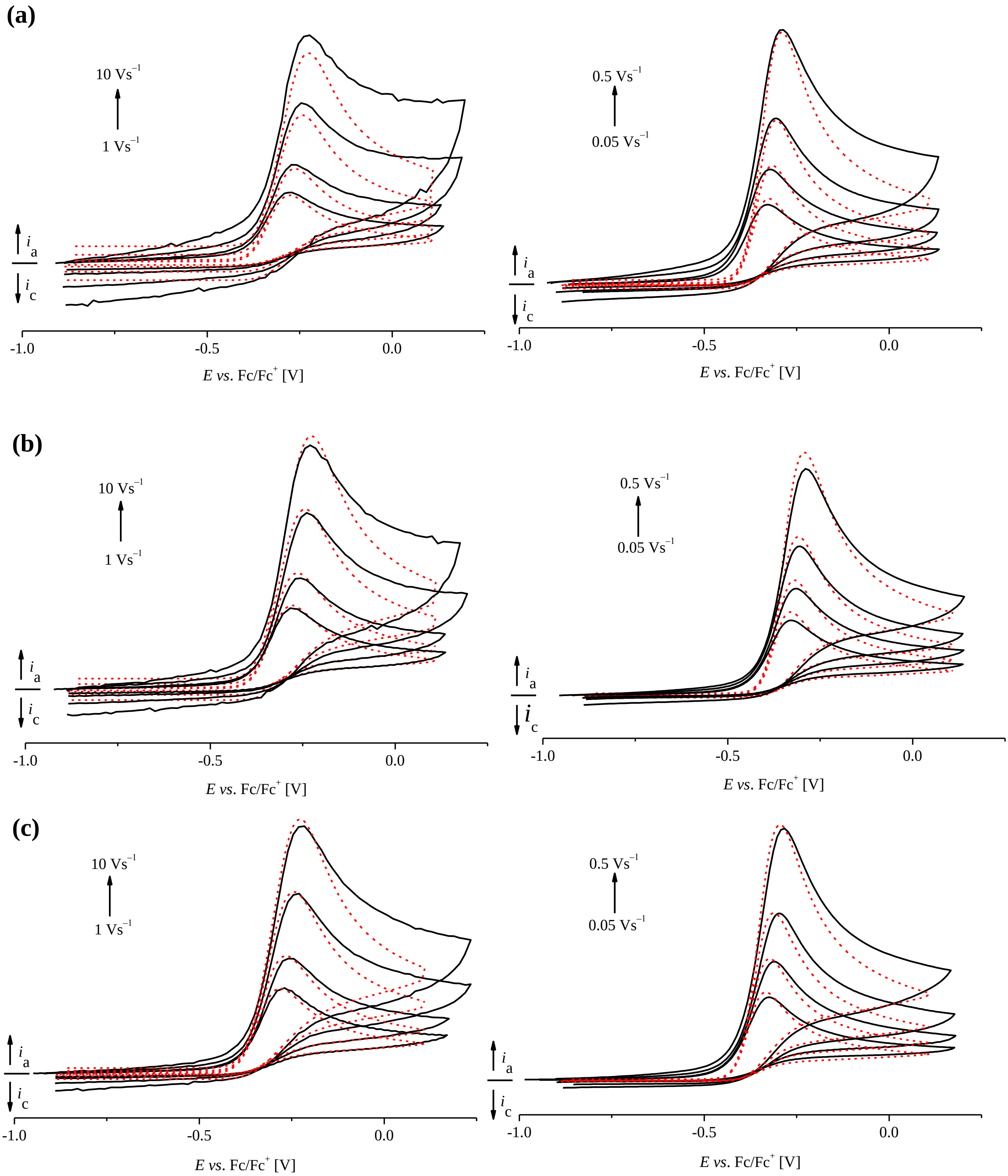

Figure 7.14: Concentration and scan rate dependent CV measurements of **[L^6Ni_2S]PF_6** ((**a**) 0.5 mM, (**b**) 1.0 mM and (**c**) 2.0 mM, scan rates: 50 $mV\cdot s^{-1}$ to 10 $V\cdot s^{-1}$).

Kinetic data from metal linked thiyl radical dimerization reactions are much less reported, in contrast to several kinetic studies of organic thiyl radicals. Franz *et al.*[233] determined a rate constant for the dimerization reaction of $[(Cp^*)_2Mo_2S_4Me]^+$ of $6.5 \cdot 10^7$ $M^{-1} \cdot s^{-1}$ and the rate of the decay by $1.1 \cdot 10^3$ $M^{-1} \cdot s^{-1}$. In **Figure 7.14**, the corresponding experimental CV's and simulated CV's at r.t. are summarized based on **Model 1**. Furthermore, in **Table 7.2** the derived data and chosen parameters for **Model 1** are listed. The oxidation of $\mathbf{[L^6Ni_2S]PF_6}$ occurs at a potential $E_{1/2}([\mathbf{L^6Ni_2S}]^+/([\mathbf{L^6Ni_2(S\cdot)}]^{2+}) = -0.255 \pm 0.01$ V in MeCN. This potential is similar to that of the $(CO)_6Fe_2S_2Me$ cluster ($E_{1/2} = -0.26 \pm 0.05$ V *vs.* Fc/Fc$^+$ in MeCN).[322]

The determination of the parameters of **Model 2** is compared to **Model 1** more complicated, since the second step, reaction of the formed $\mathbf{[L^6Ni_2(S\cdot)]^{2+}}$ with $\mathbf{[L^6Ni_2S]^+}$ to $\mathbf{[L^6Ni_2S\therefore SNi_2L^6]^{3+}}$ includes in addition to k_1 also the equilibrium constant K_1 (**Table 7.2, Scheme 7.3**). A rate constant k_1 for the chemical reaction in **Model 2** is derived of approximately $1 \cdot 10^7$ $M^{-1} \cdot s^{-1}$ (upper limit $1 \cdot 10^{10}$ $M^{-1} \cdot s^{-1}$) and a K_1 of $1 \cdot 10^7$ M^{-1} (upper limit infinity). The oxidation of $\mathbf{[L^6Ni_2S]^+}$ occurs at a potential $E_{1/2}([\mathbf{L^6Ni_2S}]^+/([\mathbf{L^6Ni_2(S\cdot)}]^{2+}) = -0.240 \pm 0.01$ V *vs.* Fc/Fc$^+$ in MeCN. $\mathbf{[L^6Ni_2S\therefore SNi_2L^6]^{3+}}$ is oxidized in a next step to $\mathbf{[(L^6)_2Ni_4(S_2)]^{4+}}$ with $E_2 = -0.92$ V. In **Figure A.7.2** (**appendix**), the corresponding experimental CV's and simulated CV's of **Model 2** are summarized.

In general, the simulated CV's are in good agreement with the experimental CV's. No clear distinction between both models is possible, based on the experimental data and the CV simulations. Neither EPR studies, nor NMR studies provide unambiguous evidence for either of the two models. Further EPR studies, for example of the one electron reduction of $\mathbf{[(L^6)_2Ni_4(S_2)]^{4+}}$ by $CoCp_2$ or the HAT reaction of $\mathbf{[L^6Ni_2(SH)]^{2+}}$ by the 2,4,6-*tert*-butyl phenoxyl radical look on the first glance reasonable, but due to the low radical concentration in comparison to the 2,4,6-*tert*-butyl phenoxyl radical it is unlikely to see any metal-sulfur-based species. In the literature, heteroleptic nickel(II) subsulfido complexes as well as homoleptic complexes are described.[328–330,332] In all those species the $[S_2]^{3-}$ is coordinated in a *side-one* fashion, with S∴S distances between those of persulfido and bis(sulfido) complexes. The synthesis of these complexes is achieved by salt metathesis for the homoleptic complex and by two electron reduction, starting with a nickel supersulfido complex in the heteroleptic complexes. A simple MO of $[S_2]^{3-}$ shows a destabilization of the S–S bond by occupying the σ^* orbital by one electron (**Scheme 7.4**). To date no *end-on* coordinated subsulfide has been mentioned in the literature, which is not surprising based on the frontier orbital considerations of Berry and coworkers.[329,343] In addition, Franz *et al.*[233] and Wieghardt and coworkers never mentioned any observation of a subsulfido complex during their kinetic studies of the transformation of thiyl radicals to the persulfido complexes. DFT based geometry optimization of the species resulting from the one electron reduction of

$[(L^6)_2Ni_4(S_2)]^{4+}$ clearly shows the bond breaking of the $[S–S]^{2-}$ bridge and the formation of a hypothetical tetranickel disulfur adduct (**Figure 7.15**). In the calculated structure, each sulfur anion is bridged between two nickel ions of a dinuclear subunit and in addition bond to one nickel ion of a second molecule (**Figure 7.15**).

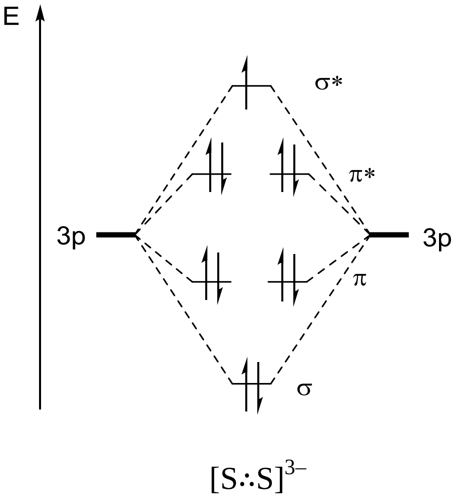

Scheme 7.4: Simple MO scheme of the electronic structure of $[S_2]^{3-\cdot}$.

Consequently, two nickel ions are coordinated in a square pyramidal fashion. No experimental evidence is currently available to show that this theoretical species is stable under real conditions in solution. It is also possible that this structure is only an energetic minimum in the DFT calculation. A key information of this DFT calculation, however, is the observation of a bond breaking of the $[S–S]^{2-}$ unit. In order to better understand the mechanism further, and to exclude the formation of a subsulfido complex, NMR experiments are performed. **$[L^6Ni_2S]^+$** is reacted with 0.5 equiv. of $[Fe(Cp^*)_2]PF_6$ at 233 K or 298 K and in the ^1H NMR spectrum a mixture of **$[(L^6)_2Ni_4(S_2)]^{4+}$** and **$[L^6Ni_2S]^+$** is monitored. The reaction of **$[(L^6)_2Ni_4(S_2)]^{4+}$** with 1.0 equiv. of $CoCp_2$ shows a mixture of **$[L^6Ni_2S]^+$** and **$[(L^6)_2Ni_4(S_2)]^{4+}$** in the ^1H NMR spectrum (see **appendix**). No further species are observed, which could justify the existence of **$[L^6Ni_2S∴SNi_2L^6]^{3+}$** as an intermediate in the solution. The difficulty in obtaining a one electron reduced complex, **$[(L^6)_2Ni_4(S_2)]^{3+}$**, can be explained by DFT calculations. The resulting complex (see **appendix**) lies 116 kJ·mol^{-1} higher in energy than the tetranickel disulfur adduct (**Figure 7.15**). This large difference between **$[L^6Ni_2S∴SNi_2L^6]^{3+}$** and the tetranickel disulfur adduct suggests most likely the mechanistic pathway of the fast S–S bond cleavage after reduction of **$[(L^6)_2Ni_4(S_2)]^{4+}$**. **$[L^6Ni_2S∴SNi_2L^6]^{3+}$** as an intermediate can be excluded. In conclusion an *in situ* formation of the subsulfido complex **$[L^6Ni_2S∴SNi_2L^6]^{3+}$** seems unlikely, due to the probably high instability of the formed $[\mathrm{S}\therefore\mathrm{S}]^{3-}$ unit, which would result in bond breaking. Even though clear experimental proof is still missing, it is more reasonable to assume the observation of a thiyl radical. **$[L^6Ni_2S\therefore SNi_2L^6]^{3+}$** will be not further considered to play a key role in the dimerization reaction of **$[L^6Ni_2(S\cdot)]^{2+}$** and in further reactivity studies. The reduction process from **$[(L^6)_2Ni_4(S_2)]^{4+}$** to **$[L^6Ni_2S]^+$** is described in **chapter 8**. Unfortunately, a simulation of the CV's of this event is not possible (**Figure 7.13** and **Figure 8.7**), since no explanation was found for the pronounced cathodic shift of the wave by increase of the complex concentration. In the next subchapter, the $\mathrm{BDFE}_{(\mathrm{sov.})}$ of the S–H bond is calculated, based on the successful deriving of $E_{1/2}$(**$[L^6Ni_2S]^+/[L^6Ni_2(S\cdot)]^{2+}$**) from the CV simulations of **Model 1** and the determination of the $\mathrm{p}K_\mathrm{a}$ value of **$[L^6Ni_2(SH)]^{2+}$**.

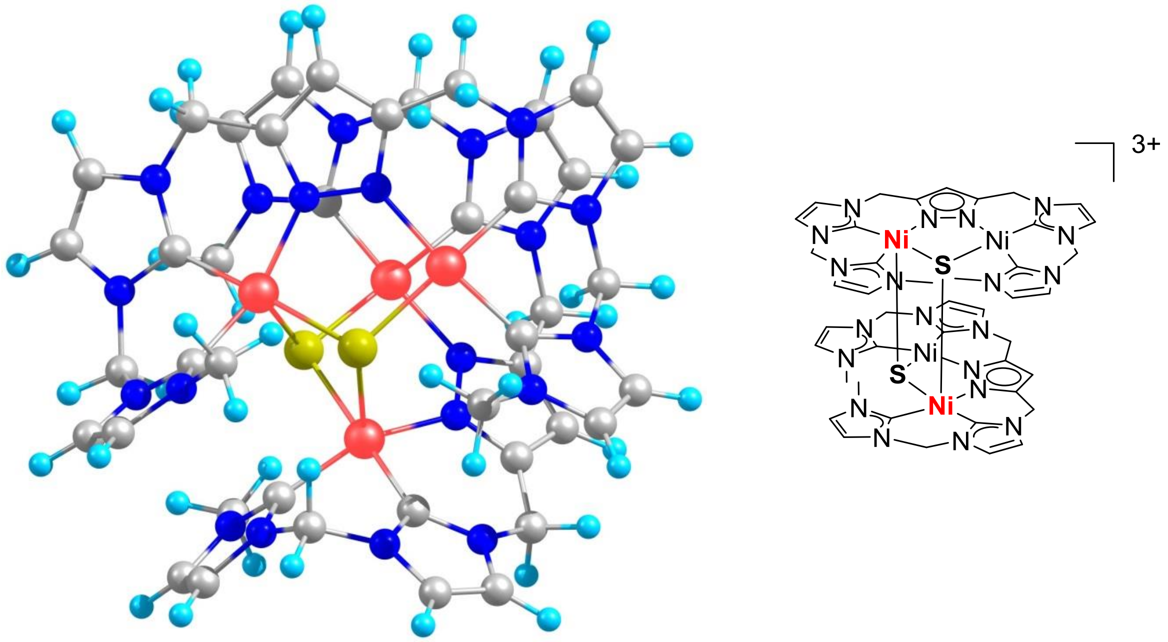

Figure 7.15: Left: Top view of calculated molecular structure of the energetic minimum of the theoretical one electron reduction of **$[(L^6)_2Ni_4(S_2)]^{4+}$**. **Right:** square pyramidal coordination of Ni.

7.3.3 Determination of the S–H bond strength and HAT reactivity studies

In nature thiyl or phenoxyl radicals are playing an important role for the transformation of substrates. One of the important steps during these reactions can be proton-coupled electron transfer (PCET) processes and more concrete hydrogen atom transfer (HAT) processes.[223,224] The terminus hydrogen atom transfer process will be used in this work, as defined by Mayer *et al.*[223] HAT describes a single kinetic step for the transfer of two particles, namely a proton and an electron, originating from the same bond, but does not necessarily mean that these are transferred in a synchronous way. In addition HAT processes will be considered where the transfer of formally H· occurs from a single donor to a single acceptor molecule.[223] In the following the properties of the *in situ* generated **$[L^6Ni_2(S\cdot)]^{2+}$** with respect to HAT processes will be investigated and analyzed. Before doing this, the thermochemistry of **$[L^6Ni_2(SH)]^{2+}$** has to be known in order to choose the substrates X–H which will be tested. This is done under consideration of the corresponding thermochemical square scheme (**Scheme 7.5**) at 298 K.[223] This scheme considers all five thermochemical parameters

- Acidity/basicity of the oxidized and reduced complexes
- Reduction potential of the protonated/deprotonated complexes
- Homolytic bond dissociation free energy ($BDFE_{(solv)}$)

While it is not possible to determine the bond dissociation free energy directly, the value can be calculated from the corresponding experimentally obtained pK_a values and electrochemical potentials $E_{1/2}$. In **chapter 6** a pK_a value of 18.42±0.06 for **$[L^6Ni_2(SH)](PF_6)(OTf)$** was determined in MeCN. $E_{1/2}$(**$[L^6Ni_2S]^+/[L^6Ni_2(S\cdot)]^{2+}$**) = –0.255±0.01 V was determined in this chapter. Based on the experimental data equations (16) and (17) can be set up. As described in **chapter 6** the CV measurements of **$[L^6Ni_2(SH)](PF_6)(OTf)$** showed no oxidative event in the measured regime and **$[L^6Ni_2(SH)]^{3+}$** was not observable.

$$\begin{array}{llll}
[L^6Ni_2(SH)]^{2+} \rightleftharpoons [Ni_2L^6S]^+ + H^+ & pK_a & (16) \\
[L^6Ni_2S]^+ \rightleftharpoons [L^6Ni_2(S\cdot)]^{2+} + e^- & E_{1/2} = E^o & (17) \\
H^+ + e^- \rightleftharpoons H\cdot & E_{1/2} & (18) \\
[L^6Ni_2(SH)]^{2+} \rightleftharpoons [L^6Ni_2(S\cdot)]^{2+} + H\cdot & BDFE_{(solv.)} & (19)
\end{array}$$

This result is not surprising, due to high instability of such systems. No values for thiyl cations ($SH\cdot^+$) have been reported in the literature either.[223] Mayer *et al.*[223] explained this observation with the suggestion that this species has to be highly energetic and highly unstable. Outer sphere oxidation of thiols to give the radical cation is unfavorable and oxidation of thiols leads to loss of H·.[223] Using Hess law[223] the energy change is independent of the path and the $\mathrm{BDFE}_{(\mathrm{solv.})}$ value can be calculated by formula (20), wherein $E_{1/2}$ is defined as E^o in good approximation and $C_{\mathrm{G,solv.}}$ (54.9 kcal/mol in MeCN)[223] is a constant which is equivalent to the H^+/H· standard reduction potential. $C_{\mathrm{G,solv.}}$ includes the free energy for the formation of H·, the free energy of solvation of H· and the nature of the reference electrode at 298 K.[223]

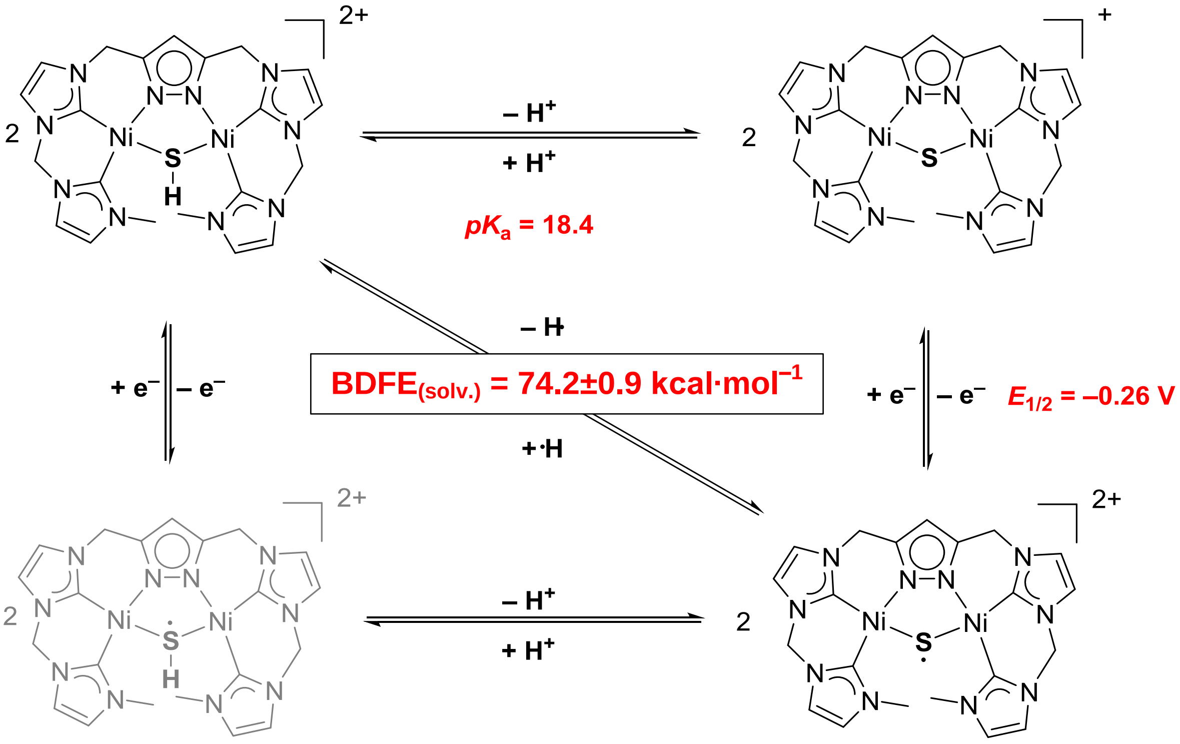

Scheme 7.5: Thermochemical square scheme of the sulfur complexes.

$$\mathrm{BDFE}_{(\mathrm{solv.})}(\mathrm{SH}) = 1.37 \cdot \mathrm{p}K_a + 23.06 \cdot E^{\mathrm{o}} + C_{\mathrm{G,solv.}} \; (20)$$

$$\mathrm{BDFE}_{(\mathrm{solv.})}(\mathrm{SH}) = 1.37 \cdot 18.4 + 23.06 \cdot (-0.255\,) + 54.9 = 74.2\ \mathrm{kcal} \cdot \mathrm{mol}^{-1}$$

Based on this equation a $\mathrm{BDFE}_{(\mathrm{solv.})}$ = 74.2±0.9 kcal/mol of the S–H bond in **[L^{6}Ni$_2$(SH)](PF$_6$)(OTf)** is determined. Unfortunately, values for cysteine or organic thiols were obtained in aqueous solution or in DMSO and are not directly comparable. For instance Borwell *et al.*[344] calculated a $\mathrm{BDFE}_{(\mathrm{solv.})}$ value for phenyl thiol in DMSO (76.9 kcal/mol). All determined bond strengths of S–H bonds in organic molecules are higher than in **[L^{6}Ni$_2$(SH)](PF$_6$)(OTf)**. One reason for this observation is the strong interaction of the metal ion with the thiol group which leads to weakening of the corresponding bond strength. A comparison with M–H bond energies (50-68 kcal/mol) showed that the bond strength in **[L^{6}Ni$_2$(SH)](PF$_6$)(OTf)** is higher.[345–348]

Knowledge about the $\text{BDFE}_{(\text{solv.})}$ of metal complexes bearing a hydrosulfido ligand is lacking. Franz, DuBois and Dupuis *et al.* published $\text{BDFE}_{(\text{solv.})}$ values of S–H bonds of dimolybdenum tertrasulfido clusters and diiron disulfido complexes with different degree of μ-sulfido protonation.[231,232,322,326] The relevant $\text{BDFE}_{(\text{solv.})}$ values are listed in **Table 7.3**. The pioneering work of these scientists is to the best of my knowledge the only example of S–H bond strength determinations of metal thiol complexes. Since 2009 no further metal thiol complexes are published with $\text{BDFE}_{(\text{solv.})}$ values.

Table 7.3: Comparison of reported $\text{BDFE}_{(\text{solv.})}$ values for S–H bond strengths in metal complexes and for the **$[\mathbf{L^6Ni_2(SH)}]^{2+}$** obtained in this work.[220,233,349] Values in ( ) are corrected numbers with $\boldsymbol{C}_{\mathbf{G,solv.}} = 54.9$.

Compound, method	$\text{BDFE}_{(\text{solv.})}$ (MeCN) [kcal/mol]
$[\text{Cp*Mo}(\mu\text{-S})_3(\mu\text{-SH})\text{MoCp*}]^+$	49.4 ± 1.3 (50.7)
$[\text{Cp*Mo}(\mu\text{-SCH}_3)(\mu\text{-S})_2(\mu\text{-SH})\text{MoCp*}]^+$	60.8 ± 1.0 (62.1)
$[\text{Cp*Mo}(\mu\text{-SCH}_3)(\mu\text{-S})(\mu\text{-SH})_2\text{MoCp*}]^+$	61.8 ± 1.6 (63.1)
$[\text{Cp*Mo}(\mu\text{-S})(\mu\text{-SH})_3\text{MoCp*}]^+$	61.9 ± 2.0 (63.2)
$(\text{CO})_3\text{Fe}(\mu\text{-SCH}_3)(\mu\text{-SH})\text{Fe(CO)}_3$	69.4 ± 1.7 (70.7)
This work: **$[\mathbf{L^6Ni_2(SH)}]^{2+}$**	74.2 ± 0.9

A comparison with the values obtained by Franz, DuBois and coworkers shows that the bond strength of the thiol group in **$[\mathbf{L^6Ni_2(SH)}]^{2+}$** is significant higher than in the molybdenum complexes, but only slightly higher than in the dinuclear iron carbonyl complex. Taking into account that Franz and DuBois *et al.*[326,345] used an older and lower $C_{\text{G,solv}}$ value (53.6 kcal/mol) than in this work (54.9 kcal/mol), the $\text{BDFE}_{(\text{solv.})}$[223] values of the latter two complexes are very close (see corrected values in brackets in **Table 7.3**). DuBois and coworkers explored their complexes in the field of proton reduction catalysis, hydrodesulfurization chemistry and hydrogenation reactions. In the latter, they demonstrate the HAT process from a bridged thiol group in their dinuclear molybdenum complex to an unsaturated carbon bond of an organic molecule, resulting in a persistent thiyl radical and an alkyl radical *via* retro-disproportionation reaction.[326] But also the reverse direction, which means HAT process at X–H substrates by a metal complex is of enormous interest.[223] HAT reactions of the reported molybdenum complexes would be quite challenging from a thermodynamic point of view as is evident from the very low $\text{BDFE}_{(\text{solv.})}$ values of the S–H bonds. In contrast to this the HAT chemistry of RO· based complexes is widely explored.[223,350–352] So far HAT processes of metal thiyl radicals are lacking. Here, the HAT reactivity of **$[L^6Ni_2(S\cdot)]^{2+}$** towards substrates is investigated.

The $BDFE_{(solv.)}$ of the S–H bond as determined above is the basis for selecting suitable substrates. Substrates are chosen which have lower but also higher $BDFE_{(solv.)}$ values than the S–H bond of **$[L^6Ni_2(SH)]^{2+}$**. In order to lower the kinetic effect of the side reaction, namely the fast dimerization reaction of **$[L^6Ni_2(S\cdot)]^{2+}$** which is estimated to be approximately $1\cdot10^8$ $M^{-1}\cdot s^{-1}$ at 239 K, all HAT reactions are conducted with a large excess of the substrate (100 equiv.) and at 238 K. In general, **$[L^6Ni_2(SH)]PF_6$** is mixed with the substrate in MeCN-d_3 and cooled down. To the cooled solution $[Fe(Cp^*)_2]PF_6$ or $[FeCp_2]PF_6$ is added under stirring (experimental section). Afterwards, the reaction product is characterized *via* ^{1}H NMR spectroscopy. **Table 7.4** summarizes the findings of the reactions.

7.3.3.1 HAT reaction of $[L^6Ni_2(S\cdot)]^{2+}$ with TEMPO–H

The formal abstraction of H· from TEMPO–H is possible ($BDFE_{(solv.)}$ = 66.5 kcal·mol^{-1}). Under presence of 100 equiv. of substrate in a MeCN-d_3 solution of **$[L^6Ni_2S]PF_6$**, $FcPF_6$ is added and an immediate color change from red-orange to pale yellow is observed. ^{1}H NMR spectroscopy of the solution shows the formation of **$[L^6Ni_2(SH)]^{2+}$**, based on the H^{pz} proton resonances of the ligand. After oxidation of **$[L^6Ni_2S]PF_6$** to the thiyl radical, a HAT reaction from TEMPO–H to **$[L^6Ni_2(S\cdot)]^{2+}$** occurs, which results in the formation of **$[Ni_2L^6SH]^{2+}$**. This reaction is possible due to the large excess of TEMPO–H in the solution and the higher $BDFE_{(solv.)}$ value of the S–H bond in the formed **$[L^6Ni_2(SH)]^{2+}$** complex (74.2 kcal/mol). The proton resonance of the S–H group is not observed in the ^{1}H NMR spectrum, due to fast proton exchange between the substrates (N–H or O–H bonds, 100 equiv.) and the S–H bridge. A ^{1}H NMR titration experiment of **$[L^6Ni_2S]PF_6$** with different equiv. of TEMPO–H (0.3 equiv. to 10 equiv.) showed no marked shift of the proton resonances of the complex. After addition of 3.0 equiv. to 10.0 equiv. of TEMPO–H, a slightly shift of the H^{pz} proton resonance by 0.02 ppm is observed. Consequently, a negligible interaction between TEMPO–H and **$[L^6Ni_2S]PF_6$** is observed (see **appendix**).

The tendency of **$[L^6Ni_2(S\cdot)]^{2+}$** to dimerize as well as the influence of the substrate amount is tested by an additional experiment. Performing the HAT experiment with only 10.0 equiv. of TEMPO–H results primarily in the formation of **$[(L^6)_2Ni_4(S_2)]^{4+}$**, while approximately 11% conversion to **$[L^6Ni_2(SH)]^{2+}$** is observed. This experiment indicated the necessity of a large excess of the substrates, to avoid the competitive formation of **$[(L^6)_2Ni_4(S_2)]^{4+}$**.

TEMPO·/TEMPO–H has an outstanding role, since it is also able to initiate a HAT process at **[L^{6}Ni$_{2}$(SH)]$^{2+}$**, which leads to the formation of **[(L^{6})$_{2}$Ni$_{4}$(S$_{2}$)]$^{4+}$**. A further discussion of this issue can be found in **chapter 8**, where the diverse synthetic routes for the synthesis of **[(L^{6})$_{2}$Ni$_{4}$(S$_{2}$)]$^{4+}$** are described.

Further thermodynamic values, like ΔG^{o}_{CPET}, ΔG^{o}_{ET} and ΔG^{o}_{PT} (21-23) for the HAT process from TEMPO–H to [**L^{6}Ni$_{2}$(S·)**]$^{2+}$ can be derived based on the thermodynamic square (**Scheme 7.5**), and by considering the equations below.[353]

$$\Delta \boldsymbol{G^{o}_{CPET}} = \mathrm{BDFE}_{(\mathrm{solv.})}\,(\mathrm{TEMPOH}) - \mathrm{BDFE}\,([\mathrm{L^6Ni_2(SH)}]^{2+}) \qquad (21)$$

$$= 66.5\ \mathrm{kcal{\cdot}mol^{-1}} - 74.2\ \mathrm{kcal{\cdot}mol^{-1}} = -7.70\ \mathrm{kcal{\cdot}mol^{-1}} \pm 0.9\ \mathrm{kcal{\cdot}mol^{-1}}$$

$$\Delta G^{o}_{ET} = -F \cdot E^{o} \qquad (22)$$

$$= -(23.06\ \mathrm{kcal \cdot mol^{-1} \cdot V^{-1}}) \cdot \left[\left(E^{o}\left([\mathrm{L^6Ni_2S}]^{2+/+}\right) - E^{o}\left(\mathrm{TEMPOH}^{+/0}\right)\right]\right.$$

$$\Delta \boldsymbol{G^{o}_{ET}} = -23.06\ \mathrm{kcal{\cdot}mol^{-1}{\cdot}V^{-1}}{\cdot}(-0.255\ \mathrm{V} - 0.710\ \mathrm{V}) = +22.3\ \mathrm{kcal{\cdot}mol^{-1}} \pm 0.2\ \mathrm{kcal{\cdot}mol^{-1}}$$

$$\Delta G^{o}_{PT} = -R \cdot T \cdot \ln(K) = -(1.37\ \mathrm{kcal \cdot mol^{-1}}) \cdot \Delta pK_{a} \qquad (23)$$

$$\Delta \boldsymbol{G^{o}_{PT}} = -1.37\ \mathrm{kcal{\cdot}mol^{-1}}{\cdot}(18.4 - 41.0) = +30.7\ \mathrm{kcal{\cdot}mol^{-1}} \pm 0.2\ \mathrm{kcal{\cdot}mol^{-1}}$$

The calculation of the barrier ($\Delta G^{\ddagger}$) is not possible, due to limitation of analytic methods. In order to obtain the reaction rate and the activation parameters $\Delta H^{\ddagger}$ and $\Delta S^{\ddagger}$ further experiments are necessary. Preliminary UV-vis experiments monitoring the reaction of TEMPO· and **[L^{6}Ni$_{2}$(SH)]$^{2+}$** show that this method is not useful to extract kinetic data, since the bands of the TEMPO· cover the bands of the complex in the relevant region (around 400 nm). Based on this observation no rate determination of this HAT process *via* UV-vis spectroscopy is possible. NMR spectroscopy as analytical method can be challenging due to the fast reaction rate of the HAT process in comparison to the NMR time scale. Preliminary HAT reaction tests with 10.0 equiv. of TEMPO· and **[L^{6}Ni$_{2}$(SH)]$^{2+}$** at 298 K show only the final product **[(L^{6})$_{2}$Ni$_{4}$(S$_{2}$)]$^{4+}$** after the first scan. In addition the high amount of paramagnetic substrate leads to NMR spectra with low resolution. Without determination of $\Delta G^{\ddagger}$, no statement concerning the mechanism of the HAT process can be made. Unfortunately it will stay unclear if the HAT process of the reaction of TEMPO–H with [**L^{6}Ni$_{2}$(S·)**]$^{2+}$ follows a concerted pathway or stepwise pathway due to the missing $\Delta G^{\ddagger}$. Mayer and coworkers have described TEMPO–H as a substrate which favors a concerted proton-coupled electron transfer process.[223] TEMPO–H is a very poor acid (pK_{a} = 41) and has a moderate oxidation potential

(E_p = 0.7 V *vs.* Fc/Fc$^+$).[353] Addition of [Fe(Cp*)$_2$]PF$_6$ to TEMPO–H showed no reactivity, proved by ^{1}H NMR spectroscopy. Based on the known HAT processes with TEMPO–H as a substrate, a concerted pathway seems most likely for the reaction of **[L^{6}Ni$_2$S]PF$_6$** with TEMPO–H and [Fe(Cp*)$_2$]PF$_6$ in agreement with previously reported examples.[352,353]

7.3.3.2 HAT reaction of [L^{6}Ni$_2$(S·)]$^{2+}$ with phenylhydrazine

Reaction of [**L^{6}Ni$_2$S]PF$_6$** with 100 equiv. of phenylhydrazine and [Fe(Cp*)$_2$]PF$_6$ leads to the formation of **[L^{6}Ni$_2$(SH)]$^{2+}$**, indicated by ^{1}H NMR spectroscopy. The addition of 100 equiv. of phenylhydrazine to [**L^{6}Ni$_2$S]PF$_6$** results in a low-field shift of all proton resonances of the complex. ESI-MS of the mixture is conducted to confirm the stability of [**L^{6}Ni$_2$S]PF$_6$** under presence of phenylhydrazine. All proton resonances observed by ^{1}H NMR spectroscopy of **[L^{6}Ni$_2$(SH)]$^{2+}$** show a high-field shift under presence of phenylhydrazine after HAT reaction. ^{1}H DOSY NMR spectroscopy of **[L^{6}Ni$_2$S]$^+$** and **[L^{6}Ni$_2$(SH)]$^{2+}$** under presence of phenylhydrazine showed similar diffusion coefficients.

In addition, the HAT reaction is followed by a stopped-flow double-mixing UV-vis experiment. In a first step, 200 equiv. of phenylhydrazine and 1.0 equiv. of [**L^{6}Ni$_2$S]PF$_6$** are mixed together (**Figure 7.16**, **black**) at –20 °C and the UV-vis spectrum of the mixture confirms the stability of [**L^{6}Ni$_2$S]PF$_6$** by its characteristic band at 393 nm, in agreement with the UV-vis spectrum of [**L^{6}Ni$_2$S]PF$_6$** (**chapter 5**). In a next step [Fe(Cp*)$_2$]PF$_6$ is added in the double-mixing set up and the reaction is monitored by UV-vis spectroscopy (**Figure 7.16** (**b**)). A decrease of the bands is observed and a broad band at 378 nm is obtained (**Figure 7.16** (**a**) and (**b**) **blue**), which is in agreement with UV-vis data of the pure **[L^{6}Ni$_2$(SH)]$^{2+}$** complex (**chapter 6**). In **Figure 7.16** (**c**), the change of the band at 401 nm is followed over time and shows an exponential decrease. The half-life, $t_{1/2}$, of the reaction is 70 s and the decrease is followed over more than 11 half-lives. The exponential fit of the decrease is first order and a k_{obs} = 6.66·10^{-3} s^{-1} for the HAT reaction of **[L^{6}Ni$_2$(S·)]$^{2+}$** with 200 equiv. of phenylhydrazine at –20 °C is obtained. The obtained k_{obs} is in the range of previously described HAT reactions with phenylhydrazine. Meyer *et al.*[352] reported the HAT reactivity of a dicopper superoxido complex with phenylhydrazine and obtained a k_{obs} = 17.9·10^{-3} s^{-1} (–20°C, 200 equiv. phenylhydrazine in MeCN).

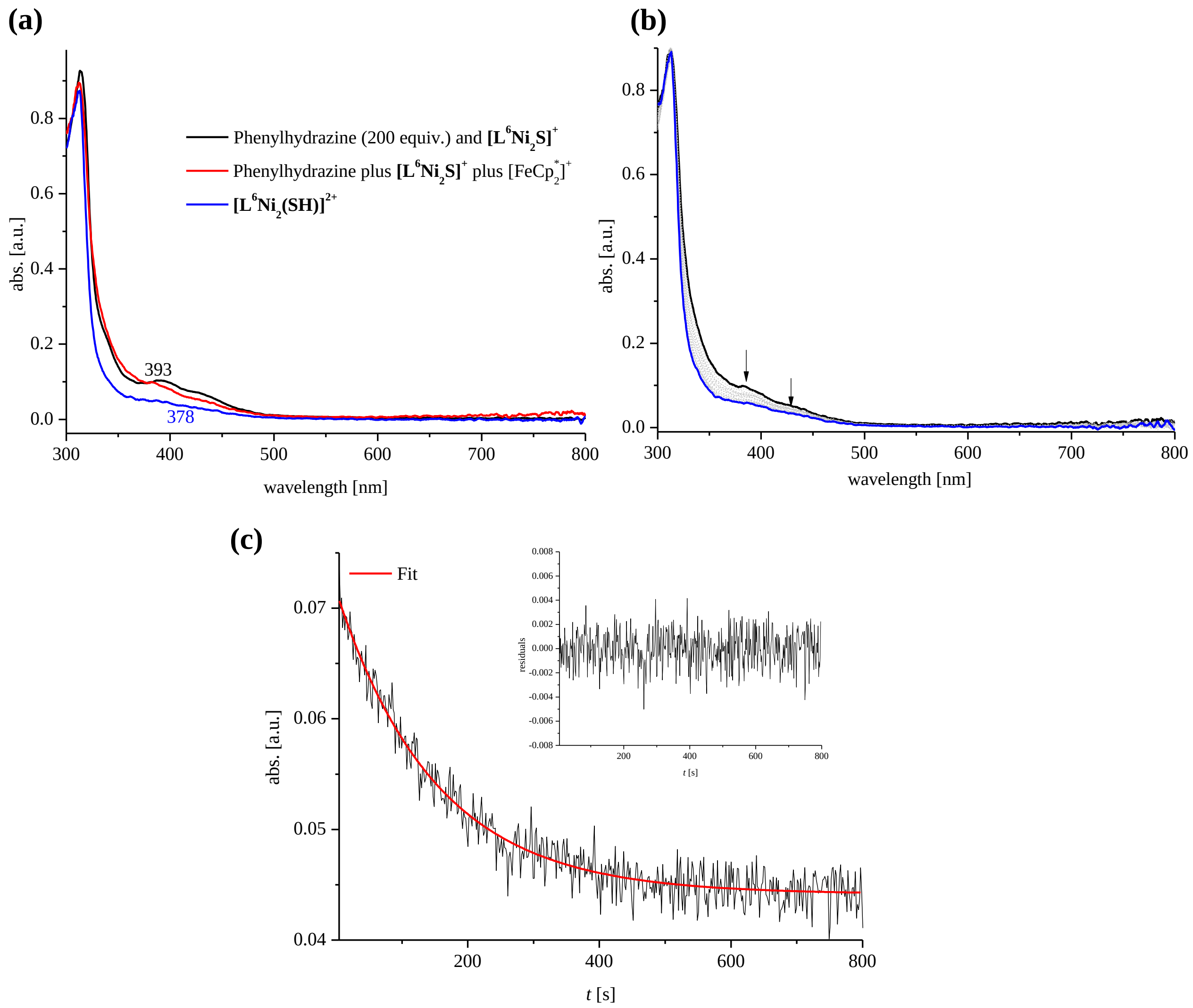

Figure 7.16: (**a**) UV-vis spectra of [**L^6Ni_2S]PF_6**/phenylhydrazine (1:200) (**black**), first spectrum after double mixing of [**L^6Ni_2S]PF_6**/phenylhydrazine with [Fe(Cp*)$_2$]PF_6 (**red**) and final UV-vis spectrum shows the band of **[$L^6Ni_2(SH)$]$^{2+}$** after HAT process (**blue**) (**b**) UV-vis spectra of the double mixing experiment. (**c**) Indirect monitoring of the reaction by decrease of the complex absorbance at 401 nm over time. **Red line** shows exponential fit and inset the residual of the fit.

7.3.3.3 HAT reaction of [L^{6}Ni$_2$(S·)]$^{2+}$ with 1,4-cyclohexadiene

After the activation of X–H bonds (X = O, N), the HAT reactivity of [**L^{6}Ni$_2$S]PF$_6$** with stronger C–H bonds is investigated. Whereas no HAT of the C–H bonds in 9,10-dihydroanthracene is observed (BDFE$_{(solv.)}$ = 75.0 kcal·mol^{-1})[223], an conversion of approximately 18 % of 1,4-cyclohexadiene is observed *via* ^{1}H NMR spectroscopy (**Scheme 7.6** and **Figure 7.17**). Unfortunately, the amount of benzene is already too high in the 2,4,6-*tert*-butylphenol stabilized 1,4-cyclohexadiene to confirm the direct formation of benzene. Consequently, the transformation is exclusively confirmed by the ratio of observed **[L^{6}Ni$_2$(SH)]$^{2+}$** and formed persulfido complex. The formation of **[L^{6}Ni$_2$(SH)]$^{2+}$** is further confirmed by ^{1}H DOSY NMR spectroscopy and ESI-MS (experimental section). The presented results of the HAT reactivity are in agreement with the determined BDFE$_{(solv.)}$ of [**L^{6}Ni$_2$S]PF$_6$** and the chosen substrates. Further substrate reactions are not possible due to the low BDFE$_{(solv.)}$ of the S–H bond and the high driving force for the dimerization reaction of [**L^{6}Ni$_2$S]PF$_6$**.

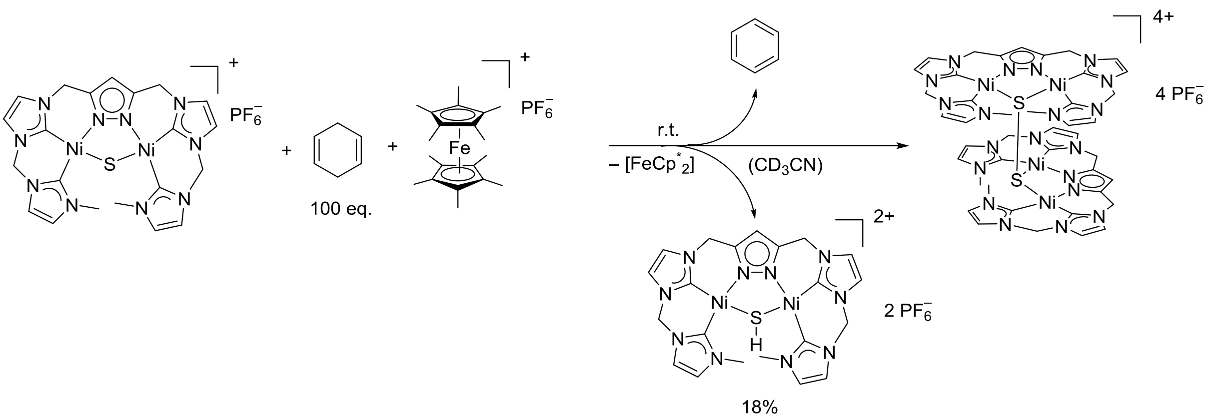

Scheme 7.6: HAT reaction of 1,4-cylohexadiene (18%) by *in situ* generated **[L^{6}Ni$_2$(S·)]$^{2+}$** and [**(L^6)$_2$Ni$_4$(S$_2$)**]$^{4+}$ *via* dimerization reaction of **[L^{6}Ni$_2$(S·)]$^{2+}$**.

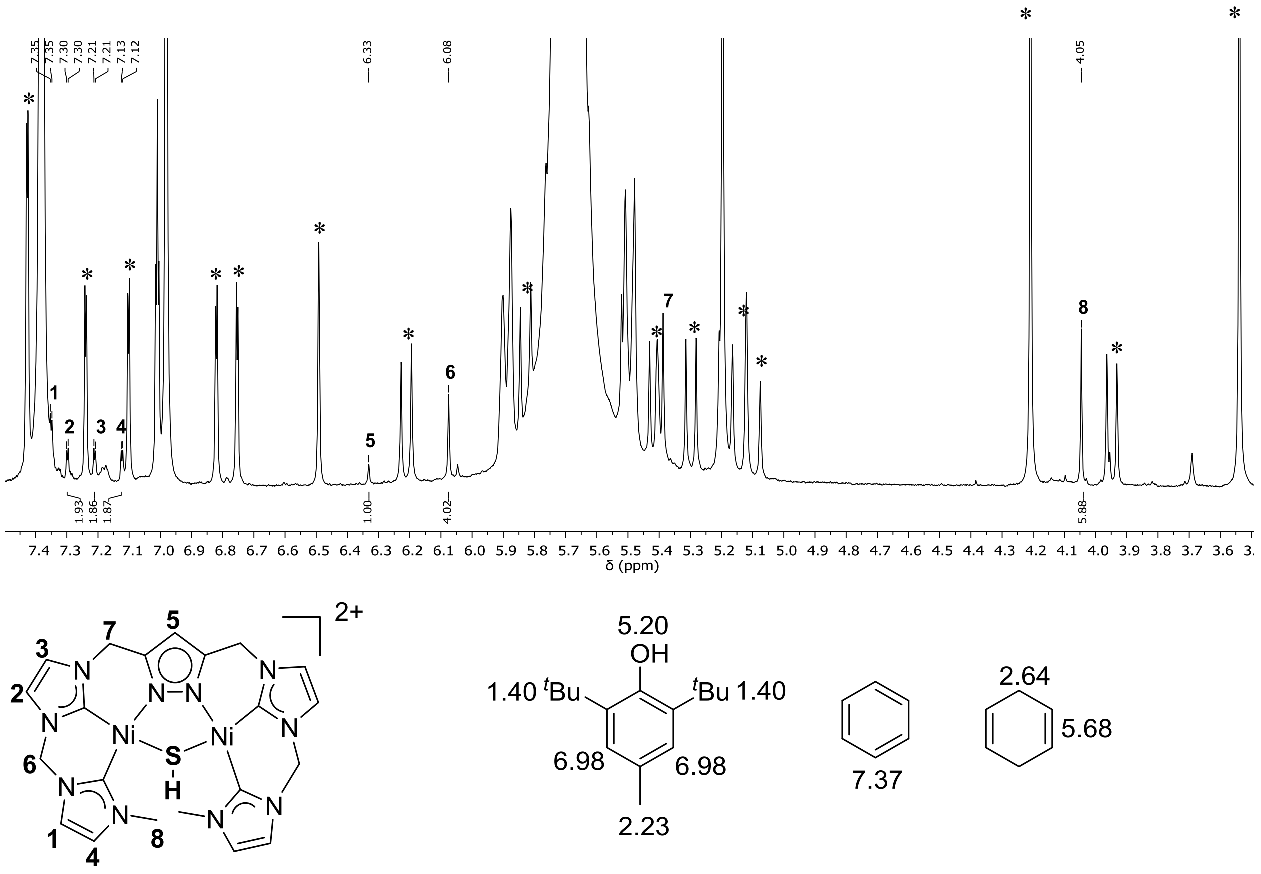

Figure 7.17: Top: ^{1}H NMR spectrum of the reaction mixture after oxidation of **[L^{6}Ni$_2$S]PF$_6$** by [Fe(Cp*)$_2$]PF$_6$ in the presence of 100 equiv. of 1,4-cyclohexadiene. (*) corresponds to the persulfido-bridged complex (**chapter 8**). **Bottom:** assignment of the proton resonance of the generated **[L^{6}Ni$_2$(SH)]$^{2+}$**complex and ^{1}H NMR chemical shifts of the organic molecules.

Table 7.4: Employed substrates for the HAT process *via* thiyl radical complex, together with their BDEF(solv.) and the observed capability of the complex to abstract H· from the substrate.[352,353]

Substrate	BDFE$_{\text{(solv.)}}$ (MeCN) [kcal/mol]	H· abstraction by **[L^{6}Ni$_2$(S·)]$^{2+}$**
9,10-Dihydroanthracene	75.0	No
1,4-Cyclohexadiene	72.9	18%
Phenylhydrazine	70.4	Yes
TEMPO–H	66.5	Yes

7.4 Conclusion and Outlook

In this chapter the first dinuclear thiyl radical-bridged complex and its spectroscopic data are presented. The EPR spectrum and DFT calculations confirmed the presence of a mainly sulfur centered radical with interaction to the two metal centers. In addition the BDFE$_{(solv.)}$ of the S–H bond of **$[L^6Ni_2(SH)]^{2+}$** is determined based on the thermodynamic square scheme. Furthermore, HAT processes with organic molecules are tested and validated the obtained BDFE$_{(solv.)}$ value. To the best of my knowledge this complex is the first example for which HAT processes starting from a thiyl radical are demonstrated. In order to further understand the mechanism of this HAT processes, kinetic studies have to be conducted, in order to give a statement about the reaction rate, and the kind of formally H· transfer (concerted or stepwise pathway). Due to lack of comparable systems this complex can be used as a model system for computational studies and also for exploring further the field of HAT processes.

8

Sulfido and hydrosulfido transformations at a preorganized dinickel center to a supramolecular tetra nickel persulfido complex

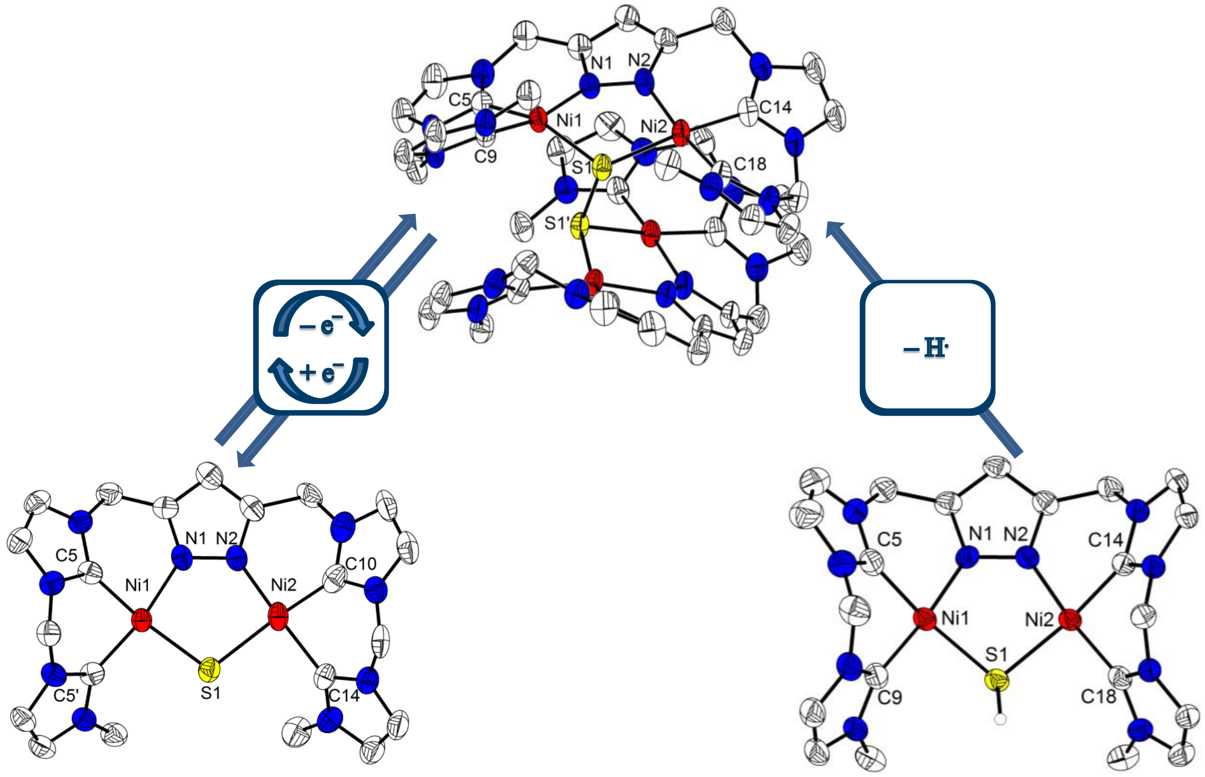

Abstract: In this chapter, the electrochemical and chemical conversion of **[L^6Ni_2S]PF_6** and a unique tetranickel(II) persulfido complex is described. In addition, the transformation of **[$L^6Ni_2(SH)$](PF_6)(OTf)** to the supramolecular complex *via* hydrogen atom abstraction reaction is investigated. Due to the important role of nitric oxide in the cellular signaling and its regulatory role in several biochemical processes, the reactivity of **[L^6Ni_2S]PF_6** and the tetranickel(II) persulfido NHC complex with NO is tested.

8.1.1 Coordination motifs of nickel sulfur complexes

In the previous **chapters 5-7** dinickel μ-sulfido, μ-hydrosulfido and μ-thiolato complexes are described with a compartmental pyrazolate/tetra-NHC ligand. The coordination of these anions is possible by the preorganized dinuclear nickel centers.

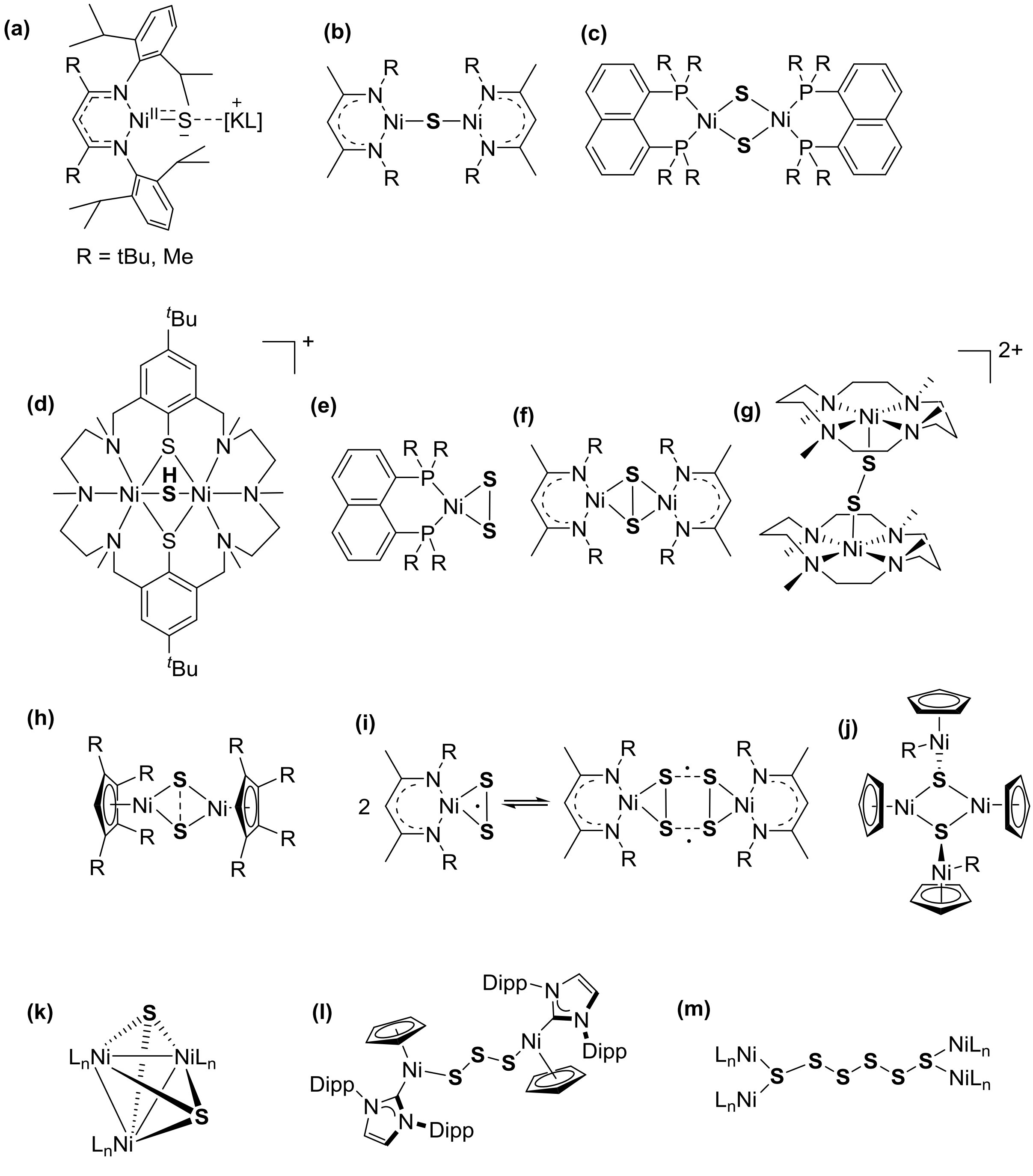

Scheme 8.1: Nickel/sulfur coordination motifs reported in the literature. (**a**) masked nickel(II) sulfido[168,354–357], (**b**) linear Ni$_2$ μ-sulfido[206,358,359], (**c**) Ni$_2$ (μ-S)$_2$[357,360] (**d**) Ni$_2$ μ-SH[235] (**e**) Ni(η^2-S$_2$)[360], (**f**) Ni$_2$(μ^2-η^2:η^2-S$_2$)[234,331,359,361], (**g**) Ni$_2$(μ-κ^1:κ^1-S$_2$)[362–364], (**h**) [Ni$_2$(μ^2-η^2:η^2-S$_2$)][328–330,332], (i) Ni(η^2-S$_2$) radical[328,330,331], (**j**) Ni$_4$(μ-S)$_2$[365] (**k**) Ni$_3$(μ-S)$_3$[366,367], (**l**) Ni$_2$(μ-κ^1, κ^1-S$_3$)[362], (**m**) Ni$_4$(μ-κ^1, κ^1-S$_6$)[235].

In the literature, several coordination motifs of di-, tri- or tetra-nickel centers with mono-, di-, tri- and hexa-chalcogenides are reported.[168,206,361,363,364,368–371,235,328–331,354,357,359] Most of these complexes are synthesized by initial reaction of a mononuclear nickel(I) complex with elemental sulfur at low temperature. In case of the dinuclear complexes a self-assembly of the mononuclear subunits and as a consequence the formation of dinuclear compounds is observed. To date, three different coordination motifs of nickel disulfido complexes are known, namely $Ni(\eta^2\text{-}S_2)$[360], $Ni_2(\mu\text{-}\eta^2\text{:}\eta^2\text{-}S_2)$[234,331,359,361] and $Ni_2(\mu\text{-}\kappa^1,\kappa^1\text{-}S_2)$[362–364] (**Scheme 8.1**, (**e**)-(**g**)).

As mentioned in **chapter 5** and **chapter 7**, the disulfido units have important functions in nature, for instance in folding and unfolding of proteins (**chapter 5**) or in reduction of nucleotides to deoxynucloetides by *E. coli* (class Ia RNR) (**chapter 7**). In the latter case, the formation of a subsulfide S_2^{3-} is proposed. A dinickel(II) μ-subsulfido complex is reported by Sitzmann *et al.*[332] (**Scheme 8.1**, (**h**)). In contrast to dinuclear sulfur complexes, only a low number of tetranuclear nickel complexes are known (**Scheme 8.1**, (**j**) and (**m**)).[235,365,366] In 2008, a macrocyclic dinickel(II) complex is reported which is transformed to a dimer with a hexasulfido bridge between the two macrocycles (**Scheme 8.1**, (**m**)) and a ligand scaffold as in (**d**). Neither such an coordination motif with a tetranickel(II) complex bearing a tetrasulfido unit, nor with a disulfido unit is reported to date, even though tetranuclear metal disulfido complexes are already isolated.[372] In 2008, Franz and coworkers[372] presented a persistent thiyl radical in a dinuclear molybdenum compound $MoS_3SMe(Cp^*)_2$ and the reversible dimerization of this metal complex under formation of a tetranuclear molybdenum μ_4-S_2 bridging subunit (**Figure 8.1**).[372]

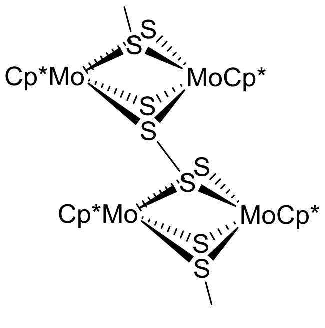

Figure 8.1: A rare tetra-molybdenum μ_4-S_2 unit in a dimerized $Mo_2S_2S(SMe)(Cp^*)_2$ cluster.[372]

A very low dimer bond dissociation free energy for the complex was determined (6.5 kcal·mol^{-1}) at 298 K in toluene-d_8. A further example of a dynamic covalent bond (DCB)[373] is shown by a 2,2,6,6-(tetramethylpiperidin-*1*-yl)disulfide (BiTEMPS) with markedly lower BDE of the S–S bond with 26-31 kcal·mol^{-1}[374,375] compared to dialkyldisulfides (60-70 kcal·mol^{-1})[376]. Such systems are finding high interest in radical reactions, such as polymerization reactions.[376]

8.1.2 *In vivo* transport of NO – H_2S/NO cross talk

NO, H_2S and CO are important gaseous transmitters and function *in vivo* as cellular signaling molecules. NO for instance is a biological regulator and mediates cardiovascular, nervous and immune functions in the body.[168,377] NO is also capable of destroying tumor cells and bacteria.[378] The NO molecule can strongly interact with H_2S in a so-called ‘cross talk’, and additionally reacts with metal sulfur-containing enzymes like iron sulfur clusters. In this case the resulting products are S, S^{2-} or H_2S. The *in vivo* transport of NO is subject of ongoing research and several possibilities have been reported. One example is the transformation of NO to *S*-nitrosylated cysteinyl thiols. In a *S*-transnitrosylation reaction formally NO^+ will be transferred from one *S*-nitrosylated cysteinyl thiol to a cysteinyl thiol under formation of another cysteine thiol and a new *S*-nitrosylated cysteinyl thiol.[379] This reaction is a reversible reaction.[379] An alternative pathway for NO transport is the generation of low molecular weight *S*-nitrosothiols.[378,380] At the moment there is an ongoing debate regarding the existence and function of $[SNO]^-$ and $[SSNO]^-$ *in vivo* as a transport vehicle or as a reservoir for nitric oxide and sulfur.[168,377,379] It is postulated that HSNO will be formed by a reaction of the gaseous transmitter H_2S with *S*-nitrosylated cysteinyl thiol, which can pass the barrier of hemoglobin membranes or smooth muscle cells and initiate the nitrosylation of hemoglobin or the relaxation of blood vessels.[378,380]

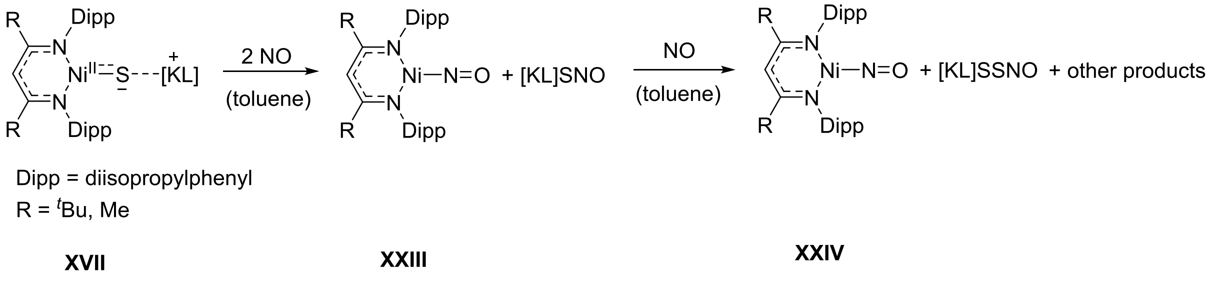

Scheme 8.2: Proposed mechanism of the formation of potassium perthionitrite **XXIV** after reaction of a complex **XVII** with excess of NO. $[KL]^+$ = potassium, chelated by 18-crown-6 ether.[168]

Furthermore, several investigations are performed to improve the knowledge of the reactivity of transition metal sulfido complexes with small molecules, especially with NO. In 2016, Hayton *et al.*[168] reported the reactivity of a complex **XVII** with the gaseous transmitters CO and NO. It is shown, that after reaction of the nickel(II) complex with excess of NO gas a nickel nitrosyl complex **XXIII** and a potassium 18-crown-6 ether perthionitrite complex **XXIV** (**Scheme 8.2**) are obtained. Furthermore, they investigated the mechanism of the reaction and proposed in the first step an abstraction of sulfide by NO under formation of the nickel nitrosyl complex and [KL]SNO. This ion pair reacts further with a second NO molecule to [KL]SSNO and further unknown products. This is the first detailed investigation of the synthesis of perthionitrite *via* reaction of NO with a metal sulfido complex.[168]

8.2 Objectives

Motivated by the lack of multinuclear nickel(II) persulfido complexes a synthetic route is investigated to obtain this still missing coordination motif (**Figure 8.2**). Detailed investigations of this unique complex are performed and an alternative approach for the synthesis of this complex is tested. In addition the properties of the complex for reversible bond cleavage, interconversion with **[L^{6}Ni$_2$S]PF$_6$** and reactivity with dihydrogen and NO are investigated.

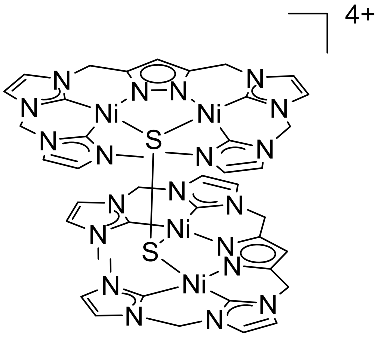

Figure 8.2: Structural proposal of the novel tetranickel(II) μ_4-S_2 coordination motif.

8.3. Results and Discussion

8.3.1 A novel coordination motif of nickel(II) sulfur complexes

The first tetranuclear nickel(II) persulfido-bridged complex **$[(L^6)_2Ni_4(S_2)](PF_6)_4$** is obtained by direct oxidation of **$[L^6Ni_2S]PF_6$** with Cp_2FePF_6 (**Scheme 8.3**). Despite the **$[L^6Ni_2S]^+/[L^6Ni_2(S\cdot)]^{2+}$** potential $E_{1/2} = –0.255$ V±0.01 V, also the quantitative transformation of **$[L^6Ni_2S]PF_6$** to the persulfdio-bridged complex by use of $[Fe(Cp^*)_2]PF_6$ ($E_{1/2} = –0.59$ V *vs.* Fc/Fc^+ in MeCN)[333] is possible and shows that the presence of small amounts of formed thiyl radical complex can shift the equilibrium quantitatively to the side of the thermodynamically stable **$[(L^6)_2Ni_4(S_2)](PF_6)_4$**.

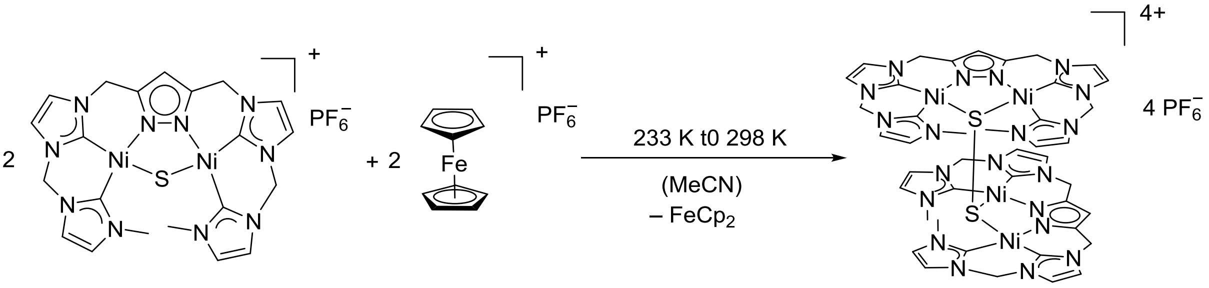

Scheme 8.3: Synthesis of **$[(L^6)_2Ni_4(S_2)](PF_6)_4$** by oxidation of **$[L^6Ni_2S]PF_6$** with $[FeCp_2]PF_6$.

Single pale-yellow crystals of **$[(L^6)_2Ni_4(S_2)](PF_6)_4$** are obtained by slow diffusion of Et_2O into a complex solution in MeCN. The molecular structure in solid state shows a C_2 symmetrical complex, which crystalizes in the space group $P2_1/c$ (**Figure 8.3**). Both dinuclear subunits are turned by around 90° to each other (**Scheme 8.3**). The CH_3 groups of each subunit are both pointing to the opposite directions away from the S–S bridge. Pöthig *et al.*[381] described an encapsulation of a halide ion by two macrocyclic dinickel(II) complexes. (**chapter 5** and **8**). They named this supramolecular complex capsoplex. A similar conformation of the two subunits, as observed in the capsoplex, can be observed in **$[(L^6)_2Ni_4(S_2)](PF_6)_4$**. Both subunits are crystallographically identical. The nickel···nickel distance is within each dinuclear subunit 3.53 Å, similar to **$[(L^6)_2Ni_4(SHS)](PF_6)_3$** (3.52 Å, **chapter 8**) and is the largest intermetallic distance for dinickel(II) complexes of the present pyrazolate/NHC ligand system, described in this thesis. Ni(1) is located 0.13 Å out of the C(9)–N(1)–C(5)–S(1) plane and Ni(2) 0.06 Å out of the C(18)-S(1)–N(2)–C(14) plane. The angle between both planes is 16.0 Å and the smallest angle of all observed complexes, obtained in this thesis. The S–S bond length is with 2.13 Å in the region of the S–S bonds found for some tetranuclear molybdenum persulfido complexes (2.17 Å-2.06 Å).[233,349] Relevant bond angles and bond lengths are listed in **Table 8.1** and **Table 8.2**.

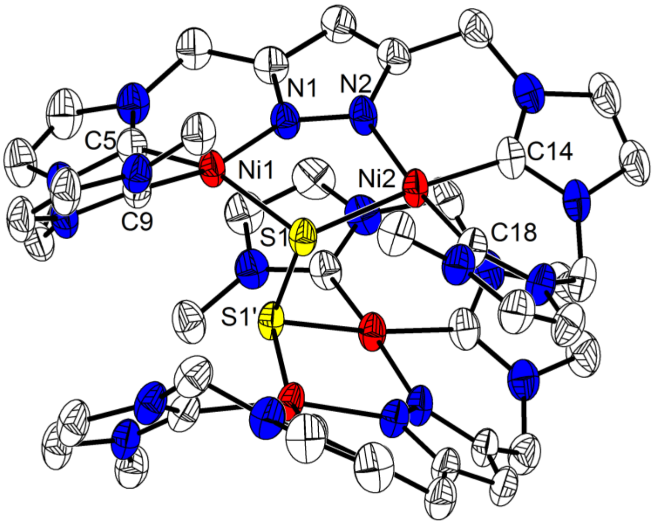

Figure 8.3: Molecular structure (50% probability thermal ellipsoids) of the cationic part of **$[(L^6)_2Ni_4(S_2)](PF_6)_4$**. H atoms are omitted for clarity.

Table 8.1: Selected bond angles for **$[(L^6)_2Ni_4(S_2)](PF_6)_4$** [°].

Atoms	Bond angles
C5–Ni1–C9	86.8(5)
C5–Ni1–N1	88.2(8)
C9–Ni1–S1	95.9(0)
N1–Ni1–S1	90.5(8)
C14–Ni2–C18	86.5(4)
C14–Ni2–N2	88.3(2)
C18–Ni2–S1	96.6(9)
N2–Ni2–S1	88.8(4)
Ni1–S1–Ni2	102.(9)

Table 8.2: Selcted bond lengths for **$[(L^6)_2Ni_4(S_2)](PF_6)_4$** [Å].

Atoms	Bond lengths
Ni1····Ni2	3.534(9)
Ni1–C5	1.862(3)
Ni1–C9	1.879(3)
Ni1–N1	1.884(2)
Ni1–S1	2.205(2)
Ni2–C14	1.865(3)
Ni2–C18	1.880(3)
Ni2–N2	1.889(2)
Ni2–S1	2.205(4)

The ^{1}H NMR spectrum of crystalline **$[(L^6)_2Ni_4(S_2)](PF_6)_4$** dissolved in MeCN-$d_3$ shows a C_2 symmetrical complex in solution (**Figure 8.4**) with the expected set of 19 signals. All 23 protons of the complex subunit can be assigned to the ^{1}H resonances by 2D NMR spectroscopic methods. All CH_2 groups of the complex show a diastereotopic splitting of the proton resonances with a pronounced chemical shift difference between the vicinal protons. A reason for these differences might be the orientation of the protons relative to the second subunit of the complex. Hereby the protons, which are orientated towards the second subunit will be more shielded than the protons which are pointing away. In addition, a markedly different chemical environment of the two CH_2 groups, located between the imidazol-*2*-ylidene units is observed. The chemical shift difference of the two centers of the spin systems is determined with approximatively $\Delta\upsilon_z = 700$ Hz ($\Delta\delta = 1.4$ ppm). Furthermore, an AB spin system for the CH_2 proton resonances H^{10} and H^{11} ($\Delta\upsilon = 192$ Hz) is found and an AX spin system for the CH_2 proton resonances H^{14} and H^{18} ($\Delta\upsilon = 676$ Hz). A possible explanation for this observation is the position of the corresponding groups within the supramolecular complex (**Figure 8.5**).

As mentioned, the two subunits of the capsoplex are twisted by approximately 90°. A result of this twist is that the CH_2 group with the protons H^{14} and H^{18} stand eclipsed with the second subunit, whereby the second CH_2 group with the protons H^{10} and H^{11} is staggered. In the latter case this leads to a higher deshielding of the proton resonances of H^{10} and H^{11} and to a low-field shift of the corresponding peaks. For the proton resonances of H^{14} and H^{18} the opposite trend is observed. ^{1}H DOSY NMR measurements confirms the presence of the tetranuclear μ-S_2 complex in solution ($D_{298\,K} = 7.15\cdot10^{-10}\ m^2\cdot s^{-1}$) in comparison with the diffusion coefficients of the dinuclear complexes reported in this work. In the $^{13}C\{^1H\}$ NMR spectrum 21 resonances are found, according to the number of the carbon atoms in the ligand of one subunit. The four carbene carbon resonate between 162.7 ppm and 158.1 ppm (**Figure 8.4**, **bottom**).

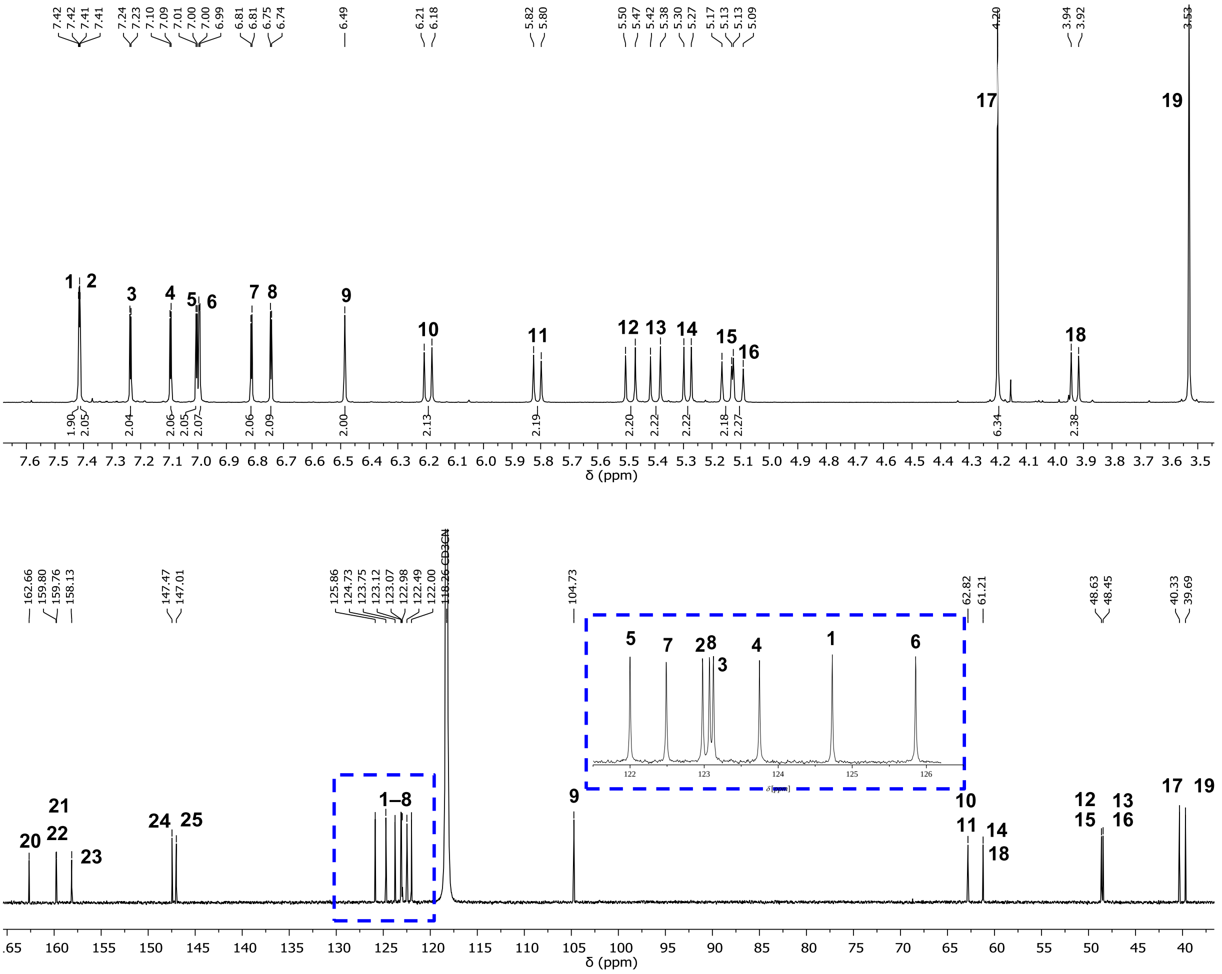

Figure 8.4: Top: ^{1}H NMR spectrum of **[(L^6)$_2$Ni$_4$(S$_2$)](PF$_6$)$_4$** in MeCN-d_3 at 500 MHz and 298 K shows a set of 19 peaks; **Bottom:** ^{13}C{^{1}H} NMR spectrum at 126 MHz showing 23 resonances. Inset shows the ^{13}C resonances of the eight chemically different imidazol-2-ylidene backbone protons.

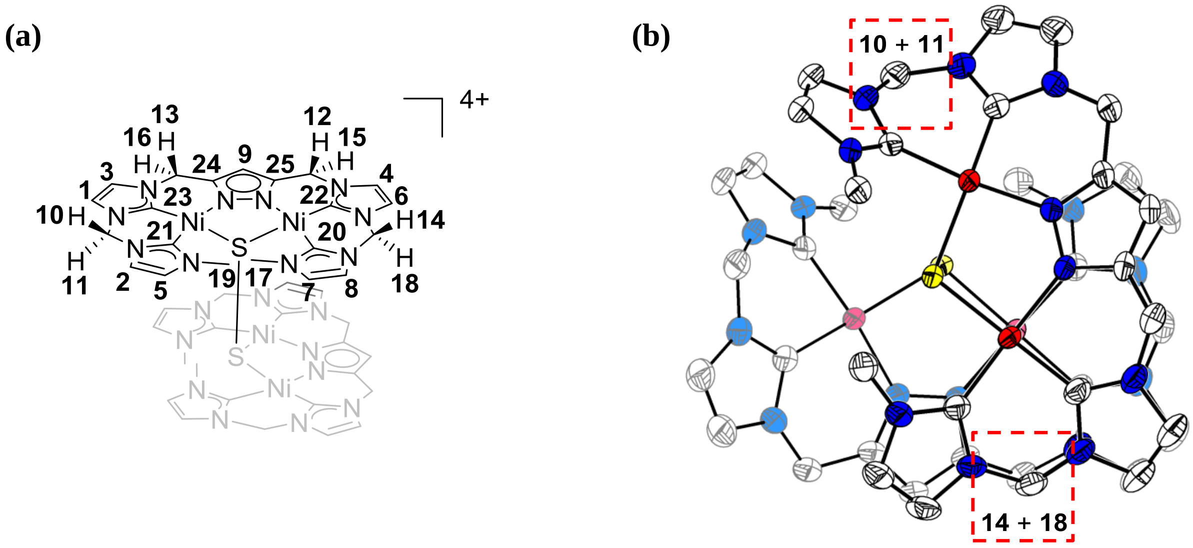

Figure 8.5: (**a**) Assignment of all peaks in the ^{1}H and ^{13}C{^{1}H} NMR spectra. (**b**) Top view of **[(L^6)$_2$Ni$_4$(S$_2$)](PF$_6$)$_4$** highlighting the position of two strongly chemical shifted CH$_2$ groups.

Possible mechanisms for the formation of **$[(L^6)_2Ni_4(S_2)](PF_6)_4$** *via* a thiyl radical intermediate are discussed in **chapter 7**. VT ^{1}H NMR experiments of **$[(L^6)_2Ni_4(S_2)](PF_6)_4$** in MeCN-$d_3$ from 233 K to 353 K does not show any change in the NMR spectra and no cleavage of the S-S bond is observed, in contrast to the S–S cleavage in BiTEMPS reported by Otsuka[374] and for a molybdenum complex at 25 °C.[372] Also the presence of H_2 at a pressure of up to 10 bar at 343 K does not lead to a homolytic cleavage of the disulfido group.

VT UV-vis spectra of **$[(L^6)_2Ni_4(S_2)](PF_6)_4$** shows three main bands (**Figure 8.6**, **left**), in agreement with previously reported spectra of **$[(L^6)Ni_2(X)](PF_6)_2$** ($X = OH^-$, Cl^- and SH^-). These bands increases upon decrease of temperature. At –40 °C bands are observed at 222 nm ($\varepsilon = 52.6\cdot10^3\ \mathrm{M^{-1}\cdot cm^{-1}}$), 301 nm ($\varepsilon = 52.6\cdot10^3\ \mathrm{M^{-1}\cdot cm^{-1}}$) and around 400 nm ($\varepsilon = 4.8\cdot10^3\ \mathrm{M^{-1}\cdot cm^{-1}}$), wherein the band at 400 nm differs the most compared to previously described complexes. The corresponding UV-vis spectrum of the complex in solid state shows a red shift of all bands (**Figure 8.6**, **right**).

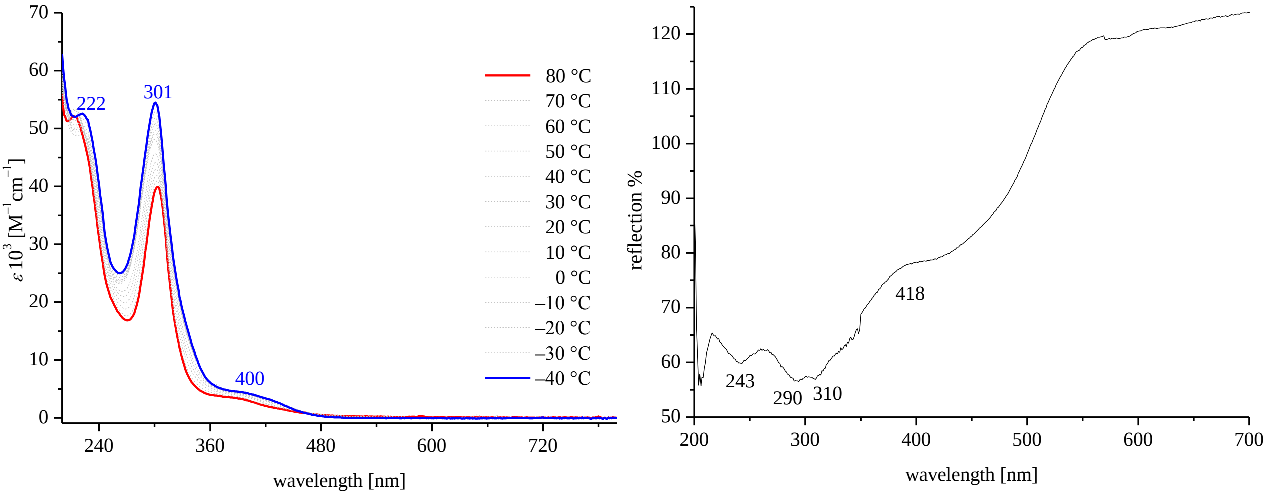

Figure 8.6: Left: UV-vis spectra of **$[(L^6)_2Ni_4(S_2)](PF_6)_4$** in MeCN in the temperature range between 80 °C to –40 °C with bands at 222 nm ($\varepsilon = 52.6\cdot10^3\ \mathrm{M^{-1}\cdot cm^{-1}}$), 301 nm ($\varepsilon = 52.6\cdot10^3\ \mathrm{M^{-1}\cdot cm^{-1}}$) and 400 nm ($\varepsilon = 4.8\cdot10^3\ \mathrm{M^{-1}\cdot cm^{-1}}$). **Right:** UV-vis spectrum of the complex in solid state.

8.3.2 Redox properties of $[(L^6)_2Ni_4(S_2)](PF_6)_4$

The redox properties of **$[(L^6)_2Ni_4(S_2)](PF_6)_4$** are investigated by CV and chemical reduction reactions. A CV of **$[(L^6)_2Ni_4(S_2)](PF_6)_4$** shows no oxidation event up to 2.0 V *vs.* Fc/Fc^+ scanning towards positive potentials (**Figure 8.7**). An electrical response at $E_\mathrm{p}^\mathrm{red}$ = –1.34 V *vs.* Fc/Fc^+ is detected by applying a negative potential first. Following the reduction a corresponding anodic wave at E_p^ox = –0.32 V is obtained.

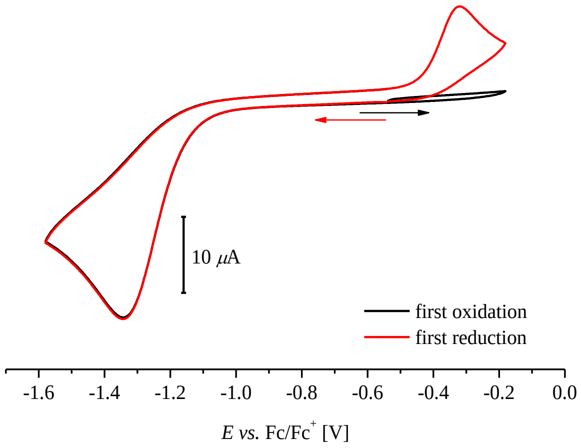

Figure 8.7: CV of **$[(L^6)_2Ni_4(S_2)](PF_6)_4$** shows no wave by applying an anodic potential first (→) and one wave at E_p^{red} = –1.34 V in the cathodic region and one wave at E_p^{red} = –0.32 V *vs.* Fc/Fc^+ in the anodic region after applying a reductive potential first (←).

In agreement with the CVs of **$[L^6Ni_2S]PF_6$** (**chapter 7** and **5**) an *EC* mechanism is assumed, starting now with the reduction of **$[(L^6)_2Ni_4(S_2)](PF_6)_4$**. In a first step **$[(L^6)_2Ni_4(S_2)](PF_6)_4$** is reduced to **$[L^6Ni_2S]PF_6$** which is oxidized again to the persulfido complex, by applying an anodic potential. This scenario is already confirmed in **chapter 7** by UV-vis SEC, wherein the reversible, electrochemical transformation from **$[L^6Ni_2S]PF_6$** to **$[(L^6)_2Ni_4(S_2)](PF_6)_4$** and *vice versa* is demonstrated. Furthermore, the chemical conversion from **$[(L^6)_2Ni_4(S_2)](PF_6)_4$** to **$[L^6Ni_2S]PF_6$** by use of two equivalents of cobaltocene as reducing agent is confirmed by ^1H NMR spectroscopy (**Scheme 8.4**). After addition of the reducing agent an immediate color change from pale yellow to red-orange is observed and the ^1H NMR spectrum shows the quantitative formation of **$[L^6Ni_2S]PF_6$**.

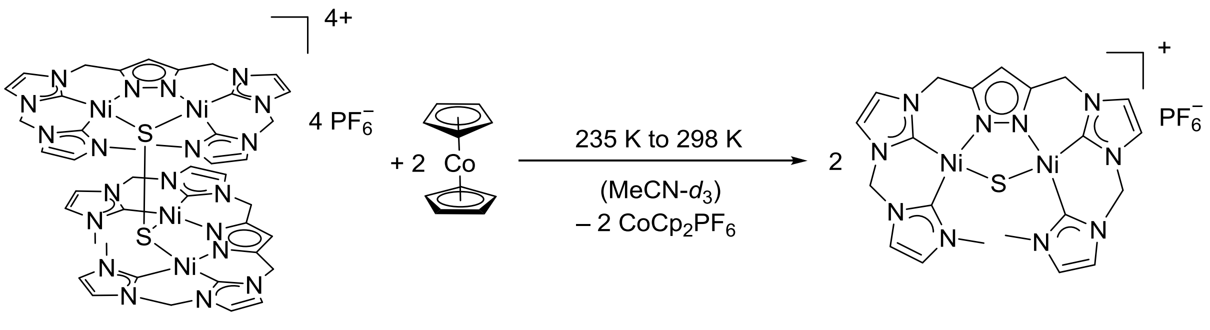

Scheme 8.4: Chemical reduction of $\mathbf{[(L^6)_2Ni_4(S_2)](PF_6)_4}$ by cobaltocene to $[\mathbf{L^6Ni_2S}]\mathbf{PF_6}$, monitored by ^{1}H NMR spectroscopy.

8.3.3 Synthesis of $[(L^6)_2Ni_4(S_2)](PF_6)_4$ *via* HAT reaction

In **chapter 7**, HAT reactions are presented, to confirm the $BDFE_{(solv.)}$ of the S–H bond in $\mathbf{[L^6Ni_2(SH)](PF_6)(OTf)}$ and to show the potential of the *in situ* generated thiyl radical complex for activation of weak C–H, O–H and N–H bonds. Furthermore, the reverse reaction, H· abstraction from $\mathbf{[L^6Ni_2(SH)](PF_6)(OTf)}$ by organic radicals is successfully tested (**Scheme 8.5**). The reaction of 1.0 equiv. of 2,4,6-*tert*-butyl-phenoxyl radical ($BDEF_{(solv.)}$ = 77.1 kcal·mol^{-1} in MeCN)[223] with $\mathbf{[L^6Ni_2(SH)](PF_6)(OTf)}$ ($BDEF_{(solv.)}$ = 74.2 kcal·mol^{-1} in MeCN) results in formation of $\mathbf{[(L^6)_2Ni_4(S_2)]^{4+}}$. This is confirmed by ^{1}H NMR spectroscopy, IR spectroscopy and crystallographic analysis of the product, with hexafluorophosphate and triflate counterions. The tetranickel(II) persulfido complex, which is obtained by oxidation of $[\mathbf{L^6Ni_2S}]^+$ has four hexafluorophosphate counter ions.

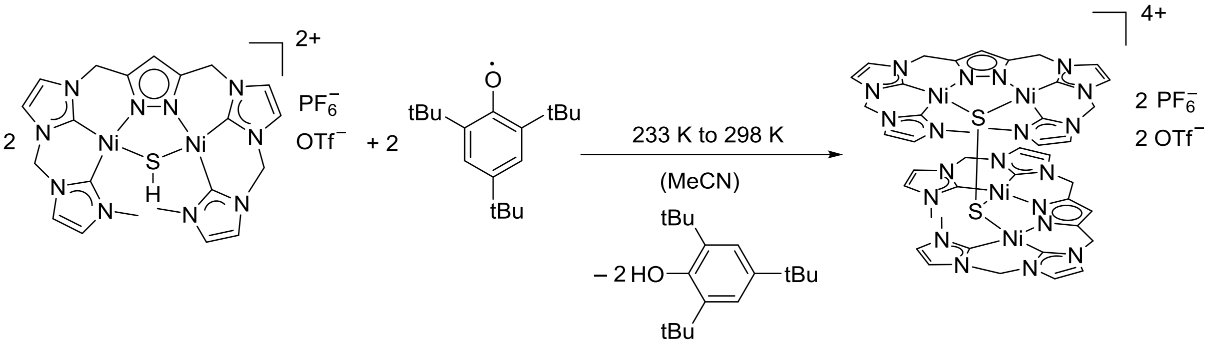

Scheme 8.5: HAT process at $\mathbf{[L^6Ni_2(SH)](PF_6)(OTf)}$ by 2,4,6-tri *tert*-butyl-phenoxyl radical results in formation of $\mathbf{[(L^6)_2Ni_4(S_2)](PF_6)_2(OTf)_2}$.

Surprisingly, this reaction is also possible with 2.0 equiv. of TEMPO radical ($BDFE_{(solv.)}$ = 66 kcal·mol^{-1} in MeCN)[223], even though the reaction is as expected slow. The

$[L^6Ni_2(SH)]^{2+}$ and the TEMPO radical and the thiyl radical complex and TEMPO–H might be in an equilibrium (**Scheme 8.6**). Since the dimerization reaction and formation of the complex **$[(L^6)_2Ni_4(S_2)]^{4+}$**is irreversible, the whole reaction is driven by the formation of the final product and the equilibrium can be shifted to the side of the thiyl radical and finally results in formation of **$[(L^6)_2Ni_4(S_2)]^{4+}$**. This reaction is slow, since it is proposed that the pre-equilibrium is primarily on the side of **$[L^6Ni_2(SH)](PF_6)(OTf)$**. The reaction can be accelerated by addition of an excess of TEMPO (10 equiv.). Mayer *et al.*[382] also described the possibility of HAT reactions with reagents which have slightly lower BDFE values than the bond strength of the substrate, but explained this behavior by tunneling effects. Unfortunately, it is not possible to derive kinetic data of this reaction, since in the UV-vis spectra of the relevant bands of the complex are covered by the bands of the HAT reagent (see also **chapter 7**).

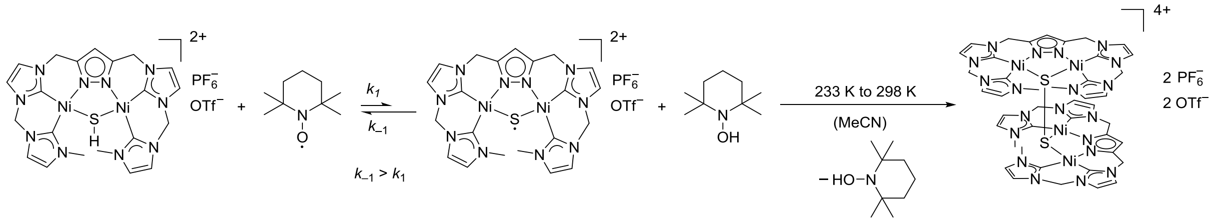

Scheme 8.6: Proposed pre-equilibrium for the HAT process of **$[L^6Ni_2(SH)](PF_6)(OTf)$** with TEMPO radical.

In conclusion, the transformation of **$[L^6Ni_2(SH)](PF_6)(OTf)$** to **$[(L^6)_2Ni_4(S_2)](PF_6)(OTf)$** by hydrogen atom abstraction reagents like TEMPO radical or 2,4,6-*tert*-butyl-phenoxyl radical is successfully demonstrated.

8.3.4 Reaction of $[L^6Ni_2S]PF_6$ with NO or $NOBF_4$

$[L^6Ni_2S]PF_6$ shows a diverse reactivity and in the previous chapters the synthesis of **$[L^6Ni_2(SCH_3)](PF_6)_2$** (**chapter 5**), **$[L^6Ni_2(SH)](PF_6)(OTf)$** (**chapter 6**) and **$[(L^6)_2Ni_4(S_2)](PF_6)_2(OTf)_2$** (**chapter 8.3**) are presented. **Scheme 5.9** in **chapter 5** summarizes the reactivity studies of the complex with respect to dioxygen and NO and NO^+. Whereby the reactivity with dioxygen is already discussed in **chapter 5**, the results of the reactions with NO and NO^+ will be presented in this subchapter. Hayton and coworkers impressively demonstrated the versatile reactivity of complex **XVII** with NO.[383] The reaction products are a nickel-NO complex and $[SNO]^-$ which further reacts to $[SSNO]^-$ (**Scheme 5.2**, **chapter 5**). The anions are of high interest, since possible reaction products of NO with sulfur containing enzymes could be $[SNO]^-$, $[SSNO]^-$ and $[ONN(O)SO_3]^{2-}$, which are controversially discussed to have the function as sulfur and NO reservoirs in organism.[383] Reaction of **$[L^6Ni_2S]PF_6$** at -30 °C in MeCN-d_3 with NO gas results in an immediately color change from red-orange to yellow-brownish. The ^{1}H NMR spectrum at –30 °C shows one set of signals corresponding to **$[L^6Ni_2(OH)]^{2+}$** but with an integral value of only 50% of the OH proton resonance (**Figure 8.8**, **left**). The ATR IR spectrum of the sample indicates that this resulted from a potential deuterium labeling of the OH group. Bands at 3593 cm^{-1} and 2655 cm^{-1} are assigned to the OH and to the OD stretch of the complex. The UV-vis spectrum exclusively shows bands from **$[L^6Ni_2(OH/D)](PF_6)_2$** (212 nm, 303 nm and 370 nm) (**Figure 8.9**, **right**).

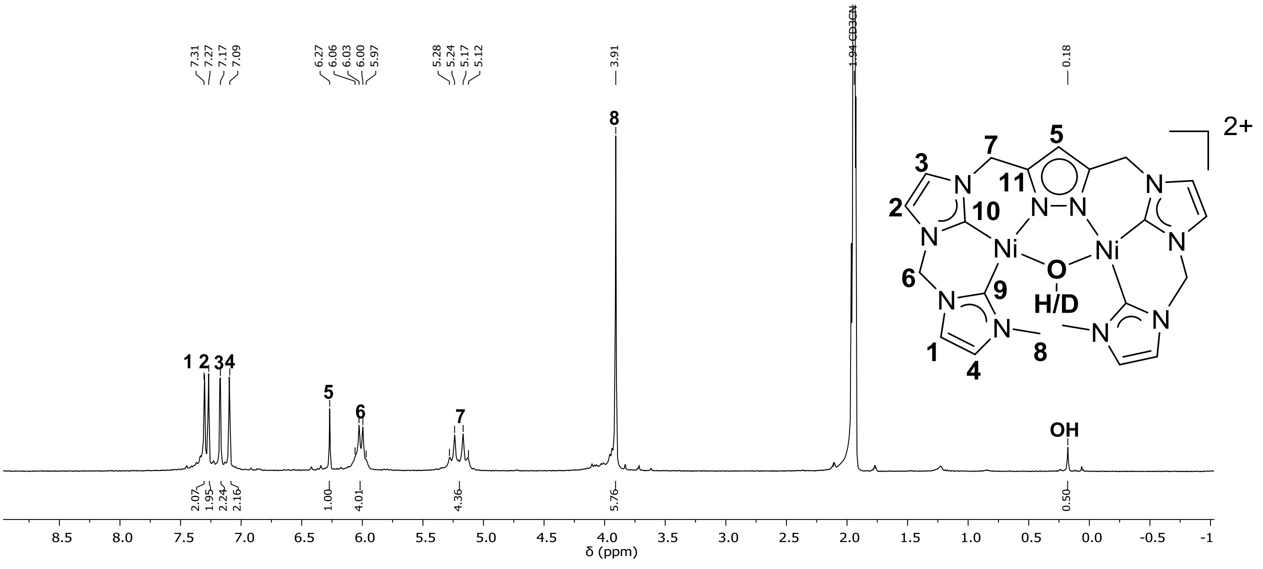

Figure 8.8: ^{1}H NMR spectrum of the reaction mixture confirmed the formation of **$[L^6Ni_2(OH)]^{2+}$** and **$[L^6Ni_2(OD)]^{2+}$** in a 1:1 ratio at 243 K in MeCN-d_3 (400 MHz).

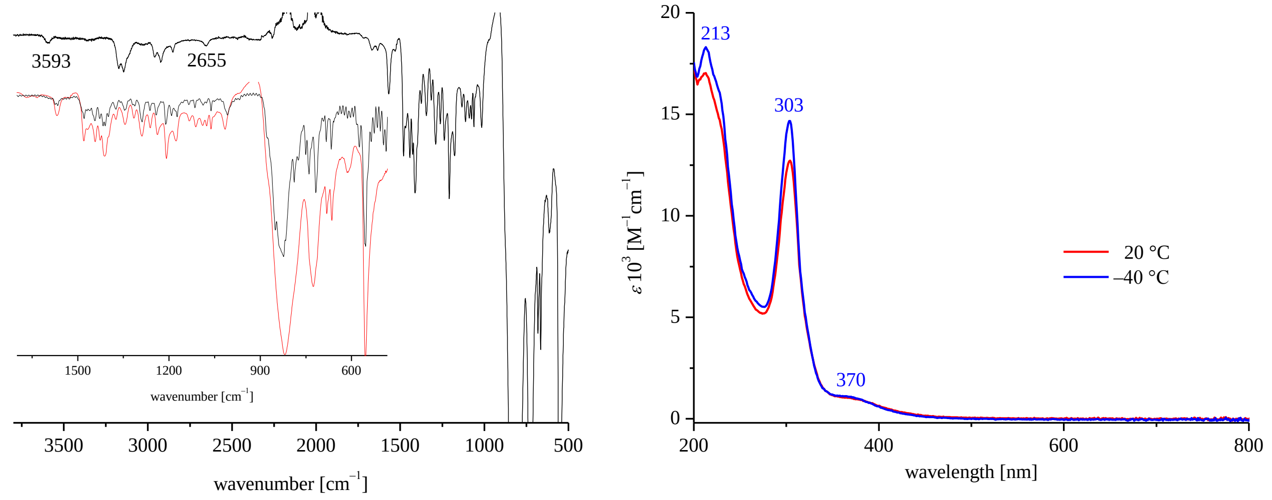

Figure 8.9: Left: ATR IR of the reaction product **[L^{6}Ni$_2$(OH/D)](PF$_6$)$_2$**. Inset shows finger print region of the **[L^{6}Ni$_2$(OH)](PF$_6$)$_2$** (**black**) and the proposed **[L^{6}Ni$_2$(OH/D)](PF$_6$)$_2$** complex (**red**). **Right:** UV-vis spectrum of the hydroxido-bridged complex as product of the NO reaction at different temperatures.

In the ESI-MS, peaks at m/z = 273 (96), m/z = 274 (95), m/z = 693 (71) and m/z = 694 (78) for the labeled and unlabeled hydroxido-bridged dinickel complexes are detected (**Figure 8.10**). In addition a peak at m/z = 643 (14) is obtained which fits to the isotopic distribution pattern of **[L^{6}Ni$_2$(OD)(SSNO)]$^+$**. However, the observation of a putative [SSNO]$^-$ complex is only possible *via* ESI-MS while IR and UV-vis data did not show any clear evidence for such a product (**Figure 8.9**). In the IR spectrum no clear assignment of bands at 595 cm^{-1} for a S–S stretch and at 1200-1358 cm^{-1} for NO stretch of SSNO$^-$ are observed.[384,385] Also in the UV-vis spectra no bands are observed at 448 nm or 350 nm, which would be characteristic for SSNO$^-$ or SNO$^-$, respectively.[384,385] In conclusion, a potential formed SSNO$^-$ cannot be confirmed by IR and UV-vis spectroscopy, and more detailed experiments are necessary.

ESI-MS, UV-vis and 1H NMR spectroscopy confirmed the formations of **[L^{6}Ni$_2$(OD)]$^{2+}$** and **[L^{6}Ni$_2$(OH)]$^{2+}$** and further investigations are performed to investigate the source of the OH/OD ion in the complex. The reaction of **[L^{6}Ni$_2$S]PF$_6$** and NO is repeated and a head space analysis of the gaseous products is performed. The IR spectrum of the gas phase shows besides bands for NO and NO$_2$ (**Figure 8.10**, **right**) bands at 2235 cm^{-1} and 1301 cm^{-1} which are assigned to N$_2$O stretches. The formation of N$_2$O is a possible explanation for the source of the oxygen ion in the **[L^{6}Ni$_2$(OH/D)](PF$_6$)$_2$** complexes. In **chapter 6** the *in situ* formation of an oxido-bridged dinickel(II) complex is reported, which undergoes a H/D exchange with MeCN-d_3. This suggests that also reaction of **[L^{6}Ni$_2$S]PF$_6$** with an excess of NO gas leads to the formation of **[L^{6}Ni$_2$O]$^+$** which abstracts a deuterium cation from the MeCN-d_3 solvent or a proton from residual water in the solvent or the silica surface of the glassware. Driess *et* *al.*[331] proposed a similar intermediate by reaction of a nickel(I) *nacnac* complex with N_2O, wherein N_2 and a dinickel(II) bis-μ-hydroxido *nanac* complex *via* **XV** is formed as final products (see **Scheme 4.10**). Onishi and coworkers[386] investigated the reversible N–N coupling of NO on dinuclear Ru complexes and they were further able to isolate a diruthenium hyponitrite complex. This complex is transformed to a diruthenium μ-oxido complex under release of N_2O, which is confirmed by several analytic methods, including a crystallographic analysis of the product.

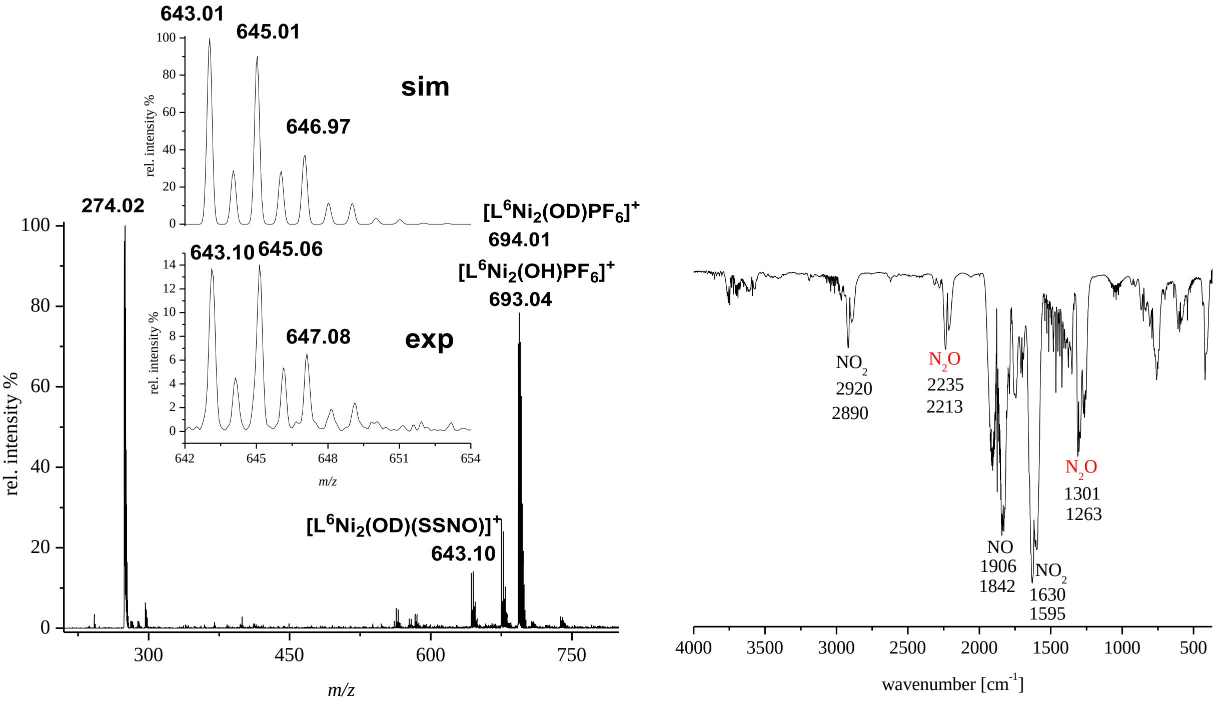

Figure 8.10: Left: ESI-MS of the reaction mixture. **Right:** Head space IR analysis after addition of NO to the complex solution.

In order to get a better understanding of the intermediates, which are formed during the reaction, single reaction steps are performed. **[L^6Ni_2S]PF_6** reacts with one equivalent of $NOBF_4$ in MeCN-d_3 at 243 K. Based on the redox potential of $NOBF_4$ in MeCN (0.87 V *vs.* Fc/Fc^+ in MeCN) this ion is able to oxidize **[L^6Ni_2S]PF_6** to the thiyl radical complex (–0.255 V), which could further recombine with the NO radical to a μ-SNO complex. Instead of the latter reaction, however the transformation of the *in situ* generated **[$L^6Ni_2(S\cdot)$]$^{2+}$** to **[$(L^6)_2Ni_4(S_2)$]$(PF_6)_4$** is monitored by ^{1}H NMR spectroscopy. Further experiments are performed. One equivalent, two equivalents (233 K to 343 K) and an excess of NO gas (233 K to 298 K) are added to **[$(L^6)_2Ni_4(S_2)$]$(PF_6)_4$** but no reaction of the complex with NO is observed. It might be that **[$(L^6)_2Ni_4(S_2)$]$^{4+}$** is stable towards NO gas. Based on these results, the formation of **[$(L^6)_2Ni_4(S_2)$]$(PF_6)_4$** as an intermediate in the reaction of **[L^6Ni_2S]PF_6** with excess of NO is excluded (**Scheme 8.7**). **Scheme 8.7** summarizes the obtained results to date.

Further experiments are planned to gain more information about the pathway of the transformation of **[L^6Ni_2S]PF_6** to **[$L^6Ni_2O(H/D)$]**$^{2+}$ and N_2O as well as the whereabouts of the decoordinated sulfur and the origin of the [SSNO]$^-$ of **[$L^6Ni_2(OH/D)$]**$^{2+}$in the ESI-MS.

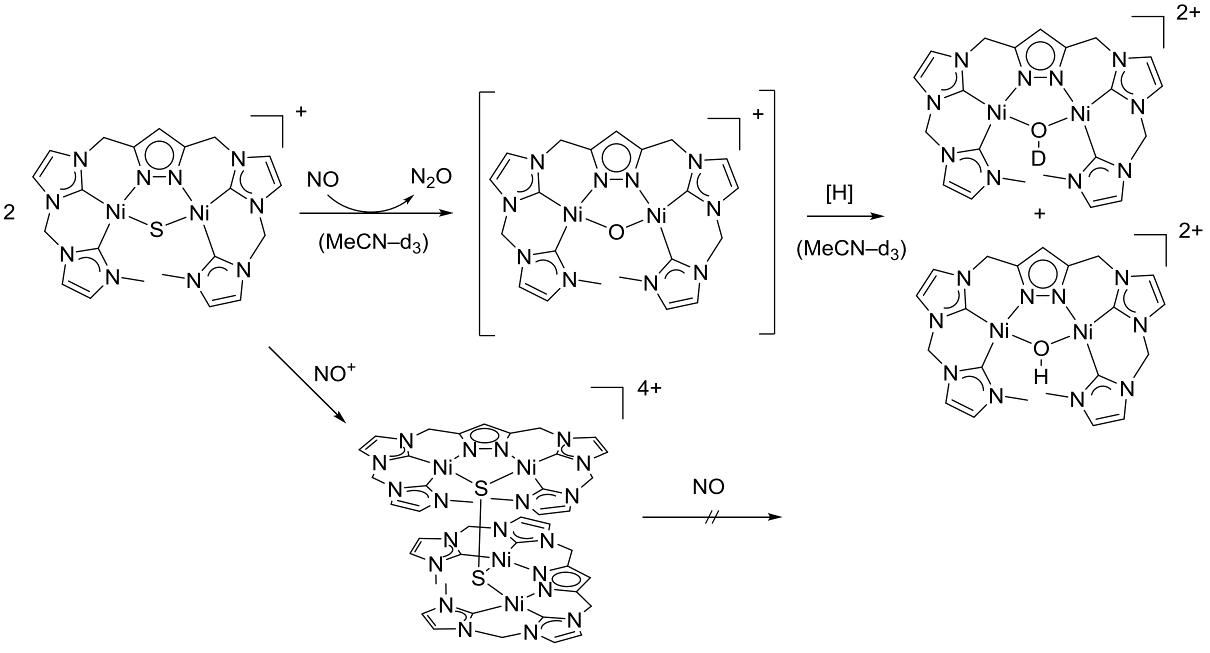

Scheme 8.7: Overview of the reaction of **[L^6Ni_2S]PF_6** with excess of NO results in formation of the labeled and unlabeled hydroxido-bridged complex under release of N_2O, which were identified by NMR, IR spectroscopy, ESI-MS and UV-vis spectroscopy of the reaction mixture and head space analysis of the gases. Bottom: addition of NO^+ to **[L^6Ni_2S]PF_6** leads to formation of **[$(L^6)_2Ni_4(S_2)$]$(PF_6)_4$**.

8.4 Conclusion and Outlook

In this chapter, the synthesis of the first tetranickel(II) persulfido complex was described. CV experiments of **$[(L^6)_2Ni_4(S_2)]^{4+}$** confirms the interconversion to [**$L^6Ni_2S]PF_6$**. Furthermore the synthesis of **$[(L^6)_2Ni_4(S_2)](PF_6)_2(OTf)_2$** by HAT from **$[L^6Ni_2(SH)](PF_6)(OTf)$** is demonstrated. The S–S bond in **$[(L^6)_2Ni_4(S_2)]^{4+}$** is stable towards dihydrogen and nitrous oxide. Furthermore, the reactivity of [**$L^6Ni_2S]PF_6$** with $NOBF_4$ and with an excess of NO is investigated. Whereby the reaction with $NOBF_4$ shows a simple redox event and the formation of **$[(L^6)_2Ni_4(S_2)](PF_6)_4$**, reaction with NO results in formation of N_2O and [**$L^6Ni_2(OH/D)]$**$^{2+}$. These reactions lead to several new questions concerning the mechanism of sulfur abstraction and the formation of N_2O *via* reaction of [**$L^6Ni_2S]$**$^+$ and NO. After analysis of all probably relevant transformations between [**$L^6Ni_2S]PF_6$**, **$[L^6Ni_2(SH)](PF_6)(OTf)$** and **$[(L^6)_2Ni_4(S_2)](PF_6)_4$**, including p$K_a$ and $BDFE_{(solv.)}$ determination of the S–H group, the reactivity of [**$L^6Ni_2S]PF_6$** and **$[L^6Ni_2(SH)](PF_6)(OTf)$** towards electrocatalytic proton reduction will be investigated in the following chapter.

9

(Electro-)catalytic proton reduction by hydrosulfido- and sulfido-bridged dinickel(II) hybrid tetra-NHC complexes

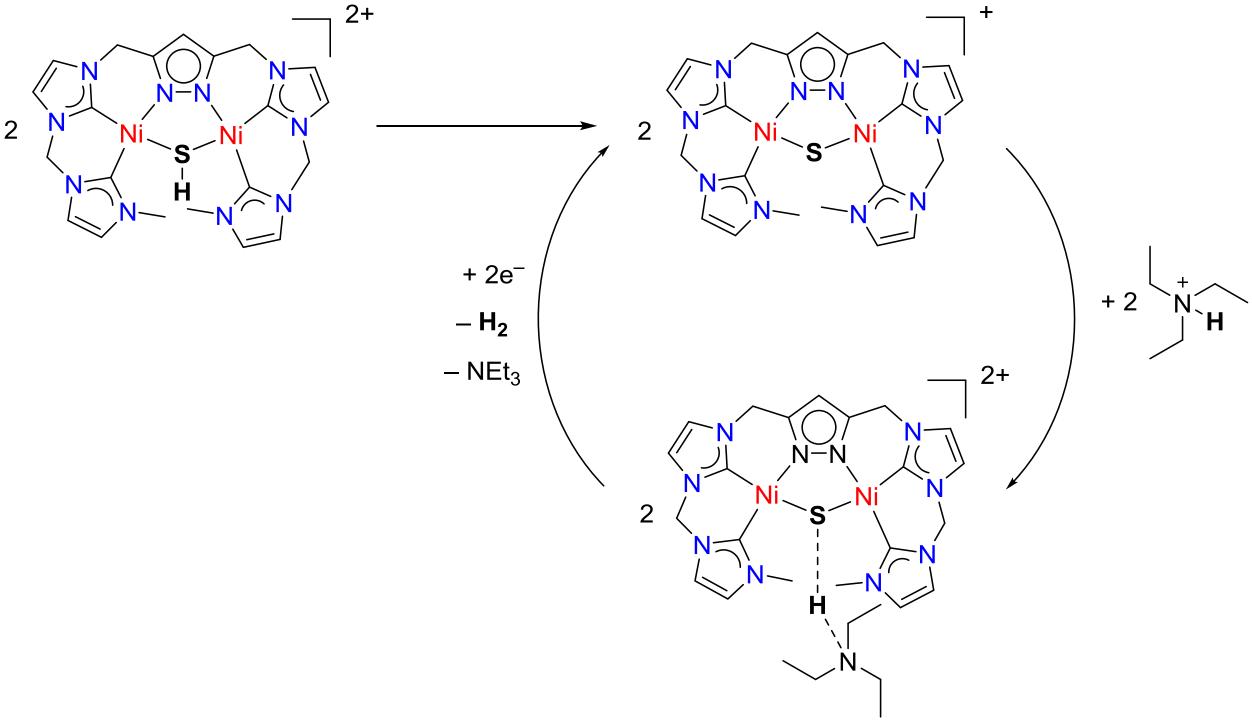

Abstract: In the previous **chapters 5** to **8** the (electro-)chemical properties of **[L^{6}Ni$_2$(SH)](PF$_6$)(OTf)** and **[L^{6}Ni$_2$S]PF$_6$** are described and the pK_a value of the S–H bond (18.42±0.06) and the BDFE(solv.) (74 kcal·mol^{-1}±0.9 kcal·mol^{-1}) are determined. Here the (electro-)catalytic properties of both complexes for proton reduction are tested and mechanistic investigations are considered.

9.1 Introduction

Finding new ways to meet the increasing energy demands is one of these enormous challenges of the 21th century. Current solutions focus on increasing the use of renewable energy sources and a complete withdrawal from fossil and nuclear fuels.[387–389] This shift is of vital importance as global warming occurs more and more rapidly, due to high CO_2 emissions from burning fossil resources.[387–390] A report from 2017 highlights that 78% of all greenhouse gases in the European Union originate from burning of fossil fuels.[391] Solar and wind energy are important renewable energy resources but they are not currently able to meet the energy demands of mankind.[391]

The idea of using dihydrogen as a renewable energy feedstock is an attractive starting point. Not only can dihydrogen be used as a fuel but also as a substrate for industrial processes like the Haber-Bosch process, which uses dihydrogen for the synthesis of ammonia. The delivery of dihydrogen is the most energy consuming step in this process. Developing sophisticated approaches to lower the energy consumption of this process will be of great benefit for mankind. Nature is able to generate dihydrogen out of water in a more efficient way than what can industrially be achieved today. Hydrogenases are able to reversibly split dihydrogen into protons and electrons or converting protons into dihydrogen.[191] The active sites of many of these enzymes contain cysteine-bridged diiron or nickel-iron metal centers.[191] [FeFe] hydrogenase enzymes are able to catalytically produce H_2 from water at 30 °C with rate constants of approximately 9000 s^{-1}.[191,392,393] [NiFe] hydrogenases with a turnover frequency of more than 1000 s^{-1} for H_2 oxidation under ambient conditions have been reported.[394,395] Research groups all over the world are trying to develop bioinspired or biomimetic model systems to gain better understanding of the natural catalytic process and to develop catalysts which will be able to provide dihydrogen as a fuel in an inexpensive and efficient way in the foreseeable future.

A proposed mechanism for the activation of H_2 by [NiFe] hydrogenase is presented in **Scheme 9.1**.[191,211,226,396] After activation of the Ni–Fe μ-OH co-factor (**Scheme 9.1**), dihydrogen can be heterolytically cleaved and the **Ni–R** state is formed. The next step of the mechanism is the formation of the **Ni–C** state by release of one proton and oxidation of the nickel ion. In oxygen sensitive [NiFe] hydrogenases, additionally the **Ni–L** state is proposed, wherein a nickel(I) species is generated.[191] The mechanistic cycle is closed by oxidation of the nickel(I) ion. In O_2 tolerant [NiFe] hydrogenases is **Ni–SI$_a$** directly regenerated from **Ni–C** under release of one electron and one proton (**Scheme 9.1**).[191] In 2016 Duboc *et al.*[211] published a biomimetic catalyst system containing a thiolato-bridged [NiFe] center which is able to generate dihydrogen from a mild acid. Mechanistic investigations of the model complex have shown that the nickel ion is the redox-catalytic center. The mechanistic investigations of this complex are of enormous importance for better understanding such proton reduction processes in model complexes and in enzymes.

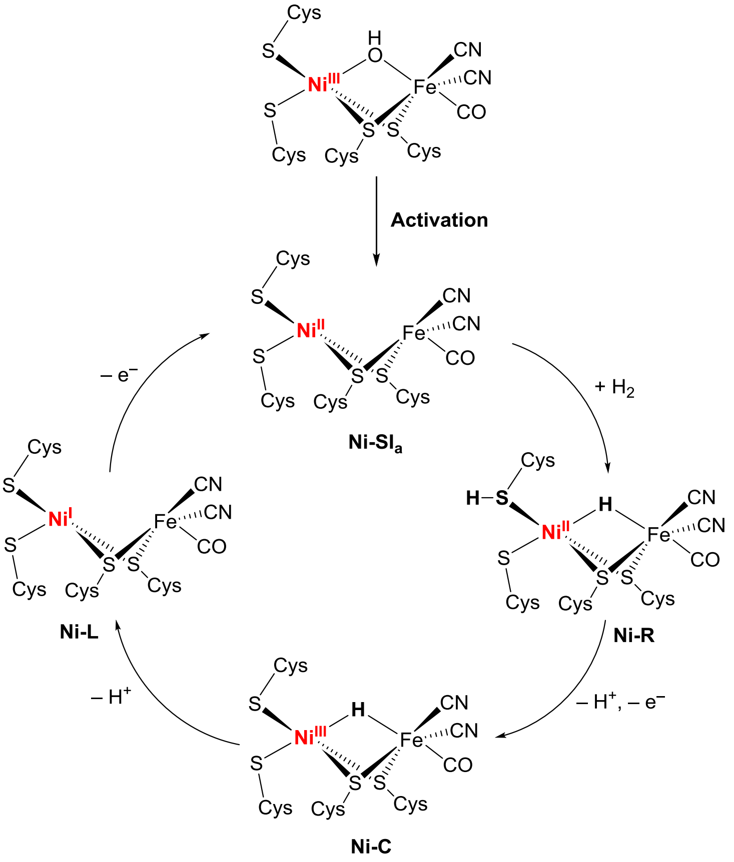

Scheme 9.1: Proposed mechanism of the interconversion of H_2 to 2 H^+ by [NiFe] hydrogenases.[191,211,226,396]

Lubitz and coworkers[226] published the subatomic resolution protein crystallography of a [NiFe] hydrogenase, wherein a protonated terminal cysteinyl thiolate, C546, is detected in the **Ni–R** state (see also **chapter 6**). Based on DFT modeling studies, Niu and Hall previously postulated the involvement of the cysteinyl in the reaction in 2001.[397,398] This observation highlights the importance of the cooperativity between the nickel center and the ligand during the conversion of protons to hydrogen or during the heterolytic cleavage of H_2. While the crystallographic structure of the protein is still part of ongoing debate, it suggests the ligand participation as a proton shuttle during the conversion of H_2 to H^+ or *vice versa*.

In contrast to [NiFe] hydrogenases, more analytically evidences are found in [FeFe] hydrogenases for the function of an amine base as proton shuttle and proton relay (**Figure 9.1**). Rauchfuss *et al.*[399,400] showed, using bioinspired model complexes, that a pendant amine plays an important role in the H_2 production. Beside bioinspired model complexes, which undergo reversible thiolate protonation[227,228], efficient electrocatalysts of non-biomimetic systems are successfully explored. Cobaloxime-based catalysts[401–405] and nickel bis(diphosphane) complexes[170,393,406–408] show even higher activity. In the nickel bis(diphosphane) complexes, the proton relay of a pendant amine plays a crucial role and catalyst of such compounds are achieved with a TOF of 106000 s^{-1}.[393] Mechanistic studies for a Cp*Rh(bipy) catalyst show that the Cp* has a non-innocent behavior and is directly involved in the formation of H_2 *via* $[(bipy)Rh(\eta^4\text{-}C_5Me_5H)]^+$.[409,410] In contrast to the large amount of organometallic catalysts for proton reduction, the number of catalysts bearing NHC ligands is comparably low.[411–413]

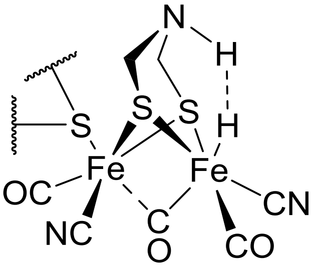

Figure 9.1: Proposed structure of the [FeFe] hydrogenases in the active state.[393]

9.2 Objectives

An overwhelming amount of organometallic complexes that are able to electrocatalytically reduce protons to dihydrogen with impressive TON and TOF values have been described in the literature. Even though the improvement of such values with cheap and earth abundant metals is a highly desired goal, the focus of this thesis is to gain further insight into the mechanistic understanding of the proton reduction by the dinickel(II) sulfur complexes (**Figure 9.2**). In this chapter, [**L^{6}Ni$_{2}$(SH)](PF$_{6}$)(OTf)** and [**L^{6}Ni$_{2}$S]PF$_{6}$** are investigated as potential catalysts for proton reduction. Furthermore, their behavior towards [HNEt$_{3}$]$^{+}$ is determined by several analytic methods, including NMR, UV-vis spectroscopy and CV, to understand mechanistic aspects of the proton reduction process.

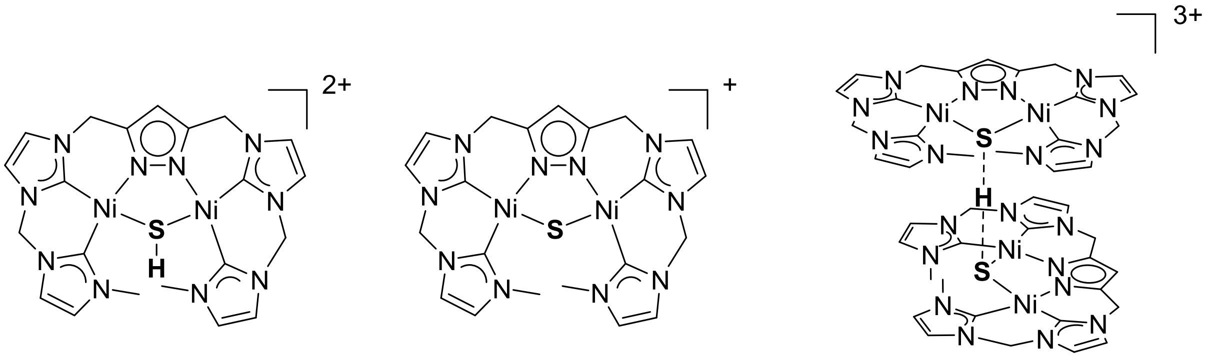

Figure 9.2: [**L^{6}Ni$_{2}$(SH)]$^{2+}$** and **[L^{6}Ni$_{2}$S]$^{+}$** complexes tested for catalytic proton reduction and encounter complex **[(L^{6})$_{2}$Ni$_{4}$(SHS)]$^{3+}$**.

9.3 Results and Discussion

The herein presented results are carried out in cooperation with Prof. Dr. Artero (CEA Grenoble), Dr. Duboc and Dr. Gennari (Université Grenoble Alpes) including a research stay in Grenoble.

9.3.1 Proton reduction by [$L^6Ni_2(SH)](PF_6)(OTf)$

CV of **[$L^6Ni_2(SH)](PF_6)(OTf)$** is presented in **chapter 6.3.3** and shows no oxidation event by applying an anodic potential up to 2.0 V *vs.* Fc/Fc$^+$, but the reduced species of **[$L^6Ni_2(SH)](PF_6)(OTf)$** ($E_\mathrm{p}^\mathrm{red.}$ = –1.93 V *vs.* Fc/Fc$^+$) can be further oxidized ($E_\mathrm{p}^\mathrm{ox.}$ = –0.28 V). At $E_\mathrm{p}^\mathrm{red.}$ = –1.5 V the oxidized species is again reduced (**Figure 6.10**, **chapter 6.3.2**, **Figure 5.8** in **chapter 5** and **Scheme 9.2**). SEC investigations of **[$L^6Ni_2(SH)](PF_6)(OTf)$** are performed and confirm **[$L^6Ni_2S]^+$** as the reduced species of **[$L^6Ni_2(SH)]^{2+}$** (**Scheme 9.2**). The SEC-UV-vis spectrum shows a marked increase of the band at 378 nm along with a red shift of the band to 393 nm after applying a cathodic potential (–2.0 V *vs.* Fc/Fc$^+$). The band at 393 nm is assigned to **[$L^6Ni_2S]PF_6$** in agreement with the UV-vis spectrum of this isolated complex presented in **chapter 5**. No intermediates are observed on the UV-vis instrument time scale at room temperature. Furthermore, the *in situ* transformed complex is oxidized at 0.0 V *vs.* Fc/Fc$^+$ causing a decrease of the band at 393 nm (**Scheme 9.2**, (**c**)). A band is observed at 400 nm in the final UV-vis spectrum, which is assigned to **[$Ni_4S_2(L^6)_2]^{4+}$** in agreement with former UV-vis measurements of **[$(L^6)_2Ni_4(S_2)](PF_6)_4$** (**chapter 8, Figure 8.6**). In **chapter 7** (**Figure 7.7**), the electrochemical conversion of **[$L^6Ni_2S]PF_6$/[$(L^6)_2Ni_4(S_2)](PF_6)_4$** is already demonstrated by UV-vis SEC, which confirmed the assignment of the wave at $E_p^{red.}$ = –1.5 V to this reduction process. In **Scheme 9.2** these transformation steps and the obtained UV-vis spectra are summarized.

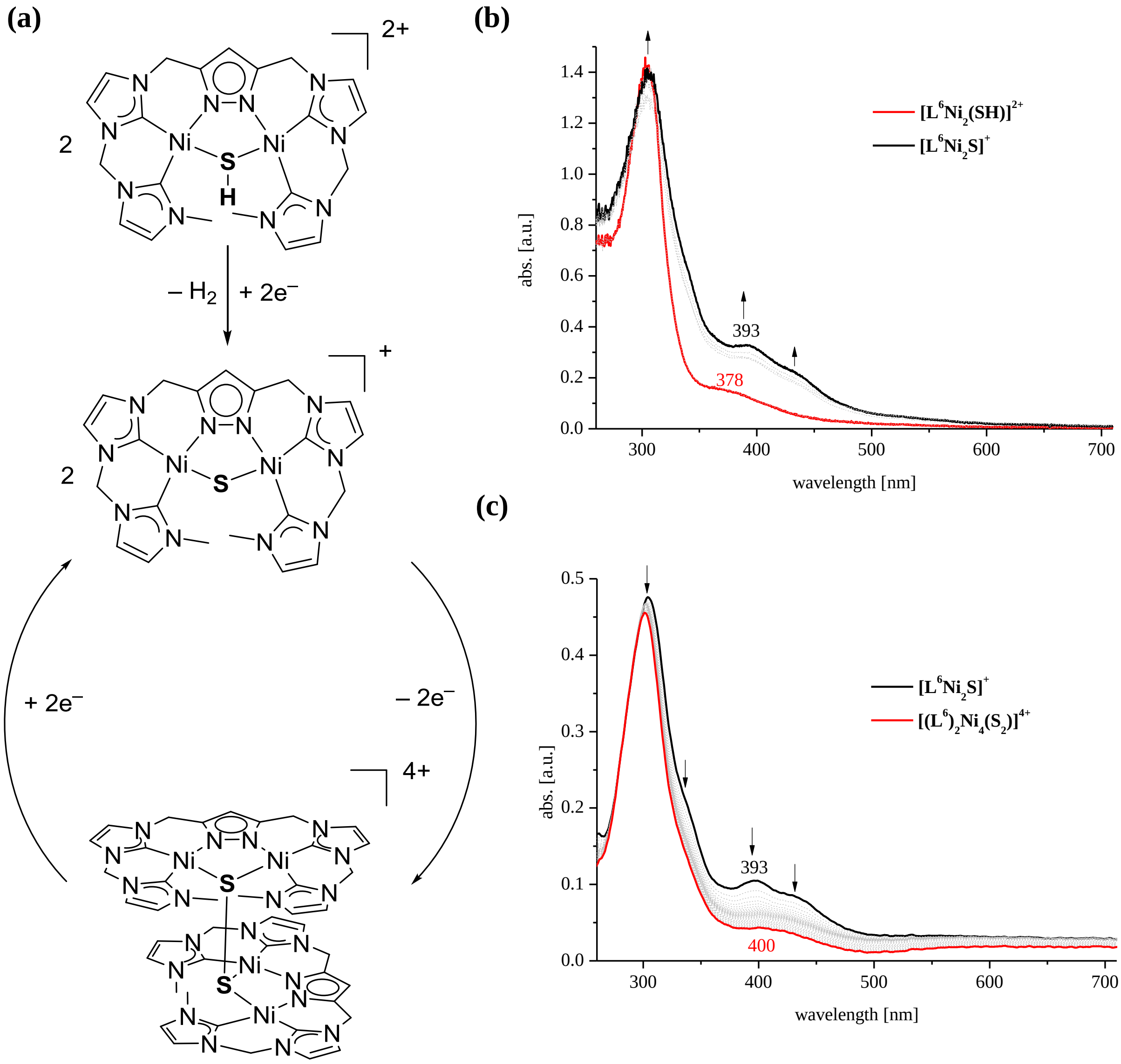

Scheme 9.2: **(a)** Proposed mechanism for the reduction of **[L^{6}Ni$_{2}$(SH)]$^{2+}$** and oxidation of the product. First reduction of **[L^{6}Ni$_{2}$(SH)]$^{2+}$** to **[Ni$_{2}$SL^{6}]$^{+}$** under release of H$_{2}$; oxidation of **[L^{6}Ni$_{2}$S]$^{+}$** to **[(L^{6})$_{2}$Ni$_{4}$(S$_{2}$)]$^{4+}$**, which is again reduced to **[L^{6}Ni$_{2}$S]$^{+}$**. (**b**) SEC monitoring of the single reaction steps *via* UV-vis spectroscopy. Starting point is **[L^{6}Ni$_{2}$(SH)]$^{2+}$** (**c**) Electrochemical oxidation of the *in situ* generated **[L^{6}Ni$_{2}$S]$^{+}$**.

The chemical transformation of **[L^{6}Ni$_{2}$(SH)]$^{2+}$** to **[L^{6}Ni$_{2}$S]$^{+}$** is also confirmed by chemical reduction of **[L^{6}Ni$_{2}$(SH)](PF$_{6}$)(OTf)** by Co(Cp*)$_{2}$ (E^{red} = –1.91 V *vs.* Fc/Fc^{+} in MeCN)[333]. After addition of Co(Cp*)$_{2}$ to **[L^{6}Ni$_{2}$(SH)]$^{2+}$** in MeCN-d_{3} an immediate color change from yellow to red-orange is observed and the proton resonances of the previously characterized **[L^{6}Ni$_{2}$S]$^{+}$** are observed in the ^{1}H NMR spectra (see **appendix**). Furthermore, the above described reaction is repeated with the *in situ* generated, deuterated complex **[L^{6}Ni$_{2}$(SD)](PF$_{6}$)(OTf)** in MeCN and the previous observed ^{2}H resonance at 0.75 ppm is gone (**Figure 9.3**). In addition, a new peak is observed at 2.54 ppm, which does not disappear by evaporation of the headspace.

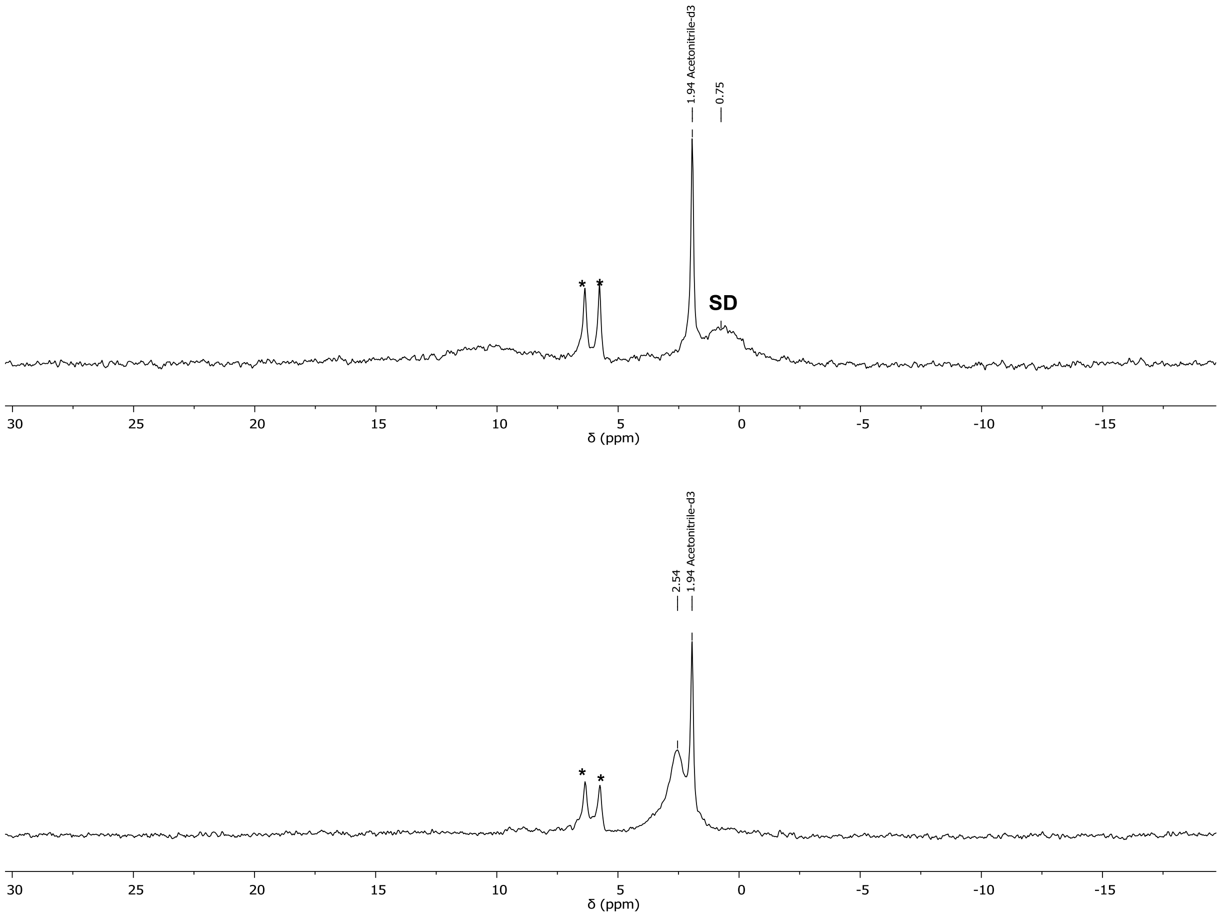

Figure 9.3: Top: ^2H NMR spectrum of **$[L^6Ni_2(SD)](PF_6)(OTf)$** in MeCN (238 K, 77 MHz). ^2H resonance of the S–D group is assigned at 0.75 ppm. **Bottom:** The signal at 0.75 ppm disappears after the reduction step and a new deuterium resonance at 2.54 ppm is observed. (*) Unknown impurities.

These experiments suggest the non-innocence of the Cp* ligand, so a control experiment of 2,6-lutidinium-*d* triflate with $Co(Cp^*)_2$ is performed. This control experiment shows the disappearance of ^2H NMR resonance of the N–D at 13.24 ppm and the appearance of a peak at 2.39 ppm (**Figure 9.4**). In agreement with reactivity studies and DFT calculations, reported in the literature, these experiments show that Cp* is a non-innocent ligand. In 2017, based on DFT calculations, Peters *et al.*[414] proposed the formation of $[Cp^*Cr(\eta^4\text{-}C_5Me_5H)]^+$ after reaction of 2,6-lutidinium with $Cr(Cp^*)_2$. In addition, by EPR spectroscopy of a solid material, they identified and characterized $[Cp^*Co(\eta^4\text{-}C_5Me_5H)]^+$ after protonation reaction of $Co(Cp^*)_2$. In 2016, Blakemore and Goddard III *et al.*[410] determined the molecular structure in solid state of $[(bipy)Rh(\eta^4\text{-}C_5Me_5H)]^+$ after reaction of Cp*Rh(bipy) with $[HNEt_3]^+$ ($pK_a = 18.8$ in MeCN). The release of dihydrogen is only possible by addition of a stronger acid, here $[DMF\text{–}H]^+$ ($pK_a = 6.1$ in MeCN).[410]

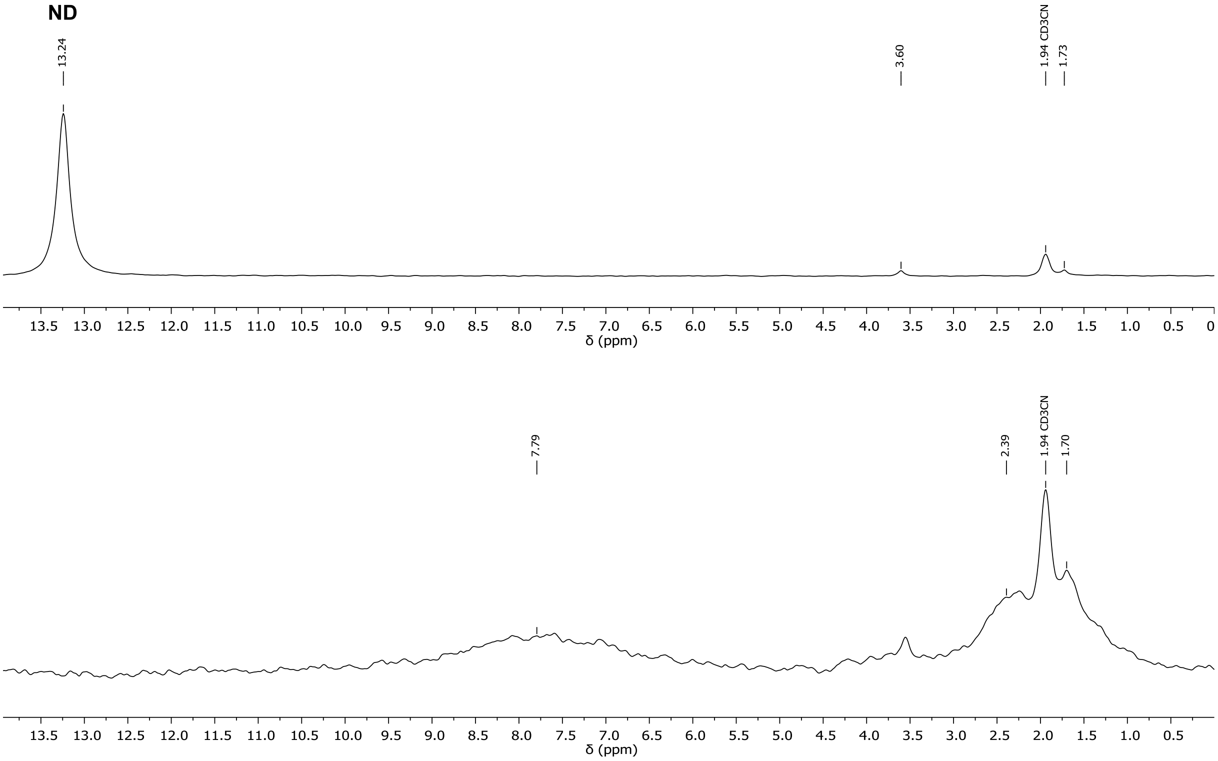

Figure 9.4: Top: ^{2}H NMR spectrum of 2,6-lutidinium-*d* in MeCN (238 K, 77 MHz). ^{2}H resonance of the N–D group is found at 13.24 ppm. **Bottom:** After addition of $Co(Cp^*)_2$ a new ^{2}H resonance at 2.39 ppm appeared.

GC-TCD analysis of the headspace following the chemical reduction of **$[L^6Ni_2(SH)](PF_6)(OTf)$** by $Co(Cp^*)_2$ indicates the evolution of only 48% of the expected amount of H_2. The pK_a value of **$[L^6Ni_2(SH)](PF_6)(OTf)$** is 18.4 (**chapter 6**) and similar to $[NEt_3H]^+$ ($pK_a = 18.8$ in MeCN) which suggests that the complex can protonate the Cp* ring in $Co(Cp^*)_2$ as an undesired reaction competing with H_2 evolution. No further information in the literature and no experimental evidences are found to explain how the protonated reducing agent further reacts, without release of H_2. EPR monitoring of the reaction of $[HNEt_3]^+$ with $Co(Cp^*)_2$ and reaction of **$[L^6Ni_2(SH)]^{2+}$** with $Co(Cp^*)_2$ give no further information. Peters reported[414] an EPR signal of $[Cp^*Co(\eta^4\text{-}C_5Me_5H)]^+$ or $[Cp^*Co(\eta^4\text{-}C_5Me_5D)]^+$ only after isolation of the complex and measurement of the solid. In conclusion, it is confirmed that the chemical reduction of **$[L^6Ni_2(SH)]^{2+}$** to **$[L^6Ni_2S]^+$** occurs with H_2 evolution and the lower H_2 yield might be due to protonation of the non-innocent Cp* ring of the reducing agent as a side reaction, which opens a unknown reaction pathway.

9.3.2 Electrochemical proton reduction by $[L^6Ni_2(SH)](PF_6)(OTf)$

The reduction process of **$[L^6Ni_2(SH)]^{2+}$** is investigated, using $[HNEt_3]^+$ as proton source. This acid is chosen, due to similar pK_a values of **$[L^6Ni_2(SH)]^{2+}$** and $[HNEt_3]^+$ and because its reduction ($E_p^{red.}$ = –2.29 V *vs.* Fc/Fc$^+$ in MeCN)[211] occurs at more negative potential than the reduction potential of **$[L^6Ni_2(SH)]^{2+}$** ($E_p^{red.}$ = –1.93V *vs.* Fc/Fc$^+$ in MeCN). In **Figure 9.5**, the CV of **$[L^6Ni_2(SH)]^{2+}$** is shown after addition of different amounts of acid. Addition of acid results in an increase of the current and a small catalytic wave is observed (– – –). After addition of 10 equiv. of acid no significant increase of the current is observed, since the separation of the catalytic wave from the reduction event of the acid is not possible.

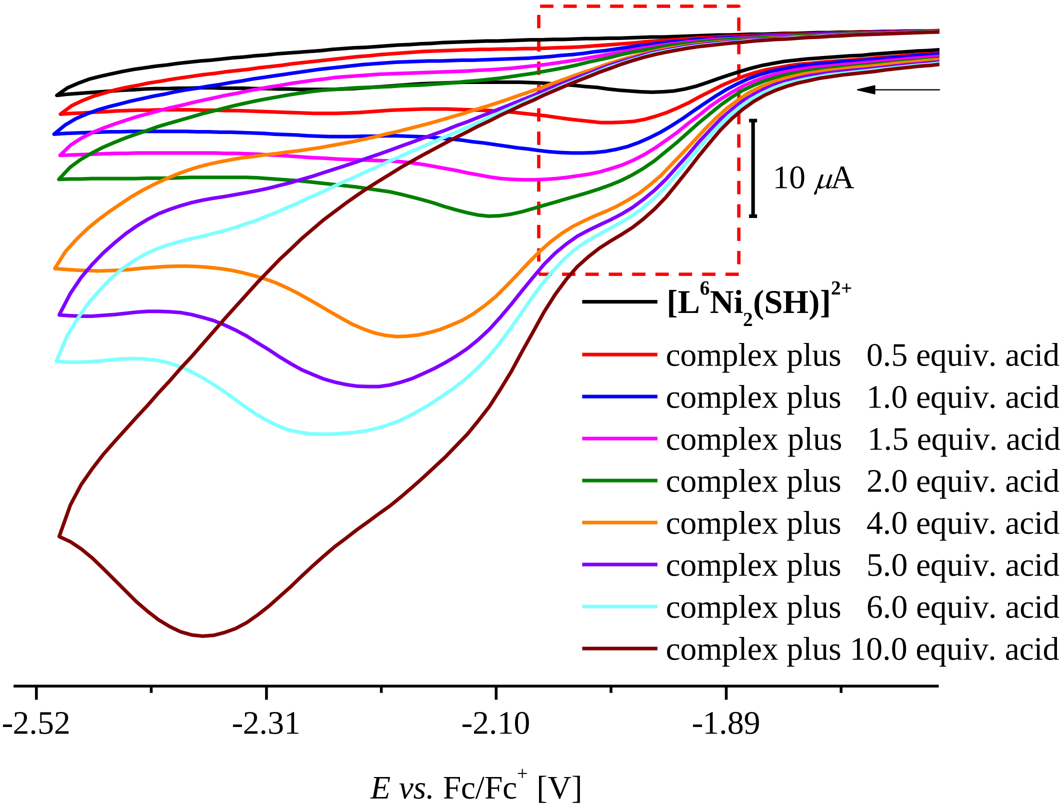

Figure 9.5: CV of **$[L^6Ni_2(SH)]^{2+}$** with different equivalents of $[HNEt_3]^+$ shows a catalytic wave (– – –).

UV-vis spectroscopy of **$[L^6Ni_2(SH)]^{2+}$** shows the stability of the complex under excess of acid (80 equiv.) (**Figure 9.6**, **left**). Furthermore, the oxidation process of the complex is investigated after its reduction event. Even after addition of 80 equiv. of $[HNEt_3]^+$ to **$[L^6Ni_2(SH)]^{2+}$** an oxidation process is observed, indicating the formation of **$[(L^6)_2Ni_4(S_2)]^{4+}$**. A two cycle modus in the CV shows in the second cycle a cathodic wave assigned to the reduction of **$[(L^6)_2Ni_4(S_2)]^{4+}$** to **$[L^6Ni_2S]^+$** (**Figure 9.6**, **right**) The oxidation process suggests the presence of **$[L^6Ni_2S]^+$** in the end of the catalytic cycle also at a high acid concentration, since **$[L^6Ni_2(SH)]^{2+}$** cannot be oxidized in the electrochemical window of MeCN (**chapter 6**).

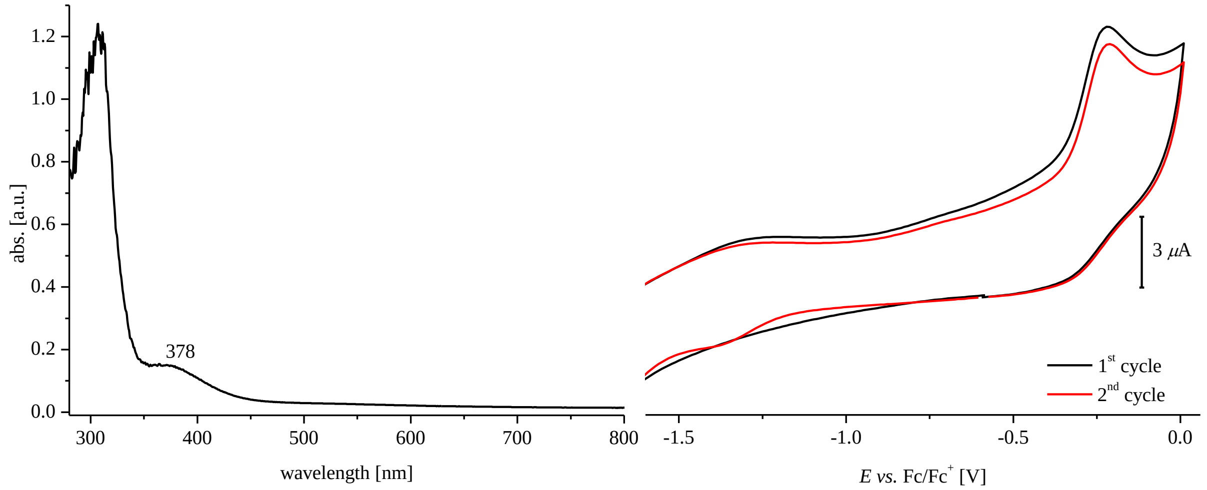

Figure 9.6: Left: UV-vis spectrum of **[L^{6}Ni$_2$(SH)]$^{2+}$**under presence of 80 equiv. of [HNEt$_3$]$^+$. **Right:** CV in a two cycle mode shows an oxidation event and one reduction event in the second cycle.

UV-vis and ^{1}H NMR spectroscopic titration experiments of **[L^{6}Ni$_2$S]$^+$** with [HNEt$_3$]$^+$ and **[L^{6}Ni$_2$(SH)]$^{2+}$** with NEt$_3$ are performed to further investigate the behavior of the complexes with the acid/base.

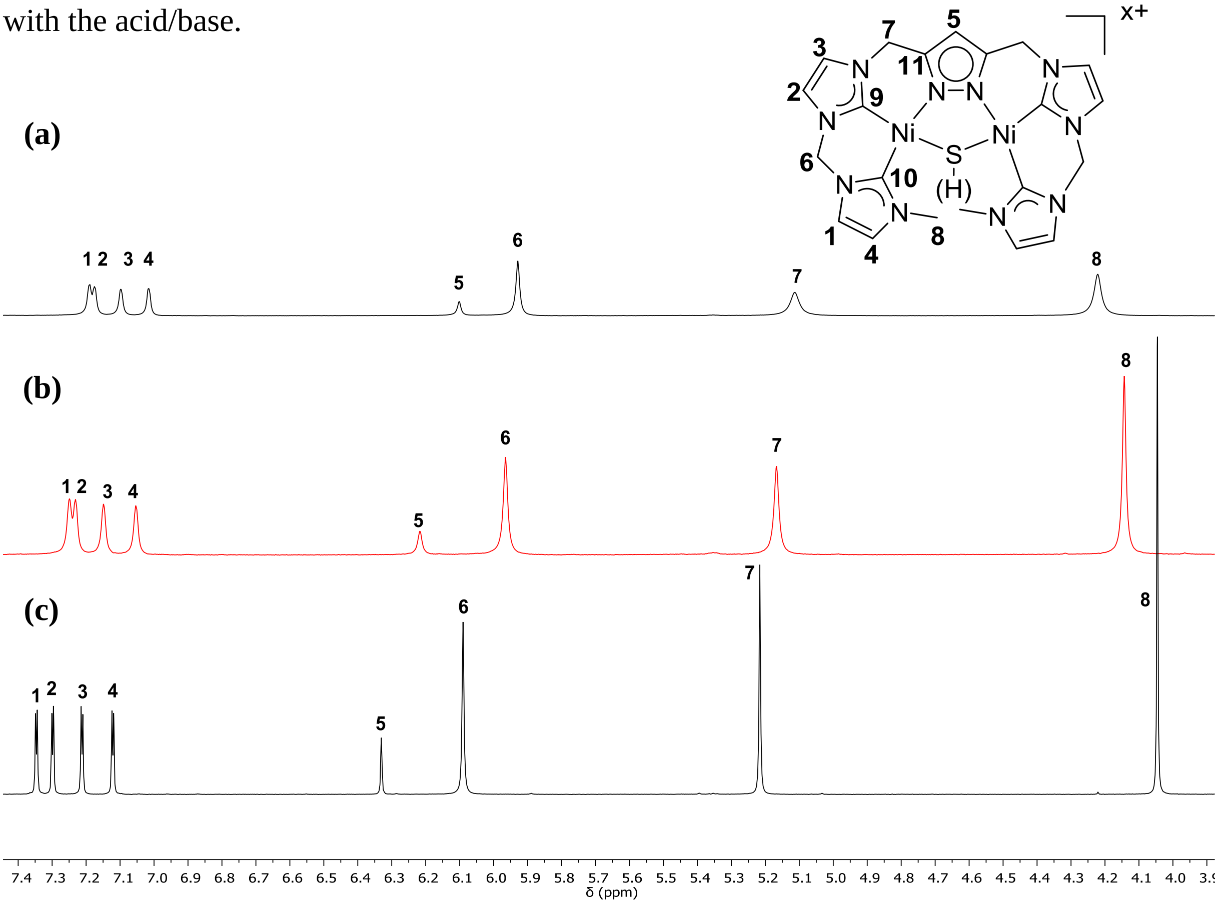

Figure 9.7: ^{1}H NMR spectra of (**a**) **[L^{6}Ni$_2$S]$^+$**, (**b**) mixture of **[L^{6}Ni$_2$S]$^+$**/[HNEt$_3$]$^+$ (1:1.23) and (**c**) **[L^{6}Ni$_2$(SH)]$^{2+}$** in MeCN-d_3 (400 MHz, 298 K).

Addition of 1.23 equiv. of [HNEt$_3$]$^+$ to **[L^{6}Ni$_2$S]$^+$** leads to a low-field shift of the proton resonances H^1-H^7, including a pronounced shift of the H^5 resonance and a high–field shift of H^8 (**red** spectra in **Figure 11.7**). The observed chemical shifts are neither similar to those of **[L^{6}Ni$_2$S]$^+$** (**Figure 9.7**, **(a)**) nor to **[L^{6}Ni$_2$(SH)]$^{2+}$** (**Figure 9.7**, **(b)**). A detailed ^{1}H NMR titration experiment of **[L^{6}Ni$_2$S]$^+$** with [HNEt$_3$]$^+$ (0.0-6.0 equiv.) in MeCN-d_3 at 298 K shows a non-linear variation of the CH$_2$ proton resonances H^6. The shape of the curve is less pronounced than in the protonation reaction of **[L^{6}Ni$_2$S]$^+$** with 2,6-lutidinium in **chapter 6** (**Figure 6.14**). No signal of a potential S–H proton resonance is observed in the ^{1}H NMR spectra after addition of six equivalents of acid.

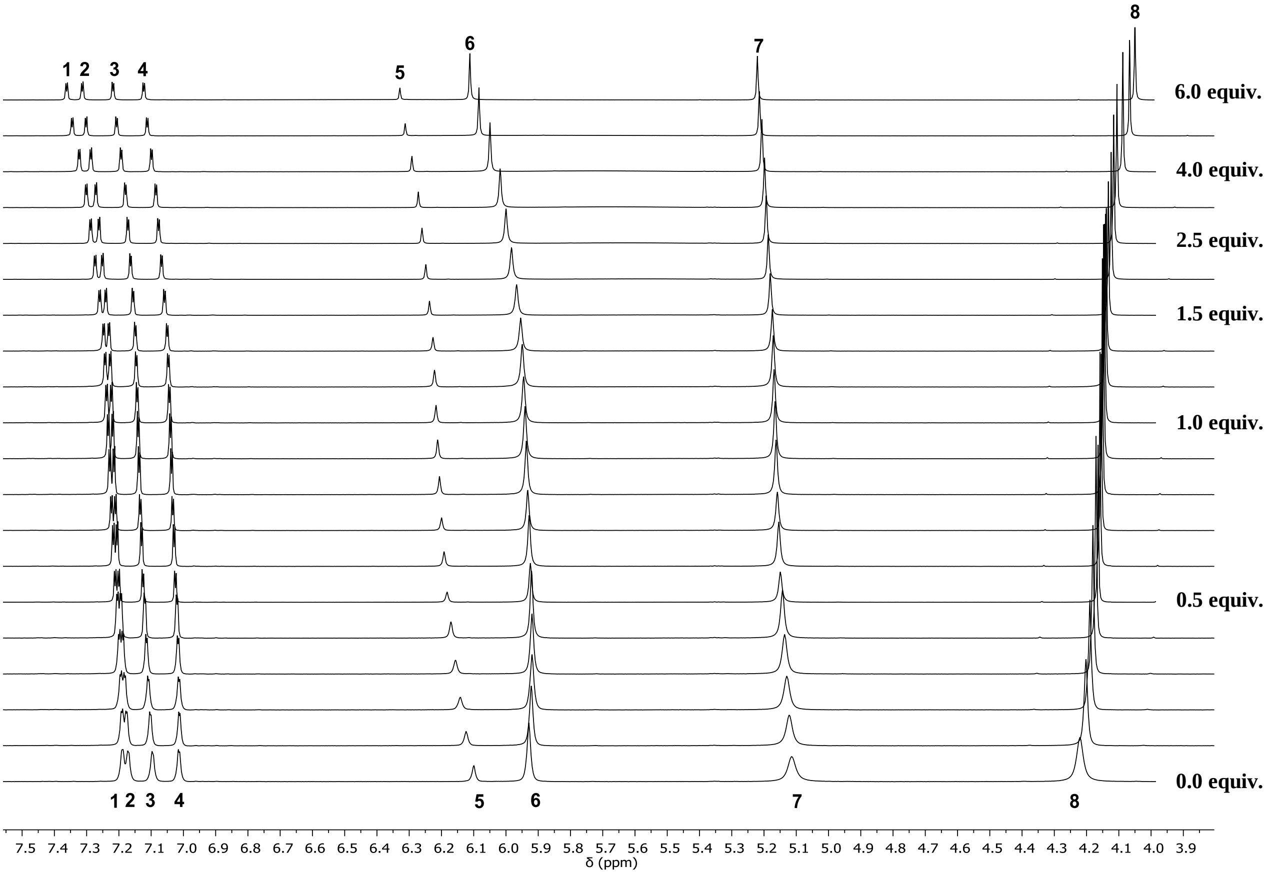

Figure 9.8: ^{1}H NMR monitoring of the titration of **[L^{6}Ni$_2$S]$^+$** with [HNEt$_3$]$^+$ (0-6 equiv.) in MeCN-d_3 at 400 MHz and 298 K.

In the temperature range between 298 K to 233 K, VT ^{1}H NMR spectra of **[L^{6}Ni$_2$S]$^+$** in the presence of 6 equiv. of acid show an additional broad peak at approximately 7 ppm and one peak at 2.5 ppm (**Figure 9.9**). A diastereotopic splitting of the CH$_2$ proton resonances H^6 and H^7 is observed upon decrease of the temperature and a coalescence temperature for both CH$_2$ groups is obtained between 273 K and 263 K (**Figure 9.9**). The ^{1}H^{1}H NOESY spectrum at 243 K shows an exchange between this two peaks 7 ppm and 2.5 ppm (see **appendix**, **Figure A.9.2**). ^{1}H DOSY NMR spectroscopy at 238 K, 243 K and 298 K cannot support a host guest complex ([**L^{6}Ni$_2$S**]$^+\cdots$H$^+\cdots$NEt$_3$) as it is also the case for the encounter complex **[(L^6)$_2$Ni$_4$(SHS)]$^{3+}$** (**chapter 6**). After addition of a further equivalent of acid (total 7.0 equiv.) to the complex, a chemical shift of all proton resonances of [**L^{6}Ni$_2$(SH)**]$^{2+}$ is observed, including a sharp singlet at 0.36 ppm for the SH proton resonance (**Figure 9.10**). A triplet at 7.10 ppm is assigned to the NH proton resonance of the acid ($^1J_{NH}$ = 53 Hz) and a broad singlet at 2.31 ppm is observed. The corresponding inverse ^{1}H NMR experiment (NEt$_3$/[**L^{6}Ni$_2$(SH)**]$^{2+}$) shows no full conversion of [**L^{6}Ni$_2$(SH)**]$^{2+}$ to [**L^{6}Ni$_2$S**]$^+$. Only one species is observable by ^{1}H NMR spectroscopy, but the complex has slightly different chemical shifts than [**L^{6}Ni$_2$S**]$^+$ (see **appendix**).

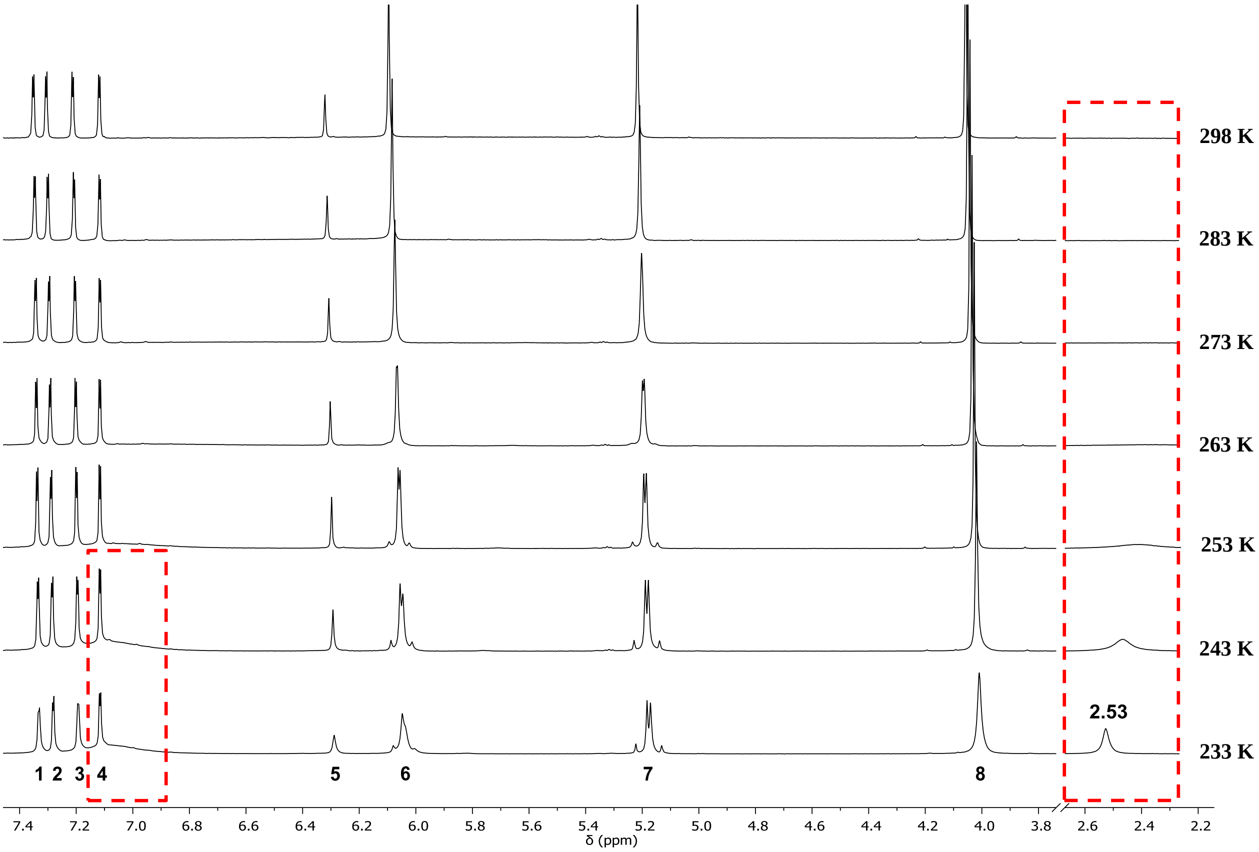

Figure 9.9: VT ^{1}H NMR spectra of the mixture [HNEt$_3$]$^+$/[**L^{6}Ni$_2$S**]$^+$ (6:1) in the temperature regime between 298-233 K in MeCN-d_3 at 400 MHz. Red dashed lines (– – –) show the appearance of new peaks at approximately 7 ppm and 2.53 ppm.

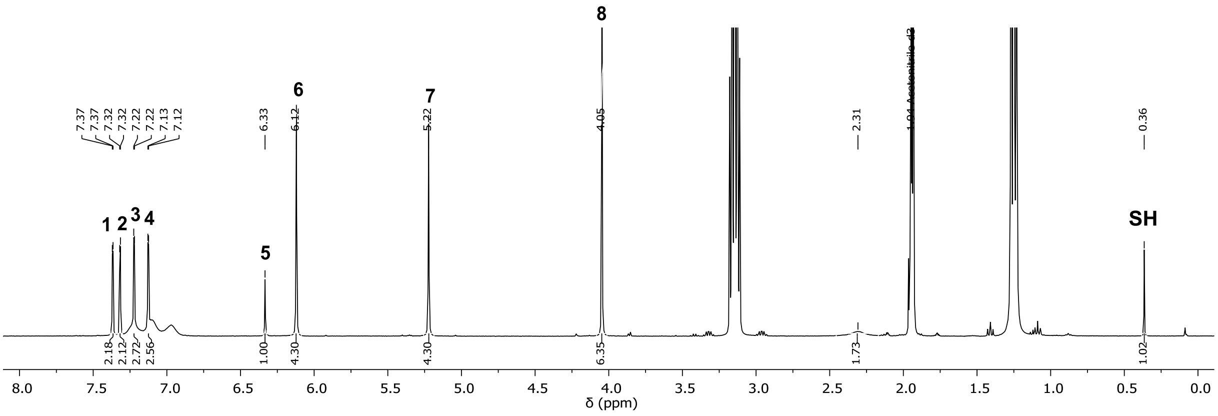

Figure 9.10: ^{1}H NMR spectrum of the mixture **[L^6Ni_2S]**$^+$/[$HNEt_3$]$^+$ (1:7) in MeCN-d_3 at 400 MHz and 298 K. Peaks are assigned to **[$L^6Ni_2(SH)$]**$^{2+}$.

Since the reaction of [$HNEt_3$]$^+$ with **[L^6Ni_2S]**$^+$ or NEt_3 with **[$L^6Ni_2(SH)$]**$^{2+}$ does not result in the pure conversion of the complex, it is not possible to determine the pK_a value of **[$L^6Ni_2(SH)$]**$^{2+}$ by these reactions, neither by ^{1}H NMR spectroscopy nor by UV-vis titration experiment (see also **chapter 6** for pK_a determination of **[$L^6Ni_2(SH)$]**$^{2+}$). The presented titration experiments are repeated and monitored by UV-vis spectroscopy but no full conversion of **[L^6Ni_2S]**$^+$/**[$L^6Ni_2(SH)$]**$^{2+}$ is observed from the use of [$HNEt_3$]$^+$/NEt_3. The plots in **Figure 9.11** summarize the non-linearity of the titrations, monitored by ^{1}H NMR or UV-vis spectroscopy. The curve shapes are similar of the UV-vis and NMR experiments are similar but different by the use of [$HNEt_3$]$^+$ or NEt_3 as the titrant. The evaluation of this data lead to different possible models (different ratios of host and guest) and a large scattering of the resulting binding equilibria K [M^{-1}], by use of the online calculation program BINDFIT v0.5 (supramolecular.org) from Thordarson and Stoddart.[415,416] Determination of K is not possible with the chosen models. A comparison of these results with the titration experiments with 2,6-lutidinium triflate, wherein a total conversion of **[L^6Ni_2S]**$^+$ to **[$L^6Ni_2(SH)$]**$^{2+}$ is observed, supports that no transformation of **[$L^6Ni_2(SH)$]**$^{2+}$ to **[L^6Ni_2S]**$^+$ occurs and *vice versa*, like in the previous case. A conversion to **[$L^6Ni_2(SH)$]**$^{2+}$ is only observed at high acid concentrations (>6.0 equiv.). Based on the presented results, an interaction between the complexes and the acid/base is reasonable.

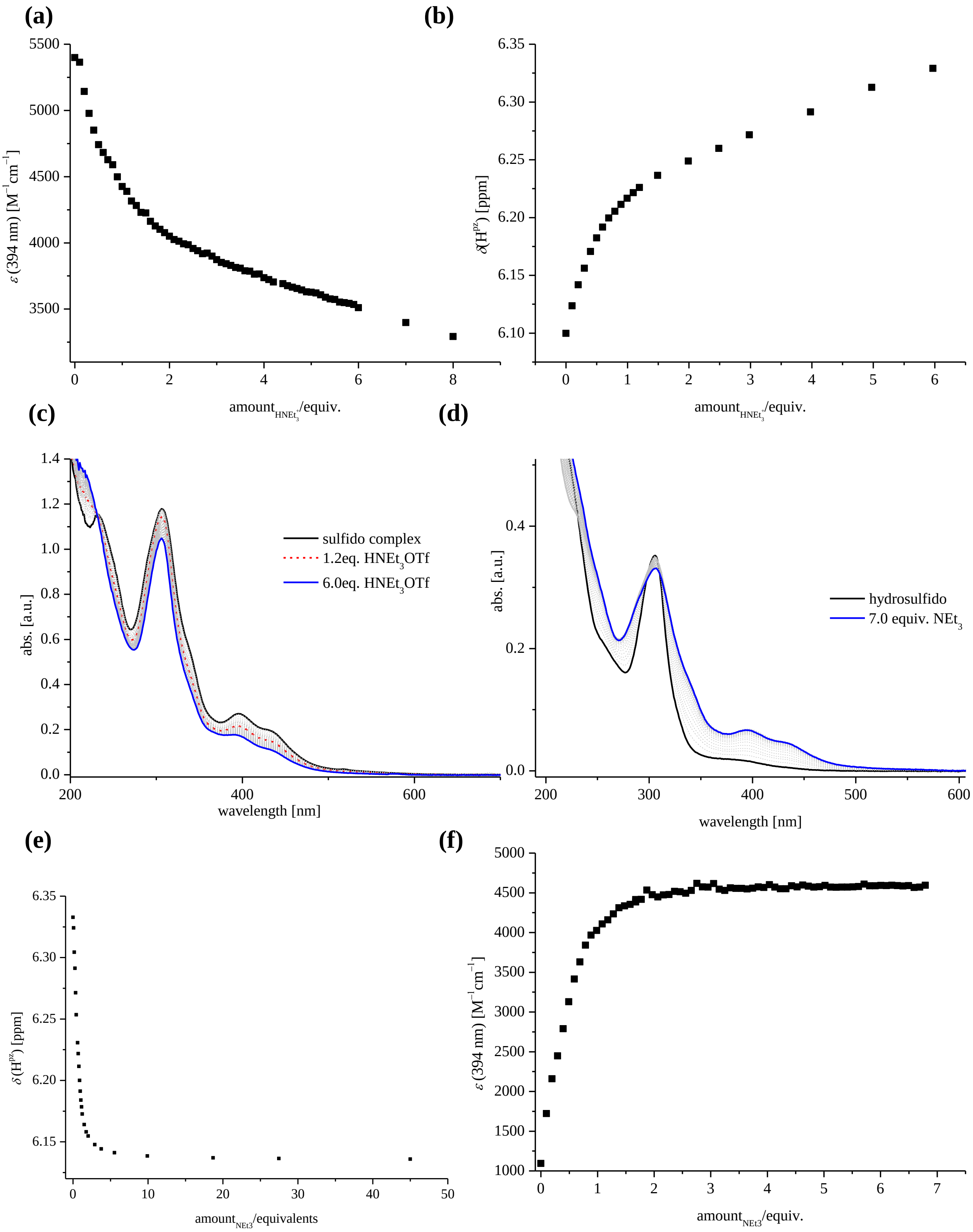

Figure 9.11: (**a**) UV-vis monitoring of the titration of **[L^6Ni_2S]$^+$** with acid, (**b**) ^1H NMR monitoring of the titration of **[L^6Ni_2S]$^+$** with acid, (**c**) UV-vis spectra during the titration of **[L^6Ni_2S]$^+$** with acid (**d**) UV-vis spectrum during the titration of **[$L^6Ni_2(SH)$]$^{2+}$** with base (**e**) ^1H NMR monitoring of the titration of **[$L^6Ni_2(SH)$]$^{2+}$** with base (**f**) UV-vis monitoring the titration of **[$L^6Ni_2(SH)$]$^{2+}$** with base.

9.3.3 Electrochemical proton reduction by [L^{6}Ni$_2$S]PF$_6$

In the literature it is well known, that in biological systems metal sulfur containing cofactors can vary their redox potentials over a broad potential range.[417–419] Mayer and Meyer *et al.*[417–419] synthesized and investigated PCET properties of their Rieske and mitoNEET model complexes. They observed in the CV anodically shifts from 65 mV to 240 mV by protonation of the 3-*N* position of the benzimidazolyl ligand backbone of the Fe_2S_2 clusters. To date, there need to be more investigations of the redox behavior of the complexes after (de)protonation of the sulfur bridge. In analogy to the previously described CV titration experiments of **[L^{6}Ni$_2$(SH)]$^{2+}$** further experiments are carried out with **[L^{6}Ni$_2$S]$^+$** and these observations are compared with results, described in the literature. By addition of one equivalent of $[HNEt_3]^+$ to **[L^{6}Ni$_2$S]$^+$** a reduction event at –2.0 V *vs.* Fc/Fc$^+$ is observed in the CV in MeCN (**Figure 9.12**). In **chapter 8**, the redox behavior of **[L^{6}Ni$_2$S]$^+$** shows that in the absence of an acid, a reduction event at –2.8 V is observed (**Figure 9.12**). This redox event is anodically shifted by around 766 mV in the presence of $[HNEt_3]^+$. The proposed localization of the proton between **[L^{6}Ni$_2$S]$^+$** and $[HNEt_3]^+$ results in a pronounced anodic shift of 766 mV. A direct comparison of the reduction events of **[L^{6}Ni$_2$S]$^+$** and **[L^{6}Ni$_2$(SH)]$^{2+}$** shows again a pronounced peak separation of approximately 810 mV. These findings underline the strong influence of the bridging donor, with less electron localization at the sulfur atom, and the higher positive charge of the complex, which affects the redox behavior of the complex (anodic shift of the peak potential).

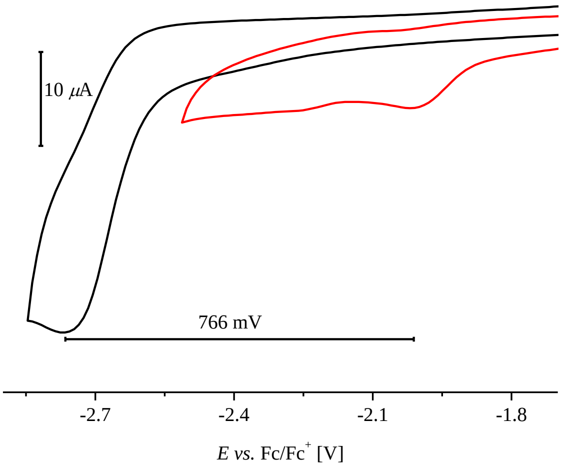

Figure 9.12: CVs of **[L^{6}Ni$_2$S]$^+$** (**black**) and **[L^{6}Ni$_2$S]$^+$**/$[HNEt_3]^+$ (**red**) with a separation of the reduction event of 766 mV.

A direct comparison of the reduction process of **[L^{6}Ni$_2$S]$^+$**/$[HNEt_3]^+$ with **[L^{6}Ni$_2$(SH)]$^{2+}$** shows a cathodic shift of approximately 50 mV (**Figure 9.13**, (**a**)). The higher anodic potential of **$[L^6Ni_2(SH)]^{2+}$**is likely caused by a smaller donor strength of the bridge, compared to **$[L^6Ni_2S]^+$**/$[HNEt_3]^+$ (see also **Figure A.9.4** in appendix). A cathodic shift of the catalytic wave of **$[L^6Ni_2(SH)]^{2+}$** is observed by comparison of the peak potentials of **$[L^6Ni_2S]^+$**/$[HNEt_3]^+$ (2.0 equiv.) (**Figure 9.13** (**b**)) with **$[L^6Ni_2(SH)]^{2+}$**/$[HNEt_3]^+$ (1.0 equiv.) in the CV's. At higher acid concentrations the reduction process of **$[L^6Ni_2(SH)]^{2+}$** approaches the catalytic process of **$[L^6Ni_2S]^+$**. At a **$[L^6Ni_2S]^+$**/$[HNEt_3]^+$ ratio of 1:3 and **$[L^6Ni_2S]^+$**/$[HNEt_3]^+$ 1:6 (**Figure 9.13** (**c**) and (**d**)) both catalytic waves are identical, which supports the same complex species in solution. **$[L^6Ni_2(SH)]^{2+}$** can be reduced under absence/presence of acid to **$[L^6Ni_2S]^+$**. The titration experiments show that **$[L^6Ni_2S]^+$** is not converted back to **$[L^6Ni_2(SH)]^{2+}$** without more than 6 equivalents of acid.

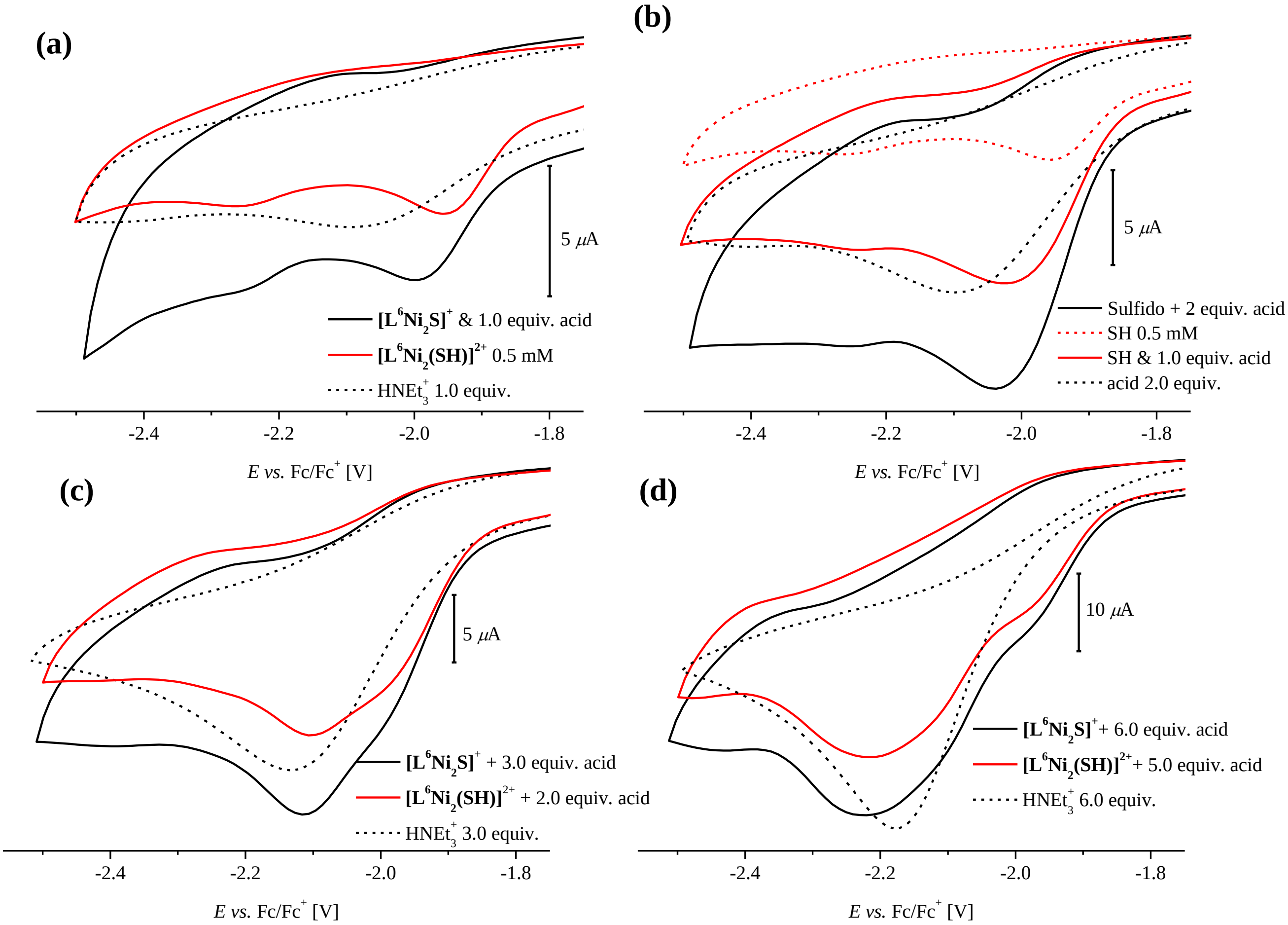

Figure 9.13: Comparison of CVs of **$[L^6Ni_2S]^+$** and **$[L^6Ni_2(SH)]^{2+}$** at different proton concentrations. (**a**) 1 equiv., (**b**) 2 equiv., (**c**) 3 equiv., (**d**) 6 equiv..

It can be proposed that **$[L^6Ni_2S]^+$** interacts with $[HNEt_3]^+$ *via* hydrogen bond interaction (**Scheme 9.3**), which probably results into an equilibrium of **$[L^6Ni_2S]^+$**/$[HNEt_3]^+$ and **$[L^6Ni_2(SH)]^{2+}$**/$[NEt_3]^+$. This equilibrium seems to be more on the side of **$[L^6Ni_2S]^+$**/$[HNEt_3]^+$. The host **$[L^6Ni_2S]^+$** can be oxidized to **$[(L^6)_2Ni_4(S_2)]^{4+}$**, which can be a possible explanation for the observation of the oxidation event in the CVs (for instance **Figure 9.6**, **left**). Similar waves at proton concentration of 6 equivalents indicate that only one species exist in solution, wherein the host-guest complex can be the catalytic active species (**Scheme 9.3**). At higher acid concentrations (>6 equiv.) only **[L^{6}Ni$_2$(SH)]$^{2+}$** exists in the resting state.

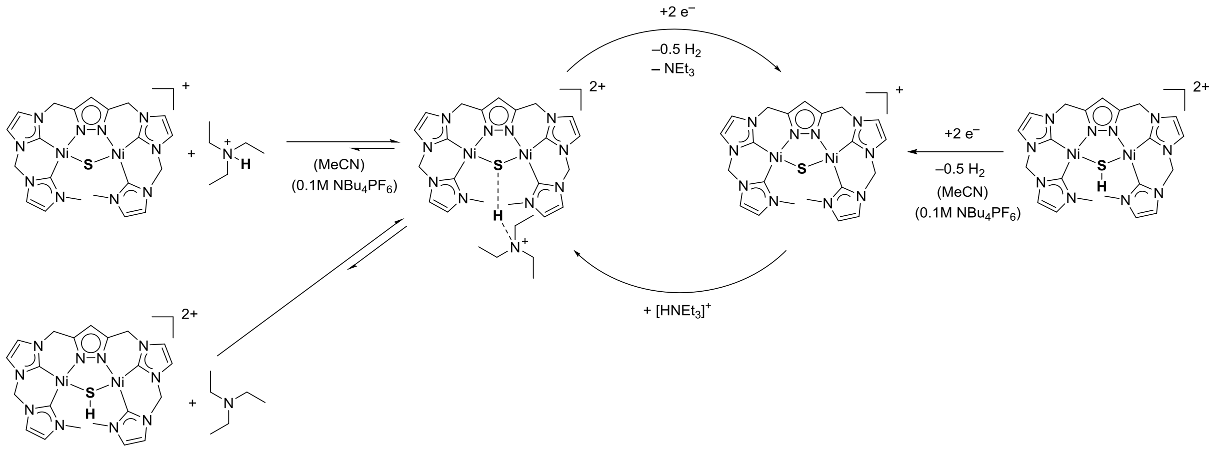

Scheme 9.3: Postulated possibilities for the catalytic proton reduction by **[L^{6}Ni$_2$S]$^+$** and [**L^{6}Ni$_2$(SH)]$^{2+}$**.

The CVs of **[L^{6}Ni$_2$S]$^+$**/[HNEt$_3$]$^+$ (1:1, 1:1.5 and 1:2) are compared with the CV's of **[L^{6}Ni$_2$(SH)]$^{2+}$**/[NEt$_3$]/ [HNEt$_3$]$^+$ (1:1:0, 1:1:0.5 and 1:1:1) in **Figure 9.14**, to further confirm the hypothesis of the same species in solution (**Scheme 9.3**). Indeed, both mixtures show the same reduction potentials, which further support this assumption.

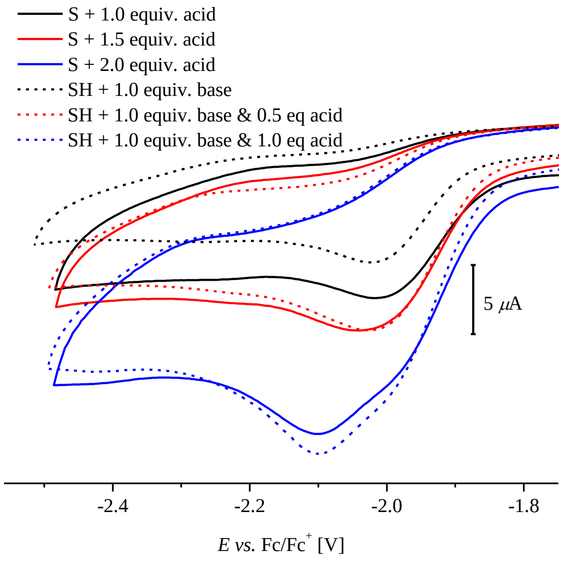

Figure 9.14: Comparison of CVs of **[L^{6}Ni$_2$S]$^+$**/[HNEt$_3$]$^+$ (1:1, 1:1.5 and 1:2) with **[L^{6}Ni$_2$(SH)]$^{2+}$**/[NEt$_3$]/ [HNEt$_3$]$^+$ (1:1:0, 1:1:0.5 and 1:1:1).

9.3.4 Catalytic proton reduction by nickel sulfur derivates

After gaining a better understanding of the possible mechanistic steps in the electrochemical reduction of protons, the (electro-)catalytic performance of [$\mathbf{L^6Ni_2S}$]$^+$ and [$\mathbf{L^6Ni_2(SH)}$]$^{2+}$ is tested in cooperation with Prof. Dr. Artero at CEA Grenoble. Unfortunately, it is not possible to evaluate the catalytic performance of the systems electrochemically using the given setup, since the sulfur containing complexes react with the mercury working electrode (see **appendix**, **Figure A.9.5**) and studies with GC rod are excluded due to the high background reduction of the acid at the working electrode at such close potentials of complex and acid. To confirm the catalytic behavior of the complexes [$\mathbf{L^6Ni_2S}$]$^+$ and [$\mathbf{L^6Ni_2(SH)}$]$^{2+}$, GC-TCD analysis of a reaction using [$HNEt_3$]$^+$ and chemical reductant ($Co(Cp^*)_2$) are performed to determine the TON values (see experimental section, **10.2.4**). An average TON for both complexes of approximately 5 is determined, which confirms catalytic performance of the system. A detailed description of the experiments and the determination of the TON values can be found in the experimental section.

9.4 Conclusion and Outlook

The catalytic dihydrogen evolution by **$[L^6Ni_2(SH)]^{2+}$** and **$[L^6Ni_2S]^+$** is confirmed. Even though the TON with approximately 5 is very low, first successful mechanistic investigations of the (electro-)chemical proton reduction by **$[L^6Ni_2(SH)]^{2+}$** and **$[L^6Ni_2S]^+$** by use of $[HNEt_3]^+$ as proton source are presented. An important parameter of these investigations is the pK_a value of the S–H group and the redox potentials of the complexes. NMR and UV-vis titration experiments and a comparison of the CVs of **$[L^6Ni_2(SH)]^{2+}$** and **$[L^6Ni_2S]^+$** with equal amounts of protons indicate that the same host-guest complex for both complexes is present in solution and might be the catalytically active species for the proton reduction process. Based on the performed experiments, it is proposed that the transfer of the proton from the acid to the complex is not necessary for proton reduction, since both are in equilibrium. Also the interaction, probably *via* the S bridge, is sufficient for dihydrogen evolution. An anodic shift of the reduction event of **$[L^6Ni_2S]^+$** around 766mV is observed under presence of acid. In order to understand the further elementary reaction steps in the catalytic mechanism, much more experiments are necessary in the future. The observed interconversion of **$[L^6Ni_2(SCH_3)]^{2+}$** and **$[L^6Ni_2(SCH_3)]^+$**gives space for speculations about the first step in the mechanism of the proton reduction by **$[L^6Ni_2(SH)]^{2+}$** or **$[L^6Ni_2S]^+$** and leads to the question if the first step is a metal centered reduction process under formation of a mixed valent Ni^INi^{II} complex. At this stage of research also both mechanism for proton reduction (heterolytic pathway and homolytic pathway) are possible and a radical pathway cannot be excluded based on the $BDFE_{(solv.)}$ of the S–H bond.

Part III

Experimental Section

10 Experimental Section

10.1.1 Materials and Methods

Unless stated otherwise, all reactions with air- and moisture sensitive chemicals were performed in an oxygen-free, dry atmosphere of inert gas (argon or nitrogen) using standard Schlenk or glovebox techniques. Inert gases (Argon and nitrogen 5.0 (99.999 Vol.-% pure)) were obtained from LINDE AG (Munich, Germany) and used without further purification. The used *UNIlab* gloveboxes from M. BRAUN INERTGAS-SYSTEME GmbH (Garching, Germany) are equipped with a build-in purification system and under inert gas atmospheres with < 0.1 ppm dioxygen and water. Inert gases (argon or nitrogen) 5.0 were used as purchased. The vacuum at the Schlenk line was at least $3.8 \cdot 10^{-2}$ mbar. Not-Schlenk glassware was stored in an oven at 120 °C for at least 12 hours and immediately transferred into the glovebox prior to use. Schlenk glassware was stored at 120 °C, heated-up three times each for 15 minutes prior to use and cooled down to room temperature *in vacuo*. Gastight syringes, quartz cuvettes, EPR tubes and caps and septa for the CV cells for water sensitive compounds and reactions were permanently stored at 60 °C.

10.1.2 Chemicals

Dry, oxygen-free and purified solvents were obtained by standard procedures, distilled and stored under inert gas. Acetonitrile and propionitrile were dried by heating to reflux over calciumhydride for several days. Acetone was stirred over B_2O_3 for 24 hours. Dimethyl sulfoxide was pre-dried over calcium hydride and distillated. Diethyl ether and tetrahydrofuran were dried over sodium. All dry solvents were stored over molecular sieves (4 Å for benzene, tetrahydrofuran, toluene and diethyl ether or 3 Å for nitriles). Oxygen-free solvents were degassed by bubbling with argon for at least 30 minutes. Absolutely oxygen-free solvents were degassed by three freeze-pump-thaw cycles and stored under argon. Other solvents and chemicals were used as purchased. Dioxygen and nitrous oxide were dried by passage through a P_2O_5 column and stored in a Schlenk tube for several days over sulfuric acid (96%). Nitric oxide was used by passed through a P_2O_5 column and a U-tube, cooled down by a Et_2O/dry ice bath to –78 °C and was directly used.

10.2 Analytics

10.2.1 Density Functional Theory (DFT) Calculations

DFT calculations were performed by Dr. Dechert of the group of Prof. Dr. Meyer. The ORCA package (version 3.0.3) was employed.[420] A geometry optimization was performed based on the coordinates of the complexes from the crystallographic structure determinations (BP86 functional, def2-tzvp basis set[421,422], RI approximation using the auxiliary def2-tzvp/J basis set, D3 dispersion correction with zero damping[423], tight convergence, and optimization criteria). The spin density calculation was carried out on the optimized coordinates by using the B3LYP functional and the RIJCOSX approximation with the same basis sets and dispersion correction as stated above.

TD-DFT calculations were performed with the coordinates obtained from the geometry optimizations (B3LYP functional, RIJCOSX approximation, def2-tzvp and def2-tzvp/j basis sets). 80 excited states were calculated; the maximum dimension of the expansion space in the Davidson procedure (MaxDim) was 800.

DFT calculation of EPR signatures were performed by Dr. Finger of the group of Prof. Dr. Schneider (Institute of Inorganic Chemistry, Georg-August-University Göttingen). This paragraph has been adapted from Ref. [219]. EPR data were evaluated applying the PBE0[424] functional including spin-orbit coupling within the Breit-Pauli approximation as implemented in ORCA (SOMF(1X) keyword) using the geometry from the optimization as described above. Relativistic effects were treated at the all-electron level with the ZORA method[425] in conjunction with the corresponding recontracted def2-TZVP basis sets[426] employing the model potential approach of van Wüllen.[427] Picture change effects[428] were also included as a correction within the scalar relativistic framework. The density-fitting procedure was used within the RIJCOSX approximation[429] in conjunction with the corresponding def2-Coulomb fit basis sets[430] and large integration grids (Grid6 and GridX6 in ORCA convention). Grimme’s dispersion correction with Becke-Johnson damping (D3(BJ)) was employed as well.

10.2.1.1 DFT Calculations of the water exchange

DFT calculations were performed by Prof. Dr. Mata from the Institute of Physical Chemistry. A geometry optimization of the structures (starting complex, transition state and intermediate) were performed based on the coordinates of the complex **$[L^6Ni_2(OH)]^{2+}$**$\cdot H_2O$ from the crystallographic structure determinations (BP86-D3/def2-SVP level of theory, with use of Coulomb density fitting approximations). A connected path between all structures was obtained by applying a harmonic potential to the coordinate: r(Ni-O1)-r(Ni-O2).

Energy calculations are performed by use of the optimized structures (BP86-D3/def2-SVP level of theory). Activation parameters were calculated by three different density functionals: BP86-D3; B3LYP-D3 and PBE0-D3/def2-QZVP level of theory. The basis set used for the electronic energy corrections was def2-QZVPP. Results are provided with and without solvent effects. The latter were included through the use of the continuum model CPCM, **Table A.4.6** (**appendix**). All calculations were carried out with the program package Orca v4.0.1.[420]

10.2.2 Determination of rate constants by ^{1}H NMR spectroscopy

This paragraph has been adapted from *Z. Anorg. Allg. Chem.* **2019**, *645*, 605:

To determine the rate constants for fast exchange (above the T_c) equation (24) was used, at T_c (25) was used and for slow and intermediate exchange (below T_c) expression (26) was used. $(\Delta\upsilon_e)_{1/2}$ is equal to exchanging singlet peak width at half height at a certain temperature, $(\Delta\upsilon_0)_{1/2}$ is the singlet peak width at half height of the peak at a temperature where no exchange occurs and $\Delta\upsilon_0$ the distance of the peak separation in [Hz] at the lowest temperature. The values of $(\Delta\upsilon_e)_{1/2}$ and $(\Delta\upsilon_0)_{1/2}$ in [Hz] were obtained by using the GSD method of the NMR program MestreNova[431].

$$k = \frac{\pi\cdot\Delta\upsilon_0{}^2}{2}\cdot\left[(\Delta\upsilon_e)_{1/2} - (\Delta\upsilon_0)_{1/2}\right]^{-1} \qquad (24)$$

$$k_c = \frac{\pi\cdot\Delta\upsilon_0}{\sqrt{2}} \qquad (25)$$

$$k = \pi\cdot\left[(\Delta\upsilon_e)_{1/2} - (\Delta\upsilon_0)_{1/2}\right] \qquad (26)$$

Equation (26) cannot be used for an AB spin system, like it was observed for **$[L^6Ni_2(OH)](PF_6)_2$** and **$[L^6Ni_2(SCH_3)](PF_6)_2$**. Determination of $\Delta\upsilon_e$ and $\Delta\upsilon_0$is not possible in an accurate way, due to an inter-spin exchange of the AB system which leads to a decrease of the outer peaks of the two doublet and to a broadening of this peaks. (26) is not considering this situation.

A possible way to determine k values for slow and intermediate exchange rates for AB spin systems is the use of computational programs. Using the simulation program WINDNMR (WINDNMR–Pro **2016**, Dnmr71, *http://www.chem.wisc.edu/areas/reich/plt/windNMR.htm.*) k values for these interconversions were obtained. Here experimentally determined υ_a, υ_b values and the υ_0 value at the lowest temperature as well as coupling constants J_{AB} for each temperature were used in order to obtain the general peak signal and peak shape of an AB spin system. Based on generated k values a simulated spectrum was derived where the $\Delta\upsilon_e$ values were manually determined. This procedure was repeated several times and the obtained $\Delta\upsilon_e$values were plotted *vs*. the predefined k values. The resulting calibration curve gives the possibility to derive directly the k values in dependence on the real $\Delta\upsilon_e$values, which were again obtained by line shape analysis, using GSD method of the NMR program MESTRENOVA.

$$\Delta H^{\ddagger} = -m \cdot R \tag{27}$$

$$\Delta S^{\ddagger} = \left(y - \ln\frac{k_B}{h}\right) \cdot R \tag{28}$$

$$E_a = -\mathrm{m} \cdot R \tag{29}$$

10.2.2.1 Determination of rate constants of $[L^6Ni_2(OH)]^{2+}$ and $[L^6Ni_2(SCH_3)]^{2+}$

The coalescence temperature of **$[L^6Ni_2(OH)]^{2+}$** is determined between 273 K and 263 K. Using the simulation program WinDNMR[432] k values for these interconversions are obtained between 243 K and 223 K. Here, real υ_a, υ_b values and the υ_0 value at 223 K as well as coupling constants J_{AB} for each temperature are used in order to obtain the general peak signal and peak shape of an AB spin system. Based on generated k values, a simulated spectrum is derived where the $\Delta\upsilon_e$values are manually determined. This procedure is repeated several times and the obtained $\Delta\upsilon_e$values are plotted *vs*. the predefined k values. The resulting calibration curve gives the possibility to derive directly the k values depending on the real $\Delta\upsilon_e$values (**Figure 13.1** (**a**)), which are again obtained by line shape analysis, using the GSD method of the NMR program MestreNova. This procedure was also applied for the determination of the rate constants of **$[L^6Ni_2(SCH_3)]^{2+}$** (**Figure 10.1** (**b**)).

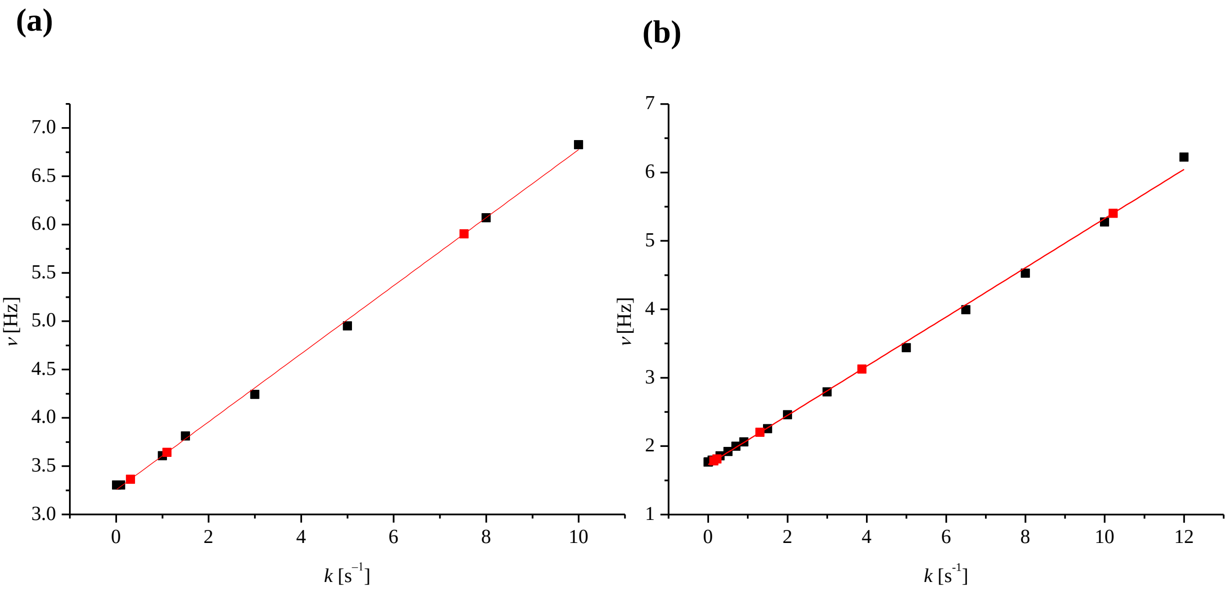

Figure 10.1: Calibration curve based on the computational derived υ and k values (**black**) and experimental determined υ values from GSD line fitting analysis for (**a**) **$[L^6Ni_2(OH)]^{2+}$** and (**b**) **$[L^6Ni_2(SCH_3)]^{2+}$**. **Black dotes** were generated by manual determination of υ from the simulation of the AB spin system. **Red dots** are the crossing points of the linear fit for an experimental υ value

10.2.3 Determination of the rate constants of H/D and $^{16}OH/^{17}OH$ exchange reactions at $[L^6Ni_2(OH)](PF_6)_2$

A defined amount of **$[L^6Ni_2(OH)](PF_6)_2$** was dissolved in MeCN-*d*$_3$ (0.5 mL) and transferred into a J Young valve NMR tube. A defined volume of labeled water was added in the neck of the J Young valve NMR tube. The solution was tempered to the desired temperature. The NMR tube was shaken four times and was immediately transferred into the 400 MHz NMR instrument. ^{1}H NMR spectra were recorded after a defined time with a defined delay time in between each measurement. Quantification of the interconversion was carried out by calculating the ratio between the proton resonance of the pyrazolate H proton and the O–H proton resonance of each NMR spectrum. All further values were graphically derived (**appendix**).

10.2.4 Determination of the TON values for chemical proton reduction

The determination of the TON values was done *via* detection of the dihydrogen evolution by GC-TCD analysis (AutosystemXL from PERKINELMER, capillary column ELITE5 with a constant temperature of 32 °C and argon as vector gas) and carried out by the following procedure. The complex, acid and reduction agent were weighed-in a GC vial. A defined volume of MeCN was added to the mixture und the suspension was shaken for several minutes. After a specific time, a defined volume of the headspace was removed by a gastight syringe and was injected into the GC instrument. The GC vial was filled up with MeCN and the volume of the headspace was determined *via* mass balance. $n(H_2)$ was calculated under consideration of a calibration curve for the area of the GC-TCD value and the mass of the headspace by the following formula (30)[433]:

$$n(\mathrm{H_2})[\mathrm{mol}] = \frac{\mathrm{area} \cdot V_{(\mathrm{headspace})} \cdot 0.01}{\mathrm{slope} \cdot 24.5} \tag{30}$$

After abstraction of background reactions of the reducing agent with the acid as well as the initial dihydrogen evolution from **$[Ni_2SHL^6]^{2+}$** the following TON values were determined:

Compound	TON
$[L^6Ni_2(SH)]^{2+}$	4.6
$[L^6Ni_2S]^{+}$	6.1

A detailed description for the calculation of dihydrogen evolution can be found below.

1) Reaction of **$[L^6Ni_2(SH)](PF_6)(OTf)$** with decamethyl cobaltocene

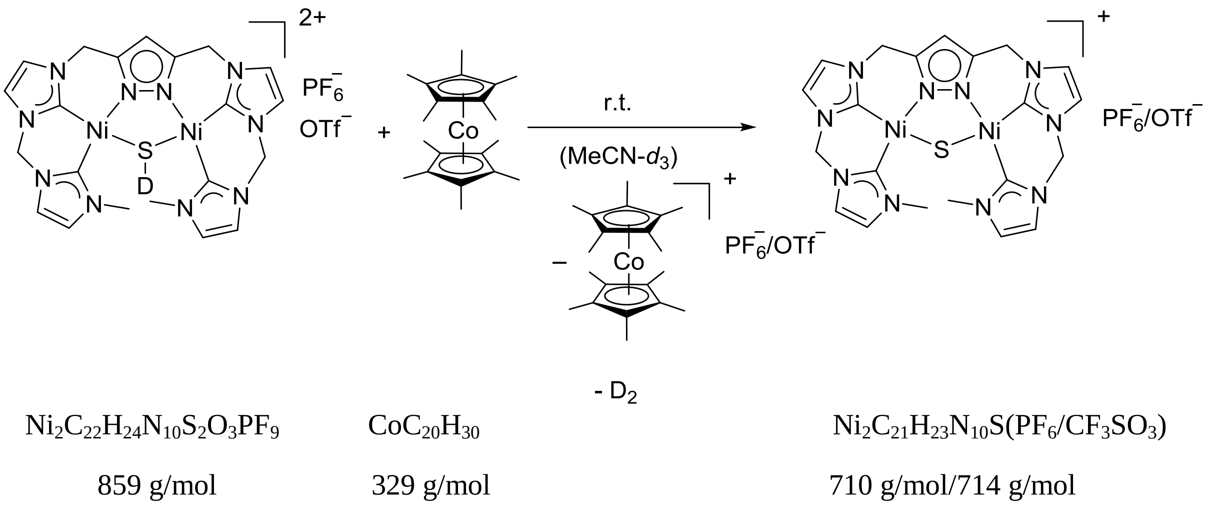

$Ni_2C_{22}H_{24}N_{10}S_2O_3PF_9$ $CoC_{20}H_{30}$ $Ni_2C_{21}H_{23}N_{10}S(PF_6/CF_3SO_3)$

859 g/mol 329 g/mol 710 g/mol/714 g/mol

Compound	*m* [mg]	*n* [µmol]	equiv.	*V* (MeCN) [µL]	*V* (gas) [µL]	area 210 s	*m* [g] (headspace)
$[L^6Ni_2SH]^{2+}$	3.246	3.775	1.00	200	25	0.46	1.1813
$Co(Cp^*)_2$	2.464	7.480	1.98				

Determination of the slope for the different volumes: The slope for 25 μL: 0.315

$$V_{(\text{headspace})} = \frac{m_{(\text{headspace})}}{\rho_{(\text{MeCN})}} = \frac{1.18\ \text{g}}{0.780\ \frac{\text{g}}{\text{mL}}} = 1.51 \cdot 10^{-3}\text{L}$$

$$n(H_2)[mol] = \frac{area \cdot V_{(headspace)} \cdot 0.01}{slope \cdot 24.5} = \frac{0.460 \cdot 1.5 \cdot 10^{-3} \cdot 0.01}{0.315 \cdot 24.5} = 0.904 \cdot 10^{-7}$$

This value corresponds to $n(\text{H}^+)$ = 1.81 μmol

Only 48% of the protons from **[L^{6}Ni$_2$(SH)](PF$_6$)(OTf)** are interconverted to H_2. This also belongs in addition to the “blank” reduction of the acid and this value will be considered for further calculations under presence of the hydrosulfido complex.

Increase of the reaction time from 210 s to 600 s did not result in an increase of the area in the GC-TCD.

2) Proton reduction of $HNEt_3BF_4$ by decamethyl cobaltocene

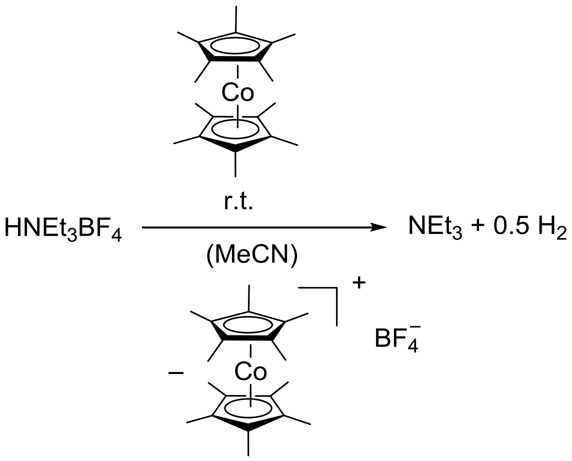

$C_6H_{16}NBF_4$	$CoC_{20}H_{30}$
189 g/mol	329 g/mol

Compound	*m* [mg]	*n* [μmol]	equiv.	*V* (MeCN) [μL]	*V* (gas) [μL]	area 880 s	*m* [g] (headspace)
[HNEt$_3$]BF$_4$	6.70	35.4	1.00	–	50	11.07	0.698
Co(Cp*)$_2$	12.2	37.0	1.04				

The determined slope for 50 μL is: 0.832

$$V_{(\text{headspace})} = \frac{m_{(\text{headspace})}}{\rho_{(\text{MeCN})}} = \frac{0.698\ \text{g}}{0.78\ \frac{\text{g}}{\text{mL}}} = 0.895 \cdot 10^{-3}\text{L}$$

$$n(\text{H}_2)[\text{mol}] = \frac{\text{area}\cdot \text{V}_{(\text{headspace})}\cdot 0.01}{\text{slope}\cdot 24.5} = \frac{11.1\cdot 0.895\cdot 10^{-3}\cdot 0.01}{0.832\cdot 24.5} = 4.86 \cdot 10^{-6}$$

This value corresponds to $n(\text{H}^+) = 9.72\ \mu\text{mol}$.

27% of the protons from $[\text{HNEt}_3]\text{BF}_4$ are converted to H_2. This value corresponds to the background reaction and will be considered for further calculations.

3) Reduction of HNEt_3BF_4 in the presence of **$[\text{L}^6\text{Ni}_2\text{S}]\text{PF}_6$** and decamethyl cobaltocene

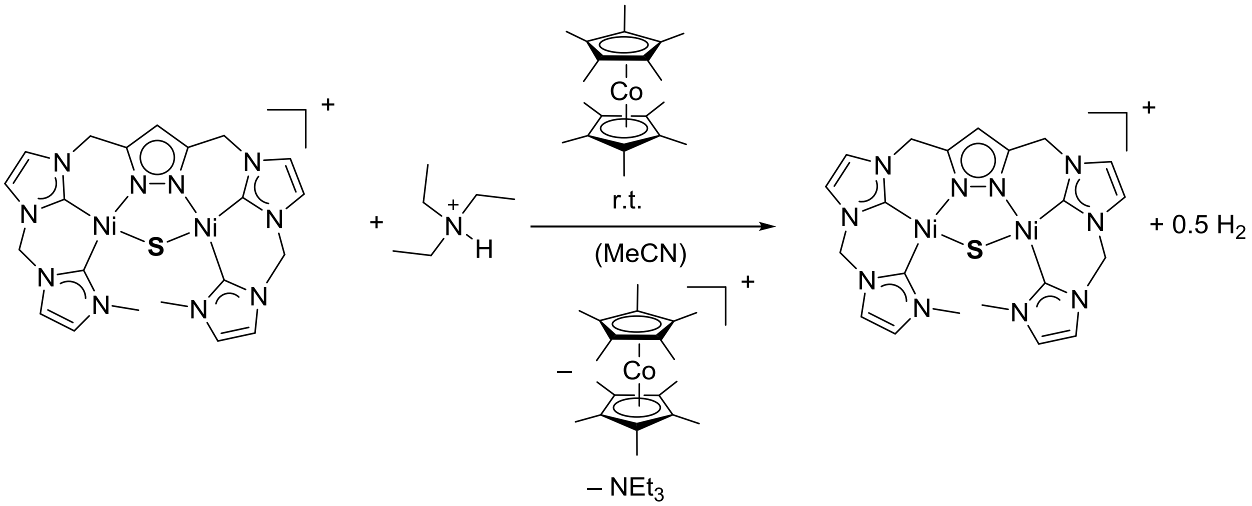

$\text{Ni}_2\text{C}_{21}\text{H}_{23}\text{N}_{10}\text{SPF}_6$

709 g/mol

Compound	*m* [mg]	*n* [μmol]	equiv.	*V* (MeCN) [μL]	*V* (gas) [μL]	area 310 s	*m* [g] (headspace)
$[\text{L}^6\text{Ni}_2\text{S}]\text{PF}_6$	2.76	3.89	1.00	400	25	9.57	1.03
Co(Cp*)_2	12.8	39.1	10.1				
$[\text{HNEt}_3]\text{BF}_4$	7.60	40.2	10.3				

The determined slope for 25 μL is: 0.315

$$V_{(headspace)} = \frac{m_{(\text{headspace})}}{\rho_{(\text{MeCN})}} = \frac{1.03\ \text{g}}{0.780\ \frac{\text{g}}{\text{mL}}} = 1.32 \cdot 10^{-3}\text{L}$$

$$n(\text{H}_2)[\text{mol}] = \frac{\text{area}\cdot V_{(\text{headspace})}\cdot 0.01}{\text{slope}\cdot 24.5} = \frac{9.57\cdot 1.32\cdot 10^{-3}\cdot 0.01}{0.315\cdot 24.5} = 16.4 \cdot 10^{-6}$$

This value corresponds to $n(\mathrm{H}^+)_{\mathrm{gross}} = 32.8\ \mu\mathrm{mol}$

More acid was used than reducing agent was present.

4) Reduction of $HNEt_3BF_4$ under presence of **[L^{6}Ni$_2$S]PF$_6$** and decamethyl cobaltocene

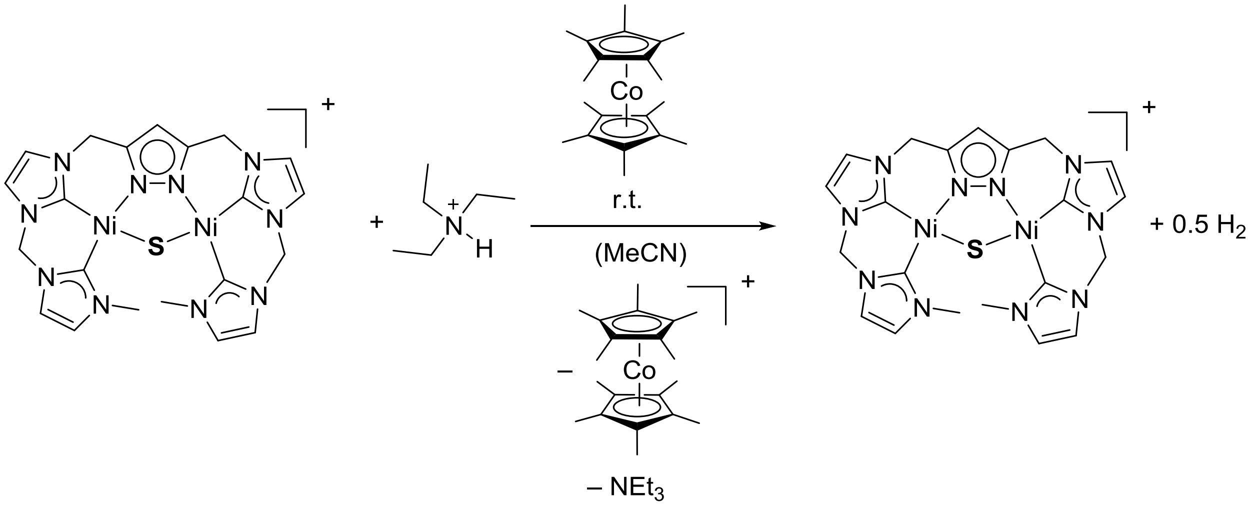

$Ni_2C_{21}H_{23}N_{10}SPF_6$

709 g/mol

Compound	m [mg]	n [μmol]	equiv.	V (MeCN) [μL]	V (gas) [μL]	area 1170 s	m [g] (headspace)
[L^{6}Ni$_2$S]PF$_6$	2.50	3.52	1.00				
Co(Cp*)$_2$	12.9	39.2	11.1	500	25	8.98	1.02
[HNEt$_3$]BF$_4$	6.60	34.9	9.92				

Determined slope for 25 μL: 0.315

$$V_{(\mathrm{headspace})} = \frac{m_{(\mathrm{headspace})}}{\rho_{(\mathrm{MeCN})}} = \frac{1.02\ \mathrm{g}}{0.780\ \frac{\mathrm{g}}{\mathrm{mL}}} = 1.31 \cdot 10^{-3}\mathrm{L}$$

$$n(\mathrm{H}_2)[\mathrm{mol}] = \frac{\mathrm{area} \cdot V_{(\mathrm{headspace})} \cdot 0.01}{\mathrm{slope} \cdot 24.5} = \frac{8.98 \cdot 1.31 \cdot 10^{-3} \cdot 0.01}{0.315 \cdot 24.5} = 15.3 \cdot 10^{-6}$$

This value corresponds to $n(\mathrm{H}^+)_{\mathrm{gross}} = 30.5\ \mu\mathrm{mol}$

Less acid was used than reduction agent was present.

5) Reduction of $HNEt_3BF_4$ under presence of **$[L^6Ni_2(SH)](PF_6)(OTf)$** and decamethyl cobaltocene

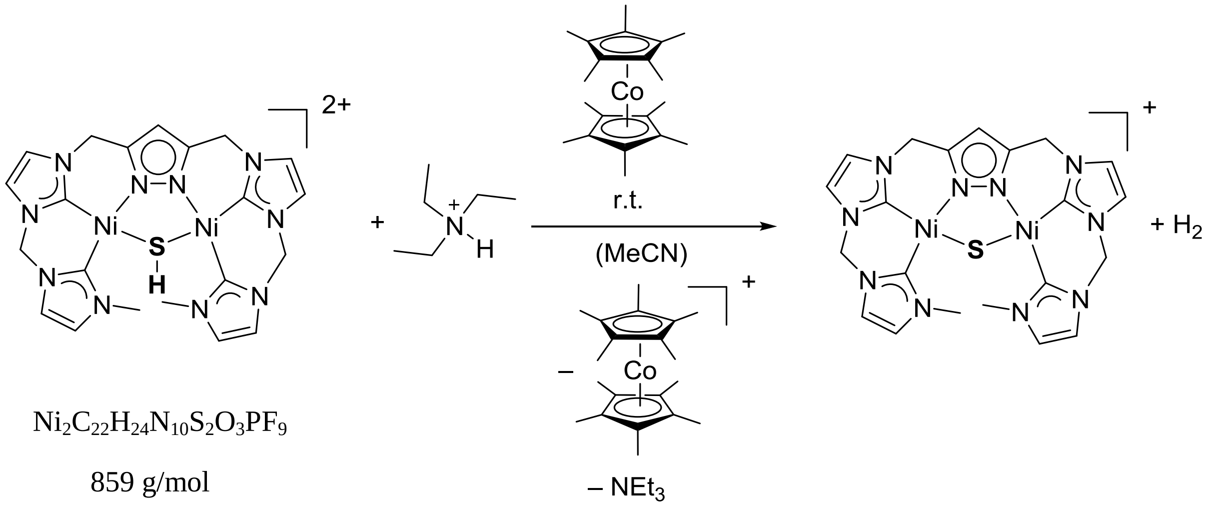

$Ni_2C_{22}H_{24}N_{10}S_2O_3PF_9$

859 g/mol

Compound	m [mg]	n [μmol]	equiv.	V (MeCN) [μL]	V (gas) [μL]	area 360 s	m [g] (headspace)
$[L^6Ni_2(SH)]^{2+}$	3.134	3.644	1.00	–	25	6.57	1.2698
$Co(Cp^*)_2$	13.104	39.783	10.92				
$[HNEt_3]BF_4$	7.359	38.936	10.68				

Determined slope for 25 μL: 0.315

$$V_{(\text{headspace})} = \frac{m_{(\text{headspace})}}{\rho_{(\text{MeCN})}} = \frac{1.27\ \text{g}}{0.780\ \frac{\text{g}}{\text{mL}}} = 1.63 \cdot 10^{-3}\text{L}$$

$$n(\text{H}_2)[\text{mol}] = \frac{\text{area}\cdot V_{(\text{headspace})}\cdot 0.01}{\text{slope}\cdot 24.5} = \frac{6.57\cdot 1.63\cdot 10^{-3}\cdot 0.01}{0.315\cdot 24.5} = 13.9 \cdot 10^{-6}$$

This value corresponds to $n(H^+)_{\text{gross}} = 27.8\ \mu\text{mol}$

10.2.5 Determination of water content in solvents

The determination of the water content in MeCN, THF and Et_2O was done by a Routine-Karl-Fischer-Coulometer C20S from METTLER TOLEDO. Determination of water contents between 1 ppm and 5% are possible.

10.2.6 Electrochemical measurements

Cyclic voltammetry (CV) experiments were exclusively conducted under inert conditions within gloveboxes of the groups of Duboc (Université Grenoble Alpes), Meyer and Siewert (Georg-August-University Göttingen). Bulk electrolysis attempts for the determination of the catalytic activity of the sulfur containing complexes with triethylammonium tetrafluroroborate were conducted outside of a glovebox under inert conditions and in a two neck electrolysis cell at the group of Prof. Dr. Artero at CEA Grenoble. All other electrochemical measurements were carried out in a three-electrode chemical cell set-up. All experiments were performed in dry and inert 0.1 M NBu_4PF_6 electrolyte solution in MeCN. Bulk electrolysis and coulometry experiments at CEA were carried out with a mercury pool cathode. The reference electrode was a silver wire in a 0.01 M $AgNO_3$ electrolyte solution, closed by a Vycor frit (P4) and dipped directly into the CV solution. A platinum wire counter electrode was located in a 0.1 M electrolyte solution in a separated compartment by a diaphragm (glass fritt). The part of the cell, which contained the complex solution and the working electrode was continously flushed by nitrogen as a carrier gas for the GC detector. The gas rate was fixed to a mass flow of 5 $mL{\cdot}min^{-1}$. The left gas from the CV cell was analyzed with a Perkin-Elmer Clarus 500 gas chromatograph and equipped with a porapack Q 80/100 column. The column is thermostated at 40 °C and a TCD detector is heated at 100 °C. The measurement of the carrier gas from the CV cell was analyzed in a continuous flow mode. Controll calibration with the pure acid in 0.1 M electrolyte solution was performed under the same conditions.

Electrochemical measurements in Grenoble were carried out in commercially purchased, dry and inert MeCN, stored over 3 Å MS, 0.1 M NBu_4PF_6, under nitrogen (cyclic voltammetry and bulk electrolysis) at 20 °C, at –40 °C and –25 °C (bulk electrolysis experiments), using a PGSTAT100N Metrohm potentiostat/galvanostat. If not mentioned otherwise, the potentials of all CV experiments in Grenoble were referred to an Ag/0.01 M $AgNO_3$ reference electrode and the potentials were calibrated by use of Fc/Fc^+ as internal standard. The working electrode was a vitreous carbon disk (3 mm in diameter) which was polished with 2 μm diamond paste (Mecaprex Presi) after each measurement.The auxiliary electrode was a Pt wire in 0.1 M electrolyte solution. $E_{\mathrm{p}}^{\mathrm{red.}}$= cathodic peak potential, $E_p^{ox.}$= anodic peak potential, $E_{1/2} = \frac{E_p^{red.} + E_p^{ox.}}{2}$, $\Delta E = E_p^{ox.} – E_p^{red.}$.

CV experiments in the group of Prof. Dr. Meyer and Prof. Dr. Siewert were conducted with dry MeCN in a 0.1 M NBu_4PF_6 electrolyte solution at 20 °C by a Gamry Interface 1000B and a Gamry reference 600 potentiostat in nitrogen gloveboxes. In a 3 mL cell as electrodes were used Pt wire (counter electrode), glassy carbon (working electrode, 3 mm in diameter), and silver wire (reference electrode) in a diaphragm (Vycor glass). All measurements were performed under inert conditions in a 0.1 M MeCN electrolyte solution (NBu_4PF_6 as electrolyte). The current *I* is given in *micro* ampere [μA], the potential in Volt [V] and the scanrates in millivolt *per* second [$mV \cdot s^{-1}$]. If possible, the data were background corrected and referenced *versus* the internal redox couple ferrocene/ferrocenium ion (Fc/Fc^+), which was added in the end of each measurement.

10.2.7 Electron ionization mass spectrometry (EI-MS)

Electron ionization mass spectrometry measurements were conducted on a BRUKER APEX IV (FTICR-MS) of the central analytic institute of the department of chemistry of the Georg-August-University Göttingen. All data are given as mass per charge *m/z* and relative intensities in percent (%).

10.2.8 Electrospray ionization mass spectrometry (ESI-MS)

Electrospray ionization mass spectrometry measurements were conducted on a HTC ULTRA from BRUKER in the group of Prof. Dr. Meyer and on a BRUKER MAXIS (ESI-QTOF-MS) at the analytic institute of the department of chemistry of the Georg-August-University Göttingen. All data are given as mass per charge *m/z* and relative intensities percent (%).

10.2.9 Elemental analysis

Standard C, H, N, S elemental analysis were measured on ELEMENTAR 4.1 VARIO EL 3 instrument by the analytical laboratory of the Institute of Inorganic Chemistry at the Georg-Auguts-University Göttingen. Oxygen sensitive compounds were sealed in aluminia capsules inside of a glovebox.

10.2.10 Electron paramagnetic resonance spectroscopy (EPR)

EPR spectra in Göttingen were recorded on a BRUKER E500 ELEXSYS X-band spectrometer with a standard cavity (ER4102ST, 9.45 GHz). The measurement was done at microwave frequency with the built-in frequency counter. The magnetic field was calibrated by a NMR field probe by BRUKER ER035M. The regulation of the temperature was achieved with an OXFORD instrument Helium flow cryostat (ESP910) and an OXFORD temperature controller (ITC-4). X-band EPR spectra in Grenoble at 100 K were recorded on a Bruker EMX spectrometer, equipped with the ER4102ST Bruker cavity. Helium EPR experiments at 22 K and 7 K were performed on a Bruker EMX spectrometer, equipped with the ER4116DM Bruker cavity, a ESR900 continuos-flow Oxford instrument cryostat and a ER4131VT Bruker temperature controller. All spectra presented were recorded under non-saturating conditions. EPR spectra were simulated using EASYSPIN, a toolbox of the MATLAB program.

10.2.11 Infrared spectroscopy (ATR and Transmission)

Infrared spectroscopic measurements were done, if not otherwise mentioned, under inert conditions by a CARY 630 FT-IR spectrometer of AGILENT. Solid materials were measured by attenuated total reflection (ATR) spectroscopy and liquids by transmission IR spectroscopy using DIALPATH TECHNOLOGY. The wavenumber υ is given in reciprocal centimeter [cm^{-1}]. The strengths of the bands are as following: strong (s), medium (m), weak (w).

10.2.12 Nuclear magnetic resonance experiments (NMR)

Room temperature and variable temperature nuclear magnetic resonance experiments of ^{1}H, ^{2}H, ^{13}C{^{1}H}, ^{19}F, ^{15}N, ^{17}O and ^{31}P nuclei as well as correlated spectroscopy (COSY), heteronuclear multiple bond coherence (HMBC) spectroscopy, heteronuclear multiple quantum coherence (HMQC) spectroscopy, diffusion-ordered spectroscopy (DOSY), nuclear Overhauser effect spectroscopy (NOESY) and exchange spectroscopy (EXSY) experiments were measured on a BRUKER *AVANCE* 300 MHz, 400 MHz, BRUKER *AVANCE DRX* 400 MHz and 500 MHz NMR instruments (Rheinstetten, Germany).

NMR chemical shifts δ are given in *parts per million* [ppm]. In case of ^{1}H and ^{13}C{^{1}H} NMR spectroscopy, the chemical shift is related to the residual ^{1}H signals and the deuterium coupled ^{13}C signals of the deuterated solvents (**Table 13.1**) or by internal standard (TMS).

Table 10.1: Residual ^{1}H signals and the deuterium coupled ^{13}C signals of the used deuterated solvents.[434]

solvent	Chemical shifts δ [ppm], multiplicity and ^nJ coupling [Hz]	
	residual ^{1}H	^{13}C
Acetonitrile–d_3, MeCN-d_3	1.94 , p, ^2J = 2.5	118.26, s 1.32, hpt, ^2J =19.4
Benzene–d_6, C_6D_6	7.16 , s,	128.06, t, ^3J = 24.3
Dimethylsulfoxide–d_6, DMSO-d_6	2.51, p, ^2J = 1.9	39.52, hpt, ^2J = 21.0
Tetrahydrofuran–d_8, THF-d_8	3.58, s, 1.72 s,	67.57 p, ^2J = 22.2 25.37 p, ^2J = 20.2
Acetone-d_6	2.05, p, ^2J = 2.2	206.26 s 29.84 hpt, ^2J = 19.4

Abbreviations of the signal multiplicity observed in the ^{1}H NMR spectra are as following: s = singlet, d = doublet, t = triplet, q = quartet, qu = quintet, sxt = sextet, hpt = septet, m = multiplet. The scalar coupling constant ^nJ between two spins is given in Hertz [Hz]. The process and evaluation of the spectra are done with the Software MestReNova (version 10.0.2) by MESTRENOVA. Inc. (Spain) and TopSpin™ by BRUKER (Rheinstetten, Germany). Determination of the $\Delta\upsilon$ values was carried out by GSD line shape analysis of the signal peaks. The determination of the exchange rate between the two conformers of **[Ni_2SL^6]PF_6** was done by the program EXSY CALC by MESTRENOVA. Inc.

10.2.13 Single-crystal X-ray structure determination

The single crystal X-ray measurements were performed at 123(2) K on a STOE IPDS II diffractometer (graphite monochromated Mo K_α radiation, λ = 0.71073 Å. The structures were solved using SHELXT[435] or SHELXS software package and refined on F^2 using all reflections with SHELXL-2013/14/16[436]. Face-indexed absorption corrections were performed numerically with the program X-RED.[437] Single-crystal X-ray structure determination was performed by Dr. Dechert from the group of Prof. Dr. Meyer.

10.2.14 Stopped-Flow UV-vis experiments

Single mixing and double mixing experiments of **[Ni_2SL^6]PF_6** with DeMeFcPF_6 or with oxidation reagent and phenylhydrazine were carried out at a HI+TECH Cryo Stopped-Flow system, capable for double mixing experiments from TGK SCIENTIFIC. The possible UV-vis spectral width was 300–800 nm feasible by a CCD chip. Data processing was done by the software kinetic studios 4.12.

10.2.15 UV-vis spectroscopy

UV-vis spectroscopy was conducted on a VARIAN CARY 60 spectrometer from AGILENT TECHNOLOGIES. Temperature dependend measurements were done between –40 °C and 80 °C, using a UNISPEK CPPL SPEK cooling unit from UNISOKO SCIENTIFIC INSTRUMENTS. For standard measurements quartz cuvettes (10 mm path length) were used. If not otherwise mentioned, all experiments were done under inert conditions using cuvettes with septa or screw caps. The wavelength λ is given in nanometer [nm], the absorbance in arbitrary units [a.u.] and the extinction coefficient ε per molarity and reciprocal centimeters [$M^{-1}\cdot cm^{-1}$]. Solid state UV-vis spectroscopy was performed on an AGILENT CARY 5000 UV-vis–NIR in a PRAYING MANTIS™ vacuum sample cell. Solid state samples were prepared inside of a glovebox by grinding solid material of the analyte with dry potassium bromide.

UV-vis spectra in Grenoble were conducted on a ZEISS MCS 601 UV–NIR photodiode-array spectrophotometer. A quartz cuvette was used (0.2 mm path length). For *in situ* measurements of the bulk electrolysis experiments at low temperatures was a transmission dip probe used (0.2 cm path length, SMA-905 connector, AVANTES).

10.2.16 UV-vis spectro-electro chemistry

UV-vis spectro-electro chemistry was recorded on an AGILENTDEUTERO (Deuterium/Tungsten light source, BWTEK EXAMPLAR LS) in a 0.1 M solution of NBu_4PF_6 as electrolyte in MeCN, using a quartz cuvette (1 mm path length). Pt mesh electrode (counter electrode), glassy carbon (working electrode) and silver wire (reference electrode) were used. The previously measured cyclic voltammogram was referenced *versus* Fc/Fc^+. SEC at room temperature was done in the glove box of the group of Prof. Dr. Meyer and also in a glove box in the group of Prof. Dr. Schneider at the institute of inorganic chemistry at the Georg-August-University Göttingen. Low temperature SEC experiments were performed in Grenoble by bulk electrolysis with a GC sponge at –25 °C and –40 °C and were monitored by a dip probe (FALCATA 6 micro immersion probe) with an optical pathway of 2 mm from HELLMA ANALYTICS. The wavelength λ is given in nanometer [nm], the absorbance in arbitrary units [a.u.] and the extinction coefficient ε per molarity and reciprocal centimeters [$M^{-1}\cdot cm^{-1}$]. Data were recorded in a wavelength range between 1100 nm–250 nm for variable temperature and 280 nm to 820 nm for SEC experiments and 280 nm to 900 nm for dip probe measurements.

10.3 Syntheses

The synthetic routes of 1,3-bis(2,4,6-trimethylphenyl)imidazolium chloride[438–440], **[H$_2$L^1](PF$_6$)$_2$**[35,51], **[H$_2$L^2](PF$_6$)$_2$**[51,441], **[H$_2$L^3](PF$_6$)$_2$**[51], **[H$_2$L^4](PF$_6$)$_2$**[51,57] and **[H$_2$L^5](PF$_6$)$_4$**[442] were already described in the literature and will not be described again in this thesis, except of new analytic data, which are relevant for the results and discussion sections. 1,2-Bis(*N*-imidazolyl)ethane[105], decamethyl ferrocenium hexafluorophophate[443], mesitylcopper(I)[444], 3,5-dimethylpyrazole[76] 3,5-bis(hydroxymethyl)pyrazole[76], 3,5-bis(chloromethyl)pyrazole hydrochloride[76], 3,5-bis(chloromethyl)-1-tetrahydropyran-2-yl-pyrazole **x**[103], TEMPO–H[445], bis(iodomethyl)-1-tetrahydropyran-2-yl-pyrazole[101,104] triethylammonium triflate[446] 2,6-lutidinium triflate[447], 2,4,6-tri-*tert*-butylphenoxyl radical[448] were synthesized according to literature known procedures. The synthesis protocol and analytic data of **[L^{4}Cu](PF$_6$)**[51] as well as additional analytic data of **[H$_2$L^4](PF$_6$)$_2$**[31,51] were already published in *Angew. Chem. Int. Ed.* **2019**, *58*, 2. **m**[105], **n**, **p**, **[H$_6$L^6]X$_5$**, **[H$_5$L^6](PF$_6$)$_4$**, **[H$_5$L^8](PF$_6$)$_4$**, **[L^{6}Ag$_6$](PF$_6$)$_4$** and **[L^{8}Ag$_6$](PF$_6$)$_4$** were published in *Z. Anorg. Allg. Chem.* **2019**, *645*, 605.

1

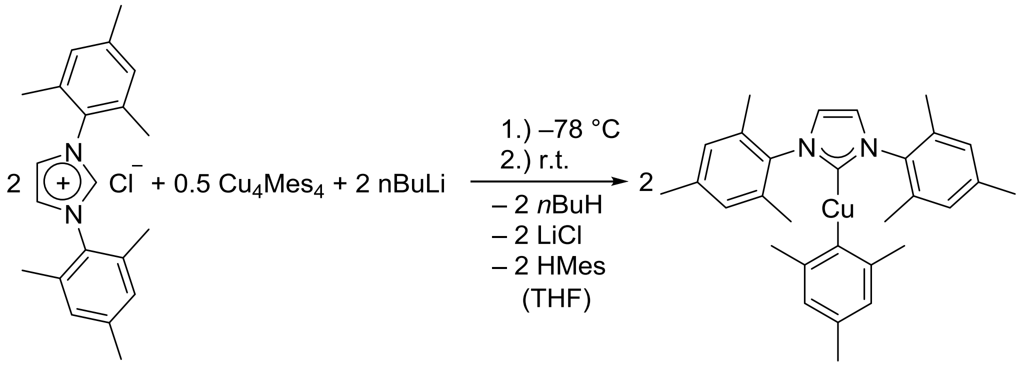

$C_{21}H_{25}N_2Cl$	CuC_9H_{11}	C_4H_9Li	$CuC_{30}H_{35}N_2$
341 g/mol	182 g/mol	64 g/mol	487 g/mol

The synthesis of **1** was carried out in analogy to the synthesis route of complex **I**[8]. 1,3-Dimesityl-2*H*-imidazolium chloride (961 mg, 2.82 mmol, 1.00 equiv.) was suspended in tetrahydrofuran (30 mL) and cooled down to –78 °C. *n*-butyl lithium (1.6 M in hexanes, 1.76 mL, 180 mg, 2.82 mmol, 0.990 equiv.) was slowly added to the suspension within 15 min. The color of the suspension turned from white to yellow and was stirred for additional 10 min at –78 °C. Afterwards, the suspension was warmed up to room temperature for additional 10 min and cooled down again to –78 °C. Mesitylcopper(I) (567 mg, 3.10 mmol, 1.09 equiv.) was dissolved in THF (20 mL), cooled down to –78°C and the green solution was slowly cannulated to the reaction mixture. The brownish solution was stirred for additional 2 hours at –78 °C and was allowed to warm to room temperature. After 17 hours stirring at room temperature, the solvent was removed under reduced pressure and the white solid was dried *in vacuo* for 2 hours. Toluene (60 mL) was added to the solid and the suspension was filtered through celite and the filter cake was washed with toluene (15 mL). The obtained solution was concentrated under reduced pressure to 20 mL and was afterwards stored at -24 °C. Colorless crystals were obtained (310 mg, 0.636 mmol, 23%), which were purified by filtering off the solution and washing the crystals with cooled toluene (2 x 3 mL). The mother liquor was concentrated under reduced pressure and stored again at –24 °C for improving the yield. Colorless crystals were obtained with an overall yield of 70% (961 mg, 1.97 mmol).

Elemental analysis of $CuC_{30}H_{35}N_2$

Calculated: **C** 73.96%; **H** 7.24%; **N** 5.75%.

Found: **C** 74.29%; **H** 7.25%; **N** 5.65%.

ESI-MS (THF) *m/z* (%): 853.4 (40) $[Cu_2C_{51}H_{59}N_4]^+$, 671.4 (100) $[CuC_{42}H_{48}N_4]^+$.

2

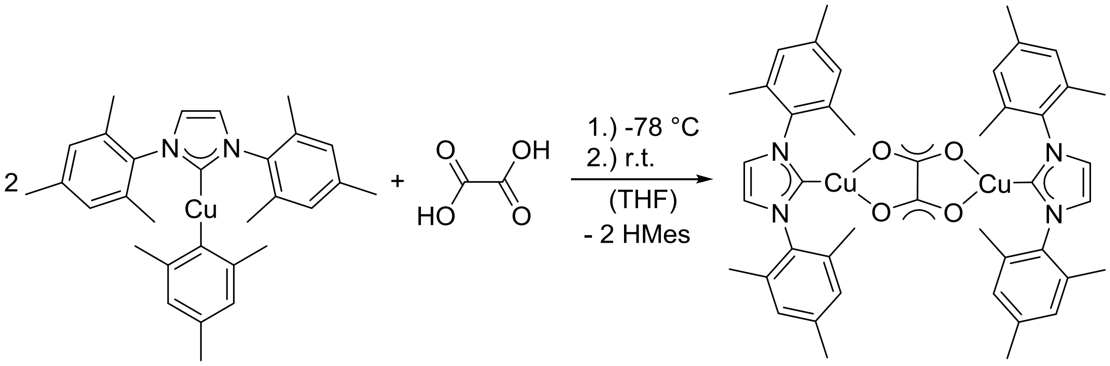

$CuC_{30}H_{35}N_2$	$C_2H_2O_4$	$Cu_2C_{44}H_{48}N_4O_4$
487 g/mol	90 g/mol	487 g/mol

The synthesis of **2** was carried out in analogy to the synthesis route of complex **II**[8]. **1** (260 mg, 0.534 mmol, 1.90 equiv.) was dissolved in tetrahydrofuran (50 mL) and cooled down to -80 °C. A cooled solution (–80 °C) of oxalic acid (25.3 mg, 0.281 mmol, 1.00 equiv.) in THF was added to the stirred complex solution. The reaction mixture was stirred overnight in the cooling bath and was allowed to warm to 20 °C. Afterwards, the solution was concentrated to 8 mL under reduced pressure and the obtained precipitate was filtered off, washed with cooled diethyl ether (3 x 5 mL) and was dried *in vacuo* for one day (57.5 mg, 0.118 mmol, 42%). Single crystals were obtained by dissolving 18.6 mg of white solid in THF (6 mL) and layering the solution with cooled Et_2O at 4 °C.

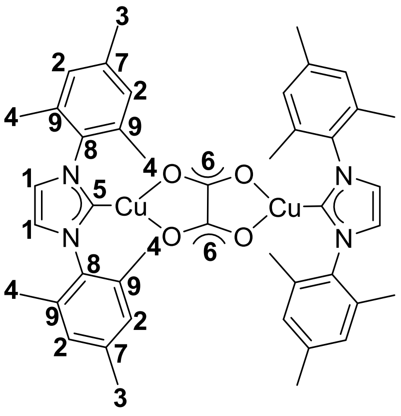

^{1}**H NMR** (300 MHz, 298 K, THF-d_8): δ [ppm] = 7.16 (s, 4 H, $_{\mathrm{Im}}$H **1**), 6.93 (s, 8 H, H$^{\mathrm{meta}}$ **2**), 2.28 (s, 12 H, H$^{\mathrm{para}}$ **3**), 2.09 (s, 24 H, H$^{\mathrm{ortho}}$ **4**).

$^{13}C\{^1H\}$ NMR (126 MHz, 298 K, THF-d_8): δ [ppm] = 185.2 ($C_{carbene}$–**5**), 170.8 (COO–**6**), 139.1 ($C_{quart.}$–**7**), 137.3 (C_{ipso}–**8**), 135.9 ($C_{quart.}$–**9**), 129.8 (C^{meta}–**2**), 122.4 (C–**1**), 21.2 (C^{para}–**3**), 17.9 (C^{ortho}–**4**).

$^1H^1H$ COSY NMR (300 MHz, 298 K, THF-d_8): δ [ppm] = 6.93/2.28 (H^{meta} **2** & H^{para} **3**), 6.93/2.09 (H^{meta} **2** & H^{ortho} **4**).

$^1H^1H$ NOESY NMR (300 MHz, 298 K, THF-d_8): δ [ppm] = 7.16/2.09 ($_{Im}H$ **1** & H^{ortho} **4**), 6.93/2.28 (H^{meta} **2** & H^{para} **3**), 6.93/2.09 (H^{meta} **2** & H^{ortho} **4**).

$^1H^{13}C$ HSQC NMR (^{1}H NMR, 300 MHz, ^{13}C NMR**,** 75.5 MHz**,** 298 K, THF-d_8): δ [ppm] = 7.16/122.4, 6.93/129.8, 2.28/21.2, 2.09/17.9.

$^1H^{13}C$ HMBC NMR (^{1}H NMR, 500 MHz, ^{13}C NMR**,** 126 MHz**,** 298 K, THF-d_8): δ [ppm] = 7.16/185.2 ($_{Im}H$ **1** & $C_{carbene}$–**5**), 7.16/137.3 ($_{Im}H$ **1** & C_{ipso}–**8**), 7.16/122.4 ($_{Im}H$ **1** & C–**1**), 6.93/137.3 (H^{meta} **2** & C_{ipso}–**8**), 6.93/129.8 (H^{meta} **2** & C^{meta}–**2**), 6.93/21.2 (H^{meta} **2** & C^{para}–**3**), 6.93/17.9 (H^{meta} **2** & C^{ortho}–**4**), 2.28/139.1 (H^{para} **3** & $C_{quart.}$–**7**), 2.28/137.3 (H^{para} **3** & C_{ipso}–**8**), 2.28/135.9 (H^{para} **3** & $C_{quart.}$–**9**), 2.28/129.8 (H^{para} **3** & C^{meta}–**2**), 2.09/137.3 (H^{ortho} **4** & C_{ipso}–**8**), 2.09/135.9 (H^{ortho} **4** & $C_{quart.}$–**9**), 2.09/129.8 (H^{ortho} **4** & C^{meta}–**2**).

$^1H^{15}N$ HMBC NMR (^{1}H NMR, 500 MHz, ^{15}N NMR, 50.7 MHz**,** 298 K, THF-d_8): δ [ppm] = 7.16/–188.2.

Elemental analysis of $Cu_2C_{44}H_{48}N_4O_4$

Calculated: **C** 64.13%; **H** 5.87%; **N** 6.80%.

Found: **C** 63.83%; **H** 5.96%; **N** 6.55%.

ESI-MS (THF) *m/z* (%): 671.4 (100) $[CuC_{42}H_{48}N_4]^+$.

IR (ATR): υ [cm^{-1}] = 3174.1 (w), 3144.3 (w), 3015.7 (w), 2971.9 (w), 2960.7 (w), 2945.8 (w), 2914.1 (w), 2856.3 (w), 2849.8 (w), 2737.0 (w), 2734.2 (w), 1628.9 (COO_{as} s), 1607.6 (s), 1564.7 (m), 1547.9 (m), 1486.4 (m), 1457.5 (m), 1435.2 (m), 1395.1 (m), 1376.4 (m), 1360.6 (m), 1329.8 (m), 1301.9 (m), 1269.3 (m), 1244.1 (w), 1229.2 (m), 1162.1 (w), 1108.1 (w), 1083.8 (w), 1036.3 (m), 1026.0 (m), 1009.3 (m), 960.8 (m), 928.2 (s), 897.4 (w), 882.5 (w), 862.0 (m), 848.0 (s), 826.6 (w), 783.7 (s), 742.7 (w), 725.0 (s), 686.8 (s), 643.9 (w), 595.5 (w), 574.9 (m), 568.5 (w), 487.4 (m), 449.2 (m), 423.1 (s).

$[H_2L^1](PF_6)_2$[35,51]

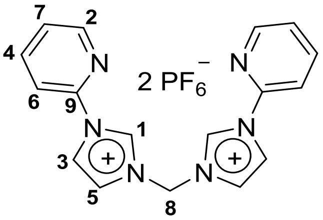

^{1}H NMR (500 MHz, 298 K, MeCN-d_3): δ [ppm] = 9.68 (t, $^3J_{HH}$ = 1.7 Hz, 2H, $_{Im}$H **1**), 9.68 (ddd, $^3J_{HH}$ = 7.6, $^4J_{HH}$ = 4.8, $^5J_{HH}$ = 0.9 Hz, 2H, H^{py-6} **2**), 8.20 (dd, $^3J_{HH}$ = 2.3, $^4J_{HH}$ = 1.7 Hz, 2H, $_{Im}$H **3**), 8.15 (dd, $^3J_{HH}$ = 1.8, 0.6 Hz, 2H, H^{py-4} **4**), 7.88 (m, 2H, $_{Im}$H **5**), 7.81 (t, $^3J_{HH}$ = 0.9 Hz, 1H, H^{py-3} **6**), 7.79 (t, $^3J_{HH}$ = 0.9 Hz, 1H, H^{py-3} **6**), 7.65 (ddd, $^3J_{HH}$ = 7.6, 4.8 Hz, $^4J_{HH}$ = 0.9 Hz, 2H, H^{py-5} **7**), 6.64 (s, 2H, **8**).

^{13}C{^{1}H} NMR (126 MHz, 298 K, MeCN-d_3): δ [ppm] = 150.6 (C–**2**), 146.6 ($C_{quart.}$–**9**), 141.7 (C–**4**), 136.6 (C–**1**), 127.1 (C–**7**), 124.3 (C–**5**), 121.6 (C–**3**), 115.4 (C–**2**), 60.6 (C–**8**).

^{1}H^{1}H COSY NMR (500 MHz, 298 K, MeCN-d_3): δ [ppm] = 9.68/8.20 ($_{Im}$H **1** & $_{Im}$H **3**), 9.68/7.88 ($_{Im}$H **1** & $_{Im}$H **5**), 9.68/8.20 ($_{Im}$H **1** & H **9**), 9.68/7.65 (H^{py-6} **2** & H^{py-5} **7**), 8.20/7.88 ($_{Im}$H **3** & $_{Im}$H **5**), 8.15/7.65 (H^{py-4} **4** & H^{py-5} **7**), 8.15/7.81//7.79 (H^{py-4} **4** & H^{py-3} **6**).

^{1}H^{1}H NOESY NMR (500 MHz, 298 K, MeCN-d_3): δ [ppm] = 9.68/8.20 ($_{Im}$H **1** & $_{Im}$H **3**), 9.68/7.88 ($_{Im}$H **1** & $_{Im}$H **5**), 9.68/7.81//7.79 ($_{Im}$H **1** & H^{py-3} **6**), 9.68/6.64 ($_{Im}$H **1** & H **8**), 7.88/6.64 ($_{Im}$H **5** & H **8**).

^{1}H^{13}C HSQC NMR (^{1}H NMR, 500 MHz, ^{13}C NMR, 126 MHz, 298 K, MeCN-d_3): δ [ppm] = 9.68/136.6, 8.64/150.6, 8.20/121.6, 8.15/141.7, 7.88/124.3, 7.81/115.4, 7.79/115.4, 7.65/127.1, 6.64/60.6.

^{1}H^{13}C HMBC NMR (^{1}H NMR, 500 MHz, ^{13}C NMR, 126 MHz, 298 K, MeCN-d_3): δ [ppm] **=** 9.68/124.3 ($_{Im}$H **1** & C–**5**), 9.68/121.6 ($_{Im}$H **1** & C–**3**), 8.20/136.6 ($_{Im}$H **3** & C–**1**), 8.20/124.3 ($_{Im}$H **3** & C–**5**), 6.64/124.3 (H **8** & C–**5**), 6.64/136.6 (H **8** & C–**1**), 8.15/146.6 (H^{py-4} **4** & $C_{quart.}$–**9**), 8.15/150.6 (H^{py-4}& C–**2**), 7.88/121.6 ($_{Im}$H **5** & C–**2**), 7.81//7.79/127.1 (H^{py-3} **6** & H^{py-5} **7**), 7.64/115.4 (H^{py-5} **7** & H^{py-3} **6**).

^{1}H^{15}N HMBC NMR (^{1}H NMR, 500 MHz, ^{15}N NMR, 50.7 MHz, 298 K, MeCN-d_3): δ [ppm] = 8.20/–202.2, 7.88/–202.2, 6.64/–202.2, 8.20/–181.7, 7.88/–181.7, 7.81//7.79/–181.7, 8.64/-94.0, 7.79/-94.0, 7.65/-94.0.

^{1}H^{1}H DOSY NMR (500 MHz, 298 K, MeCN-d_3): D_{298K} [$m^2 \cdot s^{-1}$] = $1.07 \cdot 10^{-5}$

$[L^1Cu_3](PF_6)_3$[36,51]

The synthesis of $\mathbf{[L^1Cu_3](PF_6)_3}$ was carried out following a route described in the Master thesis of Resch[51]. Since, the characterization of $\mathbf{[L^1Cu_3](PF_6)_3}$ was already described in the literature[36], only new analytic data and data which are necessary for the understanding of the rearrangement of the complex in solution are mentioned here.

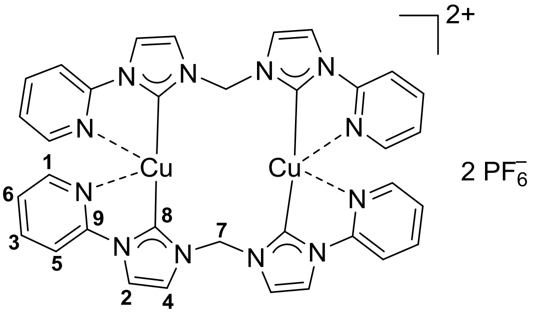

^{1}H NMR (500 MHz, 298 K, MeCN-d_3): δ [ppm] = 7.78 (br s, 4H, $H^{py\text{-}6}$ **1**), 7.76 (d, $^3J_{HH}$ = 2.1 Hz, 4H, $_{Im}H$ **2**), 7.73 (ddd, $^3J_{HH}$ = 8.3, 7.5, $^4J_{HH}$ = 1.8 Hz, 4H, $H^{py\text{-}4}$ **3**), 7.56 (d, $^3J_{HH}$ = 2.1 Hz, 4H, $_{Im}H$ **4**), 7.46 (d, $^3J_{HH}$ = 7.7 Hz, 4H, $H^{py\text{-}3}$ **5**), 7.18 (ddd, $^3J_{HH}$ = 8.3, 7.5 Hz, $^4J_{HH}$ = 1.8 Hz, 4H, $H^{py\text{-}5}$ **6**), 6.36 (s, 2H, H **7**).

^{13}C{^{1}H} NMR (126 MHz, 298 K, MeCN-d_3): δ [ppm] = 183.1 ($C_{carbene}$–**8**), 150.6 ($C_{quart.}$–**9**), 148.7 (C–**1**), 141.1 (C–**3**), 124.2 (C–**6**), 123.6 (C–**4**), 118.8 (C–**2**), 113.2 (C–**5**), 65.9 (C–**7**).

^{1}H^{1}H NOESY NMR (500 MHz, 298 K, MeCN-d_3): δ [ppm] = 7.76/7.56 ($_{Im}H$ **2** & $_{Im}H$ **4**), 7.76/7.46 ($_{Im}H$ **2** & $H^{py\text{-}3}$ **5**), 7.76/7.18 ($_{Im}H$ **2** & $H^{py\text{-}5}$ **6**), 7.73/7.46 ($H^{py\text{-}4}$ **3** & $H^{py\text{-}3}$ **5**), 7.73/7.18 ($H^{py\text{-}4}$ **3** & $H^{py\text{-}5}$ **6**), 7.56/6.36 ($_{Im}H$ **4** & H **7**).

^{1}H^{15}N HMBC NMR (^{1}H NMR, 500 MHz, ^{15}N NMR, 50.7 MHz, 298 K, MeCN-d_3): δ [ppm] = 7.76/–189.9, 7.57/–189.9, 6.36/–189.9, 7.76/–173.2, 7.57/–173.2, 7.18/–108.7.

^{1}H^{1}H DOSY NMR (500 MHz, 298 K, MeCN-d_3): D_{298K} [$m^2 \cdot s^{-1}$] = $8.97 \cdot 10^{-6}$

ESI-MS (MeCN) *m/z* (%): 875.1 (100) $[Cu_2(C_{38}H_{34}N_{14})_2PF_6]^+$, 365.1 (99) $[Cu_2(C_{38}H_{34}N_{14})_2]^{2+}$.

$\mathbf{[H_2L^2](PF_6)_2}$[441]

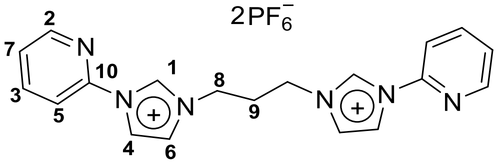

^{1}H NMR (500 MHz, 298 K, MeCN-d_3): δ [ppm] = 9.33 (t, $^3J_{HH}$ = 1.7 Hz, 2H, $_{Im}$H **1**), 8.60 (ddd, $^3J_{HH}$ = 4.8, $^4J_{HH}$ = 1.8 Hz, $^5J_{HH}$ = 0.9 Hz, 2H, H$^{py\text{-}6}$ **2**), 8.13 (m, 4H, H$^{py\text{-}4}$ **3** & $_{Im}$H **4**), 7.76 (t, 2H, $^3J_{HH}$ = 0.9 Hz, H$^{py\text{-}3}$ **5**), 7.75 (t, $^3J_{HH}$ = 0.9 Hz, 1H, H$^{py\text{-}3}$ **5**), 7.64 (t, $^3J_{HH}$ = 1.96 Hz, 2H, $_{Im}$H **6**), 7.60 (ddd, $^3J_{HH}$ = 7.6, 4.8 Hz, $^4J_{HH}$ = 0.9 Hz, 2H, H$^{py\text{-}5}$ **7**), 4.39 (t, $^3J_{HH}$ = 7.30 Hz, 4H, H **8**), 2.59 (qu, $^3J_{HH}$ = 7.30 Hz, 2H, H **9**).

^{13}C{^{1}H} NMR (126 MHz, 298 K, MeCN-d_3): δ [ppm] = 150.6 (C–**2**), 147.3 (C$_{quart.}$–**10**), 141.6 (C–**3**), 135.3 (C–**1**), 126.6 (C–**7**), 124.6 (C–**6**), 120.8 (C–**4**), 115.1 (C–**5**), 47.9 (C–**8**), 30.5 (C–**9**).

^{1}H^{1}H NOESY NMR (500 MHz, 298 K, MeCN-d_3): δ [ppm] = 9.33/8.13 ($_{Im}$H **1** & H$^{py\text{-}4}$ **3** & $_{Im}$H **4**), 9.33/7.75 ($_{Im}$H **1** & H$^{py\text{-}3}$ **5**), 9.33/7.64 ($_{Im}$H **1** & $_{Im}$H **6**), 9.33/4.39 ($_{Im}$H **1** & H **8**), 9.33/2.59 ($_{Im}$H **1** & H **9**), 8.60/8.13 (H$^{py\text{-}6}$ **2** & $_{Im}$H **4** & H$^{py\text{-}4}$ **3**), 8.13/7.75 ($_{Im}$H **4** & H$^{py\text{-}3}$ **5**).

^{1}H^{15}N HMBC NMR (^{1}H NMR, 500 MHz, ^{15}N NMR, 50.7 MHz, 298 K, MeCN-d_3): δ [ppm] = 9.33/–196.7, 8.13/–196.7, 7.64/–196.7, 4.39/–196.7, 2.59/–196.7, 9.33/–185.2, 8.13/–185.2, 7.64/–185.2, 8.60/–94.4, 7.60/–94.4.

^{1}H^{1}H DOSY NMR (500 MHz, 298 K, MeCN-d_3): D_{298K} [m^2·s^{-1}] = 1.03·10^{-5}.

$[L^2Cu_3](PF_6)_3$[51]

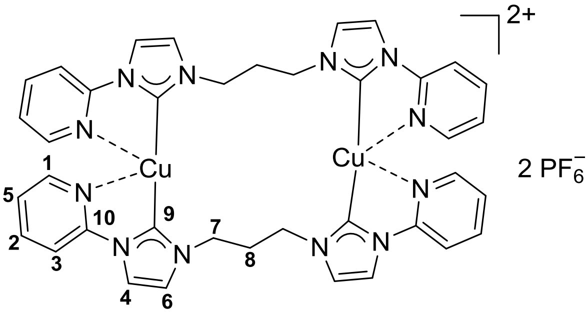

^{1}H NMR (500 MHz, 298 K, MeCN-d_3): δ [ppm] = 8.12 (ddd, $^3J_{HH}$ = 4.9, 1.0 Hz, 4H, H^{py-6} **1**), 7.95 (ddd, $^3J_{HH}$ = 8.2, 7.5 Hz, $^4J_{HH}$ = 1.8 Hz, 4H, H^{py-4} **2**), 7.50 (d, $^3J_{HH}$ = 8.2 Hz, 4H, H^{py-3} **3**), 7.39 (d, $^3J_{HH}$ = 2.0 Hz, 4H, $_{Im}H$ **4**), 7.33 (ddd, $^3J_{HH}$ = 7.5, 4.9 Hz, $^4J_{HH}$ = 0.9 Hz, 4H, H^{py-5} **5**), 7.18 (d, $^3J_{HH}$ = 2.0 Hz, 4H, $_{Im}H$ **6**), 4.13 (t, $^3J_{HH}$ = 6.3 Hz, H **7**), 2.31 (qu, $^3J_{HH}$ = 6.3 Hz, H **8**).

^{13}C{^{1}H} NMR (126 MHz, 298 K, MeCN-d_3): δ [ppm] = 181.6 ($C_{carbene}$–**9**), 151.1 ($C_{quart.}$–**10**), 149.3 (C–**1**), 141.0 (C–**2**), 124.2 (C–**5**), 122.6 (C–**6**), 119.4 (C–**4**), 114.4 (C–**3**), 48.8 (C–**7**), 31.5 (C–**8**).

^{1}H^{1}H NOESY NMR (500 MHz, 298 K, MeCN-d_3): δ [ppm] = 8.12/7.18 (H^{py-6} **1** & $_{Im}H$ **6**), 8.12/7.33 (H^{py-6} **1** & H^{py-5} **5**), 8.12/4.13 (H^{py-6} **1** & H **7**), 8.12/2.31 (H^{py-6} **1** & H **8**), 7.95/7.50 (H^{py-4} **2** & H^{py-3} **3**), 7.95/7.33 (H^{py-4} **2** & H^{py-5} **5**), 7.95/4.13 (H^{py-4} **2** & H **7**), 7.50/7.39 (H^{py-3} **3** & $_{Im}H$ **4**), 7.50/4.13 (H^{py-3} **3** & H **7**), 7.33/4.13 (H^{py-5} **5** & H **7**), 7.18/7.39 ($_{Im}H$ **6** & $_{Im}H$ **4**), 7.18/4.13 ($_{Im}H$ **6** & H **7**), 7.18/2.31 ($_{Im}H$ **6** & H **8**).

^{1}H^{15}N HMBC NMR (^{1}H NMR, 500 MHz, ^{15}N NMR, 50.7 MHz, 298 K, MeCN-d_3): δ [ppm] = 7.39/–188.9, 7.18/–188.9, 4.13/–188.9, 2.31/–188.9, 7.50/–175.7, 7.39/–175.7, 7.18/–175.7, 8.12/–105.5, 7.50/–105.5, 7.33/–105.5.

^{1}H^{1}H DOSY NMR (500 MHz, 298 K, MeCN-d_3): D_{298K} [$m^2 \cdot s^{-1}$] = $8.69 \cdot 10^{-6}$

ESI-MS (MeCN) *m/z* (%): 395.1 (100) $[Cu_2C_{38}H_{36}N_{12}]^{2+}$, 933.2 (99) $[Cu_2C_{38}H_{36}N_{12}(PF_6)]^+$.

UV-vis (EtCN, 193 K): $\lambda_{max.}$ [nm] (ε 10^3 [$M^{-1} \cdot cm^{-1}$]) = 304 (36.84), 371 (32.82).

Elemental analysis of $CuC_{30}H_{35}N_2$

Calculated: **C** 39.31%; **H** 3.13%; **N** 14.48%.

Found: **C** 39.48%; **H** 3.37%; **N** 14.73%.

$[\mathbf{L^3Cu_2}](\mathbf{PF_6})_3$[51]

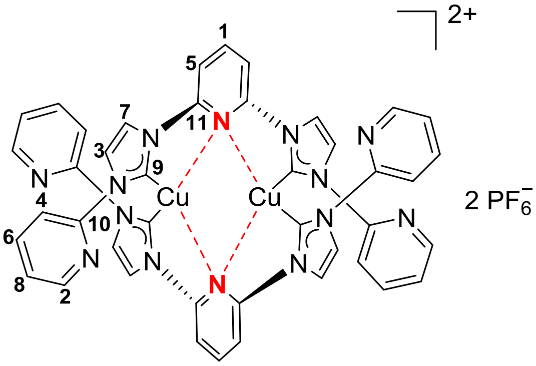

^{1}H NMR (400 MHz, 353 K, MeCN-d_3): δ [ppm] = 8.31 (t, $^3J_{HH}$ = 8.0 Hz, 2H, H$^{py\text{-}4}$ **1**), 8.10 (dd, $^3J_{HH}$ = 4.79 Hz, 2H, H$^{py\text{-}6}$ **2**), 7.86 (d, $^3J_{HH}$ = 2.1 Hz, 4H, $_{Im}$H **3**), 7.74 (d, $^3J_{HH}$ = 8.2 Hz, 4H, H$^{py\text{-}3}$ **4**), 7.70 (d, $^3J_{HH}$ = 8.0 Hz, 4H, H$^{py\text{-}3}$ **5**), 7.57 (ddd, $^3J_{HH}$ = 7.9, 1.8 Hz, 4H, H$^{py\text{-}4}$ **6**), 7.52 (d, $^3J_{HH}$ = 2.1 Hz, 4H, $_{Im}$H **7**), 7.26 (ddd, $^3J_{HH}$ = 7.4, 4.8 Hz, $^4J_{HH}$ = 0.7 Hz, 4H, H$^{py\text{-}5}$ **8**).

^{13}C{^{1}H} NMR (101 MHz, 353 K, MeCN-d_3): δ [ppm] = 181.6 (C$_{carbene}$–**9**), 151.3 (C$_{quart.}$–**10**), 150.0 (C–**11**), 149.6 (C–**2**), 145.1 (C–**1**), 140.4 (C–**6**), 121.2 (C–**3**), 120.0 (C–**7**), 115.0 (C–**5** & C–**4**).

^{1}H^{1}H NOESY NMR (400 MHz, 353 K, MeCN-d_3): δ [ppm] = 8.10/7.57 (H$^{py\text{-}6}$ **2** & H$^{py\text{-}4}$ **6**), 7.86/7.74 ($_{Im}$H **3** & H$^{py\text{-}3}$ **4**), 7.70/7.52 (H$^{py\text{-}3}$ **5** & $_{Im}$H **7**).

^{1}H NMR (400 MHz, 293 K, MeCN-d_3): δ [ppm] = 8.28 (t, $^3J_{HH}$ = 7.3 Hz, 2H, H$^{py\text{-}4}$ **1**), 8.09 (m, 2H, H$^{py\text{-}6}$ **2**), 7.86 (d, $^3J_{HH}$ = 1.9 Hz, 4H, $_{Im}$H **3**), 7.74 (d, $^3J_{HH}$ = 8.2, 4H, H$^{py\text{-}3}$ **4**), 7.71 (d, $^3J_{HH}$ = 7.9 Hz, 4H, H$^{py\text{-}3}$ **5**), 7.55 (m, 4H, H$^{py\text{-}4}$ **6**), 7.53 (m, 4H, $_{Im}$H **7**), 7.25 (ddd, $^3J_{HH}$ = 7.4, 4.8 Hz, $^4J_{HH}$ = 0.7 Hz, 4H, H$^{py\text{-}5}$ **8**).

^{13}C{^{1}H} NMR (101 MHz, 293 K, MeCN-d_3): δ [ppm] = 182.3 (C$_{carbene}$–**9**), 150.8 (C$_{quart.}$–**10**), 149.4 (C–**11**), 149.1 (C–**2**), 144.7 (C–**1**), 140.1 (C–**6**), 124.8 (C–**8**), 120.7 (C–**3**), 119.7 (C–**7**), 114.5 (C–**5**), 114.4 (C–**4**).

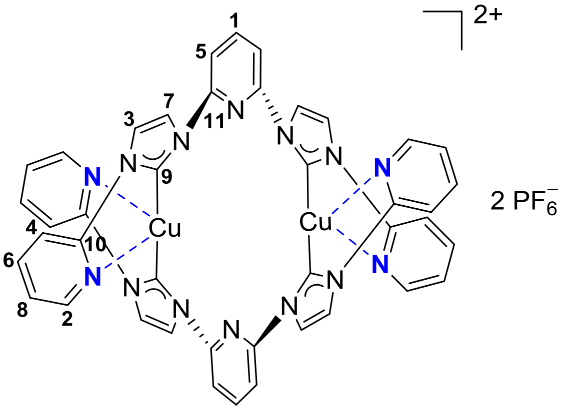

^{1}H NMR (400 MHz, 233 K, MeCN-d_3): δ [ppm] = 8.57 (s, 4H, $_{\text{Im}}$H **7**), 8.40 (d, $^3J_{\text{HH}}$ = 8.1, 4H, H$^{\text{py-3}}$ **5**), 8.15 (s, 4H, $_{\text{Im}}$H **3**), 8.09 (d, $^3J_{\text{HH}}$ = 3.7, 2H, H$^{\text{py-6}}$ **2**), 8.07 (d, $^3J_{\text{HH}}$ = 7.9, 4H, H$^{\text{py-4}}$ **6**), 7.88 (d, $^3J_{\text{HH}}$ = 8.3, 4H, H$^{\text{py-3}}$ **4**), 7.39 (t, $^3J_{\text{HH}}$ = 8.1, 2H, H$^{\text{py-4}}$ **1**), 7.30 (*ps* t, $^3J_{\text{HH}}$ = 6.0, 4H, H$^{\text{py-5}}$ **8**).

^{13}C{^{1}H} NMR (101 MHz, 233 K, MeCN-d_3): δ [ppm] = 184.3 (C$_{\text{carbene}}$–**9**), 150.5 (C$_{\text{quart.}}$–**10**), 149.5 (C–**11**), 148.7 (C–**2**), 142.6 (C–**1**), 141.0 (C–**6**), 123.8 (C–**8**), 120.3 (C–**7**), 117.5 (C–**7**), 112.4 (C–**4**), 112.1 (C–**5**).

^{1}H^{1}H NOESY NMR (400 MHz, 233 K, MeCN-d_3): δ [ppm] = 8.15/7.88 ($_{\text{Im}}$H **3** & H$^{\text{py-3}}$ **4**), 8.40/8.57 (H$^{\text{py-3}}$ **5** & $_{\text{Im}}$H **7**).

$[H_2L^4](PF_6)_2$[31,51]

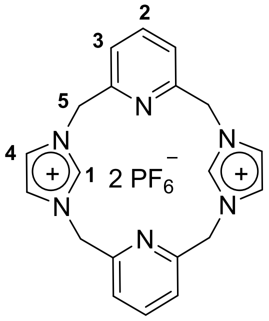

^{1}H NMR (500 MHz, 298 K, MeCN-d_3): δ [ppm] = 8.50 (s, 2H, $H^{py\text{-}4}$ **2**), 7.93 (t, $^3J_{HH}$ = 7.8 Hz, 4H, $H^{py\text{-}4}$ **2**), 7.51 (d, $^3J_{HH}$ = 7.8 Hz, 4H, $H^{py\text{-}3}$ **3**), 7.31 (d, 4H, $^3J_{HH}$ = 1.5 Hz, $_{im}$H **4**), 5.42 (s, 8H, H **5**).

^{1}H^{1}H NOESY NMR (500 MHz, 298 K, MeCN-d_3): δ [ppm] = 8.50/7.31 ($_{Im}$H **1** & $_{Im}$H **4**), 8.50/5.42 ($_{Im}$H **1** & H **5**), 7.93/7.51 ($H^{py\text{-}4}$ **2** & $H^{py\text{-}3}$ **3**), 7.51/7.31 ($H^{py\text{-}3}$ **3** & $_{Im}$H **4**), 7.51/5.42 ($H^{py\text{-}3}$ **3** & H **5**), 7.31/5.42 ($_{Im}$H **4** & H **5**).

^{1}H^{15}N HMBC NMR (^{1}H NMR, 500 MHz, ^{15}N NMR, 50.7 MHz, 298 K, MeCN-d_3): δ [ppm] = 8.50/–202.9, 7.31/–202.9, 5.42/–202.9, 7.51/–77.6, 5.42/–77.6.

^{1}H DOSY NMR (500 MHz, 298 K, MeCN-d_3): D_{298K} [$m^2 \cdot s^{-1}$] = $9.40 \cdot 10^{-6}$

The analytic data were published in *Angew. Chem. Int. Ed.* **2019**, *58*, 2.

$[L^4Cu](PF_6)$[51]

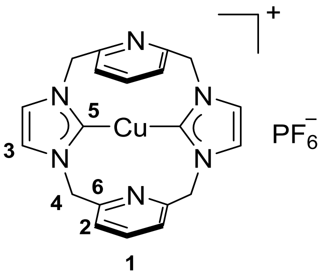

^{1}H NMR (500 MHz, 298 K, MeCN-d_3): δ [ppm] = 7.75 (t, $^3J_{HH}$ = 7.7 Hz, 2H, **1**), 7.34 (d, $^3J_{HH}$ = 7.7 Hz, 4H, **2**), 6.96 (s, 4H, **3**), 5.20 (s, 8H, H **4**).

^{13}C{^{1}H} NMR (126 MHz, 298 K, MeCN-d_3): δ [ppm] = 178.4 ($C_{carbene}$–**5**), 155.9 ($C_{quart.}$–**6**), 139.7 (C–**1**), 123.9 (C–**3**), 122.7 (C–**2**), 56.2 (C–**4**).

^{1}H^{1}H NOESY NMR (500 MHz, 298 K, MeCN-d_3): δ [ppm] = 7.75/7.34 ($H^{py\text{-}4}$ **1** & $H^{py\text{-}3/5}$ **2**), 7.33/6.96 ($H^{py\text{-}3/5}$ **2** & $_{im}$H **3**), 7.33/5.20 ($H^{py\text{-}3/5}$ **2** & H **4**), 6.96/5.20 ($_{Im}$H **3** & $_{Im}$H **3**).

^{1}H^{13}C HSQC NMR (^{1}H NMR, 500 MHz, ^{13}C NMR, 126 MHz, 298 K, MeCN-d_3): δ [ppm] = 7.75/139.7, 7.34/123.9, 6.96/122.7, 5.20/56.2.

^{1}H^{13}C HMBC NMR (^{1}H NMR, 500 MHz, ^{13}C NMR, 126 MHz, 298 K, MeCN-d_3): δ [ppm] = 7.75/155.9 ($H^{py\text{-}4}$ **1**/$C_{quart.}$–**6**), 7.34/155.9 ($H^{py\text{-}3}$ **2**/$C_{quart.}$–**6**), 7.34/123.9 ($H^{py\text{-}3}$ **2**/C-**2**), 7.34/56.2 ($H^{py\text{-}3}$ **2**/C–**4**), 6.96/178.4 ($_{Im}$H **3**/$C_{carbene}$–**5**), 6.96/122.7 ($_{Im}$H **3**/C–**3**), 6.96/56.2 ($_{Im}$H **3**/C–**4**), 5.20/178.4 (H **4**/$C_{carbene}$–**5**), 5.20/155.9 (H **4**/$C_{quart.}$–**6**), 5.20/123.9 (H **4**/ C–**2**), 5.20/122.7 (H **4**/ C–**3**).

^{1}H^{15}N HMBC NMR (^{1}H NMR, 500 MHz, ^{15}N NMR, 50.7 MHz, 298 K, MeCN-d_3): δ [ppm] = 6.97/–190.41, 5.20/–190.41, 7.34/–67.45, 5.20/–67.45.

^{1}H DOSY NMR (500 MHz, 298 K, MeCN-d_3): D_{298K} [$m^2\cdot s^{-1}$] = $1.04\cdot10^{-5}$

Elemental analysis of $CuC_{20}H_{18}N_6PF_6$

Calculated: **C** 43.60%; **H** 3.29%; **N** 15.25%.

Found: **C** 42.55%; **H** 3.47%; **N** 14.91%.

ESI-MS (MeCN) *m/z* (%): 405.1 (100) $[CuC_{20}H_{18}N_6]^+$.

UV-vis (MeCN, 238 K): $\lambda_{max.}$ [nm] (ε 10^3 [$M^{-1}\cdot cm^{-1}$]) = 331 (2.17).

The synthesis route *via* Mes_4Cu_4[51] as well as the analytic data of the complex were published in *Angew. Chem. Int. Ed.* **2019**, *58*, 2.

$[L^5Cu](PF_6)_2$

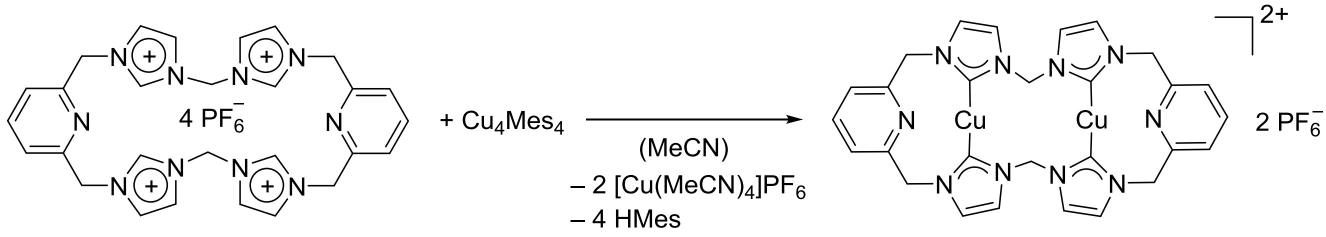

$C_{28}H_{30}N_{10}P_4F_{24}$	CuC_9H_{11}	$Cu_2C_{28}H_{26}N_{10}P_2F_{12}$
1086 g/mol	182 g/mol	2832 g/mol

$[H_2L^5](PF_6)_2$ (542 mg, 0.499 mmol, 1.00 equiv.) and mesitylcopper(I) (381 mg, 2.09 mmol, 4.20 equiv.) were suspended in MeCN (40 mL). The yellow-orange solution was stirred for 5 days at ambient temperature. The solvent volume was reduced to 3 mL *in vacuo* and a precipitate was formed after addition of diethyl ether (11 mL) to the solution. The solution was removed by cannulation and the orange solid was washed several times with diethyl ether. After the solution was removed by cannulation, the solid was dried under reduced pressure. A yellow solid was obtained in 95% yield (434 mg, 0.472 mmol).

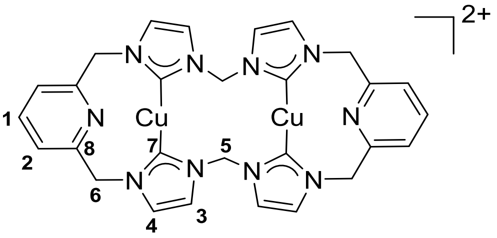

^{1}H NMR (500 MHz, 298 K, MeCN-d_3): δ [ppm] = 7.90 (t, $^3J_{HH}$ = 7.7 Hz, 2H, $H^{py\text{-}4}$ **1**), 7.52 (d, $^3J_{HH}$ = 7.7 Hz, 4H, $H^{py\text{-}3/5}$ **2**), 7.42 (s, 4H, H **3**), 7.28 (s, 4H, H **4**), 6.95 (d, $^2J_{HH}$ = 14.1 Hz, 2H, H **5**), 6.10 (d, $^2J_{HH}$ = 14.1 Hz, 2H, H **5**), 5.22 (s, 8H, H **6**).

^{13}C{^{1}H} NMR (126 MHz, 298 K, MeCN-d_3): δ [ppm] = 182.4 ($C_{carbene}$–**7**), 154.3 ($C_{quart.}$–**8**), 140.7 (C–**1**), 124.9 (C–**4**), 124.6 (C–**2**), 120.1 (C–**3**), 65.5 (C–**5**), 54.9 (C–**6**).

^{1}H^{1}H COSY NMR (500 MHz, 298 K, MeCN-d_3): δ [ppm] = 7.90/7.52 ($H^{py\text{-}4}$ **1** & $H^{py\text{-}3/5}$ **2**), 7.52/5.22 ($H^{py\text{-}3/5}$ **2** & H **6**), 7.42/7.28 ($_{Im}$H **3** & $_{Im}$H **4**), 7.28/5.22 ($_{Im}$H **4** & H **6**), 6.95/6.10 (H **5**/ H **5**).

^{1}H^{1}H NOESY NMR (500 MHz, 298 K, MeCN-d_3): δ [ppm] = 7.90/7.52 ($H^{py\text{-}4}$ **1** & $H^{py\text{-}3/5}$ **2**) 7.52/5.22 ($H^{py\text{-}3/5}$ **2** & H **6**), 7.42/7.28 ($_{Im}$H **3** & $_{Im}$H **4**), 7.42/6.95 ($_{Im}$H **3** & H **5**), 7.42/6.10 ($_{Im}$H **3** & H **5**), 7.28/5.22 ($_{Im}$H **4** & CH_2 **6**).

^{1}H^{13}C HSQC NMR (^{1}H NMR, 500 MHz, ^{13}C NMR, 126 MHz, 298 K, MeCN-*d*$_3$): δ [ppm] = 7.90/140.7, 7.52/124.6, 7.42/120.1, 7.28/124.9, 6.95/65.5, 6.10/65.5.

^{1}H^{13}C HMBC NMR (^{1}H NMR, 500 MHz, ^{13}C NMR, 126 MHz, 298 K, MeCN-*d*$_3$): δ [ppm] = 7.90/154.3 (H$^{\text{py-4}}$ **1** & C$_{\text{quart.}}$–**8**), 7.52/154.3 (H$^{\text{py-3/5}}$ **2** & C$_{\text{quart.}}$–**8**), 7.42/124.9 ($_{\text{Im}}$H **4** & C–**4**), 7.28/120.1 ($_{\text{Im}}$H **4** & C–**3**), 6.95/120.1 (H **5** & C–**3**), 5.22/182.4 (H **6** & C$_{\text{carbene}}$–**7**), 5.22/154.3 (H **6** & C$_{\text{quart.}}$–**8**), 5.22/124.9 (H **6** & C–**4**) 5.22/124.6 (H **6** & C–**2**),

^{1}H^{15}N HMBC NMR (^{1}H NMR, 500 MHz, ^{15}N NMR, 50.7 MHz, 298 K, MeCN-*d*$_3$): δ [ppm] = 7.41/–191.11, 7.52/–88.44, 7.28/–191.11, 7.28/–184.72, 5.22/–191.11, 5.22/–88.44.

^{1}H DOSY NMR (500 MHz, 298 K, MeCN-*d*$_3$): $D_{298\text{K}}$ [m$^{2}\cdot$s^{-1}] = $9.35\cdot10^{-6}$

Elemental analysis of $Cu_2C_{28}H_{26}N_{10}P_2F_{12}$

Calculated: **C** 36.57%; **H** 2.85%; **N** 15.23%.

Found: **C** 38.56%; **H** 3.33%; **N** 16.66%.

ESI-MS (MeCN) *m/z* (%): 314.1 (100) $[Cu_2C_{28}H_{26}N_{10}]^{2+}$, 773.1 (22) $[Cu_2C_{28}H_{26}N_{10}PF_6]^{+}$.

UV-vis (EtCN, 193 K): $\lambda_{\text{max.}}$ [nm] (ε 10^{3} [M$^{-1}\cdot$cm^{-1}]) = 465 (0.31).

m[105]

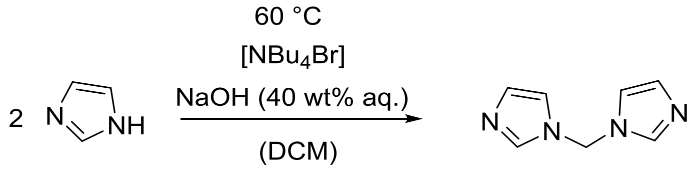

$C_3H_4N_2$	$C_{16}H_{36}NBr$	$C_7H_8N_4$
68 g/mol	322 g/mol	148 g/mol

1*H*-Imidazole (30.0 g, 441 mmol, 1.00 equiv.) and tetrabuthylammonium bromide (TBAB, 7.12 g, 22.1 mmol, 0.0500 equiv.) were dissolved in dichloromethane (400 mL). An aqueous solution of sodium hydroxide (40 wt%) was slowly added to the organic solution under stirring. The two phase layer was heated to reflux at 47 °C for 14 hours. Afterwards, DCM was removed under reduced pressure. The solid was removed by filtration and dried *in vacuo* for one hour. The white raw product was sublimed at a high vacuum line Kugelrohr apparatus at 140 °C (10^{-5} mbar) for one day. A white, crystalline solid was isolated in 78% yield (25.3 g, 171 mmol).

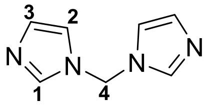

^{1}H NMR (500 MHz, 298 K, DMSO-d_6): δ [ppm] = 7.93 (dd, $^3J_{HH}$ = 2.2 Hz, $^4J_{HH}$ = 1.1 Hz, 2H, $_{Im}$H **1**), 7.39 (dd, $^3J_{HH}$ = 2.6 Hz, $^4J_{HH}$ = 1.3 Hz, 2H, $_{Im}$H **2**), 6.91 (dd, $^3J_{HH}$ = 2.2 Hz, $^4J_{HH}$ = 1.1 Hz, 2H, $_{Im}$H **3**), 6.21 (s, 2H, H **4**).

^{13}C{^{1}H} NMR (126 MHz, 298 K, DMSO-d_6): δ [ppm] = 137.3 (C–**1**), 129.2 (C–**3**), 119.1 (C–**2**), 54.8 (C–**4**).

^{1}H^{1}H COSY NMR (500 MHz, 298 K, DMSO-d_6): δ [ppm] = 7.93/7.39 ($_{Im}$H **1** & $_{Im}$H **2**), 7.93/6.91 ($_{Im}$H **1** & $_{Im}$H **3**), 7.93/6.21 ($_{Im}$H **1** & H **4**), 7.39/6.91 ($_{Im}$H **2** & $_{Im}$H **3**), 7.39/6.21 ($_{Im}$H **2** & H **4**), 6.91/6.21 ($_{Im}$H **3** & H **4**).

^{1}H^{1}H NOESY NMR (500 MHz, 298 K, DMSO-d_6): δ [ppm] = 7.93/6.21 ($_{Im}$H **1** & H **4**), 7.39/6.91 ($_{Im}$H **2** & $_{Im}$H **2**), 7.39/6.21 ($_{Im}$H **2** & H **4**), 6.91/6.21 ($_{Im}$H **3** & H **4**).

^{1}H^{13}C HSQC NMR (^{1}H NMR, 500 MHz, ^{13}C NMR, 126 MHz, 298 K, DMSO-d_6): δ [ppm] = 7.93/137.3, 7.39/119.1, 6.91/129.2, 6.21/54.8.

^{1}H^{13}C HMBC NMR (^{1}H NMR, 500 MHz, ^{13}C NMR, 126 MHz, 298 K, DMSO-d_6): δ [ppm] = 7.93/129.2 ($_{Im}$H **1** & C–**3**), 7.93/119.1 ($_{Im}$H **1** & C–**2**), 7.93/54.8 ($_{Im}$H **1** & C–**4**), 7.39/137.3 ($_{\text{Im}}$H **2** & C–**1**), 7.39/129.2 ($_{\text{Im}}$H **2** & C–**3**), 7.39/54.8 ($_{\text{Im}}$H **2** & C–**4**), 6.91/137.3 ($_{\text{Im}}$H **3** & C–**1**), 6.91/119.1 ($_{\text{Im}}$H **3** & C–**2**), 6.91/54.8 ($_{\text{Im}}$H **3** & C–**4**), 6.21/137.3 (H **4** & C–**1**), 6.21/119.1 (H **4** & C–**2**).

^{1}H^{15}N HMBC NMR (^{1}H NMR, 500 MHz, ^{15}N NMR, 50.7 MHz, 298 K, DMSO-d_6): δ [ppm] = 7.93/–202.0, 7.39/–202.0, 6.91/–202.0, 6.21/–202.0, 7.93/–116.1, 7.39/–116.1, 6.91/–116.1.

Elemental analysis of $C_7H_8N_4$

Calculated: **C** 56.74%; **H** 5.44%; **N** 37.81%.

Found: **C** 56.61%; **H** 5.46%; **N** 38.27%.

EI-MS *m/z* (%): 148 (63) $[C_7H_8N_4]^+$, 81 (100) $[C_4H_5N_2]^+$.

IR (ATR): υ [cm^{-1}] = 3131.2 (w), 3111.7 (m), 3002.6 (m), 1683.9 (m), 1659.7 (m), 1601.9 (m), 1509.7 (s), 1492.0 (s), 1388.6 (s), 1353.1 (s), 1307.5 (m), 1278.6 (s), 1223.6 (s), 1101.5 (s), 1076.4 (s), 1034.4 (s), 999.0 (s), 906.8 (s), 851.8 (s), 825.7 (s), 769.8 (s), 743.7 (s), 711.9 (s), 658.9 (s), 619.7 (s), 609.5 (s), 568.5 (s), 443.6 (s).

The synthesis route as well as the analytic data of **m** were published in *Z. Anorg. Allg. Chem.* **2019**, *645*, 605. © 2019 JOHN WILEY AND SONS.

.

n[449]

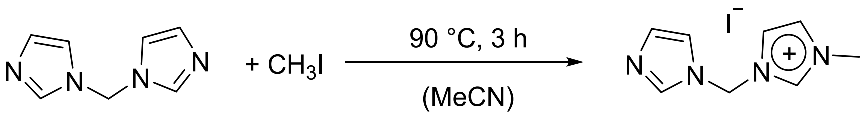

$C_3H_4N_4$	C_3H_3I	$C_8H_{11}N_4I$
148 g/mol	142 g/mol	290 g/mol

1,1’-Bis(*N*-imidazolyl)methane (10.3 g, 69.7 mmol, 1.00 equiv.) was dissolved in MeCN (200 mL). Iodomethane (1.74 mL, 3.40 g, 27.9 mmol, 0.400 equiv.) was added and the solution was heated to reflux for 3 h. The solvent was removed and the resulting colorless solid was dried *in vacuo*. The solid was dissolved in MeOH (250 mL) and Et_2O (200 mL) was slowly added and the white precipitate was filtered off. Additionally, Et_2O (500 mL) was added to the filtrate. The resulting, cloudy suspension was rest for one hour. A colorless oil was formed. The two phase solution was stored at –30 °C overnight. The colorless solid was filtered off, washed with Et_2O and was dried at a high vacuum line. A white solid was obtained in 66% yield (5.31 g, 18.3 mmol). The solvent of the filtrate was removed *in vacuo* and the obtained solid was sublimed at a high vacuum Kugelrohr apparatus in order to regain the bis(*N*-imidazolyl)methane.

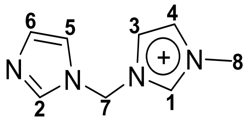

^{1}H NMR (500 MHz, 298 K, DMSO-d_6): δ [ppm] = 9.33 (s, 1H, $_{\text{Im}}$H **1**), 8.01 (dd, $^3J_{HH}$ = 2.2 Hz, $^4J_{HH}$ = 1.1 Hz, 1H, $_{\text{Im}}$H **2**), 7.94 (dd, $^3J_{HH}$ = 3.7 Hz, $^4J_{HH}$ = 1.9 Hz, 1H, $_{\text{Im}}$H **3**), 7.74 (dd, $^3J_{HH}$ = 3.6 Hz, $^4J_{HH}$ = 1.8 Hz, 1H, $_{\text{Im}}$H **4**), 7.48 (dd, $^3J_{HH}$ = 2.6 Hz, $^4J_{HH}$ = 1.3 Hz, 1H, $_{\text{Im}}$H **5**), 6.99 (dd, $^3J_{HH}$ = 2.2 Hz, $^4J_{HH}$ = 1.1 Hz, 1H, $_{\text{Im}}$H **6**), 6.47 (s, 2H, H **7**), 3.87 (s, 3H, H **8**).

^{13}C{^{1}H} NMR (126 MHz, 298 K, DMSO-d_6): δ [ppm] = 137.8 (C–**2**), 137.0 (C–**1**), 129.7 (C-**6**),124.3 (C–**4**), 121.6 (C–**3**), 119.3 (C–**5**), 56.7 (C–**7**), 36.2 (C–**8**).

^{1}H^{1}H COSY NMR (500 MHz, 298 K, DMSO-d_6): δ [ppm] = 9.33/7.94 ($_{\text{Im}}$H **1** & $_{\text{Im}}$H **3**), 9.33/7.74 ($_{\text{Im}}$H **1** & $_{\text{Im}}$H **4**), 9.33/6.47 ($_{\text{Im}}$H **1** & H **7**), 9.33/3.87 ($_{\text{Im}}$H **1** & H **8**), 8.01/7.48 ($_{\text{Im}}$H **2** & $_{\text{Im}}$H **5**), 8.01/6.99 ($_{\text{Im}}$H **2** & $_{\text{Im}}$H **6**), 8.01/6.47 ($_{\text{Im}}$H **2** & H **7**), 7.94/7.74 ($_{\text{Im}}$H **3** & $_{\text{Im}}$H **4**), 7.94/6.47 ($_{\text{Im}}$H **3** & H **7**), 7.94/3.87 ($_{\text{Im}}$H **3** & H **8**), 7.74/6.47 ($_{\text{Im}}$H **4** & H **7**), 7.74/3.87 ($_{\text{Im}}$H **4** & H **8**), 7.48/6.99 ($_{\text{Im}}$H **5** & $_{\text{Im}}$H **6**), 7.48/6.47 ($_{\text{Im}}$H **5** & H **7**), 6.99/6.47 ($_{\text{Im}}$H **5** & H **7**).

^{1}H^{1}H NOESY NMR (500 MHz, 298 K, DMSO-d_6): δ [ppm] = 9.33/8.01 ($_{\mathrm{Im}}$H **1** & $_{\mathrm{Im}}$H **2**), 9.33/7.48 ($_{\mathrm{Im}}$H **1** & $_{\mathrm{Im}}$H **5**), 9.33/6.47 ($_{\mathrm{Im}}$H **1** & H **7**), 9.33/3.87 ($_{\mathrm{Im}}$H **1** & H **8**), 8.01/6.47 ($_{\mathrm{Im}}$H **2** & H **7**), 7.94/7.74 ($_{\mathrm{Im}}$H **3** & $_{\mathrm{Im}}$H **4**), 7.94/7.48 ($_{\mathrm{Im}}$H **3** & $_{\mathrm{Im}}$H **5**), 7.94/6.47 ($_{\mathrm{Im}}$H **3** & H **7**), 7.74/3.87 ($_{\mathrm{Im}}$H **4** & H **8**), 7.48/6.99 ($_{\mathrm{Im}}$H **5** & $_{\mathrm{Im}}$H **6**), 7.48/6.47 ($_{\mathrm{Im}}$H **5** & H **7**).

^{1}H^{13}C HSQC NMR (^{1}H NMR, 500 MHz, ^{13}C NMR, 126 MHz, 298 K, DMSO-d_6): δ [ppm] = 9.33/137.0, 8.01/137.8, 7.94/121.6, 7.74/124.3, 7.48/119.3, 6.99/129.7, 6.47/56.7, 3.87/36.2.

^{1}H^{13}C HMBC NMR (^{1}H NMR, 500 MHz, ^{13}C NMR, 126 MHz, 298 K, DMSO-d_6): δ [ppm] = 9.33/124.3 ($_{\mathrm{Im}}$H **1** & C–**4**), 9.33/121.6 ($_{\mathrm{Im}}$H **1** & C–**3**), 9.33/56.7 ($_{\mathrm{Im}}$H **1** & C–**7**), 9.33/36.2 ($_{\mathrm{Im}}$H **1** & C–**8**), 8.01/129.7 ($_{\mathrm{Im}}$H **2** & C–**6**), 8.01/119.3 ($_{\mathrm{Im}}$H **2** & C–**5**), 8.01/56.7 ($_{\mathrm{Im}}$H **2** & C–**7**), 7.94/137.0 ($_{\mathrm{Im}}$H **3** & C–**1**), 7.94/124.3 ($_{\mathrm{Im}}$H **3** & C–**4**), 7.94/56.7 ($_{\mathrm{Im}}$H **3** & C-**7**), 7.74/137.0 ($_{\mathrm{Im}}$H **4** & C–**1**), 7.74/121.6 ($_{\mathrm{Im}}$H **4** & C–**3**), 7.74/36.2 ($_{\mathrm{Im}}$H **4** & C–**8**), 7.48/137.8 ($_{\mathrm{Im}}$H **5** & C–**2**), 7.48/129.7 ($_{\mathrm{Im}}$H **5** & C–**6**), 7.48/56.7 ($_{\mathrm{Im}}$H **5** & C–**7**), 6.99/137.8 ($_{\mathrm{Im}}$H **6** & C–**2**), 6.99/119.3 ($_{\mathrm{Im}}$H **6** & C–**5**), 6.47/137.8 (H **7** & C–**2**), 6.47/137.0 (H **7** & C–**1**), 6.47/121.6 (H **7** & C–**3**), 6.47/119.3 (H **7** & C–**5**), 3.87/137.0 (H **8** & C–**1**), 3.87/124.3 (H **8** & C–**4**).

^{1}H^{15}N HMBC NMR (^{1}H NMR, 500 MHz, ^{15}N NMR, 50.7 MHz, 298 K, DMSO-d_6): δ [ppm] = 8.01/–208.1, 7.48/–208.1, 6.99/–208.1, 6.47/–208.1, 9.33/–205.9, 7.94/–205.9, 7.74/–205.9, 3.87/–205.9, 9.33/–195.5, 7.94/–195.5, 7.74/–195.5, 6.47/–195.5, 8.01/–114.8, 7.48/–114.8, 6.99/–114.8.

Elemental analysis of $C_8H_{11}N_4I$

Calculated: **C** 33.12%; **H** 3.82%; **N** 19.31%.

Found: **C** 33.02%; **H** 3.72%; **N** 19.49%.

ESI-MS (MeCN) *m/z* (%): 163.1 (100) $[C_8H_{11}N_4]^+$.

IR (ATR): υ [cm^{-1}] = 3106.1 (w), 3082.8 (m), 3063.2 (m), 2992.4 (m), 1628.1 (m), 1584.3 (m), 1573.1 (m), 1555.4 (m), 1515.3 (m), 1493.9 (m), 1431.4 (m), 1408.1 (m), 1384.8 (m), 1355.9 (m), 1328.9 (m), 1322.4 (m), 1294.4 (m), 1284.2 (s), 1231.9 (s), 1224.5 (s), 1198.4 (w), 1163.0 (s), 1153.7 (s), 1108.9 (m), 1098.7 (m), 1083.8 (s), 1077.3 (s), 1031.6 (s), 992.5 (w), 982.2 (w), 908.6 (s), 903.0 (s), 837.8 (s), 821.0 (s), 762.3 (s), 749.3 (s), 719.4 (s), 657.9 (s), 643.9 (s), 622.5 (s), 617.9 (s), 612.3 (s), 604.8 (s), 573.1 (m).

The synthesis route as well as the analytic data of **n** were published in *Z. Anorg. Allg. Chem.* **2019**, *645*, 605. © 2019 JOHN WILEY AND SONS.

q

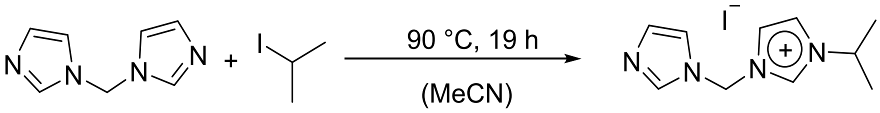

$C_3H_4N_4$	C_3H_7I	$C_{10}H_{15}N_4I$
148 g/mol	170 g/mol	318 g/mol

1,1’-Bis(*N*-imidazolyl)methane (3.00 g, 20.3 mmol, 1.00 equiv.) was dissolved in MeCN (100 mL). 2-Iodopropane (0.800 mL, 1.37 g, 8.06 mmol, 0.400 equiv.) was added and the solution was heated to reflux for 19 h. The solvent was removed and the solid was dried at a high vacuum line overnight. The white solid was dissolved in methanol (70 mL). Et$_2$O (150 mL) was slowly added to the solution and the white emulsion was stored for several hours at –30 °C. The resulting colorless solid was filtered off, washed with Et$_2$O and dried at a high vacuum line. A white solid was obtained in 27% yield (0.705 g, 2.22 mmol).

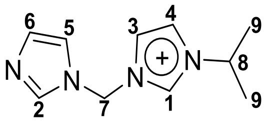

^{1}H NMR (300 MHz, 298 K, DMSO-d_6): δ [ppm] = 9.48 (dd, $^3J_{HH}$ = 3.07 Hz, $^4J_{HH}$ = 1.52 Hz 1H, $_{Im}$H **1**), 8.02 (dd, $^3J_{HH}$ = 2.03 Hz, $^4J_{HH}$ = 0.96 Hz, 1H, $_{Im}$H **2**), 7.96 (dd, $^3J_{HH}$ = 3.20 Hz, $^4J_{HH}$ = 1.6 Hz, 2H, $_{Im}$H **3** & $_{Im}$H **4**), 7.49 (dd, $^3J_{HH}$ = 2.60 Hz, $^4J_{HH}$ = 1.31 Hz, 1H, $_{Im}$H **5**), 7.00 (dd, $^3J_{HH}$ = 2.17 Hz, $^4J_{HH}$ = 1.02 Hz, 1H, $_{Im}$H **6**), 6.44 (s, 2H, H **7**), 4.67 (hpt, $^3J_{HH}$ = 6.70 Hz, 1H, H **8**), 1.48 (d, $^3J_{HH}$ = 6.70 Hz, 6H, H **9**).

^{13}C{^{1}H} NMR (75.5 MHz, 298 K, DMSO-d_6): δ [ppm] = 137.8 (C–**2**), 135.4 (C–**1**), 129.7 (C–**6**),121.9 (C–**3**), 121.3 (C–**4**), 119.3 (C–**5**), 52.7 (C–**8**), 22.1 (C–**9**).

^{1}H^{1}H COSY NMR (300 MHz, 298 K, DMSO-d_6): δ [ppm] = 9.48/7.96 ($_{Im}$H **1** & $_{Im}$H **3** & $_{Im}$H **4**), 8.02/7.49 ($_{Im}$H **2** & $_{Im}$H **5**), 7.49/7.00 ($_{Im}$H **5** & $_{Im}$H **6**), 4.67/1.48 (H **8** & H **9**).

^{1}H^{13}C HSQC NMR (^{1}H NMR, 300 MHz, ^{13}C NMR, 75.5 MHz, 298 K, DMSO-d_6): δ [ppm] = 9.48/135.9, 8.02/137.8, 7.96/121.9, 7.96/121.3, 7.49/119.3, 7.00/129.7, 4.67/52.7.

^{1}H^{13}C HMBC NMR (^{1}H NMR, 500 MHz, ^{13}C NMR, 126 MHz, 298 K, DMSO-d_6): δ [ppm] = 9.48/121.9 ($_{Im}$H **1** & C–**3**), 9.48/121.3 ($_{Im}$H **1** & C–**4**), 8.02/129.7 ($_{Im}$H **2** & C–**6**), 8.02/119.3 ($_{Im}$H **2** & C–**5**), 7.96/135.9 ($_{Im}$H **3**/ $_{Im}$H **4** & C–**1**), 7.96/121.9 ($_{Im}$H **4** & C–**3**), 7.96/121.3 ($_{Im}$H **3** & C–**4**), 7.49/137.8 ($_{Im}$H **5** & C–**2**), 7.49/129.7 ($_{Im}$H **5** & C–**6**), 7.00/137.8 ($_{Im}$H **6** & C–**2**), 7.00/119.3 ($_{Im}$H **6** & C–**5**), 6.44/137.8 (CH$_2$ **7** & C–**2**), 6.44/135.4 (CH$_2$ **7** &

C–**1**), 6.44/121.9 (H **7** & C–**3**), 6.44/119.3 (H **7** & C–**5**), 4.67/22.1 (H **8** & C–**9**), 1.48/52.7 (H **9** & C–**8**).

p

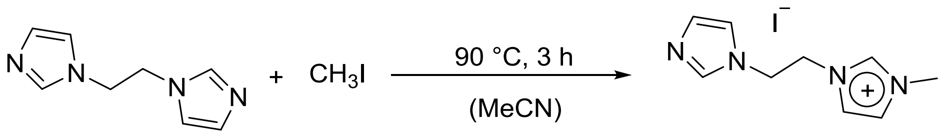

$C_8H_{10}N_4$	CH_3I	$C_9H_{13}N_4I$
162 g/mol	142 g/mol	304 g/mol

1,2-Bis(*N*-imidazolyl)ethane (1.00 g, 6.17 mmol, 2.50 equiv.) was dissolved in MeCN (50 mL). Methyl iodide (154 µL, 350 mg, 2.47 mmol, 1.00 equiv.) was added to the solution. Afterwards, the solution was refluxed for 3 h and the solvent was removed *in vacuo*. The colorless oil was dried at a high vacuum line overnight. The raw product was dissolved in methanol (60 mL). Et_2O (150 mL) was slowly added to the solution and the white emulsion was stored for five days at –30 °C. The white solid was filtered off, washed with ethyl acetate and was dried *in vacuo*. A white solid was obtained in 82% yield (616 mg, 2.03 mmol).

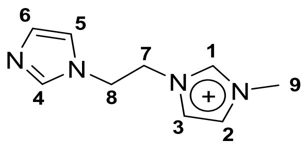

^{1}H NMR (300 MHz, 298 K, DMSO-d_6): δ [ppm] = 8.92 (s, 1H, $_{\mathrm{Im}}$H **1**), 7.67 (dd, $^3J_{HH}$ = 2.2 Hz, $^4J_{HH}$ = 1.1 Hz, 1H, $_{\mathrm{Im}}$H **2**), 7.49 (m, 2H, $_{\mathrm{Im}}$H **3**, & $_{\mathrm{Im}}$H **4**), 7.10 (dd, $^3J_{HH}$ = 2.2 Hz, $^4J_{HH}$ = 1.1 Hz, 1H, $_{\mathrm{Im}}$H **5**), 6.89 (dd, $^4J_{HH}$ = 2.2 Hz, $^4J_{HH}$ = 1.1 Hz, 1H, 1H, $_{\mathrm{Im}}$H **6**), 4.57 (m, 2H, H **7**), 4.46 (m, 2H, H **8**), 3.82 (s, 3H, H **9**).

^{13}C{^{1}H} NMR (75 MHz, 298 K, DMSO-d_6): δ [ppm] = 137.4 (C–**4**), 136.7 (C–**1**), 128.9 (C–**6**),123.7 (C–**2**), 122.2 (C–**3**), 119.1 (C–**5**), 49.4 (C–**7**), 45.5 (C–**8**), 35.8 (C–**9**).

^{1}H^{1}H COSY NMR (300 MHz, 298 K, DMSO-d_6): δ [ppm] = 8.92/7.67 ($_{\mathrm{Im}}$H **1** & $_{\mathrm{Im}}$H **2**), 8.92/7.49 ($_{\mathrm{Im}}$H **1** & $_{\mathrm{Im}}$H **3**), 8.93/3.84 ($_{\mathrm{Im}}$H **1** & H **9**), 7.67/7.49 ($_{\mathrm{Im}}$H **2** & $_{\mathrm{Im}}$H **3**), 7.67/3.80 ($_{\mathrm{Im}}$H **2** & H **9**), 7.49/7.10 ($_{\mathrm{Im}}$H **4** & $_{\mathrm{Im}}$H **5**), 7.49/6.89 ($_{\mathrm{Im}}$H **4** & $_{\mathrm{Im}}$H **6**).

^{1}H^{1}H NOESY NMR (300 MHz, 298 K, DMSO-d_6): δ [ppm] = 8.92/4.57 ($_{\mathrm{Im}}$H **1** & H **7**), 8.92/3.82 ($_{\mathrm{Im}}$H **1** & H **9**), 7.67/7.49 ($_{\mathrm{Im}}$H **2** & $_{\mathrm{Im}}$H **3**), 7.67/3.82 ($_{\mathrm{Im}}$H **2** & H **9**), 7.49/4.57 ($_{\mathrm{Im}}$H **3** & $_{\mathrm{Im}}$H **7**), 7.49/4.46 ($_{\mathrm{Im}}$H **3** & H **8**), 7.10/4.57 ($_{\mathrm{Im}}$H **5** & $_{\mathrm{Im}}$H **7**), 7.10/4.46 ($_{\mathrm{Im}}$H **5** & H **8**).

^{1}H^{13}C HSQC NMR (^{1}H NMR, 300 MHz, ^{13}C NMR, 75 MHz, 298 K, DMSO-d_6): δ [ppm] = 8.93/136.7, 7.67/123.7, 7.49/137.4, 7.49/122.2, 7.10/119.1, 6.89/128.9, 4.57/49.4, 4.46/45.5, 3.83/35.8.

Elemental analysis of $C_9H_{13}N_4$

Calculated: **C** 35.54%; **H** 4.31%; **N** 18.42%.

Found: **C** 35.57%; **H** 4.22%; **N** 18.46%.

ESI-MS (MeCN) *m/z* (%): 83.0 (81) $[C_4H_7N_2]^+$, 95.0 (100) $[C_5H_7N_2]^+$, 177 (71) $[C_9H_{13}N_4]^+$.

The synthesis route as well as the analytic data of **p** were published in *Z. Anorg. Allg. Chem.* **2019**, *645*, 605. © 2019 JOHN WILEY AND SONS.

r

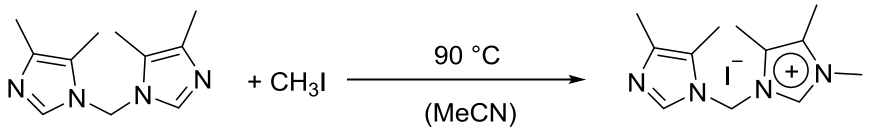

$C_{11}H_{16}N_4$ C_3H_3I $C_{12}H_{19}N_4I$

204 g/mol 142 g/mol 346 g/mol

1,1’-Bis(4,5-dimethylimidazolyl) methane (3.01 g, 0.0147 mol, 1.00 equiv.) was dissolved in MeCN (100 mL). Methyl iodide (0.4 mL, 0.912 g, 0.00643 mol, 0.437 equiv.) was added and the solution was heated to reflux at 90 °C for 3.5 hours. Afterwards the solvent was removed under reduced pressure and the white solid was dried *in vacuo* overnight. The white solid was dissolved in MeOH (30 mL) and diethyl ether was added to the solution and stored at 0 °C for several hours. Afterwards the precipitate was filtered off and diethyl ether was added again to the solution and two fractions were isolated afterwards as white solid in 98% yield (2.18 g, 6.28 mmol).

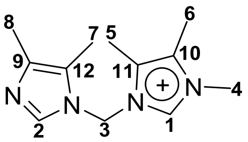

^{1}H NMR (300 MHz, 298 K, DMSO-d_6): δ [ppm] = 9.01 (s, 1H, $_{\text{Im}}$H **1**), 7.78 (s, 1H, $_{\text{Im}}$H **2**), 6.34 (s, 1H, H **3**), 3.73 (s, 3H, H **4**), 2.26 (s, 3H, H **5**), 2.20 (s, 3H, H **6**), 2.10 (s, 3H, H **7**), 2.02 (s, 3H, H **8**).

^{13}C{^{1}H} NMR (75.5 MHz, 298 K, DMSO-d_6): δ [ppm] = 136.9 (C–**2**), 135.4 (C–**1**), 134.5 ($C_{\text{quart.}}$–**9**), 128.6 ($C_{\text{quart.}}$–**10**), 126.2 ($C_{\text{quart.}}$–**11**), 122.4 ($C_{\text{quart.}}$–**12**), 54.8 (C–**3**), 34.1 (C–**4**), 12.9 (C–**8**), 8.6 (C–**5**), 8.5 (C–**7**), 8.1 (C–**6**).

^{1}H^{1}H COSY NMR (300 MHz, 298 K, DMSO-d_6): δ [ppm] = 9.01/6.34 ($_{\text{Im}}$H **1** & H **3**), 9.01/3.73 ($_{\text{Im}}$H **1** & H **4**), 7.78/6.34 ($_{\text{Im}}$H **2** & H **4**).

^{1}H^{1}H NOESY NMR (300 MHz, 298 K, DMSO-d_6): δ [ppm] = 9.01/7.78 ($_{\text{Im}}$H **1** & $_{\text{Im}}$H **2**), 9.01/6.34 ($_{\text{Im}}$H **1** & H **3**), 9.01/3.73 ($_{\text{Im}}$H **1** & H **4**), 9.01/2.10 ($_{\text{Im}}$H **1** & H **7**), 7.78/6.34 ($_{\text{Im}}$H **2** & H **3**), 7.78/2.26 ($_{\text{Im}}$H **2** & H **5**), 6.34/2.26 (H **3** & H **5**), 6.34/2.20 (H **3** & H **6**), 6.34/2.10 (H **3** & H **7**), 3.73/2.20 (H **4** & H **6**).

^{1}H^{13}C HSQC NMR (^{1}H NMR, 300 MHz, ^{13}C NMR, 75.5 MHz, 298 K, DMSO-d_6): δ [ppm] = 9.01/135.4, 7.78/136.9, 6.34/54.8, 3.73/34.1, 2.26/8.6, 2.20/8.1, 2.10/8.5, 2.02/12.9.

^{1}H^{13}C HMBC NMR (^{1}H NMR, 500 MHz, ^{13}C NMR, 126 MHz, 298 K, DMSO-d_6): δ [ppm] = 9.01/128.6 ($_{\mathrm{Im}}$H **1** & $C_{\mathrm{quart.}}$–**10**), 9.01/126.2 ($_{\mathrm{Im}}$H **1** & $C_{\mathrm{quart.}}$–**11**), 7.78/134.5 ($_{\mathrm{Im}}$H **2** & $C_{\mathrm{quart.}}$–**9**), 7.78/122.4 ($_{\mathrm{Im}}$H **2** & $C_{\mathrm{quart.}}$–**12**), 6.34/136.9 (H **3** & C–**2**), 6.34/135.4 (H **3** & C–**1**), 6.34/126.2 (H **3** & $C_{\mathrm{quart.}}$–**11**), 6.34/122.4 (H **3** & $C_{\mathrm{quart.}}$–**12**), 3.73/135.4 (H **4** & C–**1**), 3.73/128.6 (H **3** & $C_{\mathrm{quart.}}$–**10**), 2.26/128.6 (H **5** & $C_{\mathrm{quart.}}$–**10**), 2.26/126.2 (H **5** & $C_{\mathrm{quart.}}$–**11**), 2.20/128.6 (H **6** & $C_{\mathrm{quart.}}$–**10**), 2.20/126.2 (H **6** & $C_{\mathrm{quart.}}$–**10**), 2.10/134.5 (H **7** & $C_{\mathrm{quart.}}$–**9**), 2.10/122.4 (H **7** & $C_{\mathrm{quart.}}$–**12**), 2.02/134.5 (H **8** & $C_{\mathrm{quart.}}$–**9**), 2.02/122.4 (H **8** & $C_{\mathrm{quart.}}$–**12**).

$[H_6L^6]X_5$ (X = Cl or I)

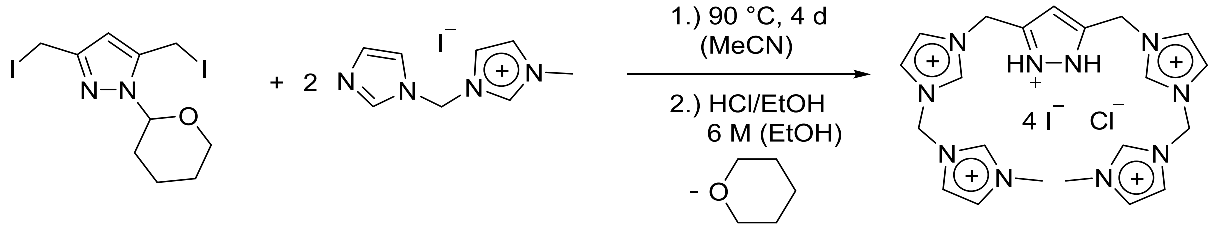

$C_3H_4N_2$	$C_8H_{11}N_4I$	$C_{21}H_{29}N_{10}I_4Cl$
432 g/mol	290 g/mol	965 g/mol

3,5-bis(iodomethyl)-1-tetrahydropyran-2-yl pyrazole (1.30 g, 3.01 mmol, 1.00 equiv.) was dissolved in MeCN (215 mL). **n** (2.01 g, 6.92 mmol, 2.30 equiv.) was added in portions to the solution. The solution was heated to reflux for 4 days at 90 °C. Afterwards, the solvent was removed *in vacuo*. The red-brownish solid was dried at a high vacuum line overnight. The dried solid was suspended in ethanol (16 mL) and a mixture of HCl/EtOH (6 M) was added. The suspension was stirred for 30 min and Et_2O was added until a precipitation appeared. The brownish solid was filtered off, washed with Et_2O and was dried at the high vacuum line for several hours. An off-white solid was obtained in 54% yield (1.56 g, 1.62 mmol).

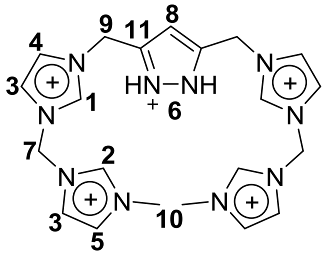

^{1}H NMR (300 MHz, 298 K, DMSO-*d*$_6$): δ [ppm] = 10.08 (s, 2H, $_{\mathrm{Im}}$H **1**), 9.93 (s, 2H, $_{\mathrm{Im}}$H **2**), 8.35 (s, 4H, $_{\mathrm{Im}}$H **3**), 8.00 (s, 2H, $_{\mathrm{Im}}$H **4**), 7.84 (s, 2H, $_{\mathrm{Im}}$H **5**), 7.30 (br s, 2H, NH **6**), 6.95 (s, 4H, H **7**), 6.66 (s, 1H, H$^{\mathrm{pz}}$ **8**), 5.56 (s, 4H, H **9**), 3.90 (s, 6H, H **10**).

^{13}C{^{1}H} NMR (101 MHz, 298 K, DMSO-*d*$_6$): δ [ppm] = 140.8 C$_{\mathrm{quart.}}$ **11**, 138.3, 137.9, 124.1, 123.2, 122.4, 122.1, 106.2, 57.6, 44.9, 36.2.

^{1}H^{1}H COSY NMR (300 MHz, 298 K, DMSO-*d*$_6$): δ [ppm] = 10.08/8.35 ($_{\mathrm{Im}}$H **1** & $_{\mathrm{Im}}$H **3**), 10.08/8.00 ($_{\mathrm{Im}}$H **1** & $_{\mathrm{Im}}$H **4**), 9.93/8.35 ($_{\mathrm{Im}}$H **2** & $_{\mathrm{Im}}$H **3**), 9.93/7.84 ($_{\mathrm{Im}}$H **2** & $_{\mathrm{Im}}$H **5**), 9.93/3.90 ($_{\mathrm{Im}}$H **2** & H **10**), 8.35/7.84 ($_{\mathrm{Im}}$H **3** & $_{\mathrm{Im}}$H **5**), 8.35/8.00 ($_{\mathrm{Im}}$H **3** & $_{\mathrm{Im}}$H **4**).

^{1}H^{13}C HSQC NMR (^{1}H NMR, 300 MHz, ^{13}C NMR, 101 MHz, 298 K, DMSO-*d*$_6$):
δ [ppm] = 10.08/137.9, 9.93/138.3, 8.35/122.4, 8.35/122.1, 8.00/123.2, 7.84/124.1, 6.95/57.6, 6.66/106.2, 3.90/36.2. Results of **$[H_6L^6]^{5+}$** were published in *ZAAC* **2019**, *645*, 605.

$[H_5L^6](PF_6)_4$

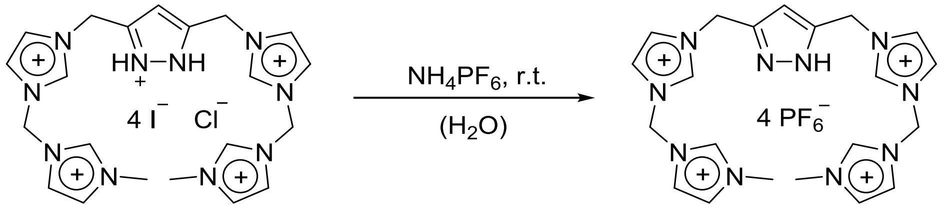

$C_{21}H_{29}N_{10}I_4Cl$	H_4NPF_6	$C_{21}H_{28}N_{10}P_4F_{24}$
432 g/mol	163 g/mol	1000 g/mol

$[H_5L^6]I_4Cl$ (1.54 g, 1.60 mmol, 1.00 equiv.) was dissolved in demineralized water (250 mL). Excess of NH_4PF_6 was added in portions to the solution and stored at –30 °C overnight. The off-white precipitate was filtered off, washed several times with water and was dried at the high vacuum line. An off-white solid was obtained in 52% yield (0.829 g, 0.829 mmol).

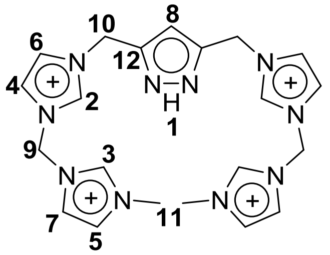

333 K:

^{1}H DOSY NMR (500 MHz, 333 K, MeCN-d_3): D_{333K} [$m^2 \cdot s^{-1}$] = $1.21 \cdot 10^{-9}$

298 K:

^{1}H NMR (500 MHz, 298 K, MeCN-d_3): δ [ppm] = 11.45 (br s, 1H, NH **1**), 8.80 (br s, 2H, $_{Im}$H **2**), 8.70 (s, 2H, $_{Im}$H **3**), 7.59 (br s, 2H, $_{Im}$H **4**), 7.57 (dd, $^3J_{HH}$ = 1.99 Hz, 2H, $_{Im}$H **5**), 7.48 (br s, 2H, $_{Im}$H **6**), 7.45 (dd, $^3J_{HH}$ = 1.80 Hz, 2H, $_{Im}$H **7**), 6.59 (s, 1H, H^{pz} **8**), 6.36 (s, 4H, H **9**), 5.45 (s, 2H, H **10**), 5.38 (s, 2H, H **10**), 3.88 (s, 6H, H **11**).

^{13}C{^{1}H} NMR (126 MHz, 298 K, MeCN-d_3): δ [ppm] = 146.4 ($C_{quart.}$–**12**), 138.4 (C–**3**), 137.9 (C–**2**), 126.0 (C–**7**), 124.8 (C–**6**), 124.6 (C–**6**), 123.6 (C–**4**), 123.3 (C–**4**), 123.0 (C–**5**), 108.0 (C–**8**), 59.8 (C–**9**), 48.0 (C–**10**), 44.8 (C–**10**), 37.5 (C–**11**).

^{1}H^{1}H COSY-NMR (500 MHz, 298 K, MeCN-d_3): δ [ppm] = 8.80/7.59 ($_{Im}$H **2** & $_{Im}$H **4**), 8.80/7.48 ($_{Im}$H **2** & $_{Im}$H **6**), 8.80/6.36 ($_{Im}$H **2** & $_{Im}$H **9)**, 8.70/7.57 ($_{Im}$H **3** & $_{Im}$H **5**), 8.70/7.45 ($_{Im}$H **3** & $_{Im}$H **7**), 8.70/6.36 ($_{Im}$H **3** & $_{Im}$H **9)**, 8.70/3.88 ($_{Im}$H **3** & H **11**), 7.57/3.88 ($_{Im}$H **5** & H **11**), 7.45/6.36 ($_{Im}$H **7** & $_{Im}$H **9**), 6.59/5.41 (H^{pz} **8** & H **10**).

^{1}H^{1}H NOESY NMR (500 MHz, 298 K, MeCN-d_3): δ [ppm] = 8.80/6.36 ($_{\mathrm{Im}}$H **2** & H **9**), 8.80/5.45 ($_{\mathrm{Im}}$H **2** & H **10**), 8.70/6.36 ($_{\mathrm{Im}}$H **3** & H **9**), 8.70/3.88 ($_{\mathrm{Im}}$H **3** & H **11**), 7.59/6.36 ($_{\mathrm{Im}}$H **4** & H **9**), 7.59/3.88 ($_{\mathrm{Im}}$H **4** & H **11**), 7.57/3.88 ($_{\mathrm{Im}}$H **5** & H **11**), 7.45/3.88 ($_{\mathrm{Im}}$H **7** & H **11**).

^{1}H^{13}C HSQC NMR (^{1}H NMR, 500 MHz, ^{13}C NMR, 126 MHz, 298 K, MeCN-d_3): δ [ppm] = 8.80/137.9, 8.70/138.4, 7.59/123.4, 7.57/123.0, 7.48/124.6, 7.45/126.0, 6.59/108.0, 6.36/59.8, 5.41/48.0, 5.41/44.8, 3.88/37.5.

^{1}H^{13}C HMBC NMR (^{1}H NMR, 500 MHz, ^{13}C NMR, 126 MHz, 298 K, MeCN-d_3): δ [ppm] = 8.70/126.0 ($_{\mathrm{Im}}$H **3** & C–**7**), 8.70/123.0 ($_{\mathrm{Im}}$H **3** & C–**5**), 7.59/137.9 ($_{\mathrm{Im}}$H **4** & C–**2**), 7.59/124.8 ($_{\mathrm{Im}}$H **4** & C–**6**), 7.59/124.6 ($_{\mathrm{Im}}$H **4** & C–**6**), 7.57/138.4 ($_{\mathrm{Im}}$H **5** & C–**3**), 7.57/126.0 ($_{\mathrm{Im}}$H **5** & C–**7**), 7.48/137.9 ($_{\mathrm{Im}}$H **6** & C–**2**), 7.45/138.4 ($_{\mathrm{Im}}$H **7** & C–**3**), 7.45/123.0 ($_{\mathrm{Im}}$H **7** & C-**5**), 6.59/146.4 (H$^{\mathrm{pz}}$ **8** & C$_{\mathrm{quart.}}$–**12**), 6.36/138.4 (H **9** & C–**3**), 6.36/137.9 (H **9** & C–**2**), 6.36/123.0 (H **9** & C–**5**), 3.88/138.4 (H **11** & C–**3**), 3.88/126.0 (H **11** & C–**7**).

^{1}H^{15}N HMBC NMR (^{1}H NMR, 500 MHz, ^{15}N NMR, 50.7 MHz, 298 K, MeCN-d_3): δ [ppm] = 8.70/–205.2, 7.57/–205.2, 7.45/–205.2, 6.36/–205.2, 8.70/–203.9, 7.57/–203.9, 7.45/–203.9, 3.88/–203.9, 6.36/–203.6, 6.59/–176.5 (**NH**), 6.59/–75.4.

^{31}P NMR (202.5 MHz, 298 K, MeCN-d_3): δ [ppm] = –144.63 (hpt., $^{1}J_{\mathrm{PF}}$ = 707.0 Hz)

^{19}F NMR (471 MHz, 298 K, MeCN-d_3): δ [ppm] = –72.68 (d, $^{1}J_{\mathrm{PF}}$ = 707.0 Hz).

^{1}H^{1}H DOSY NMR (500 MHz, 298 K, MeCN-d_3): $D_{298\mathrm{K}}$ [m$^{2}\cdot$s^{-1}] = $7.74\cdot10^{-10}$.

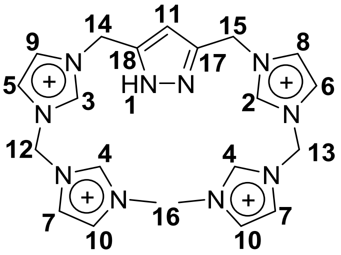

243 K:

^{1}H NMR (500 MHz, 243 K, MeCN-d_3): δ [ppm] = 11.52 (s, 1H, NH **1**), 8.79 (s, 1H, $_{\mathrm{Im}}$H **2**), 8.76 (s, 1H, $_{\mathrm{Im}}$H **3**), 8.68 (s, 2H, $_{\mathrm{Im}}$H **4**), 7.57 (d, $^{3}J_{\mathrm{HH}}$ = 1.68 Hz, 1H, $_{\mathrm{Im}}$H **5**), 7.56 (d, $^{3}J_{\mathrm{HH}}$ = 1.61 Hz, 1H, $_{\mathrm{Im}}$H **6**) 7.54 (dd, $^{3}J_{\mathrm{HH}}$ = 1.98 Hz, 2H, $_{\mathrm{Im}}$H **7**), 7.45 (d, $^{3}J_{\mathrm{HH}}$ = 1.58 Hz, 1H, $_{\mathrm{Im}}$H **8**), 7.44 (d, $^{3}J_{\mathrm{HH}}$ = 1.58 Hz, 1H, $_{\mathrm{Im}}$H **9**), 7.42 (br s, 2H, $_{\mathrm{Im}}$H **10**), 6.56 (s, 1H, H$^{\mathrm{pz}}$ **11**), 6.32 (s, 2H, H **12**), 6.31 (s, 2H, H **13**), 5.41 (s, 2H, H **14**), 5.34 (s, 2H, H **15**), 3.84 (s, 6H, H **16**).

^{13}C{^{1}H} NMR (126 MHz, 243 K, MeCN-d_3): δ [ppm] = 146.1 (C$_{\mathrm{quart.}}$–**17**), 146.0 (C$_{\mathrm{quart.}}$–**18**), 137.9 (C–**4**), 137.6 (C–**3**), 137.4 (C–**2**), 125.6 (C–**10**), 124.3 (C–**8**), 124.0 (C–**9**), 123.2 (C–**5**), 122.9 (C–**6**), 122.6 (C–**7**), 107.5 (C–**11**), 59.1 (C–**12**), 59.1 (C–1**3**), 47.3 (C–**15**), 44.2 (C–**14**), 37.1 (C–**16**).

^{1}H^{1}H NOESY NMR (500 MHz, 243 K, MeCN-d_3): δ [ppm] = 11.52/8.79 (NH **1** & $_{\text{Im}}$H **2**), 11.52/8.76 (NH **1** & $_{\text{Im}}$H **3**), 11.52/6.56 (NH **1** & H$^{\text{pz}}$ **11**), 11.52/5.41 (NH **1** & H **14**), 11.52/5.34 (NH **1** & H **15**), 8.79//8.76/7.57 ($_{\text{Im}}$H **2**/$_{\text{Im}}$H **3** & $_{\text{Im}}$H **5**), 8.79//8.76/7.56 ($_{\text{Im}}$H **2**/$_{\text{Im}}$H **3** & $_{\text{Im}}$H **6**), 8.79//8.76/7.54 ($_{\text{Im}}$H **2**/$_{\text{Im}}$H **3** & $_{\text{Im}}$H **7**), 8.79//8.76/7.45 ($_{\text{Im}}$H **2**/$_{\text{Im}}$H **3** & $_{\text{Im}}$H **8**), 8.79//8.76/7.44 ($_{\text{Im}}$H **2**/$_{\text{Im}}$H **3** & $_{\text{Im}}$H **9**), 8.79//8.76/6.56 ($_{\text{Im}}$H **2**/$_{\text{Im}}$H **3** & H$^{\text{pz}}$ **11**), 8.79//8.76/6.32 ($_{\text{Im}}$H **2**/$_{\text{Im}}$H **3** & H **12**), 8.79//8.76/6.31 ($_{\text{Im}}$H **2**/$_{\text{Im}}$H **3** & H **13**), 8.79//8.76/5.41 ($_{\text{Im}}$H **2**/$_{\text{Im}}$H **3** & H **14**), 8.79//8.76/5.34 ($_{\text{Im}}$H **2**/$_{\text{Im}}$H **3** & H **15**), 8.68/7.57 ($_{\text{Im}}$H **4** & $_{\text{Im}}$H **5**), 8.68/7.56 ($_{\text{Im}}$H **4** & $_{\text{Im}}$H **6**), 8.68/7.54 ($_{\text{Im}}$H **4** & $_{\text{Im}}$H **7**), 8.68/7.42 ($_{\text{Im}}$H **4** & $_{\text{Im}}$H **10**), 8.68/6.32 ($_{\text{Im}}$H **4** & H **12**), 8.68/6.31 ($_{\text{Im}}$H **4** & H **13**), 8.68/3.84 ($_{\text{Im}}$H **4** & H **16**), 7.57//7.56/7.45 ($_{\text{Im}}$H **5**/ $_{\text{Im}}$H **6** & $_{\text{Im}}$H **8**), 7.57//7.56/7.44 ($_{\text{Im}}$H **5**/ $_{\text{Im}}$H **6** & $_{\text{Im}}$H **9**), 7.57//7.56/6.32 ($_{\text{Im}}$H **5**/ $_{\text{Im}}$H **6** & H **12**), 7.57//7.56/6.31 ($_{\text{Im}}$H **5**/$_{\text{Im}}$H **6** & H **13**), 7.57//7.56/5.41 ($_{\text{Im}}$H **5**/$_{\text{Im}}$H **6** & H **14**), 7.57//7.56/5.34 ($_{\text{Im}}$H **5**/$_{\text{Im}}$H **6** & H **15**), 7.54/7.42 ($_{\text{Im}}$H **7** & $_{\text{Im}}$H **10**), 7.54/6.32 ($_{\text{Im}}$H **7** & H **12**), 7.54/6.31 ($_{\text{Im}}$H **7** & H **13**), 7.45//7.44/6.56 ($_{\text{Im}}$H **8**/$_{\text{Im}}$H **9** & H$^{\text{pz}}$ **11**), 7.45//7.44/6.32 ($_{\text{Im}}$H **8**/$_{\text{Im}}$H **9** & H **12**), 7.45//7.44/5.41 ($_{\text{Im}}$H **8**/$_{\text{Im}}$H **9** & H **14**), 7.45//7.44/5.34 ($_{\text{Im}}$H **8**/$_{\text{Im}}$H **9** & H **15**), 7.42/6.32 ($_{\text{Im}}$H **10** & H **12**), 7.42/6.31 ($_{\text{Im}}$H **10** & H **13**), 7.42/3.84 ($_{\text{Im}}$H **10** & H **16**), 6.56/5.41 (H$^{\text{pz}}$ **11** & H **14**), 6.56/5.34 (H$^{\text{pz}}$ **11** & H **15**).

^{1}H^{13}C HSQC NMR (^{1}H NMR, 500 MHz, ^{13}C NMR, 126 MHz, 243 K, MeCN-d_3): δ [ppm] = 8.79/17.4, 8.76/137.6, 8.68/137.9, 7.57/123.2, 7.56/122.9, 7.54/122.6, 7.45/124.3, 7.44/124.0, 7.42/125.6, 6.56/107.5, 6.32/59.1, 6.31/59.1, 5.41/44.2, 5.34/47.3, 3.84/37.1.

^{1}H^{13}C HMBC NMR (^{1}H NMR, 500 MHz, ^{13}C NMR, 126 MHz, 243 K, MeCN-d_3): δ [ppm] = 11.52/146.1 (NH **1** & C$_{\text{quart.}}$–**17**), 11.52/146.0 (NH **1** & C$_{\text{quart.}}$–**18**), 11.52/107.5 (NH **1** & C–**11**), 8.79/124.3 ($_{\text{Im}}$H **2** & C–**8**), 8.79/122.9 ($_{\text{Im}}$H **2** & C–**6**), 8.76/124.0 ($_{\text{Im}}$H **3** & C–**9**), 8.76/123.2 ($_{\text{Im}}$H **3** & C–**5**), 8.76/44.2 ($_{\text{Im}}$H **3** & C–**14**), 8.68/125.6 ($_{\text{Im}}$H **4** & C–**10**), 8.68/122.6 ($_{\text{Im}}$H **4** & C–**7**), 8.68/59.1 ($_{\text{Im}}$H **4** & C–**12**/C–**13**), 8.68/37.1 ($_{\text{Im}}$H **4** & C–**16**), 7.57/137.6 ($_{\text{Im}}$H **5** & C–**3**), 7.57/124.0 ($_{\text{Im}}$H **5** & C–**9**), 7.56/137.4 ($_{\text{Im}}$H **6** & C–**2**), 7.56/124.3 ($_{\text{Im}}$H **6** & C–**8**), 7.54/137.9 ($_{\text{Im}}$H **7** & C–**4**), 7.54/125.6 ($_{\text{Im}}$H **7** & C–**10**), 7.54/59.1 ($_{\text{Im}}$H **7** & C–**12**/C–**13**), 7.45/137.4 ($_{\text{Im}}$H **8** & C–**2**), 7.45/122.9 ($_{\text{Im}}$H **8** & C–**6**), 7.44/137.6 ($_{\text{Im}}$H **9** & C–**3**), 7.44/123.2 ($_{\text{Im}}$H **9** & C–**5**), 7.42/137.9 ($_{\text{Im}}$H **10** & C–**4**), 7.42/122.6 ($_{\text{Im}}$H **10** & C–**7**), 7.42/37.1 ($_{\text{Im}}$H **10** & C–**16**), 6.56/146.1 (H$^{\text{pz}}$ **11** & C$_{\text{quart.}}$–**17**), 6.56/146.0 (H$^{\text{pz}}$ **11** & C$_{\text{quart.}}$–**17**), 6.56/44.2 (H$^{\text{pz}}$ **11** & C–**14**), 6.32//6.31/137.9 (H **12**/**13** & C–**4**), 6.32//6.31/137.6 (H **12**/**13** & C–**3**), 6.32//6.31/137.4 (H **12**/**13** & C–**2**), 6.32//6.31/123.2 (H **12**/**13** & C–**5**), 6.32//6.31/122.9 (H **12**/**13** & C–**6**), 6.32//6.31/122.6 (H **12**/**13** & C–**7**), 5.41/146.0 (H **14** & C$_{\text{quart.}}$–**18**), 5.34/146.1 (H **15** & C$_{\text{quart.}}$–**17**), 5.41/137.6 (H **14** & C–**3**), 5.41/124.0 (H **14** & C–**9**), 5.41/107.5 (H **14** &

C–**11**), 5.34/137.4 (H **15** & C–**2**), 5.34/124.3 (H **15** & C–**8**), 5.34/107.5 (H **15** & C–**11**), 3.84/137.9 (H **16** & C–**4**), 3.84/125.6 (H **16** & C–**10**).

^{1}H^{15}N HSQC NMR (^{1}H NMR, 500 MHz, ^{15}N NMR**,** 50.7 MHz**,** 243 K, MeCN-d_3): δ [ppm] = 11.45/–176.1.

^{1}H^{15}N HMBC NMR (^{1}H NMR, 500 MHz, ^{15}N NMR, 50.7 MHz, 243 K, MeCN-d_3): δ [ppm] = 11.52/–76.3, 8.79/–203.6, 8.79/–194.5, 8.76/–203.1, 8.76/–196.2, 8.68/–205.0, 8.68/–204.0, 7.57/–203.1, 7.57/–196.2, 7.56/–194.5, 7.54/–205.0, 7.54/–204.0, 7.45/–203.6, 7.45/–194.5, 7.44/–203.1, 7.44/–196.2, 7.42/–205.0, 7.42/–204.0, 6.56/–176.1, 6.56/–76.3, 6.32/–205.0, 6.32/–203.1, 6.31/–205.0, 6.31/–203.6, 5.41/–196.2, 5.41/–176.1, 5.34/–194.5, 5.34/–76.3, 3.84/–204.0.

^{1}H DOSY NMR (500 MHz, 243 K, MeCN-d_3): D_{243K} [$m^2 \cdot s^{-1}$] = $3.17 \cdot 10^{-10}$.

Elemental analysis of $C_{21}H_{28}N_{10}P_4F_{24}$

Calculated: **C** 25.21%; **H** 2.82%; **N** 14.00%.

Found: **C** 25.35%; **H** 2.71%; **N** 14.02%.

ESI-MS (MeCN) *m/z* (%): 855 (18.8) $[C_{21}H_{28}N_{10}(PF_6)_3]^+$, 401 (36.5) $[C_{20}H_{21}N_{10}]^+$ 355 (100) $[C_{21}H_{28}N_{10}(PF_6)_2]^{2+}$, 163 (91.3) $[C_8H_{11}N_4]^+$.

IR (MeCN): υ [cm^{-1}] = 3171.0 (w), 3152.4 (w), 3116.9 (w), 2945.5 (w), 1586.4 (w), 1552.9 (w), 1334.8 (w), 1172.6 (m), 848.2 (P–F$_{asym.}$, s).

The synthesis route as well as the analytic data of **$[H_5L^6](PF_6)_4$** were published in *Z. Anorg. Allg. Chem.* **2019**, *645*, 605. © 2019 JOHN WILEY AND SONS.

$[H_5L^7](PF_6)_4$

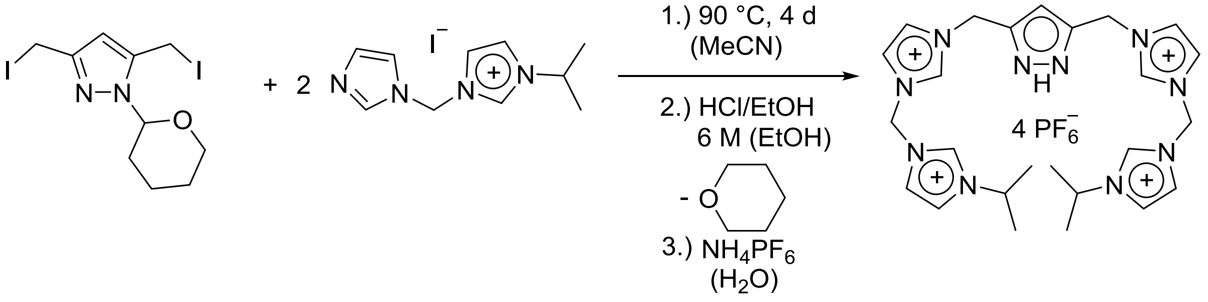

$C_3H_4N_2$	$C_{10}H_{15}N_4I$	$C_{25}H_{36}N_{10}P_4F_{24}$
432 g/mol	318 g/mol	1056 g/mol

3,5-bis(iodomethyl)-1-tetrahydropyran-*2*-yl pyrazole (0.402 g, 0.930 mmol, 1.00 equiv.) was dissolved in MeCN (150 mL). **q** (0.681 g, 2.14 mmol, 2.30 equiv.) was added in portions to the solution. The solution was heated for 4 days at 90 °C. Afterwards, the solvent was removed *in vacuo*. The gained red-brownish solid was dried at a high vacuum line overnight. The dried solid was dissolved in MeOH (30 mL) and a mixture of HCl/EtOH (6 M, 30 mL) was added. The solution was stirred for 20 min and diethylether was added until a precipitation appeared. The brownish solid was filtered off, washed with Et_2O and was dried at the high vacuum line for several hours. An off-white solid was dissolved in demineralized water (150 mL). Excess of NH_4PF_6 was added in portions to the solution and stored at –30 °C overnight. The off-white precipitate was filtered off, washed several times with water and was dried at the high vacuum line. An off-white solid was obtained in 8% yield (76.7 mg, 0.0725 mmol).

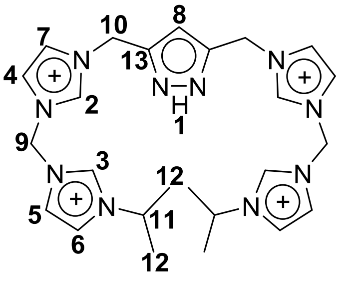

^{1}H NMR (500 MHz, 298 K, MeCN-d_3): δ [ppm] = 11.48 (br s, 1H, NH **1**), 8.81 (br s, 2H, $_{\text{Im}}$H **2**), 8.77 (dd, $^3J_{HH}$ = 1.50 Hz, 2H, $_{\text{Im}}$H **3**), 7.63 (br s, 2H, $_{\text{Im}}$H **4**), 7.60 (dd, $^3J_{HH}$ = 1.90 Hz, 2H, $_{\text{Im}}$H **5**), 7.57 (dd, $^3J_{HH}$ = 1.76 Hz, 2H, $_{\text{Im}}$H **6**), 7.49 (br s, 2H, $_{\text{Im}}$H **7**), 6.60 (s, 1H, H^{pz} **8**), 6.35 (s, 4H, H **9**), 5.41 (br s, 2H, H **10**), 4.65 (hpt, $^3J_{HH}$ = 6.70 Hz, 2H, H **11**), 1.53 (d, $^3J_{HH}$ = 6.70 Hz, 12H, H **12**).

^{13}C{^{1}H} NMR (126 MHz, 298 K, MeCN-d_3): δ [ppm] = 146.4 (C$_{\text{quart.}}$–**13**), 138.0 (C–**2**), 136.5 (C–**3**), 124.6 (C–**7**), 123.8 (C–**4**), 123.7 (C–**4**), 123.4 (C–**5**), 122.9 (C–**6**), 108.0 (C–**8**), 59.8 (C–**9**), 55.1 (C–**11**), 48.0 (C–**10**), 44.8 (C–**10**), 22.5 (C–**12**).

^{1}H^{1}H COSY NMR (500 MHz, 298 K, MeCN-d_3): δ [ppm] = 8.81/7.49 ($_{\text{Im}}$H **2** & $_{\text{Im}}$H **7**), 8.81/7.63 ($_{\text{Im}}$H **2** & $_{\text{Im}}$H **4**), 8.81/6.35 ($_{\text{Im}}$H **2** & $_{\text{Im}}$H **9)**, 8.77/7.57 ($_{\text{Im}}$H **3** & $_{\text{Im}}$H **6**), 8.77/7.60 ($_{\text{Im}}$H **3** & $_{\text{Im}}$H **5**), 8.77/6.35 ($_{\text{Im}}$H **3** & $_{\text{Im}}$H **9)**,7.63/7.49 ($_{\text{Im}}$H **4** & $_{\text{Im}}$H **7**), 7.63/6.35 ($_{\text{Im}}$H **4** & $_{\text{Im}}$H **9**), 7.60/7.7.57 ($_{\text{Im}}$H **5** & $_{\text{Im}}$H **6**), 7.60/6.35 ($_{\text{Im}}$H **5** & H **9**), 4.65/1.53 (H **11** & H **12**).

^{1}H^{1}H NOESY NMR (500 MHz, 298 K, MeCN-d_3): δ [ppm] = 8.81/6.60 ($_{\text{Im}}$H **2** & H$^{\text{pz}}$ **8**), 8.81/6.35 ($_{\text{Im}}$H **2** & H **9**), 8.81/5.41 ($_{\text{Im}}$H **2** & H **10**), 8.77/7.60 ($_{\text{Im}}$H **3** & $_{\text{Im}}$H **5**), 8.77/7.57 ($_{\text{Im}}$H **3** & $_{\text{Im}}$H **6**), 8.77/6.35 ($_{\text{Im}}$H **3** & H **9**), 8.77/4.65 ($_{\text{Im}}$H **3** & H **11**), 8.77/1.53 ($_{\text{Im}}$H **3** & H **12**), 7.63/7.49 ($_{\text{Im}}$H **4** & $_{\text{Im}}$H **7**), 7.63/6.35 ($_{\text{Im}}$H **4** & H **9**), 7.60/6.35 ($_{\text{Im}}$H **5** & H **9**), 7.57/4.65 ($_{\text{Im}}$H **6** & H **11**), 7.57/1.53 ($_{\text{Im}}$H **6** & H **12**), 7.49/6.60 ($_{\text{Im}}$H **7** & H$^{\text{pz}}$ **8**), 7.49/5.41 ($_{\text{Im}}$H **7** & H **10**), 6.60/5.41 (H$^{\text{pz}}$ **8** & H **10**), 6.35/1.53 (CH$_2$ **9** & H **12**), 4.65/1.53 (H **11** & H **12**).

^{1}H^{13}C HSQC NMR (^{1}H NMR, 500 MHz, ^{13}C NMR, 126 MHz, 298 K, MeCN-d_3): δ [ppm] = 8.81/138.0, 8.77/136.5, 7.63/123.8, 7.63/123.7, 7.60/123.4, 7.57/122.9, 7.49/124.6, 6.60/108.0, 6.35/59.8, 5.41/48.0, 5.41/44.8, 4.65/55.1, 1.53/22.5.

^{1}H^{13}C HMBC NMR (^{1}H NMR, 500 MHz, ^{13}C NMR, 126 MHz, 298 K, MeCN-d_3): δ [ppm] **=** 8.77/122.9 ($_{\text{Im}}$H **3** & C–**6**), 8.77/123.4 ($_{\text{Im}}$H **3** & C–**5**), 8.77/59.8 ($_{\text{Im}}$H **3** & C–**9**), 7.63/138.0 ($_{\text{Im}}$H **4** & C–**2**), 7.63/124.6 ($_{\text{Im}}$H **4** & C–**7**), 7.60/136.5 ($_{\text{Im}}$H **5** & C–**3**), 7.60/122.9 ($_{\text{Im}}$H **5** & C–**6**), 7.57/136.5 ($_{\text{Im}}$H **6** & C–**3**), 7.57/123.4 ($_{\text{Im}}$H **6** & C–**5**), 7.49/138.0 ($_{\text{Im}}$H **7** & C-**2**), 6.35/138.0 (H **9** & C–**2**), 6.35/136.5 (H **9** & C–**3**), 6.35/123.4 (H **9** & C–**5**), 6.35/123.8 (H **9** & C–**4**), 6.35/123.7 (H **9** & C–**4**), 4.65/136.5 (H **11** & C–**3**), 4.65/122.9 (H **11** & C–**6**), 4.65/22.5 (H **11** & C–**12**), 1.53/55.1 (H **12** & C–**11**).

^{1}H^{15}N HMBC NMR (^{1}H NMR, 500 MHz, ^{15}N NMR, 50.7 MHz, 298 K, MeCN-d_3): δ [ppm] = 8.77/–205.9, 7.60/–205.9, 7.57/–205.9, 6.35/–205.9, 8.77/–178.2, 7.60/–178.2, 7.57/–178.2, 1.53/–178.2, 6.60/–175.9.

ESI-MS (MeCN) *m/z* (%): 911 (85) [$C_{25}H_{37}N_{10}(PF_6)_3$]$^{+}$.

$[H_5L^8](PF_6)_4$

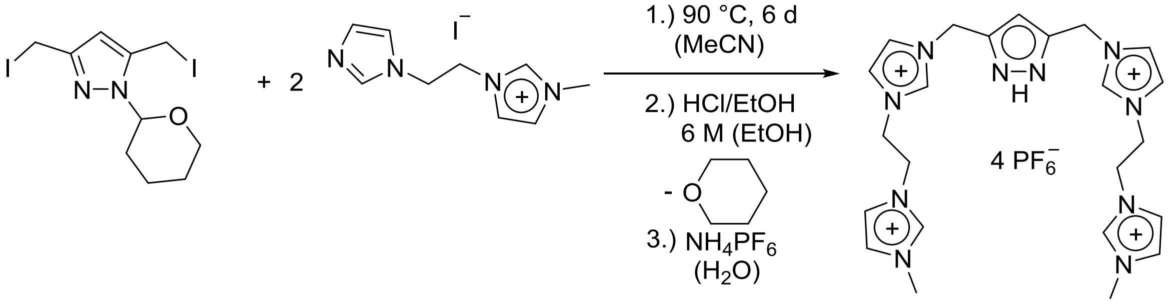

$C_3H_4N_2$	$C_9H_{13}N_4I$	$C_{23}H_{32}N_{10}P_4F_{24}$
432 g/mol	304 g/mol	1028 g/mol

3,5-bis(iodomethyl)-1-tetrahydropyran-2-yl pyrazole (621 mg, 1.43 mmol, 1.00 equiv.) was dissolved in MeCN (150 mL). **p** (1.06 g, 3.48 mmol, 2.42 equiv.) was added in portions to the solution. The solution was heated to reflux for 6 days at 90 °C. $[\mathbf{H_5L^8}]\mathbf{I_4}$ was isolated from a red-orange solution in 15% yield as a white precipitate and was washed with Et_2O. Afterwards, the solvent of the separated solution was removed *in vacuo*. The red-brownish solid was dried at a high vacuum line overnight. The dried solid was dissolved in EtOH (30 mL) and a mixture of HCl/EtOH (6 M, 15 mL) was added. The solution was stirred for 30 min and diethylether (60 mL) was added until a precipitation appeared. The yellow solid was filtered off, washed with Et_2O and was dried at the high vacuum line for several hours. An off-white solid was dissolved in demineralized water (150 mL). Excess of NH_4PF_6 was added in portions to the solution and stored at –30 °C overnight. The off-white precipitate was filtered off, washed several times with water and was dried at the high vacuum line. An off-white solid was obtained in 44% yield (650 mg, 0.632 mmol).

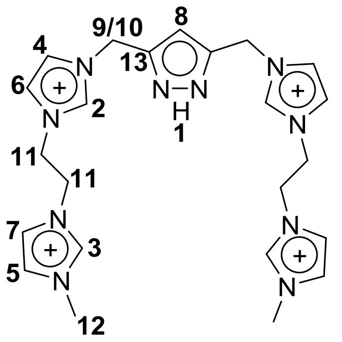

^{1}H NMR (300 MHz, 298 K, DMSO-d_6): δ [ppm] = 13.22 (br s, 1H, NH **1**), 9.07 (d, $^{3}J_{\text{HH}}$ = 10.5 Hz, 2H, $_{\text{Im}}$H **2**), 8.96 (s, 2H, $_{\text{Im}}$H **3**), 7.72 (t, $^{3}J_{\text{HH}}$ = 1.70 Hz, 2H, $_{\text{Im}}$H **4**), 7.69 (dd, $^{3}J_{\text{HH}}$ = 1.70 Hz, 2H, $_{\text{Im}}$H **5**), 7.63 (br s, 2H, $_{\text{Im}}$H **6**), 7.54 (dd, $^{3}J_{\text{HH}}$ = 1.70 Hz, 2H, $_{\text{Im}}$H **7**), 6.43 (s, 1H, H$^{\text{pz}}$ **8**), 5.48 (s, 2H, H **9**), 5.39 (s, 2H, H **10**), 4.66 (s, 8H, H **11**), 3.84 (dd, $^{3}J_{\text{HH}}$ = 1.50 Hz, 2H, H **12**).

^{13}C{^{1}H} NMR (75 MHz, 298 K, DMSO-d_6): δ [ppm] = 145.8 (C$_{\text{quart.}}$–**13**), 137.1 (C–**3**), 136.8 (C–**2**), 124.0 (C–**5**), 123.1 (C–**4** & C–**6**), 122.3 (C–**7**), 105.2 (C–**8**), 48.6 (C–**11**), 48.3 (C–**11**), 46.2 (C–**9** & C–**10**), 43.2 (C–**9** & C–**10**), 36.0 (C–**12**).

^{1}H^{1}H COSY NMR (300 MHz, 298 K, DMSO-d_6): δ [ppm] = 9.07/7.72 ($_{\text{Im}}$H **2** & $_{\text{Im}}$H **4**), 9.07/7.63 ($_{\text{Im}}$H **2** & $_{\text{Im}}$H **6**), 8.96/7.54 ($_{\text{Im}}$H **3** & $_{\text{Im}}$H **7**), 8.96/7.69 ($_{\text{Im}}$H **3** & $_{\text{Im}}$H **5**).

^{1}H^{1}H NOESY NMR (300 MHz, 298 K, DMSO-d_6): δ [ppm] = 9.07/5.48 ($_{\text{Im}}$H **2** & H **9**), 9.07/5.39 ($_{\text{Im}}$H **2** & H **10**), 9.07/4.66 ($_{\text{Im}}$H **2** & H **11**), 8.96/4.66 ($_{\text{Im}}$H **3** & H **11**), 8.96/3.84 ($_{\text{Im}}$H **3** & H **12**), 7.72/6.43 ($_{\text{Im}}$H **4** & H$^{\text{pz}}$ **8**), 7.72/5.48 ($_{\text{Im}}$H **4** & H **9**), 7.72/5.39 ($_{\text{Im}}$H **4** & H 10), 7.69/3.84 ($_{\text{Im}}$H **5** & H **12**), 7.63/4.66, ($_{\text{Im}}$H **5** & H **11**), 7.54/4.66 ($_{\text{Im}}$H **7** & H **11**), 6.43/5.48 (H$^{\text{pz}}$ **8** & H **9**), 6.43/5.39 (H$^{\text{pz}}$ **8** & H **10**).

^{1}H^{13}C HSQC NMR (^{1}H NMR, 300 MHz, ^{13}C NMR, 75 MHz, 298 K, DMSO-d_6): δ [ppm] = 9.07/136.8, 8.96/137.1, 7.72/123.1, 7.69/124.0, 7.63/123.1, 7.54/122.3, 6.43/105.2, 5.48/43.2, 5.39/46.2, 4.66/48.6, 4.66/48.3, 3.84/36.0.

^{1}H^{13}C HMBC NMR (^{1}H NMR, 300 MHz, ^{13}C NMR, 75 MHz, 298 K, DMSO-d_6): δ [ppm] **=** 7.72/136.8 ($_{\text{Im}}$H **4** & C–**2**), 7.69/137.1 ($_{\text{Im}}$H **5** & C–**3**), 7.54/137.1 ($_{\text{Im}}$H **7** & C–**3**), 6.43/145.8 (H$^{\text{pz}}$ **8** & C$_{\text{quart.}}$–**13**), 5.48/136.8 (H **9/10** & C–**2**), 5.39/145.8 (H **10** & C$_{\text{quart.}}$–**13**).

^{31}P NMR (121.5 MHz, 298 K, MeCN-d_3): δ [ppm] = –144.20 (hpt., $^{1}J_{\text{PF}}$ = 711.3 Hz)

^{19}F NMR (471 MHz, 298 K, MeCN-d_3): δ [ppm] = –72.68 (d, $^{1}J_{\text{PF}}$ = 707.0 Hz).

Elemental analysis of $C_{23}H_{32}N_{10}P_4F_{24}$

Calculated: **C** 26.86%; **H** 3.14%; **N** 13.62%.

Found: **C** 27.34%; **H** 3.28%; **N** 13.82%.

ESI-MS $H_5L^8(PF_6)_4$ (MeCN) *m/z* (%):883 (100) [$C_{23}H_{32}N_{10}(PF_6)_3$]$^{+}$.

ESI-MS $H_5L^8(ClO_4)_4$ (MeCN) *m/z* (%):747 (90) [$C_{23}H_{32}N_{10}(ClO_4)_3$]$^{+}$.

The synthesis route as well as the analytic data of **[H_5L^8](PF_6)$_4$** were published in *Z. Anorg. Allg. Chem.* **2019**, *645*, 605. © 2019 JOHN WILEY AND SONS.

$[H_5L^9](PF_6)_4$

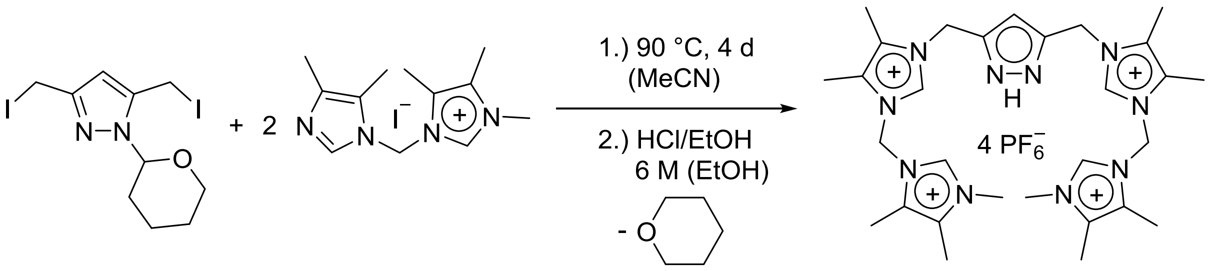

$C_3H_4N_2$	$C_{12}H_{19}N_4I$	$C_{29}H_{43}N_{10}P_4F_{24}$
432 g/mol	346 g/mol	1112 g/mol

3,5-bis(iodomethyl)-1-tetrahydropyran-*2*-yl pyrazole (1.24 g, 2.87 mmol, 1.00 equiv.) was dissolved in MeCN (150 mL). **r** (2.18 g, 6.29 mmol, 2.19 equiv.) was added in portions to the solution. The solution was heated for 4 days at 90 °C. Afterwards, the solvent was removed *in vacuo*. The gained red-brownish solid was dried at a high vacuum line overnight. The dried solid was suspended in MeOH (40 mL) and a mixture of HCl/EtOH (6 M, 30 mL) was added. The solution was stirred for 20 min and Et_2O was added until a precipitation appeared. The yellow solid was filtered off, washed with Et_2O and was dried at the high vacuum line for several hours. An off-white solid was dissolved in demineralized water (150 mL). Excess of NH_4PF_6 was added in portions to the solution and stored at –30 °C overnight. The off-white precipitate was filtered off, washed several times with water and was dried at the high vacuum line. An off-white solid was obtained in 13% yield (430 mg, 0.386 mmol).

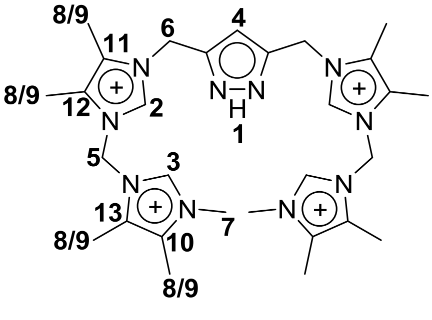

^{1}H NMR (300 MHz, 298 K, DMSO-*d*$_6$): δ [ppm] = 11.36 (br s, 1H, NH **1**), 8.56 (s, 2H, $_{\mathrm{Im}}$H **2**), 8.48 (s, 2H, $_{\mathrm{Im}}$H **3**), 6.41 (s, 1H, H$^{\mathrm{pz}}$ **4**), 6.24 (s, 4H, H **5**), 5.31 (br s, 4H, H **6**), 3.73 (s, 6H, H **7**), 2.20 (m, 24H, H **8** & **9**).

^{13}C{^{1}H} NMR (75 MHz, 298 K, DMSO-*d*$_6$): δ [ppm] = 136.4 (C–**2**), 136.1 (C–**3**), 130.6 (C–**10**), 130.3 (C–**11**), 128.9 (C–**12**), 128.1 (C–**13**), 106.8 (C–**4**), **57.2** (C–**5**), 34.9 (C–**6**), 8.76–8.34 (C–**8** & C–**9**).

$^1H^1H$ NOESY NMR (300 MHz, 298 K, MeCN-d_3): δ [ppm] = 8.56/6.24 ($_{Im}$H **2** & H **5**), 8.56/5.31 ($_{Im}$H **2** & H **6**), 8.56/2.20 ($_{Im}$H **2** & H **8** & **9**), 8.48/6.24 ($_{Im}$H **3** & H **5**), 8.48/3.73 ($_{Im}$H **3** & H **7**), 8.48/2.20 ($_{Im}$H **3** & H **8** & **9**), 6.41/5.31 (H^{pz} **4** & H **6**), 6.41/2.20 (H^{pz} **4** & H **8** & **9**), 6.24/2.20 (H **5** & H **8** & **9**), 5.31/2.20 (H **6** & H **8** & **9**), 3.73 (H **7** & H **8** & **9**).

$^1H^{13}C$ HSQC NMR (^{1}H NMR, 300 MHz, ^{13}C NMR, 75 MHz, 298 K, MeCN-d_3): δ [ppm] = 8.56/136.2, 8.48/136.1, 6.41/106.8, 6.24/57.2, 5.31/34.9, 2.20/8.76–8.34.

$^1H^{13}C$ HMBC NMR (^{1}H NMR, 300 MHz, ^{13}C NMR, 75 MHz, 298 K, MeCN-d_3): δ [ppm] **=** 8.56/130.3 ($_{Im}$H **2** & C–**11**), 8.56/128.9 ($_{Im}$H **2** & C–**12**), 8.48/130.6 ($_{Im}$H **3** & C–**10**), 8.48/128.1 ($_{Im}$H **3** & C–**13**), 6.24/136.2 (H **5** & C–**2**), 6.24/136.1 (H **5** & C–**3**), 6.24/128.9 (H **5** & C–**12**), 6.24/128.1 (H **5** & C–**13**), 5.31/136.2 (H **6** & C–**2**), 5.31/130.3 (H **6** & C–**11**), 5.31/106.8 (H **6** & C–**4**), 3.73/136.1 (H **7** & C–**3**), 3.73/130.6 (H **7** & C–**10**).

ESI-MS (MeCN) *m/z* (%):967 (100) $[C_{29}H_{43}N_{10}(PF_6)_3]^+$.

$[L^6Ag_6](PF_6)_4$

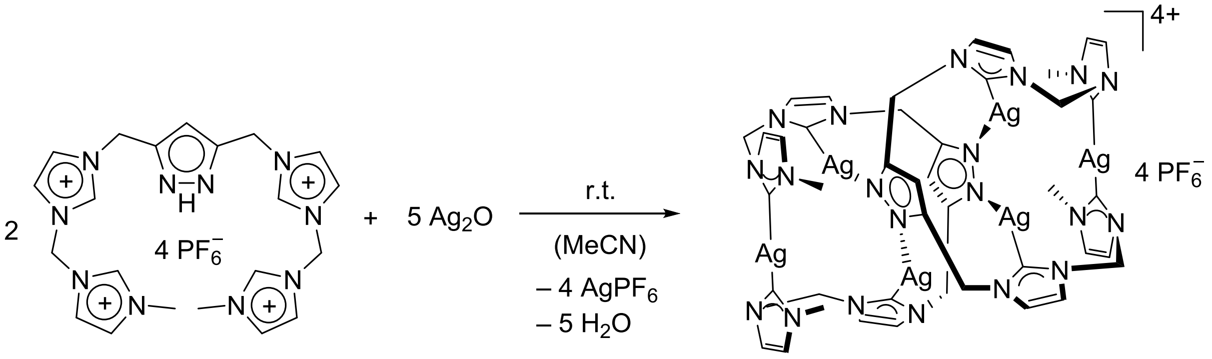

$C_{21}H_{28}N_{10}P_4F_{24}$	Ag_2O	$Ag_6C_{42}H_{46}N_{20}P_4F_{24}$
1000 g/mol	232 g/mol	2058 g/mol

$[H_5L^6](PF_6)_4$ (350 mg, 350 μmol, 1.00 equiv.) was dissolved in MeCN (100 mL) and silver(I) oxide (243 mg, 1.05 mmol, 3.00 equiv.) was added. The resulting suspension was heated at 55 °C for 25 hours. The solid material was removed by filtration over Celite®, after the suspension was cooled down to room temperature. The solvent of the brown solution was removed under reduced pressure and MeCN (50 mL) was added to the black residue. A white solid was obtained in 54% yield (195 mg, 94.8 μmol) by fractionated precipitation of the compound with diethyl ether.

ESI-MS (MeCN) *m/z* (%): 1912 (100) $[Ag_6(C_{21}H_{23}N_{10})_2(PF_6)_3]^+$.

Elemental analysis of $Ag_6C_{42}H_{46}N_{20}P_4F_{24}$

Calculated: **C** 24.51%; **H** 2.25%; **N** 13.61%.

Found: **C** 24.27%; **H** 2.70%; **N** 12.83%.

The synthesis route as well as the analytic data of **$[L^6Ag_6](PF_6)_4$** were published in *Z. Anorg. Allg. Chem.* **2019**, *645*, 605. © 2019 JOHN WILEY AND SONS.

[L^{8}Ag$_6$](PF$_6$)$_4$

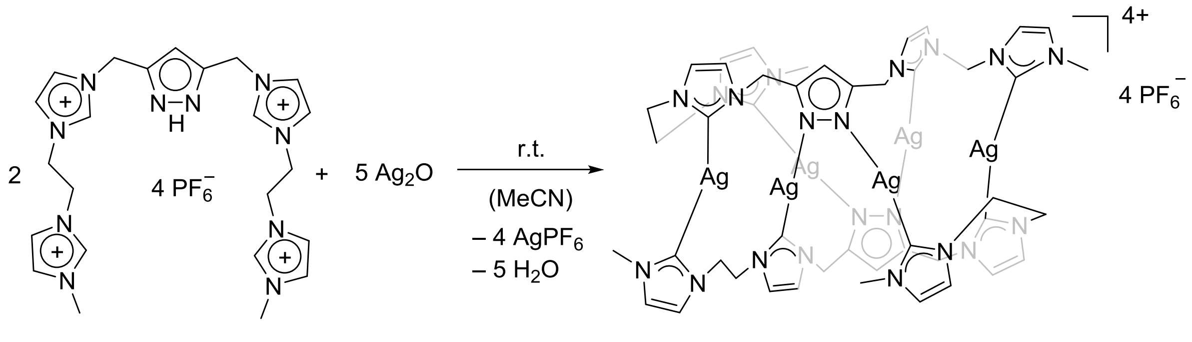

$C_{23}H_{32}N_{10}P_4F_{24}$	Ag_2O	$Ag_6C_{46}H_{54}N_{20}P_4F_{24}$
1028 g/mol	232 g/mol	2114 g/mol

[H$_5$L^8](PF$_6$)$_4$ (350 mg, 340 *µ*mol, 1.00 equiv.) was dissolved in MeCN (100 mL) and silver(I) oxide (237 mg, 1.02 mmol, 3.00 equiv.) was added. The resulting suspension was heated at 55 °C for 25 hours. The solid material was removed by filtration over Celite®, after the suspension was cooled down to room temperature. The solvent of the brown solution was removed under reduced pressure and acetone (50 mL) was added to the brown oil. A white solid was obtained in 60% yield (214 mg, 101 *µ*mol) by fractionated precipitation of the compound with diethyl ether.

ESI-MS (MeCN) *m/z* (%): 1969 (5) $[Ag_6(C_{23}H_{27}N_{10})_2(PF_6)_3]^+$, 912 (63) $[Ag_5(C_{23}H_{27}N_{10})_2(PF_6)_2]^+$.

Elemental analysis of $Ag_6C_{46}H_{54}N_{20}P_4F_{24}$

Calculated: **C** 26.13%; **H** 2.58%; **N** 13.25%.

Found: **C** 26.04%; **H** 2.91%; **N** 13.10%.

The synthesis route as well as the analytic data of **[L^{8}Ag$_6$](PF$_6$)$_4$** were published in *Z. Anorg. Allg. Chem.* **2019**, *645*, 605. © 2019 JOHN WILEY AND SONS.

$[L^6Cu_6](PF_6)_4$

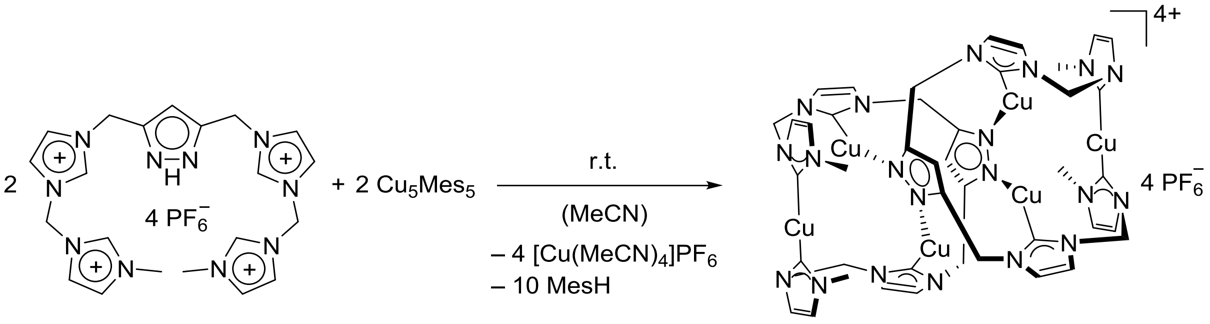

$C_{21}H_{28}N_{10}P_4F_{24}$ CuC_9H_{11} $Cu_6C_{42}H_{46}N_{20}P_4F_{24}$

1000 g/mol 183 g/mol 1792 g/mol

$[H_5L^6](PF_6)_4$ (308 mg, 308 μmol, 1.00 equiv.) and mesitylcopper(I) (290 mg, 1.58 mmol, 5.15 equiv.) were suspended in MeCN (50 mL). The yellow solution was allowed to react for 3 days at ambient temperature. The solvent volume was reduced to 5 mL *in vacuo* and a precipitation was formed after addition of Et_2O to the solution. The solution was removed by cannulation and the colorless solid was washed several times with Et_2O. After the solution was removed by cannulation, the solid was dried under reduced pressure. A colorless solid was obtained in 74% yield (203 mg, 0.113 mmol).

ESI-MS (MeCN) *m/z* (%): 646 (9) $[Cu_5(C_{21}H_{23}N_{10})_2PF_6]^{2+}$, 382 (100) $[Cu_5(C_{21}H_{23}N_{10})_2]^{3+}$
UV-vis (EtCN, 293 K): $\lambda_{max.}$ [nm] (ε 10^3 [$M^{-1}\cdot cm^{-1}$]) = 266 (38.32), 315 (16.90).

$[\mathbf{L^8Cu_6}](\mathbf{PF_6})_4$

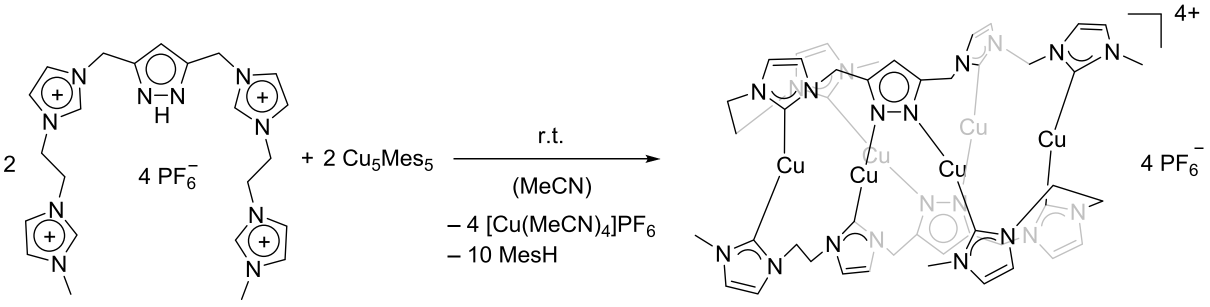

$C_{23}H_{32}N_{10}P_4F_{24}$	CuC_9H_{11}	$Cu_6C_{46}H_{54}N_{20}P_4F_{24}$
1028 g/mol	183 g/mol	1848 g/mol

$[H_5L^8](PF_6)_4$ (420 mg, 409 μmol, 1.00 equiv.) and mesitylcopper(I) (385 mg, 2.10 mmol, 5.14 equiv.) were suspended in MeCN (40 mL). The yellow solution was allowed to react for 4 days at ambient temperature. The solvent volume was reduced to 4 mL *in vacuo* and a precipitation was formed after addition of Et_2O to the solution. The solution was removed by cannulation and the colorless solid was washed several times with Et_2O. After the solution was removed by cannulation, the solid was dried under reduced pressure. A colorless solid was obtained in 73% yield (275 mg, 0.148 mmol).

ESI-MS (MeCN) *m/z* (%): 1993 (5) $[Cu_6(C_{23}H_{27}N_{10})_2(PF_6)_5]^-$, 1783 (20) $[Cu_5(C_{23}H_{27}N_{10})_2(PF_6)_4]^-$.
UV-vis (EtCN, 293 K): $\lambda_{max.}$ [nm] (ε 10^3 [$M^{-1}\cdot cm^{-1}$]) = 310 (16.71), 357 (6.45)

$[L^6Ni_2(OH)](PF_6)_2$

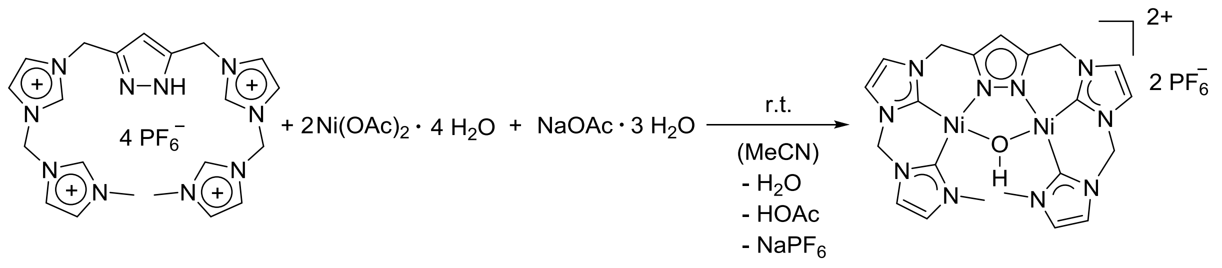

$C_{21}H_{28}N_{10}P_4F_{24}$	$NiC_4H_{14}O_8$	$NaC_2H_9O_5$	$Ni_2C_{21}H_{24}N_{10}OP_2F_{12}$
1000 g/mol	249 g/mol	136 g/mol	840 g/mol

$[H_5L^6](PF_6)_4$ (536 mg, 0.536 mmol, 1.00 equiv.) was dissolved in MeCN (p.a., 50 mL). Nickel(II) acetate tetra hydrate (89.7 mg, 0.360 mmol, 3.00 equiv.) and sodium acetate tri-hydrate (400 mg, 1.61 mmol, 2.00 equiv.) were added to the yellowish solution. The suspension was stirred for 3 days at room temperature. Afterwards, the suspension was filtered and the filtrate was dried *in vacuo*. The obtained pale yellow solid was washed several times with demineralized water and dried under high vacuum. Yellow crystals were obtained by slow diffusion of Et_2O or THF in a solution of acetone or MeCN at 0 °C. Yield: 70% (312.8 mg, 0.373 mmol).

^{1}H NMR (500 MHz, 298 K, MeCN-d_3): δ [ppm] = 7.32 (d, $^3J_{HH}$ = 2.0 Hz, 2H, $_{Im}$H **1**), 7.28 (d, $^3J_{HH}$ = 2.0 Hz, 2H, $_{Im}$H **2**), 7.19 (d, $^3J_{HH}$ = 2.0 Hz, 2H, $_{Im}$H **3**), 7.10 (d, $^3J_{HH}$ = 2.0 Hz, 2H, $_{Im}$H **4**), 6.29 (s, 1H, H^{pz}, **5**), 6.05 (s, 4H, H **6**), 5.22 (s, 4H, H **7**), 3.95 (s, 6H, H **8**), –0.04 (s, 1H, **OH**).

^{13}C{^{1}H} NMR (126 MHz, 298 K, MeCN-d_3): δ [ppm] = 161.3 ($C_{carbene}$–**9**), 156.7 ($C_{carbene}$–**10**), 144.6 ($C_{quart.}$–**11**), 124.8 (C–**4**), 123.7 (C–**3**), 123.3 (C–**1**), 121.9 (C–**2**), 101.9 (C–**5**), 62.6 (C–**6**), 48.0 (C–**7**), 38.4 (C–**8**).

^{1}H^{1}H COSY NMR (500 MHz, 298 K, MeCN-d_3): δ [ppm] = 7.32/7.10 ($_{Im}$H **1** & $_{Im}$H **4**), 7.28/7.19 ($_{Im}$H **2** & $_{Im}$H **3**), 6.29/5.22 (H^{pz} **5** & H **7**).

^{1}H^{1}H NOESY NMR (500 MHz, 298 K, MeCN-d_3): δ [ppm] = 7.32/6.05 ($_{Im}$H **1** & H **6**), 7.28/6.05 ($_{Im}$H **2** & H **6**), 7.19/5.22 ($_{Im}$H **3** & H **7**), 7.10/3.96 ($_{Im}$H **4** & H **8**), 6.29/5.22 (H^{pz} **5** & H **7**), 3.95/(–0.04) (H **8** & **OH**).

^{1}H^{13}C HSQC NMR (^{1}H NMR, 500 MHz, ^{13}C NMR, 126 MHz, 298 K, MeCN-d_3): δ [ppm] = 7.32/123.3, 7.28/121.9, 7.19/123.7, 7.10/124.8, 6.29/101.9, 6.05/62.6, 5.22/48.0, 3.95/38.4.

^{1}H^{13}C HMBC NMR (^{1}H NMR, 500 MHz, ^{13}C NMR, 126 MHz, 298 K, MeCN-d_3): δ [ppm] = 7.32/161.3 ($_{Im}$H **1** & $C_{carbene}$–**9**), 7.32/124.8 ($_{Im}$H **1** & C–**4**), 7.32/62.6 ($_{Im}$H **1** & C–**6**), 7.28/156.7 (${}_{\text{Im}}$H **2** & $\text{C}_{\text{carbene}}$–**10**), 7.28/123.7 (${}_{\text{Im}}$H **2** & C–**3**), 7.28/62.6 (${}_{\text{Im}}$H **2** & C–**6**), 7.19/156.7 (${}_{\text{Im}}$H **3** & $\text{C}_{\text{carbene}}$–**10**), 7.19/121.9 (${}_{\text{Im}}$H **3** & C–**2**), 7.19/48.0 (${}_{\text{Im}}$H **3** & C–**7**), 7.10/161.3 (${}_{\text{Im}}$H **4** & $\text{C}_{\text{carbene}}$–**9**), 7.10/123.3 (${}_{\text{Im}}$H **4** & C–**1**), 7.10/38.4 (${}_{\text{Im}}$H **4** & C–**8**), 6.29/144.6 (H^{pz} **5** & C–**11**), 6.05/161.33 (H **6** & $\text{C}_{\text{carbene}}$–**9**), 6.05/156.7 (H **6** & $\text{C}_{\text{carbene}}$–**10**), 6.05/123.3 (H **6** & C–**1**), 6.05/121.9 (H **6** & C–**2**), 5.22/156.7 (H **7** & $\text{C}_{\text{carbene}}$–**10**), 5.22/144.6 (H **7** & $\text{C}_{\text{quart.}}$–**11**), 5.22/123.7 (H **7** & C–**3**), 5.22/101.9 (H **7** & C–**5**), 3.95/161.3 (H **8** & $\text{C}_{\text{carbene}}$–**9**), 3.95/124.8 (H **8** & C–**4**).

^{1}H^{15}N HMBC NMR (^{1}H NMR, 500 MHz, ^{15}N NMR, 50.7 MHz, 298 K, MeCN-d_3): δ [ppm] = 7.32/–199.4, 7.32/–195.9, 7.28/–199.9, 7.28/–197.7, 7.19/–199.9, 7.19/–197.7, 7.10/–199.4, 7.10/–195.9, 6.29/–138.9, 6.05/–199.4, 6.05/–197.7, 5.22/–199.9, 5.22/–138.9, 3.95/–195.9.

^{31}P NMR (121.5 MHz, 298 K, MeCN-d_3): δ [ppm] = –144.6 (hpt., $^{1}J_{\text{PF}}$ = 706.8 Hz)

^{19}F NMR (282 MHz, 298 K, MeCN-d_3): δ [ppm] = –72.8 (d, $^{1}J_{\text{PF}}$ = 706.8 Hz)

^{1}H DOSY NMR (500 MHz, 333 K, MeCN-d_3): $D_{333\text{K}}$ [m^2s^{-1}] = $1.50\cdot10^{-9}$

^{1}H DOSY NMR (500 MHz, 298 K, MeCN-d_3): $D_{298\text{K}}$ [m^2s^{-1}] = $9.77\cdot10^{-10}$

^{1}H DOSY NMR (500 MHz, 243 K, MeCN-d_3): $D_{243\text{K}}$ [m^2s^{-1}] = $3.89\cdot10^{-10}$

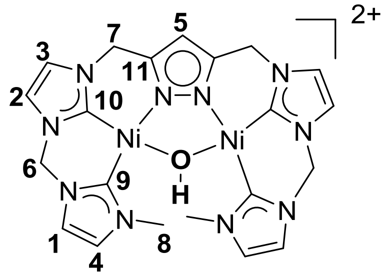

^{1}H NMR (300 MHz, 298 K, Acetone-d_6): δ [ppm] = 7.58 (t, $^{3}J_{\text{HH}}$ = 1.8 Hz, 4H, ${}_{\text{Im}}$H **1** & ${}_{\text{Im}}$H **2**), 7.49 (d, $^{3}J_{\text{HH}}$ = 2.0 Hz, 2H, ${}_{\text{Im}}$H **3**), 7.35 (d, $^{3}J_{\text{HH}}$ = 2.0 Hz, 2H, ${}_{\text{Im}}$H **4**), 6.42 (s, 4H, H **6**), 6.41 (s, 1H, H^{pz} **5**), 5.45 (s, 4H, H **7**), 4.19 (s, 6H, H **8**), 1.15 (s, 1H, **OH**).

^{13}C{^{1}H} NMR (75.5 MHz, 298 K, Acetone-d_6): δ [ppm] = 161.4 ($\text{C}_{\text{carbene}}$–**9**), 156.9 ($\text{C}_{\text{carbene}}$–**10**), 144.6 ($\text{C}_{\text{quart.}}$–**11**), 124.9 (C–**4**), 123.8 (C–**3**), 123.2 (C–**1**), 122.1 (C–**2**), 101.9 (C–**5**), 62.5 (C–**6**), 47.9 (C–**7**), 38.2 (C–**8**).

^{1}H NMR (300 MHz, 298 K, DMSO-d_6): δ [ppm] = 7.61 (m, 4H, ${}_{\text{Im}}$H **1** & ${}_{\text{Im}}$H **2**), 7.52 (d, $^{3}J_{\text{HH}}$ = 2.0 Hz, 2H, ${}_{\text{Im}}$H **3**), 7.40 (d, $^{3}J_{\text{HH}}$ = 2.0 Hz, 2H, ${}_{\text{Im}}$H **4**), 6.36 (s, 1H, H^{pz} **5**), 6.26 (s, 4H, H **6**), 5.33 (s, 4H, H **7**), 3.90 (s, 4H, H **8**), 1.88 (s, 1H, **OH**).

^{31}P NMR (121.5 MHz, 298 K, DMSO-d_6): δ [ppm] = –144.2 (hpt., $^{1}J_{\text{PF}}$ = 711.4 Hz).

^{19}F NMR (282 MHz, 298 K, DMSO-d_6): δ [ppm] = –70.1 (d, $^{1}J_{\text{PF}}$ = 711.4 Hz).

ESI-MS (MeCN) *m/z* (%): 693.04 (100) $[\text{Ni}_2\text{C}_{21}\text{H}_{24}\text{N}_{10}\text{O}(\text{PF}_6)]^{+}$, 274.02 (42.5) $[\text{Ni}_2\text{C}_{21}\text{H}_{24}\text{N}_{10}\text{O}]^{2+}$.

Elemental analysis of $Ni_2C_{21}H_{24}N_{10}OP_2F_{12}$

Calculated: **C** 30.03%; **H** 2.88%; **N** 16.68%.

Found: **C** 29.80%; **H** 2.85%; **N** 16.07%.

IR (ATR–solid): υ [cm^{-1}] = 3599.8 (OH, w), 1479.1 (w), 1443.6 (w), 1374.7 (w), 1345.9 (w), 1288.4 (w), 1242.1 (w), 1210.8 (w), 1173.3 (w), 1007.7 (w), 823.4 (s, P–F$_{asym.}$)

IR (MeCN): υ [cm^{-1}] = 3518.3 (OH, w), 3172.9 (w, C–H$_{carbene}$), 3143.1 (w, C-H$_{carbene}$), 3116.9 (w, C–H$_{carbene}$), 2943.6 (w, C–H$_{carbene}$), 1714.01 (m, acetone), 1571.5 (m), 1482.1 (m), 1444.8 (m), 1409.3 (m), 1345.9 (w), 1314.3 (m), 1291.9 (w), 1262.1 (w), 1239.7 (w), 1209.9 (w), 1176.3 (m), 1133.4 (w), 1112.9 (w), 1090.6 (w), 1075.7 (w), 1062.6 (m), 823.4 (s, P–F$_{asym.}$), 736.4 (s).

IR (DMSO): υ [cm^{-1}] = 3389.4 (OH, w), 3102.3 (m), 2267.1 (w), 2129.6 (w), 1565.0 (w), 1481.8 (w), 1447.1 (w), 1411.0 (w), 1371.3 (w), 1341.5 (w),, 1316.7 (w), 1289.4 (w), 1268.2 (w), 1244.7 (w), 1209.9 (w), 1187.5 (w), 1175.1 (w), 1137.8 (w), 1115.5 (w), 1044.4 (s), 851.0 (w), 846.3 (m), 825.9 (m), 757.4 (m), 738.6 (w).

UV-vis (MeCN, 293 K): $\lambda_{max.}$ [nm] (ε 10^3 [M^{-1}·cm^{-1}]) = 374 (1.10), 303 (22.03), 213 (25.43).

Labeling of [L^{6}Ni$_2$(OH)](PF$_6$)$_2$

[L^{6}Ni$_2$(OD)](PF$_6$)$_2$

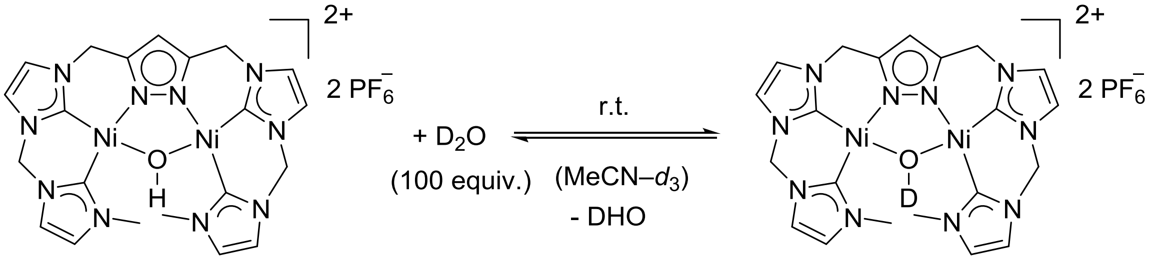

$Ni_2C_{21}H_{24}N_{10}OP_2F_{12}$ D_2O $Ni_2C_{21}H_{23}DN_{10}OP_2F_{12}$

840 g/mol 20 g/mol 841 g/mol

[L^{6}Ni$_2$(OH)](PF$_6$)$_2$ (18.0 mg, 0.0214 mmol, 1.00 equiv.) was dissolved in MeCN-d_3 (0.5 mL). Deuterated water (D_2O, 38.8 μL, 42.9 mg, 2.14 mmol, 100 equiv.) was added and the solution is shaken several times.

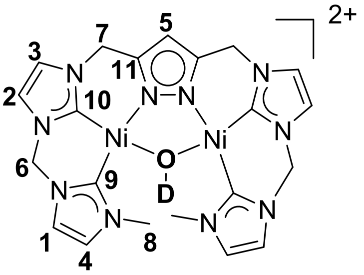

^{1}H NMR (500 MHz, 298 K, MeCN-d_3): δ [ppm] = 7.33 (d, $^3J_{HH}$ = 2.0 Hz, 2H, $_{Im}$H **1**), 7.29 (d, $^3J_{HH}$ = 2.0 Hz, 2H, $_{Im}$H **2**), 7.20 (d, $^3J_{HH}$ = 2.0 Hz, 2H, $_{Im}$H **3**), 7.10 (d, $^3J_{HH}$ = 2.0 Hz, 2H, $_{Im}$H **4**), 6.28 (s, 1H, H^{pz} **5**), 6.06 (s, 4H, H **6**), 5.22 (s, 4H, H **7**), 3.94 (s, 4H, H **8**).

^{2}H NMR (61 MHz, 298 K, MeCN): δ [ppm] = –0.03 (s, **OD**).

IR (MeCN-d_3): υ [cm^{-1}] = 3172.9 (w), 3143.1 (w), 3116.9 (w), 3029.4 (w), 2964.1 (w), 2606.2 (**OD**, w), 1569.7 (m), 1532.4 (w), 1482.1 (m), 1444.7 (m), 1427.9 (m), 1416.8 (m), 1375.8 (w), 1345.9 (w), 1316.1 (w), 1291.9 (m), 1263.9 (w), 1241.6 (w), 1209.9 (m), 1178.2 (w), 850.1 (s), 738.2 (m).

ESI-MS (MeCN) *m/z* (%): 694 (100) $[Ni_2C_{21}H_{24}N_{10}OPF_6]^+$, 274 (43) $[Ni_2C_{21}H_{24}N_{10}O]^{2+}$.

$[L^6Ni_2(^{18}O/^{17}OH)](PF_6)_2$

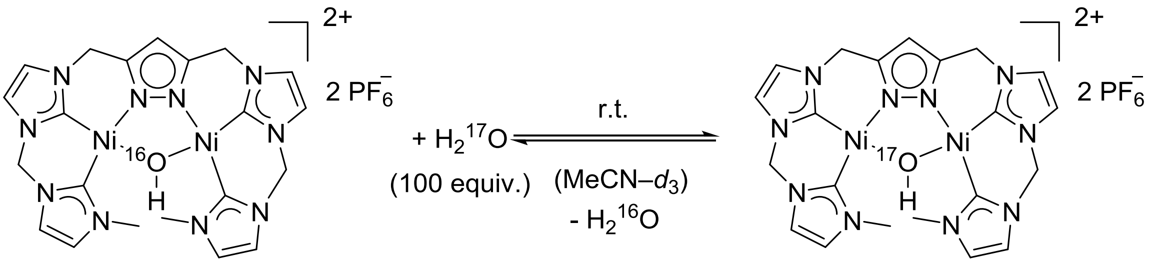

$Ni_2C_{21}H_{24}N_{10}{}^{16}OP_2F_{12}$	$H_2{}^{17}O$	$Ni_2C_{21}H_{24}N_{10}{}^{17}OP_2F_{12}$
840 g/mol	19 g/mol	841 g/mol

$[L^6Ni_2(OH)](PF_6)_2$ (18.2 mg, 0.0217 mmol, 1.00 equiv.) was dissolved in MeCN-d_3 (0.5 mL). Labeled water ($H_2{}^{17}O$ or $H_2{}^{18}O$, 100 equiv.) was added and the solution is shacken several times.

ESI-MS ($H_2{}^{18}O$, MeCN) *m/z* (%): 695 (100) $[Ni_2C_{21}H_{24}N_{10}{}^{18}OPF_6]^+$, 275 (15) $[Ni_2C_{21}H_{24}N_{10}{}^{18}O]^{2+}$
^{17}O NMR (54 MHz, 298 K, MeCN-d_3): δ [ppm] = –119.6 (br s, ^{17}**OH**).

Reaction of **$[L^6Ni_2(OH)](PF_6)_2$** with $KHBEt_3$

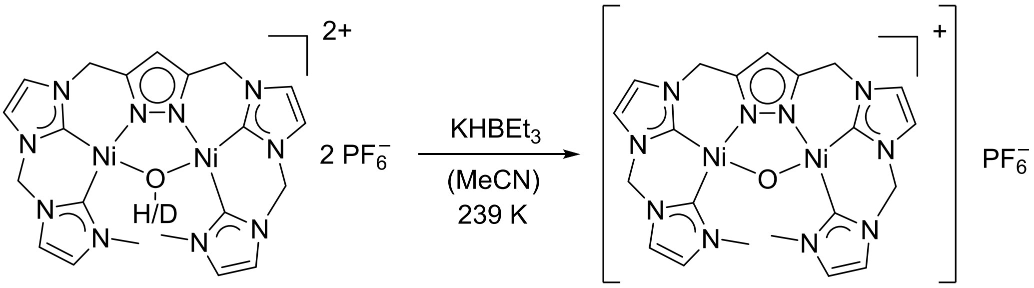

$Ni_2C_{21}H_{24}N_{10}OP_2F_{12}$	KBC_6H_{16}	$Ni_2C_{21}H_{23}N_{10}OPF_6$
840 g/mol	138 g/mol	694 g/mol

$[L^6Ni_2(OH)](PF_6)_2$ (34.5 mg, 41 μmol, 1.00 equiv.) was dissolved in MeCN-d_3 or MeCN (0.5 mL) and cooled to 238 K. A cooled $KHBEt_3$ solution (1.0 M in THF, 62 μL, 8.56 mg, 62 μmol, 1.50 equiv.) was slowly added under stirring. A color change from yellow to red-orange was observed. Afterwards ESI-MS and ^{1}H NMR spectra were measured.

- **(a)** For long time ^{1}H NMR studies: Et_2O was added to the solution and the formed precipitate was dried *in vacuo* and redisolved in MeCN-d_3.
- **(b)** For IR spectroscopic investigations: Et_2O was added to the solution and the formed precipitate was dried *in vacuo* and redisolved in MeCN-d_3 for one day. Afterwards a IR spectrum was conducted.
- **(c)** Queching of the reaction: D_2O was added in excess to the reaction mixture after addition of $KHBEt_3$ to the complex solution and an observed color change. Afterwards an ESI-MS was measured.
- **(d)** ^{2}H NMR experiment: After addition of $KHBEt_3$ to **$[L^6Ni_2(OD)](PF_6)_2$** in a J Young valve NMR tube, the reaction mixture was shaken and freeze quenched in liquid nitrogen. Afterwards a ^{2}H NMR spectrum was conducted.

$[L^7Ni_2(OH)](PF_6)_2$

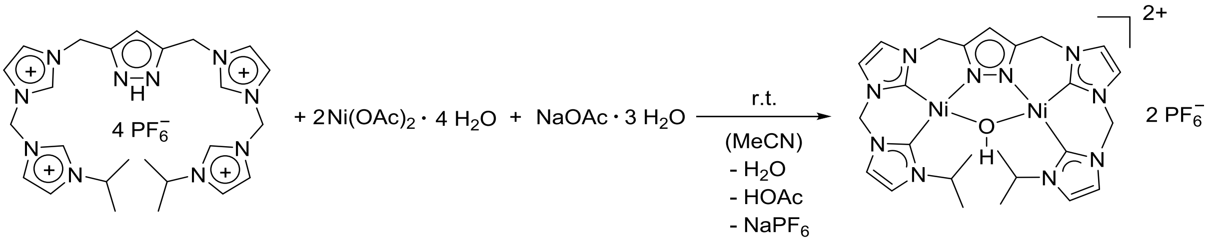

$C_{25}H_{36}N_{10}P_4F_{24}$	$NiC_4H_{14}O_8$	$NaC_2H_9O_5$	$Ni_2C_{25}H_{32}N_{10}OP_2F_{12}$
1056 g/mol	249 g/mol	136 g/mol	896 g/mol

$[H_5L^7](PF_6)_4$ (54.7 mg, 51.7 µmol, 1.00 equiv.) was dissolved in MeCN (p.a., 20 mL). $Ni(OAc)_2 \cdot 4H_2O$ (36.0 mg, 0.145 mmol, 2.80 equiv.) and $NaOAc \cdot 3H_2O$ (12.7 mg, 93.2 µmol, 1.80 equiv.) were added to the yellowish solution. The suspension was stirred for 3 days at room temperature. Afterwards, the suspension was filtered off and the filtrate was dried *in vacuo*. The obtained pale yellow solid was washed several times with demineralized water and dried under high vacuum. Yellow crystals were obtained by slow diffusion of THF in a solution of acetone or MeCN at 0 °C.

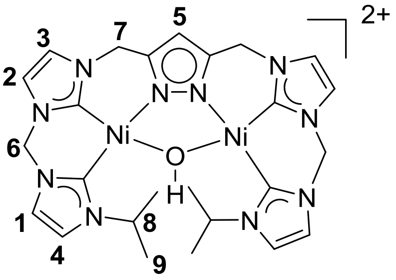

^{1}H NMR (300 MHz, 298 K, MeCN-d_3): δ [ppm] = 7.35 (d, $^3J_{HH}$ = 2.0 Hz, 2H, $_{Im}$H **1**), 7.29 (d, $^3J_{HH}$ = 2.0 Hz, 2H, $_{Im}$H **2**), 7.24 (d, $^3J_{HH}$ = 2.0 Hz, 2H, $_{Im}$H **3**), 7.18 (d, $^3J_{HH}$ = 2.0 Hz, 2H, $_{Im}$H **4**), 6.30 (s, 1H, H^{pz}, **5**), 6.09 (s, 4H, H **6**), 5.22 (s, 4H, H **7**), 5.13 (dt, $^3J_{HH}$ = 13.2 Hz, 6.6 Hz, 2H, H **8**), 1.61 (d, $^3J_{HH}$ = 6.6 Hz, 12H, H **9**), 0.07 (s, 1H, **OH**).

ESI-MS (MeCN) *m/z* (%): 749 (100) $[Ni_2C_{25}H_{31}N_{10}OHPF_6]^+$, 302 (80) $[Ni_2C_{25}H_{31}N_{10}OH]^{2+}$.

[$L^9Ni_2(OH)](PF_6)_2$

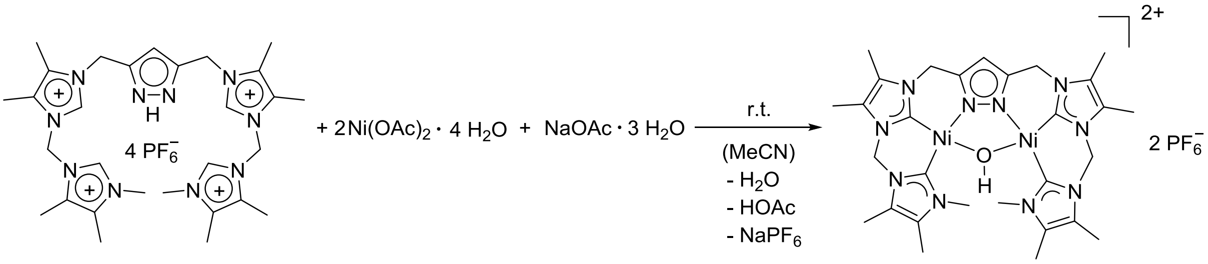

$C_{29}H_{43}N_{10}P_4F_{24}$	$NiC_4H_{14}O_8$	$NaC_2H_9O_5$	$Ni_2C_{29}H_{39}N_{10}OP_2F_{12}$
1112 g/mol	249 g/mol	136 g/mol	952 g/mol

[H_5L^9](PF_6)$_4$ (127 mg, 0.114 mmol, 1.00 equiv.) was dissolved in MeCN (p.a., 20 mL). Nickel(II) acetate tetra-hydrate (85.4 mg, 0.343 mmol, 3.00 equiv.) and sodium acetate tri-hydrate (31.1 mg, 0.228 mmol, 2.00 equiv.) were added to the yellowish solution. The suspension was stirred for 3 days at room temperature. Afterwards, the suspension was filtered off and the filtrate was dried *in vacuo*. The obtained pale yellow solid was washed several times with demineralized water and dried *in vacuo*.

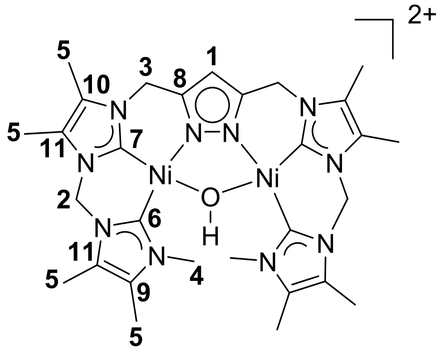

^{1}H NMR (300 MHz, 298 K, MeCN-*d*$_3$): δ [ppm] = 6.29 (s, 1H, H^{pz} **1**), 5.79 (s, 4H, H **2**), 5.10 (s, 4H, H **3**), 3.84 (s, 6H, H **4**), 2.23-2.21 (2 s, 24 H, H **5**), –0.21 (s, 1H, **OH**).

^{13}C{^{1}H} NMR (75 MHz, 298 K, MeCN-*d*$_3$): δ [ppm] = 159.2 ($C_{carbene}$–**6**), 154.1 ($C_{carbene}$–**7**), 144.1 ($C_{quart.}$–**8**), 127.9 (C-**9**), 127.0 (C–**10**), 126.2 (C–**11**), 125.8 (C–**11**), 101.4 (C–**1**), 57.0 (C–**2**), 44.6 (C–**3**), 35.3 (C-**4**), 8.4 (C–**5**).

^{1}H^{1}H COSY NMR (300 MHz, 298 K, MeCN-*d*$_3$): δ [ppm] = 6.29/5.10 (H^{pz} **5** & H **3**).

^{1}H^{1}H NOESY NMR (300 MHz, 298 K, MeCN-*d*$_3$): δ [ppm] = 6.29/5.11 (H^{pz} **1** & CH_2 **3**), 5.79/2.23 (H **2** & H **5**), 5.10/2.23 (H **2** & H **5**), 3.84/2.23–2.21 (H **4** & H **5**) 3.84/(–0.21) (H **4** & **OH**).

$^1H^{13}C$ HSQC NMR (^{1}H NMR, 300 MHz, ^{13}C NMR, 75 MHz, 298 K, MeCN-d_3): δ [ppm] = 6.29/101.4, 5.79/57.0, 5.10/44.6, 3.84/35.3, 2.23–2.21/8.4.

$^1H^{13}C$ HMBC NMR (^{1}H NMR, 500 MHz, ^{13}C NMR, 126 MHz, 298 K, MeCN-d_3): δ [ppm] = 6.29/144.1 (H^{pz} **1** & C–**8**), 5.79/159.2 (H **2** & $C_{carbene}$–**6**), 5.79/154.1 (H **2** & $C_{carbene}$–**7**), 5.10/144.1 (CH_2 **3** & $C_{quart.}$–**8**), 3.84/159.2 (H **4** & $C_{carbene}$–**6**).

ESI-MS (MeCN) *m/z* (%): 805 (41) $[Ni_2C_{29}H_{39}N_{10}OHPF_6]^+$, 330 (100) $[Ni_2C_{29}H_{39}N_{10}OH]^{2+}$.

$[L^6Ni_2Cl](PF_6)_2$

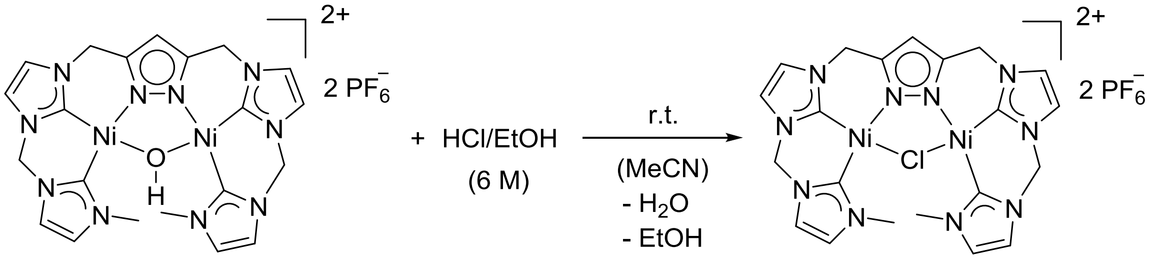

$Ni_2C_{21}H_{24}N_{10}OP_2F_{12}$ HCl/C_2H_6O $Ni_2C_{21}H_{23}N_{10}ClP_2F_{12}$

840 g/mol 858 g/mol

$[L^6Ni_2(OH)](PF_6)_2$ (99.6 mg, 0.119 mmol, 1.00 equiv.) was dissolved in MeCN (3 mL). An ethanolic hydrogen chloride solution (6.0 M, 20.7 μL, 0.125 mmol, 1.05 equiv.) was added dropwise to the solution. The yellow solution immediately turned to greenish. The solution was further stirred for 15 min.. Afterwards, the solvent was removed at the high vacuum line overnight. A yellow-greenish solid was obtained in 86% yield (87.2 mg, 0.102 mmol). Greenish crystals were received by slow diffusion of Et_2O into a solution of the product in MeCN.

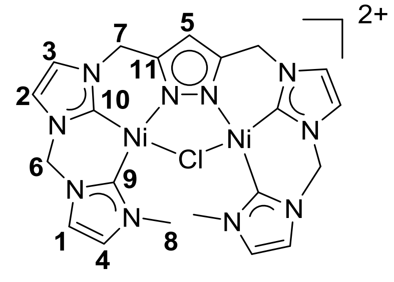

^{1}H NMR (500 MHz, 298 K, MeCN-d_3): δ [ppm] = 7.34 (d, $^3J_{HH}$ = 2.0 Hz, 4H, $_{Im}$H **1** & $_{Im}$H **2**), 7.23 (d, $^3J_{HH}$ = 2.0 Hz, 2H, $_{Im}$H **3**), 7.12 (d, $^3J_{HH}$ = 2.0 Hz, 2H, $_{Im}$H **4**), 6.33 (s, 1H, H^{pz}, **5**), 6.13 (s, 4H, CH_2, **6**), 5.26 (s, 4H, CH_2, **7**), 3.99 (s, 6H, CH_3, **8**).

^{13}C{^{1}H} NMR (126 MHz, 298 K, MeCN-d_3): δ [ppm] = 156.2 ($C_{carbene}$–**9**), 152.9 ($C_{carbene}$–**10**), 146.6 ($C_{quart.}$–**11**), 125.8 (C–**4**), 123.4 (C–**3**), 123.3 (C–**1**), 122.2 (C–**2**), 103.6 (C–**5**), 62.8 (C–**6**), 47.9 (C–**7**), 39.3 (C–**8**).

^{1}H^{1}H COSY NMR (500 MHz, 298 K, MeCN-d_3): δ [ppm] = 7.34/7.23 ($_{Im}$H **2** & $_{Im}$H **3**), 7.34/7.12 ($_{Im}$H **1** & $_{Im}$H **4**), 7.34/6.12 ($_{Im}$H **1/2** & H **6**), 7.34/3.97 ($_{Im}$H **1** & H **8**), 7.23/5.26 ($_{Im}$H **3** & H **7**), 7.12/3.97 ($_{Im}$H **4** & H **8**), 6.33/5.25 (H^{pz} **5** & H **7**), 6.13/5.26 (H **6** & H **7**), 6.13/3.99 (H **6** & H **8**).

^{1}H^{1}H NOESY NMR (500 MHz, 298 K, MeCN-d_3): δ [ppm] = 7.34/6.13 ($_{\text{Im}}$H **1/2** & H **6**), 7.23/5.26 ($_{\text{Im}}$H **3** & H **7**), 7.12/3.97 ($_{\text{Im}}$H **4** & H **8**), 6.33/5.26 (H$^{\text{pz}}$ **5** & H **7**).

^{1}H^{13}C HSQC NMR (^{1}H NMR, 500 MHz, ^{13}C NMR, 126 MHz, 298 K, MeCN-d_3): δ [ppm] = 7.34/123.3, 7.34/122.2, 7.23/123.4, 7.12/125.8, 6.33/103.6, 6.13/62.8, 5.3/47.9, 3.97/39.3.

^{1}H^{13}C HMBC NMR (^{1}H NMR, 500 MHz, ^{13}C NMR, 126 MHz, 298 K, MeCN-d_3): δ [ppm] = 7.34/156.2 ($_{\text{Im}}$H **1** & C$_{\text{carbene}}$–**9**), 7.34/152.9 ($_{\text{Im}}$H **2** & C$_{\text{carbene}}$–**10**), 7.34/125.8 ($_{\text{Im}}$H **1** & C–**4**), 7.34/123.4 ($_{\text{Im}}$H **2** & C–**3**), 7.34/62.8 ($_{\text{Im}}$H **1/2** & C$_{\text{carbene}}$–**6**), 7.23/152.9 ($_{\text{Im}}$H **3** & C$_{\text{carbene}}$–**10**), 7.23/122.2 ($_{\text{Im}}$H **3** & C–**2**), 7.23/47.9 ($_{\text{Im}}$H **3** & C–**7**), 7.12/156.2 ($_{\text{Im}}$H **4** & C$_{\text{carbene}}$–**9**), 7.12/123.4 ($_{\text{Im}}$H **4** & C–**1**), 7.12/39.3 ($_{\text{Im}}$H **4** & C–**8**), 6.33/146.6 (H$^{\text{pz}}$ **5** & C$_{\text{quart.}}$–**11**), 6.33/47.9 (H$^{\text{pz}}$ **5** & C–**7**), 6.13/156.2 (H **6** & C$_{\text{carbene}}$–**9**), 6.13/152.9 (H **6** & C$_{\text{carbene}}$–**10**), 6.13/123.3 (H **6** & C–**1**), 6.13/122.2 (H **6** & C–**2**), 5.26/152.9 (H **7** & C$_{\text{carbene}}$–**10**), 5.26/146.6 (H **7** & C$_{\text{quart.}}$–**11**), 5.26/123.4(H **7** & C–**3**), 5.26/103.6 (H **7** & C–**5**), 3.99/156.2 (H **8** & C$_{\text{carbene}}$–**9**), 3.99/125.8 (H **8** & C–**4**).

^{1}H^{15}N HMBC NMR (^{1}H NMR, 500 MHz, ^{15}N NMR, 50.7 MHz, 298 K, MeCN-d_3): δ [ppm] = 7.34/–199.7, 7.34/–197.9, 7.34/–195.5, 7.23/–199.7, 7.23/–197.7, 7.12/–197.9, 7.12/–195.5, 6.33/–137.9, 6.13/–197.9, 5.26/–199.7, 5.26/–137.9, 3.99/–195.5.

^{1}H DOSY NMR (500 MHz, 298 K, MeCN-d_3): $D_{298\text{K}}$ [m^{2}s^{-1}] = $-9.80 \cdot 10^{-10}$.

^{31}P NMR (121.5 MHz, 298 K, MeCN-d_3): δ [ppm] = –144.6 (hpt., $^1J_{\text{PF}}$ = 706.6 Hz).

^{19}F NMR (282 MHz, 298 K, MeCN-d_3): δ [ppm] = –72.9 (d, $^1J_{\text{PF}}$ = 706.6 Hz).

Elemental analysis of $Ni_2C_{21}H_{23}N_{10}ClP_2F_{12} \cdot CH_3CN$

Calculated: **C** 30.72%; **H** 2.91%; **N** 17.13%.

Found: **C** 30.95%; **H** 2.80%; **N** 17.17%.

Elemental analysis of $Ni_2C_{21}H_{23}N_{10}ClP_2F_{12}$

Calculated: **C** 29.39%; **H** 2.70%; **N** 16.32%.

Found: **C** 30.08%; **H** 2.92%; **N** 16.39%.

ESI-MS (MeCN) *m/z* (%): 713.05 (100) $[Ni_2C_{21}H_{23}N_{10}Cl(PF_6)]^+$, 283.98 (7.8) $[Ni_2C_{21}H_{23}N_{10}Cl]^{2+}$.

IR (MeCN-d_3): υ [cm^{-1}] = 3172.9 (w), 3144.9 (w), 3120.7 (w), 1685.3 (w), 1571.5 (w), 1483.9 (w), 1444.7 (w), 1429.9 (w), 1416.8 (w), 1409.3 (w), 1349.7 (w), 1318.0 (w), 1297.5 (w), 1239.7 (w), 1208.0 (w), 1180.1 (w), 850.1 (s), 740.1 (m).

UV-vis (MeCN, 293 K): $\lambda_{\text{max.}}$ [nm] (ε 10^3 [M$^{-1}\cdot$cm^{-1}]) = 375 (0.84), 297 (21.9), 211 (35.5).

$[L^6Ni_2(CN)_2](PF_6)_2$

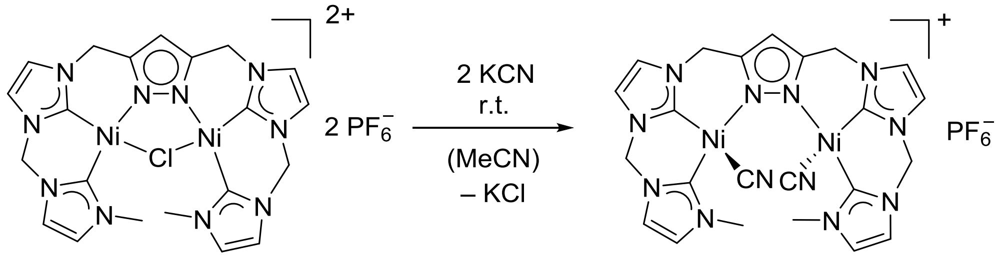

$Ni_2C_{21}H_{23}N_{10}ClP_2F_{12}$	KCN	$Ni_2C_{23}H_{23}N_{12}PF_6$
858 g/mol	65 g/mol	730 g/mol

$[L^6Ni_2Cl](PF_6)_2$ (23.8 mg, 27.7 μmol, 1.00 equiv.), was dissolved in MeCN-d_3 (0.8 mL) and stored over molecular sieves (3 Å) for two days. The yellow solution was filtered off and the solution was added to potassium cyanide (3.6 mg, 55.3 μmol, 2.00 equiv.). The suspension was stirred for one hour. After one hour, the off-white solution was filtered off.

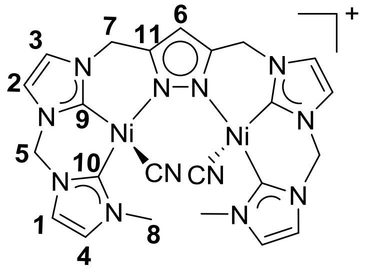

^{1}H NMR (500 MHz, 298 K, MeCN-d_3): δ [ppm] = 7.29 (d, $^3J_{HH}$ = 1.9 Hz, 2H, $_{\mathrm{Im}}$H **1**) 7.21 (d, $^3J_{HH}$ = 1.8 Hz, 2H, & $_{\mathrm{Im}}$H **2**), 7.13 (d, $^3J_{HH}$ = 1.8 Hz, 2H, $_{\mathrm{Im}}$H **3**), 6.97 (d, $^3J_{HH}$ = 1.7 Hz, 2H, $_{\mathrm{Im}}$H **4**), 6.39 (d, $^2J_{HH}$ = 12.0 Hz, 2H, H **5**), 6.28 (s, 1H, H^{pz} **6**), 5.91 (d, $^2J_{HH}$ = 12.0 Hz, 2H, H **5**), 5.24 (d, $^2J_{HH}$ = 16.0 Hz, 2H, H **7**), 5.16 (d, $^2J_{HH}$ = 16.0 Hz, 2H, H **7**), 3.87 (br s, 6H, H **8**).

^{13}C{^{1}H} NMR (126 MHz, 298 K, MeCN-d_3): δ [ppm] = 169.5 (C$_{\mathrm{carbene}}$–**9**), 163.4 (C$_{\mathrm{carbene}}$–**10**), 146.2 (C$_{\mathrm{quart.}}$–**11**), 143.1 (**CN**), 124.3 (C–**4**), 123.0 (C–**1**), 122.6 (C–**3**), 120.5 (C–**2**), 102.1 (C–**6**), 62.9 (C–**5**), 47.8 (C–**7**), 39.8 (C–**8**).

^{1}H^{1}H COSY NMR (500 MHz, 298 K, MeCN-d_3): δ [ppm] = 7.29/7.6.97 ($_{\mathrm{Im}}$H **1** & $_{\mathrm{Im}}$H **4**), 7.21/7.13 ($_{\mathrm{Im}}$H **2** & $_{\mathrm{Im}}$H **3**), 6.39/5.91 (H **5** & H **5**), 5.24/5.16 (H **7** & H **7**).

^{1}H^{1}H NOESY NMR (500 MHz, 298 K, MeCN-d_3): δ [ppm] = 7.29/5.91 ($_{\mathrm{Im}}$H **1** & H **5**), 7.21/5.91 ($_{\mathrm{Im}}$H **2** & H **5**), 7.13/5.16 ($_{\mathrm{Im}}$H **3** & H **7**), 6.28/5.16 (H^{pz} **6** & H **7**).

^{1}H^{13}C HSQC NMR (^{1}H NMR, 500 MHz, ^{13}C NMR, 126 MHz, 298 K, MeCN-d_3): δ [ppm] = 7.29/123.0, 7.21/120.5, 7.13/122.6, 6.97/124.3, 6.39//5.91/62.9, 6.28/102.1, 5.16/47.8, 3.87/39.8.

^{1}H^{13}C HMBC NMR (^{1}H NMR, 500 MHz, ^{13}C NMR, 126 MHz, 298 K, MeCN-d_3): δ [ppm] = 6.28/146.2 (H^{pz} **6** & $C_{quart.}$–**11**), 5.91/169.5 (H **5** & $C_{carbene}$–**9**), 5.91/163.4 (H **5** & $C_{carbene}$–**10**), 5.16/169.5 (H **7** & $C_{carbene}$–**9**), 5.17/146.2 (H **7** & $C_{quart.}$–**11**).

ESI-MS (MeCN) *m/z* (%): 583.30 (100) $[Ni_2C_{23}H_{23}N_{12}]^+$.

IR (MeCN-d_3): υ [cm^{-1}] = 3170.8 (w), 3143.1 (w), 3028.7 (w), 2116 (m, CN), 1480.7 (m), 1425.6 (m), 1410.4 (m), 1345.7 (m), 1299.8 (m),1236.6 (m), 1204.1 (m),1171.8 (m), 849.8 (s).

$[L^6Ni_2(NH_2)](PF_6)_2$

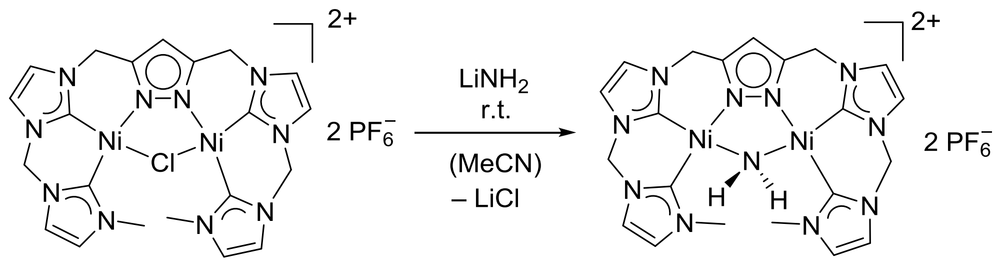

$Ni_2C_{21}H_{23}N_{10}ClP_2F_{12}$ LiH$_2$N $Ni_2C_{21}H_{25}N_{11}P_2F_{12}$

858 g/mol 23 g/mol 839 g/mol

$[L^6Ni_2Cl](PF_6)_2$ (9.37 mg, 10.3 μmol, 1.00 equiv.), was dissolved in MeCN (1 mL) and stored over molecular sieves (3 Å) for two days. The yellow solution was filtered off and lithium amide (0.38 mg, 16.5 μmol, 1.60 equiv.) was added to the solution. After three days the yellow solution was filtered again and ESI-MS and IR spectra of the solution were recorded. Afterwards, the solution was filled into a J Young valve NMR tube and the solvent was removed *in vacuo*. MeCN-d_3 (0.5 mL) was added and NMR experiments were conducted. The synthesis of **$[L^6Ni_2(NH_2)](PF_6)_2$** was also accessible by reaction of **$[L^6Ni_2Cl](PF_6)_2$** with liquid ammonia. **$[L^6Ni_2Cl](PF_6)_2$** (21.1 mg, 24.5 μmol, 1.00 equiv.) was added into a Schlenk flask and cooled down to –78 °C. Approximately 5 mL of NH_3 was condensed into the flask and the suspension was stirred for 20 minutes. Afterwards the sample was warmed up to r.t. over a period of 3 hours, the atmosphere was removed *in vacuo* and a yellow solid was obtained.

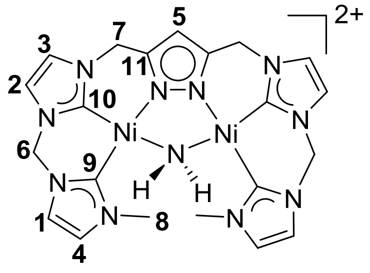

^{1}H NMR (400 MHz, 298 K, MeCN-d_3): δ [ppm] = 7.31 (d, $^3J_{HH}$ = 2.0 Hz, 2H, $_{\text{Im}}$H **1**), 7.26 (d, $^3J_{HH}$ = 2.0 Hz, 2H, $_{\text{Im}}$H **2**), 7.19 (d, $^3J_{HH}$ = 2.0 Hz, 2H, $_{\text{Im}}$H **3**), 7.10 (d, $^3J_{HH}$ = 2.0 Hz, 2H, $_{\text{Im}}$H **4**), 6.27 (s, 1H, H^{pz} **5**), 6.04 (s, 4H, H **6**), 5.18 (s, 4H, H **7**), 3.90 (s, 6H, H **8**).

^{13}C{^{1}H} NMR (126 MHz, 298 K, MeCN-d_3): δ [ppm] = 164.7 (C_{carbene}–**9**), 164.6 (C_{carbene}–**10**), 145.1 ($C_{\text{quart.}}$–**11**), 125.1 (C–**4**), 125.4 (C–**1**), 123.1 (C–**3**), 121.2 (C–**2**), 102.9 (C–**5**), 62.8 (C–**6**), 47.9 (C–**7**), 38.6 (C–**8**).

^{1}H^{1}H COSY NMR (400 MHz, 298 K, MeCN-d_3): δ [ppm] = 7.31/7.10 ($_{\text{Im}}$H **1** & $_{\text{Im}}$H **4**), 7.31/6.04 ($_{\text{Im}}$H **1** & H **6**), 7.26/7.19 ($_{\text{Im}}$H **2** & $_{\text{Im}}$H **3**), 7.26/6.04 ($_{\text{Im}}$H **2** & H **6**), 7.19/5.18 ($_{\text{Im}}$H **3** & H **7**), 6.27/5.18 (H$^{\text{pz}}$ **5** & H **7**).

^{1}H^{1}H NOESY NMR (500 MHz, 298 K, MeCN-d_3): δ [ppm] = 7.31/6.04 ($_{\text{Im}}$H **1** & H **6**), 7.26/6.04 ($_{\text{Im}}$H **2** & H **6**), 7.19/5.18 ($_{\text{Im}}$H **3** & H **7**), 7.10/3.90 ($_{\text{Im}}$H **4** & H **8**), 6.27/5.18 (H$^{\text{pz}}$ **5** & H **7**).

^{1}H^{13}C HSQC NMR (^{1}H NMR, 500 MHz, ^{13}C NMR, 126 MHz, 298 K, MeCN-d_3): δ [ppm] = 7.31/123.1, 7.26/121.2, 7.19/123.4, 7.10/125.1, 6.27/102.9, 6.04/62.8, 5.18/47.9, 3.90/38.6.

^{1}H^{13}C HMBC NMR (^{1}H NMR, 500 MHz, ^{13}C NMR, 126 MHz, 298 K, MeCN-d_3): δ [ppm] = 7.31/164.7 ($_{\text{Im}}$H **1** & C$_{\text{carbene}}$–**9**), 7.31/125.1 ($_{\text{Im}}$H **1** & C–**4**), 7.26/164.6 ($_{\text{Im}}$H **2** & C$_{\text{carbene}}$–**10**), 7.26/123.4 ($_{\text{Im}}$H **2** & C–**3**), 7.19/164.6 ($_{\text{Im}}$H **3** & C$_{\text{carbene}}$–**10**), 7.19/121.2 ($_{\text{Im}}$H **3** & C–**2**), 7.10/164.7 ($_{\text{Im}}$H **4** & C$_{\text{carbene}}$–**9**), 7.10/123.1 ($_{\text{Im}}$H **4** & C–**1**), 6.27/145.1 (H$^{\text{pz}}$ **5** & C$_{\text{quart.}}$–**11**), 6.04/164.7 (H **6** & C$_{\text{carbene}}$–**9**), 6.04/164.6 (H **6** & C$_{\text{carbene}}$–**10**), 6.04/123.1 (H **6** & $_{\text{Im}}$H **1**), 6.04/121.2 (H **6** & $_{\text{Im}}$H **2**), 5.18/164.6 (H **7** & C$_{\text{carbene}}$–**10**), 5.18/145.1 (H **7** & C$_{\text{quart.}}$–**11**), 5.18/123.4 (H **7** & $_{\text{Im}}$H **3**), 5.18/102.9 (H **7** & C–**5**), 3.90/164.7 (H **8** & C$_{\text{carbene}}$–**9**), 3.90/125.1 (H **8** & C–**4**).

^{1}H^{15}N HMBC NMR (^{1}H NMR, 500 MHz, ^{15}N NMR, 50.7 MHz, 298 K, MeCN-d_3): δ [ppm] = 7.31/–198.3, 7.31/–196.6, 7.26/–199.1, 7.26/–198.6, 7.19/–199.1, 7.19/–198.6, 7.10/–198.3, 7.10/–196.6, 6.27/–131.1, 6.03/–198.62, 6.03/–198.3, 5.18/–198.6, 5.18/–131.1, 3.90/–196.6.

^{1}H DOSY NMR (500 MHz, 298 K, MeCN-d_3): $D_{298\text{K}}$ [m^{2}s^{-1}] = $9.95 \cdot 10^{-10}$

ESI-MS (MeCN) *m/z* (%): 692.10 (100) $[Ni_2C_{21}H_{25}N_{11}PF_6]^+$, 273.53 (83) $[Ni_2C_{21}H_{25}N_{11}]^{2+}$.

IR (MeCN): υ [cm^{-1}] = 3474.9 (**NH$_2$**, m), 3379.8 (**NH$_2$**, m), 3256.8 (w), 3174.8 (w), 3143.1 (w), 3118.8 (w), 3098.3 (w), 3020.0 (w), 2943.6 (w), 2306.0 (m), 2276.2 (m), 2194.2 (m), 2138.3 (m), 1644.2 (m), 1605.1 (m), 1573.4 (w), 1564.1 (w), 1528.7 (w), 1478.3 (w), 1444.8 (m), 1418.7 (m), 1413.1 (m), 1372.1 (w), 1344.1 (w), 1312.4 (w), 1293.8 (w), 1262.1 (w), 1237.8 (w), 1208.0 (w), 1194.9 (w), 1172.6 (w), 878.0 (s), 848.2 (s), 736.4 (m).

$[L^6Ni_2(ND)_2](PF_6)_2$

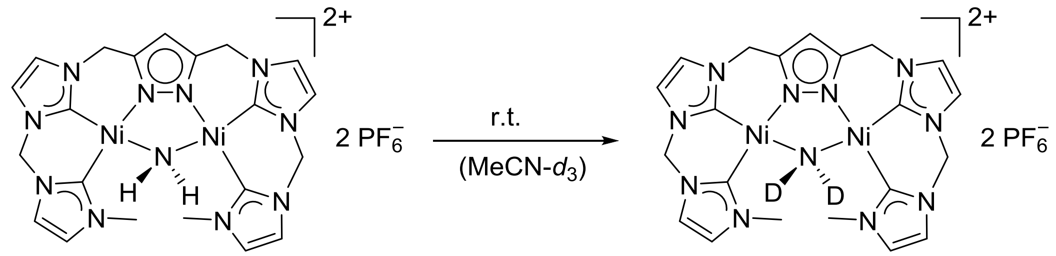

$Ni_2C_{21}H_{25}N_{11}P_2F_{12}$ $Ni_2C_{21}H_{23}D_2N_{11}P_2F_{12}$

839 g/mol 841 g/mol

An ESI-MS and solution IR spectrum of **$[L^6Ni_2(NH_2)](PF_6)_2$** were measured after the complex was dissolved in MeCN-d_3 (0.5 mL) and stored in the solution for one month.

ESI-MS (MeCN-d_3) *m/z* (%): 694.31 (100) $[Ni_2C_{21}H_{23}D_2N_{11}PF_6]^+$, 693.38 (8.45) $[Ni_2C_{21}H_{24}DN_{11}PF_6]^+$, 274.63 (27) $[Ni_2C_{21}H_{23}D_2N_{11}]^{2+}$.

IR (MeCN-d_3): υ [cm^{-1}] = 3169.2 (w), 3143.1 (w), 2977.2 (w), 2943.6 (w), 2613.6 (**ND_2**, w), 2466.4 (**ND_2**, w), 2287.4 (m), 2190.5 (m), 1595.8 (m), 1573.4 (w), 1478.3 (m), 1463.4 (m), 1444.8 (m), 1424.3 (m), 1409.3 (m), 1375.8 (m), 1342.2 (m), 1312.4 (m), 1282.6 (m), 1263.9 (m), 1237.8 (m), 1208.0 (m), 1172.6 (m), 874.0 (m), 849.0 (s), 829.6 (m), 738.2 (m).

[L^{6}Ni$_2$S]PF$_6$

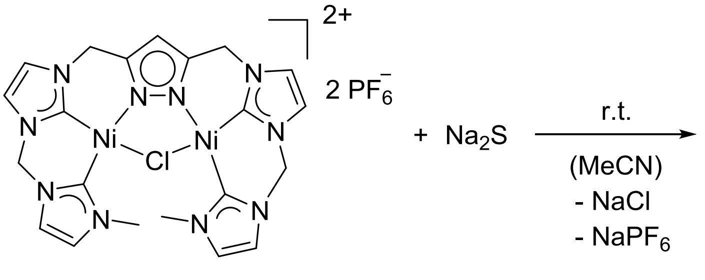

Ni$_2$C$_{21}$H$_{23}$N$_{10}$ClP$_2$F$_{12}$	Na$_2$S	Ni$_2$C$_{21}$H$_{23}$N$_{10}$SPF$_6$
858 g/mol	20 g/mol	710 g/mol

[L^{6}Ni$_2$Cl](PF$_6$)$_2$ (125 mg, 146 mmol, 1.00 equiv.) was dissolved in MeCN (3 mL). Solid sodium sulfide (95%, 13.2 mg, 0.169 mmol, 1.10 equiv.) was added to the greenish solution and crushed. Immediately, a color change from greenish to orange appeared. The suspension was stirred for three days. Afterwards, the reddish solution was filtered and the solvent was removed *in vacuo*. A red-orange solid was obtained in 78% yield (81.2 mg, 0.114 mmol). Red crystals can be received by slow diffusion of diethyl ether into a solution of in MeCN.

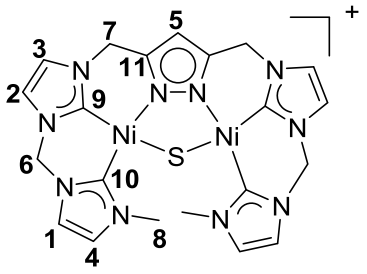

^{1}H NMR (400 MHz, 298 K, MeCN-d_3): δ [ppm] = 7.18 (d, $^3J_{HH}$ = 2.0 Hz, 2H, $_{Im}$H **1**), 7.16 (d, $^3J_{HH}$ = 2 Hz, 2H, $_{Im}$H **2**), 7.09 (d, $^3J_{HH}$ = 2 Hz, 2H, $_{Im}$H **3**), 7.01 (d, $^3J_{HH}$ = 2 Hz, 2H, $_{Im}$H **4**), 6.09 (s, 1H, H^{pz} **5**), 5.92 (s, 4H, H **6**), 5.11 (s, 4H, H **7**), 4.21 (s, 4H, H **8**).

^{13}C{^{1}H} NMR (101 MHz, 298 K, MeCN-d_3): δ [ppm] = 173.3 (C$_{carbene}$–**9**), 171.4 (C$_{carbene}$–**10**), 145.6 (C$_{quart.}$–**11**), 124.3 (C–**4**), 121.9 (C–**1**), 121.6 (C–**3**), 119.9 (C–**2**), 102.1 (C–**5**), 62.6 (C–**6**), 48.3 (C–**7**), 39.9 (C–**8**).

^{1}H^{1}H COSY NMR (400 MHz, 298 K, MeCN-d_3): δ [ppm] = 7.18/7.01 ($_{Im}$H **1** & $_{Im}$H **4**), 7.16/7.09 ($_{Im}$H **2** & $_{Im}$H **3**), 6.09/5.11 (H^{pz} **5** & H **7**).

^{1}H^{1}H NOESY NMR (400 MHz, 298 K, MeCN-d_3): δ [ppm] = 7.18/5.92 ($_{Im}$H **1** & H **6**), 7.16/5.92 ($_{Im}$H **2** & H **6**), 7.09/5.11 ($_{Im}$H **3** & H **7**), 7.01/4.21 ($_{Im}$H **4** & H **8**), 6.09/5.11 (H^{pz} **5** & H **7**).

^{1}H^{13}C HSQC NMR (^{1}H NMR, 400 MHz, ^{13}C-NMR, 101 MHz, 298 K, MeCN-d_3): δ [ppm] = 7.18/121.9, 7.16/119.9, 7.09/121.6, 7.01/124.3, 6.09/102.1, 5.92/62.6, 5.11/48.3, 4.21/39.9.

^{1}H^{13}C HMBC NMR (^{1}H NMR, 400 MHz, ^{13}C NMR, 101 MHz, 298 K, MeCN-d_3): δ [ppm] = 7.18/171.4 ($_{\text{Im}}$H **1** & C$_{\text{carbene}}$–**10**), 7.18/124.3 ($_{\text{Im}}$H **1** & C–**4**), 7.32/62.6 ($_{\text{Im}}$H **1** & C–**6**), 7.16/173.3 ($_{\text{Im}}$H **2** & C$_{\text{carbene}}$–**9**), 7.16/121.6 ($_{\text{Im}}$H **2** & C–**3**), 7.16/62.6 ($_{\text{Im}}$H **2** & C–**6**), 7.09/173.3 ($_{\text{Im}}$H **3** & C$_{\text{carbene}}$–**9**), 7.09/119.9 ($_{\text{Im}}$H **3** & C–**2**), 7.09/48.3 ($_{\text{Im}}$H **3** & C–**7**), 7.01/171.4 ($_{\text{Im}}$H **4** & C$_{\text{carbene}}$–**10**), 7.01/121.9 ($_{\text{Im}}$H **4** & C–**1**), 7.01/39.9 ($_{\text{Im}}$H **4** & C–**8**), 6.09/145.6 (H$^{\text{pz}}$ **5** & C–**11**), 5.92/173.3 (H **6** & C$_{\text{carbene}}$–**9**), 5.92/171.4 (H **6** & C$_{\text{carbene}}$–**10**), 5.92/121.9 (H **6** & C–**1**), 5.92/119.9 (H **6** & C–**2**), 5.11/173.3 (H **7** & C$_{\text{carbene}}$–**9**), 5.11/145.6 (H **7** & C$_{\text{quart.}}$–**11**), 5.11/121.6 (H **7** & C–**3**), 4.22/171.4 (H **8** & C$_{\text{carbene}}$–**10**), 4.22/124.3 (H **8** & C–**4**).

^{1}H^{15}N HMBC NMR (^{1}H NMR, 500 MHz, ^{15}N NMR, 50.7 MHz, 298 K, MeCN-d_3): δ [ppm] = 7.18/–201.3, 7.18/–198.9, 7.16/–203.4, 7.16/–200.6, 7.09/–203.4, 7.09/–200.6, 7.01/–201.3, 7.01/–198.9, 5.92/–200.6, 6.09/–113.9.

^{1}H DOSY NMR (500 MHz, 298 K, MeCN-d_3): $D_{298\text{K}}$ [m^{2}s^{-1}] = $1.06 \cdot 10^{-9}$

^{31}P NMR (121.5 MHz, 298 K, MeCN-d_3): δ [ppm] = –144.6 (hpt., $^1J_{\text{PF}}$ = 706.4 Hz).

^{19}F NMR (282 MHz, 298 K, MeCN-d_3): δ [ppm] = –72.9 (d, $^1J_{\text{PF}}$ = 706.4 Hz).

ESI-MS (MeCN) *m/z* (%): 563.20 (100) $[\text{Ni}_2\text{C}_{21}\text{H}_{23}\text{N}_{10}\text{S}]^+$.

IR (ATR): υ [cm^{-1}] = 3169.5 (w), 3144.9 (w), 3135.9 (w), 2938.3 (w), 1572.1 (w), 1475.2 (w), 1438.9 (w), 1422.1 (m), 1404.4 (m), 1384.8 (m), 1346.6 (w), 1307.5 (w), 1288.8 (w), 1258.1 (w), 1235.7 (w), 1204.0 (m), 1173.3 (m), 1084.7 (w), 1070.8 (w), 1043.7 (w), 834.1 (s), 725.0 (s), 682.2 (m), 660.7 (m).

UV-vis (MeCN, 293 K): $\lambda_{\text{max.}}$ [nm] (ε 10^3 [M^{-1}·cm^{-1}]) = 395 (10.8), 306 (48.3), 230 (49.9).

$[L^6Ni_2(SCH_3)](PF_6)_2$

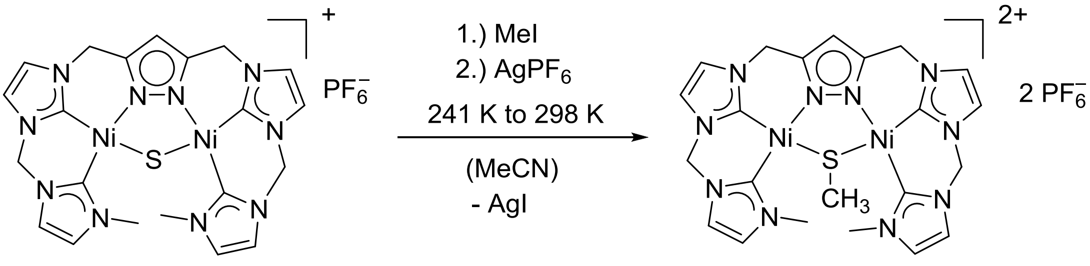

$Ni_2C_{21}H_{23}N_{10}SPF_6$ — CH_3I — $AgPF_6$ — $Ni_2C_{22}H_{26}N_{10}SP_2F_{12}$

710 g/mol — 142 g/mol — 253 g/mol — 870 g/mol

$[L^6Ni_2S]PF_6$ (40.8 mg, 0.0574 mmol, 1.00 equiv.) was dissolved in MeCN (3.0 mL). The solution was cooled down to 241 K. Under absence of light, iodomethane (3.60 μL, 8.21 mg, 0.0578 mmol, 1.01 equiv.) was slowly added to the cooled solution under stirring. Immediately, a color change from red to yellow appeared and a yellow precipitate was formed. The suspension was stirred for additional 5 min at 241 K. $AgPF_6$ (14.5 mg, 0.0574 mmol, 1.00 equiv.) was suspended in MeCN (1 mL) and also cooled down to 241 K. The $AgPF_6$ suspension was slowly added to the complex suspension. The previously formed yellow precipitate was re-dissolved and a white precipitate was formed. The yellow solution was filtered. Amber colored crystals were obtained by slow diffusion of Et_2O into the complex solution.

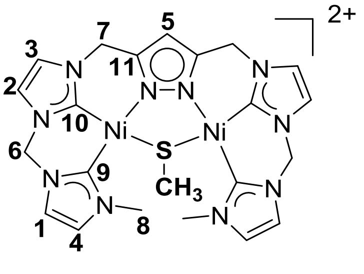

^{1}H NMR (400 MHz, 298 K, MeCN-d_3): δ [ppm] = 7.37 (d, $^3J_{HH}$ = 2.0 Hz, 2H, $_{Im}$H **1**), 7.31 (d, $^3J_{HH}$ = 2.0 Hz, 2H, $_{Im}$H **2**), 7.19 (d, $^3J_{HH}$ = 2.0 Hz, 2H, $_{Im}$H **3**), 7.13 (d, $^3J_{HH}$ = 2.0 Hz, 2H, $_{Im}$H **4**), 6.32 (s, 1H, H^{pz} **5**), 6.19 (d, $^2J_{HH}$ = 12.5 Hz, 2H, H **6**), 6.06 (d, $^2J_{HH}$ = 12.5 Hz, 4H, H **6**), 5.20 (d, $^2J_{HH}$ = 7.9 Hz, 4H, H **7**), 4.15 (s, 6H, H **8**), 1.57 (s, 1H, **SCH_3**).

^{13}C{^{1}H} NMR (126 MHz, 298 K, MeCN-d_3): δ [ppm] = 163.6 ($C_{carbene}$–**9**), 163.2 ($C_{carbene}$–**10**), 147.1 ($C_{quart.}$–**11**), 125.3 (C–**4**), 123.7 (C–**1**), 122.7 (C–**3**), 121.5 (C–**2**), 104.3 (C–**5**), 62.9 (C–**6**), 47.9 (C–**7**), 38.7 (C–**8**), 15.9 (**S–CH_3**).

^{1}H^{1}H COSY NMR (500 MHz, 298 K, MeCN-d_3): δ [ppm] = 7.37/7.13 ($_{Im}$H **1** & $_{Im}$H **4**), 7.37/4.15 ($_{Im}$H **1** & H **8**), 7.31/7.19 ($_{Im}$H **2** & $_{Im}$H **3**), 7.13/4.15 ($_{Im}$H **4** & H **8**), 6.32/5.20 (H^{pz} **5** & H **7**).

^{1}H^{1}H NOESY NMR (500 MHz, 298 K, MeCN-d_3): δ [ppm] = 7.37/6.12 ($_{Im}$H **1** & H **6**), 7.31/6.12 ($_{Im}$H **2** & H **6**), 7.19/5.20 ($_{Im}$H **3** & H **7**), 7.13/4.15 ($_{Im}$H **4** & H **8**), 6.32/5.20 (H^{pz} **5** & H **7**), 4.15/1.57 (H **8** & **SCH$_3$**).

^{1}H^{13}C HSQC NMR (^{1}H NMR, 500 MHz, ^{13}C NMR, 126 MHz, 298 K, MeCN-d_3): δ [ppm] = 7.37/123.7, 7.31/121.5, 7.19/122.7, 7.13/125.3, 6.32/104.3, 6.12/62.9, 5.20/47.9, 4.15/38.7, 1.57/15.9.

^{1}H^{13}C HMBC NMR (^{1}H NMR, 500 MHz, ^{13}C NMR, 126 MHz, 298 K, MeCN-d_3): δ [ppm] = 7.37/163.6 ($_{Im}$H **1** & C$_{carbene}$–**9**), 7.37/125.3 ($_{Im}$H **1** & C–**4**), 7.31/163.2 ($_{Im}$H **2** & C$_{carbene}$–**10**), 7.31/122.7 ($_{Im}$H **2** & C–**3**), 7.19/163.2 ($_{Im}$H **3** & C$_{carbene}$–**10**), 7.19/121.5 ($_{Im}$H **3** & C–**2**), 7.13/163.6 ($_{Im}$H **4** & C$_{carbene}$–**9**), 7.13/123.7 ($_{Im}$H **4** & C–**1**), 6.32/147.1 (H^{pz} **5** & C$_{quart.}$–**11**), 5.20/163.2 (H **7** & C$_{carbene}$–**10**), 5.20/147.1 (H **7** & C$_{quart.}$–**11**), 5.20/122.7 (H **7** & $_{Im}$H **3**), 5.20/104.3 (H **7** & C–**5**), 4.15/163.6 (H **8** & C$_{carbene}$–**9**), 4.15/125.3 (H **8** & C–**4**), 1.57/163.2 (**SCH$_3$** & C$_{carbene}$–**10**).

^{1}H^{15}N HMBC NMR (^{1}H NMR, 500 MHz, ^{15}N NMR, 50.7 MHz, 298 K, MeCN-d_3): δ [ppm] = 7.37/–197.2, 7.37/–196.3, 7.31/–200.2, 7.31/–198.0, 7.19/–200.2, 7.19/–198.0, 7.13/–197.2, 7.13/–196.3, 6.32/–131.0, 5.20/–200.2, 5.20/–131.0, 4.15/–197.2.

ESI-MS (MeCN-d_3) *m/z* (%): 723.18 (100) $[Ni_2C_{22}H_{26}N_{10}SPF_6]^+$, 289.15 (22.8) $[Ni_2C_{22}H_{26}N_{10}S]^{2+}$.

$[L^6Ni_2(SCH_3)]PF_6$

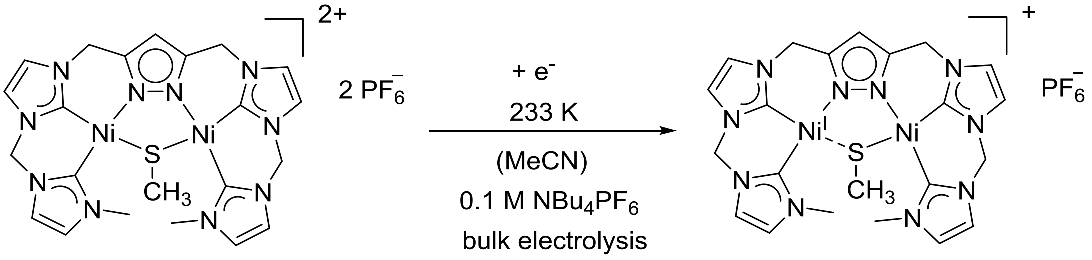

$[L^6Ni_2(SCH_3)](PF_6)_2$ (9.40 mg, 0.0574 mmol, 1.00 equiv.) was dissolved in a 0.1 M MeCN NBu_4PF_6 solution (15.0 mL). The solution was cooled down to 233 K. The solution was electrolysed at –2.1 V *vs.* Ag/$AgNO_3$ for 68 min. and the reaction was followed *via* EPR spectroscopy and UV-vis spectroscopy.

UV-vis (MeCN, 298 K): $\lambda_{max.}$ [nm] (abs. [a.u.]) = 383 (0.81), 525 (0.26).
UV-vis (MeCN, 233 K): $\lambda_{max.}$ [nm] (abs. [a.u.]) = 385 (0.74), 525 (0.36), 786 (0.15).
EPR (9.44 GHz, 100 K, MeCN, dark purple/black): g_1 =2.18, g_2 =2.05, g_3 =2.04, $g_{av.}$ =2.09.
CV (0.7 mM, 0.1 M NBu_4PF_6/MeCN, 298 K): $E_{1/2}$ [V] *vs.* Ag/$AgNO_3$ = –1.93
CV (0.7 mM, 0.1 M NBu_4PF_6/MeCN, 233 K): $E_{1/2}$ [V] *vs.* Ag/$AgNO_3$ = –1.97
CV (1.0 mM, 0.1 M NBu_4PF_6/MeCN, 298 K): $E_{1/2}$ [V] *vs.* Fc/Fc^+ = –2.03

$[(L^6)_2Ni_2(SHS)](PF_6)_3$

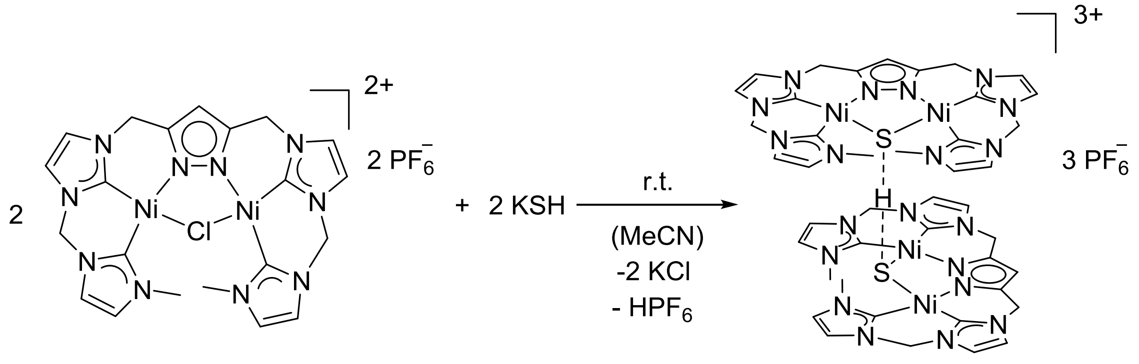

$Ni_2C_{21}H_{23}N_{10}ClP_2F_{12}$ KSH $Ni_4C_{42}H_{47}N_{20}S_2P_3F_{18}$

858 g/mol 72 g/mol 1566 g/mol

$[L^6Ni_2Cl](PF_6)_2$ (70.0 mg, 0.0816 mmol, 1.00 equiv.) was dissolved in MeCN (6 mL). Solid KSH (95%, 6.82 mg, 0.0944 mmol, 1.10 equiv.) was added to the greenish solution and the solid particles were crushed. The solution turned over time from greenish to orange. The suspension was stirred for three days and the solid was filtered. Red crystals were obtained by slow diffusion of Et_2O to the red filtrate.

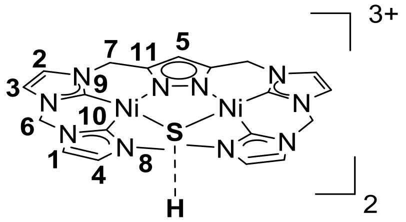

^{1}H NMR (500 MHz, 298 K, MeCN-d_3): δ [ppm] = 7.22 (d, $^3J_{HH}$ = 2.0 Hz, 4H, $_{Im}$H **1**), 7.21 (d, $^3J_{HH}$ = 1.9 Hz, 4H, $_{Im}$H **2**), 7.14 (d, $^3J_{HH}$ = 1.9 Hz, 4H, $_{Im}$H **3**), 7.02 (d, $^3J_{HH}$ = 2 Hz, 4H, $_{Im}$H **4**), 6.23 (s, 2H, H^{pz} **5**), 5.93 (s, 8H, H **6**), 5.16 (s, 8H, H **7**), 4.12 (s, 12H, H **8**), 1.01 (s, 1H, **S–H**).
^{13}C{^{1}H} NMR (126 MHz, 298 K, MeCN-d_3): δ [ppm] = 166.8 ($C_{carbene}$–**9**), 165.0 ($C_{carbene}$–**10**), 146.5 ($C_{quart.}$–**11**), 125.1 (C–**4**), 122.7 (C–**1**), 122.4 (C–**3**), 120.7 (C–**2**), 103.5 (C–**5**), 62.5 (C–**6**), 48.1 (C–**7**), 39.9 (C–**8**).
^{1}H DOSY NMR (500 MHz, 298 K, MeCN-d_3): D_{298K} [m^2s^{-1}] = $9.47\cdot10^{-10}$.
^{1}H DOSY NMR (500 MHz, 243 K, MeCN-d_3): D_{243K} [m^2s^{-1}] = $3.77\cdot10^{-10}$.
ESI-MS (MeCN) *m/z* (%):708.90 (19.1) $[Ni_2C_{21}H_{24}N_{10}S(PF_6)]^+$, 563.09 (100) $[Ni_2C_{21}H_{23}N_{10}S]^+$, 281.94 (12.2) $[Ni_2C_{21}H_{24}N_{10}S]^{2+}$.
IR (ATR): υ [cm^{-1}] = 3172.2 (w), 3146.2 (w), 3112.6 (w), 1570.3 (w), 1561.8 (w), 1527.4 (w), 1475.3 (w), 1461.2 (w), 1441.7 (w), 1423.0 (m), 1405.3 (m), 1385.8 (m), 1346.6 (w),

1309.3 (w), 1290.7 (m), 1260.9 (w), 1239.5 (w), 1205.9 (m), 1176.1 (m), 1126.7 (w), 1106.2 (w), 1071.7 (w), 1043.7 (w), 1012.1 (w), 967.3 (w), 828.5 (s), 793.1 (s), 731.6 (s), 717.6 (s), 693.3 (s), 681.2 (s), 659.8 (s), 642.1 (s), 554.5 (s).

UV-vis (MeCN, 293 K): $\lambda_{\text{max.}}$ [nm] (ε 10^3 [$\text{M}^{-1}\cdot\text{cm}^{-1}$]) = 394 (7.9), 306 (48.9), 230 (50.9).

$[(L^6)_2Ni_2(SHS)](PF_6)_2(OTf)$

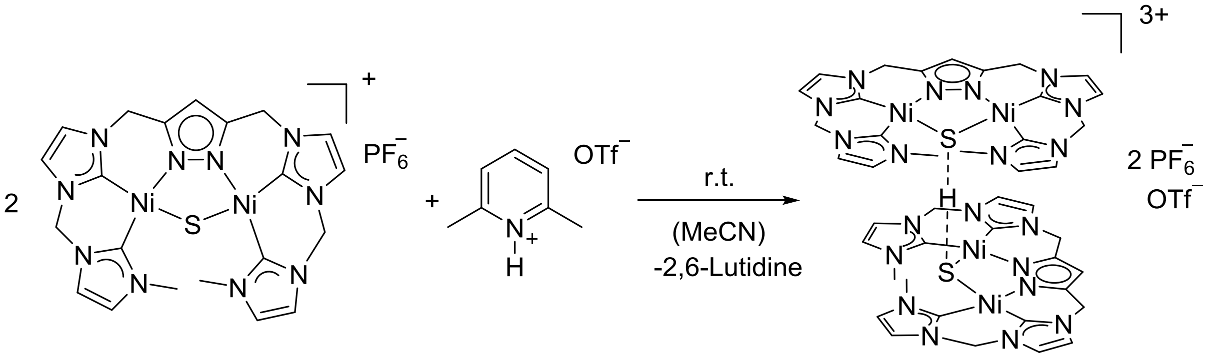

$Ni_2C_{21}H_{23}N_{10}SPF_6$ $C_8H_{10}NSO_3F_3$ $Ni_4C_{43}H_{47}N_{20}S_3O_3P_2F_{15}$

710 g/mol 257 g/mol 1570 g/mol

[L^{6}Ni$_2$S]PF$_6$ (6.36 mg, 0.00896 mmol, 1.00 equiv.) was dissolved in MeCN-d_3 (0.5 mL) and filled into a J Young valve NMR tube. A stock solution was prepared by dissolving 2,6-lutidinium triflate (14.0 mg, 0.0542 mmol, 6.05 equiv.) in MeCN-d_3 (0.2 mL). Aliquotes of 0.1 equiv. 2,6–lutidinium triflate (3 μL) were added to the complex solution and a ^{1}H NMR spectra were measured at three different temperatures (298 K, 253 K and 233 K). For detailed information according the whole titration experiment see **appendix**.

$[L^6Ni_2S]PF_6$

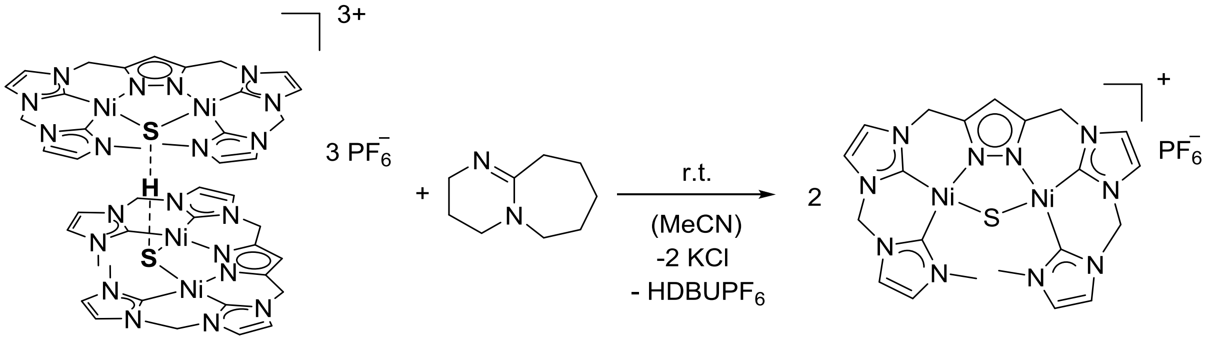

$Ni_4C_{42}H_{47}N_{20}S_2P_3F_{18}$	$C_9H_{16}N_2$	$Ni_2C_{21}H_{23}N_{10}SPF_6$
1566 g/mol	152 g/mol	710 g/mol

$[L^6Ni_4(SHS)](PF_6)_3$ (6.82 mg, 0.00436 mmol, 1.00 equiv.) was dissolved in MeCN-d_3 (0.5 mL). 1,8-Diazabicyclo[5.4.0]undec-7-en (DBU) (≥99%, 0.4 μL, 0.408 mg, 0.00268 mmol, 0.60 equiv.) was added to the orange solution. Crystals can be obtained by slow diffusion of Et_2O into the complex solution.

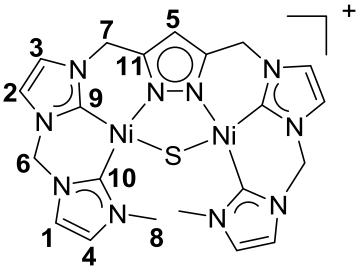

^{1}H NMR (400 MHz, 298 K, MeCN-d_3): δ [ppm] = 7.19 (d, $^3J_{HH}$ = 1.8 Hz, 2H, $_{Im}$H **1**), 7.17 (d, $^3J_{HH}$ = 1.7 Hz, 2H, $_{Im}$H **2**), 7.10 (d, $^3J_{HH}$ = 1.7 Hz, 2H, $_{Im}$H **3**), 7.01 (d, $^3J_{HH}$ = 1.8 Hz, 2H, $_{Im}$H **4**), 6.10 (s, 1H, H^{pz} **5**), 5.93 (s, 4H, H **6**), 5.12 (s, 4H, H **7**), 4.22 (s, 4H, H **8**).

ESI-MS (MeCN) *m/z* (%): 563.15 (100) $[Ni_2C_{21}H_{23}N_{10}S]^+$.

[$L^6Ni_2(SH)](PF_6)(OTf)$

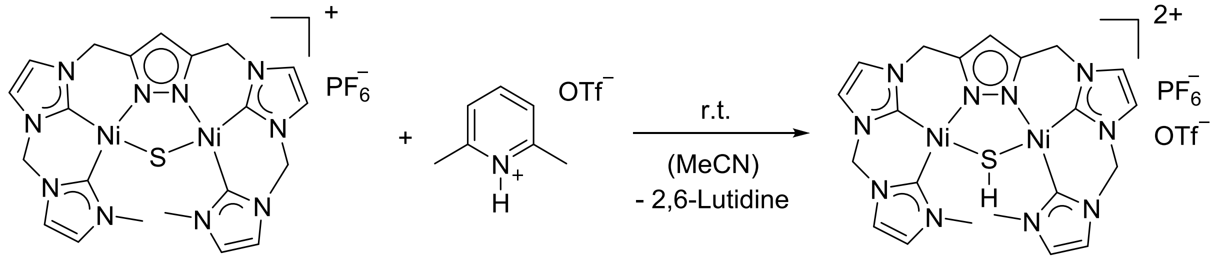

$Ni_2C_{21}H_{23}N_{10}SPF_6$	$C_8H_{10}NSO_3F_3$	$Ni_2C_{22}H_{24}N_{10}S_2O_3PF_9$
710 g/mol	257 g/mol	860 g/mol

[$L^6Ni_2S]PF_6$ (37.9 mg, 0.0534 mmol, 1.00 equiv.) was dissolved in MeCN (3 mL). 2,6-Lutidiniumtriflate (15.1 mg, 0.0587 mmol, 1.10 equiv.), dissolved in MeCN (0.1 mL) was slowly added to the stirred, red solution. Immediately, a color change appears from red to yellow. The solution was stirred for additional 10 min. and Et_2O (6 mL) was added. The yellow precipitate was filtered off and washed several times with Et_2O. Afterwards, the pale yellow solid was dried *in vacuo*. A pale yellow solid was obtained in 75% yield (34.5 mg, 0.0401 mmol). Pale yellow crystals were obtaned by slow Et_2O diffusion into a solution of MeCN.

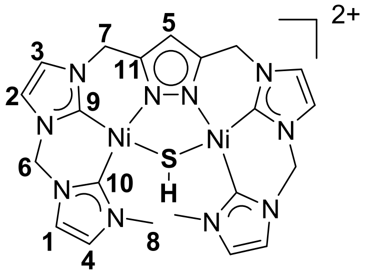

^{1}H NMR (500 MHz, 298 K, MeCN-d_3): δ [ppm] = 7.35 (d, $^3J_{HH}$ = 2.0 Hz, 2H, $_{Im}$H **1**), 7.30 (d, $^3J_{HH}$ = 2.0 Hz, 2H, $_{Im}$H **2**), 7.21 (d, $^3J_{HH}$ = 2.0 Hz, 2H, $_{Im}$H **3**), 7.12 (d, $^3J_{HH}$ = 2.0 Hz, 2H, $_{Im}$H **4**), 6.33 (s, 1H, H^{pz} **5**), 6.09 (s, 4H, H **6**), 5.22 (s, 4H, H **7**), 4.04 (s, 6H, H **8**), 0.34 (s, 1H, **SH**).

^{13}C{^{1}H} NMR (126 MHz, 298 K, MeCN-d_3): δ [ppm] = 162.3 ($C_{carbene}$–**9**), 160.7 ($C_{carbene}$–**10**), 147.1 ($C_{quart.}$–**11**), 125.7 (C–**4**), 123.7 (C–**1**), 123.1 (C–**3**), 121.4 (C–**2**), 104.3 (C–**5**), 62.9 (C–**6**), 47.9 (C–**7**), 39.9 (C–**8**).

^{1}H^{1}H COSY NMR (500 MHz, 298 K, MeCN-d_3): δ [ppm] = 7.35/7.12 ($_{Im}$H **1** & $_{Im}$H **4**), 7.35/6.09 ($_{Im}$H **1** & H **6**), 7.35/4.04 ($_{Im}$H **1** & H **8**), 7.30/7.21 ($_{Im}$H **2** & $_{Im}$H **3**), 7.30/6.09 ($_{Im}$H **2**

& H **6**), 7.21/5.22 ($_{\mathrm{Im}}$H **3** & H **7**), 7.12/6.09 ($_{\mathrm{Im}}$H **4** & H **6**), 7.12/4.04 ($_{\mathrm{Im}}$H **4** & H **8**), 6.33/5.25 (H$^{\mathrm{pz}}$ **5** & H **7**), 6.09/5.21 (H **6** & H **7**), 6.09/4.04 (H **6** & H **8**).

^{1}H^{1}H NOESY NMR (500 MHz, 298 K, MeCN-d_3): δ [ppm] = 7.35/6.09 ($_{\mathrm{Im}}$H **1** & H **6**), 7.35/4.04 ($_{\mathrm{Im}}$H **1** & H **8**), 7.30/6.09 ($_{\mathrm{Im}}$H **2** & H **6**), 7.30/5.22 ($_{\mathrm{Im}}$H **2** & H **7**), 7.22/5.22 ($_{\mathrm{Im}}$H **3** & H **7**), 7.21/6.09 ($_{\mathrm{Im}}$H **3** & H **6**), 7.12/6.09 ($_{\mathrm{Im}}$H **4** & H **6**), 7.12/4.04 ($_{\mathrm{Im}}$H **4** & H **8**), 6.33/5.22 (H$^{\mathrm{pz}}$ **5** & H **7**).

^{1}H^{13}C HSQC NMR (^{1}H NMR, 400 MHz, ^{13}C NMR, 101 MHz, 298 K, MeCN-d_3): δ [ppm] = 7.35/123.7, 7.30/121.4, 7.21/123.1, 7.12/125.7, 6.33/104.3, 6.09/62.9, 5.22/47.9, 4.04/39.9.

^{1}H^{13}C HMBC NMR (^{1}H NMR, 400 MHz, ^{13}C NMR, 101 MHz, 298 K, MeCN-d_3): δ [ppm] = 7.35/160.7 ($_{\mathrm{Im}}$H **1** & C$_{\mathrm{carbene}}$–**10**), 7.35/125.7 ($_{\mathrm{Im}}$H **1** & C–**4**), 7.35/62.9 ($_{\mathrm{Im}}$H **1** & C–**6**), 7.30/162.3 ($_{\mathrm{Im}}$H **2** & C$_{\mathrm{carbene}}$–**9**), 7.30/123.1 ($_{\mathrm{Im}}$H **2** & C–**3**), 7.21/162.3 ($_{\mathrm{Im}}$H **3** & C$_{\mathrm{carbene}}$–**9**), 7.21/121.4 ($_{\mathrm{Im}}$H **3** & C–**2**), 7.12/160.7 ($_{\mathrm{Im}}$H **4** & C$_{\mathrm{carbene}}$–**10**), 7.12/123.7 ($_{\mathrm{Im}}$H **4** & C–**1**), 7.12/39.9 ($_{\mathrm{Im}}$H **4** & C–**8**), 6.33/147.1 (H$^{\mathrm{pz}}$ **5** & C–**11**), 6.09/162.3 (H **6** & C$_{\mathrm{carbene}}$–**9**), 6.09/160.7 (H **6** & C$_{\mathrm{carbene}}$–**10**), 6.09/123.7 (H **6** & C–**1**), 6.09/121.4 (H **6** & C–**2**), 5.22/162.3 (H **7** & C$_{\mathrm{carbene}}$–**9**), 5.22/147.1 (H **7** & C$_{\mathrm{quart.}}$–**11**), 5.22/123.1 (H **7** & C–**3**), 5.22/104.3 (H **7** & C–**5**), 4.04/160.7 (H **8** & C$_{\mathrm{carbene}}$–**10**), 4.04/125.7 (H **8** & C–**4**).

^{1}H^{15}N HMBC NMR (^{1}H NMR, 500 MHz, ^{15}N NMR, 50.7 MHz, 298 K, MeCN-d_3): δ [ppm] = 7.35/–197.5, 7.35/–194.9, 730/–199.5, 7.30/–198.7, 7.21/–199.5, 7.21/–198.7, 7.12/–197.5, 7.12/–194.9, 6.33/–134.7, 6.09/–198.7, 6.09/–197.5, 5.22/–199.5, 5.22/–134.7, 4.04/–194.9.

^{1}H DOSY NMR (500 MHz, 298 K, MeCN-d_3): $D_{298\mathrm{K}}$ [m^{2}s^{-1}] = $1.00 \cdot 10^{-9}$.

^{31}P NMR (121.5 MHz, 298 K, MeCN-d_3): δ [ppm] = –144.6 (hpt., $^1J_{\mathrm{PF}}$ = 706.4 Hz).

^{19}F NMR (282 MHz, 298 K, MeCN-d_3): δ [ppm] = –79.4 (s, CF$_3$), –72.9 (d, $^1J_{\mathrm{PF}}$ = 706.5 Hz).

ESI-MS (MeCN) *m/z* (%): 713.13 (73.7) [$\mathrm{Ni_2C_{21}H_{24}N_{10}S(OTf)}$]$^+$, 709.13 (58.2), [$\mathrm{Ni_2C_{21}H_{24}N_{10}S(PF_6)}$]$^+$, 563.20 (36.0) [$\mathrm{Ni_2C_{21}H_{23}N_{10}S}$]$^+$, 282.21 (100) [$\mathrm{Ni_2C_{21}H_{24}N_{10}S}$]$^{2+}$.

IR (ATR): υ [cm^{-1}] = 3172.2 (w), 3141.5 (w), 2959.8 (w), 2587.0 (**SH**, w), 1570.3 (w), 1562.8 (w), 1529.3 (w), 1481.7 (m), 1467.8 (w), 1445.4 (m), 1410.9 (m), 1405.3 (m), 1387.6 (w), 1340.1 (m), 1300.0 (m), 1232.9 (s), 1201.2 (s), 1179.8 (s), 117.6 (s), 1029.8 (s), 981.3 (s), 824.7 (s), 731.6 (s), 683.1 (m), 665.4 (m), 635.6 (s), 556.4 (s).

UV-vis (MeCN, 293 K): $\lambda_{\mathrm{max.}}$ [nm] (ε 10^3 [M$^{-1}\cdot$cm^{-1}]) = 376 (2.8), 305 (10.8), 306 (40.1), 220 (51.2).

$[L^6Ni_2(SD)](PF_6)(OTf)$

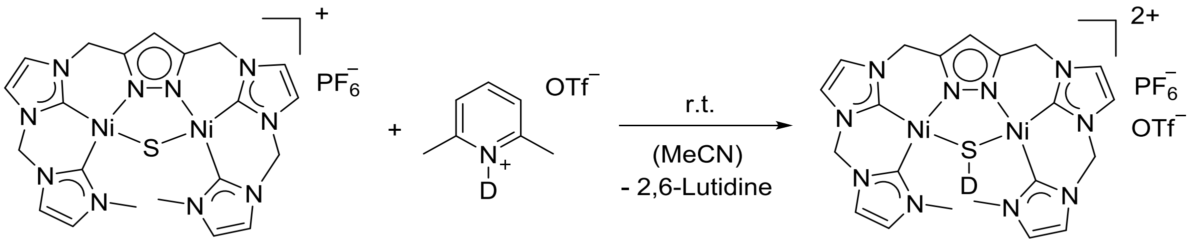

$Ni_2C_{21}H_{23}N_{10}SPF_6$ $C_8H_9DNSO_3F_3$ $Ni_2C_{22}H_{23}DN_{10}S_2O_3PF_9$

710 g/mol 258 g/mol 861 g/mol

$[L^6Ni_2S]$ (12.6 mg, 0.0178 mmol, 1.00 equiv.) was dissolved in MeCN (0.5 mL). 2,6-Lutidinium–*d* triflate (4.55 mg, 0.0176 mmol, 0.990 equiv.), dissolved in MeCN (0.1 mL), was slowly added to the red solution. Immediately, a color change appeared from red to yellow. Yellow crystals were obtained in 23% yield (3.50 mg, 0.00406 mmol) by slow diffusion of diethyl ether in a MeCN solution.

^{1}H NMR (500 MHz, 298 K, MeCN-d_3): δ [ppm] = 7.35 (d, $^3J_{HH}$ = 2.0 Hz, 2H, $_{Im}$H **1**), 7.30 (d, $^3J_{HH}$ = 2.0 Hz, 2H, $_{Im}$H **2**), 7.22 (d, $^3J_{HH}$ = 2.0 Hz, 2H, $_{Im}$H **3**), 7.13 (d, $^3J_{HH}$ = 2.0 Hz, 2H, $_{Im}$H **4**), 6.33 (s, 1H, H^{pz} **5**), 6.09 (s, 4H, H **6**), 5.22 (s, 4H, H **7**), 4.04 (s, 6H, H **8**).
^{2}H NMR (61 MHz, 238 K, MeCN): δ [ppm] = 0.75 (s, **SD**).
IR (ATR): υ [cm^{-1}] = 3169.5 (w), 3134.0 (w), 3109.8 (w), 2957.9 (w), 2866.6 (w), 1896.5 (**SD**, w), 1574.0 (w), 1561.9 (w), 1530.2 (w), 1480.8 (m), 1467.8 (m), 1447.3 (m), 1426.8 (w), 1414.7 (m), 1404.4 (m), 1388.6 (m), 1371.8 (w), 1357.8 (w), 1342.9 (m), 1314.0 (m),1300.0 (m), 1257.2 (s), 1222.7 (s), 1207.8 (s), 1166.8 (s), 1112.7 (m), 1075.4 (m), 1054.9 (m), 1026.9 (s), 835.9 (s), 826.6 (s), 795.9 (s), 731.6 (s), 681.2 (s), 664.5 (s), 633.7 (s), 573.1 (s), 556.4 (s), 516.3 (s).

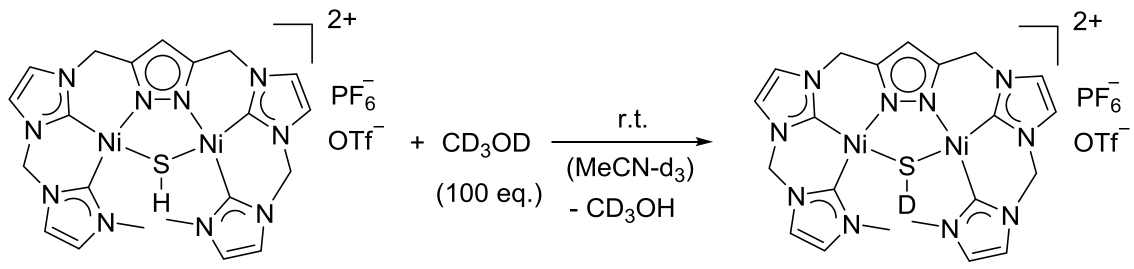

$Ni_2C_{22}H_{23}DN_{10}S_2O_3PF_9$ — CD_4O — $Ni_2C_{22}H_{23}DN_{10}S_2O_3PF_9$

860 g/mol — 36 g/mol — 861 g/mol

[L^{6}Ni$_2$(SH)](PF$_6$)(OTf) (6.00 mg, 0.00698 mmol, 1.00 equiv.) was dissolved in MeCN-*d*$_3$ (0.5 mL). Methanol-*d*$_4$ (28.3 μL, 25.2 mg, 0.698 mmol, 100 equiv.) was added to the yellow solution. Afterwards the solvent was removed *in vacuo* for several days. A yellow solid was obtained.

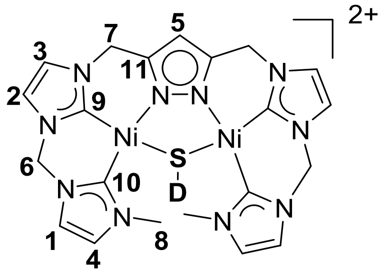

^{1}H NMR (400 MHz, 298 K, MeCN-*d*$_3$): δ [ppm] = 7.35 (d, $^3J_{HH}$ = 2.0 Hz, 2H, $_{Im}$H **1**), 7.30 (d, $^3J_{HH}$ = 2.0 Hz, 2H, $_{Im}$H **2**), 7.22 (d, $^3J_{HH}$ = 2.0 Hz, 2H, $_{Im}$H **3**), 7.13 (d, $^3J_{HH}$ = 2.0 Hz, 2H, $_{Im}$H **4**), 6.33 (s, 1H, H^{pz} **5**), 6.09 (s, 4H, H **6**), 5.22 (s, 4H, H **7**), 4.04 (s, 6H, H **8**).

ESI-MS (MeCN-*d*$_3$) *m/z* (%): 714.08 (70.0) $[Ni_2C_{21}H_{23}DN_{10}S(OTf)]^+$, 713.13 (51.1) $[Ni_2C_{21}H_{24}N_{10}S(OTf)]^+$, 710.16 (100) $[Ni_2C_{21}H_{23}DN_{10}S(PF_6)]^+$ 709.22 (34.5), $[Ni_2C_{21}H_{24}N_{10}S(PF_6)]^+$, 563.27 (29.5) $[Ni_2C_{21}H_{23}N_{10}S]^+$, 282.64 (70.3) $[Ni_2C_{21}H_{23}DN_{10}S]^{2+}$, 282.19 (23.6) $[Ni_2C_{21}H_{24}N_{10}S]^{2+}$.

Determination of pK_a([L^{6}Ni$_2$(SH)]$^{2+}$)

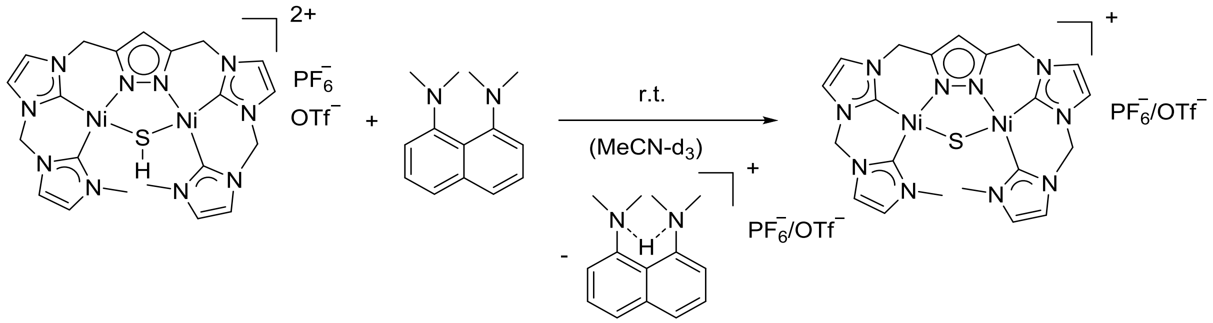

$Ni_2C_{22}H_{24}N_{10}S_2O_3PF_9$	$C_{14}H_{18}N_2$	$Ni_2C_{21}H_{23}N_{10}S(PF_6/CF_3SO_3)$
860 g/mol	214 g/mol	710 g/mol/714 g/mol

^{1}H NMR: [L^{6}Ni$_2$(SH)](PF$_6$)(OTf) (4.08 mg, 0.00474 mmol, 1.00 equiv.) was dissolved in MeCN-d_3 (0.5 mL). A stock solution (0.475 M) of *N*,*N*,*N*’,*N*’-tetramethylnaphthalene-1,8-diamine (protone-sponge®, 99%) (10.2 mg, 0.0475 mmol, 10.0 equiv.) in MeCN-d_3 (100 μL) was prepared. ^{1}H NMR experiments were conducted after addition of aliquots of protone-sponge® to the complex solution at 298 K (**Table 10.2**). The experiment was finished after addition of 10.0 equiv. (100 μL) of *N*,*N*,*N*’,*N*’-tetramethylnaphthalene-1,8-diamine. See **appendix** for evaluation of the obtained ^{1}H NMR spectra.

Table 10.2: Detailed information of the titration experiment

Experiment number #	Total *V* (Proton-sponge®) [μL]	Total amount of equivalents
#1	0	0.0
#2	1	0.1
#3	2	0.2
#4	3	0.3
#5	4	0.4
#6	5	0.5
#7	7	0.7
#8	8	0.8
#9	9	0.9
#10	10	1.0
#11	11	1.1
#12	12	1.2
#13	13	1.3
#14	14	1.4
#15	15	1.5
#16	16	1.6
#17	17	1.7
#18	18	1.8
#19	19	1.9
#20	20	2.0
#21	25	2.5
#22	30	3.0
#23	35	3.5
#24	40	4.0
#25	50	5.0
#26	60	6.0
#27	70	7.0
#28	100	10.0

UV-vis (MeCN, 293 K): **[L^6Ni_2(SH)](PF_6)(OTf)** (50 μM, 4.08 mg, 0.0950 μmol, 1.00 equiv.) in MeCN (1.9 mL) was filled into a UV-vis cuvette. A solution of *N*,*N*,*N*',*N*'-tetramethylnaphthalene-1,8-diamine (proton-sponge®, 99%) (10.2 mg, 0.0475 mmol, 10.0 equiv.) in MeCN (100 μL) was prepared. UV-vis spectra were conducted after addition of aliquots of protone-sponge® to the complex soltion at 293 K. Aliquots of 0.1 equivalents (1.0 μL) were added to the complex solution. The experiment was finished after addition of 2.70 equiv. (27 μL) of *N*,*N*,*N*',*N*'-tetramethylnaphthalene-1,8-diamine. See **appendix** and results and discussion for evaluation of the obtained spectra.

Reduction of [L^{6}Ni$_2$(SH)](PF$_6$)(OTf) by Co(Cp*)$_2$

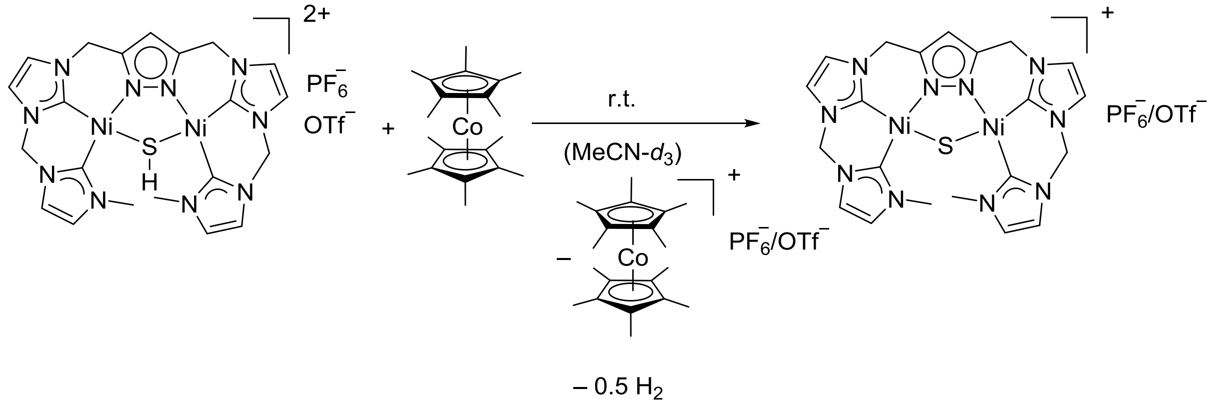

$Ni_2C_{22}H_{24}N_{10}S_2O_3PF_9$	$CoC_{20}H_{30}$	$Ni_2C_{21}H_{23}N_{10}S(PF_6/CF_3SO_3)$
860 g/mol	329 g/mol	710 g/mol/714 g/mol

[L^{6}Ni$_2$(SH)](PF$_6$)(OTf) (3.96 mg, 0.00460 mmol, 1.00 equiv.) was dissolved in MeCN-d_3 (0.5 mL). and cooled down to 241 K. Co(Cp*)$_2$ (1.55 mg, 0.00471 mmol, 1.02 equiv.) was solved in MeCN-d_3 (0.1 mL) and also cooled down to 241 K. Under stirring, the brownish Co(Cp*)$_2$ solution was slowly added to the complex solution. The yellow solution turned to red-brownish, was warmed up to room temperature and the solid was filtered.

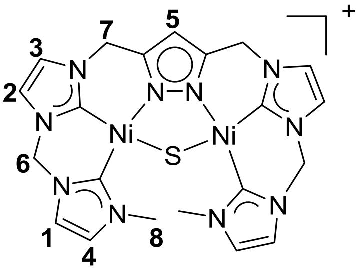

^{1}H NMR (400 MHz, 299 K, MeCN-d_3): δ [ppm] = 7.20 (d, $^3J_{HH}$ = 1.9 Hz, 2H, $_{\mathrm{Im}}$H **1**), 7.19 (d, $^3J_{HH}$ = 1.9 Hz, 2H, $_{\mathrm{Im}}$H **2**), 7.11 (d, $^3J_{HH}$ = 1.9 Hz, 2H, $_{\mathrm{Im}}$H **3**), 7.02 (d, $^3J_{HH}$ = 1.9 Hz, 2H, $_{\mathrm{Im}}$H **4**), 6.12 (s, 1H, H$^{\mathrm{pz}}$ **5**), 5.94 (s, 4H, H **6**), 5.12 (s, 4H, H **7**), 4.21 (s, 4H, H **8**).

Oxidation of $[L^6Ni_2S]PF_6$ by $[Fe(Cp^*)_2]PF_6$

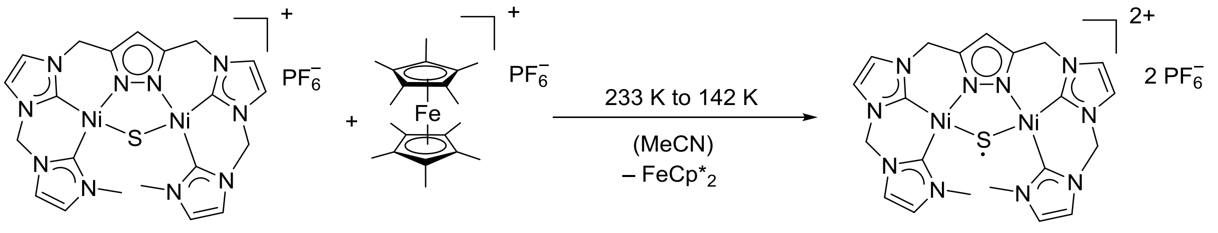

$Ni_2C_{21}H_{23}N_{10}SPF_6$	$FeC_{20}H_{30}PF_6$	$Ni_2C_{21}H_{23}N_{10}SP_2F_{12}$
710 g/mol	471 g/mol	855 g/mol

$[L^6Ni_2S]PF_6$ (3.06 mg, 0.00431 mmol, 1.00 equiv.) was dissolved in MeCN (200 μL) and transferred into an EPR tube. $[Fe(Cp^*)_2]PF_6$ (2.03 mg, 0.00431 mmol, 1.00 equiv.) was dissolved in MeCN (20 μL) and cooled down to 233 K. The green solution of $[Fe(Cp^*)_2]PF_6$ was transferred into the neck of the EPR tube. Afterwards, the complex solution was cooled down to 233 K. The $[Fe(Cp^*)_2]PF_6$ was rinsed slowly into the complex solution. The solution in the EPR tube was immediately freeze quenched in liquid nitrogen after the solution turned slightly orange. A X-band EPR measurement of the frozen solution was conducted at 142 K at. Afterwards the solution was warmed up to room temperature. Immediately, a color change from orange-green to yellow appeared. The solution was again frozen in liquid nitrogen and again an EPR measurement was done at 142 K.

EPR (9.43 GHz, 142 K, MeCN, orange solution): g_1 =2.17, g_2 =2.10, g_3 =2.04, $g_{av.}$ =2.10.
EPR (9.43 GHz, 142 K, MeCN, yellow solution): EPR silent.

HAT reaction with 100 equiv. TEMPO–H

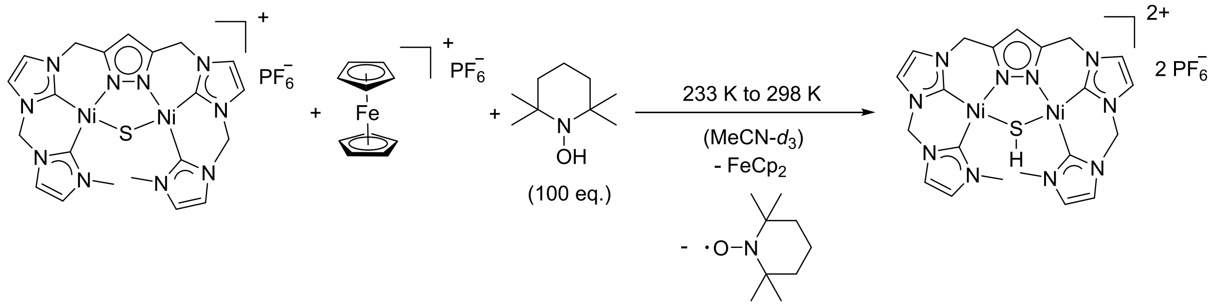

$Ni_2C_{21}H_{23}N_{10}SPF_6$	$FeC_{10}H_{10}PF_6$	$C_9H_{19}NO$	$Ni_2C_{21}H_{24}N_{10}SP_2F_{12}$
710 g/mol	331 g/mol	157 g/mol	856 g/mol

[L^{6}Ni$_2$S]PF$_6$ (5.40 mg, 0.00761 mmol, 1.00 equiv.) was dissolved in MeCN-d_3 (0.5 mL). 2,2,6,6-Tetramethyl-piperidinylol (TEMPO–H) (120 mg, 0.761 mmol, 100 equiv.) was dissolved in MeCN-d_3 (0.2 mL). [FeCp$_2$]PF$_6$ (2.76 mg, 0.00836 mmol, 1.09 equiv.) was dissolved in MeCN-d_3 (0.2 mL). All three solutions were cooled down to 233 K. TEMPO–H was added to the complex solution. Under stirring, [FeCp$_2$]PF$_6$ was slowly added to the orange complex solution. A color change was observed from orange to yellow. The solution was stirred for additional 10 min. and was warmed up to room temperature. The yellow solution was filtered. Same results were obtained by use of [Fe(Cp*)$_2$]PF$_6$ instead of [FeCp$_2$]PF$_6$.

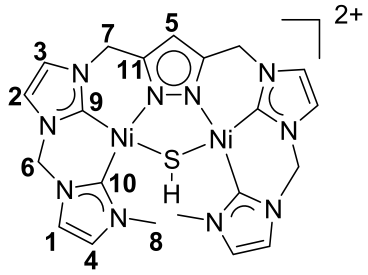

^{1}H NMR (400 MHz, 298 K, MeCN-d_3): δ [ppm] = 7.33 (*ps* s, 2H, $_{\mathrm{Im}}$H **1**), 7.29 (*ps* s, 2H, $_{\mathrm{Im}}$H **2**), 7.20 (*ps* s, 2H, $_{\mathrm{Im}}$H **3**), 7.11 (*ps* s, 2H, $_{\mathrm{Im}}$H **4**), 6.31 (s, 1H, H$^{\mathrm{pz}}$, **5**), 6.07 (s, 4H, CH$_2$, **6**), 5.20 (s, 4H, H **7**), 4.06 (s, 6H, H **8**).

^{31}P NMR (121.5 MHz, 298 K, MeCN-d_3): δ [ppm] = –144.6 (hpt., $^1J_{\mathrm{PF}}$ = 706.4 Hz).

^{19}F NMR (282 MHz, 298 K, MeCN-d_3): δ [ppm] = –72.7 (d, $^1J_{\mathrm{PF}}$ = 706.7 Hz).

HAT reaction with 100 equiv. of phenylhydrazine

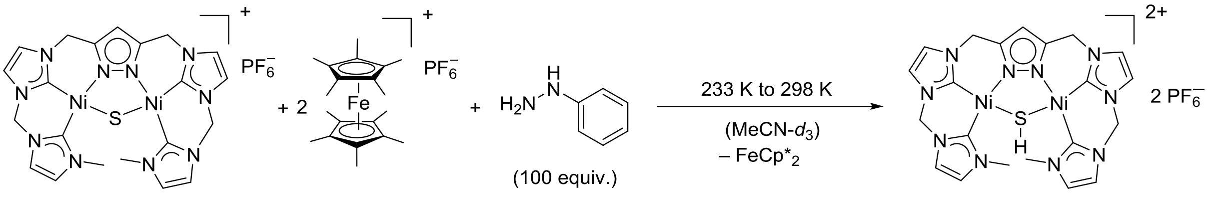

$Ni_2C_{21}H_{23}N_{10}SPF_6$	$FeC_{20}H_{30}PF_6$	C_6H_8N	$Ni_2C_{21}H_{24}N_{10}SP_2F_{12}$
710 g/mol	471 g/mol	108 g/mol	856 g/mol

[L^{6}Ni$_2$S]PF$_6$ (5.39 mg, 0.00759 mmol, 1.00 equiv.) was dissolved in MeCN-d_3 (0.2 mL). Phenylhydrazine (75 μL, 82.1 mg, 0.759 mmol, 100 equiv.) was dissolved in MeCN-d_3 (0.2 mL) and the complex solution was added. [Fe(Cp*)$_2$]PF$_6$ (3.58 mg, 0.00759 mmol, 1.00 equiv.) was dissolved in MeCN-d_3 (0.1 mL). The two solutions were cooled down to 233 K. Under stirring, [Fe(Cp*)$_2$]PF$_6$ was slowly added to the orange complex solution. A color change was observed from orange to yellow. The solution was stirred for additional 10 min. and was warmed up to room temperature.

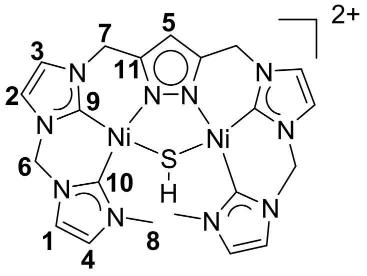

^{1}H NMR (400 MHz, 298 K, MeCN-d_3): δ [ppm] = 7.33 (d, $^3J_{HH}$ = 1.7 Hz, 2H, $_{Im}$H **2**), 7.16 (d, $^3J_{HH}$ = 1.8 Hz, 2H, $_{Im}$H **3**), 7.11 (d, $^3J_{HH}$ = 1.7 Hz, 2H, $_{Im}$H **4**), 6.32 (s, 1H, H^{pz} **5**), 5.96 (s, 4H, H **6**), 5.15 (s, 4H, H **7**), 4.00 (s, 6H, H **8**).

^{1}H DOSY NMR [L^{6}Ni$_2$(SH)](PF$_6$)$_2$ plus 100 equiv. phenylhydrazine
(500 MHz, 298 K, MeCN-d_3): D_{298K} [m^2·s^{-1}] = 7.94·10^{-10}

^{1}H DOSY NMR [L^{6}Ni$_2$S]PF$_6$ plus 100 equiv. phenylhydrazine
(500 MHz, 298 K, MeCN-d_3): D_{298K} [m^2·s^{-1}] = 7.94·10^{-10}

ESI-MS (MeCN) *m/z* (%) (**[L^{6}Ni$_2$S]PF$_6$** plus 100 equiv. phenylhydrazine): 562.94 (100) $[Ni_2C_{21}H_{23}N_{10}S]^+$

Stopped-flow UV-vis (MeCN, 253 K): $\lambda_{max.}$ [nm] (abs.) [a.u.] = 378 (0.05).

HAT reaction with 100 equiv. of 1,4-cyclohexadiene

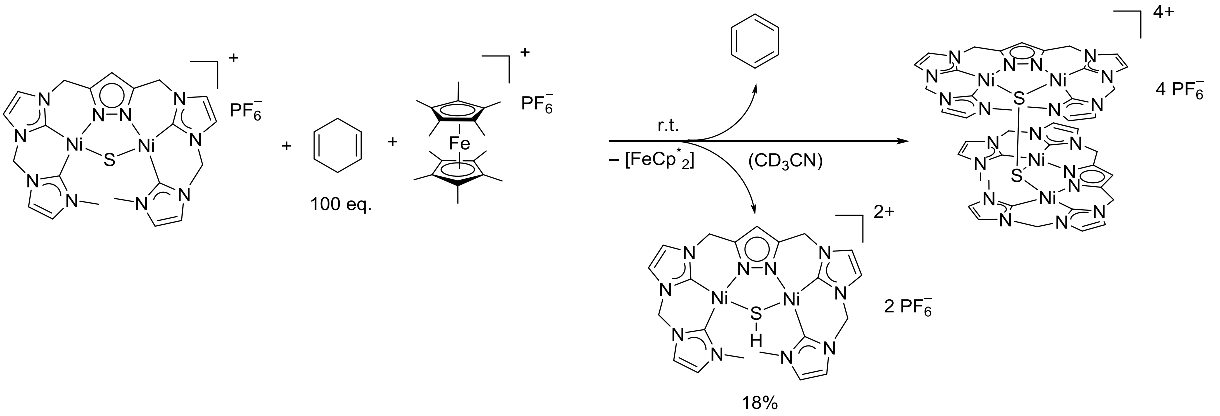

$Ni_2C_{21}H_{23}N_{10}SPF_6$	C_6H_8	$FeC_{20}H_{30}PF_6$	$Ni_4C_{42}H_{46}N_{20}S_2P_4F_{24}$
710 g/mol	80 g/mol	471 g/mol	1710 g/mol

[L^{6}Ni$_2$S]PF$_6$ (5.38 mg, 0.00758 mmol, 1.00 equiv.) was dissolved in MeCN-*d*$_3$ (0.4 mL). 1,4-Cyclohexadiene (71 μL, 60.7 mg, 0.758 mmol, 100 equiv.) was added to the complex solution. [Fe(Cp*)$_2$]PF$_6$ (3.61 mg, 0.00758 mmol, 1.01 equiv.) was dissolved in MeCN-*d*$_3$ (0.1 mL). The two solutions were cooled down to 233 K. Under stirring, [Fe(Cp*)$_2$]PF$_6$ was slowly added to the red-orange complex solution. A color change was observed from orange to yellow. The solution was stirred for additional 10 min. and was warmed up to room temperature.

^{1}H NMR (400 MHz, 298 K, MeCN-*d*$_3$): δ [ppm] = 7.42 (d, $^3J_{HH}$ = 0.9 H 2H, $_{\mathrm{Im}}$H **1**), 7.41 (d, $^3J_{HH}$ = 0.9 Hz, 2H, $_{\mathrm{Im}}$H **2**), 7.24 (d, $^3J_{HH}$ = 2.0 Hz, 2H, $_{\mathrm{Im}}$H **3**), 7.10 (d, $^3J_{HH}$ = 2.0 Hz, 2H, $_{\mathrm{Im}}$H **4**), 7.00 (d, $^3J_{HH}$ = 2.0 Hz, 2H, $_{\mathrm{Im}}$H **5**), 6.99 (d, $^3J_{HH}$ = 2.0 Hz ,2H, $_{\mathrm{Im}}$H **6**), 6.81 (d, $^3J_{HH}$ = 2.0 Hz, 2H, $_{\mathrm{Im}}$H **7**), 6.74 (d, $^3J_{HH}$ = 2.0 Hz, 2H, $_{\mathrm{Im}}$H **8**), 6.49 (s, 2H, H$_{\mathrm{pz}}$ **9**), 6.19 (d, $^2J_{HH}$ = 13.5 Hz, 2H, H **10**), 5.81 (d, $^2J_{HH}$ = 13.4 Hz, 2H, H **11**), 5.49 (d, $^2J_{HH}$ = 17.1 Hz, 2H, H **12**), 5.40 (d, $^2J_{HH}$ = 17.4 Hz, 2H, H **13**), 5.29 (d, $^2J_{HH}$ = 13.0 Hz, 2H, H **14**), 5.15 (d, $^2J_{HH}$ = 17.0 Hz, 2H, H **15**), 5.11 (d, $^2J_{HH}$ = 17.4 Hz, 2H, H **16**), 4.20 (s, 6H, H **17**), 3.93 (d, $^2J_{HH}$ = 12.9 Hz, 2H, H **18**), 3.53 (s, 6H, H **19**).

[L^{6}Ni$_2$(SH)]$^{2+}$ (18%): 7.35 (d, $^3J_{HH}$ = 2.0 Hz, 2H, $_{\mathrm{Im}}$H **1**), 7.30 (d, $^3J_{HH}$ = 2.0 Hz, 2H, $_{\mathrm{Im}}$H **2**), 7.21 (d, $^3J_{HH}$ = 2.0 Hz, 2H, $_{\mathrm{Im}}$H **3**), 7.12 (d, $^3J_{HH}$ = 2.0 Hz, 2H, $_{\mathrm{Im}}$H **4**), 6.33 (s, 1H, H$^{\mathrm{pz}}$ **5**), 6.08 (s, 4H, H **6**), 5.22 (s, 4H, H **7**), 4.05 (s, 6H, H **8**).

ESI-MS (MeCN) *m/z* (%): 709.03 (17) [$Ni_2C_{21}H_{23}N_{10}SHPF_6$]$^+$

$[(L^6)_2Ni_4(S_2)](PF_6)_4$

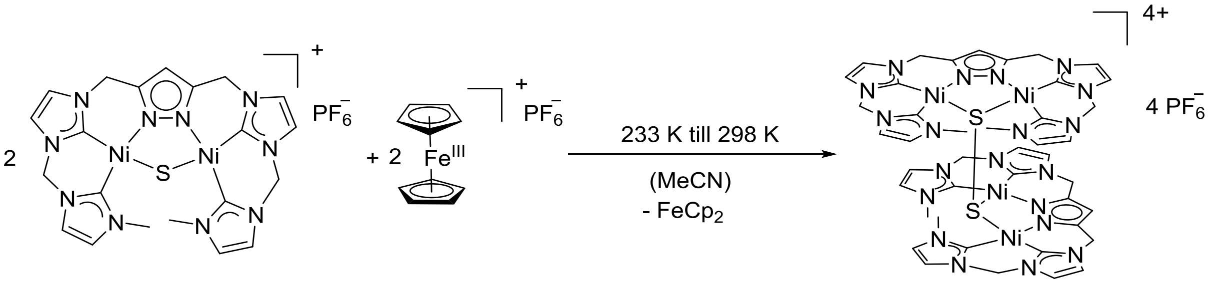

$Ni_2C_{21}H_{23}N_{10}SPF_6$ $FeC_{10}H_{10}PF_6$ $Ni_4C_{42}H_{46}N_{20}S_2P_4F_{24}$

710 g/mol 331 g/mol 1710 g/mol

$[L^6Ni_2S]PF_6$ (29.8 mg, 0.0420 mmol, 1.00 equiv.) was dissolved in MeCN (1.2 mL). The solution was cooled down to 241 K. $[FeCp_2]PF_6$ (14.0 mg, 0.0421 mmol, 1.00 equiv.) was dissolved in MeCN (0.5 mL) and also cooled down to 241 K. The dark blue solution of $[FeCp_2]PF_6$ was, under stirring, dropwise added to the red complex solution. A slow color change can be observed from red to yellow-greenish. The solution was stirred for additional 10 min. under ambient conditions. Afterwards, the solution was filtered off and orange crystals were obtained by slow diffusion of Et_2O to the solution. Orange-yellow crystals were obtained in 53% yield (18.9 mg, 0.0111 mmol).

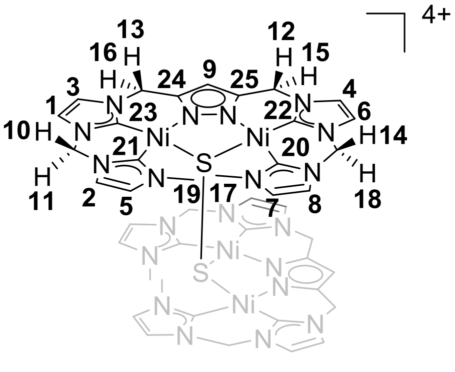

^{1}H NMR (500 MHz, 298 K, MeCN-d_3): δ [ppm] = 7.42 (d, $^3J_{HH}$ = 0.9 H 2H, $_{Im}$H **1**), 7.41 (d, $^3J_{HH}$ = 0.9 Hz, 2H, $_{Im}$H **2**), 7.24 (d, $^3J_{HH}$ = 2.0 Hz, 2H, $_{Im}$H **3**), 7.10 (d, $^3J_{HH}$ = 2.0 Hz, 2H, $_{Im}$H **4**), 7.00 (d, $^3J_{HH}$ = 2.0 Hz, 2H, $_{Im}$H **5**), 6.99 (d, $^3J_{HH}$ = 2.0 Hz ,2H, $_{Im}$H **6**), 6.81 (d, $^3J_{HH}$ = 2.0 Hz, 2H, $_{Im}$H **7**), 6.74 (d, $^3J_{HH}$ = 2.0 Hz, 2H, $_{Im}$H **8**), 6.49 (s, 2H, H_{pz} **9**), 6.19 (d, $^2J_{HH}$ = 13.5 Hz, 2H, H **10**), 5.81 (d, $^2J_{HH}$ = 13.4 Hz, 2H, H **11**), 5.49 (d, $^2J_{HH}$ = 17.1 Hz, 2H, H **12**), 5.40 (d, $^2J_{HH}$ = 17.4 Hz, 2H, H **13**), 5.29 (d, $^2J_{HH}$ = 13.0 Hz, 2H, H **14**), 5.15 (d, $^2J_{HH}$ = 17.0 Hz, 2H, H **15**), 5.11 (d, $^2J_{HH}$ = 17.4 Hz, 2H, H **16**), 4.20 (s, 6H, H **17**), 3.93 (d, $^2J_{HH}$ = 12.9 Hz, 2H, H **18**), 3.53 (s, 6H, H **19**).

^{13}C{^{1}H} NMR (126 MHz, 298 K, MeCN-d_3): δ [ppm] = 162.7 (C$_{\text{carbene}}$–**20**), 159.8 (C$_{\text{carbene}}$–**21**), 159.8 (C$_{\text{carbene}}$–**22**), 158.1 (C$_{\text{carbene}}$–**23**), 147.5 (C$_{\text{quart.}}$–**24**), 147.0 (C$_{\text{quart.}}$–**25**), 125.9 (C–**5**), 124.7 (C–**7**), 123.8 (C–**2**), 123.1 (C–**8**), 123.1 (C–**3**), 123.0 (C–**4**), 122.5 (C–**1**), 122.0 (C–**6**), 104.7 (C–**9**), 62.8 (C–**10/11**), 61.2 (C–**14/18**), 48.6 (C–**12/15**), 48.5 (C–**13/16**), 40.3 (C–**17**), 39.7 (C–**19**).

^{1}H^{1}H NOESY NMR (500 MHz, 298 K, MeCN-d_3): δ [ppm] = 3.53/4.20 (H **19** & H **17**), 3.53/7.00 (H **19** & $_{\text{Im}}$H **4**), 4.20/5.81 (H **17** & H **11**), 4.20/6.81 (H **17** & $_{\text{Im}}$H **7**), 6.49/5.49 (H$^{\text{pz}}$ **9** & H **12**), 6.49/5.40 (H$^{\text{pz}}$ **9** & H **13**), 6.49/5.15 (H$^{\text{pz}}$ **9** & H **15**), 6.49/5.11 (H$^{\text{pz}}$ **9** & H **16**), 3.93/5.29 (H **18** & H **14**), 5.11/5.40 (H **16** & H **13**), 5.15/5.49 (H **15** & H **12**), 5.81/6.19 (H **11** & H **10**), 5.29/6.74 (H **14** & $_{\text{Im}}$H **8**), 5.29/6.99 (H **14** & $_{\text{Im}}$H **6**), 5.40/7.24 (H **13** & $_{\text{Im}}$H **3**), 5.49/7.10 (H **12** & $_{\text{Im}}$H **4**), 6.19/7.40 (H **10** & $_{\text{Im}}$H **8**), 6.19/7.40 (H **10** & $_{\text{Im}}$H **2**), 6.19/7.42 (H **10** & $_{\text{Im}}$H **1**), 6.74/5.29 ($_{\text{Im}}$H **8** & H **14**), 6.81/4.20 ($_{\text{Im}}$H **7** & H **17**), 6.81/5.81 ($_{\text{Im}}$H **7** & H **11**), 7.00/3.53 ($_{\text{Im}}$H **5** & H **19**), 6.99/5.29 ($_{\text{Im}}$H **6** & H **14**), 7.10/5.49 ($_{\text{Im}}$H **4** & H **12**), 7.24/5.40 ($_{\text{Im}}$H **3** & H **13**), 7.42/6.19 ($_{\text{Im}}$H **1** & H **10**).

^{1}H^{1}H COSY NMR (500 MHz, 298 K, MeCN-d_3): δ [ppm] = 7.42/7.24 ($_{\text{Im}}$H **1** & $_{\text{Im}}$H **3**), 6.99/7.10 ($_{\text{Im}}$H **6** & $_{\text{Im}}$H **4**), 6.74/6.81 ($_{\text{Im}}$H **8** & $_{\text{Im}}$H **7**), 6.49/5.15 (H$^{\text{pz}}$ **9** & CH$_2$ **15**), 6.49/5.11 (H$^{\text{pz}}$ **9** & H **16**), 5.81/6.19 (H **11** & H **10**), 3.93/5.29 (H **18** & H **14**), 5.15/5.49 (H **15** & H **12**), 5.11/5.40 (H **16** & H **13**), 4.20/6.81 (H **17** & $_{\text{Im}}$H **7**), 3.53/7.00 (H **19** & $_{\text{Im}}$H **5**).

^{1}H^{13}C HSQC NMR (500 MHz, 298 K, MeCN-d_3): δ [ppm] = 7.00/125.9, 6.81/124.7, 7.41/123.8, 6.74/123.1, 7.24/123.1, 7.10/123.0, 7.42/122.5, 6.99/ 122.0, 6,48/104.7, 6.19/62.8, 5.81/62.8, 5.29/61.2, 3.93/61.2, 5.49/48.6, 5.15/48.6, 5.40/48.5, 5.11/48.5, 4.20/40.3, 3.53/39.7.

^{1}H^{13}C HMBC NMR (500 MHz, 298 K, MeCN-d_3): δ [ppm] = 3.53/159.8 (H **19** & C$_{\text{carbene}}$–**21**), 3.53/125.9 (H **19** & C–**5**), 4.20/124.7 (H **17** & C–**7**), 3.93/123.1 (H **18** & C–**8**), 4.20 (H **17** & C$_{\text{carbene}}$–**20**), 5.11/104.7 (H **16** & C–**9**), 5.11/147.5 (H **16** & C$_{\text{quart.}}$–**24**), 5.15/147.0 (H **15** & C$_{\text{quart.}}$–**25**), 5.29/162.6 (H **14** & C$_{\text{carbene}}$–**20**), 5.29/159.8 (H **14** & C$_{\text{carbene}}$–**20**), 5.40/104.7 (H **13** & C$_{\text{carbene}}$–**9**), 5.49/104.73 (H **12** & C$_{\text{carbene}}$–**9**), 5.40/123.1 (H **13** & C–**3**), 6.81/162.7 ($_{\text{Im}}$H **7** & C$_{\text{carbene}}$–**20**), 6.81/213.1 ($_{\text{Im}}$H **7** & C–**8**), 7.24/122.5 ($_{\text{Im}}$H **3** & C–**1**), 7.10/122.0 ($_{\text{Im}}$H **4** & C–**6**), 6.74/124.7 ($_{\text{Im}}$H **8** & C–**7**), 5.40/158.1 (H **13** & C$_{\text{carbene}}$–**23**), 5.40/147.5 (H **13** & C$_{\text{quart.}}$–**24**). 7.10/159.8 ($_{\text{Im}}$H **4** & C$_{\text{carbene}}$–**21**), 7.10/159.8 ($_{\text{Im}}$H **4** & C$_{\text{carbene}}$–**22**), 5.40/147.5 (H **13** & C$_{\text{quart.}}$–**24**), 5.11/147.5 (H **16** & C$_{\text{quart.}}$–**24**), 5.49/147.0 (H **12** & C$_{\text{quart.}}$–**25**), 5.15/147.01 (H **15** & C$_{\text{quart.}}$–**25**), 7.41//7.42/158.1 ($_{\text{Im}}$H **1/2** & C$_{\text{carbene}}$–**23**), 7.24/158.1 ($_{\text{Im}}$H **3** & C$_{\text{carbene}}$–**23**), 6.19/158.13 (H **10** & C$_{\text{carbene}}$–**23**), 5.40/158.1 (H **13** & C$_{\text{carbene}}$–**23**), 6.81/162.7 ($_{\text{Im}}$H **7** & C$_{\text{carbene}}$–**20**), 6.74/162.7 ($_{\text{Im}}$H **8** & C$_{\text{carbene}}$–**20**), 5.29/162.6 (H **14** & C$_{\text{carbene}}$–**20**), 4.20/162.6

(CH_2 **17** & $C_{carbene}$–**20**), 5.29/162.7 (CH_2 **14** & $C_{carbene}$–**20**), 5.29/159.8 (CH_2 **14** & $C_{carbene}$–**21**), 5.29/122.0 (CH_2 **14** & C–**6**).

^{1}H DOSY NMR (500 MHz, 298 K, MeCN-*d*$_3$): D_{298K} [m^2s^{-1}] = $7.08 \cdot 10^{-10}$.

^{31}P NMR (121.5 MHz, 298 K, MeCN-*d*$_3$): δ [ppm] = –144.6 (hpt., $^1J_{PF}$ = 706.8 Hz).

^{19}F NMR (282 MHz, 298 K, MeCN-*d*$_3$): δ [ppm] = –72.7 (d, $^1J_{PF}$ = 706.8 Hz).

IR (ATR): υ [cm^{-1}] = 3173.2 (w), 3148.9 (w), 2959.8 (w), 3137.8 (w), 3120.1 (w), 3043.6 (w), 2956.9 (w), 1569.4 (m), 1535.8 (w), 1477.1 (m), 1468.7 (m), 1443.5 (m), 1428.6 (m), 1413.7 (m), 1402.5 (m), 1391.4 (m), 1344.8 (m), 1310.3 (m), 1293.5 (m), 1278.6 (m), 1268.3 (m), 1254.4 (w), 1243.2 (w), 1212.4 (m), 1186.3 (m), 1134.1 (w), 1113.6 (w), 1103.4 (w), 1077.3 (m), 1046.5 (m), 1013.9 (m), 828.4 (s), 785.6 (s), 768.8 (s), 757.6 (s), 738.1 (s), 725.9 (s), 673.8 (s), 659.8 (s), 552.6 (s).

UV-vis (MeCN, 293 K): $\lambda_{max.}$ [nm] (ε 10^3 [$M^{-1} \cdot cm^{-1}$]) = 400 (2.8), 305 (3.99), 302 (48.1), 224 (48.7).

Elemental analysis of $Ni_4C_{42}H_{46}N_{20}S_2P_4F_{24}$

Calculated: **C** 29.50%; **H** 2.71%; **N** 16.39%; S 3.75.

Found: **C** 30.16%; **H** 2.95%; **N** 16.62%; S 4.29.

$[(L^6)_2Ni_4(S_2)](PF_6)_4$ *via* oxidation reaction

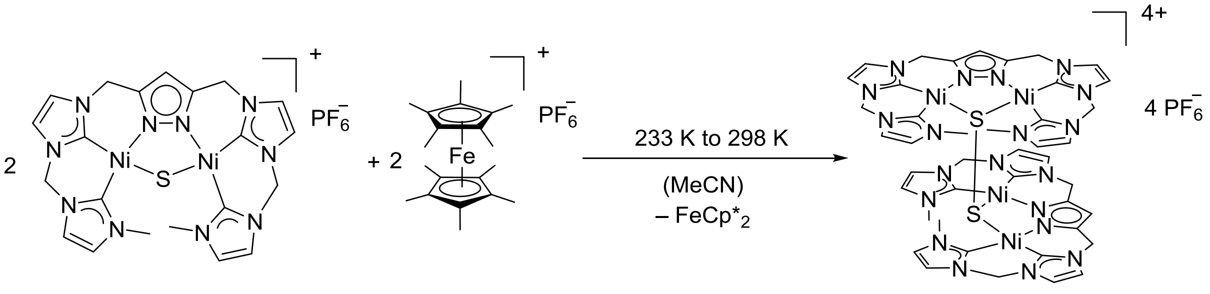

$Ni_2C_{21}H_{23}N_{10}SPF_6$ $FeC_{20}H_{30}PF_6$ $Ni_4C_{42}H_{46}N_{20}SP_4F_{24}$

710 g/mol 471 g/mol 1710 g/mol

$[L^6Ni_2S]PF_6$ (2.84 mg, 0.00400 mmol, 1.00 equiv.) was dissolved in MeCN-d_3 (0.4 mL). The solution was cooled down to 241 K. $[Fe(Cp^*)_2]PF_6$ (2.07 mg, 0.00439 mmol, 1.09 equiv.) was dissolved in MeCN-d_3 (0.2 mL) and also cooled down to 241 K. The green solution of $[Fe(Cp^*)_2]PF_6$ was, under stirring, dropwise added to the red complex solution. A color change can be observed from red to yellow-greenish. The solution was stirred for additional 10 min under ambient conditions. Afterwards, a ^{1}H NMR spectrum was measured. Orange crystals were obtained by slow diffusion of diethyl ether to the solution.

^{1}H-NMR (400 MHz, 298 K, MeCN-d_3): δ [ppm] = 7.42 (d, $^3J_{HH}$ = 0.9 H 2H, $_{Im}$H **1**), 7.41 (d, $^3J_{HH}$ = 0.9 Hz, 2H, $_{Im}$H **2**), 7.24 (d, $^3J_{HH}$ = 2.0 Hz, 2H, $_{Im}$H **3**), 7.10 (d, $^3J_{HH}$ = 2.0 Hz, 2H, $_{Im}$H **4**), 7.00 (d, $^3J_{HH}$ = 2.0 Hz, 2H, $_{Im}$H **5**), 6.99 (d, $^3J_{HH}$ = 2.0 Hz ,2H, $_{Im}$H **6**), 6.81 (d, $^3J_{HH}$ = 2.0 Hz, 2H, $_{Im}$H **7**), 6.74 (d, $^3J_{HH}$ = 2.0 Hz, 2H, $_{Im}$H **8**), 6.49 (s, 2H, H_{pz} **9**), 6.19 (d, $^2J_{HH}$ = 13.5 Hz, 2H, H **10**), 5.81 (d, $^2J_{HH}$ = 13.4 Hz, 2H, H **11**), 5.49 (d, $^2J_{HH}$ = 17.1 Hz, 2H, H **12**), 5.40 (d, $^2J_{HH}$ = 17.4 Hz, 2H, H **13**), 5.29 (d, $^2J_{HH}$ = 13.0 Hz, 2H, H **14**), 5.15 (d, $^2J_{HH}$ = 17.0 Hz, 2H, H **15**), 5.11 (d, $^2J_{HH}$ = 17.4 Hz, 2H, H **16**), 4.20 (s, 6H, H **17**), 3.93 (d, $^2J_{HH}$ = 12.9 Hz, 2H, CH_2, **18**), 3.53 (s, 6H, H **19**).

$[(L^6)_2Ni_4(S_2)](PF_6)_2(OTf)_2$ *via* HAT from $[L^6Ni_2(SH)](PF_6)(OTf)$

(a) by 2,4,6-tri-tert-butyl phenoxyl radical

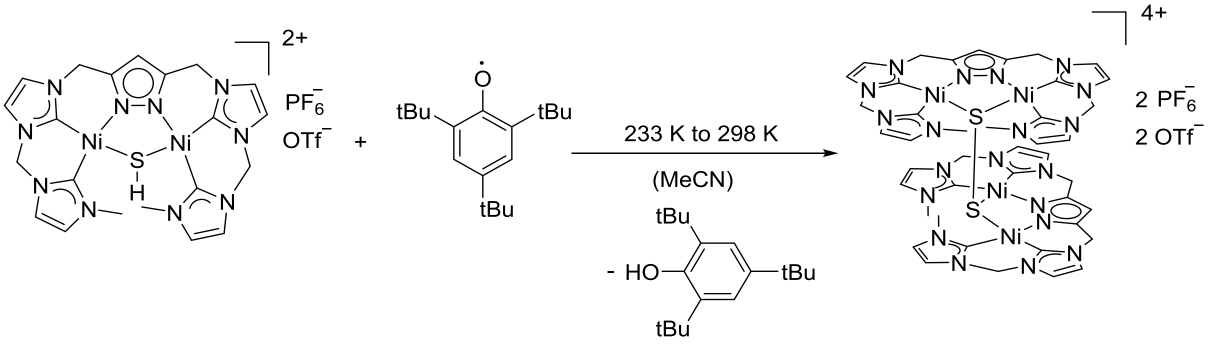

$Ni_2C_{22}H_{24}N_{10}S_2O_3PF_9$	$C_{18}H_{29}O$	$Ni_4C_{44}H_{46}N_{20}S_3O_6P_2F_{18}$
860 g/mol	261 g/mol	2004 g/mol

$[L^6Ni_2(SH)](PF_6)(OTf)$ (13.7 mg, 15.9 μmol, 1.00 equiv.) was dissolved in MeCN (0.4 mL). A solution of 2,4,6-tri-*tert*-butylphenoxyl radical (4.16 mg, 15.9 μmol, 1.00 equiv.) in MeCN (0.1 mL) was slowly added to the yellow solution. Immediately, a color change appeared from pale yellow to yellow.

^{1}H NMR (400 MHz, 298 K, MeCN-d_3): δ [ppm] = 7.42 (d, $^3J_{HH}$ = 0.9 H 2H, $_{Im}$H **1**), 7.41 (d, $^3J_{HH}$ = 0.9 Hz, 2H, $_{Im}$H **2**), 7.24 (d, $^3J_{HH}$ = 2.0 Hz, 2H, $_{Im}$H **3**), 7.10 (d, $^3J_{HH}$ = 2.0 Hz, 2H, $_{Im}$H **4**), 7.00 (d, $^3J_{HH}$ = 2.0 Hz, 2H, $_{Im}$H **5**), 6.99 (d, $^3J_{HH}$ = 2.0 Hz ,2H, $_{Im}$H **6**), 6.81 (d, $^3J_{HH}$ = 2.0 Hz, 2H, $_{Im}$H **7**), 6.74 (d, $^3J_{HH}$ = 2.0 Hz, 2H, $_{Im}$H **8**), 6.49 (s, 2H, H_{pz} **9**), 6.19 (d, $^2J_{HH}$ = 13.5 Hz, 2H, H **10**), 5.81 (d, $^2J_{HH}$ = 13.4 Hz, 2H, H **11**), 5.49 (d, $^2J_{HH}$ = 17.1 Hz, 2H, H **12**), 5.40 (d, $^2J_{HH}$ = 17.4 Hz, 2H, H **13**), 5.29 (d, $^2J_{HH}$ = 13.0 Hz, 2H, H **14**), 5.15 (d, $^2J_{HH}$ = 17.0 Hz, 2H, H **15**), 5.11 (d, $^2J_{HH}$ = 17.4 Hz, 2H, H **16**), 4.20 (s, 6H, H **17**), 3.93 (d, $^2J_{HH}$ = 12.9 Hz, 2H, H **18**), 3.53 (s, 6H, H **19**).

(b) by TEMPO·

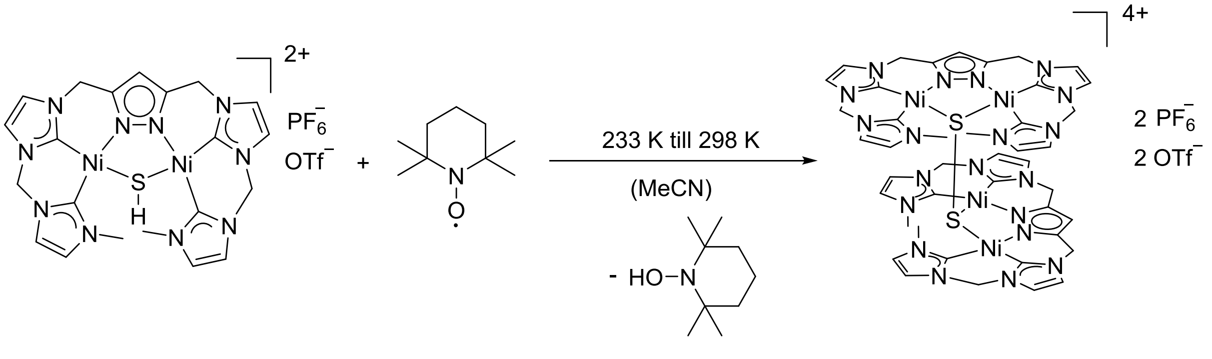

$Ni_2C_{22}H_{24}N_{10}S_2O_3PF_9$ $C_9H_{18}NO$ $Ni_4C_{44}H_{46}N_{20}S_3O_6P_2F_{18}$

860 g/mol 156 g/mol 2004 g/mol

[L^{6}Ni$_2$(SH)](PF$_6$)(OTf) (5.10 mg, 0.00593 mmol, 1.00 equiv.) was dissolved in MeCN-d_3 (0.5 mL). The pale yellow solution was cooled down to 241 K. A solution of 2,2,6,6-tetramethyl-piperidinyloxyl (TEMPO) (1.80 mg, 0.0115 mmol, 1.94 equiv.) was dissolved in MeCN (0.2 mL) and also cooled down to 241 K. The red solution was slowly added to the yellow complex solution. Immediately, the intensity of the yellow color increased.

^{1}H NMR (400 MHz, 298 K, MeCN-d_3): δ [ppm] = 7.42 (d, $^3J_{HH}$ = 0.9 H 2H, $_{Im}$H **1**), 7.41 (d, $^3J_{HH}$ = 0.9 Hz, 2H, $_{Im}$H **2**), 7.24 (d, $^3J_{HH}$ = 2.0 Hz, 2H, $_{Im}$H **3**), 7.10 (d, $^3J_{HH}$ = 2.0 Hz, 2H, $_{Im}$H **4**), 7.00 (d, $^3J_{HH}$ = 2.0 Hz, 2H, $_{Im}$H **5**), 6.99 (d, $^3J_{HH}$ = 2.0 Hz ,2H, $_{Im}$H **6**), 6.81 (d, $^3J_{HH}$ = 2.0 Hz, 2H, $_{Im}$H, **7**), 6.74 (d, $^3J_{HH}$ = 2.0 Hz, 2H, $_{Im}$H **8**), 6.49 (s, 2H, H$_{pz}$ **9**), 6.19 (d, $^2J_{HH}$ = 13.5 Hz, 2H, CH$_2$ **10**), 5.81 (d, $^2J_{HH}$ = 13.4 Hz, 2H, H **11**), 5.49 (d, $^2J_{HH}$ = 17.1 Hz, 2H, H **12**), 5.40 (d, $^2J_{HH}$ = 17.4 Hz, 2H, H **13**), 5.29 (d, $^2J_{HH}$ = 13.0 Hz, 2H, H **14**), 5.15 (d, $^2J_{HH}$ = 17.0 Hz, 2H, H **15**), 5.11 (d, $^2J_{HH}$ = 17.4 Hz, 2H, H **16**), 4.20 (s, 6H, H **17**), 3.93 (d, $^2J_{HH}$ = 12.9 Hz, 2H, H **18**), 3.53 (s, 6H, H **19**).

^{1}H DOSY NMR (500 MHz, 298 K, MeCN-d_3): D_{298K} [m^{2}s^{-1}] = 7.08·10^{-10}.

IR (ATR): υ [cm^{-1}] = 3179.7 (w), 3149.9 (w), 2964.4 (w), 1572.1 (w), 1480.8 (m), 1462.2 (w), 1444.5 (m), 1427.7 (m), 1413.7 (m), 1406.3 (m), 1374.6 (w), 1346.6 (m), 1314.9 (w), 1293.5 (w), 1284.2 (w), 1260.9 (w), 1243.2 (w), 1236.7 (w), 12078 (m), 1182.6 (m), 1132.3 (m), 1112.7 (m), 1102.5 (w), 1086.6 (w), 1076.4 (w), 1061.5 (m), 1053.1 (w), 1013.9 (w), 822.9 (s), 790.3 (s), 784.7 (s), 769.8 (s), 732.5 (s), 722.2 (s), 695.2 (s), 681.2 (s), 664.5 (s), 637.4 (s), 617.9 (s), 574.9 (s), 555.4 (s).

Reduction of $[(L^6)_2Ni_4(S_2)](PF_6)_4$ with 2.0 equiv. of $CoCp_2$

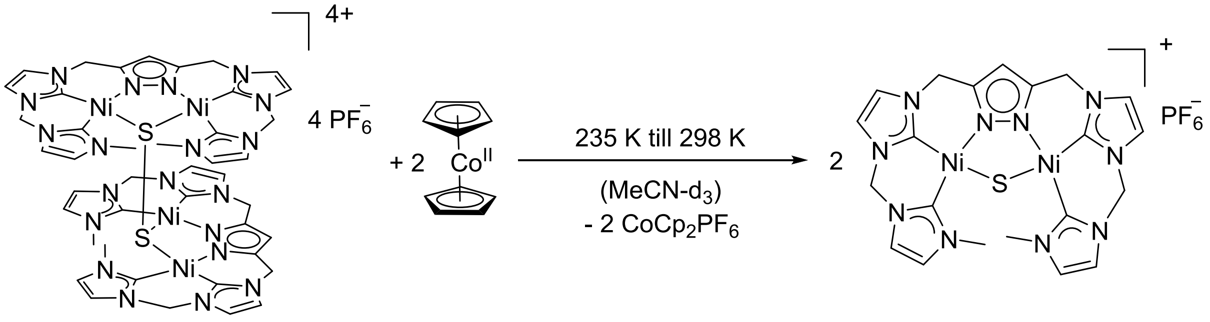

$Ni_4C_{42}H_{46}N_{20}SP_4F_{24}$	$CoC_{10}H_{10}$	$Ni_2C_{21}H_{23}N_{10}SPF_6$
1710 g/mol	189 g/mol	710 g/mol

$[(L^6)_2Ni_4S_2](PF_6)_4$ (4.04 mg, 0.00236 mmol, 1.00 equiv.) was dissolved in MeCN-*d*$_3$ (0.5 mL) and cooled down to 235 K. Cobaltocene (0.890 mg, 0.00471 mmol, 1.99 equiv.) was dissolved in MeCN-*d*$_3$ (0.3 mL) and slowly added to the cooled complex solution. Immediately, a color change from yellow to orange was observed.

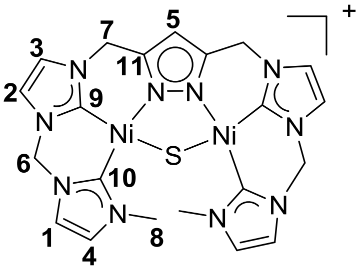

^{1}H NMR (400 MHz, 298 K, MeCN-*d*$_3$): δ [ppm] = 7.19 (d, $^3J_{HH}$ = 2.0 Hz, 2H, $_{Im}$H **1**), 7.18 (d, $^3J_{HH}$ = 1.9 Hz, 2H, $_{Im}$H **2**), 7.10 (d, $^3J_{HH}$ = 1.9 Hz, 2H, $_{Im}$H **3**), 7.02 (d, $^3J_{HH}$ = 2 Hz, 2H, $_{Im}$H **4**), 6.11 (s, 1H, H^{pz} **5**), 5.93 (s, 4H, H **6**), 5.11 (s, 4H, H **7**), 4.23 (s, 4H, H **8**).

Titration of $[HNEt_3]OTf$ to $[L^6Ni_2S]PF_6$

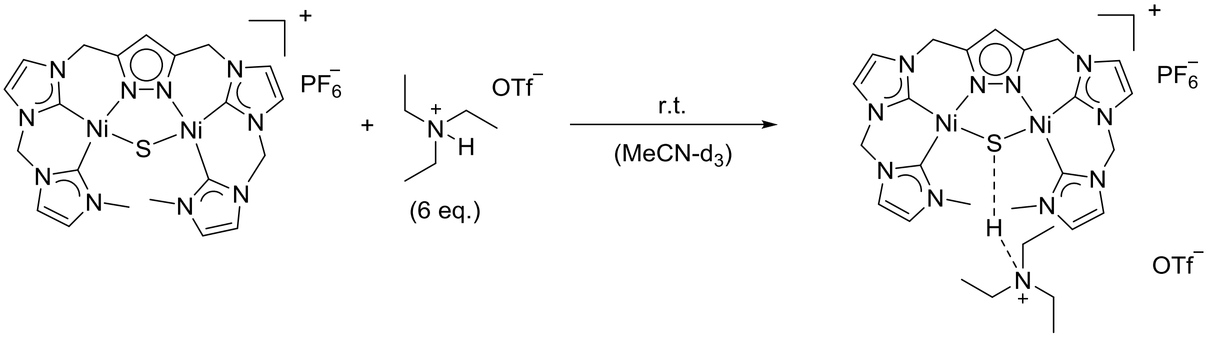

$Ni_2C_{21}H_{23}N_{10}SPF_6$ — 710 g/mol

$C_7H_{16}NSO_3F_3$ — 251 g/mol

$Ni_2C_{28}H_{39}N_{11}S_2O_3PF_9$ — 961 g/mol

^{1}H NMR spectroscopy:

$[L^6Ni_2S]PF_6$ (5.02 mg, 0.00707 mmol, 1.00 equiv.) was dissolved in MeCN-d_3 (0.5 mL) and filled into a Young NMR tube. Triethylammonium triflate (10.7 mg, 0.0425 mmol, 6.00 equiv.) was dissolved in MeCN-d_3 (60 μL). A triethylammonium triflate solution was added to the red complex solution and a ^{1}H NMR experiment was conducted. The color of the solution changed from red-orange to yellow during the titration experiment.

#1 **Starting compound**

^{1}H NMR (400 MHz, 298 K, MeCN-d_3): δ [ppm] = 7.19 (d, $^3J_{HH}$ = 2.0 Hz, 2H, $_{Im}$H **1**), 7.17 (d, $^3J_{HH}$ = 2.0 Hz, 2H, $_{Im}$H **2**), 7.10 (d, $^3J_{HH}$ = 2.0 Hz, 2H, $_{Im}$H **3**), 7.01 (d, $^3J_{HH}$ = 2.0 Hz, 2H, $_{Im}$H **4**), 6.10 (s, 1H, H^{pz} **5**), 5.93 (s, 4H, H **6**), 5.11 (s, 4H, H **7**), 4.22 (s, 6H, H **8**).

#2 0.1 eq.

^{1}H NMR (400 MHz, 298 K, MeCN-d_3): δ [ppm] = 7.19 (d, $^3J_{HH}$ = 2.0 Hz, 2H, $_{Im}$H **1**), 7.18 (d, $^3J_{HH}$ = 2.0 Hz, 2H, $_{Im}$H **2**), 7.10 (d, $^3J_{HH}$ = 2.0 Hz, 2H, $_{Im}$H **3**), 7.01 (d, $^3J_{HH}$ = 2.0 Hz, 2H, $_{Im}$H **4**), 6.12 (s, 1H, H^{pz} **5**), 5.92 (s, 4H, H **6**), 5.12 (s, 4H, H **7**), 4.20 (s, 6H, H **8**).

#3 0.2 eq.

^{1}H NMR (400 MHz, 298 K, MeCN-d_3): δ [ppm] = 7.19 (d, $^3J_{HH}$ = 2.0 Hz, 2H, $_{Im}$H **1**), 7.18 (d, $^3J_{HH}$ = 2.0 Hz, 2H, $_{Im}$H **2**), 7.11 (d, $^3J_{HH}$ = 2.0 Hz, 2H, $_{Im}$H **3**), 7.01 (d, $^3J_{HH}$ = 2.0 Hz, 2H, $_{Im}$H **4**), 6.14 (s, 1H, H^{pz} **5**), 5.92 (s, 4H, H **6**), 5.13 (s, 4H, H **7**), 4.19 (s, 6H, H **8**).

#4 0.3 eq.

^{1}H NMR (400 MHz, 298 K, MeCN-d_3): δ [ppm] = 7.20 (d, $^3J_{HH}$ = 2.0 Hz, 2H, $_{Im}$H **1**), 7.19 (d, $^3J_{HH}$ = 2.0 Hz, 2H, $_{Im}$H **2**), 7.11 (d, $^3J_{HH}$ = 2.0 Hz, 2H, $_{Im}$H **3**), 7.02 (d, $^3J_{HH}$ = 2.0 Hz, 2H, $_{Im}$H **4**), 6.16 (s, 1H, H^{pz} **5**), 5.92 (s, 4H, H **6**), 5.14 (s, 4H, H **7**), 4.18 (s, 6H, H **8**).

#5 0.4 eq.

^{1}H NMR (400 MHz, 298 K, MeCN-d_3): δ [ppm] = 7.20 (d, $^3J_{HH}$ = 2.0 Hz, 2H, $_{Im}$H **1**), 7.19 (d, $^3J_{HH}$ = 2.0 Hz, 2H, $_{Im}$H **2**), 7.12 (d, $^3J_{HH}$ = 2.0 Hz, 2H, $_{Im}$H **3**), 7.02 (d, $^3J_{HH}$ = 2.0 Hz, 2H, $_{Im}$H **4**), 6.17 (s, 1H, H^{pz} **5**), 5.92 (s, 4H, H **6**), 5.14 (s, 4H, H **7**), 4.17 (s, 6H, H **8**).

#6 0.5 eq.

^{1}H NMR (400 MHz, 298 K, MeCN-d_3): δ [ppm] = 7.21 (d, $^3J_{HH}$ = 2.0 Hz, 2H, $_{Im}$H **1**), 7.20 (d, $^3J_{HH}$ = 2.0 Hz, 2H, $_{Im}$H **2**), 7.13 (d, $^3J_{HH}$ = 2.0 Hz, 2H, $_{Im}$H **3**), 7.02 (d, $^3J_{HH}$ = 2.0 Hz, 2H, $_{Im}$H **4**), 6.18 (s, 1H, H^{pz} **5**), 5.92 (s, 4H, H **6**), 5.15 (s, 4H, H **7**), 4.16 (s, 6H, H **8**).

#7 0.6 eq.

^{1}H NMR (400 MHz, 298 K, MeCN-d_3): δ [ppm] = 7.22 (d, $^3J_{HH}$ = 2.0 Hz, 2H, $_{Im}$H **1**), 7.21 (d, $^3J_{HH}$ = 2.0 Hz, 2H, $_{Im}$H **2**), 7.13 (d, $^3J_{HH}$ = 2.0 Hz, 2H, $_{Im}$H **3**), 7.03 (d, $^3J_{HH}$ = 2.0 Hz, 2H, $_{Im}$H **4**), 6.19 (s, 1H, H^{pz} **5**), 5.93 (s, 4H, H **6**), 5.15 (s, 4H, H **7**), 4.16 (s, 6H, H **8**).

#8 0.7 eq.

^{1}H NMR (400 MHz, 298 K, MeCN-d_3): δ [ppm] = 7.22 (d, $^3J_{HH}$ = 2.0 Hz, 2H, $_{Im}$H **1**), 7.21 (d, $^3J_{HH}$ = 2.0 Hz, 2H, $_{Im}$H **2**), 7.13 (d, $^3J_{HH}$ = 2.0 Hz, 2H, $_{Im}$H **3**), 7.03 (d, $^3J_{HH}$ = 2.0 Hz, 2H, $_{Im}$H **4**), 6.20 (s, 1H, H^{pz} **5**), 5.93 (s, 4H, H **6**), 5.16 (s, 4H, H **7**), 4.15 (s, 6H, H **8**).

#9 0.8 eq.

^{1}H NMR (400 MHz, 298 K, MeCN-d_3): δ [ppm] = 7.23 (d, $^3J_{HH}$ = 2.0 Hz, 2H, $_{Im}$H **1**), 7.22 (d, $^3J_{HH}$ = 2.0 Hz, 2H, $_{Im}$H **2**), 7.14 (d, $^3J_{HH}$ = 2.0 Hz, 2H, $_{Im}$H **3**), 7.04 (d, $^3J_{HH}$ = 2.0 Hz, 2H, $_{Im}$H **4**), 6.21 (s, 1H, H^{pz} **5**), 5.94 (s, 4H, H **6**), 5.16 (s, 4H, H **7**), 4.15 (s, 6H, H **8**).

#10 0.9 equiv.

^{1}H NMR (400 MHz, 298 K, MeCN-d_3): δ [ppm] = 7.23 (d, $^3J_{HH}$ = 2.0 Hz, 2H, $_{Im}$H **1**), 7.22 (d, $^3J_{HH}$ = 2.0 Hz, 2H, $_{Im}$H **2**), 7.14 (d, $^3J_{HH}$ = 2.0 Hz, 2H, $_{Im}$H **3**), 7.04 (d, $^3J_{HH}$ = 2.0 Hz, 2H, $_{Im}$H **4**), 6.21 (s, 1H, H^{pz} **5**), 5.94 (s, 4H, H **6**), 5.17 (s, 4H, H **7**), 4.15 (s, 6H, H **8**).

#11 1.0 equiv.

^{1}H NMR (400 MHz, 298 K, MeCN-d_3): δ [ppm] = 7.24 (d, $^3J_{HH}$ = 2.0 Hz, 2H, $_{Im}$H **1**), 7.22 (d, $^3J_{HH}$ = 2.0 Hz, 2H, $_{Im}$H **2**), 7.14 (d, $^3J_{HH}$ = 2.0 Hz, 2H, $_{Im}$H **3**), 7.04 (d, $^3J_{HH}$ = 2.0 Hz, 2H, $_{Im}$H **4**), 6.22 (s, 1H, H^{pz} **5**), 5.95 (s, 4H, H **6**), 5.17 (s, 4H, H **7**), 4.14 (s, 6H, H **8**).

#12 1.1 equiv.

^{1}H NMR (400 MHz, 298 K, MeCN-d_3): δ [ppm] = 7.24 (d, $^3J_{HH}$ = 2.0 Hz, 2H, $_{Im}$H **1**), 7.23 (d, $^3J_{HH}$ = 2.0 Hz, 2H, $_{Im}$H **2**), 7.15 (d, $^3J_{HH}$ = 2.0 Hz, 2H, $_{Im}$H **3**), 7.05 (d, $^3J_{HH}$ = 2.0 Hz, 2H, $_{Im}$H **4**), 6.22 (s, 1H, H^{pz} **5**), 5.95 (s, 4H, H **6**), 5.17 (s, 4H, H **7**), 4.14 (s, 6H, H **8**).

#13 1.2 equiv.

^{1}H NMR (400 MHz, 298 K, MeCN-d_3): δ [ppm] = 7.25 (d, $^3J_{HH}$ = 2.0 Hz, 2H, $_{Im}$H **1**), 7.23 (d, $^3J_{HH}$ = 2.0 Hz, 2H, $_{Im}$H **2**), 7.15 (d, $^3J_{HH}$ = 2.0 Hz, 2H, $_{Im}$H **3**), 7.05 (d, $^3J_{HH}$ = 2.0 Hz, 2H, $_{Im}$H **4**), 6.23 (s, 1H, H^{pz} **5**), 5.95 (s, 4H, H **6**), 5.17 (s, 4H, H **7**), 4.14 (s, 6H, H **8**).

#14 1.5 equiv.

^{1}H NMR (400 MHz, 298 K, MeCN-d_3): δ [ppm] = 7.26 (d, $^3J_{HH}$ = 2.0 Hz, 2H, $_{Im}$H **1**), 7.24 (d, $^3J_{HH}$ = 2.0 Hz, 2H, $_{Im}$H **2**), 7.16 (d, $^3J_{HH}$ = 2.0 Hz, 2H, $_{Im}$H **3**), 7.06 (d, $^3J_{HH}$ = 2.0 Hz, 2H, $_{Im}$H **4**), 6.24 (s, 1H, H^{pz} **5**), 5.97 (s, 4H, H **6**), 5.18 (s, 4H, H **7**), 4.13 (s, 6H, H **8**).

#15 2.0 equiv.

^{1}H NMR (400 MHz, 298 K, MeCN-d_3): δ [ppm] = 7.27 (d, $^3J_{HH}$ = 2.0 Hz, 2H, $_{Im}$H **1**), 7.25 (d, $^3J_{HH}$ = 2.0 Hz, 2H, $_{Im}$H **2**), 7.16 (d, $^3J_{HH}$ = 2.0 Hz, 2H, $_{Im}$H **3**), 7.07 (d, $^3J_{HH}$ = 2.0 Hz, 2H, $_{Im}$H **4**), 6.25 (s, 1H, H^{pz} **5**), 5.98 (s, 4H, H **6**), 5.19 (s, 4H, H **7**), 4.12 (s, 6H, H **8**).

#16 2.5 equiv.

^{1}H NMR (400 MHz, 298 K, MeCN-d_3): δ [ppm] = 7.29 (d, $^3J_{HH}$ = 2.0 Hz, 2H, $_{Im}$H **1**), 7.26 (d, $^3J_{HH}$ = 2.0 Hz, 2H, $_{Im}$H **2**), 7.17 (d, $^3J_{HH}$ = 2.0 Hz, 2H, $_{Im}$H **3**), 7.08 (d, $^3J_{HH}$ = 2.0 Hz, 2H, $_{Im}$H **4**), 6.26 (s, 1H, H^{pz} **5**), 6.00 (s, 4H, H **6**), 5.19 (s, 4H, H **7**), 4.12 (s, 6H, H **8**).

#17 3.0 equiv.

^{1}H NMR (400 MHz, 298 K, MeCN-d_3): δ [ppm] = 7.30 (d, $^3J_{HH}$ = 2.0 Hz, 2H, $_{Im}$H **1**), 7.27 (d, $^3J_{HH}$ = 2.0 Hz, 2H, $_{Im}$H **2**), 7.18 (d, $^3J_{HH}$ = 2.0 Hz, 2H, $_{Im}$H **3**), 7.09 (d, $^3J_{HH}$ = 2.0 Hz, 2H, $_{Im}$H **4**), 6.27 (s, 1H, H^{pz} **5**), 6.02 (s, 4H, H **6**), 5.20 (s, 4H, H **7**), 4.11 (s, 6H, H **8**).

#18 4.0 equiv.

^{1}H NMR (400 MHz, 298 K, MeCN-d_3): δ [ppm] = 7.32 (d, $^3J_{HH}$ = 2.0 Hz, 2H, $_{Im}$H **1**), 7.29 (d, $^3J_{HH}$ = 2.0 Hz, 2H, $_{Im}$H **2**), 7.19 (d, $^3J_{HH}$ = 2.0 Hz, 2H, $_{Im}$H **3**), 7.10 (d, $^3J_{HH}$ = 2.0 Hz, 2H, $_{Im}$H **4**), 6.29 (s, 1H, H^{pz} **5**), 6.05 (s, 4H, H **6**), 5.21 (s, 4H, H **7**), 4.09 (s, 6H, H **8**).

#19 5.0 equiv.

^{1}H NMR (400 MHz, 298 K, MeCN-d_3): δ [ppm] = 7.34 (d, $^3J_{HH}$ = 2.0 Hz, 2H, $_{Im}$H **1**), 7.30 (d, $^3J_{HH}$ = 2.0 Hz, 2H, $_{Im}$H **2**), 7.21 (d, $^3J_{HH}$ = 2.0 Hz, 2H, $_{Im}$H **3**), 7.11 (d, $^3J_{HH}$ = 2.0 Hz, 2H, $_{Im}$H **4**), 6.31 (s, 1H, H^{pz} **5**), 6.08 (s, 4H, H **6**), 5.21 (s, 4H, H **7**), 4.07 (s, 6H, H **8**).

#20 6.0 equiv.

^{1}H NMR (400 MHz, 298 K, MeCN-d_3): δ [ppm] = 7.36 (d, $^3J_{HH}$ = 2.0 Hz, 2H, $_{Im}$H **1**), 7.31 (d, $^3J_{HH}$ = 2.0 Hz, 2H, $_{Im}$H **2**), 7.22 (d, $^3J_{HH}$ = 2.0 Hz, 2H, $_{Im}$H **3**), 7.12 (d, $^3J_{HH}$ = 2.0 Hz, 2H, $_{Im}$H **4**), 6.33 (s, 1H, H^{pz} **5**), 6.11 (s, 4H, H **6**), 5.22 (s, 4H, H **7**), 4.05 (s, 6H, H **8**).

References

[1] T.-Y. Chen, J. Vaissermann, E. Ruiz, J. P. Sénateur, P. Doppelt, *Chem. Mater.* **2001**, *13*, 3993–4004.

[2] P. L. Pai, C. H. Ting, *IEEE Electron Device Lett.* **1989**, *10*, 423–425.

[3] M. B. Small, D. J. Pearson, *IBM J. Res. Dev.* **1990**, *34*, 858–867.

[4] A. V Gelatos, A. Jain, R. Marsh, C. J. Mogab, *MRS Bull.* **1994**, *49*, 49–54.

[5] P. Doppelt, T. H. Baum, *MRS Bull.* **1994**, 41–48.

[6] K. Köhler, J. Eichhorn, F. Meyer, D. Vidovic, *Organometallics* **2003**, *22*, 4426–4432.

[7] J. Teichgräber, S. Dechert, F. Meyer, *J. Organomet. Chem.* **2005**, *690*, 5255–5263.

[8] M. Stollenz, S. Fischer, H. Gehring, S. G. Resch, S. Dechert, C. Große, F. Meyer, *J. Organomet. Chem.* **2016**, *821*, 106–111.

[9] J. Díez, S. Falagán, P. Gamasa, J. Gemeno *Polyhedron* **1988**, *7*, 37–42.

[10] A. Jakob, T. Rüffer, P. Ecorchard, B. Walfort, K. Körbitz, S. Frühauf, S. E. Schulz, T. Gessner, H. Lang, *Z. Anorg. Allg. Chem.* **2010**, *636*, 1931–1940.

[11] J. C. Y. Lin, R. T. W. Huang, C. S. Lee, A. Bhattacharyya, W. S. Hwang, I. J. B. Lin, *Chem. Rev.* **2009**, *109*, 3561–3598.

[12] M. Trose, F. Nahra, C. S. J. Cazin, *Coord. Chem. Rev.* **2018**, *355*, 380–403.

[13] A. J. Arduengo, R. L. Harlow, M. Kline, *J. Am. Chem. Soc.* **1991**, *113,* 361–363.

[14] C. Boehme, G. Frenking, *J. Am. Chem. Soc.* **1996**, *118*, 2039–2046.

[15] C. Heinemann, T. Müller, Y. Apeloig, H. Schwarz, *J. Am. Chem. Soc.* **1996**, *118,* 2023–2038.

[16] W. A. Herrmann, C. Köcher, *Angew. Chem. Int. Ed.* **1997**, 36, 2162–2187.

[17] M. Stollenz, F. Meyer, *Organometallics* **2012**, *31*, 7708–7727.

[18] M. Stollenz, J. E. Raymond, L. M. Pérez, J. Wiederkehr, N. Bhuvanesh, *Chem. Eur. J.* **2016**, *22*, 2396–2405.

[19] X. Hu, I. Castro-Rodriguez, K. Olsen, K. Meyer, *Organometallics* **2004**, *23*, 755–764.

[20] W. A. Herrmann, *Angew. Chem. Int. Ed.* **2002**, *41*, 1290–1309.

[21] M. Poyatos, J. A. Mata, E. Peris, *Chem. Rev.* **2009**, *109*, 3677–3707.

[22] F. E. Hahn, M. C. Jahnke, *Angew. Chem. Int. Ed.* **2008**, *47*, 3122–3172.

[23] D. Pugh, A. A. Danopoulos, *Coord. Chem. Rev.* **2007**, *251*, 610–641.

[24] S. Díez-González, N. Marion, S. P. Nolan, S. Diez-Gonzalez, *Chem. Rev.* **2009**, *109*, 3612–3676.

[25] P. L. Chiu, C.-L. Lai, C.-F. Chang, C.-H. Hu, H. M. Lee, *Organometallics* **2005**, *24*,

6169–6178.

[26] B. Liu, Y. Zhang, D. Xu, W. Chen, *Chem. Commun.* **2011**, *47*, 2883–2885.

[27] V. S. Thoi, C. J. Chang, *Chem. Commun.* **2011**, *47*, 6578–6580.

[28] J. Nitsch, F. Lacemon, A. Lorbach, A. Eichhorn, F. Cisnetti, A. Steffen, *Chem. Commun.* **2016**, *52*, 2932–2935.

[29] O. Kühl, *Functionalised N-Heterocyclic Carbene Complexes*, John Wiley & Sons Ltd, West Sussex, **2010**.

[30] B. Liu, Y. Zhang, D. Xu, W. Chen, *Chem. Commun.* **2011**, *47*, 2883–2885.

[31] M. V Baker, B. W. Skelton, A. H. White, C. C. Williams, *Organometallics* **2002**, *21*, 2674–2678.

[32] A. Biffis, M. Cipani, E. Bressan, C. Tubaro, C. Graiff, A. Venzo, *Organometallics* **2014**, *33*, 2182–2188.

[33] R. E. Andrew, A. B. Chaplin, *Inorg. Chem.* **2015**, *54*, 312–322.

[34] K. Riener, M. J. Bitzer, A. Pöthig, A. Raba, M. Cokoja, W. A. Herrmann, F. E. Kühn, *Inorg. Chem.* **2014**, *53*, 12767–12777.

[35] Z. Xi, X. Zhang, W. Chen, S. Fu, D. Wang, *Organometallics* **2007**, *26*, 6636–6642.

[36] B. Liu, Q. Xia, W. Chen, *Angew. Chem. Int. Ed.* **2009**, *48*, 5513–5516.

[37] S. Gu, J. Du, J. Huang, H. Xia, L. Yang, W. Xu, C. Lu, *Beilstein J. Org. Chem.* **2016**, *12*, 863–873.

[38] B. Liu, X. Ma, F. Wu, W. Chen, *Dalt. Trans.* **2015**, *44*, 1836–1844.

[39] D. H. Brown, G. L. Nealon, P. V Simpson, B. W. Skelton, Z. Wang, *Organometallics* **2009**, 1965–1968.

[40] J. C. Garrison, R. S. Simons, J. M. Talley, C. Wesdemiotis, C. A. Tessier, W. J. Youngs, *Organometallics* **2001**, *20*, 1276–1278.

[41] B. Liu, W. Chen, S. Jin, *Organometallics* **2007**, *26*, 3660–3667.

[42] Y. Zhou, W. Chen, *Organometallics* **2007**, *26*, 2742–2746.

[43] P. J. Barnard, M. V. Baker, S. J. Berners-Price, B. W. Skelton, A. H. White, *Dalt. Trans.* **2004**, 1038–1047.

[44] S. Gu, J. Huang, X. Liu, H. Liu, Y. Zhou, W. Xu, *Inorg. Chem. Commun.* **2012**, *21*, 168–172.

[45] J. Nitsch, C. Kleeberg, R. Fröhlich, A. Steffen, *Dalt. Trans.* **2015**, *44*, 6944–6960.

[46] J. Nitsch, L. P. Wolters, C. Fonseca Guerra, F. M. Bickelhaupt, A. Steffen, *Chem. Eur. J.* **2017**, *23*, 614–622.

[47] B. Hupp, J. Nitsch, T. Schmitt, R. Bertermann, K. Edkins, F. Hirsch, I. Fischer, M.

Auth, A. Sperlich, A. Steffen, *Angew. Chem. Int. Ed.* **2018**, 1–6.

[48] B. Liu, Q. Xia, W. Chen, *Angew. Chem. Int. Ed.* **2009**, *48*, 5513–5516.

[49] E. Kühnel, I. V. Shishkov, F. Rominger, T. Oeser, P. Hofmann, *Organometallics* **2012**, *31*, 8000–8011.

[50] A. A. Danopoulos, P. Cole, S. P. Downing, D. Pugh, *J. Organomet. Chem.* **2008**, *693*, 3369–3374.

[51] S. G. Resch, *Synthesis and Characterization of New Copper(I) N-Heterocyclic Carbene Complexes*, Master Thesis, Technische Universität München, Garching b. München **2013**.

[52] L. Pazderski, *Magn. Reson. Chem.* **2008**, *46*, 3–5.

[53] Ö. Öztopcu, K. Mereiter, M. Puchberger, K. A. Kirchner, *Dalt. Trans.* **2011**, *40*, 7008–7021.

[54] A. Einstein, *Ann. Phys.* **1905**, *17*, 132.

[55] T. Wagner, A. Pöthig, H. M. S. Augenstein, T. D. Schmidt, E. Herdtweck, W. Brütting, W. A. Herrmann, F. E. Kühn, *Organometallics* **2015**, 34, 1522–1529.

[56] J. C. Garrison, R. S. Simons, J. M. Talley, C. Wesdemiotis, C. A. Tessier, W. J. Youngs, *Organometallics* **2001**, *20*, 1276–1278.

[57] M. V. Baker, B. W. Skelton, A. H. White, C. C. Williams, *Organometallics* **2002**, *21*, 2674–2678.

[58] M. V. Baker, D. H. Brown, R. A. Haque, P. V. Simpson, B. W. Skelton, A. H. White, C. C. Williams, *Organometallics* **2009**, *28*, 3793–3803.

[59] I. Klawitter, M. R. Anneser, S. Dechert, S. Meyer, S. Demeshko, S. Haslinger, A. Pöthig, F. E. Kühn, F. Meyer, *Organometallics* **2015**, *34*, 2819–2825.

[60] B. P. I. Appl., **2005**.

[61] I. Klawitter, *Makrozyklische NHC-Liganden Zur Stabilisierung Hochvalenter Metallionen*, Ph.D. Thesis, Georg-August-University Göttingen, Göttingen **2015**.

[62] F. E. Hahn, C. Radloff, T. Pape, A. Hepp, *Chem. Eur. J.* **2008**, *14*, 10900–10904.

[63] Y. Zhou, W. Chen, Dalton Trans. **2007**, 5123–5125.

[64] Y. Zhou, Z. Xi, W. Chen, D. Wang, *Organometallics* **2008**, *27*, 5911–5920.

[65] P. Liang, A. Kobayashi, W. M. C. Sameera, M. Yoshida, M. Kato, *Inorg. Chem.* **2018**, *57*, 5929–5938.

[66] F. P. Gasparro, N. H. Kolodny, *J. Chem. Educ.* **1977**, *54*, 258–261.

[67] J. Sandström, *Dynamic NMR Spectroscopy*, Academic Press Inc., London, **1982**.

[68] E. Jabri, M. B. Carr, R. P. Hausinger, P. A. Karplus, *Science* **1995**, *268*, 998–1004.

[69] R. M. Haak, S. J. Wezenberg, A. W. Kleij, *Chem. Commun.* **2010**, *46*, 2713–2723.

[70] L. C. Seefeldt, B. M. Hoffman, D. R. Dean, *Annu. Rev. Biochem.* **2009**, *78*, 701–722.

[71] S. W. Ragsdale, *J. Biol. Chem.* **2009**, *284*, 18571–18575.

[72] R. Balasubramanian, S. M. Smith, S. Rawat, L. A. Yatsunyk, T. L. Stemmler, A. C. Rosenzweig, *Nature* **2010**, *465*, 115–119.

[73] S. Liu, A. Motta, A. R. Mouat, M. Delferro, T. J. Marks, *J. Organomet. Chem.* **2014**.

[74] T. Sone, A. Yamaguchi, S. Matsunaga, *J. Am. Chem. Soc.* **2008**, *130*, 10078–10079.

[75] D. G. H. Hetterscheid, S. H. Chikkali, B. deBruin, J. N. H. Reek, *ChemCatChem* **2013**, *5*, 2785–2793.

[76] T. G. Schenck, J. M. Downes, C. R. C. Milne, P. B. Mackenzie, H. Boucher, J. Whelan, B. Bosnich, *Inorg. Chem.* **1985**, *24*, 2334–2337.

[77] K. E. Dalle, F. Meyer, *Eur. J. Inorg. Chem.* **2015**, *2015*, 3391–3405.

[78] J. Klingele, S. Dechert, F. Meyer, *Coord. Chem. Rev.* **2009**, *253*, 2698–2741.

[79] T. Kamiusuki, H. Okawa, E. Kitaura, M. Koikawa, N. Matsumoto, S. Kida, H. Oshio, *J. Chem. Soc. Dalt. Trans.* **1989**, 2077–2081.

[80] N. Kindermann, E. Bill, S. Dechert, S. Demeshko, E. J. Reijerse, F. Meyer, *Angew. Chem. Int. Ed.* **2015**, *127*, 1758–1763.

[81] K. E. Dalle, T. Gruene, S. Dechert, S. Demeshko, F. Meyer, *J. Am. Chem. Soc.* **2014**, *136*, 7428–7434.

[82] L. K. Frensch, K. Pröpper, M. John, S. Demeshko, C. Brückner, F. Meyer, *Angew. Chem. Int. Ed.* **2011**, *50*, 1420–1424.

[83] S. Neudeck, S. Maji, I. López, S. Meyer, F. Meyer, A. Llobet, *J. Am. Chem. Soc.* **2014**, *136*, 24–27.

[84] Y. Zhou, X. Zhang, W. Chen, H. Qiu, *J. Organomet. Chem.* **2008**, *693*, 205–215.

[85] B. Liu, B. Liu, Y. Zhou, W. Chen, *Organometallics* **2010**, *29*, 1457–1464.

[86] U. J. Scheele, M. Georgiou, M. John, S. Dechert, F. Meyer, *Organometallics* **2008**, *27*, 5146–5151.

[87] M. Georgiou, W. Simone, V. Konstanzer, S. Dechert, M. John, F. Meyer, *Z. Naturforsch. B* **2009**, *64b*, 1542–1552.

[88] P. J. Altmann, A. Pöthig, *J. Am. Chem. Soc.* **2016**, *138*, 13171–13174.

[89] T. Ogoshi, S. Kanai, S. Fujinami, T. Yamagishi, *J. Am. Chem. Soc.* **2008**, *130*, 5022–5023.

[90] P. J. Altmann, A. Pöthig, *Chem. Commun.* **2016**, *52*, 9089–9092.

[91] P. J. Altmann, A. Pöthig, *Angew. Chem. Int. Ed.* **2017**, *56*, 15733–15736.

[92] S. Erbas-Cakmak, D. A. Leigh, C. T. McTernan, A. L. Nussbaumer, *Chem. Rev.* **2015**, *115*, 10081–10206.

[93] M. Xue, Y. Yang, X. Chi, X. Yan, F. Huang, *Chem. Rev.* **2015**, *115*, 7398–7501.

[94] P. J. Altmann, C. Jandl, A. Pöthig, *Dalt. Trans.* **2015**, *44*, 11278–11281.

[95] S. J. Jeon, R. M. Waymouth, *J. Chem. Soc. Dalt. Trans.* **2008**, 437–439.

[96] S. A. Reindl, A. Pöthig, M. Drees, B. Bechlars, E. Herdtweck, W. A. Herrmann, F. E. Kühn, *Organometallics* **2013**, *32*, 4082–4091.

[97] U. J. Scheele, M. John, S. Dechert, F. Meyer, *Eur. J. Inorg. Chem.* **2008**, 373–377.

[98] T. Guo, S. Dechert, F. Meyer, *Organometallics* **2014**, *33*, 5145–5155.

[99] S. A. Reindl, A. Pöthig, B. Hofmann, W. A. Herrmann, F. E. Kühn, *J. Organomet. Chem.* **2015**, *775*, 130–136.

[100] K. E. Dalle, S. Dechert, F. Meyer, *Z. Anorg. Allg. Chem.* **2015**, *641*, 2181–2189.

[101] S. Fischer, S. Demeshko, S. Dechert, F. Meyer, *Z. Anorg. Allg. Chem.* **2012**, *638*, 621–627.

[102] D. H. Manz, P. C. Duan, S. Dechert, S. Demeshko, R. Oswald, M. John, R. A. Mata, F. Meyer, *J. Am. Chem. Soc.* **2017**, *139*, 16720–16731.

[103] J. C. Röder, F. Meyer, H. Pritzkow, *Organometallics* **2001**, *20*, 811–817.

[104] A. Gers-Barlag, *Two-in-One Pincer Type Ligands and Their Metal Complexes for Catalysis*, Ph.D. Thesis, Georg-August-Universität Göttingen, Göttingen **2016**.

[105] E. Díez-Barra, A. de La Hoz, A. Sánchez-Migallón, J. Tejeda, *Heterocycles* **1992**, *34*, 1365–1373.

[106] D. T. Weiss, S. Haslinger, C. Jandl, A. Pöthig, M. Cokoja, F. E. Kühn, *Inorg. Chem.* **2015**, *54*, 415–417.

[107] F. Aguilar-Parrilla, F. Männle, H.-H. Limbach, J. Elguero, N. Jagerovic, *Magnet. Reson. Chem.* **1994**, *32*, 699–702.

[108] M. Veronelli, S. Dechert, A. Schober, S. Demeshko, F. Meyer, *Eur. J. Inorg. Chem.* **2017**, 446–453.

[109] M. Veronelli, S. Dechert, S. Demeshko, F. Meyer, *Inorg. Chem.* **2015**, *54*, 6917–6927.

[110] B. C. Chen, W. Philipsborn, K. Nagarajan, *Helv. Chim. Acta* **1983**, *66*, 1537–1555.

[111] M. T. Chenon, C. Coupry, D. M. Grant, R. J. Pugmire, *J. Org. Chem.* **1977**, *42*, 659–661.

[112] W. M. Litchman, *J. Am. Chem. Soc.* **1979**, *101*, 545–547.

[113] R. M. Claramunt, C. López, M. D. Santa María, D. Sanz, J. Elguero, *Prog. Nucl. Magn. Reson. Spectrosc.* **2006**, *49*, 169–206.

[114] H. Schmidbaur, A. Schier, *Angew. Chem. Int. Ed.* **2015**, *54*, 746–784.

[115] A. Bondi, *J. Phys. Chem.* **1964**, *68*, 441–451.

[116] P. C. Duan, D. H. Manz, S. Dechert, S. Demeshko, F. Meyer, *J. Am. Chem. Soc.* **2018**, *140*, 4929–4939.

[117] P. A. Karplus, M. A. Pearson, R. P. Hausinger, *Acc. Chem. Res.* **1997**, *30*, 330–337.

[118] A. Balasubramanian, K. Ponnuraj, *J. Mol. Biol.* **2010**, *400*, 274–283.

[119] H. L. Mobley, M. D. Island, R. P. Hausinger, *Microbiol. Rev.* **1995**, *59*, 451–480.

[120] E. L. Carter, N. Flugga, J. L. Boer, S. B. Mulrooney, R. P. Hausinger, *Metallomics* **2009**, *1*, 207–221.

[121] S. V Kryatov, E. V Rybak-akimova, F. Meyer, H. Pritzkow, *Eur. J. Inorg. Chem.* **2003**, 1581–1590.

[122] F. Meyer, E. Kaifer, P. Kircher, K. Heinze, H. Pritzkow, *Chem. Eur. J.* **1999**, *5*, 1617–1630.

[123] S. Buchler, F. Meyer, E. Kaifer, H. Pritzkow, *Inorg. Chim. Acta* **2002**, *337*, 371–386.

[124] A. M. Barrios, S. J. Lippard, *J. Am. Chem. Soc.* **2000**, *122*, 9172–9177.

[125] A. H. Christian, P. Müller, S. Monfette, *Organometallics* **2014**, *33*, 2134–2137.

[126] D. Huang, R. H. Holm, *J. Am. Chem. Soc.* **2010**, *132*, 4693–4701.

[127] E. Carmona, J. M. Marín, P. Palma, M. Paneque, M. L. Poveda, *Inorg. Chem.* **1989**, *28*, 1895–1900.

[128] N. Kitajima, S. Hikichi, M. Tanaka, Y. Morooka, *J. Am. Chem. Soc.* **1993**, *115*, 5496–5508.

[129] W. A. Herrmann, G. Gerstberger, M. Spiegler, *Organometallics* **1997**, *16*, 2209–2212.

[130] H. V. Huynh, C. Holtgrewe, T. Pape, L. L. Koh, E. Hahn, *Organometallics* **2006**, *25*, 245–249.

[131] K. Inamoto, J. Kuroda, K. Hiroya, Y. Noda, M. Watanabe, T. Sakamoto, *Organometallics* **2006**, *25*, 3095–3098.

[132] D. T. Richens, *Chem. Rev.* **2005**, *105*, 1961–2002.

[133] T. P. Cheeseman, A. L. Odell, H. A. Raethel, *Chem. Commun.* **1968**, 1496–1498.

[134] D. H. Manz, *Preorganized Bimetallic Nickel Complexes of Pyrazolate-Bridged Ligands for Cooperative Substrate Transformation*, Ph.D. Thesis,Georg-August-Universität Göttingen, Göttingen **2016**.

[135] T. Graef, J. Galezowska, S. Dechert, F. Meyer, *Eur. J. Inorg. Chem.* **2011**, 4161–4167.

[136] S. Yao, E. Bill, C. Milsmann, K. Wieghardt, M. Driess, *Angew. Chem. Int. Ed.* **2008**, *47*, 7110–7113.

[137] E. J. Nurminen, J. K. Mattinen, H. Lönnberg, *J. Chem. Soc. Perkin Trans.* **2002**, *2*, 2159–2165.

[138] A. L. Allred, E. G. Rochow, *J. Inorg. Nucl. Chem.* **1958**, *5*, 264–268.

[139] T. Kimura, H. Arita, K. Ishiwata, S. Kuwata, T. Ikariya, *J. Chem. Soc. Dalt. Trans.* **2009**, 2912–2914.

[140] S. Park, A. L. Rheingold, D. Max Roundhill, *Organometallics* **1991**, *10*, 615–623.

[141] M. Herberhold, W. Ehrenreich, *Angew. Chem. Int. Ed.* **1982**, *21*, 633–633.

[142] D. T. Haworth, R. S. Czernuszewicz, *Spectrosc. Lett.* **1980**, *13*, 765–776.

[143] R. L. McCullough, L. H. Jones, C. A. Crosby, *Spectrochim. Acta* **1960**, *16*, 929–944.

[144] A. Abou-Hamdan, A. Roodt, A. E. Merbach, *Inorg. Chem.* **1998**, *37*, 1278–1288.

[145] F. J. Monlien, L. Helm, A. Abou-Hamdan, A. E. Merbach, *Inorg. Chem.* **2002**, *41*, 1717–1727.

[146] J. A. Franz, J. C. Birnbaum, D. S. Kolwaite, J. C. Linehan, D. M. Camaioni, M. Dupuis, *J. Am. Chem. Soc.* **2004**, *126*, 6680–6691.

[147] S. C. Sendlinger, J. R. Nicholson, E. B. Lobkovsky, J. C. Huffman, D. Rehder, G. Christou, *Inorg. Chem.* **1993**, *32*, 204–210.

[148] M. Dey, R. C. Kunz, D. M. Lyons, S. W. Ragsdale, *Biochemistry* **2007**, *46*, 11969–11978.

[149] M. Dey, J. Telser, R. C. Kunz, N. S. Lees, S. W. Ragsdale, B. M. Hoffman, *J. Am. Chem. Soc.* **2007**, *129*, 11030–11032.

[150] R. C. Kunz, M. Dey, S. W. Ragsdale, *Biochemistry* **2008**, *47*, 2661–2667.

[151] S. Scheller, M. Goenrich, S. Mayr, R. K. Thauer, B. Jaun, *Angew. Chem. Int. Ed.* **2010**, *49*, 8112–8115.

[152] W. Grabarse, F. Mahlert, E. C. Duin, M. Goubeaud, S. Shima, R. K. Thauer, V. Lamzin, U. Ermler, *J. Mol. Biol.* **2001**, *309*, 315–330.

[153] E. C. Duin, M. L. McKee, *J. Phys. Chem. B* **2008**, *112*, 2466–2482.

[154] J. P. Donahue, *Chem. Rev.* **2006**, *106*, 4747–4783.

[155] D. D. Whitehurst, T. Isoda, I. Mochida, *Adv. Catal.* **1998**, *42*, 345–471.

[156] P. Grange, X. Vanhaeren, *Catal. Today* **1997**, *36*, 375–391.

[157] C. Bianchini, A. Meli, *Acc. Chem. Res.* **1998**, *31*, 109–116.

[158] M. R. DuBois, M. C. VanDerveer, D. L. DuBois, R. C. Haltiwanger, W. K. Miller, *J. Am. Chem. Soc.* **1980**, *102*, 7456–7461.

[159] A. Travert, H. Nakamura, R. A. Van Santen, S. Cristol, J. F. Paul, E. Payen, *J. Am. Chem. Soc.* **2002**, *124*, 7084–7095.

[160] S. Kuwata, M. Hidai, *Coord. Chem. Rev.* **2001**, *213*, 211–305.

[161] S.-C. Han, H.-S. Kim, M.-S. Song, J.-H. Kim, H.-J. Ahn, J.-Y. Lee, *J. Alloys Compd.* **2003**, *351*, 273–278.

[162] C. Kong, S. Min, G. Lu, *ACS Catal.* **2014**, *4*, 2763–2769.

[163] O. Y. Gutirrez, S. Singh, E. Schachtl, J. Kim, E. Kondratieva, J. Hein, J. A. Lercher, *ACS Catal.* **2014**, *4*, 1487–1499.

[164] I. Takei, Y. Wakebe, K. Suzuki, Y. Enta, T. Suzuki, Y. Mizobe, M. Hidai, *Organometallics* **2003**, *22*, 4639–4641.

[165] F. Olechnowicz, G. L. Hillhouse, R. F. Jordan, *Inorg. Chem.* **2015**, *54*, 2705–2712.

[166] F. Olechnowicz, G. L. Hillhouse, T. R. Cundari, R. F. Jordan, *Inorg. Chem.* **2017**, *56*, 9922–9930.

[167] N. J. Hartmann, G. Wu, T. W. Hayton, *Angew. Chem. Int. Ed.* **2015**, *54*, 14956–14959.

[168] N. J. Hartmann, G. Wu, T. W. Hayton, *J. Am. Chem. Soc.* **2016**, *138*, 12352–12355.

[169] N. J. Hartmann, G. Wu, T. W. Hayton, *Dalt. Trans.* **2016**, *45*, 14508–14510.

[170] M. Rakowski Dubois, D. L. Dubois, *Acc. Chem. Res.* **2009**, *42*, 1974–1982.

[171] J. Y. Yang, S. Chen, W. G. Dougherty, W. S. Kassel, R. M. Bullock, D. L. Dubois, S. Raugei, R. Rousseau, M. Dupuis, M. R. Dubois, *Chem. Commun.* **2010**, *46*, 8618–8620.

[172] C. T. Saouma, W. Kaminsky, J. M. Mayer, *J. Am. Chem. Soc.* **2012**, *134*, 7293–7296.

[173] Y. Zu, J. A. Fee, J. Hirst, *J. Am. Chem. Soc.* **2001**, *123*, 9906–9907.

[174] D. W. Bak, J. A. Zuris, M. L. Paddock, P. A. Jennings, S. J. Elliott, *Biochemistry* **2009**, *48*, 10193–10195.

[175] R. Camba, Y. S. Jung, L. M. Hunsicker-Wang, B. K. Burgess, C. D. Stout, J. Hirst, F. A. Armstrong, *Biochemistry* **2003**, *42*, 10589–10599.

[176] W. N. Lanzilotta, J. Christiansen, D. R. Dean, L. C. Seefeldt, *Biochemistry* **1998**, *37*, 11376–11384.

[177] D. J. Ferraro, L. Gakhar, S. Ramaswamy, *Biochem. Biophys. Res. Commun.* **2005**, *338*, 175–190.

[178] K. Hsueh, W. M. Westler, J. L. Markley, *J. Am. Chem. Soc.* **2010**, *132*, 7908–7918.

[179] A. Osyczka, C. C. Moser, P. L. Dutton, *Trends Biochem. Sci.* **2005**, *30*, 176–182.

[180] E. A. Berry, M. Guergova-Kuras, L. Huang, A. R. Crofts, *Annu. Rev. Biochem.* **2000**, *69*, 1005–1075.

[181] P. Zimmermann, C. Limberg, *J. Am. Chem. Soc.* **2017**, *139*, 4233–4242.

[182] M. Goubeaud, G. Schreiner, R. K. Thauer, *Eur. J. Biochem.* **1997**, *243*, 110–114.

[183] M. Krüger, A. Meyerdierks, F. O. Glöckner, R. Amann, F. Widdel, M. Kube, R. Reinhardt, J. Kahnt, R. Böcher, R. K. Thauer, S. Shima, *Nature* **2003**, *426*, 878–881.

[184] S. Shima, M. Krueger, T. Weinert, U. Demmer, J. Kahnt, R. K. Thauer, U. Ermler, *Nature* **2012**, *481*, 98–101.

[185] G. K. Lahiri, A. M. Stolzenberg, *Inorg. Chem.* **1993**, *32*, 4409–4413.

[186] T. Wongnate, D. Sliwa, B. Ginovska, D. Smith, M. W. Wolf, N. Lehnert, S. Raugei, S. W. Ragsdale, *Science* **2016**, *352*, 953–958.

[187] S. L. Chen, M. R. A. Blomberg, P. E. M. Siegbahn, *Phys. Chem. Chem. Phys.* **2014**, *16*, 14029–14035.

[188] T. Wongnate, S. W. Ragsdale, *J. Biol. Chem.* **2015**, *290*, 9322–9334.

[189] M. Can, F. A. Armstrong, S. W. Ragsdale, *Chem. Rev.* **2014**, *114*, 4149–4174.

[190] J. Seravalli, S. W. Ragsdale, *J. Biol. Chem.* **2008**, *283*, 8384–8394.

[191] W. Lubitz, H. Ogata, O. Ru, E. Reijerse, *Chem. Rev.* **2014**, *114*, 4081–4148.

[192] R. M. Buonomo, I. Font, M. J. Maguire, J. H. Reibenspies, T. Tuntulani, M. Y. Darensbourg, *J. Am. Chem. Soc.* **1995**, *117*, 963–973.

[193] J. W. van der Zwaan, J. M. C. C. Coremans, E. C. M. Bouwens, S. P. J. Albracht, *Biochim. Biophys. Acta* **1990**, *1041*, 101–110.

[194] J. M. C. C. Coremans, J. W. van der Zwaan, S. P. J. Albracht, *Biochim. Biophys. Acta* **1992**, *1119*, 157–168.

[195] M. Y. Darensbourg, W. Weigand, *Eur. J. Inorg. Chem.* **2011**, 994–1004.

[196] C. Schäfer, B. Friedrich, O. Lenza, *Appl. Environ. Microbiol.* **2013**, *79*, 5137–5145.

[197] O. Lenz, M. Ludwig, T. Schubert, I. Bürstel, S. Ganskow, T. Goris, A. Schwarze, B. Friedrich, *Chem. Phys. Chem.* **2010**, *11*, 1107–1119.

[198] B. Friedrich, J. Fritsch, O. Lenz, *Curr. Opin. Biotechnol.* **2011**, *22*, 358–364.

[199] N. J. Lindenmaier, S. Wahlefeld, E. Bill, T. Szilvási, C. Eberle, S. Yao, P. Hildebrandt, M. Horch, I. Zebger, M. Driess, *Angew. Chem. Int. Ed.* **2017**, *56*, 2208–2211.

[200] T. Liu, B. Li, M. L. Singleton, M. B. Hall, M. Y. Darensbourg, *J. Am. Chem. Soc.* **2009**, *131*, 8296–8307.

[201] C. A. Grapperhaus, M. Y. Darensbourg, *Acc. Chem. Res.* **1998**, *31*, 451–459.

[202] T. Takagi, T. Isemura, *J. Biochem.* **1964**, *56*, 344–350.

[203] D. A. Vicic, W. D. Jones, N. York, R. V December, D. J. C. R. V, *J. Am. Chem. Soc.* **1999**, *121*, 4070–4071.

[204] S. S. Oster, R. J. Lachicotte, W. D. Jones, *Inorg. Chim. Acta* **2002**, *330*, 118–127.

[205] J. Cho, K. M. Van Heuvelen, G. P. A. Yap, T. C. Brunold, C. G. Riordan, *Inorg. Chem.*

2008, *47*, 3931–3933.

[206] C. Mealli, S. Midollini, L. Sacconi, *Inorg. Chem.* **1978**, *17*, 632–637.

[207] N. Elgrishi, K. J. Rountree, B. D. McCarthy, E. S. Rountree, T. T. Eisenhart, J. L. Dempsey, *J. Chem. Educ.* **2018**, *95*, 197–206.

[208] J. K. Kochi, *Acc. Chem. Res.* **1992**, *25*, 39–47.

[209] K. Schulbert, R. Mattes, *Z. Naturforsch.* **1994**, *49b*, 770–772.

[210] E. I. Solomon, S. I. Gorelsky, A. Dey, *J. Comput. Chem.* **2009**, *30*, 1545–1614.

[211] D. Brazzolotto, M. Gennari, N. Queyriaux, T. R. Simmons, J. Pécaut, S. Demeshko, F. Meyer, M. Orio, V. Artero, C. Duboc, *Nat. Chem.* **2016**, *8*, 1054–1060.

[212] J. Telser, *J. Braz. Chem. Soc.* **2010**, *21*, 1139–1157.

[213] C. Holliger, A. J. Pierik, W. R. Hagen, E. J. Reijerse, *J. Am. Chem. Soc.* **1993**, *115*, 5651–5656.

[214] C. Y. Lin, P. P. Power, *Chem. Soc. Rev.* **2017**, *46*, 5347–5399.

[215] P. Chmielewski, M. Grzeszczuk, L. Latos-grazynski, J. Lisowski, *Inorg. Chem.* **1989**, *28*, 3546–3552.

[216] M. P. Suh, K. Y. Oh, J. W. Lee, Y. Y. Bae, *J. Am. Chem. Soc.* **1996**, *118*, 777–783.

[217] C. Yoo, Y. Lee, *Angew. Chem. Int. Ed.* **2017**, *56*, 9502–9506.

[218] M. I. Lipschutz, X. Yang, R. Chatterjee, T. D. Tilley, *J. Am. Chem. Soc.* **2013**, *135*, 15298–15301.

[219] F. Schneck, J. Ahrens, M. Finger, A. C. Stückl, C. Würtele, D. Schwarzer, S. Schneider, *Nat. Commun.* **2018**, *9*, 1–8.

[220] J. A. Franz, S.-J. Lee, T. A. Bowden, M. S. Alnajjar, A. M. Appel, J. C. Birnbaum, T. E. Bitterwolf, M. Dupuis, *J. Am. Chem. Soc* **2009**, *131*, 15212–15224.

[221] A. M. Appel, D. L. DuBois, M. Rakowski DuBois, *J. Am. Chem. Soc.* **2005**, *127*, 12717–12726.

[222] A. Ienco, M. J. Calhorda, J. Reinhold, F. Reineri, C. Bianchini, M. Peruzzini, F. Vizza, C. Mealli, *J. Am. Chem. Soc.* **2004**, *126*, 11954–11965.

[223] J. J. Warren, T. A. Tronic, J. M. Mayer, S. V. G. Bond, *Chem. Rev.* **2010**, *110*, 6961–7001.

[224] C. C. Lawrence, M. Bennati, H. V Obias, G. Bar, R. G. Griffin, J. Stubbe, *Proc. Natl. Acad. Sci. U. S. A.* **1999**, *96*, 8979–84.

[225] R. K. Thauer, A. Kaster, M. Goenrich, M. Schick, T. Hiromoto, S. Shima, *Annu. Rev. Biochem.* **2010**, *79*, 507–536.

[226] H. Ogata, K. Nishikawa, W. Lubitz, *Nature* **2015**, *520*, 571–574.

[227] S. Ding, P. Ghosh, A. M. Lunsford, N. Wang, N. Bhuvanesh, M. B. Hall, M. Y. Darensbourg, *J. Am. Chem. Soc.* **2016**, *138*, 12920–12927.

[228] K. Weber, T. Krämer, H. S. Shafaat, T. Weyhermüller, E. Bill, M. Van Gastel, F. Neese, W. Lubitz, *J. Am. Chem. Soc.* **2012**, *134*, 20745–20755.

[229] D. Brazzolotto, L. Wang, H. Tang, M. Gennari, N. Queyriaux, C. Philouze, S. Demeshko, F. Meyer, M. Orio, V. Artero, M. B. Hall, C. Duboc, *ACS Catal.* **2018**, *8*, 10658–10667.

[230] V. Autissler, W. Clegg, R. W. Harrington, R. A. Henderson, *Inorg. Chem.* **2004**, *43*, 3098–3105.

[231] A. M. Appel, S. Lee, J. A. Franz, L. Dubois, M. R. Dubois, B. Twamley, D. L. Dubois, M. Rakowski, *Organometallics* **2009**, 749–754.

[232] A. M. Appel, S. Lee, J. A. Franz, D. L. Dubois, P. Northwest, P. O. Box, *J. Am. Chem. Soc.* **2009**, *131*, 5224–5232.

[233] A. M. Appel, S. J. Lee, J. A. Franz, D. L. DuBois, M. R. DuBois, J. C. Birnbaum, B. Twamley, *J. Am. Chem. Soc.* **2008**, *130*, 8940–8951.

[234] R. J. Pleus, H. Waden, W. Saak, D. Haase, S. Pohl, *Dalt. Trans.* **1999**, 2601–2610.

[235] V. Lozan, B. Kersting, *Inorg. Chem.* **2008**, *47*, 5386–5393.

[236] W. Beck, W. Danzer, R. Höfer, *Angew. Chem. Int. Ed.* **1973**, *2*, 87–88.

[237] I. Kaljurand, A. Kütt, L. Sooväli, T. Rodima, V. Mäemets, I. Leito, I. A. Koppel, *J. Org. Chem.* **2005**, *70*, 1019–1028.

[238] C. T. Saouma, W. Kaminsky, J. M. Mayer, *J. Am. Chem. Soc.* **2012**, *134*, 7293–7296.

[239] C. T. Saouma, M. M. Pinney, J. M. Mayer, *Inorg. Chem.* **2014**, *53*, 3153–3161.

[240] J. P. Roth, S. Lovell, J. M. Mayer, *J. Am. Chem. Soc.* **2000**, *122*, 5486–5498.

[241] R. D. Shannon, *Acta Cryst.* **1976**, *A32*, 751–767.

[242] J. A. Stubbe, *Annu. Rev. Biochem.* **1989**, *58*, 257–285.

[243] S. Licht, G. J. Gerfen, J. Stubbe, *Science* **1996**, *271*, 477–481.

[244] R. Karthein, R. Dietz, W. Nastainczyk, H. H. Ruf, *Eur. J. Biochem.* **1988**, *171*, 313–320.

[245] S. T. Kim, A. Sancar, C. Essenmacher, G. T. Babcock, *Proc. Natl. Acad. Sci.* **1993**, *90*, 8023–8027.

[246] M. Kolberg, G. Bleifuss, A. Gräslund, B. M. Sjöberg, W. Lubitz, F. Lendzian, G. Lassmann, *Arch. Biochem. Biophys.* **2002**, *403*, 141–144.

[247] J. A. Stubbe, W. A. van der Donk, *Chem. Rev.* **1998**, *98*, 705–762.

[248] P. Reichard, A. Baldesten, L. Rutberg, *J. Biol. Chem.* **1961**, *236*, 1150–1157.

[249] B. L. Greene, A. T. Taguchi, J. Stubbe, D. G. Nocera, *J. Am. Chem. Soc.* **2017**, *139*, 16657–16665.

[250] P. Nordlund, P. Reichard, *Annu. Rev. Biochem.* **2006**, *75*, 681–706.

[251] B.-M. Sjöberg, P. Reichard, A. Gräslund, A. Ehrenberg, *J. Biol. Chem.* **1978**, *253*, 6863–6865.

[252] P. Nordlund, P. Reichard, *Annu. Rev. Biochem.* **1998**, *67*, 71–98.

[253] E. C. Minnihan, N. Ando, E. J. Brignole, L. Olshansky, J. Chittuluru, F. J. Asturias, C. L. Drennan, D. G. Nocera, J. Stubbe, *Proc. Natl. Acad. Sci.* **2013**, *110*, 3835–3840.

[254] E. C. Minnihan, D. G. Nocera, J. Stubbe, *Acc. Chem. Res.* **2013**, *46*, 2524–2535.

[255] S. Y. Reece, D. G. Nocera, *Annu. Rev. Biochem.* **2009**, *78*, 673–699.

[256] K. Ravichandran, E. C. Minnihan, Q. Lin, K. Yokoyama, A. T. Taguchi, J. Shao, D. G. Nocera, J. A. Stubbe, *Biochemistry* **2017**, *56*, 856–868.

[257] J. A. Stubbe, D. G. Nocera, C. S. Yee, M. C. Y. Chang, *Chem. Rev.* **2003**, *103*, 2167–2201.

[258] S. Y. Reece, J. M. Hodgkiss, J. A. Stubbe, D. G. Nocera, *Philos. Trans. R. Soc. B Biol. Sci.* **2006**, *361*, 1351–1364.

[259] D. N. Beratan, C. Liu, A. Migliore, N. F. Polizzi, S. S. Skourtis, P. Zhang, Y. Zhang, *Acc. Chem. Res.* **2015**, *48*, 474–481.

[260] S. Hammes-Schiffer, *Acc. Chem. Res.* **2006**, *39*, 93–100.

[261] M. R. Seyedsayamdost, C. T. Y. Chan, V. Mugnaini, J. Stubbe, M. Bennati, *J. Am. Chem. Soc.* **2007**, *129*, 15748–15749.

[262] B. Wörsdörfer, D. A. Conner, K. Yokoyama, J. Livada, M. Seyedsayamdost, W. Jiang, A. Silakov, J. Stubbe, J. M. Bollinger, C. Krebs, *J. Am. Chem. Soc.* **2013**, *135*, 8585–8593.

[263] K. R. Ravichandran, A. T. Taguchi, Y. Wei, C. Tommos, D. G. Nocera, J. Stubbe, *J. Am. Chem. Soc.* **2016**, *138*, 13706–13716.

[264] T. U. Nick, K. R. Ravichandran, J. Stubbe, M. Kasanmascheff, M. Bennati, *Biochemistry* **2017**, *56*, 3647–3656.

[265] T. Argirević, C. Riplinger, J. A. Stubbe, F. Neese, M. Bennati, *J. Am. Chem. Soc.* **2012**, *134*, 17661–17670.

[266] T. U. Nick, W. Lee, S. Koßmann, F. Neese, J. Stubbe, M. Bennati, *J. Am. Chem. Soc.* **2015**, *137*, 289–298.

[267] J. Stubbe, D. Ackles, *J. Biol. Chem.* **1980**, *255*, 8027.

[268] B. M. Sjöberg, A. Gräslund, F. Eckstein, *J. Biol. Chem.* **1983**, *258*, 8060–8067.

[269] J. Stubbe, D. Ackles, R. Segal, R. L. Blakley, *J. Biol. Chem.* **1981**, *256*, 4843–4846.

[270] R. Lenz, B. Giese, *J. Am. Chem. Soc.* **1997**, *119*, 2784–2794.

[271] G. J. Gerfen, S. Licht, J. P. Willems, B. M. Hoffman, J. Stubbe, *J. Am. Chem. Soc.* **1996**, *118*, 8192–8197.

[272] M. Kumar, R. O. Day, G. J. Colpas, M. J. Maroney, *J. Am. Chem. Soc.* **1989**, *111*, 8326.

[273] N. D. J. Branscombe, A. J. Atkins, A. Marin-Becerra, E. J. L. McInnes, F. E. Mabbs, J. McMaster, M. Schröder, *Chem. Commun.* **2003**, 1098–1099.

[274] M. A. Halcrow, G. Christou, *Chem. Rev.* **1994**, *94*, 2421–2481.

[275] J. C. Fontecilla-Camps, S. W. Ragsdale, *Adv. Inorg. Chem.* **1999**, *47*, 8242.

[276] P. Amara, A. Volbeda, J. C. Fontecilla-Camps, M. J. Field, *J. Am. Chem. Soc.* **1999**, *121*, 4468–4477.

[277] L. Jia, C. Bonaventura, J. Bonaventura, J. S. Stamler, *Nature* **1996**, *380*, 221–226.

[278] J. R. Pawloski, D. T. Hess, J. S. Stamler, *Nature* **2001**, *409*, 622–626.

[279] M. T. Salgado, S. Ramasamy, A. Tsuneshige, P. T. Manoharan, J. M. Rifkind, *J. Am. Chem. Soc.* **2011**, *133*, 13010–13022.

[280] M. T. Salgado, E. Nagababu, J. M. Rifkind, *J. Biol. Chem.* **2009**, *284*, 12710–12718.

[281] M. Fontecave, S. Ollagnier-De-Choudens, E. Mulliez, *Chem. Rev.* **2003**, *103*, 2149–2166.

[282] W. Huang, W. Chen, G. Wang, J. Li, X. Cheng, G. Li, *ACS Catal.* **2016**, *6*, 7471–7474.

[283] T. M. Nguyen, N. Manohar, D. A. Nicewicz, *Angew. Chem. Int. Ed.* **2014**, *53*, 6198–6201.

[284] X. Pan, E. Lacôte, J. Lalevée, D. P. Curran, *J. Am. Chem. Soc.* **2012**, *134*, 5669–5674.

[285] B. P. Roberts, *Chem. Soc. Rev.* **1999**, *28*, 25–35.

[286] H. S. Dang, B. P. Roberts, *Tetrahedron Lett.* **1995**, *36*, 2875–2878.

[287] N. M. Mews, G. Hörner, H. Schubert, A. Berkefeld, *Inorg. Chem.* **2018**, 57, 9670–9682.

[288] K. Wang, E. I. Stiefel, *Science.* **2001**, *291*, 106–109.

[289] C. A. Grapperhaus, K. Ouch, M. S. Mashuta, *J. Am. Chem. Soc.* **2009**, *131*, 64–65.

[290] K. Ouch, M. S. Mashuta, C. A. Grapperhaus, *Inorg. Chem.* **2011**, *50*, 9904–9914.

[291] S. Poturovic, M. S. Mashuta, C. A. Grapperhaus, *Angew. Chem. Int. Ed.* **2005**, *44*, 1883–1887.

[292] G. Lassmann, M. Kolberg, G. Bleifuss, A. Gräslund, B. M. Sjöberg, W. Lubitz, *Phys. Chem. Chem. Phys.* **2003**, *5*, 2442–2453.

[293] M. Van Gastel, W. Lubitz, G. Lassmann, F. Neese, *J. Am. Chem. Soc.* **2004**, *126*, 2237–2246.

[294] M. C. R. Symons, *J.C.S. Perkin 2* **1974**, *58*, 1618–1620.

[295] H. Chandra, D. N. R. Rao, M. C. R. Symons, *J. Chem. Soc. Dalt. Trans.* **1987**, 729–732.

[296] J. Derendorf, C. Jenne, M. Keßler, *Angew. Chem. Int. Ed.* **2017**, *56*, 8281–8284.

[297] J. Springs, C. P. Janzen, M. Y. Darensbourg, J. C. Calabrese, P. J. Krusic, J. N. Verpeaux, C. Amatore, *J. Am. Chem. Soc.* **1990**, *112*, 5789–5797.

[298] J. E. McDonough, A. Mendiratta, J. J. Curley, G. C. Fortman, S. Fantasia, C. C. Cummins, E. V. Rybak-Akimova, S. P. Nolan, C. D. Hoff, *Inorg. Chem.* **2008**, *47*, 2133–2141.

[299] A. C. Lizano, M. G. Munchhof, E. K. Haub, M. E. Noble, *J. Am. Chem. Soc.* **1991**, *113*, 9204–9210.

[300] G. N. R. Tripathi, Q. Sun, D. A. Armstrong, D. M. Chipman, R. H. Schuler, *J. Phys. Chem.* **1992**, *96*, 5344–5350.

[301] J. E. McDonough, J. J. Weir, K. Sukcharoenphon, C. D. Hoff, O. P. Kryatova, E. V Rybak-Akimova, B. L. Scott, G. J. Kubas, A. Mendiratta, C. C. Cummins, *J. Am. Chem. Soc.* **2006**, *128*, 10295–10303.

[302] S. Kimura, E. Bill, E. Bothe, T. Weyhermüller, K. Wieghardt, *J. Am. Chem. Soc.* **2001**, *123*, 6025–6039.

[303] M. Bennati, J. H. Robblee, V. Mugnaini, J. Stubbe, J. H. Freed, P. Borbat, *J. Am. Chem. Soc.* **2005**, *127*, 15014–15015.

[304] J. A. Stubbe, D. G. Nocera, C. S. Yee, M. C. Y. Chang, *Chem. Rev.* **2003**, *103*, 2167–2201.

[305] S. S. Licht, S. Booker, J. Stubbe, *Biochemistry* **1999**, *38*, 1221–1233.

[306] P. Lau, H. Braunwarth, G. Huttner, D. Gunauer, K. Evertz, W. Imhof, C. Emmerich, L. Zsolnai, *Organometallics* **1991**, *10*, 3861–3873.

[307] R. M. Wing, G. C. Tustin, W. H. Okamura, *J. Am. Chem. Soc.* **1970**, *92*, 1935–1939.

[308] G. N. Schrauzer, V. P. Mayweg, *J. Am. Chem. Soc.* **1965**, *87*, 1483–1489.

[309] V. Lyaskovskyy, B. De Bruin, *ACS Catal.* **2012**, *2*, 270–279.

[310] V. K. K. Praneeth, M. R. Ringenberg, T. R. Ward, O. R. Luca, R. H. Crabtree, V. K. K. Praneeth, M. R. Ringenberg, T. R. Ward, *Angew. Chem. Int. Ed.* **2012**, *51*, 10228–10234.

[311] O. R. Luca, R. H. Crabtree, *Chem. Soc. Rev.* **2013**, *42*, 1440–1459.

[312] D. L. J. Broere, R. Plessius, J. I. Van Der Vlugt, *Chem. Soc. Rev.* **2015**, *44*, 6886–6915.

[313] M. Bose, G. Moula, A. Begum, S. Sarkar, *Inorg. Chem.* **2011**, *50*, 3852–3854.

[314] B. A. Goodman, J. B. Raynor, *Adv. Inorg. Chem. Radiochem.* **1970**, *13*, 136–341.

[315] Y. H. Chang, C. L. Su, R. R. Wu, J. H. Liao, Y. H. Liu, H. F. Hsu, *J. Am. Chem. Soc.* **2011**, *133*, 5708–5711.

[316] S. Chakrabarty, R. Banerjee, *Int. J. Chem. Kinet.* **2016**, *48*, 274–280.

[317] C. A. Grapperhaus, S. Poturovic, *Inorg. Chem.* **2004**, *43*, 3292–3298.

[318] R. Y. C. Shin, H. S. Sim, L. Y. Goh, R. D. Webster, *J. Organomet. Chem.* **2007**, *692*, 3267–3276.

[319] H. Tang, E. N. Brothers, M. B. Hall, *Inorg. Chem.* **2017**, *56*, 583–593.

[320] R. Eisenberg, H. B. Gray, *Inorg. Chem.* **2011**, *50*, 9741–9751.

[321] U. Das, T. Ghorui, B. Adhikari, S. Roy, S. Pramanik, K. Pramanik, *Dalt. Trans.* **2015**, *44*, 8625–8639.

[322] J. A. Franz, S. Lee, T. A. Bowden, M. S. Alnajjar, A. M. Appel, J. C. Birnbaum, T. E. Bitterwolf, M. Dupuis, *J. Am. Chem. Soc.* **2009**, *131*, 15212–15224.

[323] D. Herebian, E. Bothe, E. Bill, T. Weyhermu, K. Wieghardt, *J. Am. Chem. Soc.* **2001**, *123*, 10012–10023.

[324] C. U. Perotto, C. L. Sodipo, G. J. Jones, J. P. Tidey, A. J. Blake, W. Lewis, E. S. Davies, J. McMaster, M. Schröder, *Inorg. Chem.* **2018**, *57*, 2558–2569.

[325] V. Bachler, G. Olbrich, F. Neese, K. Wieghardt, *Inorg. Chem.* **2002**, *41*, 4179–4193.

[326] W. W. Ellis, J. W. Raebiger, C. J. Curtis, J. W. Bruno, D. L. DuBois, *J. Am. Chem. Soc.* **2004**, *126*, 2738–2743.

[327] E. P. Broering, S. Dillon, E. M. Gale, R. A. Steiner, J. Telser, T. C. Brunold, T. C. Harrop, *Inorg. Chem.* **2015**, *54*, 3815–3828.

[328] S. Yao, P. Hrobárik, F. Meier, R. Rudolph, E. Bill, E. Irran, M. Kaupp, M. Driess, *Chem. Eur. J.* **2013**, *19*, 1246–1253.

[329] S. a. Yao, V. Martin-Diaconescu, I. Infante, K. M. Lancaster, A. W. Götz, S. DeBeer, J. F. Berry, *J. Am. Chem. Soc.* **2015**, *137*, 4993–5011.

[330] R. Rudolph, B. Blom, S. Yao, F. Meier, E. Bill, M. Van Gastel, N. Lindenmaier, M. Kaupp, M. Driess, *Organometallics* **2014**, *33*, 3154–3162.

[331] S. Yao, C. Milsmann, E. Bill, K. Wieghardt, M. Driess, *J. Am. Chem. Soc.* **2008**, *130*, 13536–13537.

[332] H. Sitzmann, D. Saurenz, G. Wolmershäuser, A. Klein, R. Boese, *Organometallics* **2001**, *20*, 700–705.

[333] N. G. Connelly, W. E. Geiger, *Chem. Rev.* **1996**, *96*, 877–910.

[334] D. M. Duggan, D. N. Hendrickson, *Inorg. Chem.* **1975**, *14*, 955–970.

[335] M. Reiners, D. Baabe, P. Schweyen, M. Freytag, P. G. Jones, M. D. Walter, *Eur. J. Inorg. Chem.* **2017**, *2017*, 388–400.

[336] V. Mishra, F. Lloret, R. Mukherjee, *Eur. J. Inorg. Chem.* **2007**, 2161–2170.

[337] T. R. Holman, M. P. Hendrich, L. Que Jr., *Inorg. Chem.* **1992**, *31*, 937–939.

[338] F. Dénès, M. Pichowicz, G. Povie, P. Renaud, *Chem. Rev.* **2014**, *114*, 2587–2693.

[339] M. A. Cremonini, L. Lunazzi, G. Placucci, *J. Org. Chem.* **1993**, *58*, 3805–3810.

[340] M. A. Cremonini, L. Lunazzi, G. Placucci, *J. Chem. Soc. Perkin Trans. 2* **1992**, *4*, 451–452.

[341] M. Z. Hoffman, E. Hayon, *J. Am. Chem. Soc.* **1972**, *94*, 7950–7957.

[342] M. Z. Hoffman, E. Hayon, *J. Phys. Chem.* **1973**, *77*, 990–996.

[343] J. F. Berry, *Chem. Eur. J.* **2010**, *16*, 2719–2724.

[344] F. G. Bordwell, J. P. Cheng, J. A. Harrelson, *J. Am. Chem. Soc.* **1988**, *110*, 1229–1231.

[345] D. D. M. Wayner, V. D. Parker, *Acc. Chem. Res.* **1993**, *26*, 287–294.

[346] M. Tilset, *J. Am. Chem. Soc.* **1992**, *114*, 2740–2741.

[347] V. Skagestad, M. Tilset, *J. Am. Chem. Soc.* **1993**, *115*, 5077–5083.

[348] R. Ciancanelli, B. C. Noll, D. L. DuBois, M. Rakowski DuBois, *J. Am. Chem. Soc.* **2002**, *124*, 2984–2992.

[349] J. Birnbaum, G. Godziela, M. Maciejewski, T. L. Tonker, R. C. Haltiwanger, M. R. DuBois, *Organometallics* **1990**, *9*, 394–401.

[350] R. L. Peterson, R. A. Himes, H. Kotani, T. Suenobu, L. Tian, M. A. Siegler, E. I. Solomon, S. Fukuzumi, K. D. Karlin, *J. Am. Chem. Soc.* **2011**, *133*, 1702–1705.

[351] R. L. Peterson, J. W. Ginsbach, R. E. Cowley, M. F. Qayyum, R. A. Himes, M. A. Siegler, C. D. Moore, B. Hedman, K. O. Hodgson, S. Fukuzumi, E. I. Solomon, K. D. Karlin, *J. Am. Chem. Soc.* **2013**, *135*, 16454–16467.

[352] N. Kindermann, C. J. Günes, S. Dechert, F. Meyer, *J. Am. Chem. Soc.* **2017**, *139*, 9831–9834.

[353] J. J. Warren, T. A. Tronic, J. M. Mayer, S. V. G. Bond, *Chem. Rev.* **2010**, *110*, 6961–7001.

[354] N. J. Hartmann, G. Wu, T. W. Hayton, *Dalt. Trans.* **2016**, *45*, 14508–14510.

[355] N. J. Hartmann, G. Wu, T. W. Hayton, *Dalt. Trans.* **2016**, *45*, 14508–14510.

[356] N. J. Hartmann, G. Wu, T. W. Hayton, *Chem. Sci.* **2018**, *9*, 6580–6588.

[357] S. S. Oster, R. J. Lachicotte, W. D. Jones, *Inorg. Chim. Acta* **2002**, *330*, 118–127.

[358] P. Holze, B. Horn, C. Limberg, C. Matlachowski, S. Mebs, *Angew. Chem. Int. Ed.* **2014**, *53*, 2750–2753.

[359] J. Cho, K. M. Van Heuvelen, G. P. A. Yap, T. C. Brunold, C. G. Riordan, *Inorg. Chem.* **2008**, *47*, 3931–3933.

[360] V. M. Iluc, C. A. Laskowski, C. K. Brozek, N. D. Harrold, G. L. Hillhouse, *Inorg. Chem.* **2010**, *49*, 6817–6819.

[361] C. Mealli, S. Midollini, *Inorg. Chem.* **1983**, *22*, 2785–2786.

[362] S. Pelties, D. Herrmann, B. De Bruin, F. Hartl, R. Wolf, *Chem. Commun.* **2014**, *50*, 7014–7016.

[363] M. T. Kieber-Emmons, K. M. Van Heuvelen, T. C. Brunold, C. G. Riordan, *J. Am. Chem. Soc.* **2009**, *131*, 440–441.

[364] K. M. Van Heuvelen, M. T. Kieber-Emmons, C. G. Riordan, T. C. Brunold, *Inorg. Chem.* **2010**, *49*, 3104–3112.

[365] U. Denninger, J. J. Schneider, G. Wilke, R. Goddard, C. Krüger, *Inorg. Chim. Acta* **1993**, *213*, 129–140.

[366] A. V. Anyushin, P. A. Abramov, N. B. Kompankov, M. N. Sokolov, V. P. Fedin, *Russ. J. Coord. Chem.* **2013**, *39*, 77–81.

[367] H. Vahrenkamp, V. A. Uchtman, L. F. Dahl, *J. Am. Chem. Soc.* **1968**, *90*, 3272–3273.

[368] N. J. Hartmann, G. Wu, T. W. Hayton, *Angew. Chem. Int. Ed.* **2015**, *54*, 14956–14959.

[369] S. Yao, M. Driess, *Acc. Chem. Res.* **2012**, *45*, 276–287.

[370] F. Olechnowicz, G. L. Hillhouse, R. F. Jordan, *Inorg. Chem.* **2015**, *54*, 2705–2712.

[371] K. M. Van Heuvelen, J. Cho, C. G. Riordan, T. C. Brunold, *Inorg. Chem.* **2010**, *49*, 3113–3120.

[372] A. M. Appel, S. J. Lee, J. A. Franz, D. L. DuBois, M. R. DuBois, J. C. Birnbaum, B. Twamley, *J. Am. Chem. Soc.* **2008**, *130*, 8940–8951.

[373] S. J. Rowan, S. J. Cantrill, G. R. L. Cousins, J. K. M. Sanders, J. F. Stoddart, *Angew. Chem. Int. Ed.* **2002**, *41*, 898–952.

[374] A. Takahashi, R. Goseki, H. Otsuka, *Angew. Chem. Int. Ed.* **2017**, *56*, 2016–2021.

[375] J. E. Bennett, *Tetrahedron* **1967**, *23*, 1697–1699.

[376] W. C. Danen, D. D. Newkirk, *J. Am. Chem. Soc.* **1976**, *98*, 516–520.

[377] M. Cheraki, M. Mogren Al-Mogren, G. Chambaud, J. S. Francisco, M. Hochlaf, S. Arabia, *J. Phys. Chem. A* **2018**, *122*, 2877–2883.

[378] A. K. Mustafa, M. M. Gadalla, S. H. Snyder, *Sci. Signal.* **2009**, *2*, 1–8.

[379] D. Tsikas, A. Böhmer, *Nitric Oxide* **2017**, *65*, 22–36.

[380] M. R. Filipovic, J. L. Miljkovic, T. Nauser, M. Royzen, K. Klos, T. Shubina, W. H. Koppenol, S. J. Lippard, I. Ivanović-Burmazović, *J. Am. Chem. Soc.* **2012**, *134*, 12016–12027.

[381] P. J. Altmann, A. Pöthig, *Chem. Commun.* **2016**, *52*, 9089–9092.

[382] A. Wu, E. A. Mader, A. Datta, D. A. Hrovat, W. T. Borden, J. M. Mayer, *J. Am. Chem. Soc.* **2009**, *131*, 11985–11997.

[383] N. J. Hartmann, G. Wu, T. W. Hayton, *J. Am. Chem. Soc.* **2016**, *138*, 12352–12355.

[384] F. Seel, R. Kuhn, G. Simon, M. Wagner, *Z. Naturforsch. B* **1985**, *40*, 1607–1617.

[385] Y. Gao, A. Toubaei, X. Kong, G. Wu, *Chem. Eur. J.* **2015**, *21*, 17172–17177.

[386] Y. Arikawa, T. Asayama, Y. Moriguchi, S. Agari, M. Onishi, *J. Am. Chem. Soc.* **2007**, *129*, 14160–14161.

[387] P. Poizot, F. Dolhem, *Energy Environ. Sci.* **2011**, *4*, 2003–2019.

[388] C. McGlade, P. Ekins, *Nature* **2015**, *517*, 187–190.

[389] G. P. Hammond, P. J. G. Pearson, *Energy Policy* **2013**, *52*, 1–9.

[390] N. Armaroli, V. Balzani, *Angew. Chem. Int. Ed.* **2007**, *46*, 52–66.

[391] International Renewable Energy Agency, *Renewable Energy Statistics* **2017**, IRENA 1–348.

[392] M. Frey, *ChemBioChem* **2002**, *3*, 153–160.

[393] M. L. Helm, M. P. Stewart, M. R. Bullock, M. R. DuBois, D. L. DuBois, *Science* **2011**, *333*, 863–865.

[394] H. S. Shafaat, O. Rüdiger, H. Ogata, W. Lubitz, *Biochim. Biophys. Acta - Bioenerg.* **2013**, *1827*, 986–1002.

[395] K. A. Vincent, A. Parkin, F. A. Armstrong, *Chem. Rev.* **2007**, *107*, 4366–4413.

[396] H. Ogata, W. Lubitz, Y. Higuchi, *J. Biochem.* **2016**, *160*, 251–258.

[397] S. Li, M. B. Hall, *Inorg. Chem.* **2001**, *40*, 18–24.

[398] S. . C. Niu, M. B. . B. Hall, *Inorg. Chem.* **2001**, *40*, 6201–6203.

[399] B. E. Barton, M. T. Olsen, T. B. Rauchfuss, *J. Am. Chem. Soc.* **2008**, *3*, 16834–16835.

[400] F. Gloaguen, T. B. Rauchfuss, *Chem. Soc. Rev.* **2009**, *38*, 100–108.

[401] C. Chauncey, L. Mccrory, C. Uyeda, J. Peters, *J. Am. Chem. Soc.* **2012**, *134*, 3164–3170.

[402] P.-A. Jacques, V. Artero, J. Pecaut, M. Fontecave, *Proc. Natl. Acad. Sci.* **2009**, *106*, 20627–20632.

[403] N. Kaeffer, A. Morozan, V. Artero, *J. Phys. Chem. B* **2015**, *119*, 13707–13713.

[404] S. M. Laga, J. D. Blakemore, L. M. Henling, B. S. Brunschwig, H. B. Gray, *Inorg.*

Chem. **2014**, *53*, 12668–12670.

[405] C. Baffert, V. Artero, M. Fontecave, *Inorg. Chem.* **2007**, *46*, 1817–1824.

[406] A. M. Appel, D. H. Pool, M. O'Hagan, W. J. Shaw, J. Y. Yang, M. R. Dubois, D. L. Dubois, R. M. Bullock, *ACS Catal.* **2011**, *1*, 777–785.

[407] D. L. DuBois, R. Morris Bullock, *Eur. J. Inorg. Chem.* **2011**, 1017–1027.

[408] C. J. Curtis, A. Miedaner, R. Ciancanelli, W. W. Ellis, B. C. Noll, M. Rakowski DuBois, D. L. DuBois, *Inorg. Chem.* **2003**, *42*, 216–227.

[409] S. I. Johnson, H. B. Gray, J. D. Blakemore, W. A. Goddard, *Inorg. Chem.* **2017**, *56*, 11375–11386.

[410] L. M. A. Quintana, S. I. Johnson, S. L. Corona, W. Villatoro, W. A. Goddard, M. K. Takase, D. G. VanderVelde, J. R. Winkler, H. B. Gray, J. D. Blakemore, *Proc. Natl. Acad. Sci.* **2016**, *113*, 6409–6414.

[411] F. Olechnowicz, G. L. Hillhouse, T. R. Cundari, R. F. Jordan, *Inorg. Chem.* **2017**, *56*, 9922–9930.

[412] S. Luo, M. A. Siegler, E. Bouwman, *Eur. J. Inorg. Chem.* **2016**, *2016*, 4693–4700.

[413] S. Luo, M. A. Siegler, E. Bouwman, *Organometallics* **2018**, *37*, 740–747.

[414] M. J. Chalkley, T. J. Del Castillo, B. D. Matson, J. P. Roddy, J. C. Peters, *ACS Cent. Sci.* **2017**, *3*, 217–223.

[415] D. Brynn Hibbert, P. Thordarson, *Chem. Commun.* **2016**, *52*, 12792–12805.

[416] P. Thordarson, *Chem. Soc. Rev.* **2011**, *40*, 1305–1323.

[417] C. T. Saouma, W. Kaminsky, J. M. Mayer, *J. Am. Chem. Soc.* **2012**, *134*, 7293–7296.

[418] M. Bergner, S. Dechert, S. Demeshko, C. Kupper, J. M. Mayer, F. Meyer, *J. Am. Chem. Soc.* **2017**, *139*, 701–707.

[419] A. Albers, S. Demeshko, S. Dechert, C. T. Saouma, J. M. Mayer, F. Meyer, *J. Am. Chem. Soc.* **2014**, *136*, 3946–3954.

[420] F. Neese, *Wiley Interdiscip. Rev. Comput. Mol. Sci.* **2012**, *2*, 73–78.

[421] A. Schäfer, H. Horn, R. Ahlrichs, *J. Chem. Phys.* **1992**, *97*, 2571–2577.

[422] F. Weigend, R. Ahlrichs, *Phys. Chem. Chem. Phys.* **2005**, *7*, 3297–3305.

[423] S. Grimme, J. Antony, S. Ehrlich, H. Krieg, *J. Chem. Phys.* **2010**, *132*, 1–19

[424] J. P. Perdew, M. Ernzerhof, K. Burke, *J. Chem. Phys.* **1996**, *105*, 9982–9985.

[425] E. Van Lenthe, A. Van Der Avoird, P. E. S. Wormer, *J. Chem. Phys.* **1998**, *108*, 4783–4796.

[426] D. A. Pantazis, X.-Y. Chen, C. R. Landis, F. Neese, *J. Chem. Theory Comput.* **2008**, *4*, 908–919.

[427] C. Van Wüllen, *J. Chem. Phys.* **1998**, *109*, 392–399.

[428] J. Autschbach, *J. Chem. Phys.* **2012**, *136*, 1–15.

[429] F. Neese, F. Wennmohs, A. Hansen, U. Becker, *Chem. Phys.* **2009**, *356*, 98–109.

[430] F. Weigend, *Phys. Chem. Chem. Phys.* **2006**, *8*, 1057–1065.

[431] MestReNova Inc., v. 10.0 **2017**.

[432] H. J. Reich, W. S. Goldenberg, B. Ö. Gudmundsson, A. W. Sanders, K. J. Kulicke, K. Simon, I. A. Guzei, *J. Am. Chem. Soc* **2001**, *123*, 8067–8079.

[433] T. Stoll, M. Gennari, I. Serrano, J. Fortage, J. Chauvin, F. Odobel, M. Rebarz, O. Poizat, M. Sliwa, A. Deronzier, et al., *Chem. Eur. J.* **2013**, *19*, 782–792.

[434] G. R. Fulmer, A. J. M. Miller, N. H. Sherden, H. E. Gottlieb, A. Nudelman, B. M. Stoltz, J. E. Bercaw, K. I. Goldberg, *Organometallics* **2010**, *29*, 2176–2179.

[435] G. M. Sheldrick, *Acta Crystallogr. Sect. A Found. Crystallogr.* **2015**, *71*, 3–8.

[436] G. M. Sheldrick, *Acta Crystallogr. Sect. C Struct. Chem.* **2015**, *71*, 3–8.

[437] X-RED; STOE & CIE GmbH: Darmstadt, Germany, **2002**.

[438] A. J. Arduengo, H. V. R. Dias, R. L. Harlow, M. Kline, *J. Am. Chem. Soc.* **1992**, *114*, 5530–5534.

[439] M. H. Voges, C. Rømming, M. Tilset, *Organometallics* **1999**, *18*, 529–533.

[440] M. L. Cole, P. C. Junk, *CrystEngComm* **2004**, *6*, 173–176.

[441] A. Raba, M. Cokoja, S. Ewald, K. Riener, E. Herdtweck, A. Pöthig, W. A Herrmann, F. E. Kühn, *Organometallics* **2012**, *31*, 2783–2800.

[442] K. Chellappan, N. J. Singh, I. C. Hwang, W. L. Jung, K. S. Kim, *Angew. Chem. Int. Ed.* **2005**, *44*, 2899–2903.

[443] A. N. Nesmeyanov, R. B. Materikova, I. R. Lyatifov, T. K. Kurbanov, N. S. Kochetkova, *J. Organomet. Chem.* **1978**, *145*, 241–243.

[444] T. Tsuda, T. Yazawa, K. Watanabe, T. Fujii, T. Saegusa, *J. Org. Chem.* **1981**, *46*, 192–194.

[445] N. A. Giffin, M. Makramalla, A. D. Hendsbee, K. N. Robertson, C. Sherren, C. C. Pye, J. D. Masuda, J. A. C. Clyburne, *Org. Biomol. Chem.* **2011**, *9*, 3672–3680.

[446] K. Fumino, V. Fossog, K. Wittler, R. Hempelmann, R. Ludwig, *Angew. Chem. Int. Ed.* **2013**, *52*, 2368–2372.

[447] A. M. Thomas, B. L. Lin, E. C. Wasinger, T. D. P. Stack, *J. Am. Chem. Soc.* **2013**, *135*, 18912–18919.

[448] V. W. Manner, T. F. Markle, J. H. Freudenthal, J. P. Roth, J. M. Mayer, *Chem. Commun.* **2008**, *246*, 256–258.

[449] S. In, J. Kang, *Bull. Korean Chem. Soc.* **2005**, *26*, 1121–1124.

[450] P. Pirovano, B. Twamley, A. R. McDonald, *Chem. Eur. J.* **2018**, *24*, 5238–5245.

[451] H.-J. Krüger, R. H. Holm, *Inrog. Chem.* **1987**, 3645–3647.

[452] H. J. Krüger, G. Peng, R. H. Holm, *Inorg. Chem.* **1991**, *30*, 734–742.

Appendix

Crystallographic Data

Table A.1 Crystal data and refinement details for **1** and **2**.

compound	**1**	**2**
empirical formula	$C_{30}H_{35}CuN_2$	$C_{44}H_{48}Cu_2N_4O_4$
formula weight	487.14	823.94
T [K]	133(2)	133(2)
crystal size [mm³]	0.500 x 0.410 x 0.260	0.200 x 0.150 x 0.080
crystal system	*monoclinic*	*triclinic*
space group	$P2_1/c$ (No. 14)	$P\bar{1}$ (No. 2)
a [Å]	16.8835(5)	9.0641(11)
b [Å]	14.3605(6)	10.3329(16)
c [Å]	22.5450(8)	11.7878(16)
α [°]	90	72.683(11)
β [°]	96.206(3)	67.882(9)
γ [°]	90	80.536(11)
V [Å³]	5434.1(3)	974.7(2)
Z	8	1
ρ [g·cm⁻³]	1.191	1.404
$F(000)$	2064	430
μ [mm⁻¹]	0.822	1.139
T_{min} / T_{max}	0.7029 / 0.8139	0.7757 / 0.9489
θ-range [°]	1.684 - 26.783	1.930 - 25.748
hkl-range	–21 to 19, ±18, ±28	±11, ±12, ±14
measured refl.	75361	10401
unique refl. [R_{int}]	11546 [0.0788]	3677 [0.0849]
observed refl. ($I > 2\sigma(I)$)	8474	2555
data / restr. / param.	11546 / 0 / 613	3677 / 0 / 250
goodness-of-fit (F^2)	0.963	1.028
$R1$, $wR2$ ($I > 2\sigma(I)$)	0.0456 / 0.0960	0.0633 / 0.1402
$R1$, $wR2$ (all data)	0.0706 / 0.1035	0.0984 / 0.1527

Table A.2 Crystal data and refinement details for **n**, **o**, and **p**.

Identification code	**n**	**o**	**p**
empirical formula	$C_8H_{11}IN_4$	$C_8H_{10}N_4$	$C_9H_{13}IN_4$
moiety formula	$C_8H_{11}N_4^+$, I^-	$C_8H_{10}N_4$	$C_9H_{13}N_4^+$, I^-
formula weight	290.11	162.20	304.13
T [K]	133(2)	133(2)	133(2)
crystal system	*monoclinic*	*monoclinic*	*monoclinic*
space group	$P2_1/c$ (No. 14)	$P2_1/n$ (No. 14)	$P2_1/n$ (No. 14)
a [Å]	14.1586(8)	6.9960(7)	6.8458(4)
b [Å]	9.9198(3)	5.5213(4)	11.5391(6)
c [Å]	15.7922(9)	10.4952(10)	14.5874(10)
α [°]	90	90	90
β [°]	105.913(4)	104.842(8)	101.360(5)
γ [°]	90	90	90
V [Å³]	2133.03(19)	391.87(6)	1129.75(12)
Z	8	2	4
ρ [g·cm⁻³]	1.807	1.375	1.788
$F(000)$	1120	172	592
μ [mm^{-1}]	2.966	0.090	2.804
T_{min} / T_{max}	0.2071 / 0.5613	0.6407 / 0.8669	0.2012 / 0.3522
θ-range [°]	1.496 - 26.764	3.163 - 26.732	2.268 - 26.698
hkl-range	±17, ±12, -18 to 19	±8, -6 to 5, ±13	-8 to 7, ±14, ±18
measured refl.	30549	4923	14959
unique refl. [R_{int}]	4510 [0.0732]	821 [0.0449]	2390 [0.0719]
observed refl. ($I > 2\sigma(I)$)	4203	742	2146
data / restr. / param.	4510 / 0 / 245	821 / 0 / 55	2390 / 0 / 128
goodness-of-fit (F^2)	1.101	1.073	1.053
$R1$, $wR2$ ($I > 2\sigma(I)$)	0.0260 / 0.0650	0.0342 / 0.0814	0.0231 / 0.0617
$R1$, $wR2$ (all data)	0.0293 / 0.0665	0.0378 / 0.0831	0.0267 / 0.0631

Table A.3 Crystal data and refinement details for **$[(L^2)_5Cu_6](PF_6)_6$** and **$[L^5Cu_2](PF_6)_2$**.

compound	**$[(L^2)_5Cu_6](PF_6)_6$**	**$[L^5Cu_2](PF_6)_2$**
empirical formula	$C_{107}H_{108}Cu_6F_{36}N_{36}P_6$	$C_{34}H_{36}Cu_2F_{12}N_{12}P_2$
formula weight	3149.35	1029.77
T [K]	133(2)	133(2)
crystal size [mm³]	0.500 x 0.100 x 0.070	0.350 x 0.280 x 0.260
crystal system	*triclinic*	*triclinic*
space group	$P\bar{1}$ (No. 2)	$P\bar{1}$ (No. 2)
a [Å]	16.2219(5)	8.7455(5)
b [Å]	17.1833(5)	10.4944(7)
c [Å]	24.8330(7)	11.9425(7)
α [°]	99.466(2)	108.720(5)
β [°]	90.653(2)	101.853(5)
γ [°]	113.775(2)	95.837(5)
V [Å³]	6225.2(3)	999.20(11)
Z	2	1
ρ [g·cm^{-3}]	1.680	1.711
F(000)	3180	520
μ [mm^{-1}]	1.201	1.246
T_{min} / T_{max}	0.6484 / 0.8893	0.6802 / 0.7637
θ-range [°]	1.318 - 25.636	1.861 - 26.755
hkl-range	±19, ±20, ±30	±11, ±13, ±15
measured refl.	76617	13450
unique refl. [R_{int}]	23424 [0.0710]	4227 [0.0199]
observed refl. ($I > 2\sigma(I)$)	15971	3743
data / restr. / param.	23424 / 603 / 1841	4227 / 21 / 303
goodness-of-fit (F^2)	0.978	1.063
$R1$, $wR2$ ($I > 2\sigma(I)$)	0.0524 / 0.1138	0.0400 / 0.1073
$R1$, $wR2$ (all data)	0.0871 / 0.1256	0.0466 / 0.1105

Table A.4 Crystal data and refinement details for **$[(L^6)_2Ag_6](PF_6)_4$** and **$[(L^8)_2Ag_6](PF_6)_4$**.

compound	**$[Ag_6(L^6)_2](PF_6)_4$**	**$[Ag_6(L^8)_2](PF_6)_4$**
empirical formula	$C_{50}H_{58}Ag_6F_{24}N_{24}P_4$	$C_{59}H_{78}Ag_6F_{24}N_{24}OP_4$
formula weight	2222.30	2366.55
T [K]	133(2)	133(2)
crystal size [mm³]	0.410 x 0.190 x 0.170	0.500 x 0.330 x 0.190
crystal system	*triclinic*	*triclinic*
space group	$P\bar{1}$ (No. 2)	$P\bar{1}$ (No. 2)
a [Å]	12.0056(5)	12.4063(6)
b [Å]	12.4018(6)	13.3872(6)
c [Å]	13.7149(7)	14.2221(7)
α [°]	93.335(4)	62.591(3)
β [°]	108.653(4)	86.067(4)
γ [°]	107.305(4)	85.347(4)
V [Å³]	1820.46(16)	2088.71(18)
Z	1	1
ρ [g·cm^{-3}]	2.027	1.881
$F(000)$	1084	1166
μ [mm^{-1}]	1.786	1.564
T_{min} / T_{max}	0.5575 / 0.7547	0.4568 / 0.7422
θ-range [°]	1.590 - 26.761	1.614 - 26.849
hkl-range	±15, ±15, -17 to 16	±15, ±16, ±17
measured refl.	24105	29222
unique refl. [R_{int}]	7695 [0.0389]	8827 [0.0198]
observed refl. ($I > 2\sigma(I)$)	6884	7880
data / restr. / param.	7695 / 0 / 491	8827 / 224 / 621
goodness-of-fit (F^2)	1.056	1.019
$R1$, $wR2$ ($I > 2\sigma(I)$)	0.0252 / 0.0574	0.0262 / 0.0685
$R1$, $wR2$ (all data)	0.0310 / 0.0591	0.0306 / 0.0704

Table A.5 Crystal data and refinement details for **$[(L^6)_2Cu_6](PF_6)_4$** and **$[(L^6)_2Cu_8Cl_{3.4}Br_{0.6}](PF_6)_2$**.

Compound	**$[(L^6)_2Cu_6](PF_6)_4$** and **$[(L^6)_2Cu_8Cl_{3.4}Br_{0.6}](PF_6)_2$**
empirical formula	$C_{47}H_{53.50}Br_{0.30}Cl_{1.70}Cu_7F_{18}N_{22.50}P_3$
Moiety formula	$C_{42}H_{46}Br_{0.60}Cl_{3.40}Cu_8N_{20}{}^{2+}$, $C_{42}H_{46}Cu_6N_{20}{}^{4+}$, 6($F_6P^-$), 5($C_2H_3N$)
formula weight	1897.55
T [K]	133(2)
crystal system	*triclinic*
space group	$P\bar{1}$ (No. 2)
a [Å]	12.7351(7)
b [Å]	14.4552(7)
c [Å]	21.1271(14)
α [°]	78.541(5)
β [°]	82.248(5)
γ [°]	67.399(4)
V [Å^3]	3511.6(4)
Z	2
ρ [g·cm^{-3}]	1.795
F(000)	1885
μ [mm^{-1}]	2.482
θ-range [°]	1.546 - 25.723
hkl-range	±15, ±17, ±25
measured refl.	32900
unique refl. [R_{int}]	13169 [0.1656]
observed refl. ($I > 2\sigma(I)$)	6324
data / restr. / param.	13169 / 847 / 857
goodness-of-fit (F^2)	0.973
$R1$, $wR2$ ($I > 2\sigma(I)$)	0.0940 / 0.1534
$R1$, $wR2$ (all data)	0.1907 / 0.1842

Table A.6 Crystal data and refinement details for **$[L^6Ni_2(OH)](PF_6)_2\cdot MeCN$**, **$[L^6Ni_2(OH)](PF_6)_2\cdot MeCN$**, **$[L^6Ni_2(OH)](PF_6)_2\cdot OC_3H_6$**, and **$[L^6Ni_2(OH)]Cl_2\cdot(H_2O)_2$**.

compound	**$[L^6Ni_2(OH)](PF_6)_2\cdot MeCN$**	**$[L^6Ni_2(OH)](PF_6)_2\cdot MeCN$**	**$[L^6Ni_2(OH)](PF_6)_2\cdot OC_3H_6$**	**$[L^6Ni_2(OH)]Cl_2\cdot(H_2O)_2$**
empirical formula	$C_{31}H_{43}F_{12}N_{11}Ni_2O_3P_2$	$C_{27}H_{33}F_{12}N_{13}Ni_2OP_2$	$C_{30}H_{42}F_{12}N_{10}Ni_2O_{3.50}P_2$	$C_{21}H_{28}Cl_2N_{10}Ni_2O_3$
formula weight	1025.12	963.02	1006.09	656.85
T [K]	133(2)	133(2)	133(2)	133(2)
crystal size [mm³]	0.500 x 0.420 x 0.280	0.500 x 0.280 x 0.150	0.360 x 0.210 x 0.160	0.500 x 0.280 x 0.230
crystal system	*monoclinic*	*triclinic*	*triclinic*	*monoclinic*
space group	$P2_1/c$ (No. 14)	$P\bar{1}$ (No. 2)	$P\bar{1}$ (No. 2)	$P2_1/n$ (No. 14)
a [Å]	24.9610(5)	11.1446(5)	11.658(2)	14.2601(4)
b [Å]	12.6150(2)	14.1269(7)	14.162(3)	9.1285(3)
c [Å]	25.3644(5)	14.3202(7)	14.195(3)	20.0497(6)
α [°]	90	66.779(3)	110.44(3)	90
β [°]	92.189(2)	67.467(3)	112.23(3)	98.620(2)
γ [°]	90	86.779(4)	95.73(3)	90
V [Å³]	7981.0(3)	1901.74(17)	1958.8(9)	2580.45(14)
Z	8	2	2	4
ρ [g·cm⁻³]	1.706	1.682	1.706	1.691
F(000)	4192	976	1028	1352
μ [mm^{-1}]	1.130	1.177	1.150	1.713
T_{min} / T_{max}	0.4705 / 0.6397	0.5591 / 0.8606	0.7006 / 0.8656	0.4447 / 0.5972
θ-range [°]	1.123 - 25.783	1.578 - 26.762	1.593 - 26.811	1.642 - 26.822
hkl-range	±30, ±15, ±30	-14 to 12, ±17, ±18	±14, ±17, ±17	-18 to 16, ±11, ±25
measured refl.	93715	25019	23590	34180
unique refl. [R_{int}]	15069 [0.0441]	8037 [0.0706]	8299 [0.0419]	5473 [0.0360]
observed refl. ($I > 2\sigma(I)$)	13733	6665	5886	4756
data / restr. / param.	15069 / 90 / 1160	8037 / 93 / 582	8299 / 67 / 630	5473 / 0 / 365
goodness-of-fit (F^2)	1.047	1.043	0.961	1.069
$R1$, $wR2$ ($I > 2\sigma(I)$)	0.0536 / 0.1352	0.0423 / 0.1121	0.0418 / 0.0874	0.0259 / 0.0682
$R1$, $wR2$ (all data)	0.0638 / 0.1505	0.0530 / 0.1171	0.0702 / 0.0948	0.0334 / 0.0745

Table A.7 Crystal data and refinement details for **[L^{6}Ni$_2$(OH)](BPh$_4$)$_2$**, **[L^{7}Ni$_2$(OH)](PF$_6$)$_2$**, and **[L^{6}Ni$_2$Cl](PF$_6$)$_2$**.

compound	**[L^{6}Ni$_2$(OH)](BPh$_4$)$_2$**	**[L^{7}Ni$_2$(OH)](PF$_6$)$_2$**	**[L^{6}Ni$_2$Cl](PF$_6$)$_2$**
empirical formula	$C_{81}H_{88}B_2N_{10}Ni_2O_4$	$C_{41}H_{64}F_{12}N_{10}Ni_2O_5P_2$	$C_{23}H_{26}ClF_{12}N_{11}Ni_2P_2$
formula weight	1404.65	1184.38	899.36
T [K]	133(2)	133(2)	133(2)
crystal size [mm³]	0.422 x 0.398 x 0.209	0.500 x 0.490 x 0.210	
crystal system	*monoclinic*	*monoclinic*	*orthorhombic*
space group	$P2_1/c$ (No. 14)	$P2_1/n$ (No. 14)	$Pmn2_1$ (No. 31)
a [Å]	14.008(3)	12.6763(4)	14.4058(17)
b [Å]	13.187(3)	26.9582(6)	13.7284(17)
c [Å]	38.573(8)	14.3191(4)	8.3737(12)
α [°]	90	90	90
β [°]	98.51(3)	92.940(3)	90
γ [°]	90	90	90
V [Å³]	7047(2)	4886.8(2)	1656.1(4)
Z	4	4	2
ρ [g·cm^{-3}]	1.324	1.610	1.804
F(000)	2968	2456	904
μ [mm^{-1}]	0.594	0.937	1.419
T_{min} / T_{max}	0.7732 / 0.9574	0.2688 / 0.7562	
θ-range [°]	1.470 - 25.703	1.511 - 25.831	1.483 - 26.764
hkl-range	±17, ±16, -46 to 40	±15, -33 to 32, -16 to 17	-16 to 18, ±17, ±10
measured refl.	57016	51236	11279
unique refl. [R_{int}]	13195 [0.0367]	9243 [0.0729]	3649 [0.0826]
observed refl. ($I > 2\sigma(I)$)	10961	7392	3046
data / restr. / param.	13195 / 345 / 1005	9243 / 1 / 656	3649 / 370 / 358
goodness-of-fit (F^2)	1.067	1.046	1.081
$R1$, $wR2$ ($I > 2\sigma(I)$)	0.0529 / 0.1227	0.0593 / 0.1542	0.0513 / 0.1167
$R1$, $wR2$ (all data)	0.0675 / 0.1324	0.0770 / 0.1798	0.0649 / 0.1243

Table A.8 Crystal data and refinement details for **$[Ni_2SL^6]PF_6$**, **$[L^6Ni_2(SCH_3)](PF_6)_2$**, **$[(L^6)_2Ni_4(SHS)](PF_6)_3$**, **$[(L^6)_2Ni_4(S_2)](PF_6)_4$**, and **$[(L^6)_2Ni_4(S_2)](PF_6)_{3.209}(OTf)_{0.791}$**.

compound	**$[L^6Ni_2S]PF_6$**	**$[L^6Ni_2(SCH_3)](PF_6)_2$**	**$[(L^6)_2Ni_4(SHS)](PF_6)_3$**	**$[(L^6)_2Ni_4(S_2)](PF_6)_4$**	**$[(L^6)_2Ni_4(S_2)](PF_6)_3OTf$**
empirical formula	$C_{21}H_{22}F_6N_{10}Ni_2PS$	$C_{24}H_{31}F_{12}N_{10}Ni_2O_{0.50}P_2S$	$C_{52}H_{61}F_{18}N_{25}Ni_4P_3S_2$	$C_{44}H_{49}F_{24}N_{21}Ni_4P_4S_2$	$C_{46.29}H_{52}F_{20.13}N_{22}Ni_4O_{0.87}P_{3.21}S_{2.29}$
formula weight	708.93	907.01	1770.12	1750.88	1720.64
T [K]	133(2)	133(2)	133(2)	133(2)	133(2)
crystal size [mm³]	0.460 x 0.140 x 0.070	0.500 x 0.470 x 0.160	0.500 x 0.490 x 0.480	0.500 x 0.280 x 0.250	0.370 x 0.280 x 0.190
crystal system	*orthorhombic*	*monoclinic*	*monoclinic*	*monoclinic*	*triclinic*
space group	*Pnma* (No. 62)	$P2_1/c$ (No. 14)	$P2_1/n$ (No. 14)	$C2/c$ (No. 15)	$P\bar{1}$ (No. 2)
a [Å]	7.5482(3)	15.9386(4)	14.6069(6)	25.2832(8)	14.6708(3)
b [Å]	12.5017(5)	22.4145(3)	16.8404(5)	14.0809(4)	16.3671(4)
c [Å]	32.5913(17)	19.5896(4)	29.9864(14)	19.7680(6)	28.6873(6)
α [°]	90	90	90	90	92.197(2)
β [°]	90	101.743(2)	103.055(3)	120.852(2)	92.046(2)
γ [°]	90	90	90	90	90.956(2)
V [Å³]	3075.5(2)	6852.0(2)	7185.6(5)	6041.7(3)	6877.8(3)
Z	4	8	4	4	4
ρ [g·cm⁻³]	1.531	1.758	1.636	1.925	1.662
F(000)	1436	3672	3596	3520	3475
μ [mm^{-1}]	1.410	1.356	1.260	1.534	1.330
T_{min} / T_{max}	0.6901 / 0.9532	0.4401 / 0.8679	0.5391 / 0.7288	0.5264 / 0.6978	0.2005 / 0.6046
θ-range [°]	1.745 - 25.717	1.305 - 26.820	1.394 - 25.730	1.724 - 26.968	1.245 - 25.671
hkl-range	-8 to 9, -15 to 14, ±39	±20, -28 to 25, ±24	±17, -19 to 20, ±36	±32, ±17, -25 to 22	±17, ±19, ±34
measured refl.	16491	92785	81918	39319	72478
unique refl. [R_{int}]	3038 [0.0419]	14555 [0.0330]	13538 [0.0372]	6423 [0.0262]	25842 [0.0408]
observed refl. ($I > 2\sigma(I)$)	2407	12489	12327	5638	20038
data / restr. / param.	3038 / 147 / 308	14555 / 819 / 1002	13538 / 2129 / 1588	6423 / 313 / 542	25842 / 1347 / 2082
goodness-of-fit (F^2)	1.109	1.018	1.188	1.072	1.056
$R1$, $wR2$ ($I > 2\sigma(I)$)	0.0445 / 0.1046	0.0402 / 0.1043	0.0559 / 0.1444	0.0497 / 0.1260	0.0726 / 0.1916
$R1$, $wR2$ (all data)	0.0627 / 0.1147	0.0487 / 0.1106	0.0608 / 0.1472	0.0575 / 0.1337	0.0930 / 0.2056

Chapter 2

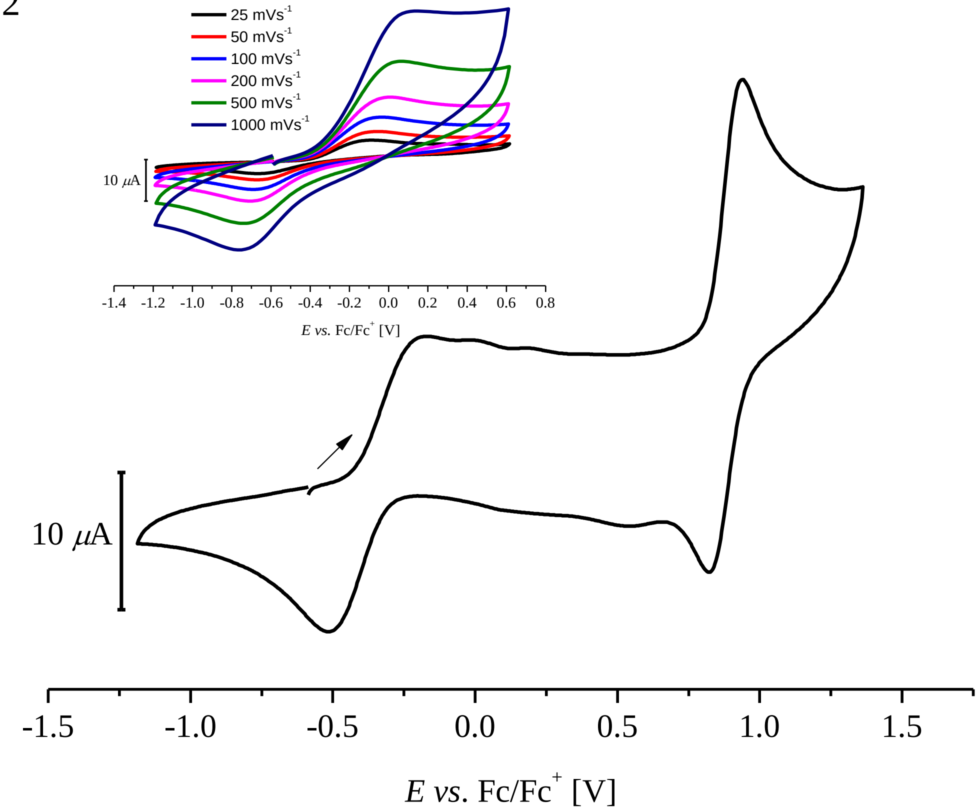

Figure A.2.1: CV of copper(I) NHC complex **6** (1.0 mM) in MeCN (0.1 M NBu_4PF_6) and a scan rate of 100 mV·s^{-1}. One irreversible, oxidative wave and one reversible oxidation process at $E_{1/2}$ = 0.88 V *vs.* Fc/Fc$^+$ were observed. **Inset** CV of the first redox event at different scan rates.

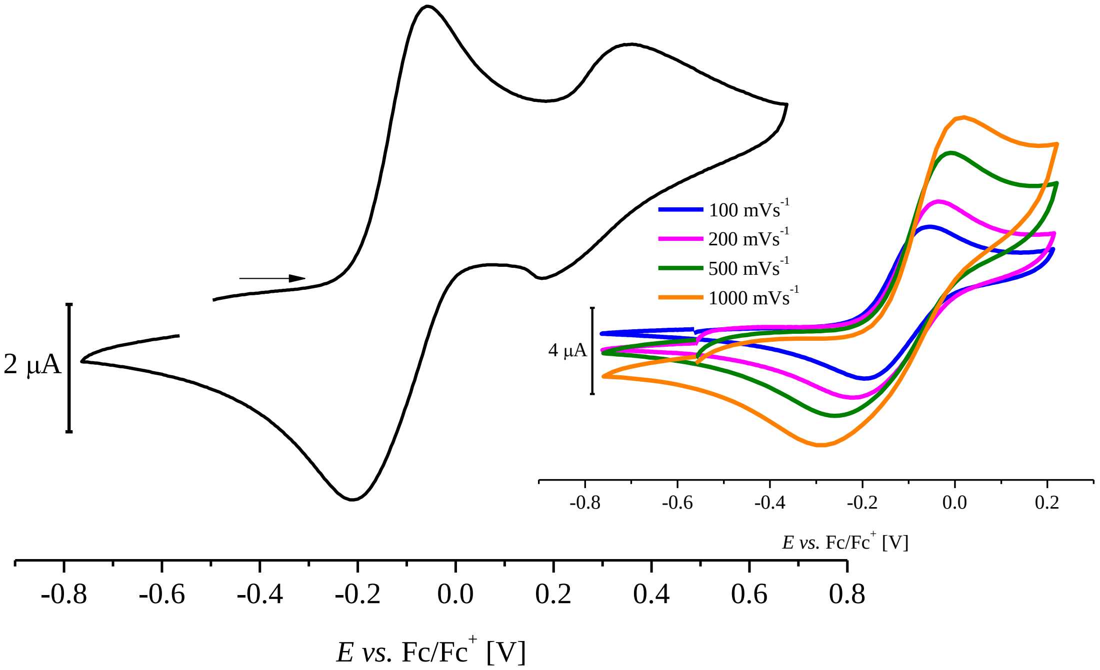

Figure A.2.2: Cyclic voltammogram of **7** (1.0 mM, 0.1 M NBu_4PF_6 in MeCN) depicts two irreversible waves at –0.13 V and 0.26 V. Inset showed the first oxidative wave at different scan rates.

Chapter 3

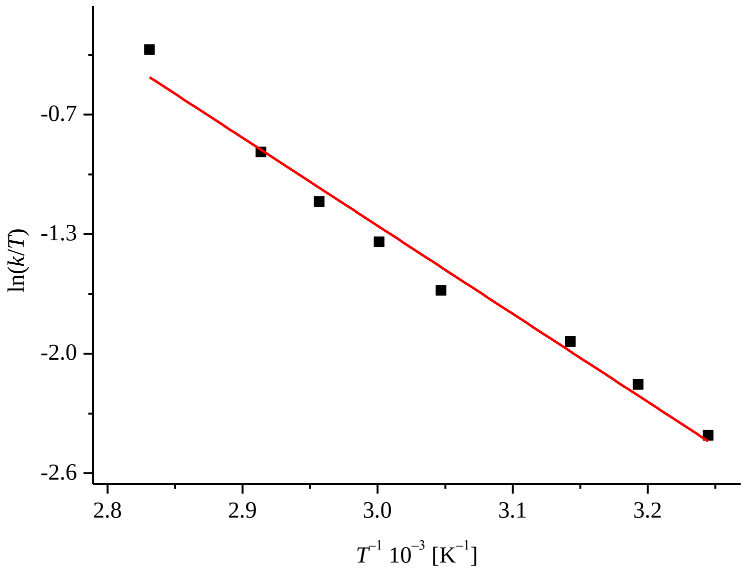

Figure A.3.1: *Eyring* plot based on the line broadening of the pyrazole tethered CH_2 group (H^{14} and H^{15}) of **$[H_5L^6](PF_6)_4$** in a temperature regime between 353 K and 308 K in DMSO-d_6. An activation enthalpy of $\Delta H^{\ddagger}$ = 40.4±0.8 kJ·mol^{-1} and an activation entropy of $\Delta S^{\ddagger}$ = –86.9±1.7 J·mol^{-1}·K^{-1}were determined. The red line shows the best fit (slope = –4860.4, intercept = 13.31, R^2 = 0.9796). © 2019 JOHN WILEY AND SONS.

Table A.3.1: Rate constants at different temperatures derived by line shape analysis of the ^{1}H NMR peaks of the CH_2 protons H^{14} and H^{15} in DMSO-d_6. © 2019 JOHN WILEY AND SONS.

T [K]	$(\Delta \upsilon_e)_{1/2}$	$(\Delta \upsilon_0)_{1/2}$	k [s^{-1}]
353.2	13.52	11.92	1151
343.2	19.08	11.92	257.9
338.2	23.48	11.92	159.8
333.2	28.01	11.92	114.8
328.2	34.97	11.92	80.16
318.2	21.60	11.92	30.43
313.2	18.26	11.92	19.92
308.2	15.27	11.92	10.54
303.2	14.50	11.92	8.121

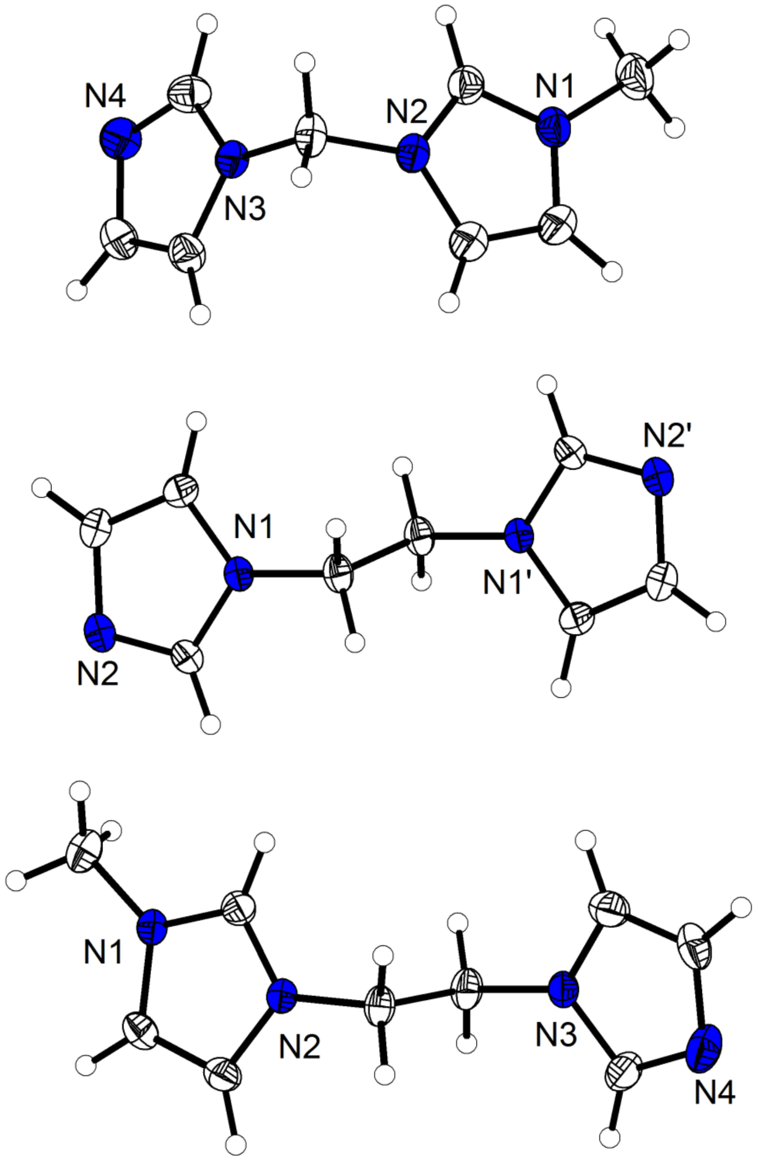

Figure A.3.2 : ORTEP plots of **n**, **o** and **p** are shown thermal ellipsoids at 50% probability level. © 2019 John Wiley and Sons.

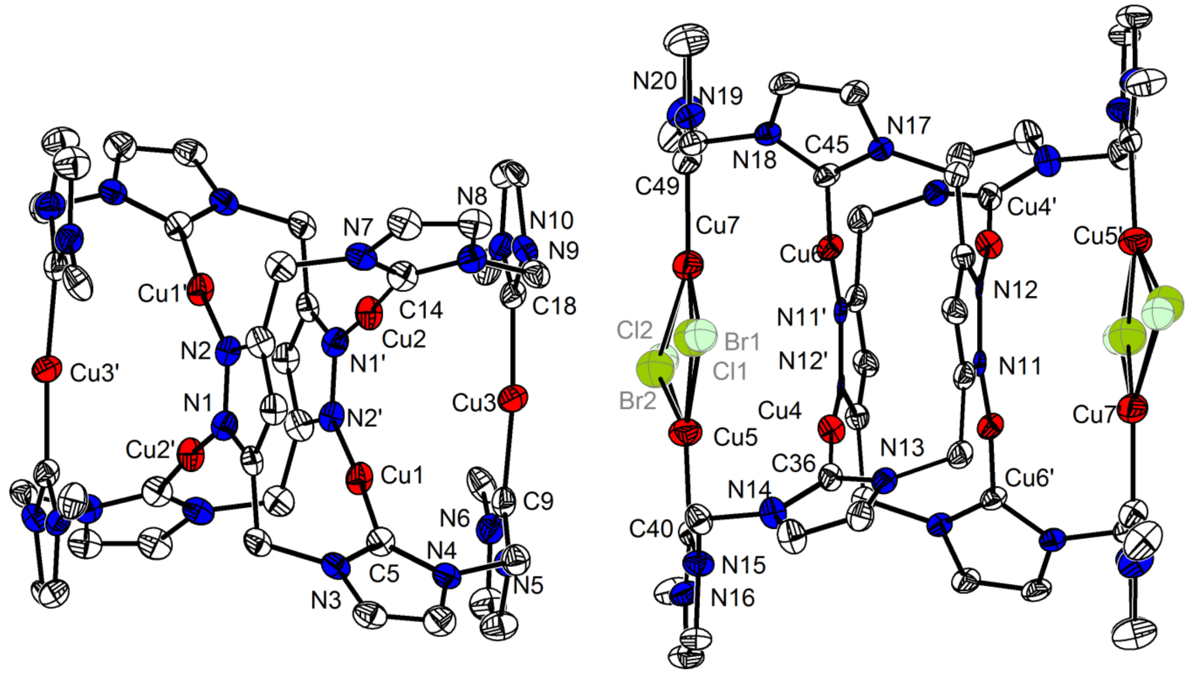

Figure A.3.3 : ORTEP plots of **$[(L^6)_2Cu_6](PF_6)_4$** and **$[(L^6)_2Cu_8Cl_{3.4}Br_{0.6}](PF_6)_2$**. Thermal ellipsoids with 50% probability. H atoms and counter ions were omitted for clarity.

Table A.3.2: Selected bond lengths [Å] for **$[(L^6)_2Cu_6](PF_6)_4$**.

Atoms	Bond lengths
Cu1–N2'	1.881(9)
Cu1–C5	1.881(1)
Cu2–N1'	1.905(1)
Cu2–C14	1.913(1)
Cu3–C18	1.901(1)
Cu3–C9	1.922(1)
Cu1····Cu2	3.062(4)
Cu1····Cu3	3.252(7)
Cu1····Cu3	3.332(2)

Table A.3.3: Selected bond angles [°] for **$[(L^6)_2Cu_6](PF_6)_4$**.

Atoms	Bond angles
N2'–Cu1–C5	176.3(5)
N1'–Cu2–C14	175.5(5)
C18–Cu3–C9	171.0(5)

Table A.3.4: Selected bond lengths [Å] for **$[(L^6)_2Cu_8Cl_{3.4}Br_{0.6}](PF_6)_2$**.

Atoms	**Bond lengths**
Cu4–C36	1.877(1)
Cu4–N12'	1.906(9)
Cu4–Cu5	2.939(2)
Cu4–Cu6'	3.009(2)
Cu4–Cu5	2.939(2)
Cu5–C40	1.903(1)
Cu5–Br2	2.22(6)
Cu5–Cl2	2.33(2)
Cu5–Br1	2.37(7)
Cu5–Cl1	2.46(3)
Cu4–Cu6'	3.009(2)
Cu6–C45	1.901(1)
Cu6–N11'	1.905(9)
Cu6–Cu7	2.939(2)
Cu7–C49	1.917(1)
Cu7–Cl2	2.25(2)
Cu7–Br2	2.37(5)
Cu7–Br1	2.50(7)
Cu7–Cl1	2.56(3)

Table A.3.5: Selected bond angles [°] for **$[(L^6)_2Cu_8Cl_{3.4}Br_{0.6}](PF_6)_2$**.

Atoms	**Bond angles**
C36–Cu4–N12'	174.1(4)
C45–Cu6–N11'	172.5(5)

Chapter 4

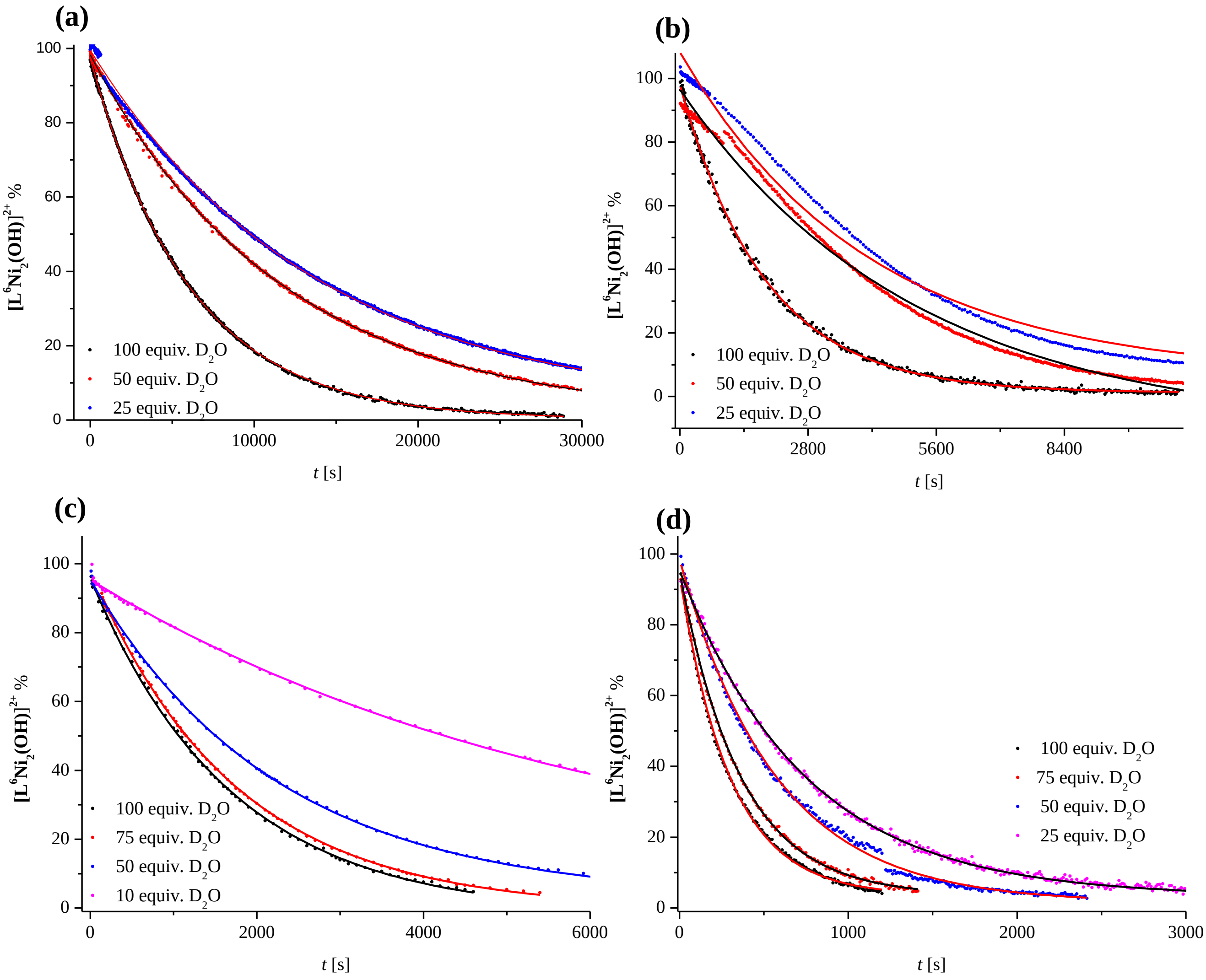

Figure A.4.1: H/D exchange at (**a**) 288 K, (**b**) 298 K, (**c**) 308 K, (**d**) 318 K plots of **$[L^6Ni_2(OH)]^{2+}$** *vs. t*.

Table A.4.1: *k* values at different temperaturesderived from a ln**$[L^6Ni_2(OH)]^{2+}$** vs *t* plot.

D_2O equiv	k_{288} 10^{-4} [s^{-1}]	k_{298} 10^{-4} [s^{-1}]	k_{308} 10^{-4} [s^{-1}]	k_{318} 10^{-4} [s^{-1}]
100	1.66	4.97	6.44	27.0
75	–	–	5.90	24.2
50	0.85	2.94	3.87	16.8
25	0.67	2.12	–	11.1
10	–	–	1.43	–

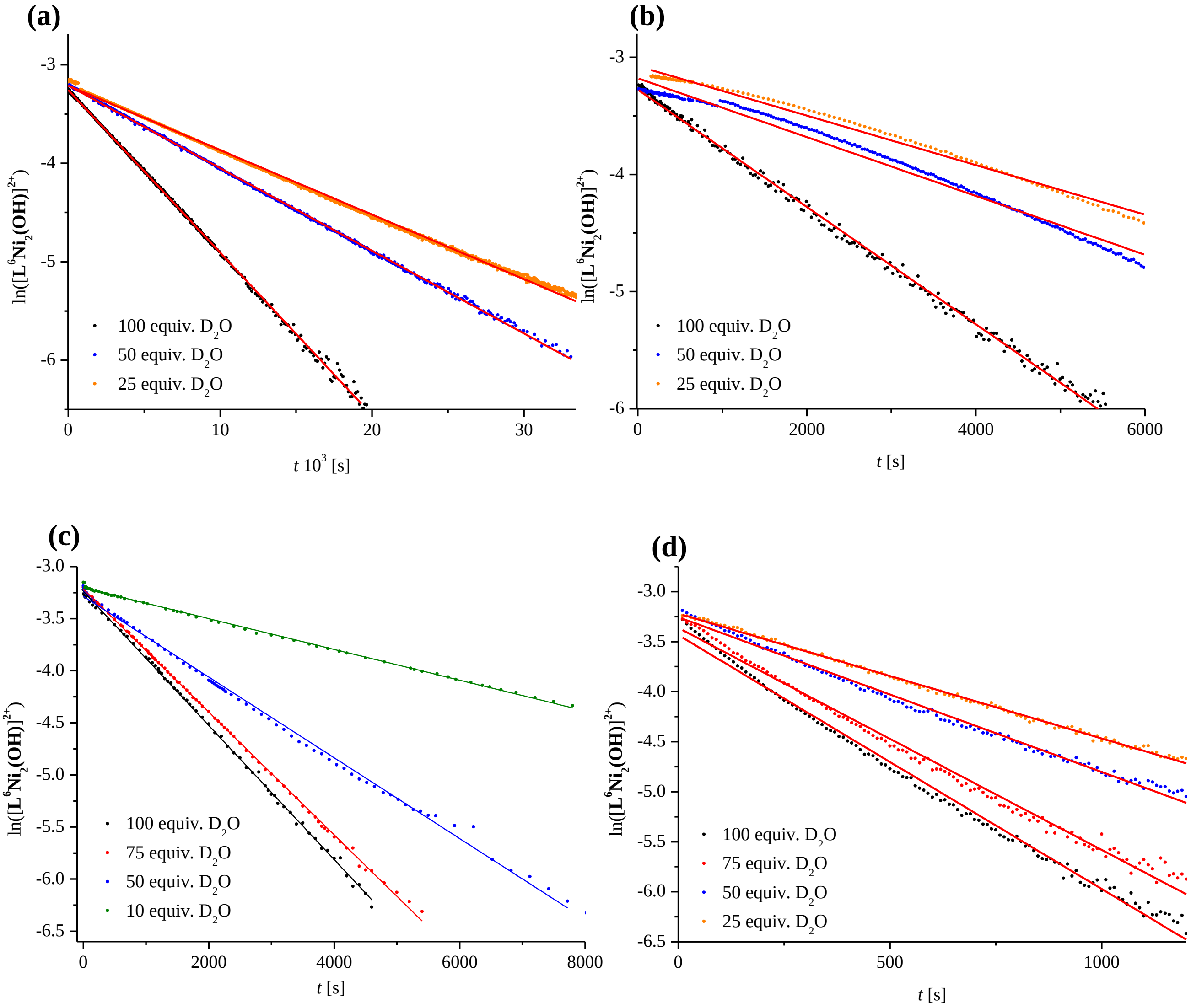

Figure A.4.2: ln(**[L^{6}Ni$_2$(OH)]$^{2+}$**) *vs.* *t* at (**a**) 288 K, (**b**) 298 K, (**c**) 308 K, (**d**) 318 K and different D_2O concentrations.

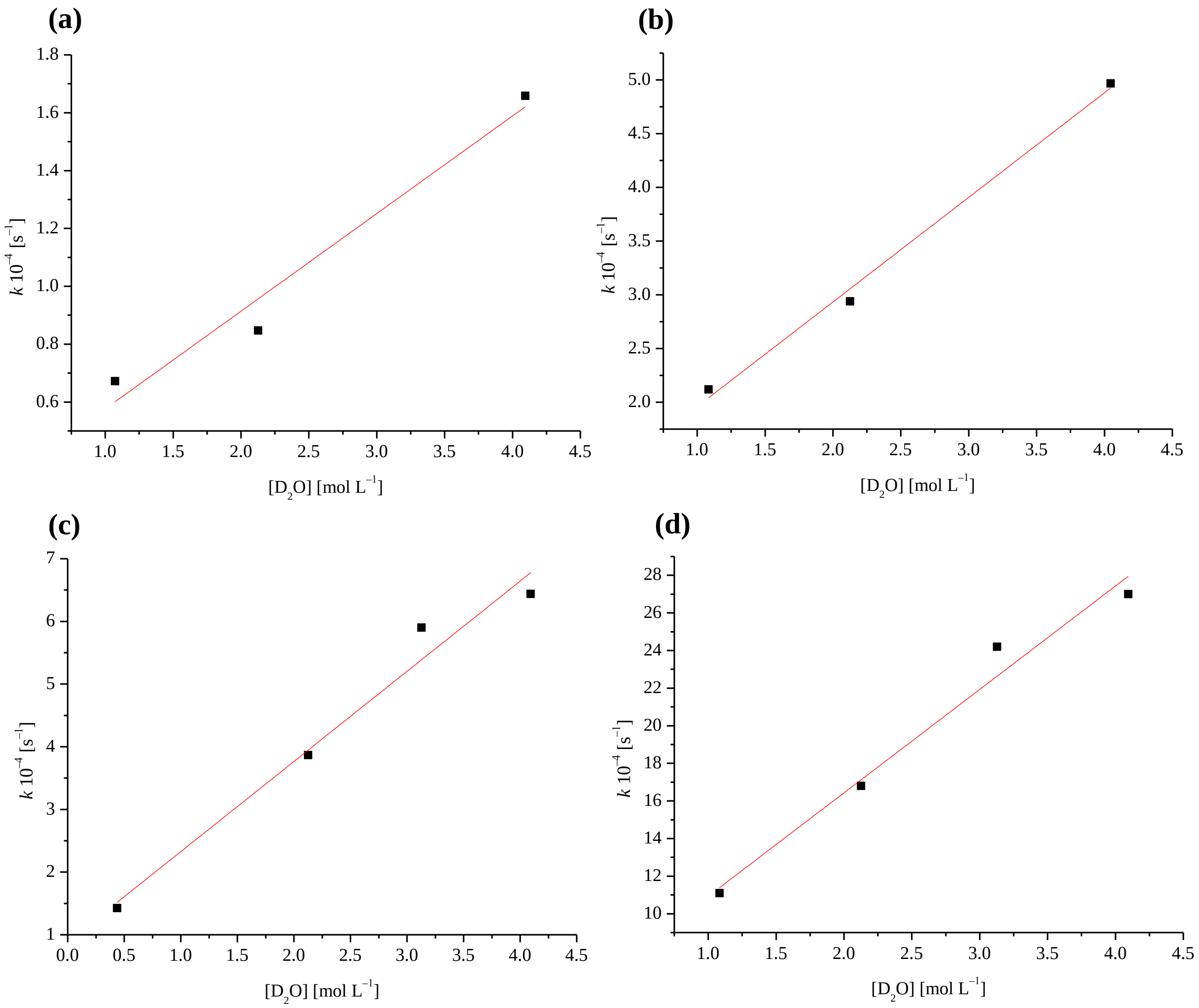

Figure A.4.3: *k vs.* [D_2O] plot at (**a**) 288 K (R^2 = 0.9338), (**b**) 298 K (R^2 = 0.9899), (**c**) 308 K (R^2 = 0.9621), (**d**) 318 K (R^2 = 0.9660).

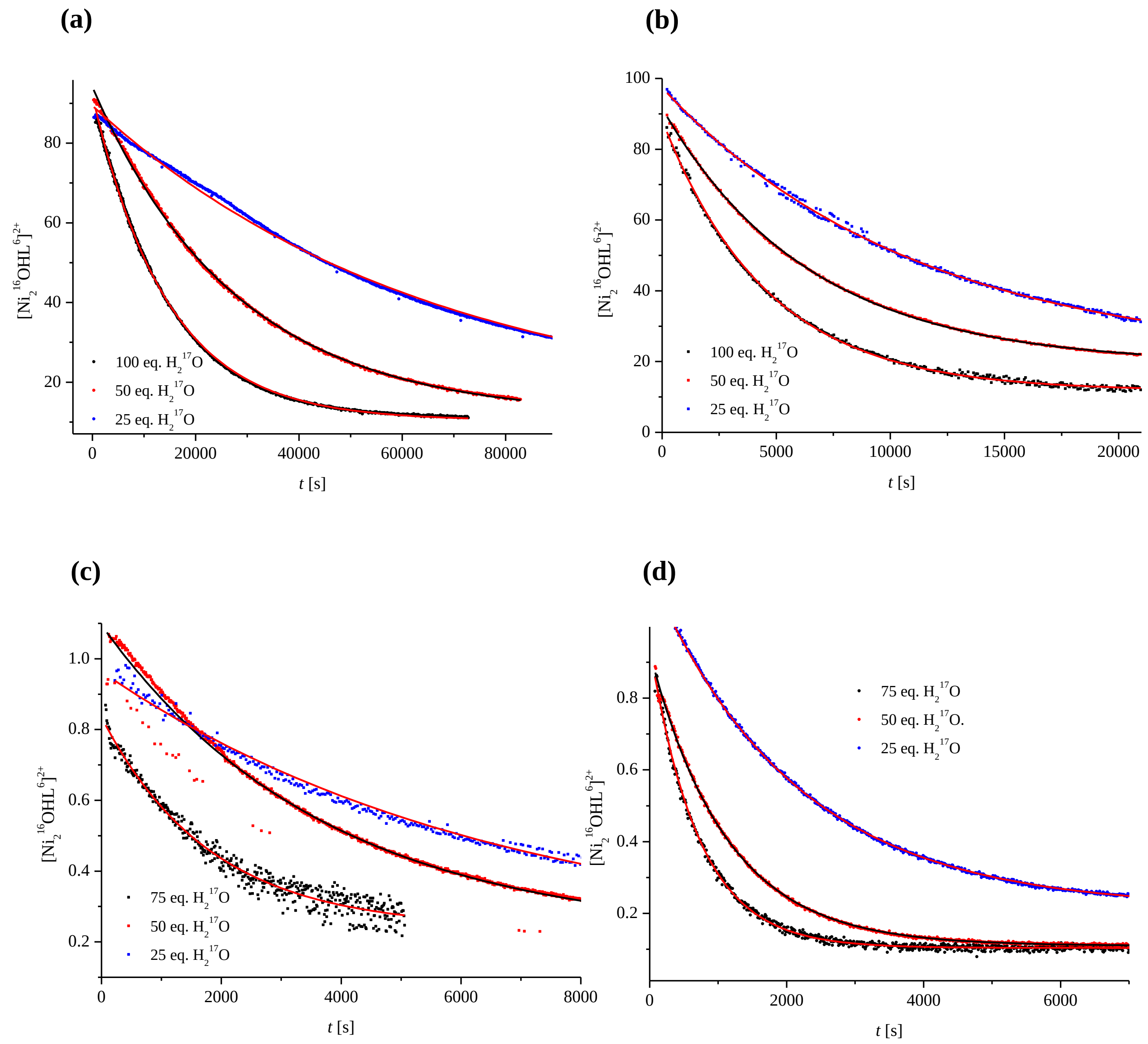

Figure A.4.4: $H_2{}^{16}O/H_2{}^{17}O$ exchange at (**a**) 298 K, (**b**) 308 K, (**c**) 318 K, (**d**) 328 K plots of **$[L^6Ni_2(OH)]^{2+}$** *vs. t*.

Table A.4.2: *k* values at different temperatures derived from a ln**$[L^6Ni_2(^{16}OH)]^{2+}$** vs *t* plot.

$H_2{}^{17}O$ equiv	k_{298} 10^{-5} [s^{-1}]	k_{308} 10^{-4} [s^{-1}]	k_{318} 10^{-4} [s^{-1}]	k_{328} 10^{-4} [s^{-1}]
100	5.69	1.65	4.49	–
75	–	–	–	10.4
50	2.85	1.02	1.86	6.71
25	1.24	0.595	1.14	3.19

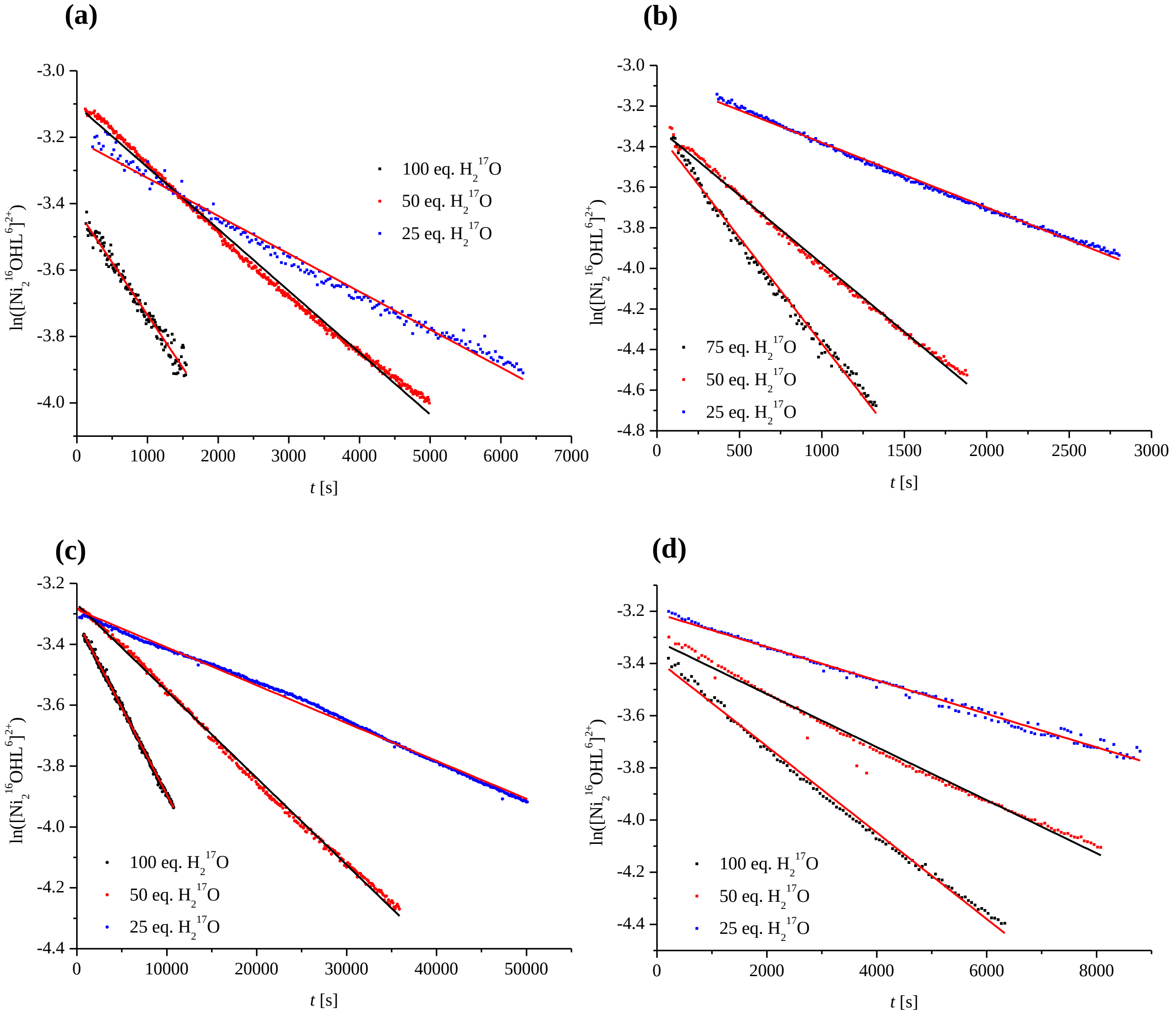

Figure A.4.5: ln($\mathbf{[L^6Ni_2(OH)]^{2+}}$) *vs.* *t* at (**a**) 298 K, (**b**) 308 K, (**c**) 318 K, (**d**) 328 K and different $H_2{}^{17}O$ concentrations.

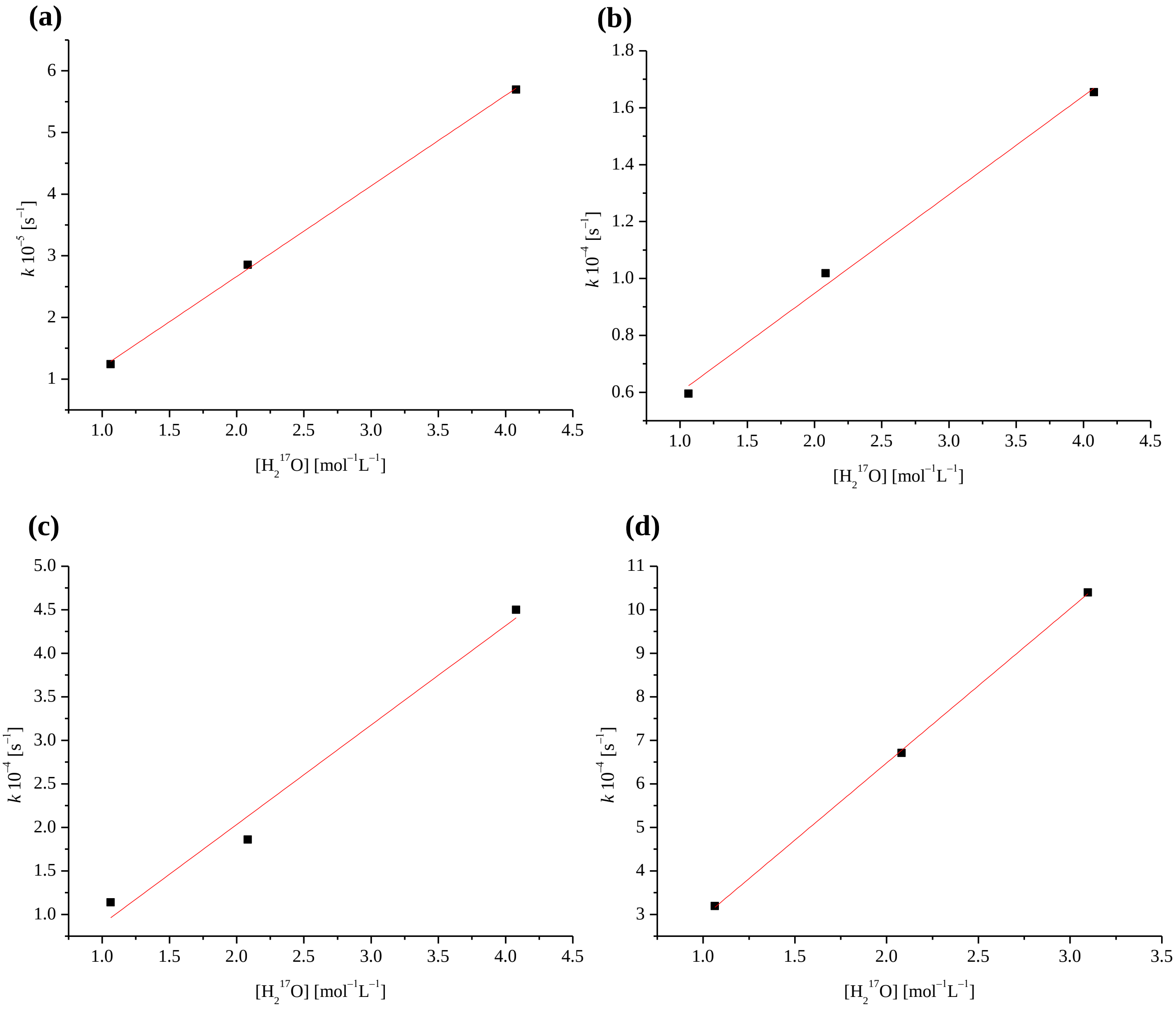

Figure A.4.6: *k vs.* [$H_2{}^{17}O$] plot at (**a**) 298 K ($R^2 = 0.998$), (**b**) 308 K ($R^2 = 0.990$), (**c**) 318 K ($R^2 = 0.965$), (**d**) 328 K ($R^2 = 0.999$).

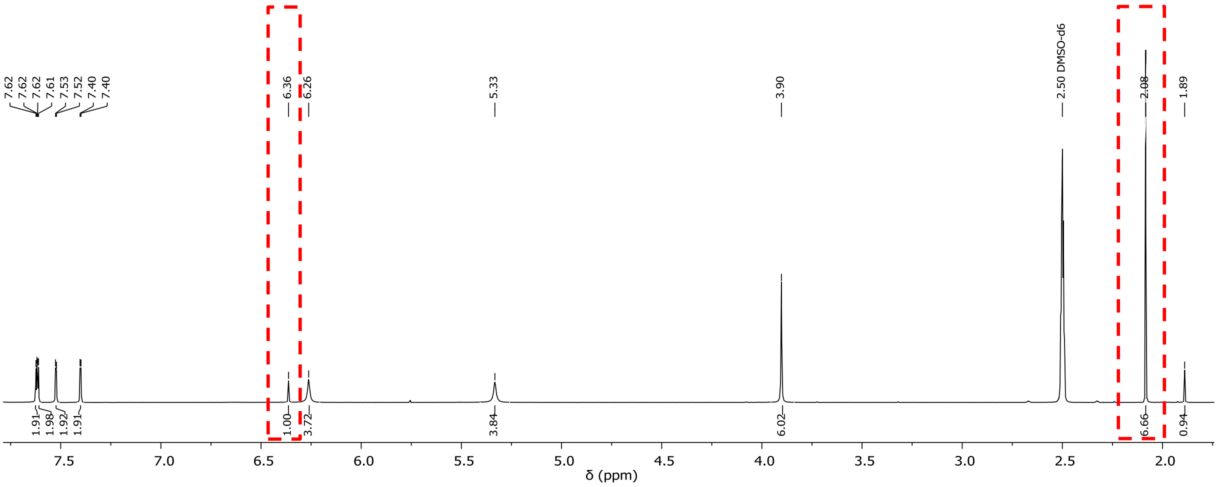

Figure A.4.7: ^{1}H NMR spectrum of **[L^{6}Ni$_2$(OH)](PF$_6$)$_2$** in DMSO-d_6 at 400 MHz and 298 K indicating the co-crystallization of one acetone molecule per complex molecule. An integral ratio of 1:6 between H^{pz} at δ = 6.36 ppm of the complex and CH$_3$ groups of acetone δ = 2.08 ppm was obtained (– – –).

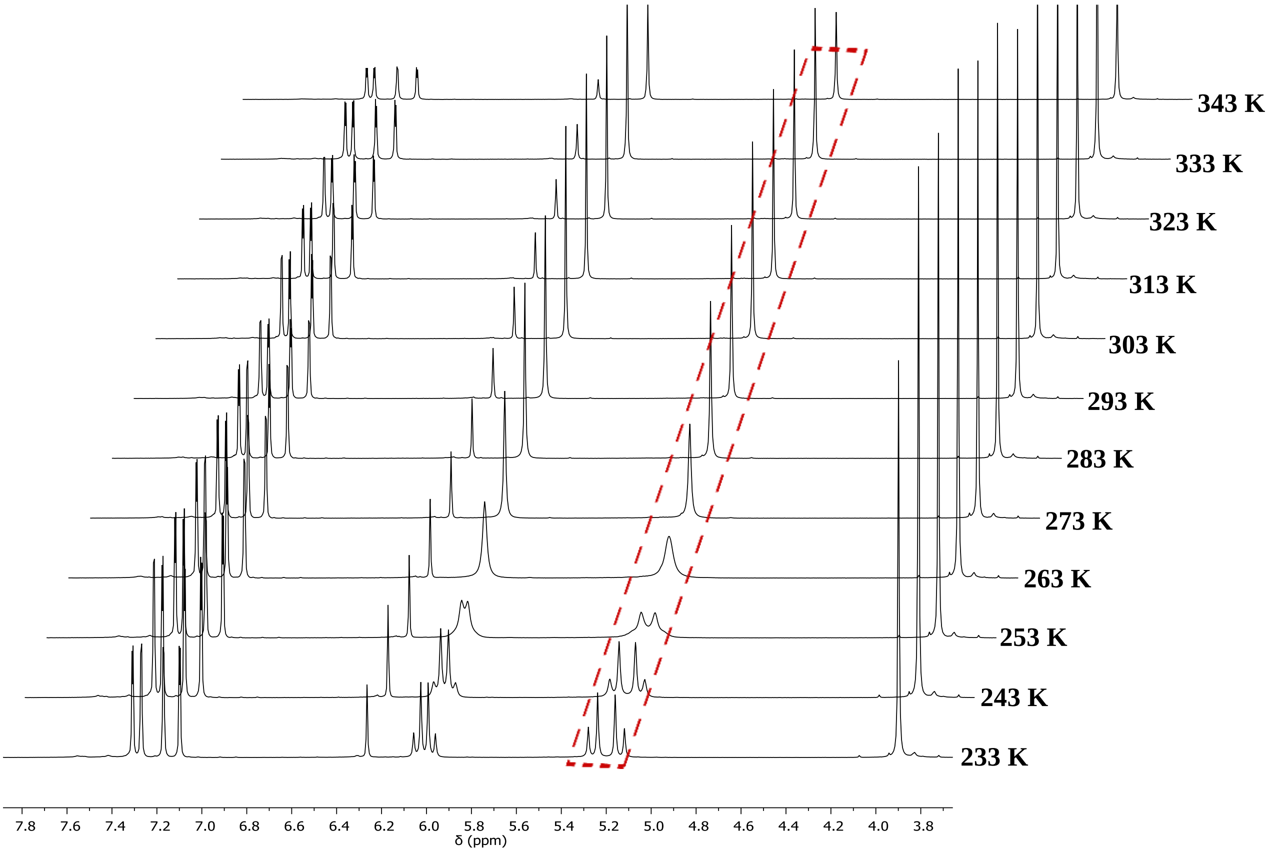

Figure A.4.8: ^{1}H VT NMR spectra of **[L^{6}Ni$_2$(OH)](PF$_6$)$_2$** in MeCN-d_3 at 400 MHz in the temperature range from 233 K to 343 K.

Table A.4.3: Selected bond lengths of **[L^{7}Ni$_2$(OH)](PF$_6$)$_2$**.

Atoms	**Bond lengths**
Ni1····Ni2	3.281(0)
Ni1–C5	1.853(4)
Ni1–N1	1.873(3)
Ni1–C9	1.884(4)
Ni1–O1	1.899(3)
Ni2–C16	1.853(4)
Ni2–N2	1.874(3)
Ni2–C20	1.881(4)
Ni2–O1	1.905(3)

Table A.4.4: Selected bond angles of **[L^{7}Ni$_2$(OH)](PF$_6$)$_2$**.

Atoms	**Bond angles**
C5–Ni1–N1	88.08(2)
C5–Ni1–C9	88.02(2)
N1-Ni1-O1	87.71(1)
C9–Ni1–O1	97.17(1)
C16–Ni2–N2	88.69(2)
C16–Ni2–C20	87.22(2)
N2–Ni2–O1	87.43(1)
C20–Ni2–O1	97.81(1)
Ni1–O1–Ni2	119.20(2)

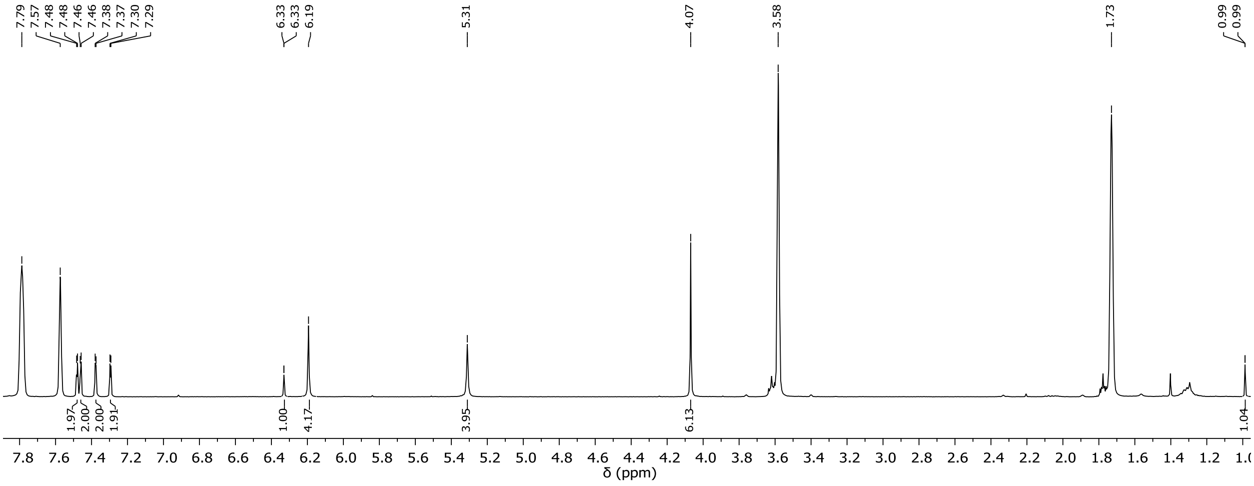

Figure A.4.9: ^{1}H NMR spectrum of **[L^{6}Ni$_2$(OH)](BAr^F)$_2$** in THF-d_8 at 400 MHz and 298 K.

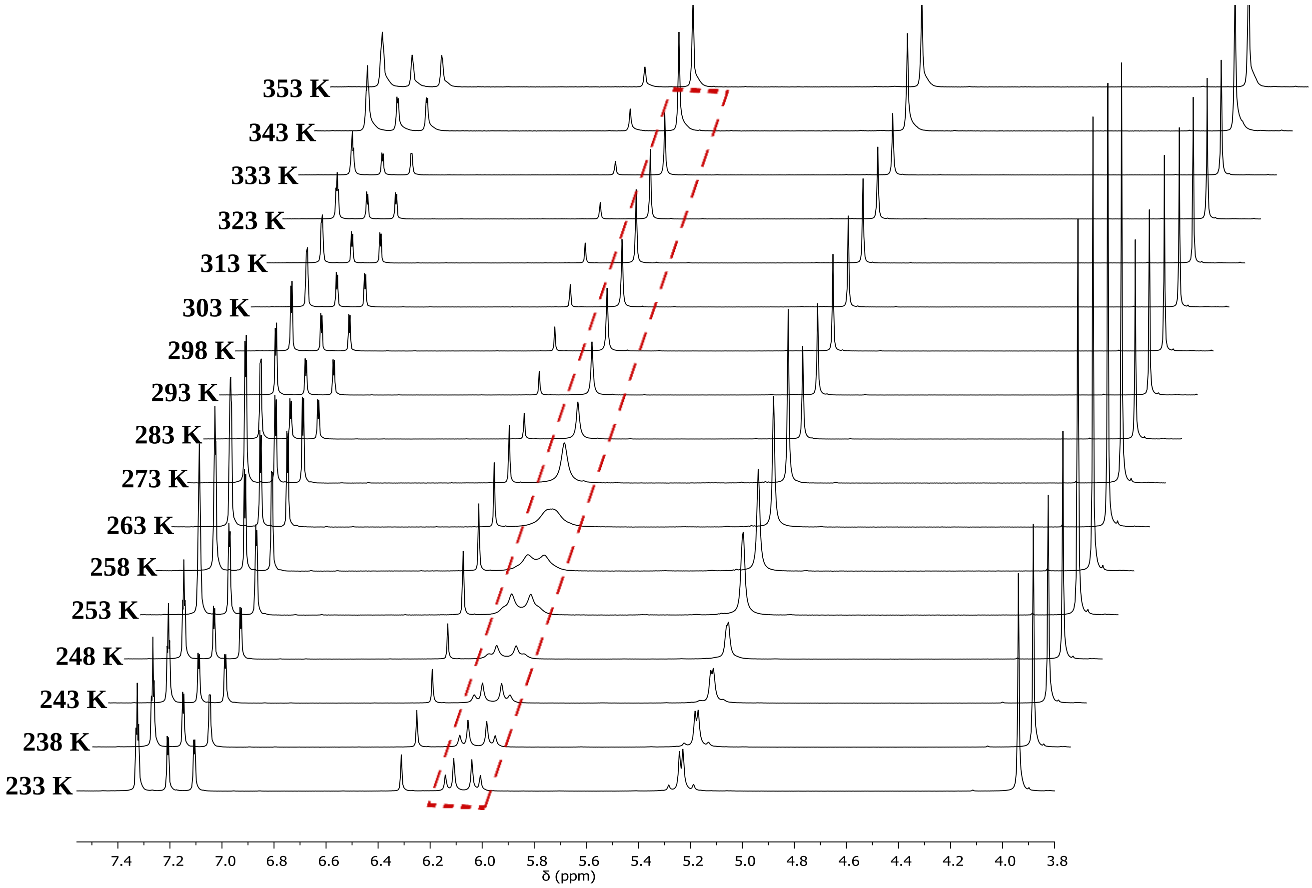

Figure A.4.10: ^{1}H VT NMR spectra of **[L^{6}Ni$_2$Cl](PF$_6$)$_2$** in MeCN-*d*$_3$ at 400 MHz in the temperature range from 233 K to 353 K.

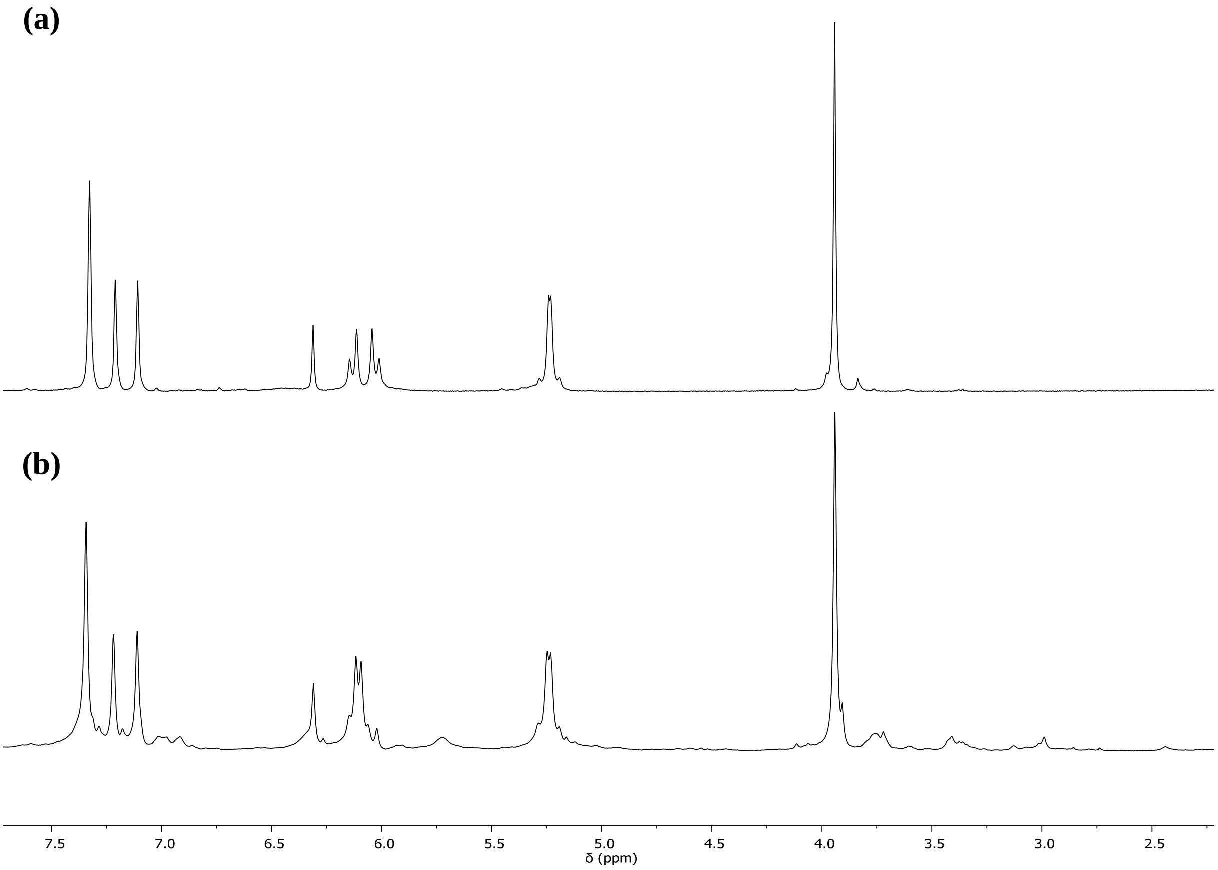

Figure A.4.11: (**a**) ^{1}H NMR spectrum of **[L^{6}Ni$_2$Cl](PF$_6$)$_2$** in MeCN-d_3 at 400 MHz and 233 K. (**b**) ^{1}H NMR spectrum of **[L^{6}Ni$_2$Cl](PF$_6$)$_2$** after addition of 1.0 equiv. of Co(Cp*)$_2$.

Chapter 5

$$\xrightarrow{\text{decrease } \theta}$$

$\mathrm{SH > Cl > SCH_3 > OH > S > SHS > S_2}$

$$\xrightarrow{\text{increase d(Ni/Ni)}}$$

$\mathrm{OH < SH < SCH_3 < Cl < S < SHS < S_2}$

$$\xrightarrow{\text{high–field} \quad \delta \text{ [ppm]} \quad \text{low–field}}$$

$\mathrm{S < SHS < NH_2 < CN < OH < SCH_3 < Cl < SH < S_2}$

$$\xrightarrow{\text{low } \lambda \quad \text{[nm]} \quad \text{high } \lambda}$$

$\mathrm{OH > SCH_3 > SH > Cl > SHS > S > S_2}$

$$\xrightarrow{\text{cathodic} \quad \text{anodic}}$$

$\mathrm{S < OH < SCH_3 < SH < Cl}$

Figure A.5.1: Summary of the observed trends of the nickel complexes by different analytic methods.

Table A.5.1: Activation parameters for the exchange of the two **[L^{6}Ni$_2$S]PF$_6$** conformers.

	Van't Hoff	Eyring		Arrhenius	
		k_1	k_2	k_1	k_2
ΔH^o [kJ/mol]	–1.1				
ΔS^o [J/mol·K]	–10.5				
$\Delta H^\ddagger$ [kJ/mol]		73.3	76.6		
$\Delta S^\ddagger$ [J/mol·K]		52.3	58.2		
E_a [kJ/mol]				75.4	78.7

Table A.5.2: Scan rates, $E_{1/2}$ potential *vs*. Fc/Fc$^+$ and peak separation of the first reduction event of **[L^{6}Ni$_2$(SCH$_3$)](PF$_6$)$_2$**.

Scan rate [mV·s^{-1}]	$E_{1/2}$ [V]	$\Delta E_{1/2}$ [mV]
25	–2.029	92.07
50	–2.029	96.09
100	–2.027	98.56
200	–2.023	108.07
500	–2.023	127.30
1000	–2.030	149.88

Chapter 6

Table A.6.1: Comparison of the inter plane angle θ, the nickel····nickel distance d, the $\delta(H^{pz})$, $\delta(^{13}C_{carbene})$ and the UV-vis band between 370-400 nm.

Compound	$\boldsymbol{\Theta}$ [°]	d(Ni····Ni) [Å]	$\boldsymbol{\delta}$ H^{pz} [ppm]	$\boldsymbol{\delta}$ $^{13}C_{carbene}$ [ppm] $C^a/C^b/C^c/C^d$	UV-vis [nm]
$[L^6Ni_2(OH)](PF_6)_2$	24.7	3.26	6.29	161.2/161.2/156.6/156.6	371
$[L^7Ni_2(OH)](PF_6)_2$	20.3	3.28	6.29	–	–
$[L^9Ni_2(OH)](PF_6)_2$	–	–	6.29	159.2/159.2/154.1/154.1	–
$[L^6Ni_2Cl](PF_6)_2$	35.7	3.46	6.33	156.0/156.0/152.8/152.8	389
$[L^6Ni_2(CN)_2](PF_6)$	–	–	6.28	163.4/163.4/169.5/169.5	–
$[L^6Ni_2(NH_2)](PF_6)_2$	–	–	6.27	164.6/164.6/164.6/164.6	–
$[L^6Ni_2S]PF_6$	17.2	3.48	6.09	171.4/171.4/173.3/173.3	393
$[L^6Ni_2(SCH_3)](PF_6)_2$	31.9	3.45	6.32	163.6/163.6/163.2/163.2	375
$[L^6Ni_2(SH)](PF_6)(OTf)$	52.1	3.29	6.33	160.7/160.7/162.2/162.2	378
$[(L^6)_2Ni_4(SHS)](PF_6)_3$	19.0/14.5	3.52/3.47	6.23	166.8/166.8/165.0/165.0	392
$[(L^6)_2Ni_4(S_2)](PF_6)_4$	16.0	3.53	6.49	159.8/162.7/158.1/159.8	400

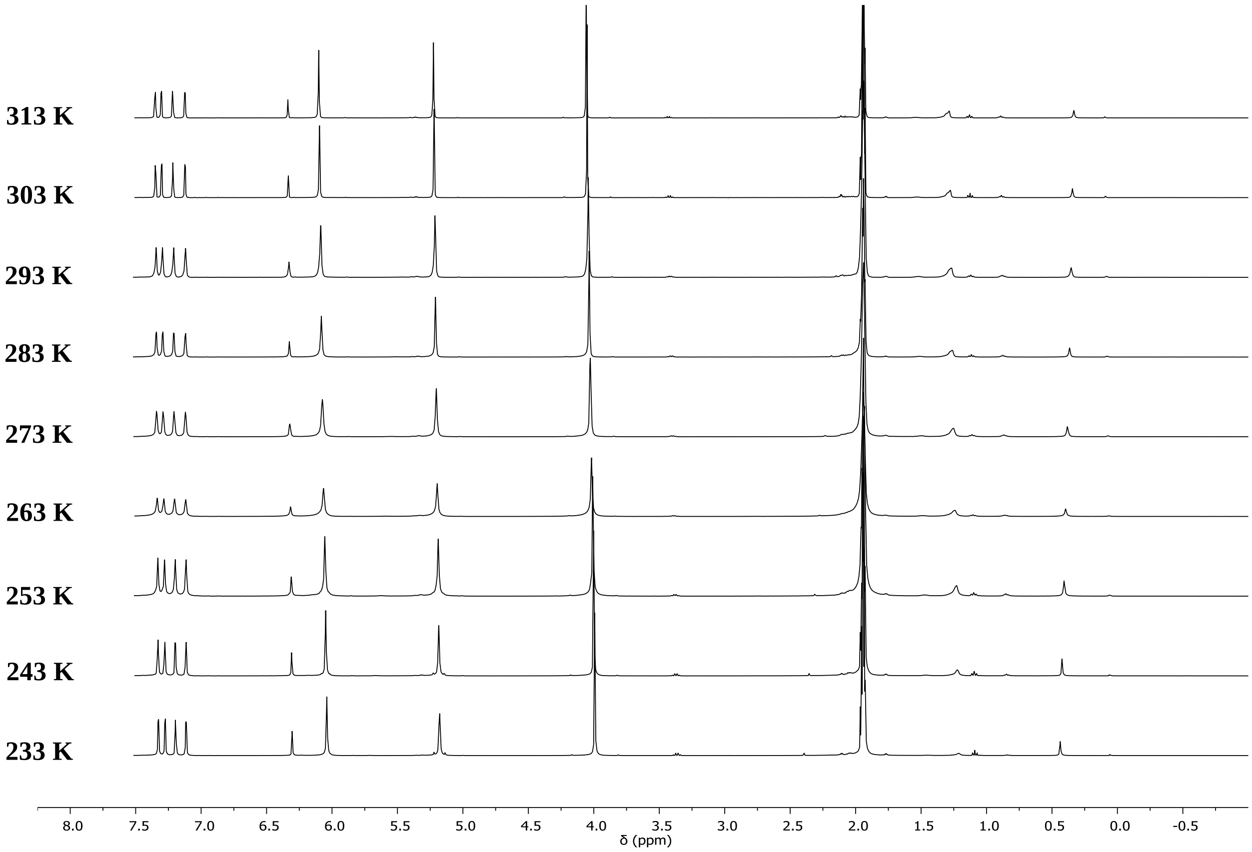

Figure A.6.1: ^{1}H VT NMR spectra of **$[L^6Ni_2(SH)](PF_6)(OTf)$** in MeCN-d_3 at 400 MHz in the temperature regime of 233 K to 313 K indicating the retention of the molecule symmetry in solution over the whole temperature regime.

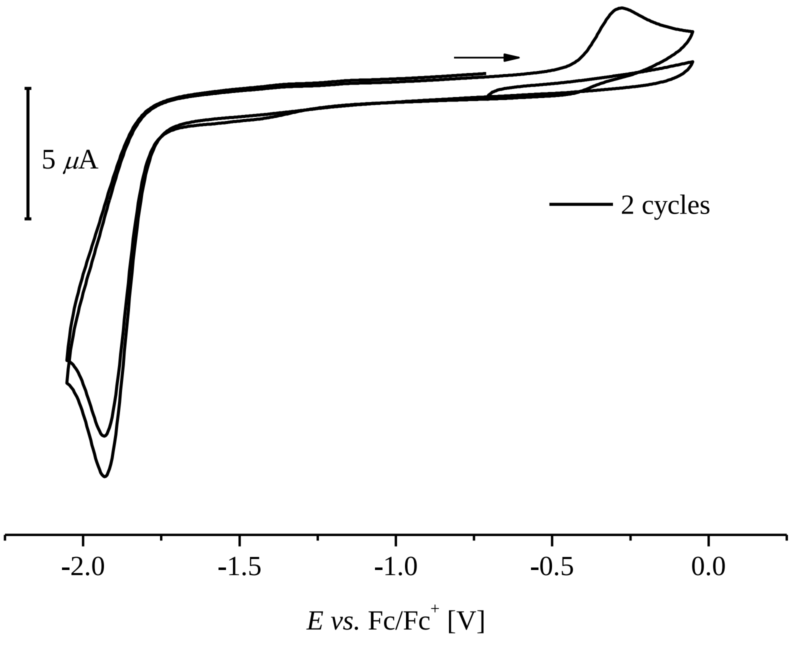

Figure A.6.2: CV of **$[L^6Ni_2(SH)]^{2+}$**. Two cycle modus showed appearance of **$[(L^6)_2Ni_2(S_2)]^{4+}$** after first reduction of **$[L^6Ni_2(SH)]^{2+}$** and oxidation of the formed **$[L^6Ni_2S]^+$**.

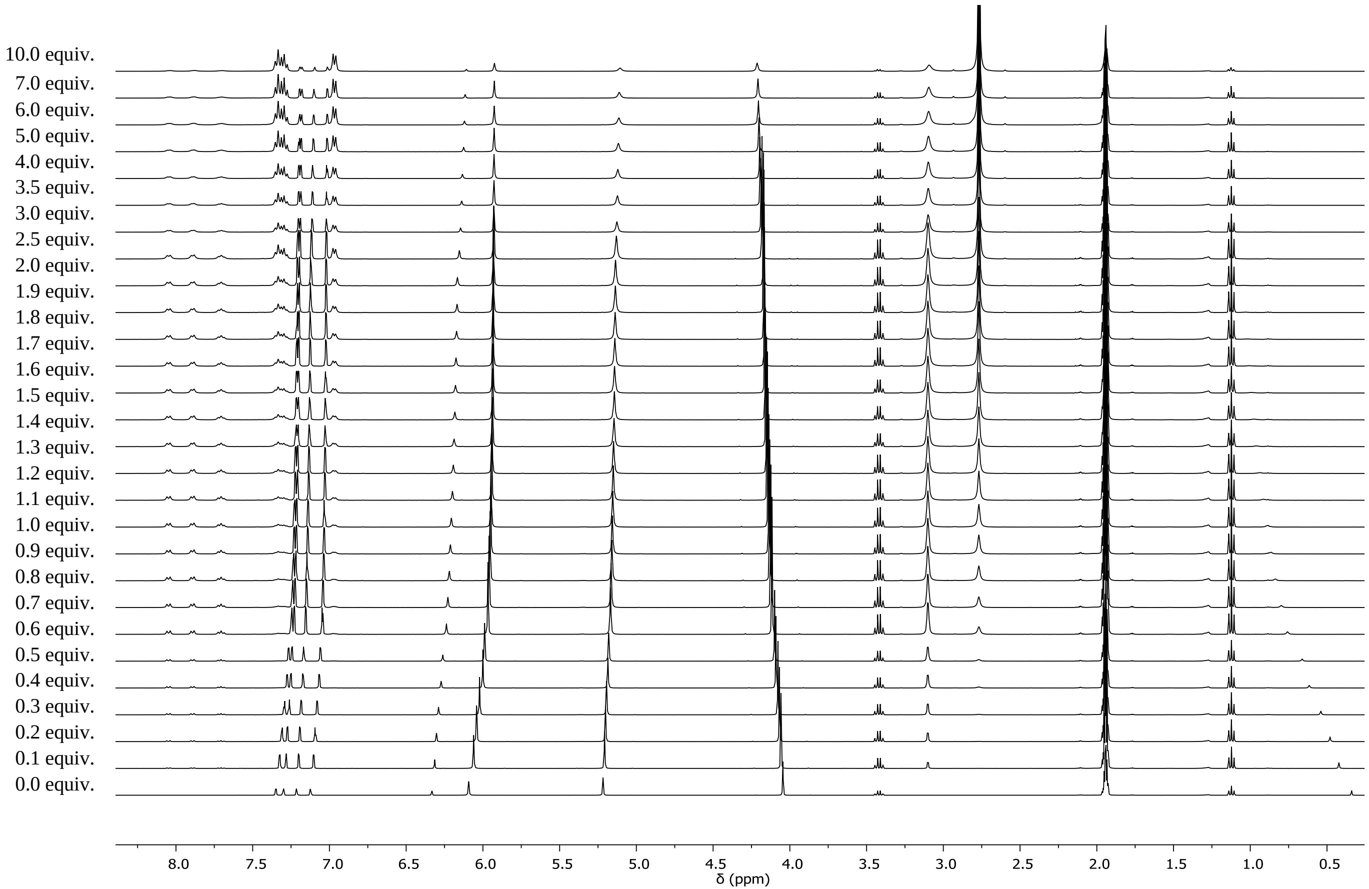

Figure A.6.3: ^{1}H NMR titration experiment. Addition of 0.1 equivalents of proton-sponge® to $\mathbf{[L^6Ni_2(SH)]^{2+}}$. At 400 MHz, 298 K, in MeCN-d_3.

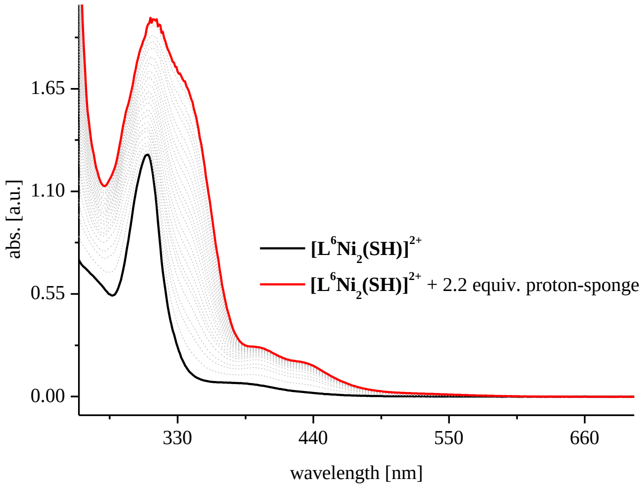

Figure A.6.4: UV-vis titration experiment. Spectrum of $\mathbf{[L^6Ni_2(SH)]^{2+}}$ with different equiv. of proton-sponge® (0.0–2.2 equiv. in 0.1 equiv. steps).

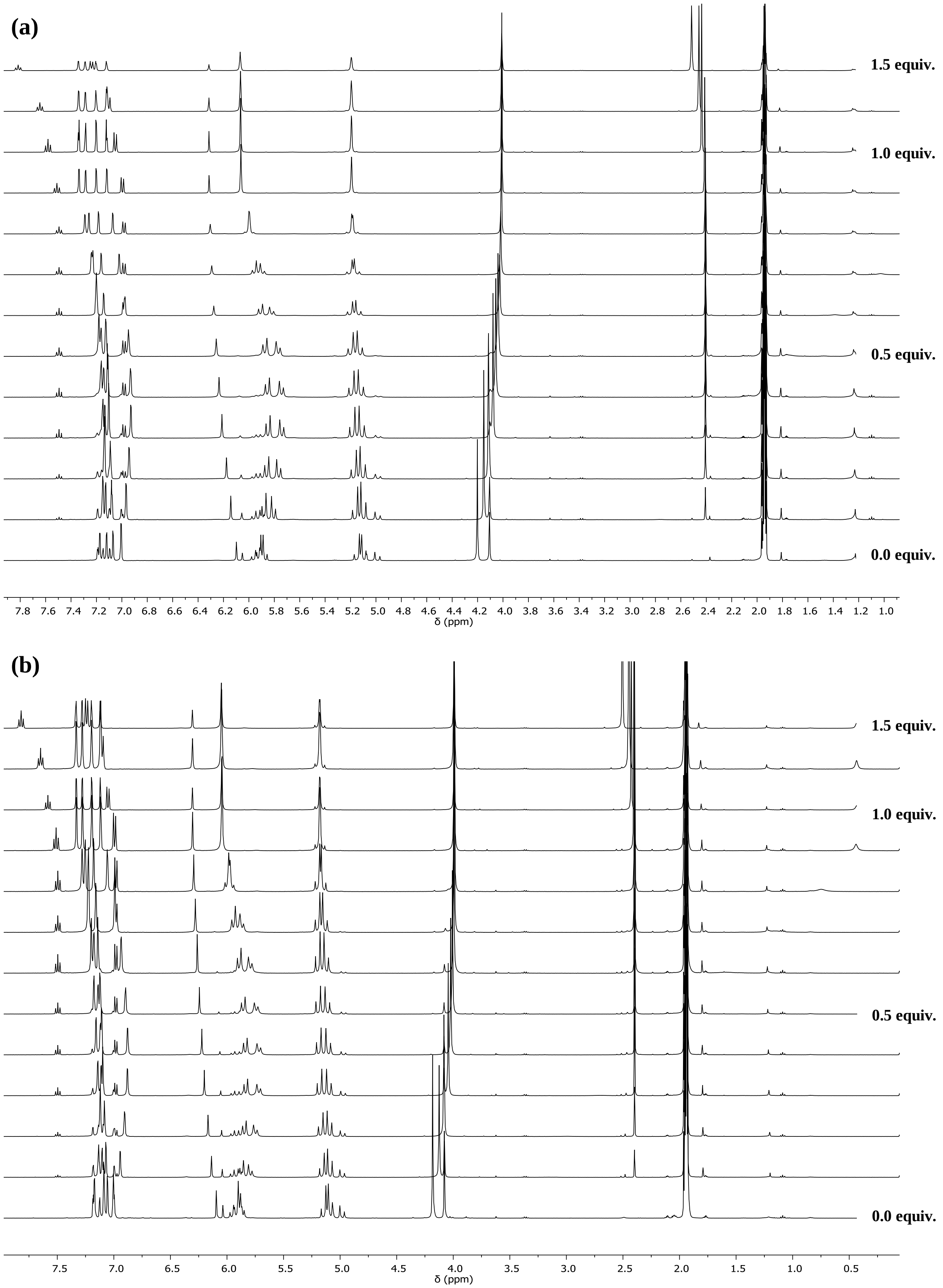

Figure A.6.5: ^{1}H NMR titration experiment: Addition of 2,6-lutidinium triflate to **[L^{6}Ni$_2$S]$^+$** at (**a**) 253 K and (**b**) 233 K at 400 MHz in MeCN-*d*$_3$.

Chapter 7

Table A.7.1: Short overview of *g* values of $\mathrm{Ni^{III}}$ complexes.

Complex	*g*–values				Reference
	g_x	g_y	g_z	g_{av}	
[NiL*OAc]	2.25	2.02	/	2.17	[450]
[NiL*acac]	2.32	2.23	2.01	2.19	[450]
[NiL*bipy]	2.19	2.16	2.02	2.12	[450]
[NiL*terpy]	2.17	2.14	2.02	2.11	[450]
[NiL*dipic]	2.22	2.19	2.01	2.14	[450]
$\mathrm{[Ni(emb)]^{-}}$	2.29	2.11	2.04	2.15	[451]
$\mathrm{[Ni(ema)]^{-}}$	2.23	2.18	2.01	2.14	[452]

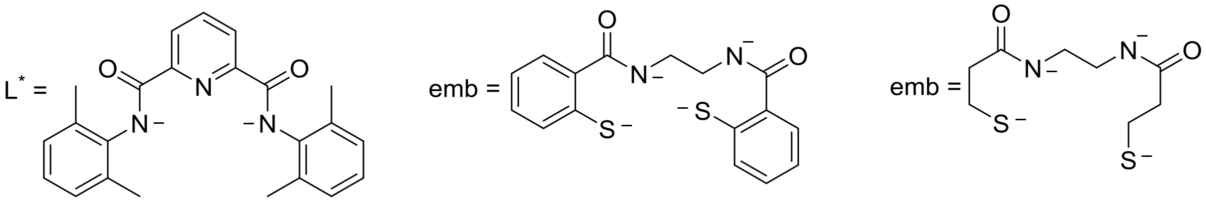

Figure A.7.1: Ligand scaffold of the $\mathrm{Ni^{III}}$ complexes, which are listed in **Table A.7.1**.[450–452]

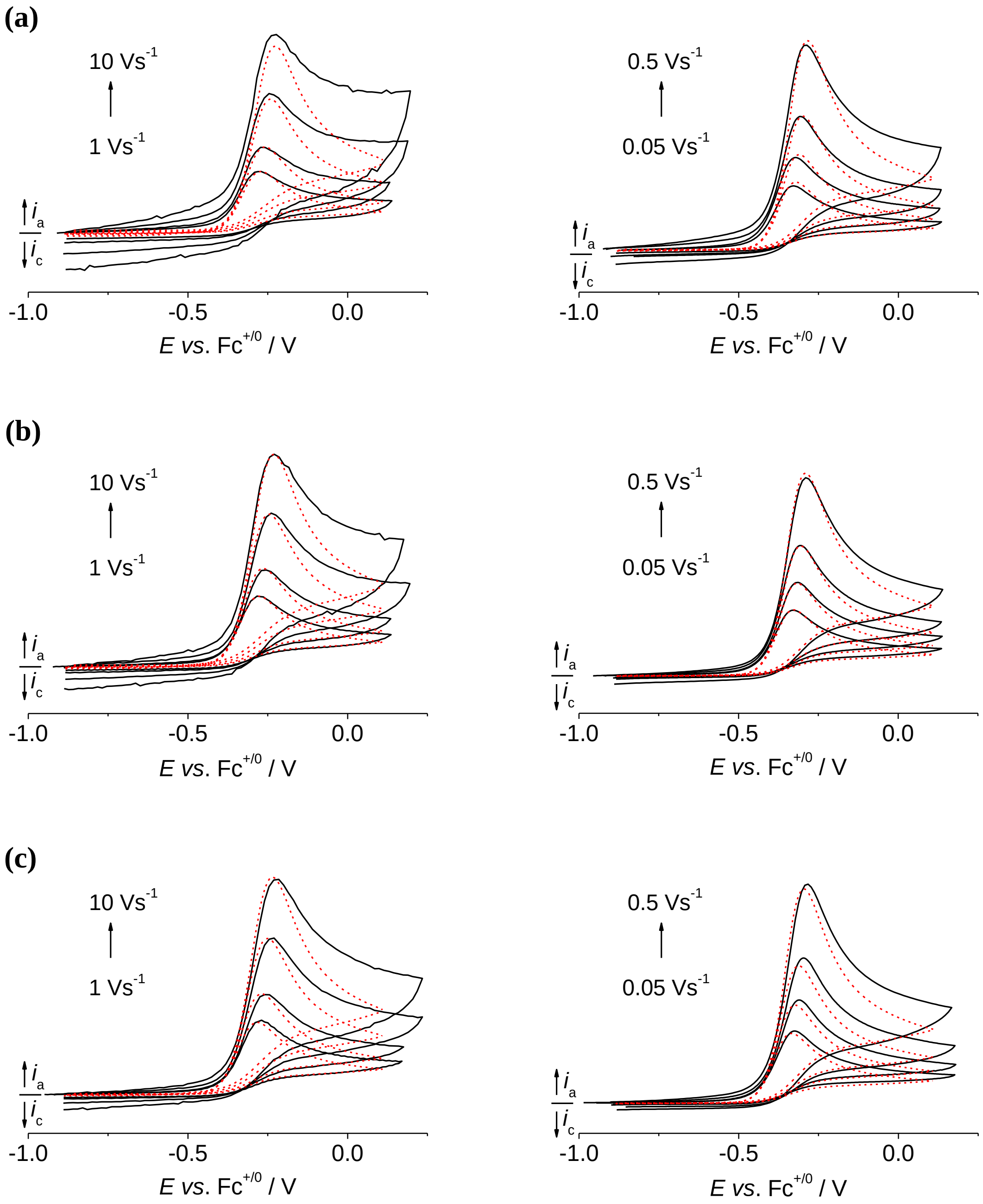

Figure A.7.2: Concentration and scan rate dependent CV measurements of **[L^{6}Ni$_2$S]PF$_6$** ((**a**) 0.5 mM, (**b**) 1.0 mM and (**c**) 2.0 mM, scan rates: 50 mV·s^{-1} to 10 V·s^{-1}) and CV simulations (– – –) under consideration of **Model 2**.

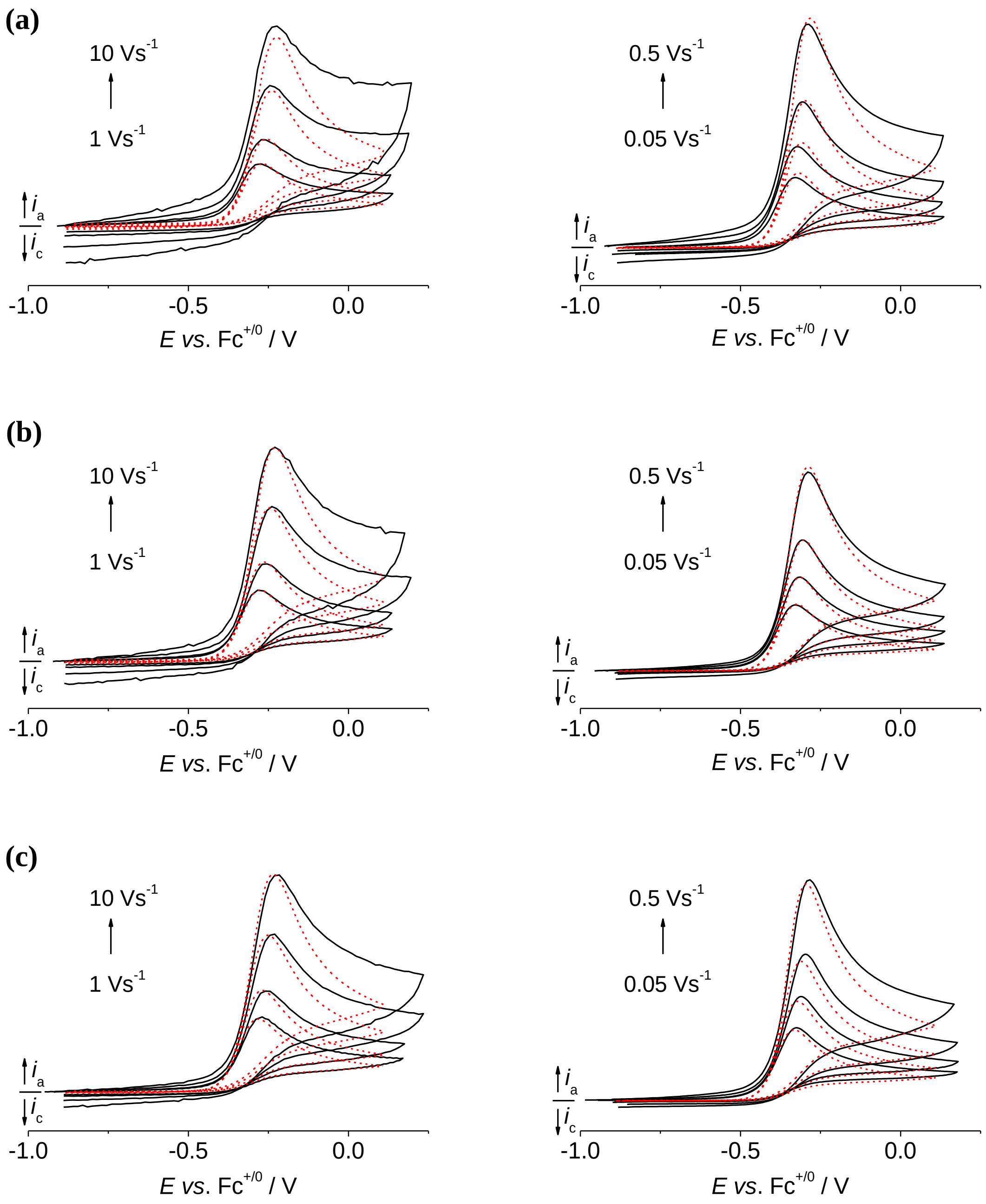

Figure A.7.3: Concentration and scan rate dependent CV measurements of **[L^{6}Ni$_2$S]PF$_6$** ((**a**) 0.5 mM, (**b**) 1.0 mM and (**c**) 2.0 mM, scan rates: 50 mV·s^{-1} to 10 V·s^{-1}) and CV simulations (– – –) under consideration of **Model 1** and **Model 2**.

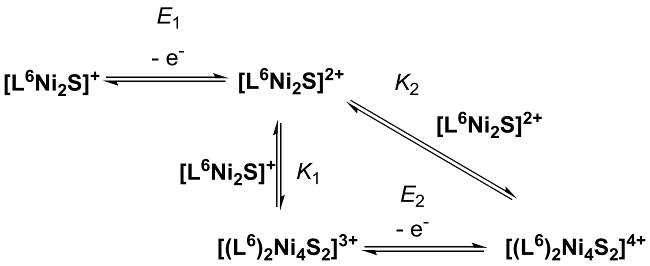

Figure A.7.4: Postulated meachanism for the interconversion of $\mathbf{[L^6Ni_2S]^+}$ and $\mathbf{[(L^6)_2Ni_4(S_2)]^{4+}}$ *via* **Model 1** and **Model 2**.

Tabelle A.7.2: Paramaters derived from CV simulation under consideration of parallel existence of **Model 1** and **Model 2**.

E_1	-0.245 (25) V
α_1	0.5 eV
$k_{s,1}$	$0.04\ \mathrm{cm \cdot s^{-1}}$
E_2	~ -0.8 V
α_2	0.5 eV
$k_{s,2}$	$\sim 1 \cdot 10^{-5}\ \mathrm{cm \cdot s^{-1}}$
k_1	$5 \cdot 10^{6}\ \mathrm{M^{-1} \cdot s^{-1}}$
K_1	$> 10^{4}\ \mathrm{M^{-1}}$
k_2	$1 \cdot 10^{7}\ \mathrm{M^{-1} \cdot s^{-1}}$
K_2	$> 2 \cdot 10^{15}\ \mathrm{M^{-1}}$
$D^{(\mathrm{Ox}\mid\mathrm{Red})}$	$5 \cdot 10^{-6}\ \mathrm{cm^2 \cdot s^{-1}}$
$D^{(\mathrm{Ox2}\mid\mathrm{Red2})}$	$2.5 \cdot 10^{-6}\ \mathrm{cm^2 \cdot s^{-1}}$

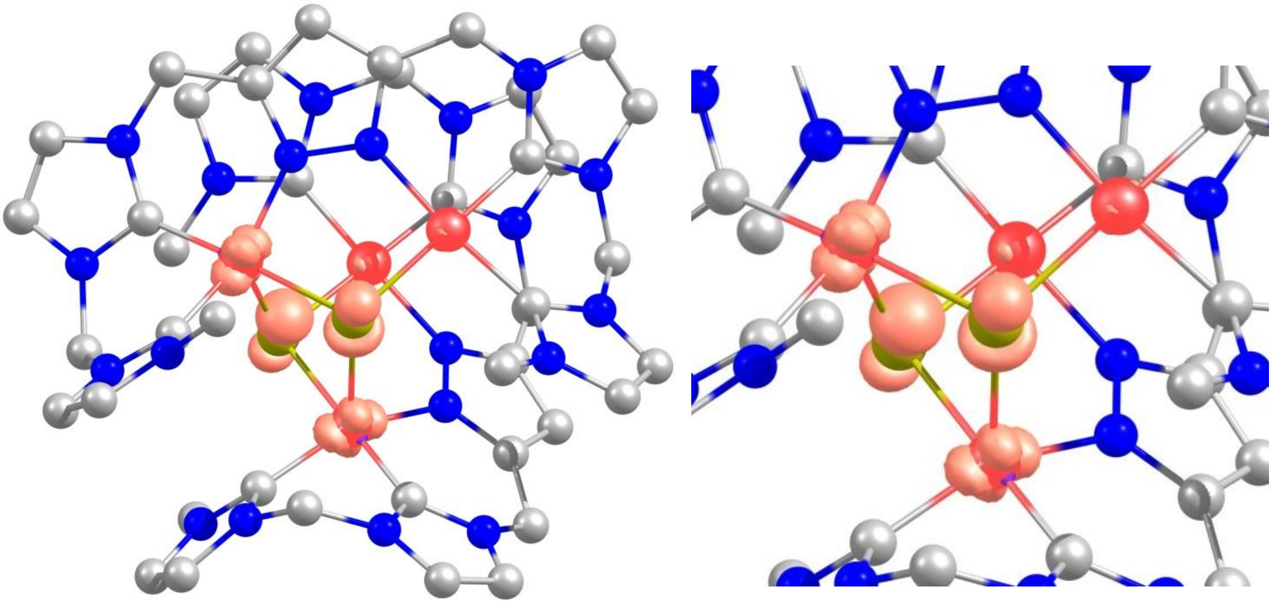

Figure A.7.5: Left: DFT optimized molecular structure of the one electron reduction of $\mathbf{[(L^6)_2Ni_4(S_2)]^{4+}}$ with spin population on one nickel ion of each subunit and the two sulfur ions. **Right:** Excerpt shows the spin density on the nickel and sulfur atoms in the molecular structure.

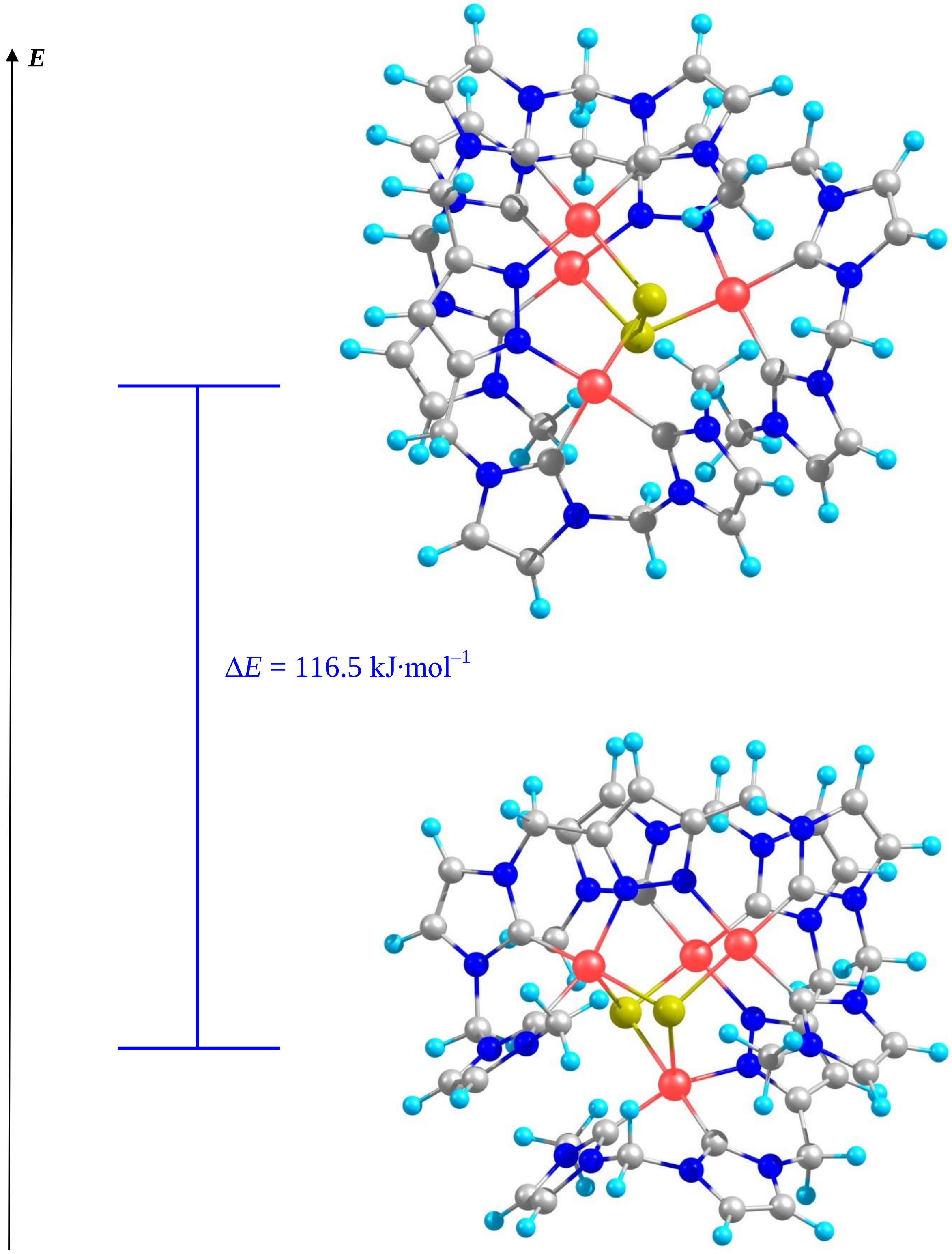

Figure A.7.6: Energy difference between the DFT optimized molecular structure of the one electron reduction of **$[(L^6)_2Ni_4(S_2)]^{4+}$** (**bottom**) and the single point calculation of the molecular structure of the one electron reduction of **$[(L^6)_2Ni_4(S_2)]^{4+}$** (**top**).

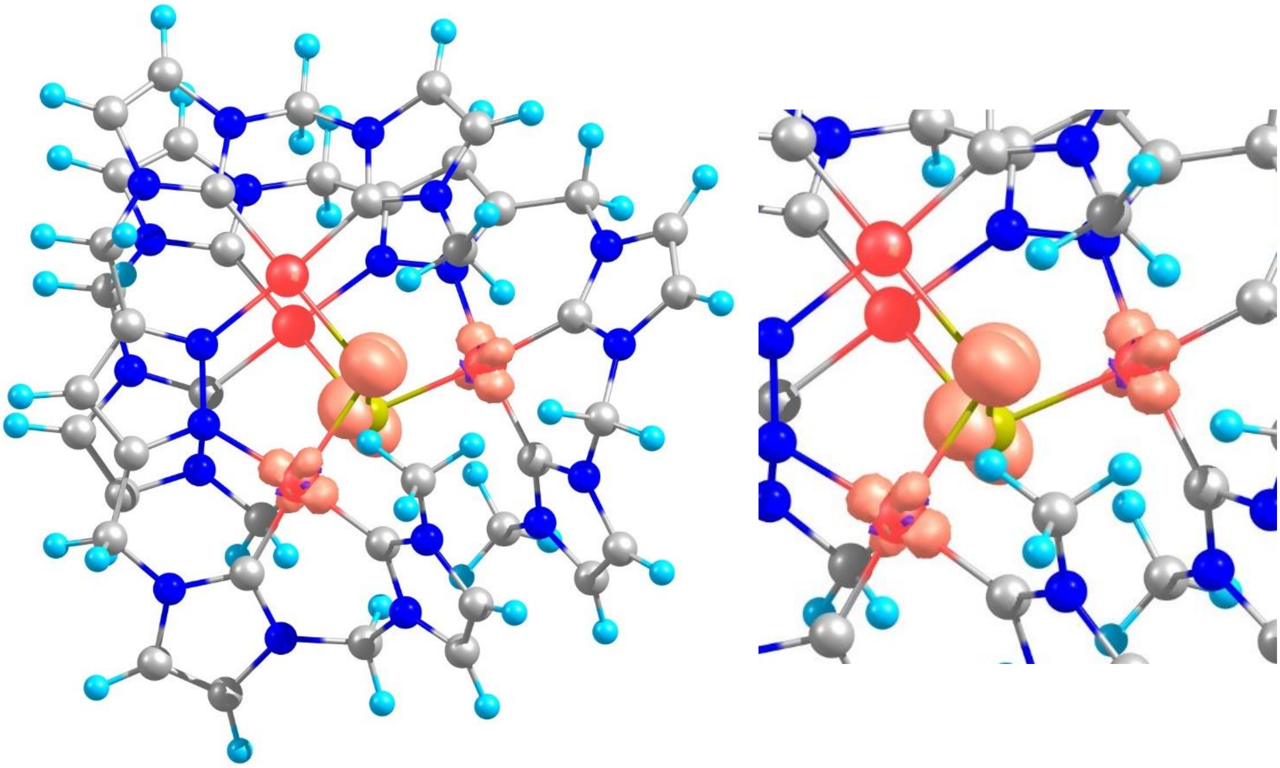

Figure A.7.7: Left: Single point calculation of the one electron reduction of **$[(L^6)_2Ni_4(S_2)]^{4+}$** with spin population on one nickel ion of each subunit and the two sulfur ion, without break of the disulfur bridge. **Right:** Excerpt shows the spin population in the molecular structure on certain atoms.

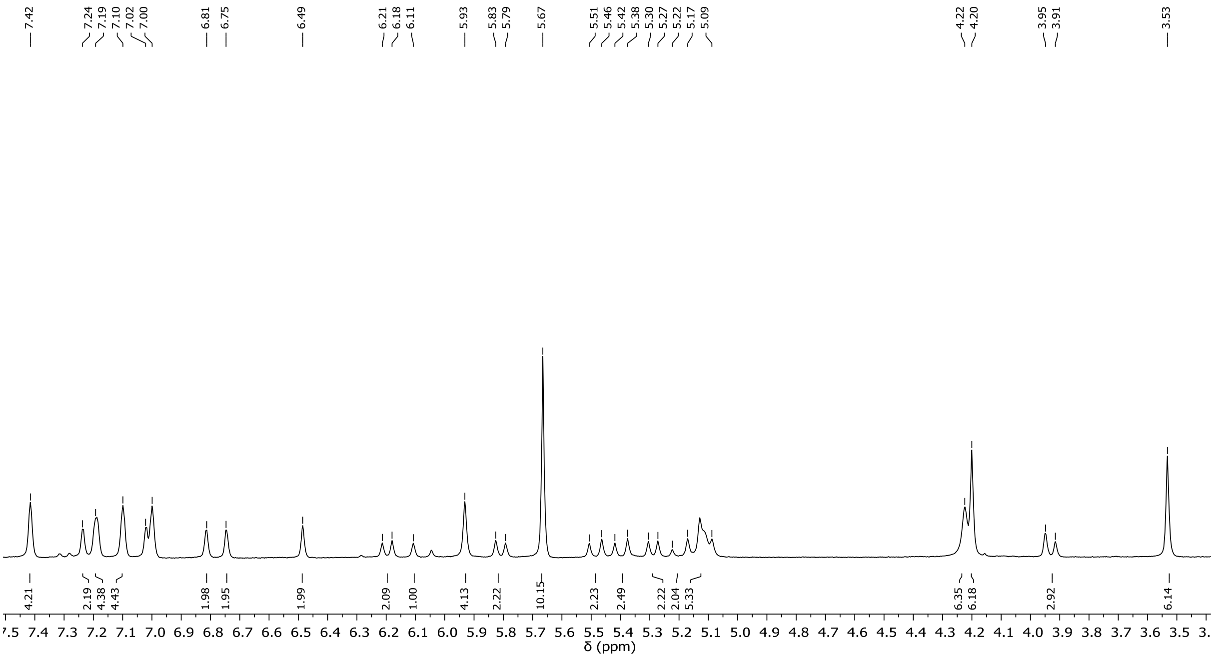

Figure A.7.8: ^{1}H NMR spectrum of the reaction of **$[(L^6)_2Ni_4(S_2)]^{4+}$** with 1.0 equiv. of $CoCp_2$ in MeCN-d_3 at 400 MHz and 298 K. (*) shows the proton resonances of the reducing agent. A 2:1 ratio of **$[(L^6)_2Ni_4(S_2)]^{4+}$:$[L^6Ni_2S]^+$** was obtained.

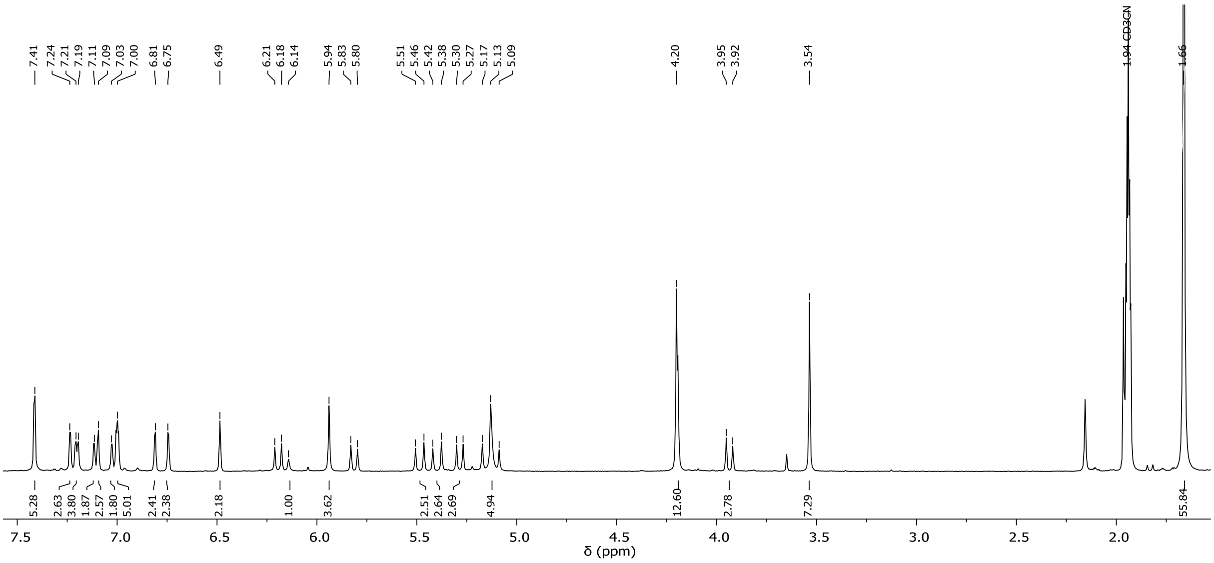

Figure A.7.9: ^{1}H NMR spectrum of the reaction of **[L^{6}Ni$_2$S]$^+$** with 0.5 equiv. of DMeFcPF$_6$ in MeCN-d_3 at 400 MHz and 298 K. (*) shows the proton resonances of the oxidation agent. A 2:1 ratio of **[(L^6)$_2$Ni$_4$(S$_2$)]$^{4+}$**:**[L^{6}Ni$_2$S]$^+$** was obtained.

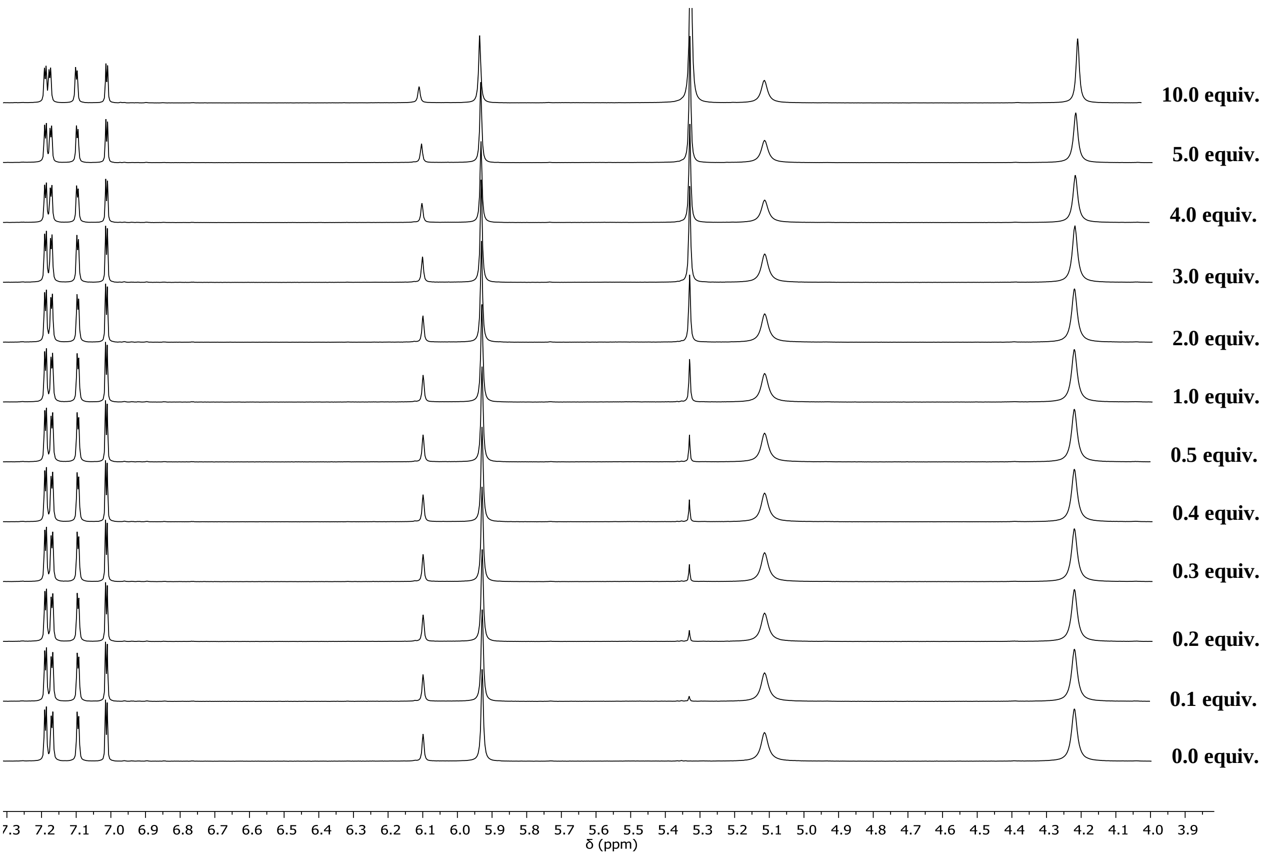

Figure A.7.10: Titration experiment: Addition of TEMPO–H to **[L^{6}Ni$_2$S]$^+$** in MeCN-d_3 at 400 MHz and 298 K. The peak at 5.33 ppm corresponds to the O–H resonance in TEMPO–H.

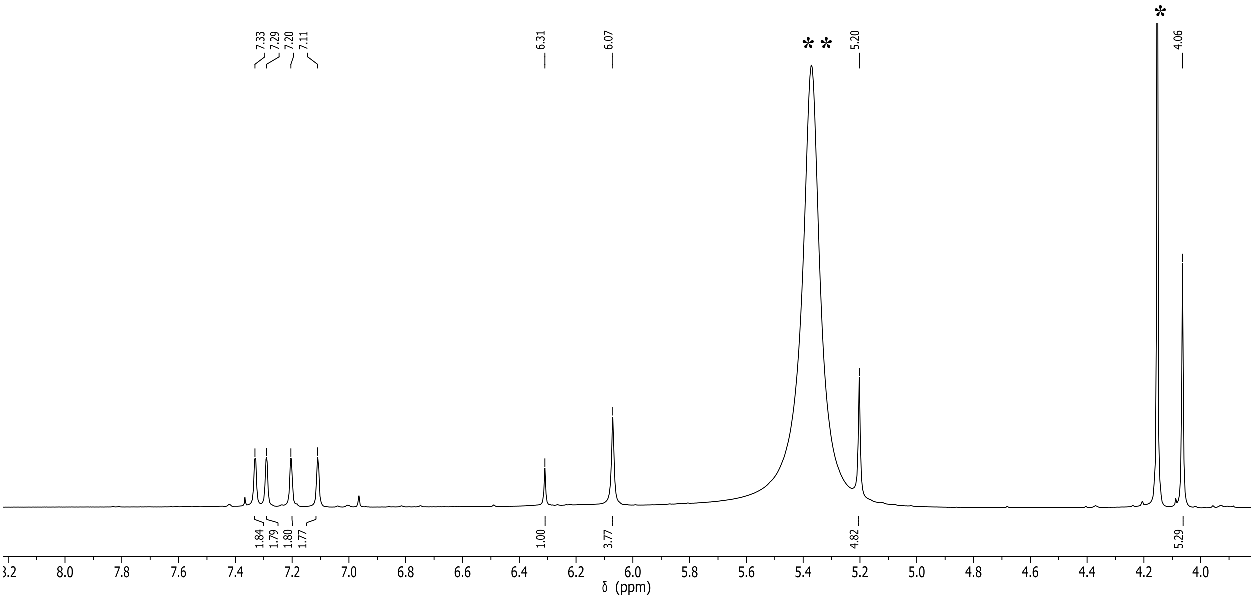

Figure A.7.11: ^{1}H NMR spectrum of the interconversion of **[L^{6}Ni$_2$S]$^+$** to **[L^{6}Ni$_2$(SH)]$^{2+}$** under presence of 100 equiv. TEMPO–H and [FeCp$_2$]PF$_6$ in MeCN-d_3 at 400 MHz and 298 K. (*) corresponds to CH$_3$ proton resonances of TEMPO· and (**) to the O–H proton resonance of TEMPO–H.

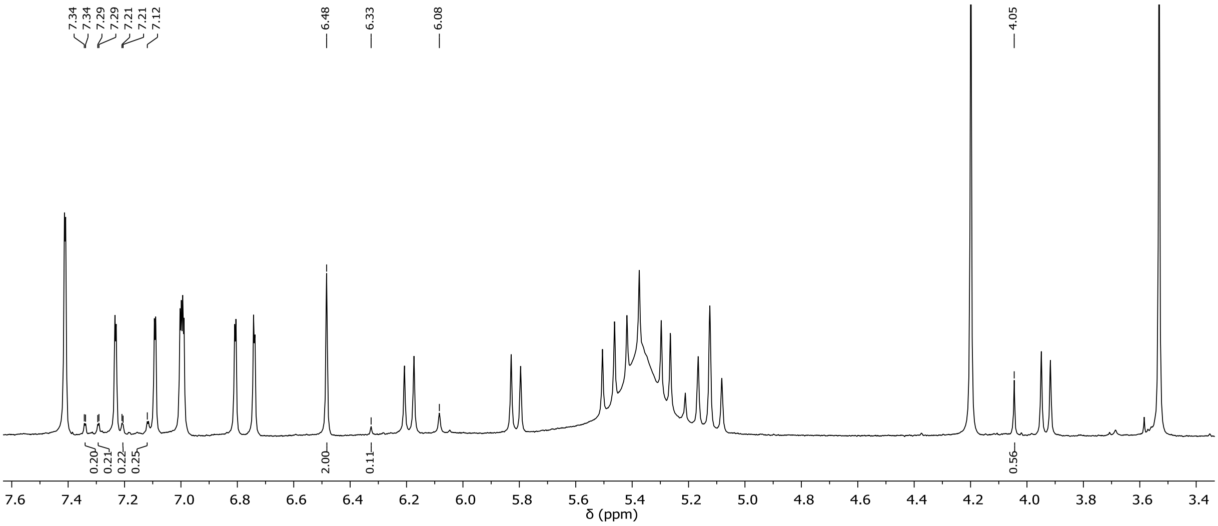

Figure A.7.12: ^{1}H NMR spectrum of the conversion of **$[L^6Ni_2S]^+$** to **$[(L^6)_2Ni_2(S_2)]^{2+}$** under presence of 10 equiv. TEMPO–H and $[Fe(Cp^*)_2]PF_6$ in MeCN-d_3 at 400 MHz and 298 K. (*) corresponds to CH_3 proton resonances of TEMPO·. 11% interconversion to **$[L^6Ni_2(SH)]^{2+}$**.

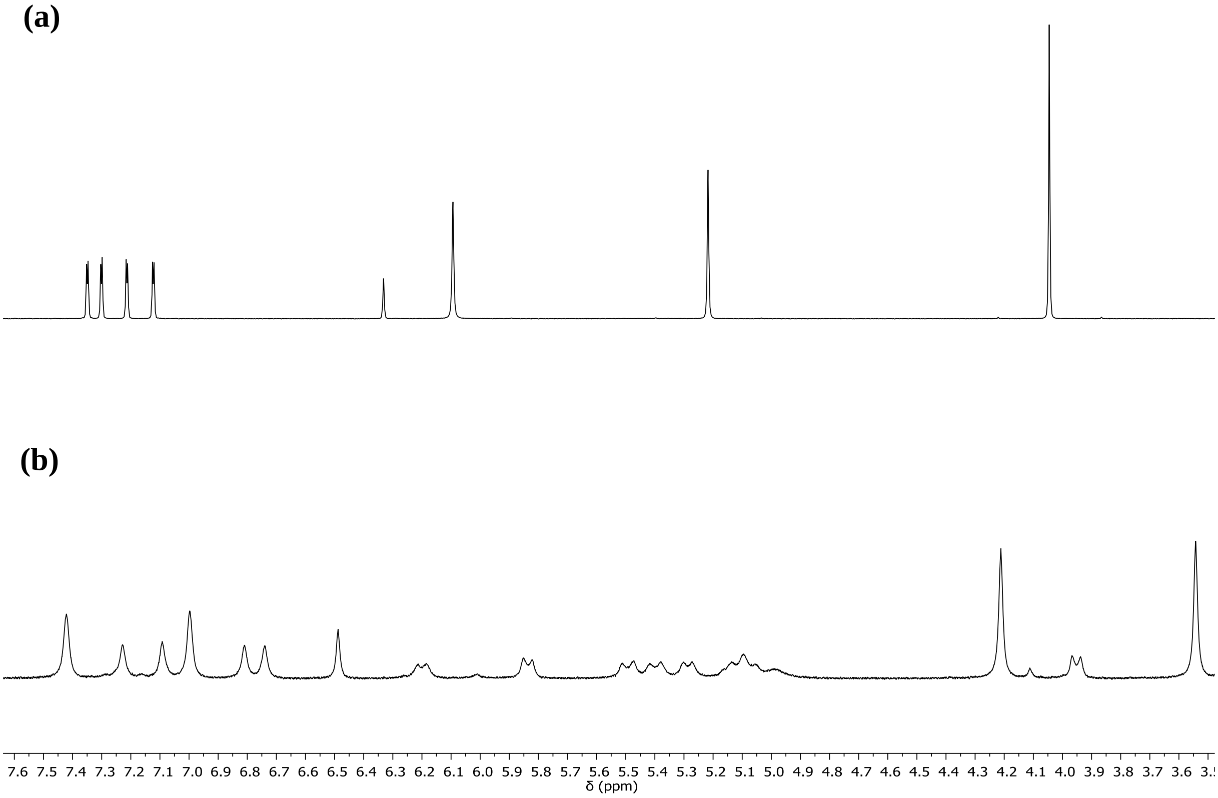

Figure A.7.13: ^{1}H NMR experiment. (**a**) **$[L^6Ni_2(SH)]^{2+}$** in MeCN-d_3 at 400 MHz and 298 K. (**b**) Addition of 10 equiv. of TEMPO· to **$[L^6Ni_2(SH)]^{2+}$**.

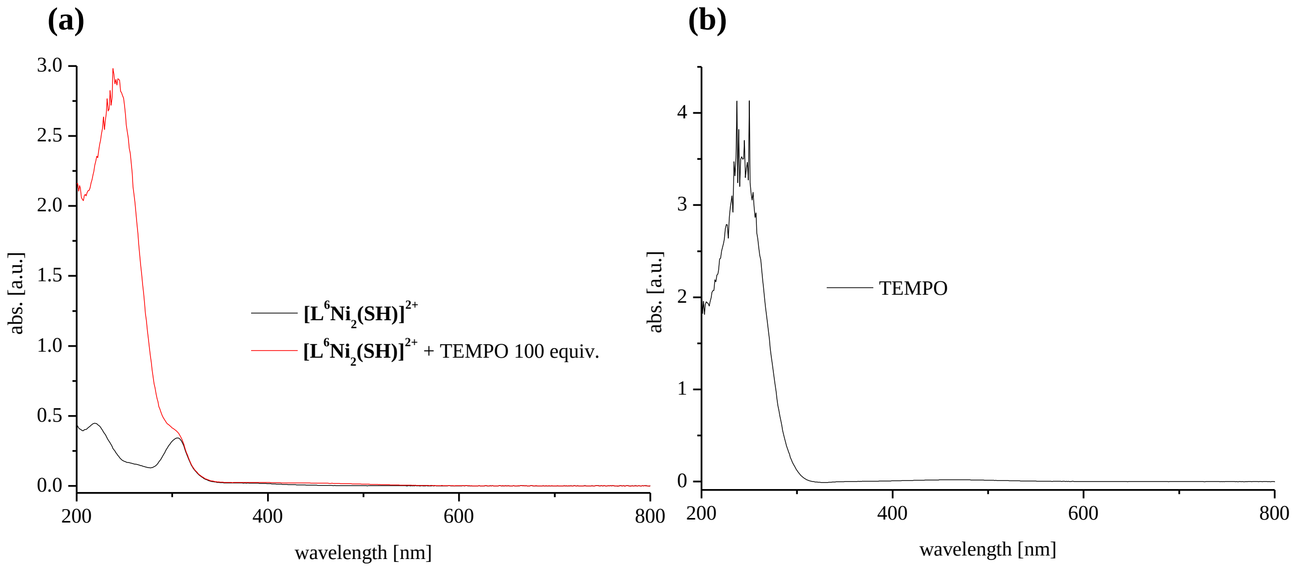

Figure A.7.14: UV-vis titration experiment. (**a**) **$[L^6Ni_2(SH)]^{2+}$**and 100 equiv. of TEMPO· (**b**) UV-vis spectrum of TEMPO· in MeCN at 20 °C.

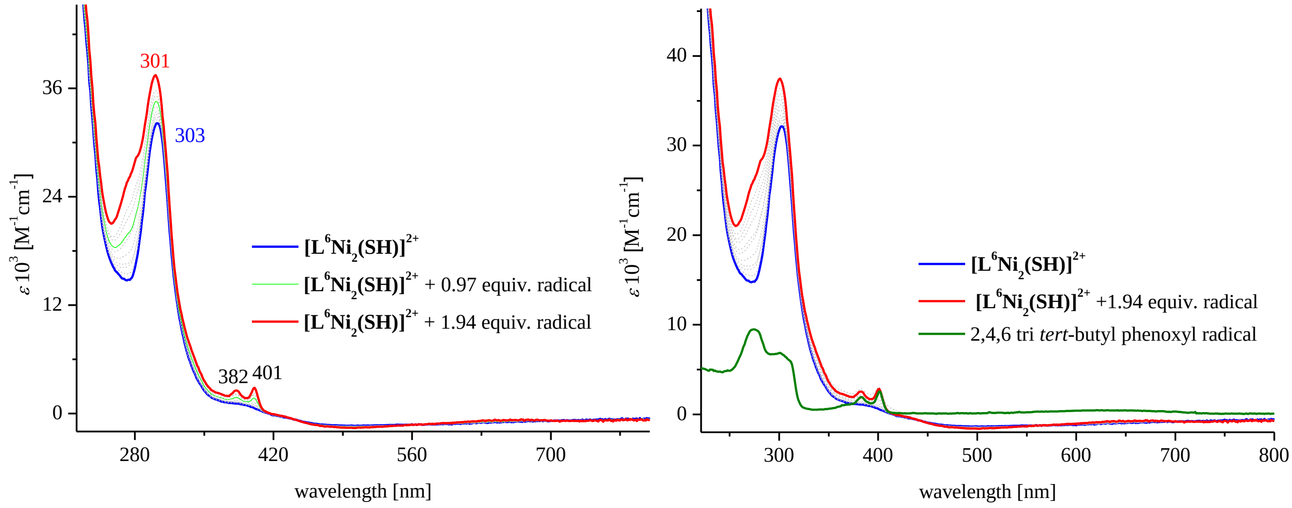

Figure A.7.15: UV-vis titration experiment. (**a**) **$[L^6Ni_2(SH)]^{2+}$** and different equiv. of 2,4,6-tri-*tert*–butylpenoxyl radical (**b**) UV-vis spectrum of (**a**) and in addition UV-vis spectrum of pure 2,4,6 tri-*tert*-butylpenoxyl radical.

Chapter 8

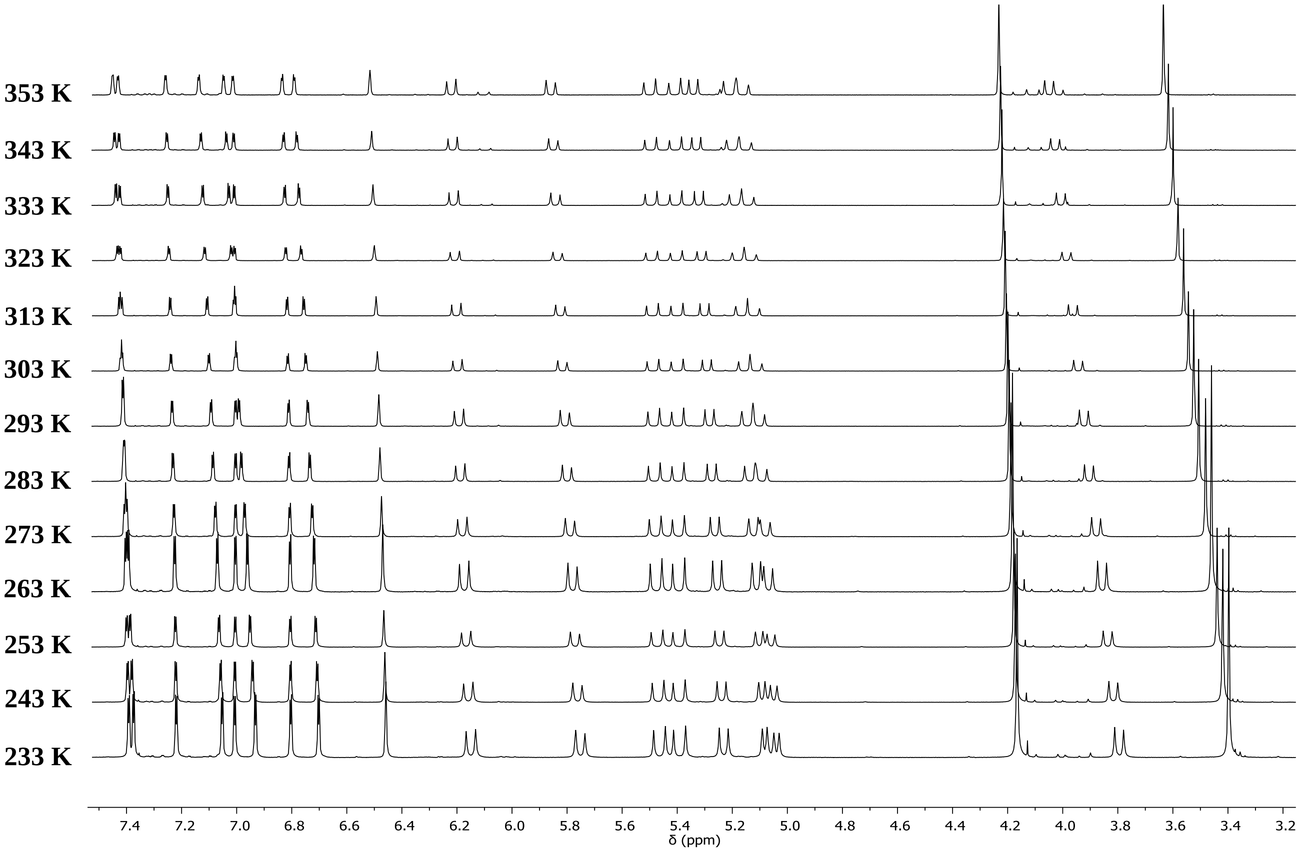

Figure A.8.1: ^{1}H VT NMR spectra of **$[(L^6)_2Ni_4(S_2)](PF_6)_4$** in MeCN-$d_3$ at 400 MHz in the temperature regime between 233 K to 353 K indicating the retention of the molecule symmetry in solution over the whole temperature regime.

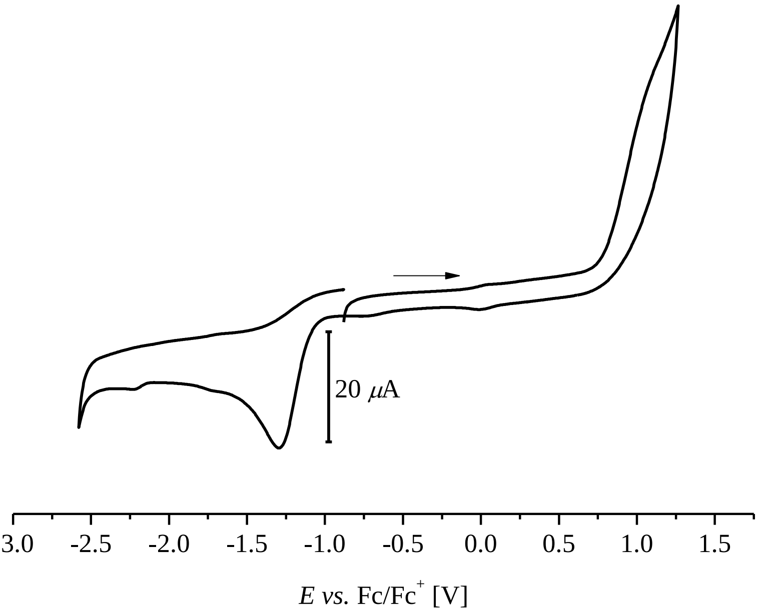

Figure A.8.2: CV of **$[(L^6)_2Ni_4(S_2)](PF_6)_4$** (1.0 mM) in 0.1 M NBu_4PF_6/MeCN solution at r.t. (range: –2.5 V to 1.5 V vs. Fc/Fc$^+$, 100 mV·s^{-1}).

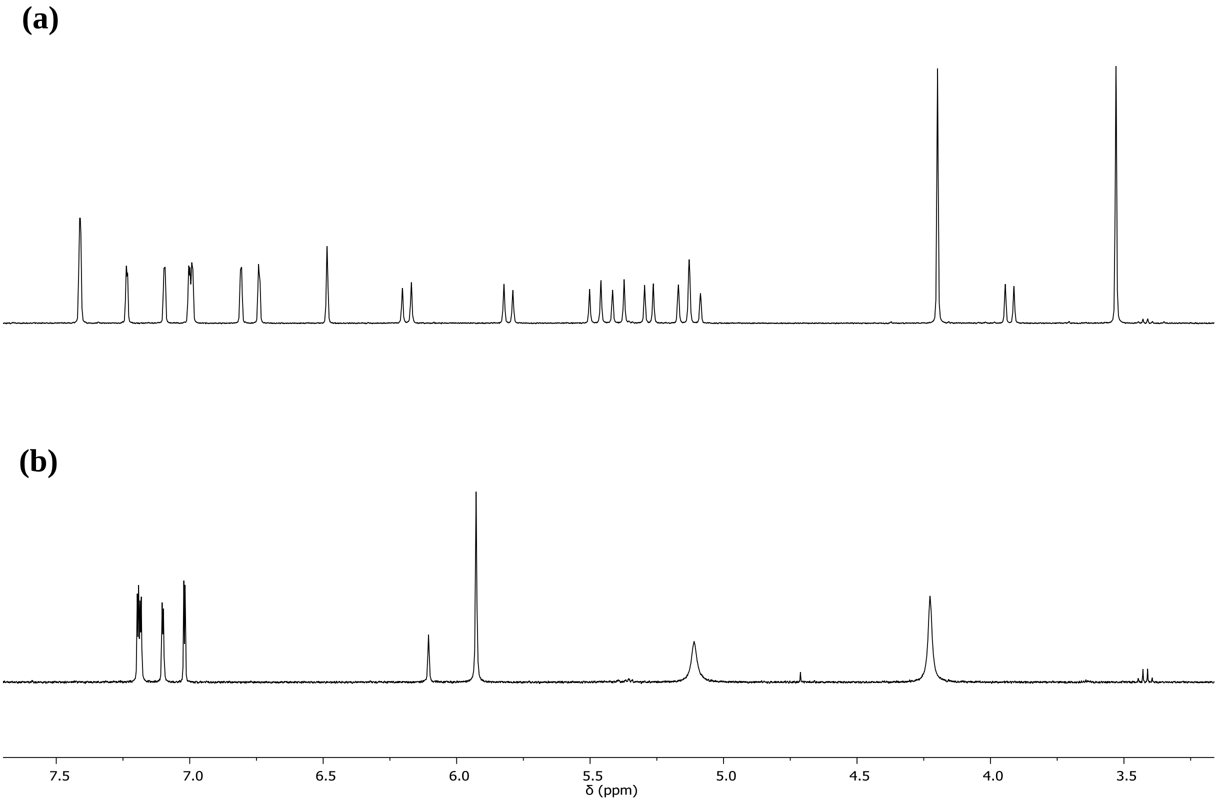

Figure A.8.3: ^{1}H NMR spectrum of the chemical reduction of **[(L^6)$_2$Ni$_4$(S$_2$)](PF$_6$)$_4$** by CoCp$_2$ (1.0 equiv.). (**a**) **[(L^6)$_2$Ni$_4$(S$_2$)](PF$_6$)$_4$**. (**b**) **[(L^6)$_2$Ni$_4$(S$_2$)](PF$_6$)$_4$** plus CoCp$_2$ in MeCN-*d*$_3$ at 298 K (400 MHz).

Chapter 9

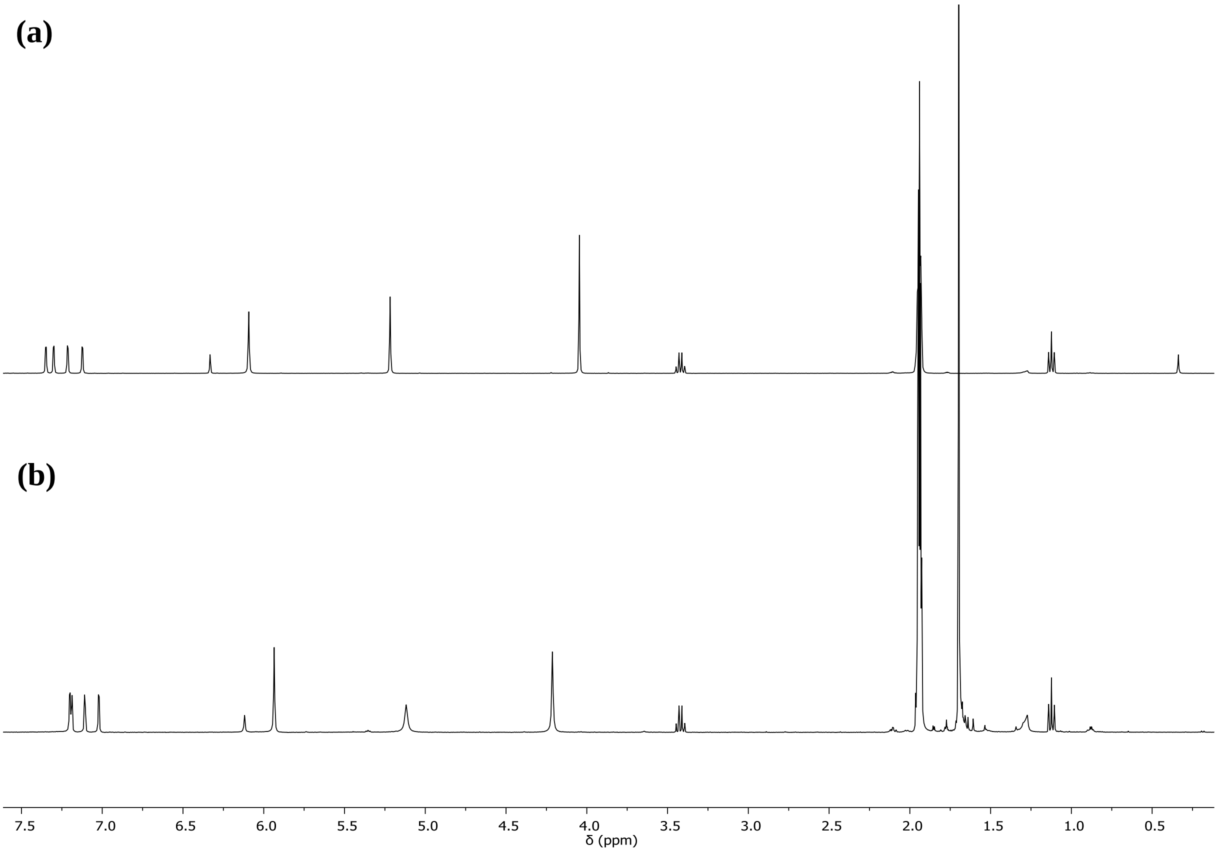

Figure A.9.1: ^{1}H NMR spectrum of the chemical reduction of **[(L^6)Ni$_2$(SH)](PF$_6$)(OTf)** by Co(Cp*)$_2$ (1.0 equiv.). (**a**) **[(L^6)Ni$_2$(SH)](PF$_6$)(OTf)** (**b**) **[(L^6)Ni$_2$(SH)](PF$_6$)(OTf)** plus Co(Cp*)$_2$ in MeCN-d_3 at 298 K (400 MHz).

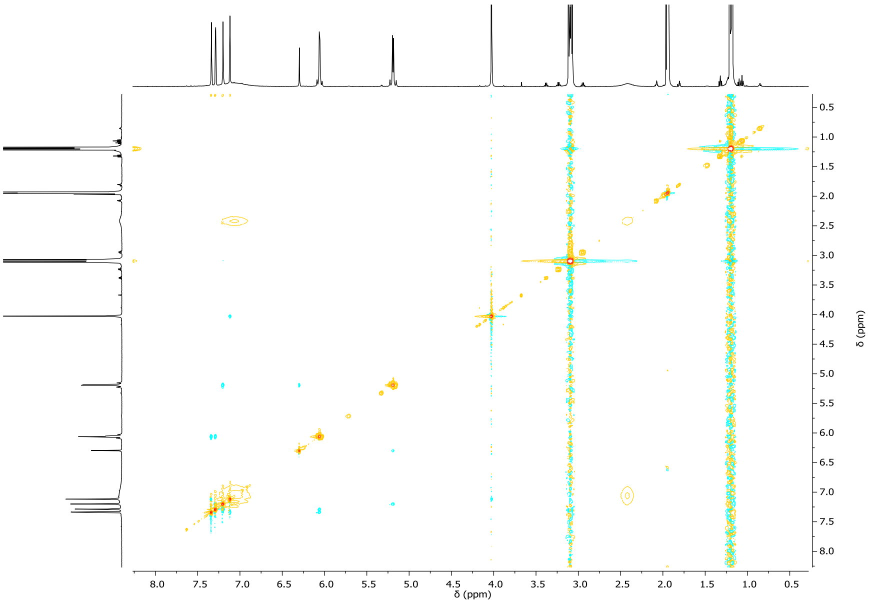

Figure A.9.2: ^{1}H^{1}H NOESY NMR spectrum of **[L^{6}Ni$_2$S]$^+$** and [HNEt$_3$]$^+$ (6.0 equiv.) in MeCN-d_3 at 243 K (400 MHz). An exchange was assigned between the signal at 7.00 ppm and 2.54 ppm.

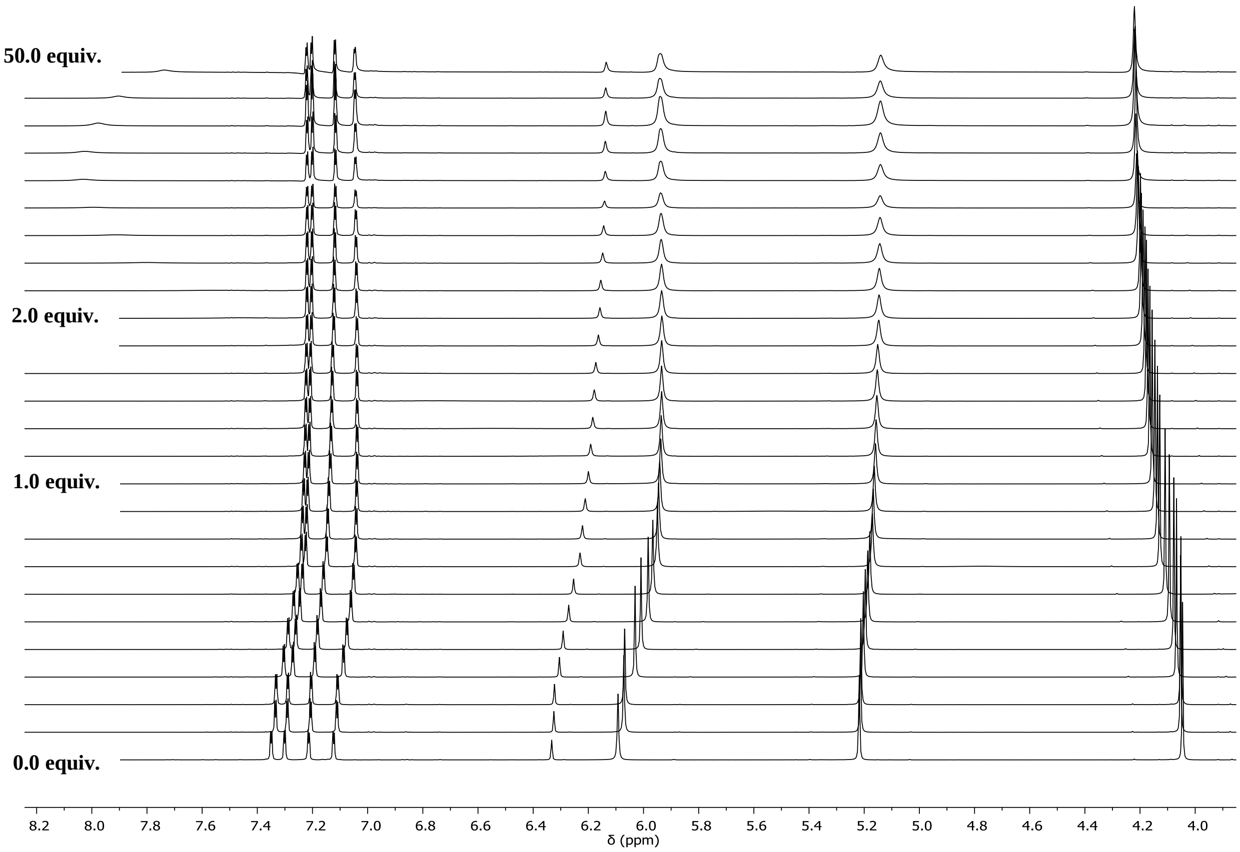

Figure A.9.3: ^{1}H NMR titration experiment: Addition of NEt$_3$ (0 equiv. to 50 equiv.) to **[L^{6}Ni$_2$(SH)]$^{2+}$** in MeCN-*d*$_3$ at 298 K (400 MHz).

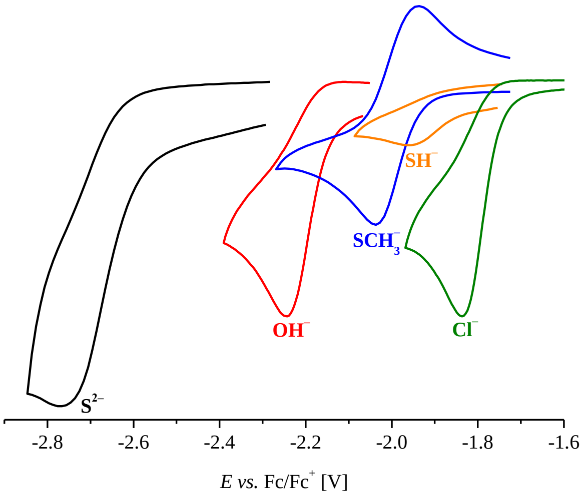

Figure A.9.4: Comparison of reduction events of **[L^{6}Ni$_2$S]PF$_6$** (S^{2-}), **[L^{6}Ni$_2$(OH)](PF$_6$)$_2$** (**OH⁻**), **[L^{6}Ni$_2$(SCH$_3$)](PF$_6$)$_2$** (**SCH$_3^-$**), **[L^{6}Ni$_2$(SH)](PF$_6$)(OTf)** (**SH⁻**) and **[L^{6}Ni$_2$(Cl)](PF$_6$)$_2$** (**Cl⁻**).

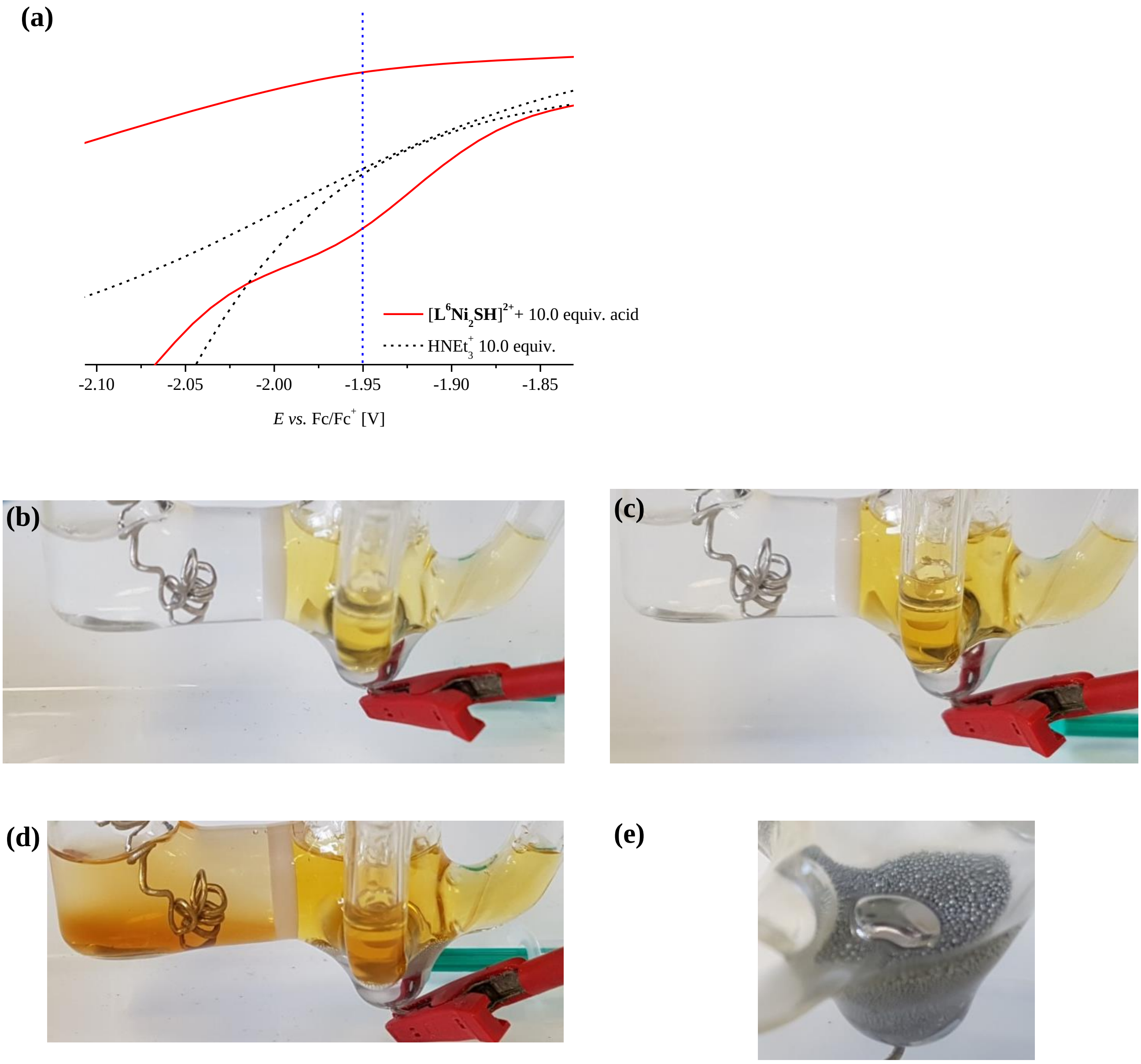

Figure A.9.5: (**a**) Excerpt of CVof **[L^{6}Ni$_2$(SH)]$^{2+}$**and 10 equiv. of [HNEt$_3$]$^+$. (– – –) shows the applied potential of the bulk electrolysis by a mercury working electrode in 0.1 M NBu$_4$PF$_6$/MeCN at r.t. Electrolysis set-up after (b) 0 minutes (c) 15 minutes and (d) 135 minutes of bulk electrolysis. (d) shows mercury balls, which are formed after reaction with the complex.

Structures of Ligands

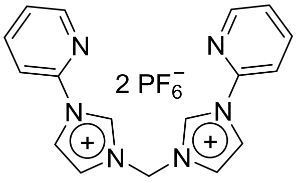

[H$_2$L^1](PF$_6$)$_2$

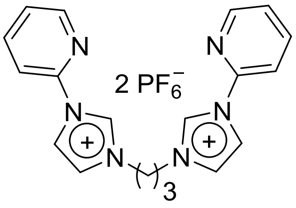

[H$_2$L^2](PF$_6$)$_2$

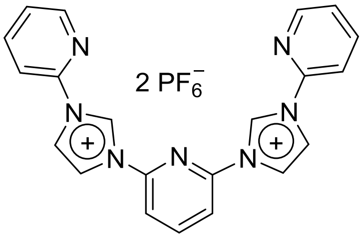

[H$_2$L^3](PF$_6$)$_2$

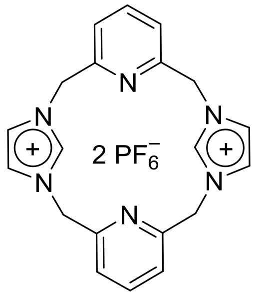

[H$_2$L^4](PF$_6$)$_2$

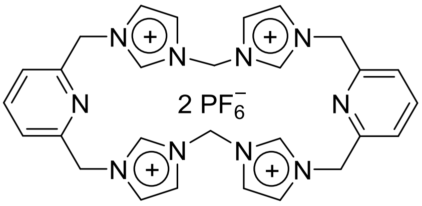

[H$_4$L^5](PF$_6$)$_4$

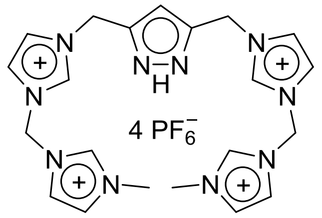

[H$_5$L^6](PF$_6$)$_4$

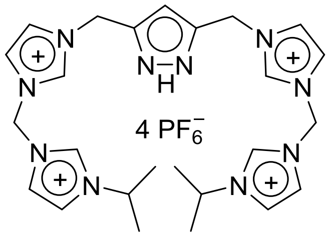

[H$_5$L^7](PF$_6$)$_4$

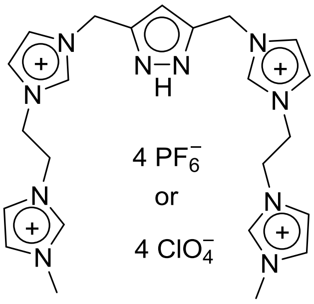

[H$_5$L^8](PF$_6$)$_4$

or

[H$_5$L^8](ClO$_4$)$_4$

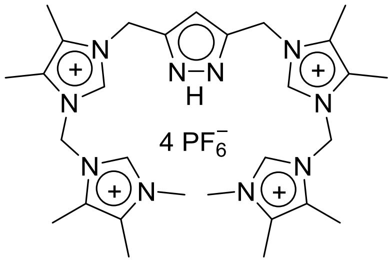

[H$_5$L^9](PF$_6$)$_4$

Structures of copper(I) complexes

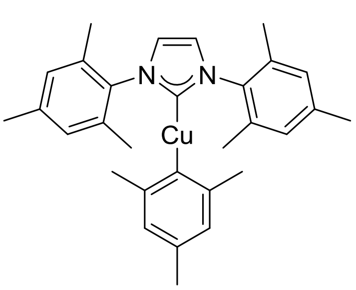

1

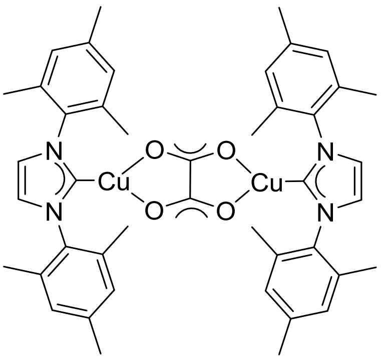

2

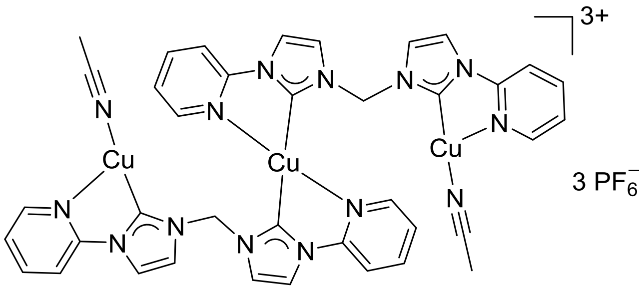

$[(L^1)_2Cu_3](PF_6)_3$

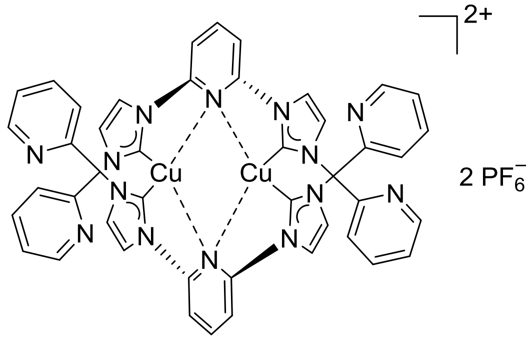

$[(L^3)_2Cu_2](PF_6)_2$

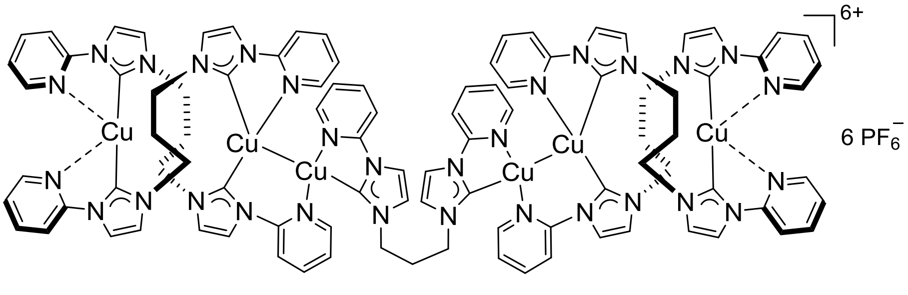

$[(L^2)_5Cu_6](PF_6)_6$

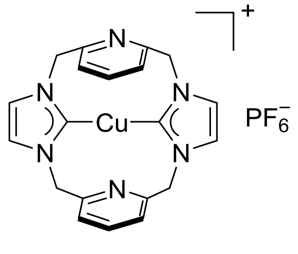

$[L^4Cu]PF_6$

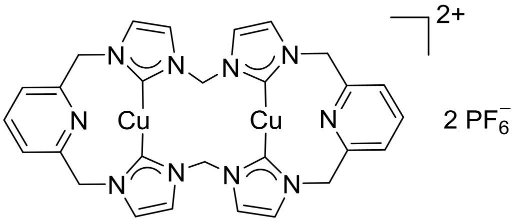

$[L^5Cu_2](PF_6)_2$

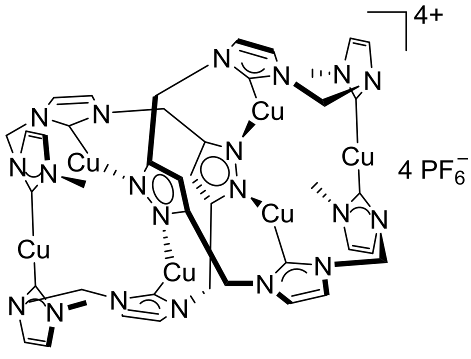

[(L^6)$_2$Cu$_6$](PF$_6$)$_4$

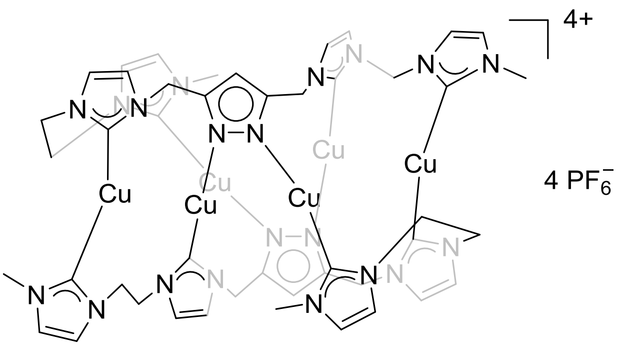

[(L^8)$_2$Cu$_6$](PF$_6$)$_4$

Structures of silver(I) complexes

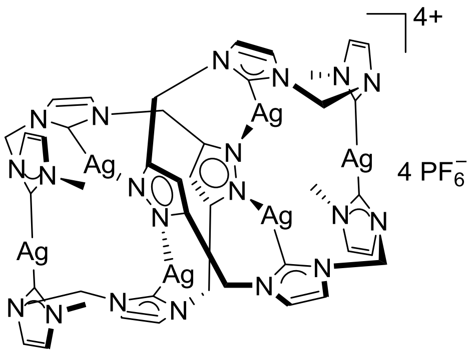

[(L^6)$_2$Ag$_6$](PF$_6$)$_4$

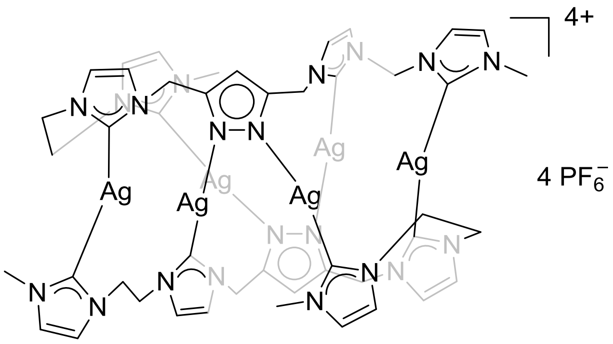

[(L^8)$_2$Ag$_6$](PF$_6$)$_4$

Structures of nickel complexes

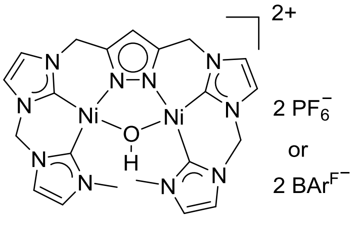

[$L^6Ni_2(OH)](PF_6)_2$

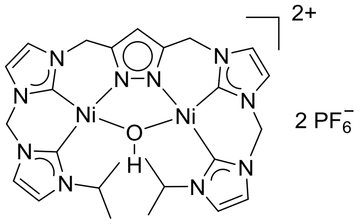

[$L^7Ni_2(OH)](PF_6)_2$

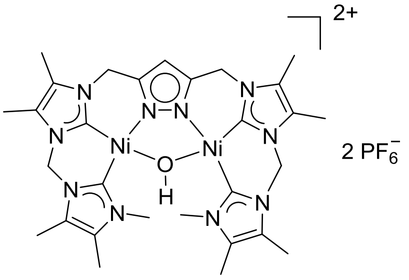

[$L^9Ni_2(OH)](PF_6)_2$

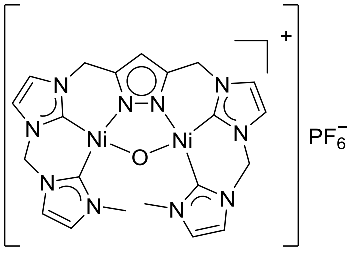

[$L^6Ni_2O]PF_6$

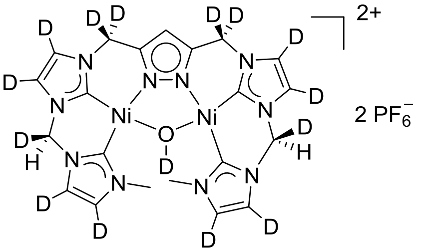

[$^DL^6Ni_2(OD)](PF_6)_2$

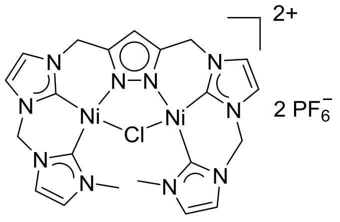

[$L^6Ni_2Cl](PF_6)_2$

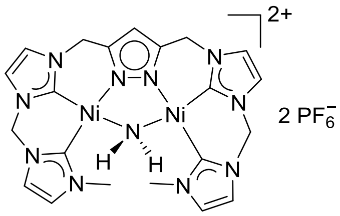

[$L^6Ni_2(NH_2)](PF_6)_2$

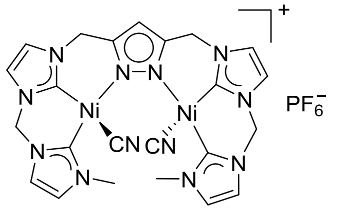

[$L^6Ni_2(CN)_2]PF_6$

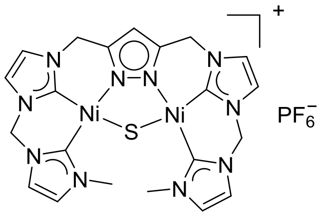

[$L^6Ni_2S]PF_6$

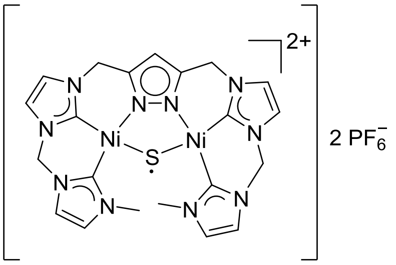

[$L^6Ni_2(S\cdot)](PF_6)_2$

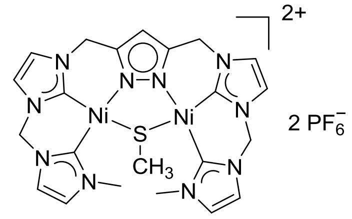

[$L^6Ni_2(SCH_3)](PF_6)_2$

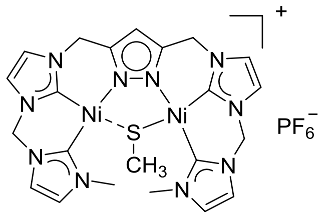

[$L^6Ni_2(SCH_3)]PF_6$

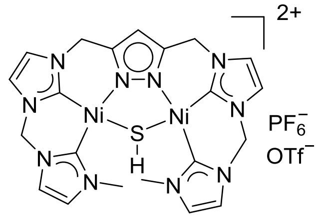

[$L^6Ni_2(SH)](PF_6)(OTf)$

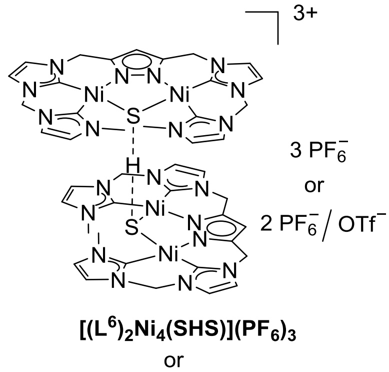

[$(L^6)_2Ni_4(SHS)](PF_6)_3$
or
[$(L^6)_2Ni_4(SHS)](PF_6)_2(OTf)$

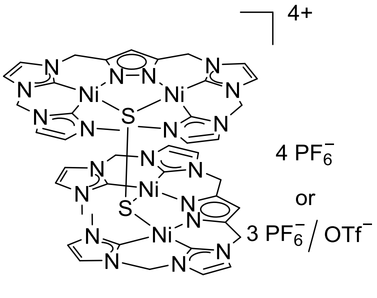

[$(L^6)_2Ni_4(S_2)](PF_6)_4$
or
[$(L^6)_2Ni_4(S_2)](PF_6)_3(OTf)$

List of scientific contributions

Publications

M. Stollenz, S. Fischer, H. Gehring, S. G. Resch, S. Dechert, C. Große, F. Meyer, *J. Organomet. Chem.* **2016**, *821*, 106–111.

S. G. Resch, S. Dechert, F. Meyer, *Z. Anorg. Allg. Chem.* **2019**, *645*, 605–612.

Y. Liu, S. G. Resch, I. Klawitter, G. E. Cutsail III, S. Demeshko, S. Dechert, F. E. Kühn, S. DeBeer, F. Meyer, *Angew. Chem. Int. Ed.* **2019**, *58*, 2.

Oral presentation at workshop

Metal N-heterocyclic Carbene Complexes for the Activation of Small Molecules. CaSuS workshop **2016**, Hanau bei Frankfurt am Main, Germany.

Poster presentations at (inter)national conferences and workshops

Synthesis, characterization and reactivity studies of new copper(I) NHC complexes for bio-inspired, oxidative C–H bond activation. CaSuS Kick-off workshop **2014**, Hildesheim, Germany.

Copper(I) Complexes with Multidentate N-heterocyclic Carbene Ligands and their Dynamics in Solution. Lower Saxony catalysis symposium (NiKaS) **2014**, Göttingen, Germany.

Copper Complexes with Multidentate N-heterocyclic Carbene Ligands and their Dynamics in Solution. Koordinationschemikertagung **2015**, Paderborn, Germany.

Copper Complexes with Multidentate N-heterocyclic Carbene Ligands and their Dynamics in Solution. 7. Göttinger Chemie-Forum **2015**, Göttingen, Germany.

Novel Dinuclear Nickel N-heterocyclic Carbene Complexes for the Activation of Small Molecules. 42nd International Conference on Coordination Chemistry **2016**, Brest, France.

Novel Dinuclear Nickel N-heterocyclic Carbene Complexes for the Activation of Small Molecules. Lower Saxony catalysis symposium (NiKaS) **2016**, Braunschweig, Germany.

Hydrosulfido, Sulfido and Persulfido Interconversions at a Preorganized Dinickel Site. CaSuS/SeleCat joint venture workshop, Bielefeld **2017**, Germany.

Hydrosulfido, Sulfido and Persulfido Interconversions at a Preorganized Dinickel Site. Anglo-German Inorganic Chemistry Meeting (AGICHEM), Göttingen **2017**, Germany.

Hydrosulfido, Sulfido and Persulfido Interconversions at a Preorganized Dinickel Site. Wissenschaftsforum Chemie, Berlin **2017**, Germany.

Sulfide Redox and Protonation Interconversions at a Preorganized Dinickel Site and HAT Reactions of a Nickel-Bounded Thiyl radical with Organic Substrates. Lower Saxony catalysis symposium (NiKaS) **2018**, Göttingen, Germany.

Copyright

All Figures, which have been adapted or reproduced from published works, the permission for adaption or reproduction has been granted by the respective publisher: ELSEVIER, JOHN WILEY AND SONS, AMERICAN CHEMICAL SOCIETY and ROYAL SOCIETY OF CHEMISTRY. Appropiate credit for the requested and used materials has been given as follows: “Adapted with permission from [Ref.]. © (YEAR) Publisher.”

Statement

The Ph.D. Thesis at hand has been drawn up by myself by exclusively using the sources and facilities indicated in the thesis.

Erklärung

Hiermit erkläre ich, dass ich die vorliegende Arbeit selbstständig verfasst und alle verwendeten Quellen und Hilfsmittel als solche gekennzeichnet habe.

Göttingen, 19.11.2018

(Stefan G. Resch)

Lebenslauf

Persönliche Daten

Stefan Günter Resch

*28.01.1988

Lebach

Berufserfahrung und akademische Ausbildung

01/2014 – 12/2018	**Promotion** (wissenschaftlicher Mitarbeiter) Georg-August-Universität Göttingen Betreuer: Prof. Dr. F. Meyer
	stellv. Doktorandenvertreter im internationalen Graduiertenkolleg Catalysis for Sustainable Synthesis (CaSuS) 11/2014 – 12/2018
	Auslandsaufenthalt Frankreich - CEA Grenoble & Université Grenoble Alpes 02/2018 - 03/2018 Betreuer: Prof. Dr. V. Artero & Dr. C. Duboc
10/2011 - 09/2013	**Master of Science Chemie** (Gesamtnote: 1,2 mit Auszeichnung) Technische Universität München
	Auslandsaufenthalt Schweiz - Eidgenössische Technische Hochschule Zürich 08/2012 - 11/2012 Betreuer: Prof. Dr. C. Copéret (Note: 1,0 (D), 6/6 Punkte (CH))
	Industrieaufenthalt Clariant SE Bruckmühl - Geschäftseinheit Catalysts 03/2012 - 04/2012 Betreuer: Dr. K. Wanninger (Note: 1,0)
10/2008 - 09/2011	**Bachelor of Science Chemie** (Gesamtnote: 2,1) Technische Universität München

Stipendien, Auszeichnungen

09/2018	Preis für das beste Poster auf dem 5. niedersächsischen Katalyse Symposium
02/2018 - 03/2018	International Research Visit Fellowship International Center for Advanced Studies of Energy Conversion
02/2018 - 03/2018	Short-Term Scientific Mission Grant European Cooperation in Science & Technology (ECOSTBio)

07/2016 - 07/2016	Reisestipendium Universitätsbund Göttingen e.V.
07/2012 - 11/2012	ERASMUS SMP Stipendium

Schlüsselkompetenzen

10/2017	Effective presentation (Schiller & Mertens)
07/2017	Communication (Schiller & Mertens)
05/2017	Teams and Leadership (Schiller & Mertens)
04/2016	Projektmanagement (Georg-August-Universität Göttingen)
10/2015	Interkulturelle Zusammenarbeit (Ideas x Skills)
03/2015	BASF Patentkurs (BASF SE)
02/2014	Führungsexzellenz in der globalen Wissenschaft (Ideas x Skills)
10/2014	Project management for young scientists (Golin Wissenschaftsmanagement)

Praktika

08/2010 - 09/2010	INM-Leibniz-Institut für Neue Materialien gGmbH (Saarbrücken)
08/2008 - 09/2008	Max-Planck-Institut für Polymerforschung (Mainz)
08/2008	Max-Planck-Institut für Kolloid- und Grenzflächenforschung (Potsdam)
07/2008	Max-Planck-Institut für biophysikalische Chemie (Göttingen)
08/2006	Laborbereich Fresenius Medical Care (St. Wendel)

Schulbildung

06/2007	Allgemeine Hochschulreife (Gesamtnote: 1,4 mit Auszeichnung)
1998 - 2007	Johannes-Kepler-Gymnasium Lebach